Doctorate Thesis
博士論文

Theoretical Studies on Halogen Centered NonCovalent Interactions in Materials Design: *From Molecular Clusters to Photovoltaic Perovskite Solar Cell Semiconductors*

(材料設計におけるハロゲンによる非共有結合相互作用に関する理論的研究：
分子クラ スターから太陽光発電用ペロブスカイト半導体に向けて)

アルピタ　バラドワージ

Arpita Varadwaj

DOCTOR OF ENGINEERING

A Dissertation submitted to the Graduate School of Engineering of the University of Tokyo, Tokyo, JAPAN

東京大学
THE UNIVERSITY OF TOKYO

Department of Chemical System Engineering
School of Engineering
The University of Tokyo
7 Chome-3-1 Hongo, Bunkyo-ku,
Tokyo 113-8654, Japan

The undersigned certify that they have read, and recommend to the Graduate School of Engineering for acceptance, a thesis entitled "**Theoretical Studies on Halogen Centered NonCovalent Interactions in Materials Design: From Molecular Clusters to Photovoltaic Perovskite Solar Cell Semiconductors**" submitted by ARPITA VARADWAJ in partial fulfilment of the requirements of the degree of DOCTOR OF ENGINEERING.

PROFESSOR DR. KOICHI YAMASHITA, DEPARTMENT OF CHEMICAL SYSTEM ENGINEERING, SCHOOL OF ENGINEERING, HONGO CAMPUS

D.Er. THESIS DIRECTOR, [FULL NAME AND DEPARTMENT]

Professor Dr. Atsuo Yamada, DEPARTMENT OF CHEMICAL SYSTEM ENGINEERING, SCHOOL OF ENGINEERING, HONGO CAMPUS

Examiner [FULL NAME AND DEPARTMENT]

Professor Dr. Takaya Kubo, RESEARCH CENTER FOR ADVANCED SCIENCE AND TECHNOLOGY, THE UNIVERSITY OF TOKYO, 4-6-1, KOMABA CAMPUS

Examiner [FULL NAME AND INSTITUTION]

Associate Prof. Dr. Ryuji Kikuchi, DEPARTMENT OF CHEMICAL SYSTEM ENGINEERING, SCHOOL OF ENGINEERING

Examiner [FULL NAME AND INSTITUTION]

Associate Prof. Dr. Hiroshi Ushiyama, DEPARTMENT OF CHEMICAL SYSTEM ENGINEERING, SCHOOL OF ENGINEERING

Examiner [FULL NAME AND INSTITUTION]

Associate Prof. Dr. Tsutomu Minegishi, DEPARTMENT OF CHEMICAL SYSTEM ENGINEERING, SCHOOL OF ENGINEERING

Examiner [FULL NAME AND INSTITUTION]

Date

A Few Related Quotations

¨With courageous simplification, one might assert that the chemistry of the last century was largely the chemistry of covalent bonding, whereas that of the present century is more likely to be the chemistry of noncovalent binding.¨

Hans-Jörg Schneider Prof. Dr.
Angew.Chem. Int. Ed. 2009, 48, 3924-3977.

¨Thus the notion of a chemical bond is too restrictive and is ill-suited to account for the physics underlying the spectrum of interactions between atoms and molecules that determine the properties of matter. What is needed is a definition of bonding rather than of a bond, one that can describe the complete range of bonded interactions that account for the properties of all matter. Such is the role fulfilled by a bond path.¨

Richard F.W. Bader Prof. Dr. (October 15, 1931 – January 15, 2012)
J. Phys. Chem. A 2009, 113, 10391-10396.

List of Publications

Referred Papers

1. Varadwaj PR, **Varadwaj A**, Jin BY (2015). Unusual bonding modes of perfluorobenzene in its polymeric (dimeric, trimeric and tetrameric) forms: Entirely negative fluorines interacting cooperatively with entirely negative fluorines. (*Physical Chemistry Chemical Physics*, 17, 31624-31645, *Cover article*).

2. **Varadwaj A**, Varadwaj PR, Jin BY (2016). Can an entirely negative fluorine in a molecule, viz. perflourobenzene, interact attractively with the entirely negative site(s) on another molecule(s)? Like liking like! (*RSC Advances,* 2016, 6, 19098-19110).

3. **Varadwaj A**, Varadwaj PR, Yamashita K (2018). Do surfaces of positive electrostatic potential on different halogen derivatives in molecules attract? Like attracting like! (*Journal of Computational Chemistry*, 39, 343-350, *Cover article*).

4. **Varadwaj A**, Varadwaj PR, Yamashita K (2017). Hybrid organic-inorganic $CH_3NH_3PbI_3$ perovskite building blocks: Revealing ultra-strong hydrogen bonding and Mulliken inner complexes and their implications in materials design (*Journal of Computational Chemistry*, 38, 2802-2818).

5. **Varadwaj A**, Varadwaj PR, Yamashita K (2018). Revealing the chemistry between bandgap and binding energy for Pb/Sn-based trihalide provskite solar cell semiconductors, *(ChemSusChem,* 11, 449-463).

Other Publications

1. Varadwaj PR, **Varadwaj A**, Jin BY (2015). Hexahalogenated and their mixed benzene derivatives as prototypes for the understanding of halogen···halogen intramolecular interactions: New insights from combined DFT, QTAIM- and RDG-based NCI analyses. (*Journal of Computational Chemistry*, 36, 2328, Cover *article*).

2. **Varadwaj A**, Varadwaj PR, Jin BY (2015). Fluorines in tetrafluoromethane as halogen bond donors: revisiting address the nature of fluorine's σ-hole (*International Journal of Quantum Chemistry*, 115, 453- 470, Cover *article).*

3. Varadwaj PR, **Varadwaj A**, Jin, BY (2015). Ligand(s)-to-metal charge transfer as a factor controlling the equilibrium constants of late first-row transition metal complexes: revealing the Irving-Williams thermodynamical series (*Physical Chemistry Chemical Physics (Communication)* 17, 805–811).

4. Varadwaj PR, **Varadwaj A**, Jin BY (2014). Halogen bonding interaction of chloromethane with several nitrogen donating molecules: addressing the nature of the chlorine surface σ-hole (*Physical Chemistry Chemical Physics 16*, 19573–19589).

5. Varadwaj PR, **Varadwaj A**, Jin BY (2014). Significant evidence of C···O andC···C long-range contacts in several heterodimeric complexes of CO with CH_3–X, should one refer to them as carbon- and dicarbon-bonds! (*Physical Chemistry Chemical Physics* 16, 17238–17252).

6. **Varadwaj A**, Varadwaj PR (2012). Can a single H_2O molecule be completely isolated within the sub-nano space inside the fullerene C_{60} cage? A Quantum chemical prospective (*Chemistry - A European Journal* 18, 15345–15360).

7. Varadwaj PR, **Varadwaj A**, Peslherbe GH (2012). An electronic structure theory investigation of the physical chemistry of the intermolecular complexes of cyclopropenylidene with hydrogen halides (*Journal of Computational Chemistry* 33, 2073–82, ***Cover article***).

8. Varadwaj PR, **Varadwaj A**, Peslherbe GH, Marques HM (2011). A conformational analysis of 18-azacrown-6 and its bonding with late first transition series divalent metals: Insights from DFT-, NPA-, and QTAIM-based studies (*Journal of Physical Chemistry A* 115, 13180–13190. **Invited article**: Richard F. W. Bader Festschrift).

9. Varadwaj PR, **Varadwaj A**, Marques HM (2011). DFT-B3LYP, NPA-, and QTAIM-based study of the physical properties of [M(II)$(H_2O)_2$(15-crown-5)] (M = Mn, Fe, Co, Ni, Cu, Zn) complexes (*Journal of Physical Chemistry A* 115, 5592–5601).

Preface

The main purpose of this dissertation is to introduce and demonstrate the "topological implication" of the halogen derivative using electronic structure calculations, which might be essential for the development of materials for photovoltaics and other optoelectronic applications. Many scientists have already been inspired using this as a tool to develop and design various experimental synthetic technologies, leading to the generation of millions of engineered crystal materials of diverse chemical origin that possess versatile functionalities. In particular, the thesis introduces the way the halogen derivative sees its interacting partners from a close vicinity, thereby forming hydrogen-, halogen-, coordinate- and other intermolecular bonding interactions to design numerous multiskilled compounds. An understanding of the nature and characteristics of these interactions in stabilizing the geometries of these compounds is a major aspect of the thesis.

Hydrogen- and halogen-bonding can be intra-molecular, or intermolecular. They are competitive, and can appear individually, or simultaneously, to stabilize chemical systems in the gas, liquid, and/or solid state. They have been referred as sister interactions, falling into area of noncovalent chemistry. The topic has continuously been cultivated by many scientists over decades. Linus Pauling, a recipient of the Nobel Prize in Chemistry in 1954, is one of the significant contributors to the fundamental understanding of chemical bonding in molecular domains and in materials. His popular book on "The Nature of the Chemical Bond" employs the underlying principles of quantum mechanics to understand and describe chemical bonding, and the way atoms cooperate with each other to design molecules, molecular complexes, and solids.

The current state-of-the-art computational approaches in modelling chemical compounds presented in this dissertation involved the Density Functional and Coupled Cluster Theories. Depending on the interest on some specific systems, electronic structure calculations were performed either non-periodically, or by employing periodic boundary condition, or by combining them together. While most of the electronic structure calculations undertaken were carried out in the gas-phase, the chemical systems investigated were limited to either single molecules, or bimolecular complexes, and/or oligomers containing a maximum of fifteen building blocks. Some of these modeled systems were either known experimentally (but ununderstood), or designed theoretically to using halogen centered topologies of bonding interactions.

For the identification and characterization of noncovalent interactions in the studied compounds three theoretical approaches were continuously invoked throughout the dissertation. The first one involves Quantum Theory of Atoms in Molecules, which is a charge density based approach originally developed by Richard Bader, since it greatly assists in identifying chemical bonding interactions through its bond critical point and bond path topologies, and several of its other bond descriptors. The second one involves the Reduced Density Gradient approach, which is also charge density approach employed for the exploration of noncovalent interactions. The third one involves the Natural Bond

Orbital approach, which is applied to explore charge transfer delocalizations involved between the most important natural electron-donating and -accepting bond orbitals.

Chapter 1 briefly outlines the background story on which this dissertation is based. It involves a brief survey of the resources and developments of materials for energy, the classification and underlying chemistry of noncovalent interactions, and their application diversities to design materials of various kinds, including those responsible for optoelectronics. It also involves a brief discussion on the current status of the trihalide perovskite solar cells, and the way noncovalent interactions assist to design them.

Chapters 2 and 3 discuss the electronic structures, energetics and charge density based studies of chemical bonding interactions of a selected number of complex systems. In particular, it is shown that the entirely negative covalently bound halogen derivative in molecules (e.g., perfluorobenzene) engage noncovalently with the negative sites on the partner molecules, forming bi- and tri-molecular clusters, and so on. While this study introduces the concept of attraction between the negative sites, which is against the Coulomb's law of electrostatics, it is demonstrated that this is not impossible when attractions arising from polarization and dispersion are dominant that have abilities to compete against repulsion (arising from electrostatics and exchange interactions).

Chapters 4–6 account for the results of electronic structures, energy landscapes, electronic properties, and charge-density based studies of the lead triiodide perovskite building blocks and their nanoclusters. These systems in the solid state have been the center of many on-going researches, especially in the area of thin film solar energy semiconductor technology. These are recently discovered as "rising stars" in the area of photovoltaics, giving some hopes to resolve the need for future energy crisis. Nevertheless, the results of various fundamentally important properties, such as the unified topologies of chemical bonding (Chapter 4), the importance of the additive and non-additive cooperative natures of hydrogen bonding interactions (Chapter 5) and the nature of the intermolecular charge transfers (Chapter 6), among several others, are discussed for enhancing our current understanding of these materials, and for assisting in the futuristic design of delicate materials of such kind and beyond. Chapter 7 introduces some new trihalide perovskite materials for photovoltaics, and proves that binding energy should be considered as a designing tool for the development of such materials. Chapter 8 deals with the general conclusion, with a perspective for future directions.

The dissertation should be of interest to a wide range of researchers who are currently focusing their research attentions on broad areas of materials science, crystal engineering, molecular and biomolecular drug designs, especially in the development of functional materials. Because this research is of fundamental origin, it should be interesting to diverse range of other scientists working in, among others, crystallography, nanotechnology, environmental and energy materials, synthetic, theoretical, computational, and supramolecular chemistry. Not only these, but it would also be useful for undergraduate and graduate students who wish to start their study research careers in halogen- and hydrogen-bonding interactions in solar cells, and who wish to use computational techniques to design halogen assisted materials for multifaceted purposes.

Acknowledgements

This thesis is made to partially fulfill the requirement of the Doctor level graduate education in Chemical System Engineering at the Department of Chemical System Engineering of the University of Tokyo, Hongo Campus, Tokyo, Japan.

Several scientific and nonscientific individuals have contributed both academically and non-academically practically to support and assist the preparation of this graduate thesis. Although it is not possible to acknowledge everyone, I am indebted to all of them for all kinds of help and assistance that I have received during the course of the preparation of this thesis.

Firstly, I am grateful, and would like to thank my current supervisor Professor Dr. Koichi Yamashita for his great time, valuable scientific and nonscientific inputs, and incredible supports that he has provided throughout my entire academic period I spent in the Yamashita-Ushiyama Laboratory.

Secondly, I am thankful to the other academic staffs of the Yamashita-Ushiyama Laboratory. Some of them include Drs. Fuji and Ushiyama for their continuous academic, technical and nontechnical supports to carry out daily computational research in the laboratory and beyond.

Thirdly, I wish to thank to the two secretaries of the Yamashita-Ushiyama Laboratory, Ms. Iyama and Ms. Sanpei, for their non-technical and academy-based supports that have made my daily life smoother in the University campus.

Fourthly, I am grateful to the staffs of one the largest supercomputing centers of Japan, Institute of Molecular Sciences (IMS), Okazaki, for their time-to-time software updates and technical supports received. Most of the results presented in this thesis were obtained using the supercomputing facilities provided by IMS.

Fifthly, I am thankful to my previous advisor Professor B.-Y. Jin of National Taiwan University (Taipei, Taiwan) for his continuous support and encouragement to conduct computational research studies on various aspects of halogen bonding at the Department of Chemistry, wherein I worked as a Research Assistant.

Not the least, I am also grateful to another senior research member of the Yamashita-Ushiyama team, Dr. Pradeep R. Varadwaj, with whom I have conducted most of my research studies on halogen and hydrogen bonding interactions in molecular and supramolecular systems, as well on perovskite solar cell semiconductors. I am greatful to his direct/indirect supervision in all aspects of this thesis work. His contributions and moral supports were very much vital for the development of my academic growth in many aspects of chemical system engineering.

Finally, I would like to thank my family, my two sons Prem and Suva, my mom and dad, and my friends for being helpful, adaptive and supportive during my time studying Chemical System Engineering at the University of Tokyo, Japan.

(Arpita Varadwaj)
Yamashita-Ushiyama Laboratory
Department of Chemical System Engineering
School and Faculty of Engineering,
The University of Tokyo, Tokyo, Japan

Dedication

To my beloved parents

Anjali & Dilip Basu

Table of Contents

Chapter 1. General Introduction

1.1 The need for energy

The resistant of human life on earth is supplemented by various forms of energy. A major part of it is filled by food energy, while the remaining ones by other forms energy, such as heat, wind, electricity and light, *etc*. Life cannot be luxurious without the latter ones.

The crisis of energy is very likely to appear in near future as soon as most of the naturally available resources (viz. coal, petroleum, natural gases, oil, nuclear energy and others) will be finished. Thus for securing the future of the human survival on earth scientists provide much efforts to discover ultimate and extractable resources for energy for use.

The best energy resources available to us are provided by Nature – the so-called God's blessings to Mankind. Researchers call some of these resources as renewables since these exist infinitely. This means these forms of energy would never run out. If they do so, then no life on earth would ever be possible!

The three major forms of renewable energy resources are wind, water and sunlight. Every animal on earth, including human, uses all the three major forms of energy for daily life. These energies are not directly interconvertible among one another. To do so, technology-based strategies must be developed which should be adopted for energy conversion.

Fig. 1 illustrates a comparison of the finite and renewable planetary energy reserves annually, reported by Perez *et al.*[1] As estimated, the world uses approximately 16 TWy (terawatt-year) energy to perform all kinds of social and technological activities. This energy is about 0.07% of the total energy of 23,000 TWy produced by the Sun annually. According to independent statistics and analysis made by Perez *et al.*,[1] as well as by the US energy information administration[12] (as discussed recently by Rui and coworkers[13]), the primary energy consumption of nearly 80% in the world is provided by fossil fuels. These include 20.8% from coal, 31.6% from natural gas, 23.3% from crude oil and 4.9% from natural gas plant liquids. The latter authors have stated that the lacking storage of the fossil fuels, as well as the rise of air pollution/global warming is mainly derived from their burning, thus boosting scientists to develop clean and renewable energies.[13] While there are many alternative renewables viable to us, such as wave, geothermal, hydro, biomass, wind and solar, the latter two are abundant enough to cover the whole need of today's world energy consumption. In fact, the solar energy alone is potentially enough to resolve all the needs for the global energy demand. This is because

only 1% area on the earth covered with photovoltaic (PV) modules with 10% power conversion efficiency can be enough to produce the energy needed by the world.

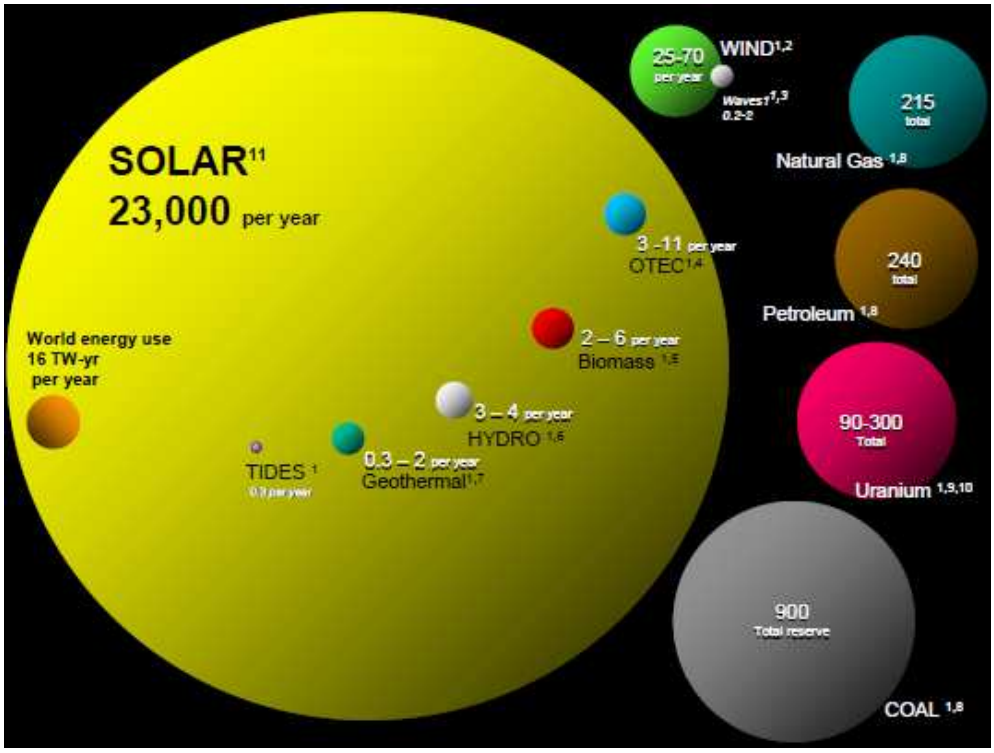

Fig. 1: Comparison of finite and renewable planetary energy reserves (Terawatt-years). Total recoverable reserves are shown for the finite resources. Yearly potentials are shown for the renewables.[12-13] The superscripts shown as numbers are references from 1 to 11.

Significant researches have currently been on-going to develop sophisticated optoelectronic nanomaterials both at molecular, cluster and supramolecular levels that can be resistant at room temperature and beyond. As said, the main reason to develop these nanomaterials is to use them to construct new optoelectronic devices, such as low bandgap semiconductors, which can be efficient to convert light energy from the renewable. The photon-to-electricity conversion process follows the working principle of the so-called *photovoltaic effect*, analogous to *photoelectric effect* originally developed by Alexandre-Edmond Becquerel. [14-16]

Photovoltaic (PV) solar cells comprise solar panels, which are semiconductors. These are potentially important candidates for converting the sun's energy directly into electric energy since these use the principle of *photovoltaic effect*.

Solar cells a class of low bandgap semiconducting materials, which are ideal and preferred over any other functional materials on earth for the aforesaid purpose. These

absorb light, covering the visible (1.68 – 3.26 eV) extending to the infrared region (1.24 meV ~ 1.68 eV) of the entire electromagnetic spectrum.

There have already been various semiconductors discovered for the above purpose. [17] Some of the important ones include: 1) Amorphous Silicon solar cell (a-Si), 2) Biohybrid solar cell, 3) Buried contact solar cell, 4) Copper indium gallium selenide solar cells (CIGS), 5) Concentrated PV cell (CVP and HCVP), 6) Cadmium telluride solar cell (CdTe), 7) Crystalline silicon solar cell (c-Si), 8) Dye-sensitized solar cell (DSSC), 9) Gallium arsenide germanium solar cell (GaAs), 10) Hybrid solar cell, 11) Luminescent solar concentrator cell (LSC), 12) Micromorph (tandem-cell using a-Si/μc-Si), 13) Monocrystalline solar cell (mono-Si), 14) Multi-junction solar cell (MJ), 15) Nanocrystal solar cell, 16) Organic solar cell (OPV), 17) Perovskite solar cell, 18) Photoelectrochemical cell (PEC), 19) Plasmonic solar cell, 20) Plastic solar cell, 21) Polycrystalline solar cell (multi-Si), 22) Polymer solar cell, 23) Quantum dot (QD) solar cell, 24) Solid-state solar cell, and 25) Thin-film solar cell (TFSC), *etc*. Most of these solar cells took decades to achive a desirable power conversion efficiency (PCE). For instance, thin-film CIGS solar cell has taken almost 40 years to achieve a PCE of 26.6%, whereas multicystalline silicon and thin-film CdTe solar cells took roughly 4 and 3 decades to achieve PCE of 21.3 and 22.1%, respectively. However, halide perovskite solar cells have only recently generated renewed interest as photovoltaic blockbusters in the history of solar cell technology. [18] Such solar cells assist in achieving a PCE of 22.7% (Fig. 2). Interestingly, this efficiency is accomplished within last 5 years, prior to the first one that reported a PCE of 2.2% in 2006, and the second one that reported PCE of 3.8% on that in 2009. Fig. 2 illustrates a summary of the PCE of various solar cells invented to date, certified by NREL (National Renewable Energy Laboratory, US).[17]

Because of several reasons (see 1.4.2), most of the solar cells so far invented might not be suitable for global use. This demands that high efficiency PV solar cells are needed to be discovered. Once this is done, the next follow up step is to convert the light energy into electric energy using the new technology, and the storage of the converted electric energies in other devices for use. This is the reason there have been simultaneous research developments currently on-going for the discovery of novel battery materials. [19]

Perovskite solar cells are categorized as the 3rd generation of PVs, [20-23] same as those of DSSC, [24-25] organic PV (OPV), [24-25] and quantum dot (QD) PVs, [26] *etc.*, since these are assumed to potentially able overcoming the Shockley–Queisser limit[27] of 31–41% PCE devised for single bandgap solar cells. Researchers honor perovskite solar cells as *the rising star* in the field of photovoltaics, [28-29] while others call them as poor man's high performance semiconductors. [30] There are other researchers who have used terms such as "holy grail" [31] and "perovskite fever", [32] *etc.*, to make the research more colorful and hot. Although the stability of these materials is under debate, [33] scientists hope that these might lead the future through appropriate "tandem" technology.[34]

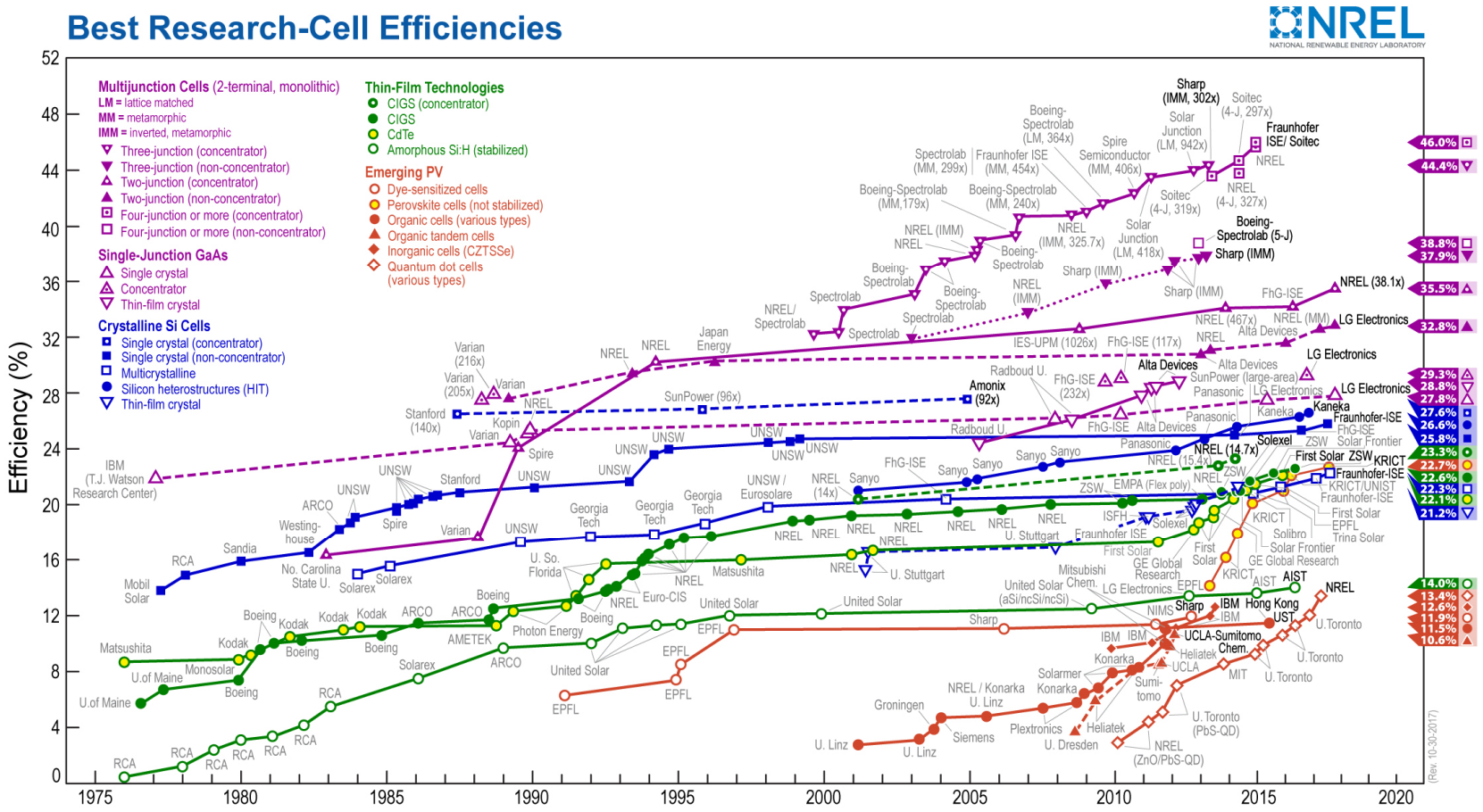

Fig. 2: Best research cell power conversion efficiencies as certified by the National Renewable Energy Laboratory (NREL).[17]

1.2 Motivation

This thesis has focussed on theoretical studies related with the fundamental understanding of noncovalent interactions of halogen derivatives in molecular domains, and a utilization of these as tools to rationalize the design principles of halide based perovskite solar cell materials. To this end, it has theoretically proposed a set of newly discovered halide perovskite compounds as possible candidates for application in photovoltaics.

Before proceeding to summarize the main theme of each Chapter of the thesis, I would like to briefly introduce below through a brief review setting the conceptual and historical importance of noncovalent interactions, as well as their super diversities and implications in materials design.

1.3 Noncovalent interactions

Studies on noncovalent interactions cover a major part of chemistry,[36] materials nanoscience[37] and crystal engineering[37-38] and biological sciences.[39-41] An obvious reason for such an upsurge of scientific interest lies in the fact that these interactions are least understood, and that these are vital for designing novel functional materials.[42] They deserve significant attention because they serve as "glue-like-adhesives",[43-44] as well as stacking spacers,[45] assisting chemical compounds to stick with each other in the form of chemical bonds. For instance, noncovalent interactions determine the packing, compactness and folding of molecular domains.[42,45-47] They are responsible for the modification of geometrical, energetic, electronic, optical and mechanical properties of the new materials that can be derived from π-conjugated molecules, ion pairs, oligomers, and polymers, among others.[48-49] According to Guo *et al.*, [50] for instance, materials design via optimized intramolecular noncovalent interactions is an efficient tool for the development of high-performance organic semiconductors. In particular, these authors have recently reported the design, synthesis, and implementation in semiconducting polymers of a novel head-to-head linkage containing the 3-alkyl-3′-alkoxy-2,2′-bithiophene donor subunit having a single strategically optimized, planarizing noncovalent S•••O interaction. Such an implementation of a head-to-head linkage with an alkyl/alkoxy substitution pattern and a single S···O interaction is a promising strategy for organic electronics materials design. Similarly, according to Sutton *et al.*, [38] an understanding of these interactions into the design of organic semiconductors can assist in developing novel materials systems from this fascinating molecular class. Zhou *et al.*[43] have asserted that “Specific noncovalent interactions that are indicative of attraction, directional intermolecular forces have always been of key interest to medicinal chemists in their search for the "glue" that holds drugs and their targets together.”

Noncovalent interactions can be intermolecular or intramolecular. These are known in many different flavors.[51-62] Decades ago, especially during the time of Pauling and later,[61] it was

understood that hydrogen bonding, van der Waals, and π•••π stacking interactions are the three major types of noncovalent interactions. However, in recent years, many of them came out (identified) from crystal studies, or even named for the first time. [63-80] These are presumably not new, which have been vastly distributed in many experimentally synthesized crystals documented in many database, such as Cambridge Structure Database (CSD).[81] The importance of these interactions were underestimated, thus are incomplete. An underlying reason for this is that these were either ununderstood, or unclear, or not characterized due to lack of appropriate experimental and theoretical tools and significant research involvements. The new chemistry of the aforesaid noncovalent interactions have become apparent in this and last decades. One of these is called σ-hole bonding.[63-67] Others are called as chalcogen bonding, [68-71] pnictogen bonding, [72] carbon bonding, [68-69] and tetrel bonding, [75-78] so on. There are several other forms of noncovalent interactions existing in the literature (e.g., Lithium bonding, [79-80] and van der Waals, [82-83] *etc.*), some of which are beyond the scope of this thesis. The above view is perhaps in line with the title of a most recent paper of Legon, "Tetrel, pnictogen and chalcogen bonds identified in the gas phase before they had names: a systematic look at non-covalent interactions".[84]

1.3.1 The hydrogen bonding

As indicated above, hydrogen bonding is a vital part of noncovalent interactions, covering a larger portion in the chemical physics and physical chemistry researches.[52-59] It has its own compartment in areas as diverse as supramolecular chemistry, [36,70,78] drug binding, medicinal chemistry,[85-86] biological science,[39-40,43] and crystal engineering,[36,53,61,69] among several other research fields. Fig. 3 illustrates the histogram, showing how largely the topic has so far been cultivated.

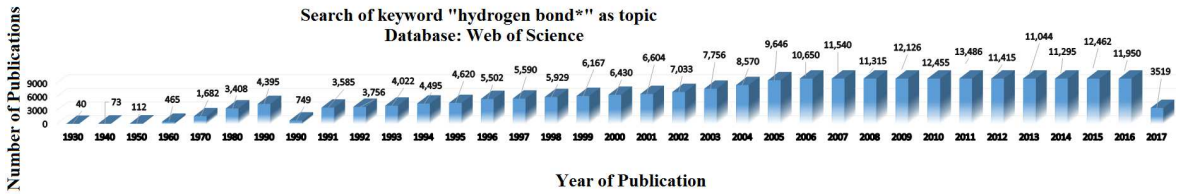

Fig: 3: Histogram chart showing the number of articles published on “hydrogen bond” for the 1900 – April 2017 period. The statistical data are obtained by searching the Web of Science Database[87] with the keyword “hydrogen bond *” as TOPIC.

Scientists have taken decades to classify hydrogen bonding interactions into three major categories.[52-59] There are various forms of this classification proposed by various authors. These were made possible because of the scattered natures of their bonding strengths and the

distinguished structural, electronic, vibrational, NMR and electron density properties. Such classification schemes were relied not only on the experimental data, but also on the level of judgement and personal feeling of scientists. For instance, and as will be discussed in detail in Chapter 4, Jeffery and Saenger have classified hydrogen bonding interactions as strong, moderate and weak.[54-55] Desiraju and Steiner have classified these interactions as very strong, strong, very weak and van der Waals.[52,53] However, Szatyłowicz has divided these as very strong, strong, moderate and weak.[60] Nevertheless, the classification schemes on hydrogen bonding proposed by various scientists are tentative. This means that there is no guarantee that the set of properties that have attributed to very strong interactions in these classification schemes would not reflect in the set of properties proposed for moderate strength hydrogen bonding interactions given molecular complexes can be of diverse varieties.

There have been over 50 definitions provided to characterize hydrogen bonding in molecular complex systems.[88] The most recent definition is put forwarded by IUPAC in 2011.[89] According to it, "The hydrogen bond is an attractive interaction between a hydrogen atom from a molecule or a molecular fragment D–H in which D is more electronegative than H, and an atom or a group of atoms in the same or a different molecule, in which there is evidence of bond formation."

A typical hydrogen bond may be depicted as D–H•••A–Y, where the three dots "•••" denote the bond. D–H represents the hydrogen bond donor. The acceptor may be an atom or an anion A, or a fragment or a molecule A–Y, where A is bonded covalently to Y. In some cases, D and A are the same. In more specific cases, D and A are the same and D–H and A–H distances are the same as well leading to symmetric hydrogen bonds. In any event, the acceptor is an electron rich region such as, but not limited to, a lone pair of Y or π-bonded pair of A–Y.

IUPAC has further suggested that the evidence for hydrogen bond formation may be experimental or theoretical, or ideally, a combination of both.

In addition to the definition provided above, IUPAC has suggested to invoke a set of six criteria (E1 – E9), a set of six characteristics (C1 – C6), and a set of nine footnotes (F1 – F9) to identify and characterize hydrogen bonding in chemical systems. Such suggestions are consistent with the fact that greater the number of criteria satisfied, the more reliable would be the characterization. However, as discussed in Chapter 4, hydrogen bonding can be readily understood as an attractive interaction of a positively charged H atom with a negative site.

1.3.2 The halogen bonding

Halogen bonding is a sister of hydrogen bonding, falling into the same category of noncovalent interactions. According to 2013 IUPAC recommendation,[90] "A halogen bond occurs when there is evidence of a net attractive interaction between an electrophilic region associated with a halogen atom in a molecular entity and a nucleophilic region in another, or the same, molecular entity."

Analogous with the hydrogen bond, a typical halogen bond is denoted by the three dots in R–X•••Y. R–X is the halogen bond donor, X (X = F, Cl, Br, I) is any halogen atom with an electrophilic (electron-poor) region, R is the chemical group (e.g., $–CH_3$) covalently bound to X, and Y is the halogen bond acceptor. In some cases, X may be covalently bound to more than one group. It may also form more than one halogen bond. A is the halogen bond acceptor and is typically a molecular entity possessing at least one nucleophilic (electron rich) region.

IUPAC has listed commonly observed halogen bond donors and acceptors are as follows:

R–X can typically be a:	dihalogen molecule (e.g., I_2, Br_2, ICl, ClF) haloalkane (e.g., CBr_4, CHI_3, $C_nF_{2n+1}I$) haloarene or haloheteroarene (e.g., iodobenzene, halopyridinium and haloimidazolium cations) 1-haloalkyne (e.g., diiodoacetylene) halonium ion (e.g., diphenyliodonium or bromonium derivatives) haloimide (e.g., N-bromo- or N-iodosuccinimide)
Y can typically be a:	lone pair possessing atom (e.g., N atom of a pyridine or an amine, O atom of a carbonyl group) π system (e.g., double or triple bonds, arene moiety) anion (e.g., halide anion, oxyanion)

There are about ten characteristic features that might be invoked to identify and characterize halogen bonding interactions in chemical systems. A detail of it can be found elsewhere.

It is to be noted that both halogen bonding, and hydrogen bonding, are electrostatically driven noncovalent interactions. However, a significant difference between them lies in the directionality, in which, the former is typically more linear (~180^o), whereas the latter is both linear and nonlinear with more freedom for making noncovalent interactions since the hydrogen atom in molecules in general is entirely positive (as in nonaromatic methane and aromatic benzene molecules, for examples). Chapters 2-4 and 7 discuss more on this specific feature.

1.3.3 The tetrel bonding

Group 14 (also called Group IV) elements are called as tetrels. The members of this group are the carbon (C), silicon (Si), germanium (Ge), tin (Sn), lead (Pb), and flerovium (Fl). The three intermediate elements of this group have been greatly assisted in the development of the semiconductor physics, e.g., the silicon technology.

Elements of this group in molecules when attract the negative sites in another molecules through a long range intermolecular interaction, a tetrel bonding interaction is developed between them.

Long range intermolecular attractions in $H_3Y\ldots TrH_3X$ molecules (Y = N, P, As; Tr = C, Si, Ge; X = F, Cl, Br) can be regarded as tetrel bonding.[91] Similar other examples can be found elsewhere.[73-78, 84]

1.3.4 The chalcogen bonding

Chalcogens are the elements in group 16 of the periodic table, the so-called oxygen family. Elements such as the oxygen (O), sulfur (S), selenium (Se), tellurium (Te), and the radioactive element polonium (Po) belong to this family.

Wang *et al.* have defined chalcogen bonding as sister of halogen bonding, which is kind of noncovalent interaction formed by the group 16 elements of the periodic table.[68] Accordingly, it is formed when there is an evidence of a net attractive interaction between an electrophilic region associated with a chalcogen atom in a molecular entity and a nucleophilic region in another.

The intermolecular attractions in $H_2CS\cdots Cl^-$, $F_2CS\cdots Cl^-$, $OCS\cdots Cl^-$, $SCS\cdots Cl^-$, [68] and $Te\cdots O–N$[70] can be regarded as models to understand chalcogen bonding in molecular complexes. Analogous examples of complexes involving chalcogen bonding can be found elsewhere.[69, 71, 84]

1.3.5 The pnictogen bonding

Pnictogens are elements in group 15 of the periodic table, the so-called nitrogen family. Elements such as nitrogen (N), phosphorus (P), arsenic (As), antimony (Sb), bismuth (Bi), and the chemically uncharacterized synthetic element moscovium (Mc) belong to the pnictogen family.

Analogous with chalcogen bonding, a pnictogen bond is formed when there is an evidence of a net attractive interaction between an electrophilic region associated with a pnictogen atom in a molecular entity and a nucleophilic region in another.

Carbenes have shown to be as electron-pair donors for $P\cdots C$ pnictogen bonds.[92] Examples of complexes involving pnictogen bonding are $(XNO_2)_2$ homodimers (X = F, Cl, Br, I).[93]

1.3.6 Other σ-hole interactions

Decades ago it was believed that halogen atoms in molecules are purely negative. This concept was not very surprising because these atoms are highly electronegative. They are

formally assigned with a charge of –1 to guarantee charge neutrality condition in molecular systems. This notion, however, does not explain stability of many crystal geometries that accompany the R–X···A interaction motif, where R is the remainder part of the molecule containing halogen, and A is the halogen bond acceptor.

While examining the computed electrostatic surface potentials of some halogenated molecules, Brinck *et al.* made a surprising discovery in 1992.[94] In specific, for H_3C–Br, CBr_4 and CCl_4, the covalently bound halogen atoms were found having areas of positive electrostatic potential on the outer axial portions of their respective surfaces, whereas their lateral sites were purely negative. This has led to an interpretation that the electron density on the surfaces of covalently bound halogen in these molecules is not isotropic. And the positive region on the halogen, which is deficient of electron density, is highly electrophilic. Because it is lying along the outer axial portion of the covalently bound halogen, it is, some years later, called as an electrophilic cap, or, simply a $\sigma_{\text{-hole}}$, (or σ_{hole}, or "sigma-hole").[63-64]

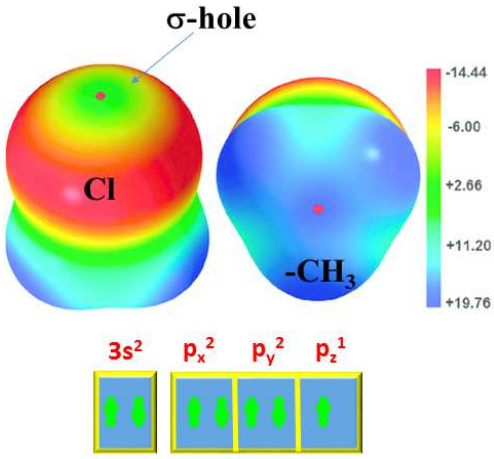

Fig. 4: The 0.001 a.u. isodensity mapped molecular electrostatic surface potential of chloromethane (H_3C–Cl), obtained with MP2(full)/6-311++G(3d,2p). It illustrates that the σ-hole (green circular region) on the chlorine's outer surface (left) is located along the C–Cl σ-bond and the methyl group (right) is facing the viewer. The color bar is shown in in kcal mol^{-1}. [95]

The concept of "sigma-hole" was originally referred to the electron-deficient outer lobe of a half-filled p (or nearly p) orbital involved in forming a covalent bond.[63-64] Accordingly, as the electron deficiency on the halogen becomes increasingly larger, this can lead to a relatively larger region of positive electrostatic potential. The attribute is not very surprising since the group R attached to X in R–X molecules pulls the electron density towards it through the σ-axis, leaving the outer region on halogen as electron deficient. Because it is positive, it can interact attractively with negative sites on other molecules (e.g., N in ammonia (NH_3)). Such attractions causing the formation of noncovalent interactions are called as σ-hole bonding.

The definition of σ-hole was initially understood by exploiting halogen centered noncovalent interactions containing positive σ-holes on group 17 elements in molecules. [63-64] It has been observed, experimentally and computationally, for many covalently-bonded atoms of Groups IV-VII. The positive character of the sigma-hole increases in going from the lighter to the heavier (more polarizable) atoms within a group, and as the remainder of the molecule becomes more electron-withdrawing.[65-66] It must therefore be understood that hydrogen- and halogen-bonding interactions are a subclass of σ-hole interactions.

The electronic configuration of ($_{17}Cl^{35}$) is $(1s^2 2s^2 2p^6) 3s^2 3p_x^2 3p_y^2 p_z^1$. If it will be bonded to a weakly electron-withdrawing group such as $–CH_3$, it will cause creating a positive σ-hole in the z-direction. This positive region can then be able to attract negative sites to form noncovalent interactions. Fig. 4 explains the nature of σ-hole on Cl along the outer portion of the C–Cl bond in $H_3C–Cl$.

1.3.7 The lump-hole concept

The concept of σ-hole introduced by Clark *et al.* [63] and Murray *et al.*[64] could explain halogen bonding (Fig. 5a) and other noncovalent interactions in many molecular systems and crystals. However, it does not explain certain noncovalent interactions formed by covalently bound halogens, such as those depicted in Fig. 5b–d. The interacting monomers in these dimers are in a sleep parallel arrangement. The intermolecular attractions (*albeit* weak!) cannot be described by σ-hole bonding because the σ-hole on the halogen in the monomers is along the

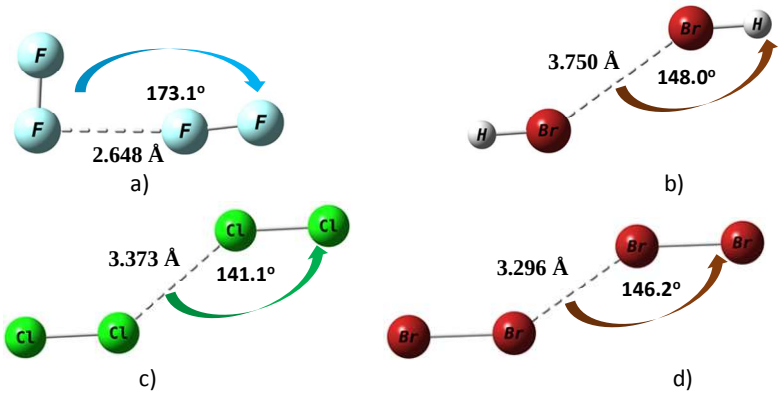

Fig. 5: The DFT-M06-2X/6-311++G(2d,2p) optimized geometry of the dimers of a) F_2, b) HBr, c) Cl_2 and d) Br_2 (this study) Intermolecular bond distances and angles are displayed. The bonding topology in a) is type-II halogen bonding equivalent, whereas those in b)-d) are type-I halogen bonding equivalent (see Chapter 2 for details). The former is typical halogen bonding (σ-hole centered), whereas the latter ones are typical halogen-halogen bonding interactions (lump-hole type).

axial direction, and is not interacting with the lateral sides of the halogen in the partner molecule.

However, the intermolecular interactions in Fig. 5b–d can be explained by the lump-hole theory. According to this concept, one does not need a true positive region on the halogen bond donor. Regions of charge-depletion and -concentration on the halogen donor and acceptor atoms/fragments interacting with each other can be sufficient to sustain attractive interaction between them. Eskandari *et al.* [97] and Duarte *et al.*[96] have provided various examples promoting the understanding of lump-hole interactions in molecular complexes.

1.4 Halogen in bimolecular and supramolecular designs

Thousands of research articles have been published within last 10 years centering the understanding of the role played by the halogen derivatives in the rationale designs of molecular clusters and supramolecular structures. Fig. 6 gives the evidence about this, showing roughly about 8000 research articles published on halogen bonding during the 1998 – 2017 (April) period (bottom). The publication growth per year shows that there is a significant interest in these interactions in various research fields.

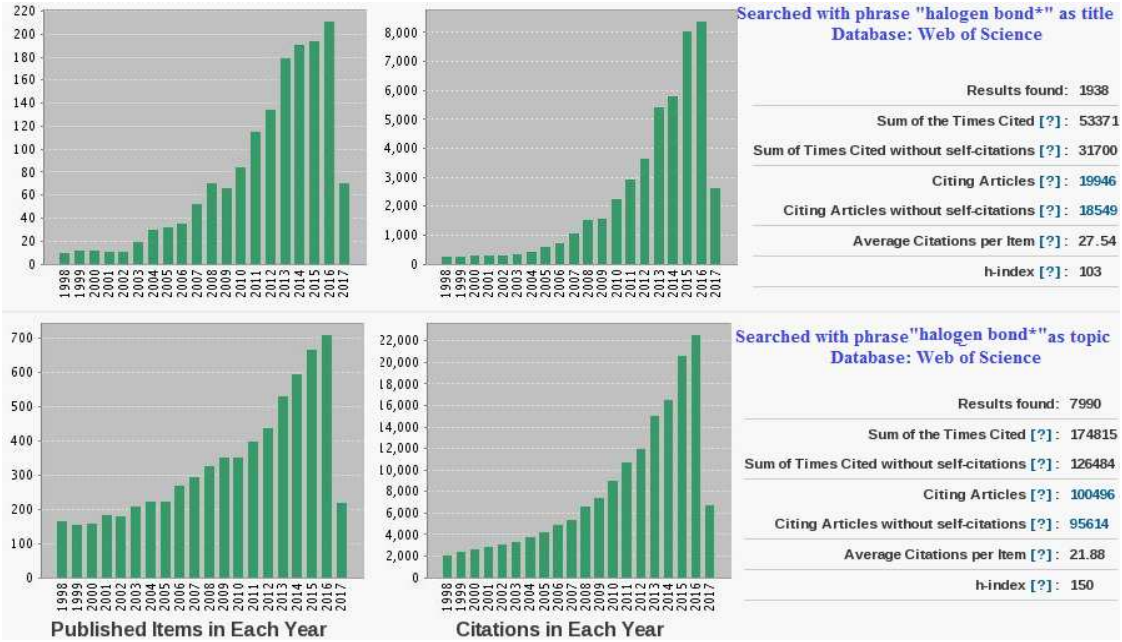

Fig. 6: a) Bar chart of the number of articles published on halogen bonding in each year for the 1998 – April 2017 period. b) Bar chart of the citation details for the same period. The statistical data are gained by searching the Web of Science Database with the keyword “halogen bond*” as TITLE. And, when the same keyword was searched as TOPIC, the resulting number of articles published/cited for the same period was dramatically different.

As indicated above, the modes of intermolecular interaction of the covalently bound halogen derivative comprising the latter three halogens come in two special flavors, type-I and type-II (Chapters 2 and 3). This is not always true for the covalently bound fluorine since in many molecules it is highly electronegative, small, reactive, least polarizable and dispersive; its bonding scenario in molecules is unpredictable.[98-99]

By contrast, the negative portions on the surface of halogen in molecules have abilities to attract hydrogen atoms in molecular species, forming intermolecular hydrogen bonding interactions.[100-101]

Note that halogen bonding is more directional than hydrogen bonding.[64-65,102] The former are easily tunable than the latter. This can be achieved easily by replacing the nature of the halogen content in molecules, as well by changing the nature of the electron-withdrawing group R in R–X (X = Cl, Br, I). This is not very surprising since increasing the halogen content in molecules from F through Cl to Br to I, the polarizability of X increases. The change of the nature of the –R group also increases the strength of the σ-hole on the halogen. In fact, larger the size of the σ-hole on the halogen, stronger would be the energy of the intermolecular interaction that it forms with the negative site, and hence the stability of the overall intermolecular complex. [64-65,102]

Both hydrogen and halogen bonding interactions can appear individually, or simultaneously in molecular systems. If they appear simultaneously, they develop collective phenomena of chemical bonding. These have been explained assembly in many molecular clusters and supramolecular structures synthesized in the solid state, including dimers, trimers and oligomers.

Many supramolecular structures are formed by reinforced derivatives of halogenated compounds. Fig. 7 illustrates the nature of halogen surfaces on fully halogenated aromatic compounds, showing the nature of σ– and π–holes.

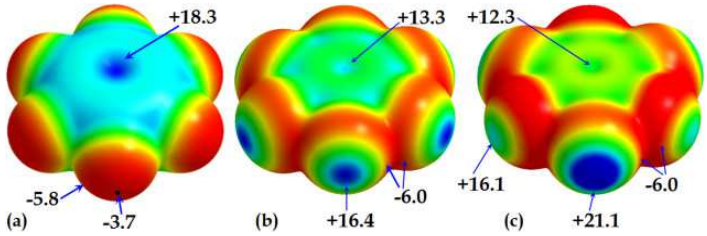

Fig 7: DFT-M06-2X/aug-cc-pVTZ molecular electrostatic potential surface of (a) perfluorobenzene (C_6F_6), (b) perchlorobenzene (C_6Cl_6), and (c) 1,3,5-tribromo-2,4,6-trichloro-benzene ($C_6Br_3Cl_3$), mapped with the 0.001 a.u. (electrons per $bohr^3$) isodensity. Colors in red and deep blue represent the most negative and most positive regions of electrostatic potential, while those in yellow, green, and cyan represent the least negative, least positive and more positive regions of electrostatic potential, respectively. The tiny blue/cyan region at the center of the aromatic ring in these compounds is a positive π-hole, not unexpected for aromatic compounds. The σ-holes on F, Cl and Br on compounds in a), b) and c) are having strengths of –3.7, +16.4 and +21.1 kcal mol^{-1}, respectively. [103]

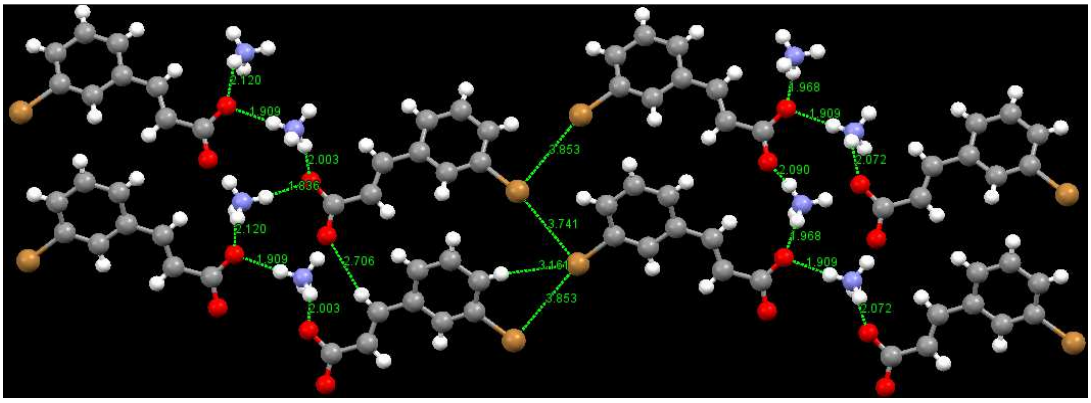

(a) Ammonium ion in directing self-assembly. Shown are intermolecular hydrogen and halogen bond distances.[105]

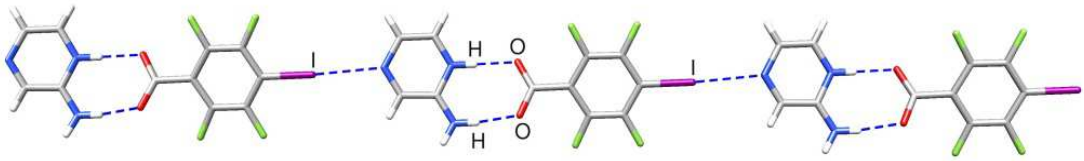

(b) Halogen bond and hydrogen bond contacts in the linear chain assembly of 2-aminopyrazin-1-ium and 2,3,5,6-tetrafluoro-4-iodobenzoate.[106]

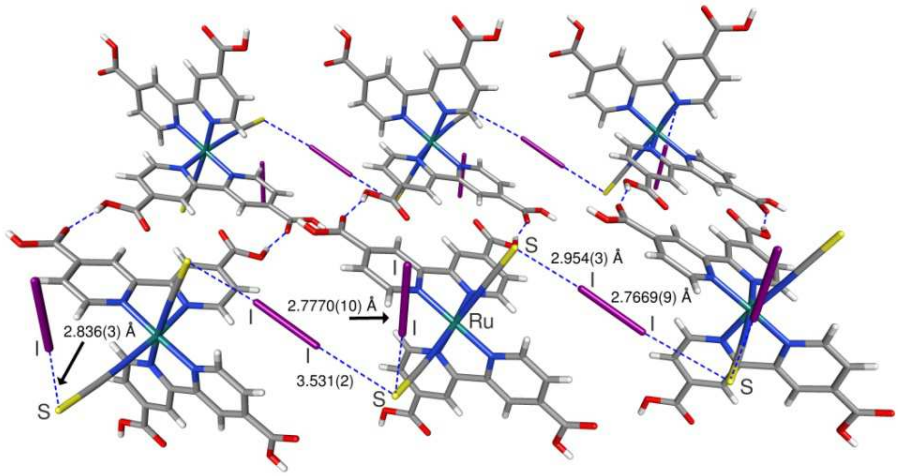

c) Halogen bonding interactions in $[RuI_2(H_2dcbpy)(CO)_2]\cdot 2I_2$.[106]

Fig. 8: Illustration of intermolecular interactions in the design of supramolecular materials.

Figs. 8 and 9. Illustrate, as examples, geometries of a few complex supramolecular structures that are formed either by pure halogen bonding interactions, or by the joint venture involvement of intermolecular hydrogen bonding with halogen bonding interactions.

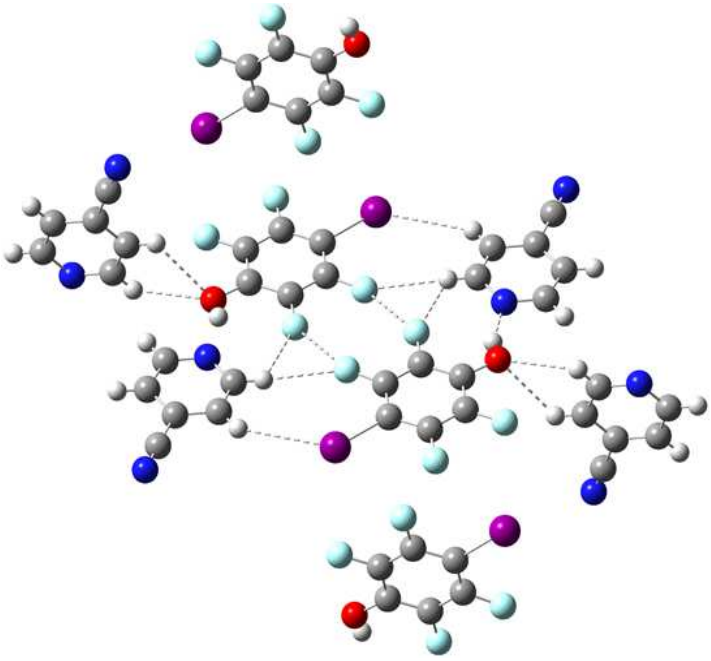

(a) An example showing halogen bonding *vs.* hydrogen bonding within a competitive supramolecular system.[107]

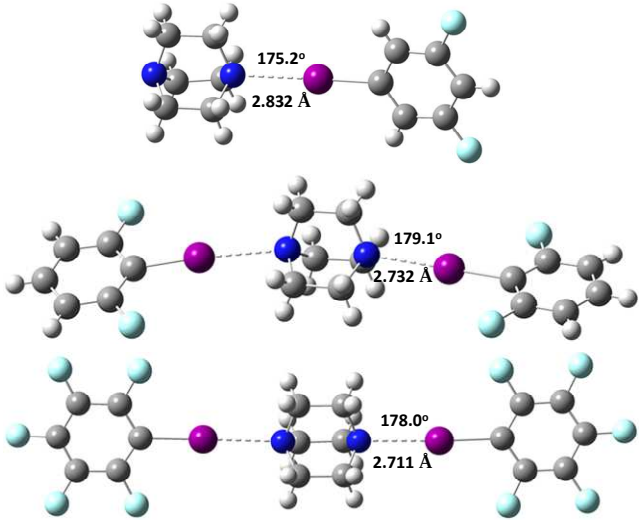

(b) Formation of supramolecular rotors assembled through halogen bonding.[105]

Fig. 9: Illustration of intermolecular interactions in the design of supramolecular materials.

1.5 Halogen for the development of perovskite solar cell materials

Numerous previous studies reported on perovskite materials are largely halide free. These are entirely inorganic materials, mainly metal oxides.[108] In 1893, Wells has mentioned that the crystals of the general compositions $CsPbX_3$ with X = Cl, Br or I, and Cs_4PbX_6 with X = Cl or Br, can be prepared from aqueous solutions. [127] In 1957 and 1958, Møller was probably next scientist who has reported two articles mentioning the importance of the $CsPbCl_3$ and $CsPbBr_3$ crystals, and has recognized these to have the perovskite structure. He found that at room temperature these systems are tetragonally or monoclinically distorted. Both of them, however, show transition to pure cubic perovskite structure, at 47 and 130 °C, respectively and with cell dimensions a = 5.605 Å for $CsPbCl_3$, a = 5.874 Å for $CsPbBr_3$.[128-129]

Since then Kojima *et al.*[109] have published their study in 2009 on methylammonium lead iodide ($MAPbI_3$) perovskite, there have been a significant interest in it, as well as in analogous halide containing metal perovskites. Fig. 10 illustrates cubic $MAPbI_3$. An obvious reason for this is due to the fact that these compounds have displayed good photovoltaic abilities suitable for the development of solar cells. [110-111] As Monser noted in his recent article of *Nature Materials*, [130] one of the most silent features of hybrid lead halide perovskites is the extended lifetime of their photogenerated charge carriers, which has been shown experimentally to originate from a slow, thermally activated recombination process, exceeding the Langevin limit[131-132] for direct recombination by several orders of magnitude.[133]

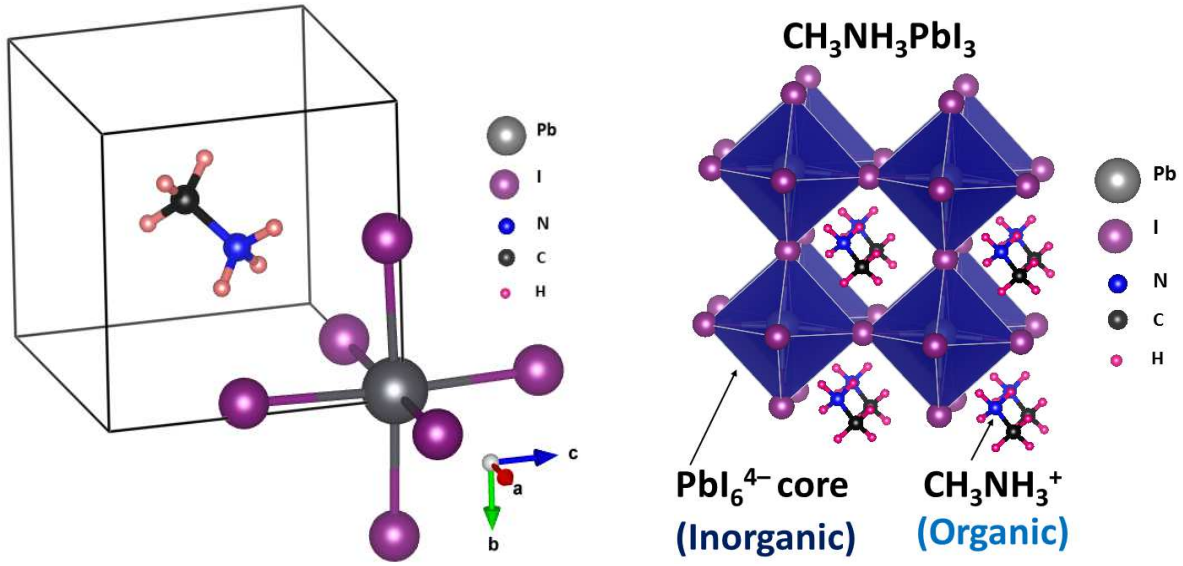

Fig. 10: The organic-inorganic hybrid framework of bulk $MAPbI_3$ in cubic phase (left) and its 2×2×2 polyhedral representation in 3D (right), with the MA cation aligned along the (111) direction.[112]

The trihalide perovskites can be understood in terms of the generic formula BMY_3. In this formula, it must be realized that the B-site cations are linked with the metal ion M through intermolecular interactions, and the halogen derivatives Y are such that Y = $I_{(3-x)}Br_{x=1-3}$, $I_{(3-x)}Cl_{x=1-3}$, $Br_{(3-x)}Cl_{x=1-3}$, and IBrCl.[8] The coordinate bonding interactions between Y and M forms the inorganic MY_3^- metal trihalide anion (lattice) topology. This then attracts the organic/inorganic B-site cations through the wondrous power of electrostatic, induction and dispersion interactions to form perovskite geometries. The molecular analogue of this attraction between B^+ and MY_3^- is an ion-pair. Its repetition may lead to the large-scale emergence of supramolecular BMY_3 (Chapters 5 and 6).

The BMY_3 topology is derived from the aristotype structures of ternary oxides called perovskites, $CaTiO_3$ (Scheme 1), a mineral that was discovered by Gustav Rose in the Ural Mountains of Russia a century ago in 1839. It has been honored in the name of Russian mineralogist Lev Perovski.[134] Victor Goldschmidt was probably the first person who have described the topology of perovskite in 1926 through the wonders of the so-called Goldschmidt tolerance factor.[135]

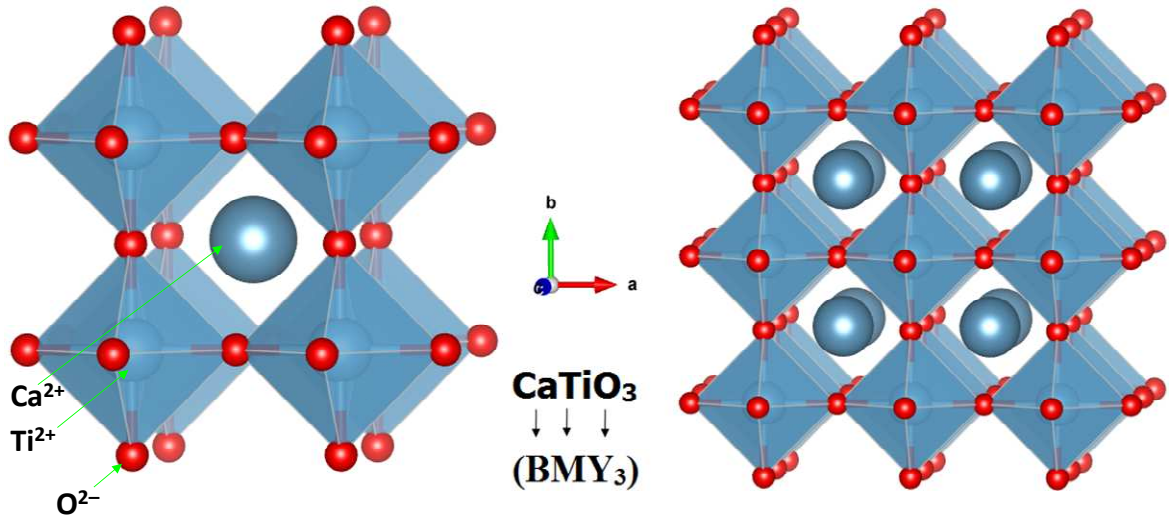

Scheme 1: The structure of the $CaTiO_3$ perovskite, with ($^{XII}A^{2+VI}B^{4+}X^{2-}_3$) architecture. a) Unit cell; b) 2×2×2 supercell; both illustrated in polyhedral representation.

In a recent study, Minns *et al.* have proposed the actual formula for $MAPbI_3$ to be $(CH_3NH_3)PbI_{3-2x}(I_2)_x$, where x ~ 0.007 at room temperature.[113] This proposal was made possible based on the rationalization that there could be the formation of I_2 molecules, suggesting a $2I^- \rightarrow I_2 + 2e^-$ redox couple.

It is well-known that the CH_3NH_3I and PbI_2 are the precursors for the synthesis of crystalline $CH_3NH_3PbI_3$.[115] However, most recent results have demonstrated that there can be another three simple precursors, i.e. PbI_2, methylamine (CH_3NH_2) and hydrogen iodide (HI) gases, which when mixed would lead to the formation of high quality perovskite films.[114] The CH_3NH_2 gas in ambient air reacts directly with PbI_2 to form stoichiometric $CH_3NH_3PbI_3$ perovskite, and the reaction completes within a few seconds.[114]

Nevertheless, there have been many halide based perovskite compounds synthesized and theoretically discussed in the recent literature.[116-117] These include different B-site cations. These are either organic or inorganic. The cations such as formamidinium ($HC(NH_2)_2^+$), guanidinium ($C(NH_2)_3^+$), and cesium cation (Cs^+), *etc.*, have been vastly exploited. One of the B-site cations exploited in this thesis work concerns the $CH_3NH_3^+$ cation. The intermolecular interactions formed by the coordinated halogens in MY_3^- with the hydrogen atoms of the organic cation(s) give structural stability and shape to the resulting perovskite geometries, causing them to become functional, suitable for application in photovoltaics. An understanding of the characteristic properties of these intermolecular hydrogen bonding interactions and their utility cover a major part of this thesis work (Chapter 4–7).

It must be understood that trihalide perovskites are not new materials. These have been studied theoretically and experimentally previously several decades ago.[118-119, 128-129] As already indicated above, these systems have gained significant renewed interest because scientists have found these to serve as materials for photovoltaics. This specific theme may be new to the community, thereby researchers have recognized this as a new era in photovoltaics.[120-121] The research area is rapidly expanding, both area of solar energy technology[122] and fundamentally.[136-137]

Other than the BMY_3 stoichiometry, there have been a variety of perovskite systems reported.[108, 123-125] These include $B_3M_2Y_9$, B_2MY_6 and $B_2MM'Y_6$, among others. [125] The former are called layered/dimer perovskites (trivalent), whereas the latter two are regarded as metal deficient perovskites (tetravalent) and double perovskites (mixed valent), respectively. A detail of the nature of the M and Y-site ions is listed in Table 1. A classification detail of perovskites can be found in recently published articles, [108,123-125,138] which will no more be discussed in this thesis.

While the $CH_3NH_3^+$ cation has covered a major part of the research related to photovoltaics, there are hundreds of other B-site cations that have also been exploited. Figs. 11 and 12 illustrate various ligand cations that are either halogen-free or halogenated, which have been used as B-site cations for synthesizing various perovskite systems in various dimensions. These are obtained from our survey of the Cambridge Structure Database (CSD).[81] Note that there are many other tri-, tetra- and penta-valent B-site ligand cations that have also been used for the synthesis of various 1D and 2D layered perovskites, but a great majority of them have

PCEs very low, and are not so good for photovoltaics. A few B-site cations, as examples, synthesized with oxidation states varying between +2, +3 and +4 are summarized in Fig. 12b.

Fig. 13, for example, shows the two-dimensional map of the DFT predicted bandgap of the Platonic model of PbI_3-based perovskites as a function of the apical and equatorial metal–halide–metal bond angles for various B-site cations. It illustrates that the bandgap of the triiodide perovskites can be efficiently tuned by varying the steric size of the B-site cation. [139-140] An analogous result can be obtainable by varying the M-site anion and its oxidation state, [141-143] as well as by changing the Y-site cations (halogen by cations such as $HCOO^-$). [144-151] Similar other studies can be found elsewhere.

Table 1: A few important class of halide based perovskites that have been exploited in the literature.

	BMY_3	$B_3M_2Y_9$	B_2MY_6	$B_2MM'Y_6$
B-site cations	Inorganic: Cs^+, Rb^+, Tl^+ Organic: $CH_3NH_3^+$, $HC(NH_2)_2^+$, $C(NH_2)_3^+$	Inorganic: Cs^+, Rb^+, Tl^+ Organic: $CH_3NH_3^+$, $HC(NH_2)_2^+$, $C(NH_2)_3^+$	Cs^+, Rb^+, Tl^+	Inorganic: Cs^+, Rb^+, Tl^+ Organic: $CH_3NH_3^+$, $HC(NH_2)_2^+$, $C(NH_2)_3^+$
M-site cations	Pb^{2+}, Sn^{2+}, *etc.*	Sb^{3+}, Bi^{3+}, *etc.*	Sn^{4+}, Ge^{4+}, *etc.*	M = K^+, Cu^+, Ag^+, Au^+ M′ = Sb^{3+}, Bi^{3+}
Y-site anions	Cl^-, Br^-, I^-	Cl^-, Br^-, I^-	Cl^-, Br^-, I^-	Cl^-, Br^-, I^-

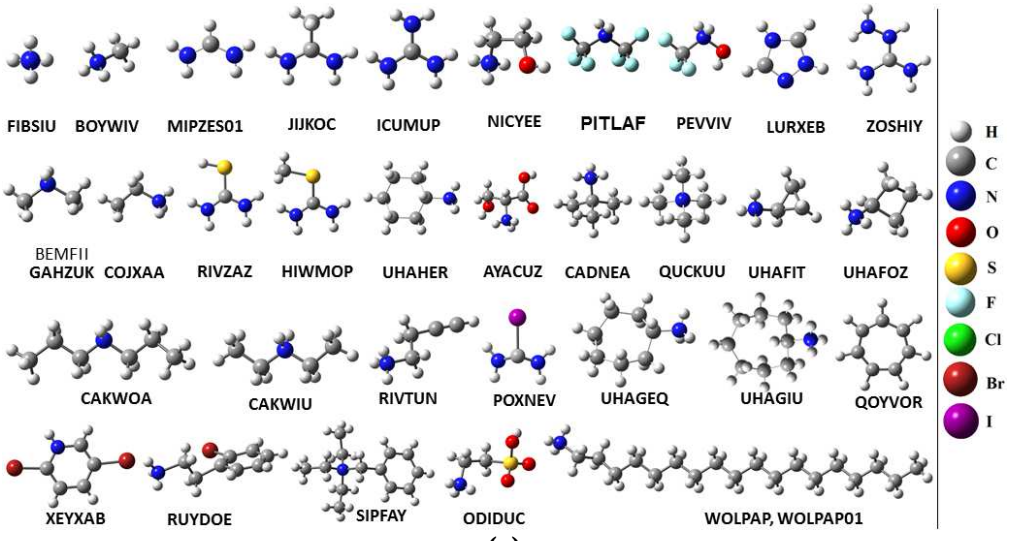

(a)

Fig. 11: List of a few monovalent organic cations that have been used for synthesis of perovskite architectures in various dimensions. Cambridge Structure Database (CSD) [81] reference codes are shown.

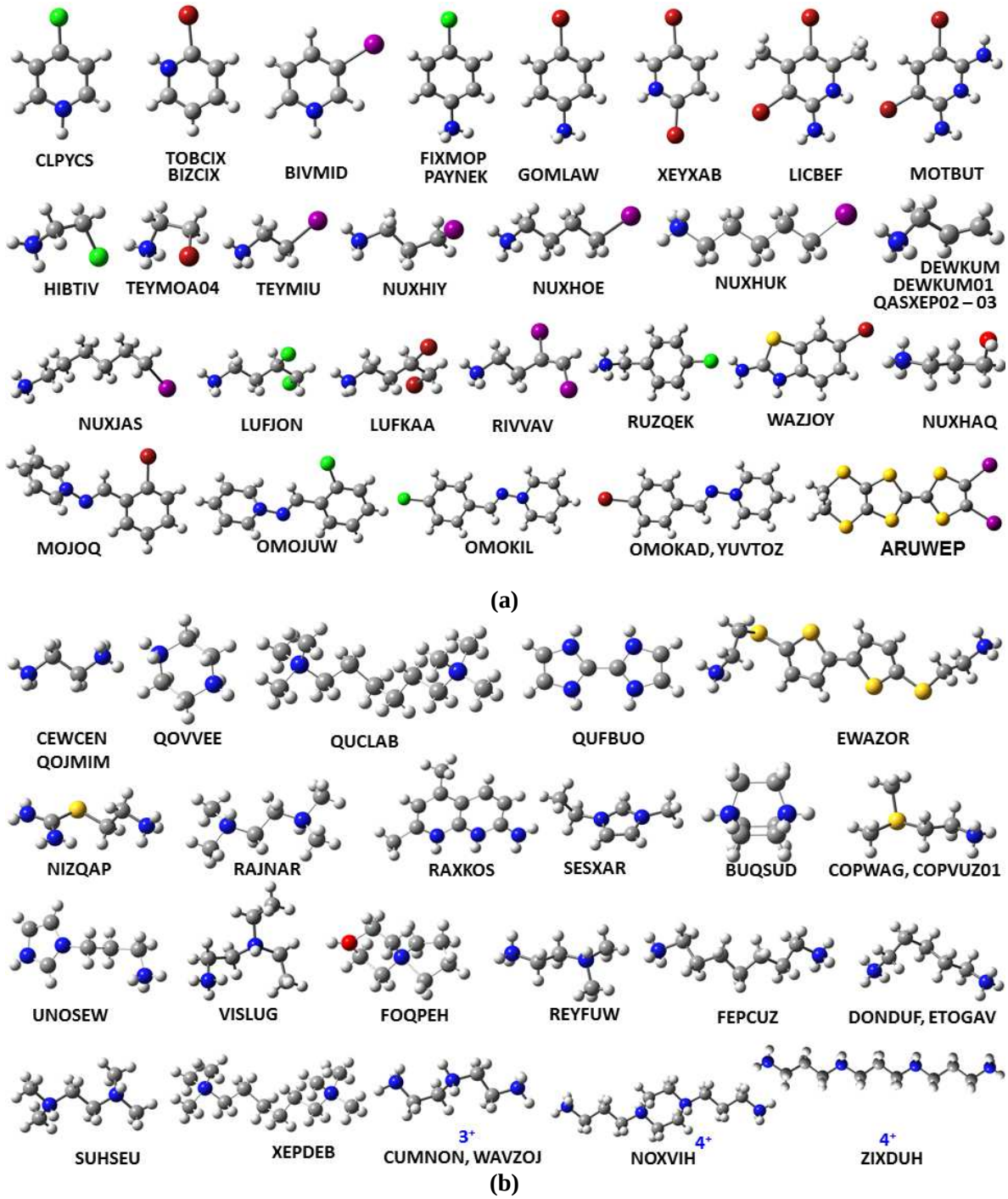

Fig. 12: a) List of a few a) monovalent divalent organic cations that have been used for synthesis of various perovskite architectures in 0-2 dimensions. b) Unless otherwise indicated, all ligand systems are divalent cations. Cambridge Structure Database (CSD) [81] reference code is shown for each case. For atom type and color, see Fig. 11.

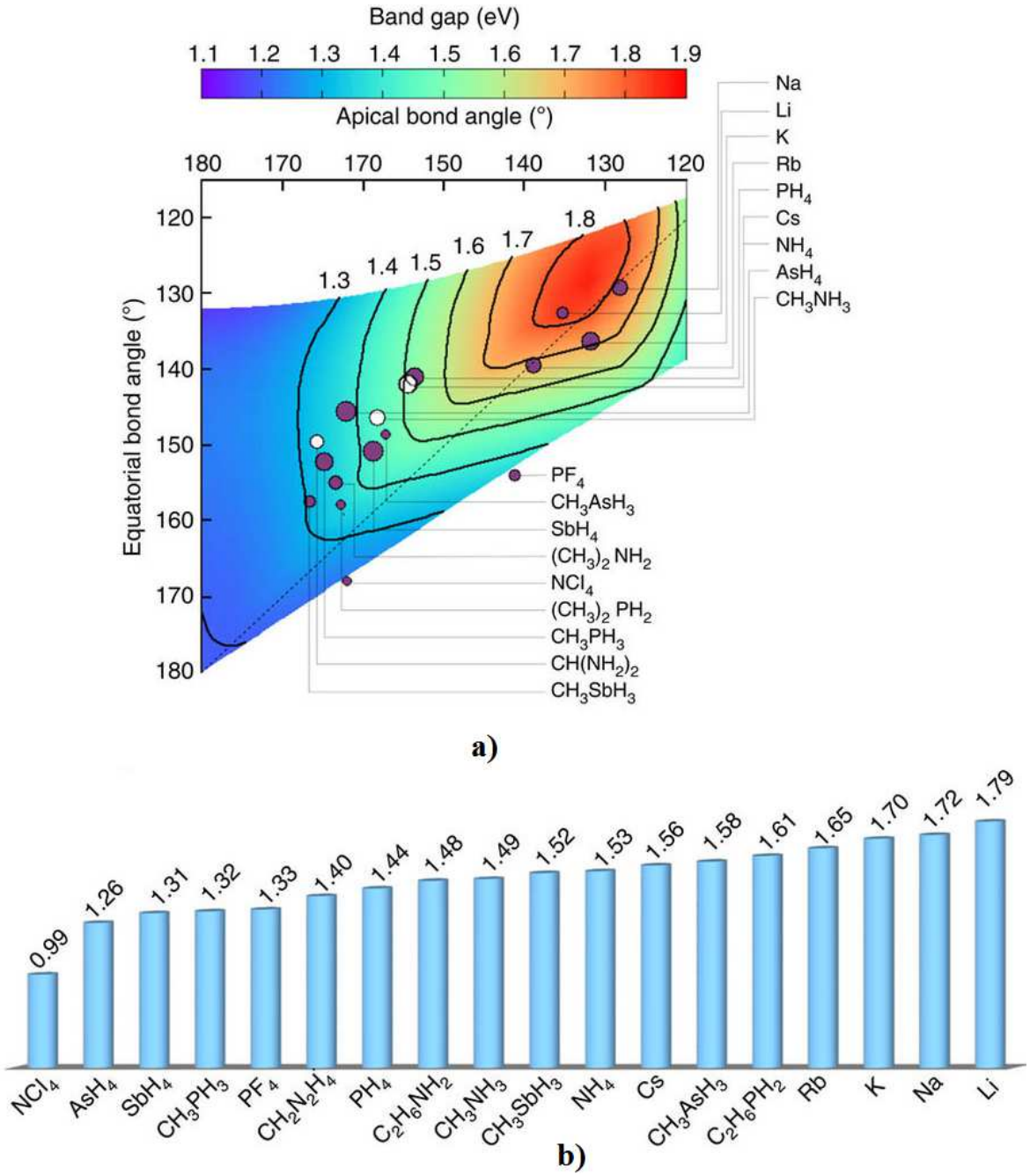

Fig. 13: a) Two-dimensional map of the DFT band gap of the Platonic model of PbI_3-based perovskites as a function of the apical and equatorial metal–halide–metal bond angles. b) Tuning the band gap of metal-halide perovskites via the steric size of the cation.[139-140]

1.5.1 The working principle of photovoltaic perovskite solar cells

The temperature T of the sun on its surface is approximately 5800 K. This is about 19.3 times larger than temperature of the earth on its surface, T = 300 K. The apparent temperature difference between the two surfaces is the driving force for any solar-energy conversion technology. This technology works with the principle of photoelectric effect – first discovered in 1839 by a French physicist named Edmund Becquerel.[14-16] Since the perovskite compounds are good light absorbing materials, [152] the energy of the absorbed light creates mobile charge carriers in it, which are positively and negatively charged species – holes and electrons. This is the working principle of most of the photovoltaic devices, in which, the electrons and holes have to be separated with minimal loss of energy (primary step), and this is presumably the reason hole transport and electron transport layered materials are attached to the perovskite layer to make the separation of carriers more efficient and is to avoid recombination close to the interface. The second step involves light absorption by the carriers. And in the third step, the carriers are need to be transported to an external circuit in order to produce electricity. Jung *et al.* have rationalized these into four principal steps: i) light absorption, ii) charge separation, iii) charge transport, and iv) charge collection.[153]

Apparently, like any other photovoltaic cell, perovskite solar cell also comprises p-type and n-type semiconductors joined together, forming the p-n junction since these have showed both electron and hole transport properties. Because the charge carriers move in opposite directions the electrons and holes are to be collected in the n-type and p-type semiconductors, respectively. Since these two are need to be connected with an external load, electricity would flow in the cell. A detail of it is discussed elsewhere.[111,154-156]

1.5.2 Device architectures

Design of stable perovskite solar cells is a challenge for materials scientists since the high performer $MAPbI_3$ and many of its derivatives are not environmentally friendly and stable.[138, 157-158] Tin analogous may be good for this purpose, but Sn oxidizes from +2 to +4 oxidation state, thus showing poor longivity.[123, 158] Nevertheless, the architectures of solar cell devices have been experimentally tested in two different flavors. These are the so-called p-i-n and n-i-p PVs.[159] These can be fabricated both as mesoscopic[152,160] and planar thin-film type.[152] The solar cell architecture in which the BMY_3 absorber coats a layer of nanocrystalline anatase TiO_2 is called mesoscopic, and the planar thin-film solar cell is composed of a layer of BMY_3 sandwiched between two selective contacts. The coating serves as scaffold for the sensitizer and assists in transporting electrons from the sensitized surface to the conductive substrate.

A p-i-n diode architecture comprises three layered regions. These include the **P**ositive-region layer, the **I**ntrinsic-region layer and the **N**egative-region layer. Similarly, an n-i-p diode architecture comprises three layered regions, the **N**egative-region layer, the **I**ntrinsic-region layer, and the **P**ositive-region layer.

The schematic diagram in Fig. 14a represents a standard perovskite p-i-n perovskite solar cell device architecture. It consists two layers (p- and n-type) on either sides of the intermediate

perovskite layer. The latter is the so-called the Electron Transport Layer (ETL), [161-163] which has high affinity for mobile electrons, thereby efficient for electron transport. Similarly, the Hole Transport Layer (HTL) conduct holes for their efficient transportation. [164-166] Materials such as the poly(3,4-ethylenedioxythiophene) polystyrene sulfonate (PEDOT:PSS) and the poly(triarylamine) (PTAA)-class of polymers serve as hole transport layers.[167] In contrary, PCBM, C_{60}, ZnO, SiO_2 and TiO_2, etc., can be served as effective electron interfaces.[161-163] Depending on the interest and efficiency, the type of the ETL and HTL materials can be selected for device fabrication.

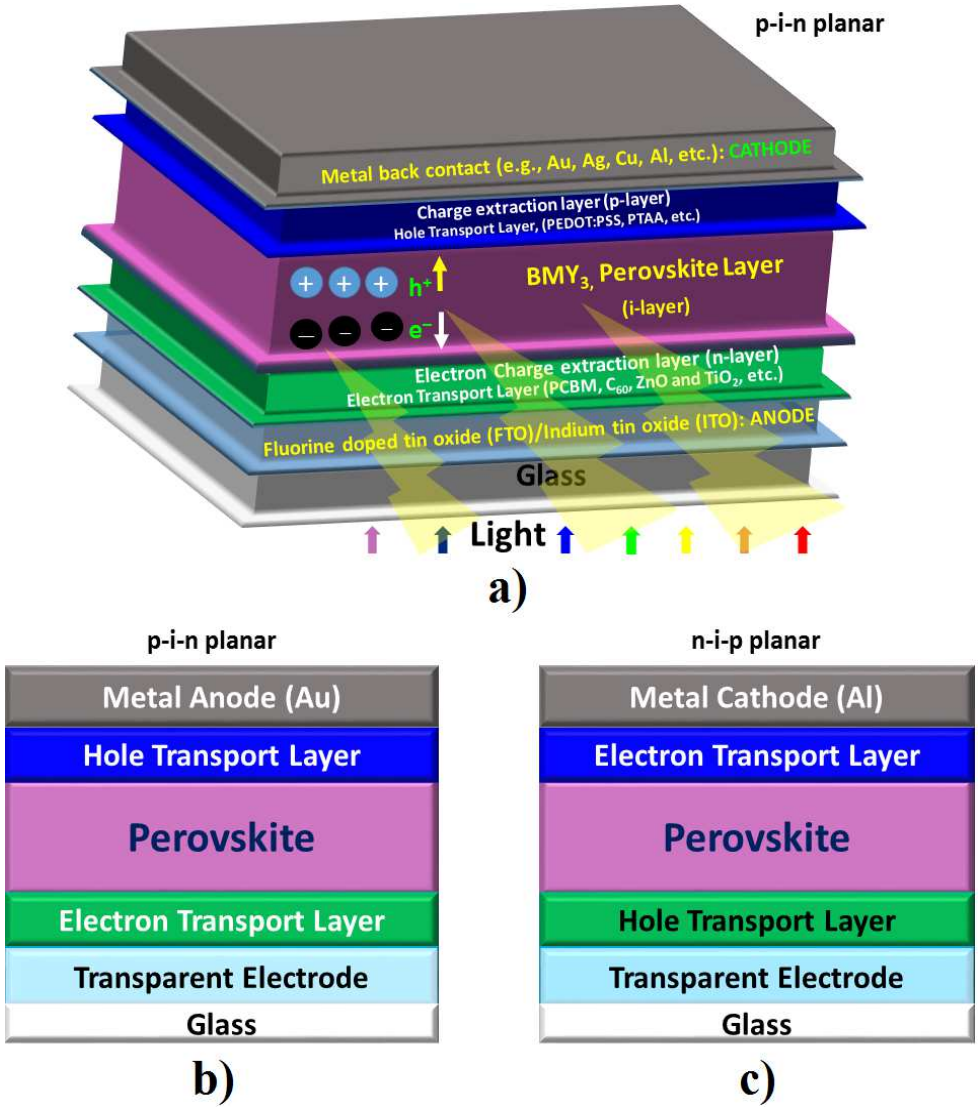

Fig. 14: Schematic of standard thin-film p-i-n and n-i-p perovskite solar cell device architectures.

1.5.3 Why are perovskite solar cells so interesting to scientists?

There can be several concerns that enable scientists to become selective in considering some specific materials for the development of the photovoltaic technology for future energy. Among others, these materials should possess the following characteristics: 1) these should show high power conversion efficiency (PCE), 2) the raw materials for to develop these synthetically should be abundant, 3) these should accompany simple device architecture, 4) the fabrication of these materials should be done with affordable rates, 5) these should be lightweight, and 6) these should be easily transportable.

From the review-type introductory discussions provided above, it is already clear that the perovskite solar cells such as $MAPbI_3$ are highly efficient.[30] The NREL certified PCE record for $MAPbI_3$ is 22.1%, [17] achieved within 10 years (since 2009[109]). [126] For instance, the crystalline silicon solar cells, the leading commercial technology, have taken several decades to convert about 25% of solar energy to electricity. This is another reason that pushes scientists to invent a best perovskite material for commercialization since the currently available ones are environmentally unstable. [168]

The raw materials to fabricate perovskites are abundant on earth. Also, these can be easily synthesized in ordinary research labs, and are lightweight. The most remarkable feature associated with them is that they can be fabricated by printing from solution. This is a common feature that the perovskite thin films share with DSSC and organic solar cell photovoltaics. [169-170] However, the PCE for the latter two technologies compared to the former is very low. Another most key feature of the perovskite materials is that the cells are well suited to solid-state hole-transport materials.

All the above characteristics might be in line with Lin *et al*, [31] who have asserted that "Organohalide perovskites can be solution processed or evaporated at low temperatures to form simple thin film photojunctions, thus delivering the potential for the holy grail of high efficiency, low embedded energy, and low cost photovoltaics. The initial device-driven "perovskite fever" has more recently given way to efforts to better understand how these materials work in solar cells, and deeper elucidation of their structure–property relationships."[31]

Dimensionality is another promising feature of perovskite materials.[171-173] These can be synthesized in various dimensions, including 0, 1, 2 and 3D, the dimensionality of the perovskites varies from 0D to 3D depending on the sizes of the ions, forming isolated polyhedron, chains, layers and cage-like perovskites. Fig. 15, as an example, presents the dimensional evolution of perovskites. Depending on the nature of the ligand cation, the dimension of the perovskite material can be determined. Fig. 16, for example, presents the longest chain ligand cation system synthesized till date that comprises a hydrophilic $–NH_3$ head and hydrophobic $(C_nH_{2n+2})_{n=18}$ tail. It serves as a spacer to connect the PbI_4 perovskite layers in 2D.[174]

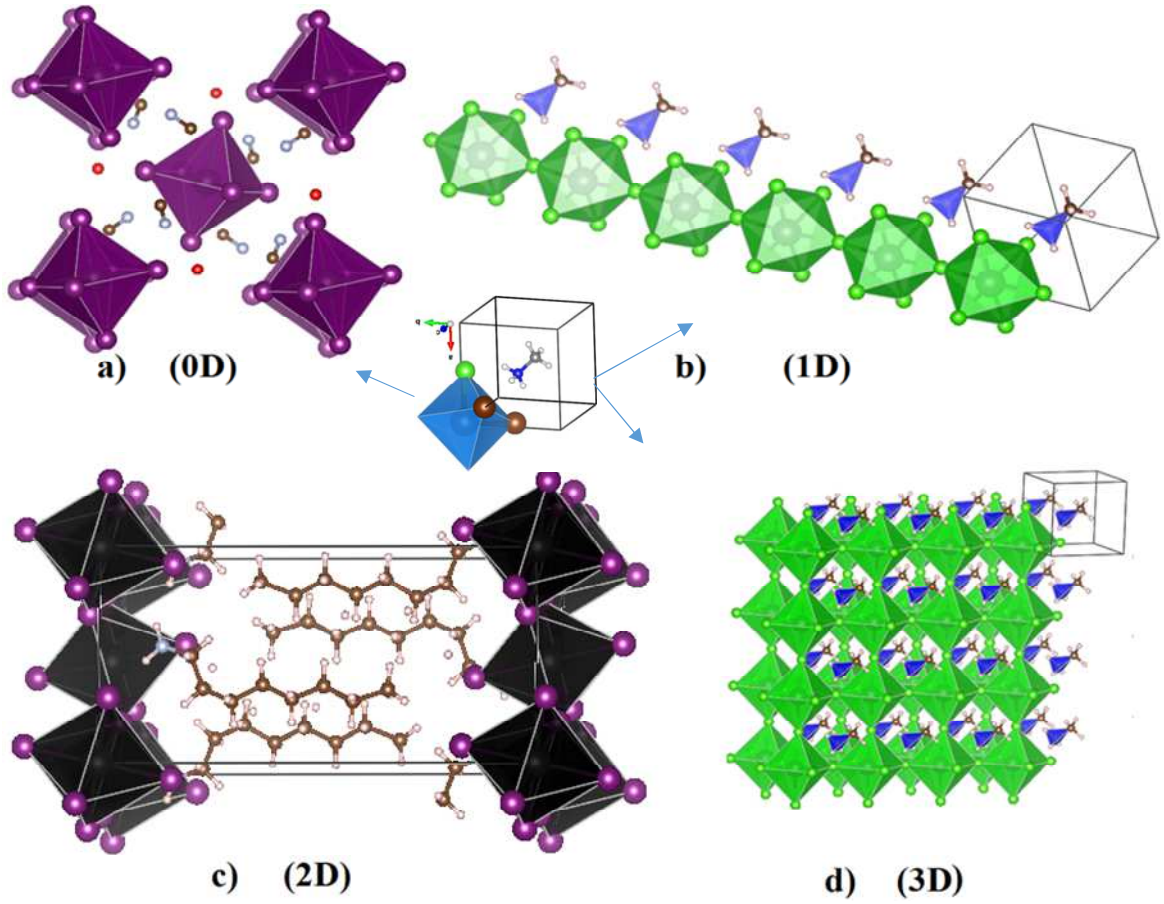

Fig. 15: Dimensional evolution of perovskites. Halide perovskites adopt various geometrical architectures, which are stable a) in 0D as quantum dot structure, b) in 1D as nanowire, c) in 2D as layer structure, and d) in 3D as cage like thin film.

As the dimensionality of the perovskite increases from 0 to 1 to 2 to 3D, the bandgap decreases. This is an essentially important attribute worth for photovoltaics. [172-173]

Another interesting feature is that the local topologies in the geometries of these materials can be fine-tuned either by the wonders of hydrogen bonding, or through the joint efforts of both halogen and hydrogen bonding interactions, presenting additional flexibility in the designing strategies of these materials. Fig. 17 illustrates the way both the interaction types essentially led to the development of octahedral tilting in some perovskite materials in 2D that have low-bandgap.

As mentioned above, the bandgap of trihalide perovskites is tunable in the entire visible range extending up to the infrared region. This is possible by triggering the extent of the nature

of the halogen content, as well as replacing the metal ion and the B-site cation in BMY_3.[139-151] This feature presents another advantage of the perovskite material over others.

$MAPbI_3$ has been regarded as a direct bandgap semiconductor with a very high absorption coefficient of 1.5×10^4 cm^{-1} at wavelength of 500 *nm*. [175] By contrast, the absorption coefficient of the indirect bandgap semiconductor s-Si is about ~ 10^2 cm^{-1}. Also, the charge carrier lifetime of $MAPbI_3$ is very high. For instance, the lifetimes of the charge carriers are roughly around 4 *ms*, 50 *ns*, 250 *ns*, and 20 *ns* for crystalline-Si, GaAs (thin film), CIGS, and CdTe semiconductors, respectively, whereas that of perovskite is 270 *ns*.[176] These two extraordinary features of $MAPbI_3$ actually have driven intense scientific interests.

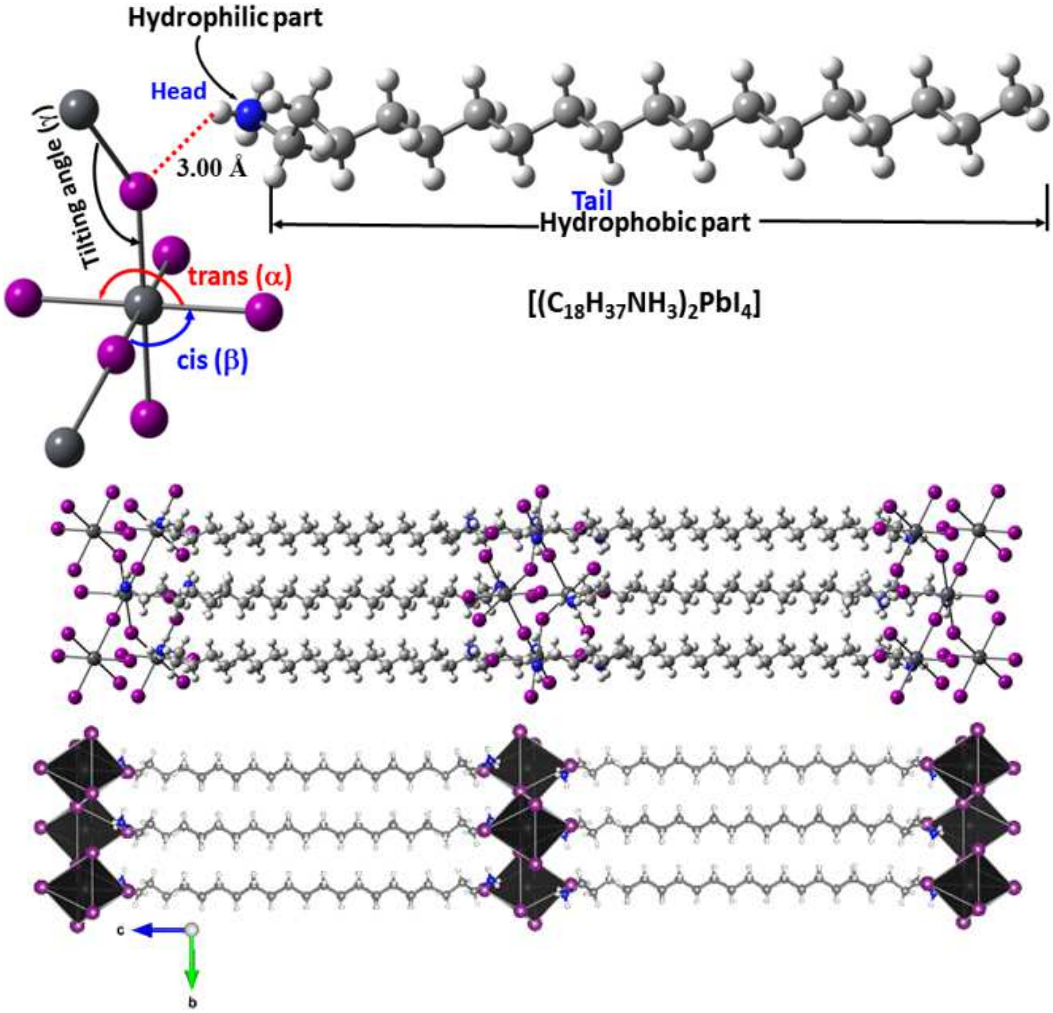

Fig. 16: a) The longest $C_{18}H_{40}N^+$ ammonium chain spacer synthesized for the development of the PbI_4 type perovskite in 2D (CSD[81] ref. code WOLPAP). It belongs to the $(C_nH_{2n+2}NH_3)_2PbI_4$ family, where n = 10, 12, 14, 16, 18. Both ball-and-stick and polyhedral models are shown for clarity.

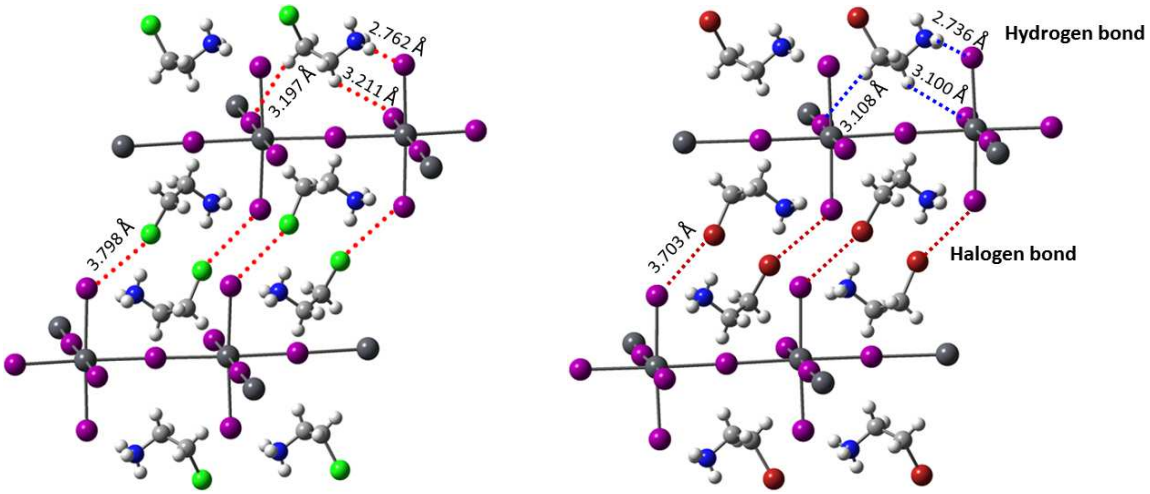

a) Ball-and-stick models of a few perovskite systems stabilized by the joint involvement of hydrogen and halogen bonding interactions (our rationalization on the reported experimental structures). Selected short intermolecular bond distances (in Å) are shown. CSD[81] ref. codes for the two geometries are TEYMUG (left) and TEYMOA04 (right), respectively.

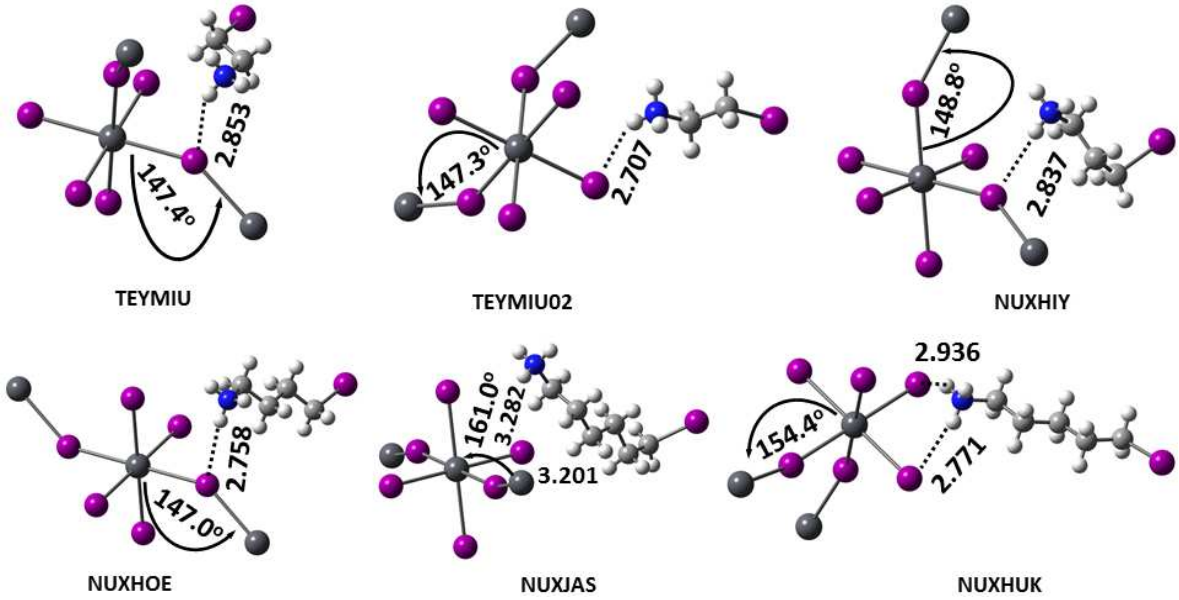

b) Examples (our rationalization on the reported experimental structures) showing B-site (halogenated) ligand cations that have been synthesized for the development of 2D perovskites. Some selected intermolecular hydrogen bond distances and tilting angles (in Å and °, respectively), together with the CSD[81] ref. codes, are illustrated.

Fig. 17: Illustration of halogenated ligand cations for the design of perovskites in 2D.

1.5.4 Is it correct to call halide perovskites as organometal/organometallic/organohalide?

As already indicated above, it might be understood that methylammonium lead/tin trihalide perovskite solar cells (CH_3NH_3Pb/SnY_3, where Y = $I_{(3-x)}Br_{x=1-3}$, $I_{(3-x)}Cl_{x=1-3}$, $Br_{(3-x)}Cl_{x=1-3}$, and IBrCl) are photonic semiconducting materials. Researches on various fundamental and technological aspects of these materials are extensively on-going to make them stable environmentally and for commercialization. However, there have been numerous research studies that address these materials to as *organometallic*. Interestingly, these studies have been massively and repeatedly appearing in reputable and high-profile peer-reviewed journal publications, such as *Nature*, *Science* and *Energy and Environmental Science*, *etc*. A question arises: whether should scientists in the perovskite and nanomaterials science communities refer $CH_3NH_3PbY_3$, as well as other perovskite derivatives falling into the same category, as organometallic? Do organometallics have any such connection with halide based perovskites?

According to IUPAC 1995 recommendation, [177] "organometallic compounds are classically compounds having bonds between one or more metal atoms and one or more carbon atoms of an organyl group. And, these compounds are classified by prefixing the metal with *organo-*, e.g. organopalladium compounds. In addition to the traditional metals and semimetals, elements such as nonmetallic boron, silicon, germanium, arsenic, selenium, and tellurium, etc., called metalloids, are also considered to form organometallic compounds, e.g. organomagnesium." Conspicuously, in the perovskite systems such as $CH_3NH_3PbY_3$ and $CH_3NH_3SnY_3$, *etc.*, there is no bonding link between the metal ion and the molecular organic cation. Also, there is no link between the metal ion of the inorganic species and the carbon atom of the molecular organic cation. From this simplicity, it should be obvious that the chemical terminology "organometallic" to refer trihalide perovskites is misleading; it is simply wrong.

Nevertheless, it has recently been demonstrated that there should not just be one term that can be referred to broadly cover all kinds of perovskite compounds that are currently at work.[178] As such, a more correct term that can be suitable to refer the hybrid organic-inorganic perovskite solar cell systems, such as the $CH_3NH_3MY_3$, $HC(NH_2)_2MY_3$ and $C(NH_2)_3MY_3$ families, *etc.*, is perhaps "hybrid organic-inorganic perovskite". For the inorganic-inorganic hybrid perovskite systems such as the $CsMY_3$, [179-180] and similar others, including double perovskites, the appropriate term is perhaps "metal halide perovskite", or "all-inorganic perovskite". The host-guest systems such as $[C(NH_2)_3M(HCOO)_3]$, $[HC(NH_2)_2M(HCOO)_3]$ and $[NH_4][M(HCOO)_3]$, *etc.*, the recommended terminology is probably "metal-organic perovskite", or simply "MOF perovskite".

1.5.5 Lead iodide perovskite as a dynamical bandgap semiconductor

There has been a great deal of confusion in the perovkite literature on whether or not the nature of the bandgap for the lead halide perovskites (especially, lead triiodie perovskite) is

direct, whether it is or indirect, or a combination of the two. Intially, it was believed that halide perovskites are direct bandgap materials. However, these materials have low defect density and long diffusion length for the charge carriers. The latter feature contradicts with what can be expected for direct bandgap semiconductors. The recent study of Wang and coworkers have resolved this controversy to some extent.[181] As can be see from Fig. 18, in addtion to the pronounced peak, there is a shoulder both in the photoluminescence (PL) emission and optical

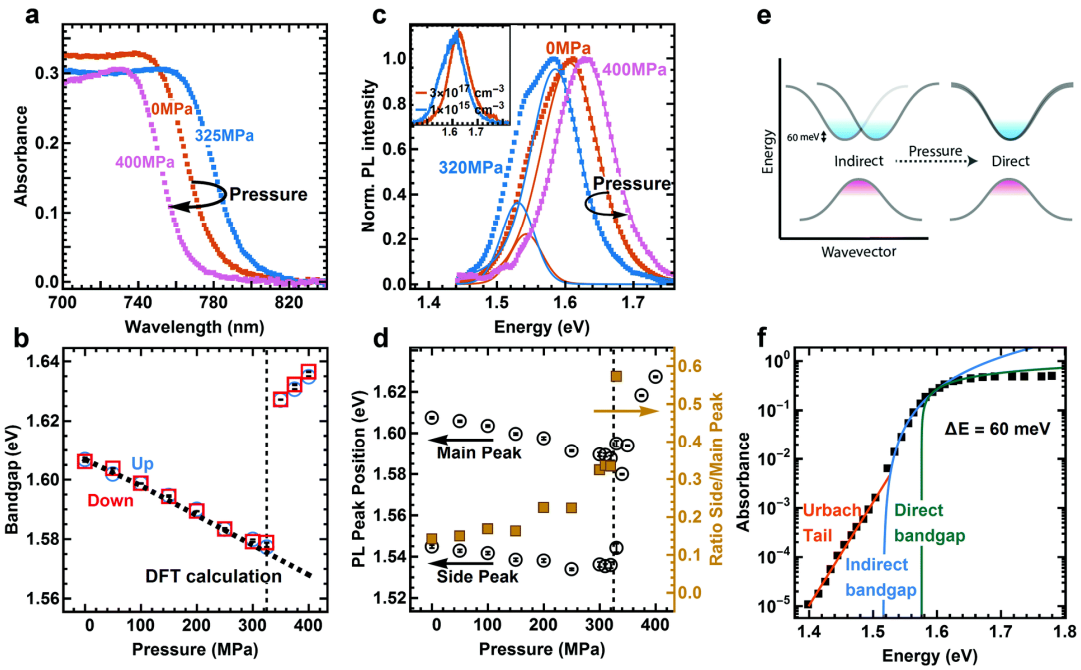

Fig. 18: Absorbance and steady state photoluminescence (PL) spectral features of lead triiodide perovskite at different pressures.[181] **a**) Absorbance spectra at three characteristic pressures. **b**) Change of the direct bandgap under pressure for pressure up (blue circles) and down (red squares) stroke. DFT calculations (dashed line) predict the bandgap change before phase transition. Black bars inside symbols represent the error from the fit. **c**) PL spectra and fits at three different pressures. At pressures below phase transition (325 MPa) the PL fit requires two peaks while above the phase transition only one peak suffices. The insert shows PL spectra at different excitation densities under ambient pressure. **d**) Position of main and side peak as extracted from fit to PL data. The ratio of side to main peak intensity increases with rising pressure. **e**) Schematics of band structure, showing direct and indirect transition showing their change with pressure. **f**) PDS data from literature fit with an exponential Urbach tail (orange) and indirect (blue) and direct (green) bandgaps.

absorption spectra. For instance, the dominant emission peak is located around 1.61 eV, with the side emission peaks around 1.55 eV. This latter peak disappears at high excitation densities. While many previous studies do not resolve this side peak in their observed spectra, thereby led to many controversial discussions noted above. Nevertheless, it has been demonstrated that the

main peak is the consequence of band-to-band recombination, whereas the side peak is speculated as the possible origin of photo-assisted recombination and exciton-photon interaction.

Using periodic density functional theory calculations,[181-182] it has been demonstrated that $CH_3NH_3PbI_3$ display both direct and indirect bandgaps in the cubic phase. The nature of this transition is controlled by changing orientation of the B-site cation inside the pseudocubic cage. In particular, and according to Motta and coworkers,[182] when the B-site cation was orientationally aligned along the [111] (corner facing) direction, the bandgap was *direct*, which measures at 1.423 eV (871 nm). The absorption peak then increases monotonically from that value, showing possibility of *direct* transitions across the band edges. By contrast, when $CH_3NH_3^+$ was orientationally aligned along the [011] (edge facing) direction, the calculated bandgap was *indirect*. Yet surprisingly, these authors have noted further that for the [011] orientation of the cation, they found the bandgap to be indirect at 1.629 eV (761 nm) and direct at 1.611 eV (769 nm). This latter result was consistent with the two-step absorption profile, with a small absoption amplitude developing at the band edge followed by a significantly more pronounced increase at around 750 nm. This reflects the indirect nature of the bandgap, which might be triggered by phonons.

The presence of an indirect bandgap can be readily understood from the band structure of the material provided the effect of spin orbit coupling is taken into account. As such, and as will be discussed in Chapter 7, there is a small displacement of the conduction band minimum in the momentum space with respect to the high symmetry R point. This suggests the rapid relaxation of the photoexcited electrons to the conduction band minimum is still possible. This process is suggested to be incoherent, [182] which is mediated by acoustic phonons and spontaneous exciton separation into free charge carriers. The direct-to-indirect bandgap transition explains the reason behind the extended carrier lifetime, although it is still topic of discussion since the unlying phenomena is not fully understood. Nevertheless, because the exact position of the the conduction band edge depends on the particular spatial arrangement of the B-site cation, thereby $CH_3NH_3PbI_3$ has been suggested as a dynamical bandgap semicounductor.[182] The same argument is applicable to $CH_3NH_3PbBr_3$ and so on.

1.5.6 Nature of carriers in lead triiodide perovskite semiconductor

Of significant interest is whether the excitonic states can be populated in the room temperature. What are the nature of charge carriers in different temperature phases of the $MAPbI_3$ system? In other words, whether in photogenerated species in $MAPbI_3$ feature strong excitonic character or are better described as free charge-carrier densities.[181-185] Despite many viewed appeared in the literature, they all differ from one another, showing the underlying chemistry is totally in the dark state.

Hutter et al.[185] have pointed that in the low temperature orthorhombic phase, both excitons and free charge carriers decay via fast non-radiative recombination pathways, which

competes effectively with charge carrier generation. In the tetragonal phase, an energetic barrier exists for the second-order and band-to-band recombination between mobile electrons of the conduction band and holes of the valence band. Accordingly, it was suggested that in the latter phase dark states are present, which are located below the optically accessible conduction band edge and are not indifferent from shallow traps. This means if, for instance, electrons were immobilized in shallow traps, the generation yield of free mobile conduction band electrons should be enhanced with i) increasing temperature, and ii) increasing charge carrier concentrations.

According to Yang et al,[186] under all excitation intensities ranging from 0.1 to 100 μJ cm^{-2}, the free charge carriers involving electrons and holes are dominant photoexcitation species, since the probability of formation of an exciton is too low. This was not so when an intermediate excitation intensity in the range 1 to 10 μJ cm^{-2} was used, since an additional recombination channel due to the formation of excitations is responsible for the PL.

Wang et al.[181] have calculated the exciton binding energy over different pressures. Their results showed that there is no change in the exciton binding energy over entire pressure range they investigated. The same conclusion was drawn when the same calculation was performed even across the phase transition, with an upper bound of a relative change of 26%. The marginal changes are suggested unlikely to result in a five-fold decrease in the charge carrier lifetime and a two-fold increase in photoluminescence quantum yield. This result might not be in line with the general believe that excitons in perovskites stabilize the excited state.

While $MAPbI_3$ in the tetragonal phase has known have a direct bandgap, Hutter et al.[185] have found this to be direct-indirect nature. It thereby explains why the recombination is enhanced with increasing temperature. This attribute is in constrast with GaAs semiconductor that has a direct bandgap, in which case the second order recombination rate is proportional to $T^{-1.7}$.

Phuong and coworkers[183] have suggested that there will be fast charge transfer from the orthorhombic to the tetragonal phase. This might explain why it should be likely to consider that this will suppress the formation of excitons in the orthorhombic phase. These authors then sugegsted the near-band-edge optical responses of the photocarriers in both the tetragonal and orthorhombic phases of the $MAPbI_3$ thin films can be more accurately described by a free-carrier model, rather than an excitonic model even at low temperatures.

It is generally understood that an incident photon on the perovskite material results in the creation of charge carriers in the form of free electrons and holes. A direct intrinsic (vertical) transition involves the excitation of electrons from the fully occupied valence band to the unoccupied conduction band of the material. On the other hand, when the transition is indirect the photo excitation of electrons of the valence band is possible, but this must be through the involvement of lattice phonons. These low-energy phonons are coupled with the rotation of the organic cations, which explain the spatial shift of the conduction band minimum to a different

location. As the temperature is raised, there can be more phonons, which cause enhancement of indirect recombination (called non-radiative recombination). Both the direct and indirect features of the bandgap of the halide perovskite material explain the broadening of the observed (emission) spectrum,[181] see Fig. 18. These also explain the enhanced life time of the charge carriers.

1.6 Outline of the Thesis

This thesis comprises eight chapters. It is structured as follows.

Except this chapter, the remaining chapters (2 to 7) has its own introduction, calculation details, results and discussion, conclusion and reference sections. Chapters 2 and 3 discuss the electronic structures and properties of a selected number of molecular cluster systems, which are either experimentally known, or theoretically proposed, to enhance the current understanding on a class of noncovalent interactions. These involve halogen-centered noncovalent bonding interactions (especially those involving fluorine), as well as π—π interactions. Chapters 3-to-6 discuss the electronic structure results of a series of dimers and oligomers of molecular lead triiodide perovskites in 0D and 1D, respectively. In specific, these studies consider metal coordinated halides as a kind of universal hydrogen bond accepting materials, and show that they have significant implications in functional materials design. The importance of the novel chemical binding topologies, the roles of both additive and non-additive cooperative effects, the inter-molecular ground state charge transfers and the binding energies on the formations and stabilities of various clustered configurations of $MAPbI_3$ is considered. Using these features as potential backgrounds, the physical chemistry and optoelectronic properties of a series of new trihalide perovskite systems, NH_3XMY_3, are discussed and proposed in Chapter 7. Thus to be more specific:

Chapter 1 deals with the general introduction of the thesis, including motivation, importance, chemical terminologies, and scientific interests to the subject matter.

Chapter 2 provides rigorous insights into the physical chemistry of $F^{\delta-}\cdots F^{\delta-}$ intermolecular synthon. For this purpose, perfluorobenzene (C_6F_6) was selected as a model compound, and have performed extensive density functional theory investigations on a number of its homomolecular dimers, trimers, and tetramers. Of the twelve $(C_6F_6)_2$ dimers investigated, a displaced-parallel arrangement was found to be the most stable. Besides, the ΔE for a minimum-energy least stable conformation of the same dimer, which involves a single $\sigma_{hole}(-)\cdots\sigma_{hole}(-)$ type $F^{\delta-}\cdots F^{\delta-}$ intermolecular bonding interaction, is amounted to –0.62, in agreement with the experimental identification of similar interactions in the solid state. Passing from this latter dimer to an analogous $(C_6F_6)_3$ trimer, as well as that from the trimer to an analogous $(C_6F_6)_4$ tetramer, we noticed windmill-type $F^{\delta-}\cdots F^{\delta-}$ intermolecular topologies causing these clusters to be stable. Because of this, we have noticed a preferential increase in the value of ΔE from –0.94 (dimer) to

–2.76 (trimer) to –4.49 kcal mol^{-1} (tetramer), thereby suggesting the presence of cooperative binding. An energy decomposed analysis has revealed that dispersion and polarization are the principal driving forces bringing the C_6F_6 molecules together in complex configurations, cause the attraction between two negative sites happening. The results of the quantum theory of atoms in molecules based source function analysis has suggested that the fully negatively charged fluorine atoms in C_6F_6 serve as sinks for the formations of the $F^{\delta-}\cdots F^{\delta-}$ bonding interactions.

Chapter 3 presented the possibility of formation of attractive intermolecular interactions between various entirely negative sites localized on a variety of atoms in molecules, leading to the formation of the thirteen isolated dimers investigated. Each of these dimers is formed upon the engagement of the totally negatively charged covalently bound fluorine in perfluorobenzene (C_6F_6) with the similarly negatively charged atoms in each of the nine Lewis bases opted, e.g., water (H_2O), ammonia (NH_3), hydrogen fluoride (HF), formaldehyde (H_2CO), fluoromethane (H_3CF), and fully fluorinated pyridine (C_5F_5N), pyrimidine ($C_4F_4N_2$), pyrazine ($C_4F_4N_2$), and pyridazine ($(CF)_4N_2$). The calculated binding energies and intermolecular contact distances for these dimers were found close to what might have envisaged for any weakly bound dimers, viz. the dimers of alkanes and polyhedranes, which involve the $C–H\cdots H–C$ dihydrogen contacts with the dissociation energies in the 0.52–12.38 kJ mol^{-1} range (Nat. Chem. 2011, 3, 323). The topological charge density results obtained upon application of quantum theory of atoms in molecules and reduced density gradient noncovalent interaction tools to the static geometries of all the thirteen dimers have enabled us to demonstrate that the $O^{\delta-}\cdots F^{\delta-}$, $F^{\delta-}\cdots F^{\delta-}$, and $N^{\delta-}\cdots F^{\delta-}$ intermolecular interactions revealed are closed-shell type. The (negative) signs and magnitudes of the local most minima and maxima of electrostatic potential calculated on the surfaces of the ten monomers examined do not support the above possibilities of attraction between the entirely negative sites, thereby witnessing limitation of the model.

Chapter 4 deals with the electronic structure and properties of the $CH_3NH_3PbI_3$ molecular building block in its conformational space. In particular, it has summarized the DFT-M06-2X/ADZP based geometrical, electronic, topological, and orbital properties of four $CH_3NH_3PbI_3$ blocks. These clusters are shown to be unusually strongly bound, with binding energies are much larger than medium-to-strongly bound intermolecular interaction documented in the literature, thereby enabled us to classify the newly identified interactions as *ultra-strong* type. Based on this, together with the unusually high charge transfers, strong hyperconjugative interactions, sophisticated topologies of the charge density, and short intermolecular distances uncovered, we have ranked the molecular $CH_3NH_3PbI_3$ perovskites as Mulliken inner complexes. Additionally, the consequences of these, as well as of the *ultra-strong* interactions, in the light of designing novel functional nanomaterials are outlined.

Chapter 5 deals with the results of the first-principles density functional theory electronic structure calculations of the zero-dimensional $MAPbI_3$ building block, and the one-dimensional $[MAPbI_3]_{n=2-15}$ nanocluster chains. This chapter, firstly, demonstrated that the orthorhombic

geometry of the system that was found to be the most stable in solid state is also likely to be stable in the gas phase. Secondly, it showed that the organic cation plays a significant role as an additive for the 1D growth of the $MAPbI_3$ material and beyond, a result which is in agreement with the experimental rationalizations. Thirdly, it introduced that the large-scale supramolecular structure emerged of the $MAPbI_3$ molecular building block is the consequence of the non-additive cooperative binding phenomena, which is strongly synergistic. All these attributes are drawn by exploiting the equilibrium structures, intermolecular hydrogen bonding interactions, energy landscapes (binding energies), and electronic and orbital properties (dipole moment, polarizability, and HOMO-LUMO gap, etc.) of the $[MAPbI_3]_{n=1-15}$ nanoclusters in zero- and one-dimensions.

Chapter 6 deals with the mechanisms of the ground state charge transfer for two classes of perovskite solar cell systems. Specifically, the molecular building blocks and 1D nanoclusters of the methylammonium and cesium lead triiodide hybrid organic-inorganic and inorganic-inorganic perovskite solar cell semiconductors have considered. It is showed using the results of the density functional theory first-principles studies on the $[MAPbI_3]$ and $[CsPbI_3]$ perovskite blocks in zero-dimension, as well as on the $[MAPbI_3]_{n=2–15}$ and $[CsPbI_3]_{n=2–10}$ nanocluster chains in one-dimension, that the equilibrium geometries of these systems evolve with the same principles of intermolecular charge transfers in their respective ground electronic states. A simplified model of charge rearrangement was used to view the charge transfer pathways as a combination of three independent mechanisms occurring separately. The first one involves within PbI_3^- (indirect), and the other two facilitates between PbI_3^- and $CH_3NH_3^+$ through intermolecular and super-exchange mechanisms, accompanying the formations of the $[MAPbI_3]_{n=1–15}$ cluster chains. Similar charge transfers mechanisms are found to operate between PbI_3^- and Cs^+, accompanying the formations of the $[CsPbI_3]_{n=1–10}$ cluster chains. The results obtained in this study show that atomic charge is not only an elegant property, but also its quantification with appropriate theoretical methods can be superb for the fundamental understanding of many physical processes in chemistry, physics, biology, materials, and supramolecular systems.

Chapter 7 deals with the results of the density functional and coupled cluster electronic structure studies of a few trihalide perovskite systems. These include the $CH_3NH_3PbY_3$, $CsPbY_3$, $CH_3NH_3SnY_3$ and $CsSnY_3$ cluster series, each comprising ten members, where $Y = I_{(3-x)}Br_{x=1–3}$, $I_{(3-x)}Cl_{x=1–3}$, $Br_{(3-x)}Cl_{x=1–3}$, and IBrCl. The latter part of this Chapter unravels the relationship between the experimental bandgap (solid) and the DFT-calculated binding energy (gas) for the first time for each of the four perovskite semiconductor series. Through the understanding of the gas phase physical chemistry of these systems, it was possible to predict a set of new competitors for $CH_3NH_3PbY_3$, $CsPbY_3$, $CH_3NH_3SnY_3$ and $CsSnY_3$. Specifically, a series of low bandgap systems, NH_3XPbY_3 and NH_3XSnY_3 (X = F, Cl, Br, I), were calculated to be stable both in the gas and solid phases. Several of these are found to have direct bandgaps in the orthorhombic and pseudocubic phases, analogous with those observed for the $MAPbI_3$ semiconductor. Based on the

nature of the bandgap and other electronic properties, it was possible to propose that some of these new materials might be ideal for application in photovoltaic solar cells.

Chapter 8 deals with the general conclusion and future directions.

1.7 References

1. R. Perez, M. Perez, A fundamental look at energy reserves for the planet; this document is available at: http://www.asrc.albany.edu/people/faculty/perez/Kit/pdf/a-fundamental-look-at%20the-planetary-energy-reserves.pdf; Also see at: https://www.iea-shc.org/data/sites/1/publications/2009-04-SolarUpdate.pdf (last retrieved on March 15, 2017).
2. S. Heckeroth, Renewables.com, adapted from Christopher Swan (1986): Sun Cell, Sierra Club Press
3. C. Archer and M. Jacobson, Evaluation of Global Wind Power -- Stanford University, Stanford, CA
4. 3. World Energy Council
5. 4. G. Nihous, An Order-of-Magnitude Estimate of Ocean Thermal Energy Conversion (OTEC) Resources, Journal of Energy Resources Technology -- December 2005 -- Volume 127, Issue 4, pp. 328-333
6. R. Whittaker (1975): The Biosphere and Man -- in Primary Productivity of the Biosphere. Springer-Verlag, 305-328. ISBN 0-3870-7083-4.
7. Environmental Resources Group, LLC, http://www.erg.com.np/hydropower_global.php, MIT/INEL, The Future of Geothermal Energy-- Impact of Enhanced Geothermal Systems [EGS] on the U.S. in the 21st Century, http://www1.eere.energy.gov/geothermal/egs_technology.html -- based on estimated energy recoverable economically in the next 50 years. Ultimate high depth potential would be much higher.
8. https://www.bp.com/content/dam/bp/pdf/energy-economics/statistical-review-2016/bp-statistical-review-of-world-energy-2016-full-report.pdf
9. WISE Uranium Project (Uranium supply and demand), this is available at: http://www.wise-uranium.org/stk.html?src=stkd03e
10. R. Price, J.R. Blaise (2002): Nuclear fuel resources: Enough to last? NEA updates, NEA News 2002 – No. 20.2
11. Solar energy received by emerged continents only, assuming 65% losses by atmosphere and clouds
12. US Energy Information Administration, Monthly Energy Review, http://www.eia.gov/totalenergy/data/monthly/ (last retrieved on March 15, 2017).
13. F. Rui, Z. WenJun, Z. ShaSha, C. Wei, The rising star in photovoltaics-perovskite solar cells : The past, present and future SCIENCE CHINA Technological Sciences 2016, 59, 989-1006(2016); 10.1007/s11431-016-6056-8.
14. E. Becquerel, Mémoire sur les effets électriques produits sous l'influence des rayons solaires". Comptes Rendus, 1839, 9, 561–567.
15. E. Becquerel, Mémoire sur le rayonnement chimique qui accompagne la lumière solaire et la lumière électrique", Comptes Rendus, 1840, 11, 702–703.
16. E. Becquerel, L'image photographique colorée du spectre solaire", Comptes Rendus 1848, 26, 181–183.
17. Photovoltaic Research, National Renewable Energy Laboratory (NREL), https://www.nrel.gov/pv/ (last retrieved on March 15, 2017); Also, see at : https://www.nrel.gov/pv/assets/images/efficiency-chart.png.
18. J. M. Frost, K. T. Butler, F. Brivio, C. H. Hendon, M. Van Schilfgaarde, A. Walsh, 2014. Atomistic origins of high-performance in hybrid halide perovskite solar cells. Nano Letters, 14, 2584-2590.
19. E. Jónsson, P. Johansson, Modern battery electrolytes: ion-ion interactions in Li+/Na+ conductors from DFT calculations, Phys. Chem. Chem. Phys. 2012, 14, 10774-9.

20. A. K. Chilvery, A. K. Batra, B. Yang, K. Xiao, P. Guggilla, M. D. Aggarwal, R. Surabhi, R. B. Lal, J. R. Currie, B. G. Penn, Perovskites: transforming photovoltaics, a mini-review, J. Photon. Energy. 5(1), 057402 (Jan 06, 2015). doi:10.1117/1.JPE.5.057402.
21. W.-J. Yin, J.-H. Yang, J. Kang, Y. Yan, S.-H. Wei, Halide perovskite materials for solar cells: a theoretical review, J. Mater. Chem. A, 2015, 3, 8926-8942.
22. J. Yana, B. R. Saunders, Third-generation solar cells: a review and comparison of polymer: fullerene, hybrid polymer and perovskite solar cells, RSC Adv., 2014,4, 43286-43314.
23. Third-generation photovoltaic cell From Wikipedia, the free encyclopedia (Redirected from Third generation photovoltaic cell). This document is available via: https://en.wikipedia.org/wiki/Third-generation_photovoltaic_cell (last retrieved on July 17, 2017).
24. G. Conibeer, Third-generation photovoltaics, materialstoday 2007, 10, 42 – 50.
25. S. Sharma, K. K. Jain, A. Sharma, Solar Cells: In Research and Applications—A Review. Materials Sciences and Applications 2015, 6, 1145-1155.
26. O. E.Semonin, J. M. Luther, M. C. Beard, Quantum dots for next-generation photovoltaics, materialstoday, 15, 2012, 508-515.
27. Y. Xu, T. Gong, J. N. Munday, The generalized Shockley-Queisser limit for nanostructured solar cells, Sci. Rep. 2015, 5, 13536, doi:10.1038/srep13536.
28. R. Fang, W. Jun, Z. Sha, S. Zhang, W. Chen, The rising star in photovoltaics-perovskite solar cells: The past, present and future, Science China Technological Sciences 2016, 59, 989–1006.
29. Q.-Y. Xu, D.-X. Yuan, H.-R. Mu, F. Igbari, Q. Bao, L.-S. Liao, Efficiency enhancement of perovskite solar cells by pumping away the solvent of precursor film before annealing, Nanoscale Research Letters, 2016, 11, 248.
30. C. C. Stoumpos, M. G. Kanatzidis, Halide Perovskites: Poor Man's High-Performance Semiconductors, Adv Mater. 2016, 28, 5778-93.
31. Q. Lin, A. Armin, P. L. Burn, P Meredith, Organohalide perovskites for solar energy conversion, Chem. Res. 2016, 49, 545–553.
32. X. Zhu, The Perovskite Fever and Beyond, Acc. Chem. Res. 2016, 49, 355-6.
33. Organometal halide perovskite solar cells: degradation and stability, T. A. Berhe, *et al.*, Energy Environ. Sci., 2016, 9, 323-356.
34. J.-W. Lee, Y.-T. Hsieh, N. De Marco, S.-H. Bae, Q. Han, Y. Yang, Halide perovskites for tandem solar cells, J. Phys. Chem. Lett., 2017, 8, 1999–2011.
35. A. S. Mahadevi, G. N. Sastry, Cooperativity in Noncovalent Interactions, Chem. Rev. 2016, 116, 2775–2825.
36. P. Gilli, G. Gilli, Noncovalent Interactions in Crystals, Supramolecular Materials Chemistry, DOI: 10.1002/9780470661345.smc110, 2012 John Wiley & Sons, Ltd.
37. P. Hobza, J. Řezáč, Introduction: Noncovalent Interactions, Chem. Rev., 2016, 116, 4911–4912.
38. C. Sutton, C. Risko, J.-L. Brédas, Noncovalent intermolecular interactions in organic electronic materials: Implications for the molecular packing vs electronic properties of acenes, Chem. Mater. 2016, 28, 3–16.
39. E. D. Głowacki, M. I.-Valdu, S. Bauer, N. S. Sariciftci, Hydrogen-bonds in molecular solids – from biological systems to organic electronics, J. Mater. Chem. B, 2013, 1, 3742-3753.
40. E. Frieden, Non-covalent interactions: Key to biological flexibility and specificity, J. Chem. Educ. 1975, 52, 754.
41. J. R. Cox, Teaching Noncovalent Interactions in the Biochemistry Curriculum through Molecular Visualization: The Search for pi Interactions, J. Chem. Educ., 2000, 77, 1424.
42. P. S. Murthy, Molecular Handshake: Recognition through Weak Noncovalent Interactions, J. Chem. Educ. 2006, 83, 1010.
43. P. Zhou, J. Huang, F. Tian, Specific noncovalent interactions at protein-ligand interface: implications for rational drug design, Curr. Med. Chem. 2012, 19, 226-38.

44. G. O. Wilson, M. M. Caruso, S. R. Schelkopf, N. R. Sottos, S. R. White, J. S. Moore, Adhesion Promotion via Noncovalent Interactions in Self-Healing Polymers, *ACS Appl. Mater. Interfaces* 2011, 3, 3072–3077.
45. S. Grimme, Do Special Noncovalent π–π Stacking Interactions Really Exist? Angew. Chem. Int. Ed. 2008, 47, 3430 –3434.
46. P. Szatyłowicz, N. Sadlej-Sosnowska, Characterizing the Strength of Individual Hydrogen Bonds in DNA Base, J. Chem. Inf. Model., 2010, 50, 2151–2161.
47. C. F. Guerra, F. M. Bickelhaupt, J. G. Snijders, E. J. Baerends, Hydrogen Bonding in DNA Base Pairs: Reconciliation of Theory and Experiment, J. Am. Chem. Soc. 2000, 122,4117-4128.
48. L. G. M. Pettersson, *et al.*, Electronic structure effects from hydrogen bonding in the liquid phase and in chemisorption: an integrated theory and experimental effort, J. Synchrotron Rad. 2001, 8, 136–140.
49. P. A. Kollman, L. C. Allen, Theory of the Hydrogen Bond: Electronic Structure and Properties of the Water Dimer View, J. Chem. Phys. 1969, 51, 3286.
50. X. Guo, *et al.*, Materials design via optimized intramolecular noncovalent interactions for high-performance organic semiconductors, Chem. Mater. 2016, 28, 2449–2460.
51. Non-covalent Interactions in the Synthesis and Design of New Compounds, A. M. Maharramov (Editor), K. T. Mahmudov (Editor), M. N. Kopylovich (Editor), A. J. L. Pombeiro (Editor), ISBN: 978-1-119-10989-1, 480 pages, 2016.
52. G. R. Desiraju, T. Steiner, The weak hydrogen bond: In structural chemistry and biology, Oxford University Press: Oxford and New York. 1999.
53. G. R. Desiraju, Hydrogen Bridges in Crystal Engineering: Interactions without Borders, *Acc. Chem. Res*. 2002, 35, 565–573.
54. G. A. Jeffrey, W. Saenger, Hydrogen Bonding in Biological Structures; Springer: Berlin, Germany, 1991.
55. G. A. Jeffrey, An introduction to hydrogen bonding, Oxford University Press: New York, 1997.
56. T. Steiner, The Hydrogen Bond in the Solid State, *Angew Chem. Int. Edn.* 2002, 41, 48 – 76.
57. G. Gilli, P. Gilli, The Nature of the Hydrogen Bond; Oxford University Press Inc.: New York, NY, USA, 2009.
58. S. Scheiner, Hydrogen Bonding a Theoretical Perspective; Oxford University Press Inc.: New York, NY, USA, 1997.
59. S. J. Grabowski, Ed.; Hydrogen Bonding—New Insights; Springer: Dordrecht, The Netherlands, 2006.
60. H. Szatyłowicz, Structural aspects of the intermolecularhydrogen bond strength: H-bondedcomplexes of aniline, phenol andpyridine derivatives, *J. Phys. Org. Chem*.2008, 21 897–914.
61. L. Pauling, The nature of the chemical bond and the structure of molecules and crystals: A introduction to modern structural chemistry, 3rd Edn, Cornell University Press, 1960.
62. S. J. Grabowski, Hydrogen Bonding - New Insights, Springer, 2006, ISBN: 978-1-4020-4852-4 (Print) 978-1-4020-4853-1 (Online).
63. T. Clark, M. Hennemann, J. S. Murray, P. Politzer, Halogen bonding: The σ-hole. *J. Mol. Model*. 2007, *13*, 291–296.
64. J. S. Murray, P. Lane, T. Clark, P. Politzer, P. σ-hole bonding: Molecules containing group VI atoms. *J. Mol. Model*. 2007, *13*, 1033–1038.
65. P. Politzer, J. S. Murray, T. Clark, Halogen bonding and other σ-hole interactions: A perspective, *Phys. Chem. Chem. Phys*. 2013, *15*, 11178–11189.
66. P. Politzer, J. S. Murray, T. Clark, Halogen bonding: An electrostatically-driven highly directional noncovalent interaction, *Phys. Chem. Chem. Phys.* 2010, 12, 7748–7757.
67. P. Politzer, J. S. Murray, Halogen bonding: An interim discussion. *Chem. Phys. Chem.* 2013, 14, 278–294.
68. W. Wang, B. Ji, Y. Zhang, Chalcogen Bond: A Sister Noncovalent Bond to Halogen Bond, China J. Phys. Chem. A, 2009, 113, 8132–8135.

69. M. E. Brezgunova, *et al.*, Chalcogen bonding: experimental and theoretical determinations from electron density analysis. Geometrical preferences driven by electrophilic–nucleophilic interactions. Crystal Growth Des. 2013, 13, 3283–3289.
70. P. C. Ho, P. Szydlowski, J. Sinclair, P. J. W. Elder, J. Kübel, C. Gendy, L. M. Lee, H. Jenkins, J. F. Britten, D. R. Morim, I. Vargas-Baca, Supramolecular macrocycles reversibly assembled by Te…O chalcogen bonding, Nat. Commun. 2016, 7, 11299.
71. S. Scheiner, Sensitivity of noncovalent bonds to intermolecular separation: hydrogen, halogen, chalcogen, and pnicogen bonds, CrystEngComm. 2013, 15, 3119–3124.
72. S. Sarkar, M. S. Pavan, T. N. G. Row, T. N. G. Experimental validation of 'pnicogen bonding' in nitrogen by charge density analysis. *Phys. Chem. Chem. Phys.* 2014, 17, 2330–2334.
73. D. Mani, E. Arunan, The X–C···Y (X = O/F, Y = O/S/F/Cl/Br/N/P) 'carbon bond' and hydrophobic interactions, Phys Chem Chem Phys. 2013, 15, 14377-83.
74. P. R. Varadwaj, A. Varadwaj, B. Y. Jin, Significant evidence of C···O and C···C long-range contacts in several heterodimeric complexes of CO with CH_3–X, should one refer to them as carbon and dicarbon bonds! *Phys. Chem. Chem. Phys.* 2014, 16, 17238.
75. S. J. Grabowski, Tetrel bond–σ-hole bond as a preliminary stage of the SN_2 reaction, Phys. Chem. Chem. Phys., 2014, 16, 1824-1834.
76. Cooperativity in Tetrel Bonds, M. Marín-Luna, I. Alkorta, J. Elguero, J. Phys. Chem. A, 2016, 120, 648–656.
77. A. Bauzá, T. J. Mooibroek, A. Frontera, Tetrel Bonding Interactions, Chem. Rec. 2016, 16, 473-87.
78. A. Bauzá, T. J. Mooibroek, A. Frontera, Tetrel bonding interaction: Rediscovered supramolecular force? Angew. Chem. Int. Ed. 2013, 52, 12317 –12321.
79. F. Wang, J. Graetz, M. S. Moreno, C. Ma, L. Wu, V. Volkov, Y. Zhu, Chemical distribution and bonding of lithium in intercalated graphite: Identification with optimized electron energy loss spectroscopy, ACS Nano, 2011, 5, 1190–1197.
80. A. Shahia, E. Arunan, Hydrogen bonding, halogen bonding and lithium bonding: an atoms in molecules and natural bond orbital perspective towards conservation of total bond order, inter- and intra-molecular bonding, Phys. Chem. Chem. Phys. 2014,16, 22935-22952.
81. C. R. Groom, I. J. Bruno, M. P. Lightfoot and S. C. Ward, Acta Cryst. 2016, B72, 171-179.
82. S. Kawai, *et al.*, Van der Waals interactions and the limits of isolated atom models at interfaces, Nat. Commun. 2016, 7, 11559.
83. M. Muruganathan, J. Sun, T. Imamura, H. Mizuta, Electrically Tunable van der Waals Interaction in Graphene–Molecule Complex, *Nano Lett.*, **2015**, *15*, 8176–8180.
84. A. C. Legon, Tetrel, pnictogen and chalcogen bonds identified in the gas phase before they had names: a systematic look at non-covalent interactions, Phys. Chem. Chem. Phys. 2017, 19, 14884-14896.
85. R. C. Wade, P. J. Goodford, The role of hydrogen-bonds in drug binding, Prog. Clin. Biol. Res. 1989, 289, 433-44.
86. B. Kuhn, P. Mohr, M. Stahl, Intramolecular Hydrogen Bonding in Medicinal Chemistry, J. Med. Chem. 2010, 53, 2601–2611.
87. Thomson Reuters Web of Science, The most comprehensive and versatile research platform. This is available at: https://webofknowledge.com/ (last retrieved on July 17, 2017).
88. E. Arunan, Definition of the hydrogen bond, http://ipc.iisc.ernet.in/~arunan/iupac/iupac/Definition_of_HydrogenBond.pdf (last retrieved on July 17, 2017).
89. E. Arunan, G. R. Desiraju, R. A. Klein, J. Sadlej, S. Scheiner, I. Alkorta, D. C. Clary, R. H. Crabtree, J. J. Dannenberg, P. Hobza, H. G. Kjaergaard, A. C. Legon, B. Mennucci, D. J. Nesbitt, Definition of the hydrogen bond (IUPAC Recommendations 2011), Pure Appl. Chem. 2011, 83, 1637–1641, 2011.

90. G. R. Desiraju, *et al.*, Definition of the halogen bond (IUPAC Recommendations 2013), *Pure Appl. Chem.* 2013, 85, 1711-1713.
91. C. J. Laconsay. J. M. Galbraith, A valence bond theory treatment of tetrel bonding interactions, Computational and Theoretical Chemistry 2017, https://doi.org/10.1016/j.comptc.2017.02.017.
92. J. E. Del Bene, I. Alkorta, J. Elguero, Carbenes as Electron-Pair Donors for P···C Pnicogen Bonds, ChemPhysChem 2017, 18, 1597–1610.
93. C. Trujillo, G. Sánchez-Sanz, I. Alkorta, J. Elguero, Halogen, chalcogen and pnictogen interactions in $(XNO_2)_2$ homodimers (X = F, Cl, Br, I).
94. Surface electrostatic potentials of halogenated methanes as indicators of directional intermolecular interactions, T. Brinck, J. S. Murray, P. Politzer Int. J. Quantum Chem. 1992, 44, 57-64.
95. P. R. Varadwaj, A. Varadwaj, B.-Y. Jin, Halogen bonding interaction of chloromethane with several nitrogen donating molecules: addressing the nature of the chlorine surface σ-hole, Phys. Chem. Chem. Phys. 2014,16, 19573-19589.
96. K. Eskandari, H. Zariny, Halogen bonding: A lump–hole interaction. Chem. Phys. Lett. 2010, 492, 9-13.
97. D. J. Duarte, N. M. Peruchena, I. Alkorta, Double Hole-Lump Interaction between Halogen Atoms, J. Phys. Chem. A. 2015, 119, 3746-52.
98. P. Panini, D. Chopra, P. Panini, D. Chopra, Understanding of noncovalent interactions involving organic fluorine, Chapter 2, Z. Li and L. Wu (eds.), Hydrogen Bonded Supramolecular Structures, Lecture Notes in Chemistry 87, DOI 10.1007/978-3-662-45756-6_2, Springer-Verlag Berlin Heidelberg 2015.
99. M. J. Vallejos, P. Auffinger, P. Shing Ho, in Halogen interactions in biomolecular crystal structures, in: International Tables of Crystallography, Volume F, ed. D. M. Himmel and M. G. Rossman, Wiley, Hoboken, NJ, 2nd Edn, Ch 23.6, 2012.
100. J. A. K. Howard, V. J. Hoy, D. O'Hagan, G. T. Smith, How good is fluorine as a hydrogen bond acceptor? *Tetrahedron* 1996, 56, 12613-12622.
101. H. -J. Schneider, Hydrogen bonds with fluorine. Studies in solution, in gas phase and by computations, conflicting conclusions from crystallographic analyses, *Chem. Sci.* 2012, 3, 1381-1394.
102. G. Cavallo, P. Metrangolo, R. Milani, T. Pilati, A. Priimagi, G. Resnati, G. Terraneo, The halogen bond, *Chem. Rev.* 2016, 116, 2478–2601.
103. P. R. Varadwaj, A. Varadwaj, B.-Y. Jin, Hexahalogenated and their mixed benzene derivatives as prototypes for the understanding of halogen···halogen intramolecular interactions: New insights from combined DFT, QTAIM-, and RDG-based NCI analyses, J. Comput. Chem. 2015, 36, 2328–2343.
104. M. Chowdhury, B. M. Kariuki, Supramolecular Assembly in Cinnamate Structures: The Influence of the Ammonium Ion and Halogen Interactions, Crystal Growth & Design, 2006, 6, 774–780.
105. L. Catalano, *et al.*, Dynamic Characterization of Crystalline Supramolecular Rotors Assembled through Halogen Bonding, J. Am. Chem. Soc. 2015, 137, 15386–15389.
106. X. Ding, M. Tuikka, M. Haukka, Halogen Bonding in Crystal Engineering, 2012, DOI: 10.5772/48592 (http://dx.doi.org/10.5772/48592).
107. C. B. Aakeröy, *et al.*, A systematic structural study of halogen bonding versus hydrogen bonding within competitive supramolecular systems, IUCrJ. 2015, 2, 498–510.
108. a) R. H. Mitchell, M. D. Welch, A. R. Chakhmouradian, Nomenclature of the perovskite supergroup: A hierarchical system of classification based on crystal structure and composition, Mineralogical Magazine 2017, DOI: 10.1180/minmag.2016.080.156; b). X-G. Zhao, *et al.*, Design of Lead-Free Inorganic Halide Perovskites for Solar Cells via Cation-Transmutation, J. Am. Chem. Soc., 2017, 139, 2630–2638.
109. K. Kojima, Y. Teshima, Y. Shirai, T. Miyasaka, Organometal halide perovskites as visible-light sensitizers for photovoltaic cells, *J. Am. Chem. Soc.* 2009, 131, 6050-6051.
110. M. M. Lee, J. Teuscher, T. Miyasaka, T. N. Murakami, H. J. Snaith, Efficient hybrid solar cells based on meso-superstructured organometal halide perovskites, *Science* 2012, 338, 643–647.

111. S. D. Stranks, H. J. Snaith, Metal-halide perovskites for photovoltaic and light-emitting devices, *Nat. Nanotech.* 2015, 10, 391–402.
112. O. B. Boggild, Crystalline form and twin formations of cryolite, perovskite and boracite, ZEITSCHRIFT FUR KRYSTALLOGRAPHIE UND MINERALOGIE 1911, 50, 349-429.
113. J. L. Minns, *et al.*, Structure and interstitial iodide migration in hybrid perovskite methylammonium lead iodide. Nature Communications 2017, 8, 15152.
114. S. R. Raga, L. K. Ono, Y. Qi, Rapid perovskite formation by CH_3NH_2 gas-induced intercalation and reaction of PbI_2, J.Mater.Chem.A, 2016, 4, 2494–2500.
115. T. Baikie, Y. Fang, J. M. Kadro, M. Schreyer, F. Wei, S. G. Mhaisalkar, M. Graetzel, T. J. White, Synthesis and crystal chemistry of the hybrid perovskite $(CH_3NH_3)PbI_3$ for solid-state sensitised solar cell applications, J. Mater. Chem. A 2013, 1, 5628 – 5641.
116. M. Konstantakoua, T. Stergiopoulos, A critical review on tin halide perovskite solar cells, J. Mater. Chem. A, 2013, 1, 5628-5641.
117. Y. Zhao, K. Zhu, Organic–inorganic hybrid lead halide perovskites for optoelectronic and electronic applications Chem. Soc. Rev.2016, 45, 655-689.
118. B.Schröder, K.Strobel, G.Wagner, R.Geick, Spectroscopy on perovskite-type layer structures in the submillimetre-millimetre wave range, Infrared Physics, 1978, 18, 893-900.
119. A. Poglitsch, D. Weber, Dynamic disorder in methylammoniumtrihalogenoplumbates (II) observed by millimeter-wave spectroscopy, J. Chem. Phys. 1987, 87, 6373.
120. H. J. Snaith, Perovskites: The Emergence of a New Era for Low-Cost, High-Efficiency Solar Cells, J. Phys. Chem. Lett., 2013, 4, 3623–3630.
121. M. A. Green, A. Ho-Baillie, Perovskite Solar Cells: The Birth of a New Era in Photovoltaics, ACS Energy Lett. 2017, 2, 822–830.
122. S. Sik Shin, *et al.*, Colloidally prepared La-doped BaSnO electrodes for efficient, photostable perovskite solar cells, Science 2017, DOI: 10.1126/science.aam6620.
123. B. Saparov, David B. Mitzi, Organic–Inorganic Perovskites: Structural Versatility for Functional Materials Design, Chem. Rev. 2016, 116, 4558–4596.
124. M. I. Saidaminov, O. F. Mohammed, O. M. Bakr, Low-Dimensional-Networked Metal Halide Perovskites: The Next Big Thing, ACS Energy Lett. 2017, 2, 889–896.
125. S. Chakraborty, *et al.*, Rational Design: A High-Throughput Computational Screening and Experimental Validation Methodology for Lead-Free and Emergent Hybrid Perovskites, ACS Energy Lett. 2017, 2, 837–845.
126. R. F. Service, Perovskite Solar Cells Get the Lead Out, http://www.sciencemag.org/news/2014/05/perovskite-solar-cells-get-lead-out (last retrieved July 18, 2017).
127. H. L. Wells, Über die Cäsium- und Kalium-Bleihalogenide, Z. anorg. Chem. 1893, 3, 195–210. This is available via: http://onlinelibrary.wiley.com/doi/10.1002/zaac.18930030124/abstract
128. C. K. Moller, A phase transition in ceaesium plumbo-chloride. Nature 1957, 180, 981–982.
129. C. K. Møller, Crystal Structure and Photoconductivity of Cæsium Plumbohalides, Nature 1958, 182, 1436.
130. J. E. Moser, Slow recombination unveiled, Nat. Mat. 2017, 16, 4-5.
131. T. M. Burke, S. Sweetnam, K. Vandewal, M. D. McGehee, Beyond Langevin Recombination: How Equilibrium Between Free Carriers and Charge Transfer States Determines the Open-Circuit Voltage of Organic Solar Cells, Adv. Energy Mater. 2015, 1500123, DOI: 10.1002/aenm.201500123.
132. P. Langevin, The recombination and mobilities of ions in gases, Ann. Chim. Phys. 1903, 28, 433−530.
133. M. B. Johnston, L. M. Herz, Hybrid Perovskites for Photovoltaics: Charge-Carrier Recombination, Diffusion, and Radiative Efficiencies, Acc. Chem. Res., 2016, 49, 146–154.

134. Perovskite Mineral Data. This is available via: http://webmineral.com/data/Perovskite.shtml#.WXxqKoSGPIU (last retrieved July 29, 2017).
135. V. M. Golschmidt, Die Gesetze der Krystallochemie, Die Naturwissenschaften 2926, 14, 477–485. This can be available via the link: https://link.springer.com/article/10.1007%2FBF01507527 (last retrieved July 29, 2017).
136. M. Park, Critical Role of Methylammonium Librational Motion in Methylammonium Lead Iodide ($CH_3NH_3PbI_3$) Perovskite Photochemistry, Nano Lett. 2017, 17, 4151–4157.
137. F. Bi, Enhanced Photovoltaic Properties Induced by Ferroelectric Domain Structures in Organometallic Halide Perovskites, J. Phys. Chem. C 2017, 121, 11151–11158.
138. F. Giustino, H. J. Snaith, Toward Lead-Free Perovskite Solar Cells. ACS Energy Lett. 2016, 1, 1233−1240.
139. M. R. Filip, G. E. Eperon, H. J. Snaith, Fe. Giustino, Steric engineering of metal-halide perovskites with tunable optical band gaps, Nature Communications 2014, 5, 5757.
140. S. M. Liga, Components-bandgap relationships in hybrid organic-inorganic perovskites, Thesis material, 2017. This is available via: https://esc.fnwi.uva.nl/thesis/centraal/files/f1454013470.pdf ((last retrieved July 29, 2017).
141. E. L. Unger, L. Kegelmann, K. Suchan, D. Sörell, L. Korte, S. Albrecht, Roadmap and roadblocks for the band gap tunability of metal halide perovskites, J. Mater. Chem. A, 2017, 5, 11401-11409.
142. L. Wang, G. D. Yuan, R. F. Duan, F. Huang, T. B. Wei, Tunable bandgap in hybrid perovskite $CH_3NH_3Pb(Br_{3-y}X_y)$ single crystals and photodetector applications, AIP Advances 2016, 6, 045115.
143. Z. Zhang, M. Wang, L. Ren, K. Jin, Tunability of Band Gap and Photoluminescence in $CH_3NH_3PbI_3$ Films by Anodized Aluminum Oxide Templates, Sci. Rep. 2017, 7, 1918.
144. C. C. Stoumpos, L. Mao, C. D. Malliakas, M. G. Kanatzidis, Structure-Bandgap Relationships in Hexagonal Polytypes and Low Dimensional Structures of Hybrid Tin Iodide Perovskites, Inorg. Chem. 2017, 56, 56–73.
145. K.-L. Hu, M. Kurmoo, Z. Wang, S. Gao, Metal−organic perovskites: Synthesis, structures, and magnetic properties of $[C(NH_2)_3][MII(HCOO)_3]$ (M=Mn, Fe, Co, Ni, Cu, and Zn;$C(NH_2)_3$= Guanidinium), Chem. -Eur. J. 2009, 15, 12050−12064.
146. Z. Wang, P. Jain, K.-Y. Choi, J. van Tol, A. K. Cheetham, H. W. Kroto, H.-J. Koo, H. Zhou, J. Hwang, E. Sang Choi, M.-H. Whangbo, N. S. Dalal, Dimethylammonium copper formate $[(CH_3)_2NH_2]Cu(HCOO)_3$: A metal-organic framework with quasi-one-dimensional antiferromagnetism and magnetostriction, Phys. Rev. *B* 2013, 87, 224406.
147. B. Pato-Doldán, M. Sánchez-Andújar, L. C. Gómez-Aguirre, S. Yáñez-Vilar, J. López-Beceiro, C. Gracia-Fernández, A. A. Haghighirad, F. Ritter, S. Castro-García, M. A. Señarís-Rodríguez, Near room temperature dielectric transition in the perovskite formate framework, $[(CH_3)_2NH_2][Mg(HCOO)_3]$, Phys. Chem. Chem. Phys. 2012, 14, 8498-8501.
148. P. Jain, N. S. Dalal, B. H. Toby, H. W. Kroto, A. K. Cheetham, Order-disorder antiferroelectric phase transition in a hybrid inorganic-organic framework with the perovskite architecture, *J. Am. Chem. Soc.* 2008, 130, 10450.
149. P. Jain, V. Ramachandran, R. J. Clark, H. D. Zhou, B. H. Toby, N. S. Dalal, H. W. Kroto, A. K. Cheetham, Multiferroic behavior associated with an order-disorder hydrogen bonding transition in metal-organic frameworks (MOFs) with the perovskite ABX_3 architecture, *J. Am. Chem. Soc.* 2009, 131, 13625.
150. M. Mączka, A. Gągor, B. Macalik, A. Pikul, M. Ptak, J. Hanuza, Order-disorder transition and weak ferromagnetism in the perovskite metal formate frameworks of $[(CH_3)_2NH_2][M(HCOO)_3]$ and $[(CH_3)_2ND_2][M(HCOO)_3]$ (M = Ni, Mn), *Inorg Chem.* 2014, 53, 457-67.

151. K. Vinod, C. S. Deepak, S. Sharma, D. Sornadurai, A. T. Satya, T. R. Ravindran, C. S. Sundara, A. Bharathi, Magnetic behavior of the metal organic framework $[(CH_3)_2NH_2]Co(HCOO)_3$, *RSC Adv.* 2015, 5, 37818-37822.
152. K. Kalyanasundaram, S. M. Zakeeruddin, M. Grätzel, Recent Advances in Hybrid Halide Perovskites-based Solar Cells, Material Matters, 2016, 11.1, 3.
153. H. S. Jung, N.-G. Park, Perovskite Solar Cells: From Materials to Devices, small 2015, 11, 1, 10–25.
154. V. Gonzalez-Pedro, *et al.*, General Working Principles of $CH_3NH_3PbX_3$ Perovskite Solar Cells, Nano Lett., 2014, 14, 888–893.
155. N. Marinova, *et al.*, Organic and perovskite solar cells: Working principles, materials and interfaces, Journal of Colloid and Interface, Science 2017, 488, 373-389.
156. K. Miyano, *et al.*, Lead Halide Perovskite Photovoltaic as a Model p–i–n Diode, Acc. Chem. Res. 2016, 49, 303–310.
157. A. Babayigit, *et al.*, Assessing the toxicity of Pb- and Sn-based perovskite solar cells in model organism Danio rerio, Sci. Rep. 2016, 6, 18721.
158. A. H. Slavney, *et al.*, Chemical Approaches to Addressing the Instability and Toxicity of Lead–Halide Perovskite Absorbers, Inorg. Chem. 2017, 56, 46–55.
159. Z. Song, S. C. Watthage, A. B. Phillips, M. J. Heben, Pathways toward high-performance perovskite solar cells: review of recent advances in organo-metal halide perovskites for photovoltaic applications, J. Photon. Energy. 2016, 6, 022001.
160. Recent trends in mesoscopic solar cells based on molecular and nanopigment light harvesters. Author links open the author workspace.CaroleGrätzel. Author links open the author workspace.Shaik M.Zakeeruddin, materialstoday 2013, 16, 11-18.
161. S. Chang, *et al.*, Transition Metal-Oxide Free Perovskite Solar Cells Enabled by a New Organic Charge Transport Layer, ACS Appl. Mater. Interfaces, 2016, 8, 8511–8519.
162. G. Yang, *et al.*, Recent progress in electron transport layers for efficient perovskite solar cells, J. Mater. Chem. A, 2016, 4, 3970-3990.
163. Z. Liu, *et al.*, Nickel oxide nanoparticles for efficient hole transport in p-i-n and n-i-p perovskite solar cells, J. Mater. Chem. A, 2017,5, 6597-6605.
164. S. Chatterjee, A. J. Pal, Introducing Cu_2O Thin Films as a Hole-Transport Layer in Efficient Planar Perovskite Solar Cell Structures, J. Phys. Chem. C, 2016, 120, 1428–1437.
165. W. Tress, *et al.*, The role of the hole-transport layer in perovskite solar cells - reducing recombination and increasing absorption, Photovoltaic Specialist Conference (PVSC), IEEE 40th 2014, 10.1109/PVSC.2014.6925216.
166. M. Moriya, *et al.*, Architecture of the Interface between the Perovskite and Hole-Transport Layers in Perovskite Solar Cells, ChemSusChem 2016 , 9,2634 –2639.
167. J.-Y. Wang, *et al.*, Bifunctional Polymer Nanocomposites as Hole-Transport Layers for Efficient Light Harvesting: Application to Perovskite Solar Cells, ACS Appl. Mater. Interfaces, 2015, 7, 27676–27684.
168. T. Leijtens, *et al.*, Towards enabling stable lead halide perovskite solar cells; interplay between structural, environmental, and thermal stability, J. Mater. Chem. A, 2017, 5, 11483-11500.
169. Z. Wei, *et al.*, Inkjet Printing and Instant Chemical Transformation of a $CH_3NH_3PbI_3$/Nanocarbon Electrode and Interface for Planar Perovskite Solar Cells, Angew. Chem. Int. Ed. 2014, 53, 13239 – 13243.
170. F. Mathies, Multipass inkjet printed planar methylammonium lead iodide perovskite solar cells, J. Mater. Chem. A 2016, 4, 19207-19213.
171. S. Sun, *et al.*, Synthesis, crystal structure, and properties of a perovskite-related bismuth phase, $(NH_4)_3Bi_2I_9$, APL Materials 2016, 4, 031101.

172. D.B. Mitzi, *et al.*, Conducting tin halides with a layered organic-based perovskite structure, Nature, 1994, 369, 467-469.
173. N.-G. Park, Perovskite solar cells: an emerging photovoltaic technology, materialstoday 2015, 18, 65-72.
174. D. G. Billing, A. Lemmerer, Synthesis, characterization and phase transitions of the inorganic–organic layered perovskite-type hybrids $[(C_nH_{2n+1}NH_3)_2PbI_4]$ (n = 12, 14, 16 and 18), New J. Chem. 2008,32, 1736-1746.
175. J.-H. Im, 6.5% efficient perovskite quantum-dot-sensitized solar cell, Nanoscale, 2011,3, 4088-4093.
176. S. Brittman, *et al.*, The expanding world of hybrid perovskites: materials properties and emerging applications, MRS Communications 2015, 5, 7–26.
177. IUPAC. Compendium of Chemical Terminology, 2nd ed. (the "Gold Book"). Compiled by A. D. McNaught and A. Wilkinson. Blackwell Scientific Publications, Oxford (1997). XML on-line corrected version: http://goldbook.iupac.org (2006-) created by M. Nic, J. Jirat, B. Kosata; updates compiled by A. Jenkins. ISBN 0-9678550-9-8. https://doi.org/10.1351/goldbook.
178. P. R. Varadwaj, Methylammonium lead trihalide perovskite solar cell semiconductors are not organometallic: A perspective, *Helv. Chim. Acta* 2017, DOI: 10.1002/hlca.201700090.
179. G. L. Protesescu, Nanocrystals of Cesium Lead Halide Perovskites ($CsPbX_3$, X = Cl, Br, and I): Novel Optoelectronic Materials Showing Bright Emission with Wide Color, Nano Lett. 2015, 15, 3692–3696.
180. V. K. Ravi, G. B. Markad, A. Nag, Band Edge Energies and Excitonic Transition Probabilities of Colloidal $CsPbX_3$ (X = Cl, Br, I) Perovskite Nanocrystals, ACS Energy Lett., 2016, 1, 665–671.
181. T. Wang, B. Daiber, J. M. Frost, S. A. Mann, E. C. Garnett, A. Walsh, B. Ehrler, Indirect to direct bandgap transition in methylammonium lead halide perovskite, Energy Environ. Sci., 2017, 10, 509-515.
182. C. Motta, F. El-Mellouhi, S. Kais, N. Tabet, F. Alharbi, S. Sanvito, Revealing the role of organic cations in hybrid halide perovskite $CH_3NH_3PbI_3$ Nature Commun. 2015, 6, 7026.
183. Le Q. Phuong, Y. Yamada, M. Nagai, N. Maruyama, A. Wakamiya, Y. Kanemitsu, Free Carriers versus Excitons in $CH_3NH_3PbI_3$ Perovskite Thin Films at Low Temperatures: Charge Transfer from the Orthorhombic Phase to the Tetragonal Phase, J. Phys. Chem. Lett. 2016, 7, 2316–2321.
184. L. M. Herz, Charge-Carrier Dynamics in Organic-Inorganic Metal Halide Perovskites, Annu. Rev. Phys. Chem. 2016. 67, 65–89.
185. E. M. Hutter, M. C. Gélvez-Rueda, A. Osherov, V. Bulović, F. C. Grozema, S. D. Stranks, T. J. Savenije, Direct-indirect character of the bandgap in methylammonium lead iodide perovskite, Nat Mater. 2017, 16, 115-120.
186. Yang, et al., Photoluminescence in Organometal Halide Perovskites: Free Carrier versus Exciton, IEEE Journal of Photovoltaics 2017, 7, 513 – 517.

Chapter 2. Unusual Noncovalent Bonding Modes of Perfluorobenzene

2.1 Introduction

Halogen bonding analogous in many senses to hydrogen bonding is a biologically and crystallographically dominant noncovalent interaction.[1] Owning to its ginormous applicability in the design of novel functional materials,[1-2] several research groups across the globe have joined together to form a Task Group in the past, which was then prompted to put forward rules governing its occurrence in compounds.[3] Although a number of characteristic properties have IUPAC recommended,[3] many of them have frequently been reflected in versatile bi- and multi-nary complexes involving medium-strong interactions of the covalently bound halogens. However, there are only a few of them that have been underrepresented. In particular, 'less than the sum of the van der Waals (vdW) radii (also called hard-sphere radii)' has recommended for its use as a geometric criterion in the search for halogen bonding and other σ_{hole} interactions, even though a use of this criterion was suggested some years ago to be a pitfall in the search for noncovalent interactions of the other type, such as hydrogen bonding.[4] The criterion often fails in border line cases wherein the covalently bound halogens involve with the negative sites in forming nocovalent interactions (i.e., for extremely weak interactions),[5] especially where the interplay between the higher order molecular momenta and/or dispersion portrays a major role in determining the interaction strength. There are two possible reasons that might explain this failure. Firstly, the vDW radii known for the atoms of the periodic table are not very accurate because they have been empirically determined based on the data measured using the varied nature of the measurement techniques and of the molecule type. Secondly, the covalently bound halogens in R–X (X = halogen, and R = remainder part of the molecule) do not occupy spherical volumes in space but are ellipsoidal due to the anisotropic distribution of charge density around the halogen nucleus, meaning that the radius of X along the extended R–X bond axis is smaller than that perpendicular to this axis, [6] and the effective vDW radii that have been evaluated and reported using the two types of radii mentioned just above might be erroneous. It must also be kept in mind that the magnitude of the vDW radius of an atom in its free state might always be different from that when it is covalently bound to other atoms in molecules, as well as when it is noncovalently bound to other atoms/bonds in other molecules (that is to say, the magnitude the vDW radius of an atom varies with the varying nature of the chemical environment). Although these issues are not the central concerns, the main focus of the study is to greatly enhance our current understanding of the efficiency of the covalent bound fluorine atom in molecules in forming noncovalent interactions with the negative sites.

Fluorine is the largest electronegative element among the four members of the halogen family. It is one of the potential candidates in medicinal chemistry, roughly 20-30% of the currently marketed drugs contain at least one fluorine atom.[7] It is also the least polarizable element in the halogen family, and its polarizability compared to the other halogens follows this order: F < Cl < Br < I, an order that is oppositely to their electronegativities (i.e., F > Cl > Br > I). [8] Because of these conspicuous eccentricities, the stability of the X'···X–R type-II halogen bonds, Scheme 1, formed between the covalently bound halogens R–X and the negative sites X' generally follows the order: (F <) Cl < Br < I, an order which is true regardless of the varying nature of the electron donor atoms X' involved.[9]

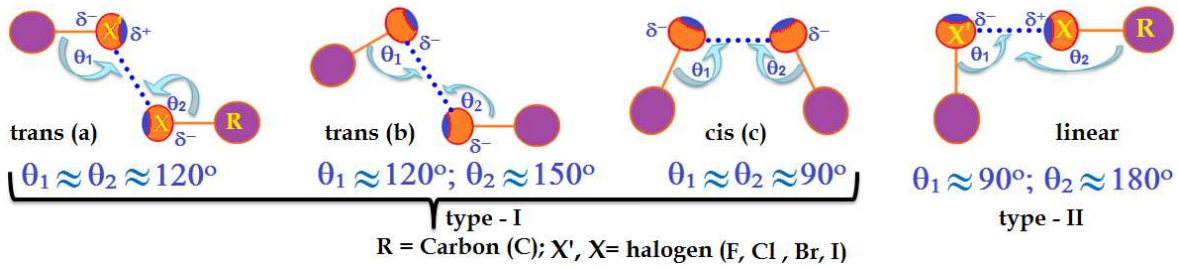

Scheme 1: Various modes of interaction of the covalently bound halogen

The covalently bound fluorine in many fluorinated compounds is fully negatively charged, e.g., H_3C–F, H_5C_6–F, H–F, H_2N–F, H_3CO–F, HO–F, and Cl–F, etc.[10a] Because of this, and because of its extremely low polarizability compared to the other three halogens it has been said that the fluorine is not proficient for forming halogen bond, [9a, b, d] and therefore not typically considered as X-bond donors, [8e] though there are scientific views existing on the opposite. [10, 12]

The fluorine atoms in perflurometh ane (CF_4) were suggested to be solely negative, [11a] and according to Politzer et al., [9a, b,d] they are incapable of forming noncovalent interactions with the negative sites on other molecules, e.g., NH_3. Contrariwise, we have recently showed that this suggestion about the fluorine's bonding temperament in CF_4 is not true. This is obviously due to the fact that the fluorine in this species accompanies a minuscule region of positive electrostatic potential (called σ_{hole}) domiciled on its surface along the outer extension of the C–F covalent bond.[5c] Consequently, such positive regions on the fluorine atoms could adequately form halogen bonded clusters when placed in close proximity to appropriate nucleophiles, such as the oxygen, nitrogen, and fluorine atoms of OCH_2, NH_3, and FH, respectively. [5c] The latter results are concordant not only with the conclusions of Osuna and coworkers, [40] as well as of Cormanich et al., [33e] both drawn theoretically, but also with the experimental results of Bol'shutkin et al. reported forty years ago, [48a] all on the dimers of CF_4. To pinpoint precisely about the experiment,

it was observed that the fluorine atoms in the CF_4 subunit in the CF_4 crystal attract the same atoms in the neighboring CF_4 subunits, leading to the formation of diverse varieties of F···F intermolecular bonding linkages (Cambrige Structural Database (CSD)[39] ref codes TFMETH, [48a] TFMETH02, [48b] and TFMETH03[48c] (Fig. S1).

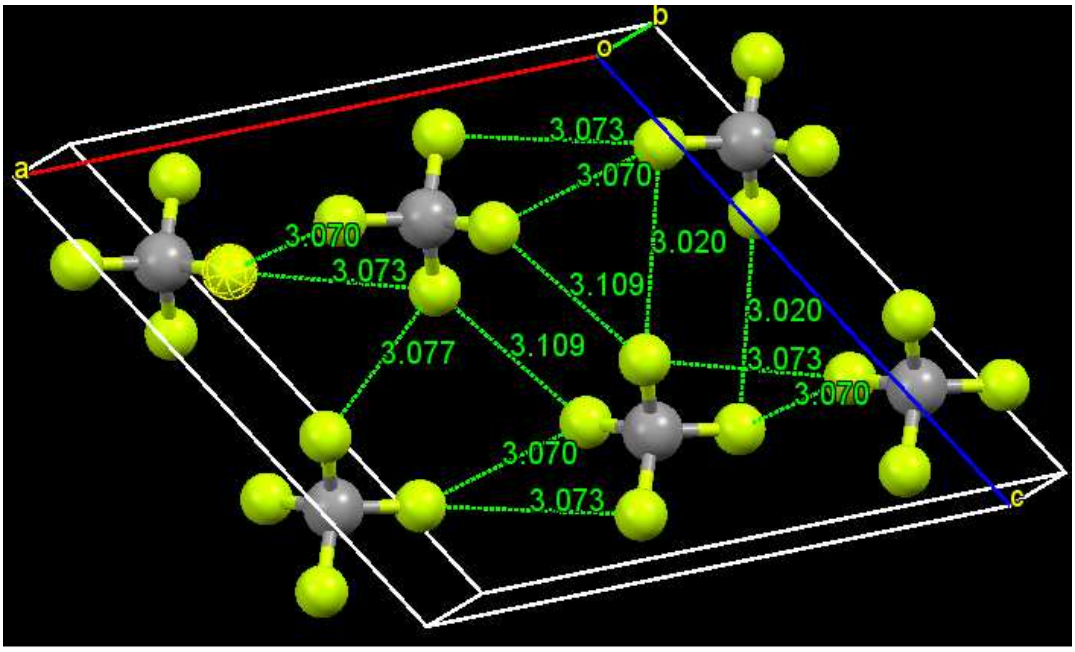

Fig. S1: The crystal of perfluoromethane CF_4 (*ref. code*: TFMETH03), obtained from Cambridge Structure Database (CSD). Selected F···F intermolecular bond distances are given in units of Å.

A suggestion homologous to the above was also presented in the past for chloromethane ($H_3C–Cl$). [11a-c] For example, it was initially suggested that the chlorine in $H_3C–Cl$ is entirely negative, thus cannot halogen bond.[11a] However, Riley et al.[11d] were able to report a detailed theoretical study on the possibility of the $H_2CO···Cl–CH_3$ gas phase dimer. Because the mechanism behind the formation of this dimer does not match with their earlier suggestion, the authors of ref.[11a] have further argued that the dimer must have formed due to the electric field of the oxygen atom in H_2CO which was sufficiently enough not only to polarize the chlorine atom in $H_3C–Cl$ on their head on approaches, but also to induce a positive region on its electrostatic surface, which was then having the ability to interact attractively with the nucleophile associated

with the oxygen atom in H_2CO.[11b-c] Contrarily, we have recently showed that this argument is perversely counterintuitive (see below further discussions), as the chlorine in $H_3C–Cl$ has inherently have a positive σ_{hole} of its own on its outermost electrostatic surface, which was not induced by its partner species upon the electrostatic interaction, which could attract favorably the covalently bound nitrogen atoms of varied strengths of negative electrostatic potential in RN molecules.[5b]

Nevertheless, whereas the covalently bound fluorine in numerous fluorinated compounds is fully negative, there are a few reported exceptions, F_2, NCCCF, F_3CCF and FCN, for examples, for which, the charge density around the fluorine's nucleus is anisotropic.[10a,12] Generally, this leads to the lay understanding that in such compounds there must be an electron-deficient electrophilic cap of positive electrostatic potential (σ_{hole}) lying along the outermost extension of the covalently bound fluorine, and the lateral portions of it lying perpendicular to the σ-bond axis must be dominated with lone pairs of electrons, the latter is generally typified by a belt of negative electrostatic potential. The former and latter regions on atoms in molecules are generally visualized by the 0.001 a.u. charge density mapped molecular electrostatic surface potential graph. They are quantified by the signs and magnitudes of the local most surface maxima and minima of electrostatic potential, often represented by the symbols $V_{s,max}$ and $V_{s,min}$, respectively. [8,9,11] It was objectified that both $V_{s,max}$ and $V_{s,min}$ are useful measures of halogen bond strength.[5b,9,13]

The domiciliation of the electropositive cap on the outer surface of the fluorine in the R–F molecules (R–F = FCCF, NCF, NCCCF, F_3CCF and F_2) *noted heretofore* in this discussion, according to Politzer et al.,[12a-b] Li et al.,[12c] Lu et al.,[12d] and Eskandari et al.,[12e] was possible only because R was sufficiently electron-deactivating. Because of this cap, the fluorine in these molecules has showed its propitious potential to attract the Lewis base centers, e.g., as in NH_3, towards itself to form N···F weakly bonded interactions. They display many characteristics comparable with hydrogen bonding, as well with halogen bonding formed by the latter three heavier halogens (X = Cl, Br, and I). Eskandari and Lesani have recently argued that these interactions should be named as 'fluorine bond' rather than referring them to as 'halogen bond',[12e] although the term 'fluorine bond' has already been referred some time ago to represent similar other noncovalent interactions.[14] According to the authors, they have so-named the interaction because unlike the latter three halogens the covalently bound fluorine in each of the above five fluorinated compounds serves as a sink rather than as a source for the N···F interactions.

By contrast, the most recent experimental observations of Kawai et al. demonstrate that fully fluorinated aromatic compounds, viz. phenyleneethynylene(bis(2,3,5,6-tetrafluoro-4-(2,3,4,5,6-pentafluorophenylethynyl)phenyl)-ethyne (BPEPE-F18), can form $C–F^{\delta-}\cdots F^{\delta-}–C$ intermolecular bonding interaction during supramolecular self-assembly.[15] To put this statement in another way, we restate that the authors of the above study have found the fluorine atoms in isolated BPEPE-F18 to be thoroughly negative, evidenced by the molecular electrostatic surface

potential map (values not reported). They then have showed that these atoms of that species can promote to develop $F^{\delta-}\cdots F^{\delta-}$ attractive intermolecular interactions with the same atoms in another BPEPE-F18, leading to the formation of a two-dimensional supramolecular layered structure. This is an observation that advocates *like attracting like*, no matter, how electronegative are the σ_{holes} and the accompanying lateral sides of the fluorine atoms in BPEPE-F18. Although the serendipitous discovery, which encompasses the geometrical arrangement between the BPEPE-F18 monomers to be regulated in such a way as to form windmill type $F^{\delta-}\cdots F^{\delta-}$ intermolecular topologies, is very rare in the vast literature, it does not come along with the assertion of Politzer et al.[9e] *halogen bonding readily be understood as the attractive interaction between the positive outer region on the halogen and the negative site*. In any case, we would like to clarify that the anisotropic fluorine in BPEPE-F18 must have an entirely negative σ_{hole} on its outer electrostatic surface along the extension of the C–F bond, a view which is in contrast with Kawai et al.[15] who have exaggerated its absence. We believe that their interpretation was fully based on the fact that the negative σ_{hole} region on the fluorine surface could be indistinguishable on the electrostatic surface of the BPEPE-F18 molecule as it merges with its negative lateral regions.

Given the profound importance of $\pi\cdots\sigma$, lone-pair$\cdots\sigma$, and π—π interactions, etc., in many areas of chemistry, biology, and crystal engineering, we have attempted in this Chapter to explore similar such bonding interactions in the dimers the perfluorobenzene (C_6F_6) molecule, and to a lesser extent, trimers, and tetramers. Our primary aim towards this Chapter is (i) to examine whether the similarly charged fluorine atoms can form $C–F^{\delta-}\cdots F^{\delta-}–C$ intermolecular bonding interactions in the conformations of the $(C_6F_6)_{n(n = 2, 3, 4)}$ clusters, and whether their bonding characteristics can be directly comparable with the ones observed experimentally in the layered supramolecular structure formed of the BPEPE-F18 molecules, [15] (ii) to verify its persuasiveness and impact in underpinning the future self-assembly, and (iii) to better understand its underlying physical chemistry in terms of the intermolecular geometries, energetics, and topological features of the charge density. A particular interest was also placed to elucidate whether the $F^{\delta-}\cdots F^{\delta-}$ metric can be treated an effective tool to enhance the stability of a complex configuration. We have tackled this problem by examining the various $(C_6F_6)_{n(n = 2, 3, 4)}$ clusters involving the $F^{\delta-}\cdots F^{\delta-}$ intermolecular interactions. In doing so, we have commented on whether the self-assembled two-dimensional supramolecular structure formed of the BPEPE-F18 molecules on the Ag(111) surface[15] was the eventual repercussion of any cooperative phenomena.

2.2 Computational details

In order to address the specific questions delineated above, we have employed Density Functional Theory (DFT) at the M06-2X/6-311++G(d,p) level of theory to calculate the

equilibrium geometries and Hessian energy eigenvalues of the twelve conformations of the $(C_6F_6)_2$ cluster, of the three conformations of the $(C_6F_6)_3$ cluster, and of the two conformations of the $(C_6F_6)_4$ cluster. The efficacy of this methodology[16a,b] in handling noncovalent interactions has been the topic of various preceding studies,[9b,16c-f] thus is suitable for the current purpose. In addition, we have performed Molecular Electrostatic Surface Potential (MESP) analysis[17] at the same level of theory to determine the various minima and maxima of electrostatic potential on the surface of the C_6F_6 monomer, which, in turn, are generally required for enlightening the most important electrophilic and nucleophilic regions. Also, we have performed Quantum Theory of Atoms in Molecules (QTAIM) [18] and Reduced Density Gradient (RDG) [19] charge density based topological analyses to elucidate the nature of the closed-shell bonding interaction involved in every pair of two atomic basins in the equilibrium structures of the $(C_6F_6)_{n(n = 2, 3, 4)}$ clusters investigated. Computer codes such as Gaussian 09,[20a] Gamess, [20b] AIMALL, [21] MultiWfn, [17] and VMD [22] were utilized for electronic-structure and -density based calculations, visualizations, and graphics generations. (Ultrafine integration grid and tight convergence criteria in lieu of default settings were invoked in the Hessian calculations performed with Gaussian 09.)

2.3 Results and discussion

2.3.1 Structural and energetic landscapes of dimers

Fig. 1 illustrates the optimized geometries of the twelve conformations of the $(C_6F_6)_2$ dimer, and Table 1 lists their energetic properties. Of these, the most stable conformation is turn out to be the one with a favorable displaced-parallel arrangement, a. Its binding energy, ΔE, calculated using a supermolecular procedure we have previously employed, [5a-c, 23] is worth –7.38 kcal mol^{-1}. It is about 1.04 and 1.19 kcal mol^{-1} (see ΔE values in Table 1) more stable than the configurations b and c (distorted and undistorted displaced-parallel), respectively. It is worth emphasizing that we had initially attempted at energy-minimizing two different sandwiched (on top parallel) geometries of the $(C_6F_6)_2$ dimer, despite the resulting conformations were turn out to be a and c. Why the on top parallel geometry of the $(C_6F_6)_2$ dimer was not found could probably be explained by the large nonbonded repulsion between the carbon faces associated with the six-membered rings of the two monomers on their head-on approaches. We believe this repulsion must have overpowered the corresponding attractive counterpart, thereby making the said geometry destabilized (unstable). This is not very dumbfound because the electrostatic potential at the outer surface the aromatic ring center in C_6F_6 is largely positive, $V_{s,max}$ = +21.4 kcal mol^{-1}, Fig. 2.

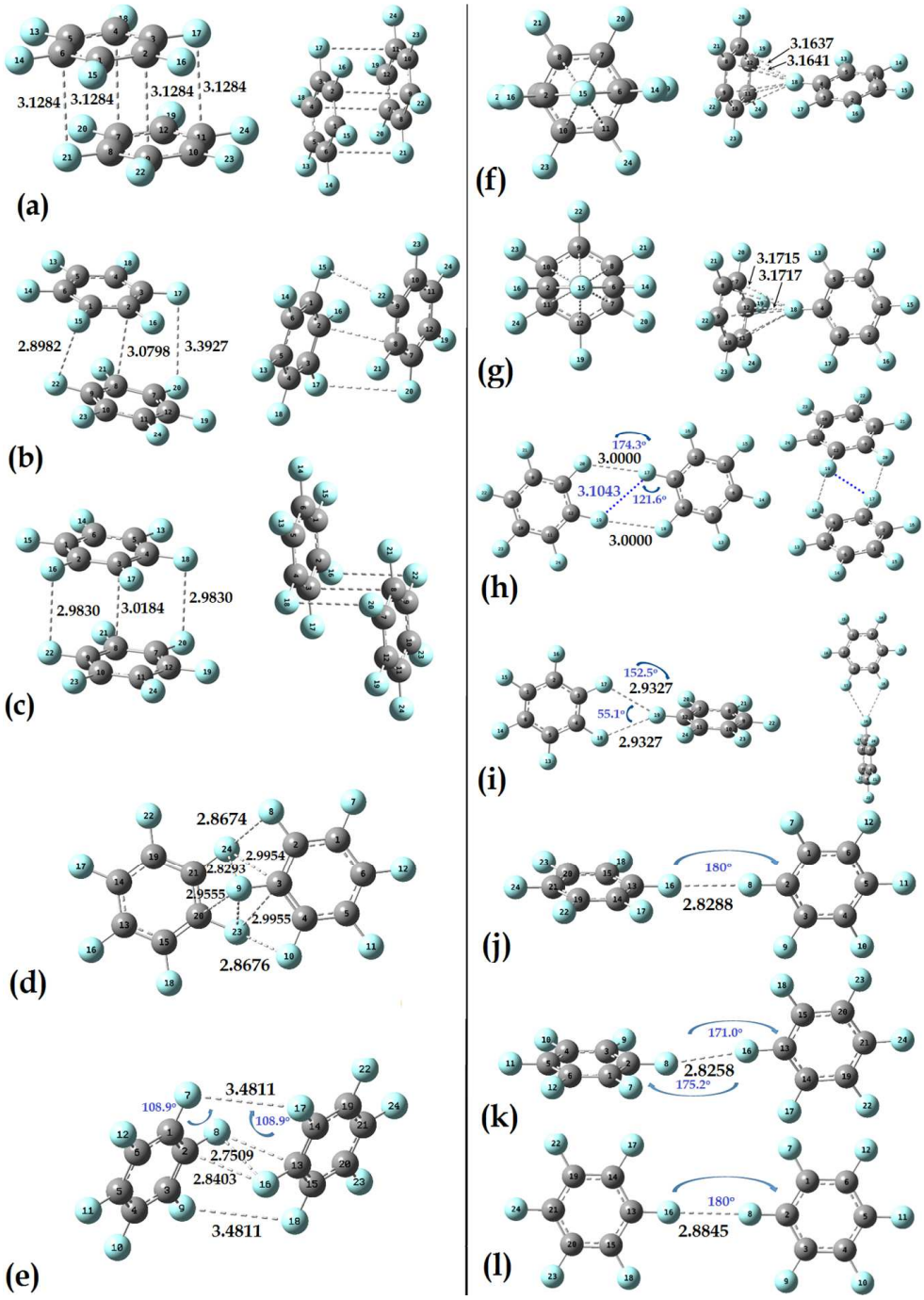

Fig. 1: The twelve optimized geometries of the $(C_6F_6)_2$ dimer, obtained using M06-2X/6-311++G(d,p). Bond-lengths (in Å) and -angles (in ^{o}) are given for some selected intermolecular contacts. For clarity, two different views are displayed for several geometries. The dotted lines between the atoms are drawn to show consistency with the QTAIM-based molecular graphs presented in Fig. 4, evocative of the presence of noncovalent interactions. Atom labeling is randomly shown. Due to symmetry, two nearly degenerate intermolecular bond distances are presented for geometries f) and g).

Compared to the previous suggestions for the $(C_6F_6)_2$ benzene dimer,[24] as well as that for similar other dimers,[25] it may be anticipated that each of the above three conformations (a-c) of the $(C_6F_6)_2$ dimer is $\pi\cdots\pi$ stabilized. This means quadrupolar and London dispersion interactions, the former supposedly yielding from the product of the polarizabilities the two π systems, are the key competitive contributing sources for the attraction between the two monomers. The incisive remark may be no wonder because C_6F_6 is a polar molecule that has a quadrupole moment (Θ) closely in magnitude but opposite in sign to C_6H_6, values of Θ –28.9±1.7 vs. +31.7±1.7 $Cm^2\times10^{-40}$ (experimental).[26] In an analogous slipped-parallel $(C_6H_6)_2$ dimer, it was argued that dispersion is the key driving force for complex stabilization, and electrostatics plays the role of repulsion.[50]

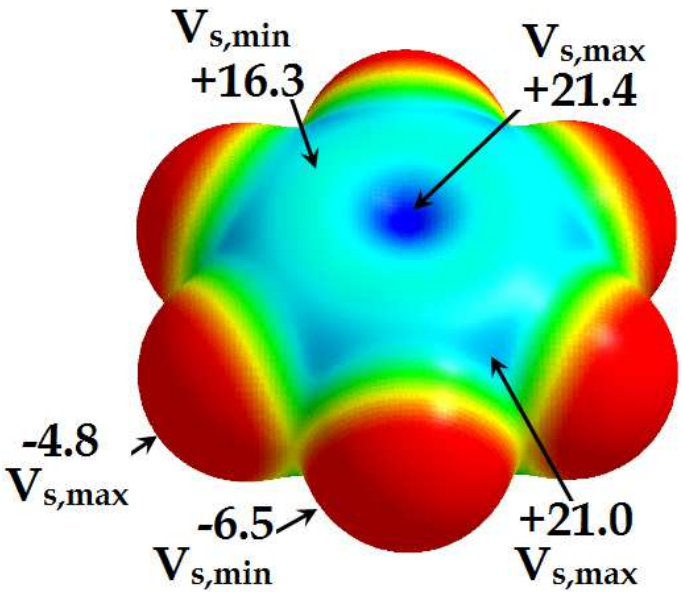

Fig. 2: M06-2X/6-311++G(d,p) computed molecular electrostatic surface potential of perfluorobenzene (C_6F_6), mapped with the 0.001 a.u. isodensity. Colors in red and deep blue represent the most negative and most positive regions of electrostatic potential, while those in yellow, green, and cyan represent the least negative, least positive, and more positive regions of electrostatic potential. $V_{s,min}$ and $V_{s,max}$ values are in units of kcal mol^{-1}. The deep-blue hole-like domain on the center of the ring surface is a π_{hole}.[9f, 13d]

The geometries d and e (Fig. 1) are the other two high energy conformations of the $(C_6F_6)_2$ dimer. The former is a minimum and latter a second order saddle point (imaginary frequencies are –9.4 and –24.4 cm^{-1}, respectively). They are about 3.09 and 3.95 kcal mol^{-1} less stable than the conformer a. They both comprise of several short C···F and F···F contacts, the shortest and longest of these are ca. 2.7509 Å and 3.4811 Å, respectively. Similar to the conformations b and c, both d and e do involve type-Ic contact, Scheme 1. This could be realized by inspecting the values of 93.5 (93.5), 91.5 (91.5), 131.8 (82.9), and 108.9 (108.9°) obtained for the angles $\angle C_7–F_{20}\cdots F_{17}$ ($\angle F_{20}\cdots F_{17}–C_3$), $\angle C_4–F_{18}\cdots F_{20}$ ($\angle F_{18}\cdots F_{20}–C_7$), $\angle C_{21}–F_{24}\cdots F_8$ ($\angle F_{24}\cdots F_8–C_2$), and $\angle C_1–F_7\cdots F_{17}$ ($\angle F_7\cdots F_{17}–C_{14}$) in b, c, d, and e, respectively.

The two C_{2v} geometries f and g (Fig. 1) of the $(C_6F_6)_2$ dimer are T-shaped (edge-face), both lying roughly at an elevated energy of 4.5 kcal mol^{-1} compared to the conformation a. These geometries, from the electrostatic surface potential point of view, are presumably stabilized by the $\pi_{hole}(+)\cdots\sigma_{hole}(-)$ interaction, the entirely positive π_{hole} in one C_6F_6 (the face of the ring) interacting with the fluorine's negative σ_{hole} in the other C_6F_6 (the edge), with the mean C$\cdots$F intermolecular distances are ca. 3.1639 and 3.1716 Å for the corresponding dimers, respectively. Both the geometries are first order saddle points with the present level of theory, with the

Table 1: Selected energetic properties of the $(C_6F_6)_2$ dimers, obtained with M06-2X in conjunction with the 6-311++G(d,p) basis set. [a]

Conformation[a]	Relative stability (Δ)	ΔE	BSSE	ΔE (BSSE)
(a)	0.00	–7.38	2.67	–4.72
(b)	1.04	–6.35	2.20	–4.14
(c)	1.19	–6.20	2.23	–3.97
(d)	3.09	–4.30	1.35	–2.95
(e)	3.95	–3.44	1.26	–2.17
(f)	4.51	–2.88	1.16	–1.72
(g)	4.53	–2.87	1.16	–1.71
(h)	6.45	–0.94	0.51	–0.43
(i)	6.49	–0.90	0.49	–0.41
(j)	6.77	–0.62	0.38	–0.24
(k)	6.78	–0.61	0.46	–0.15
(l)	6.88	–0.51	0.33	–0.17

[a]The properties include the relative stability (Δ/kcal mol^{-1}), the binding energy (ΔE/kcal mol^{-1}), the basis set superposition error energy (BSSE/kcal mol^{-1}), and the BSSE corrected binding energy (ΔE(BSSE)/kcal mol^{-1}).
[b] See Fig. 1 for conformational details.

imaginary frequencies associated with the low-frequency deformation vibrational modes of the respective dimers are ca. –7.1 and –3.5 cm^{-1}, respectively. The topology is identical to what is commonly known as the T-shaped configuration of the $(C_6H_6)_2$ dimer that enjoys preferable quadrupole/quadrupole interactions, as it facilitates a favorable environment wherein the positive quadrupole of one C_6H_6 ring interacts attractively with the negative quadrupole of the other.

The geometries associated with the other two conformations h and i (Fig. 1) of the $(C_6F_6)_2$ dimer are both minima, with the former and latter belong to the C_{2h} and C_2 point group symmetries, respectively. The geometry of the former conformation is formed due to the *quasilinear* attraction between the fluorine's negative σ_{holes} in one monomer and the negative lateral portion of the same atoms in another monomer (lone-pair$\cdots\sigma_{hole}(-)$ type). The two short F$\cdots$F distances in this geometry are equivalent, 30000 Å each, both represented by the broken lines in white-gray. The angles θ_1 (θ_1 = $\angle C_7$–$F_{20}\cdots F_7$) and θ_2 (θ_2 = $\angle F_{20}\cdots F_7$–C_3) associated

with these contacts are approximately 125.5 and 174.3°, respectively (see Scheme 1 for θ_1 and θ_2). Because the latter angle is close to 180°, one may conclude a strong directional preference of bonding in this dimer similarly with the type-II intermolecular topology (Scheme 1), which is generally formed when the covalently bound halogen with an electrophilic cap (of positive electrostatic surface potential) on it links with the nucleophilic sites through an attractive interaction. [27e-f]

In the geometry i, however, the fluorine's negative σ_{hole} in one monomer on the right is facing the mid-point of a C=C bond of another monomer on the left. The arrangement has resulted in an equivalent F···F pair formed between the lateral negative sides of the three interacting fluorine atoms. The intermolecular distance associated with the F···F equivalent pair is ca. 2.9327 Å, and the angles θ_1 and θ_2 associated with them each are approximately 122.4 and 152.5°, respectively. Interestingly, these values do not match with the previously defined type-I contacts, [27] we thus named it to be referred to as type-Ib, Scheme 1.

Noticeable in geometry h is another short F···F pair transpiring between the two C_6F_6 monomers. It is represented by the dotted line in blue, and is occurring between the lateral sides of the two fluorine atoms, each from a given monomer. Unlike the F···F pairs discussed already above, this latter is seemingly a forced interaction. The intermolecular distance for this F···F pair is ca. 3.1043 Å, with $\theta_2 \approx \theta_1 = 121.6°$. Interestingly enough, the angular feature associated with this interaction is analogous to what has been referred in the literature to as type-I contact,[6a, 27] but we called it type-Ia to discriminate it from type-Ib and –Ic contacts, Scheme 1. Such a topology of bonding is commonly observed between the carbon bound halogen atoms in the solid state,[27] crystalline $(C_6Cl_6)_3$, for example.[27a] Recently, Duarte et al. have suggested a similar interaction topology between the bromine atoms in the FBr···BrF dimer, which was formed due to the interaction of a lump on one bromine with the hole on the other.[27b] According to Brammer et al.,[27c] this kind of geometrical attribute is a repercussion of an electrostatically repulsive arrangement since at the point of interaction their MESPs are nearly identical, and their occurrences are not very surprising in the solid state as they are most likely to result from minimization of intermolecular repulsions or from weakly attractive interaction driven by dispersive forces. Awwadi and coworkers have suggested that the C–X···X–C (X = Cl, Br, I) type-Ia interaction topology which is by far most common in the solid state is electrostatically attractive for a narrow range of angles, $140 < \theta_1 \approx \theta_2 < 160$, [27d] and beyond this range they are mostly electrostatically repulsive. However, as noted by Brammer et al., [27c] there exist some specific cases, wherein the C–X···X–C interactions beyond the above angular range are still attractive (similar to those found for the geometries h and i), and in those cases, dispersion plays an intervening role.

In each of the other three conformations of the $(C_6F_6)_2$ dimer, j-l, there is a single F···F intermolecular bonding interaction. The former one and latter two geometries of the dimers are stationary and first order saddle points, respectively (imaginary frequencies associated with the

latter two are ca. –5.1 and –2.3 cm^{-1}, respectively). The F···F intermolecular distance is about 2.8288 Å in j (D_{2d}), 2.8258 Å in k (C_1), and 2.8845 Å in l (D_{2h}). The binding energies for the corresponding dimers are ca. –0.62, –0.61, and –0.51 kcal mol^{-1}, respectively, showing the F···F interaction strengths in these dimers are nearly equivalent. For the former and latter geometries, $\theta_1 \approx \theta_2 = 180^o$, revealing a prototype $\sigma_{hole}(-)\cdots\sigma_{hole}(-)$ interaction. For the intermediate geometry k, $\theta_1 = 171.0^o$ and $\theta_2 = 175.2^o$, and the F···F pair could also be described as lone-pair$\cdots\sigma_{hole}(-)$ type. In most of these unconventional interactions, one of the fluorine atoms is probably serving as a fluorine bond acceptor, and the other as a fluorine bond donor.

The electrostatic fields around covalently bound fluorine atoms in isolated C_6F_6 are ostensibly equivalent. This may be realized from the negative electrostatic potential values that are computed to be identical on the surfaces of the fluorine atoms along (or around) the outer extensions of the C–F bond axes (cf. Fig. 2). Because of it, one must not expect an induction of a positive electrostatic potential on the surface of the fluorine atom in a monomer caused by the electrostatic fields of the same atoms in another monomer when both are on their head-on approaches. This proves the fact that for the formation of an F···F link, as in the geometries h and l, one does not necessarily require an involvement of a positive site. The result is in sharp contrast with an assertion of Politzer et al. *the negative electrostatic potential associated with a* σ_{hole} *precludes the possibility of halogen bonding–unless the electric field of the negative site is strong enough to induce a positive region on the halogen.* [9a,b,d]

Nevertheless, it is well known that DFT is notoriously poor at accurately describing long-range effects, including dispersion. Although M06-2X can deliver some impressive accuracy for its expense but, like all parametrized models, is not necessarily guaranteed to perform well under all scenarios. For example, according to Zhao and Truhlar, the M06-2X outperforms many older DFT functionals, and offers reasonable chemical accuracies for applications in main-group thermochemistry, kinetics, and noncovalent interactions. [16a,b] Similarly, Kozuch and Martin have suggested only recently that the DFT functionals with high exact exchange or long-range corrections, especially M06-2X and ωB97XD, and double hybrids, are suitable for the study of halogen bonding, [16f] yet there are examples in the literature where this functional underperforms. [41] Taking this as an issue, we have reoptimized only the D_{2d} geometry of the $(C_6F_6)_2$ dimer j (Fig. 1) with eleven other very popular DFT and DFT-D functionals in conjunction with the same 6-311++G(d,p) basis set. The results listed in Table 2 manifest the F···F distances to vary widely between 2.7949 (Cam-B3LYP) and 3.0841 Å (TPSSTPSS), and the uncorrected ΔE to vary between –0.14 (B3LYP-D) to –0.77 kcal mol^{-1} (PW91PW91). Indeed such a large variation in the intermolecular distances, as in the values of the ΔE, can be attributed to the percentage of exchange and correlation mixing in the DFT functionals. Among the functionals tested, the ΔE determined with M06-2X is harmonious with that obtained with ωB97XD, as well as with that calculated with the highest level of theory applied (MP2), thereby demonstrating trustworthiness

of the M06-2X results. However, compared to M06-2X, all the other DFT/DFT-D functionals have underestimated the ΔE, except for PW91PW91, ωB97XD, and HCTH, in which cases, there were slight overestimations. In contrary, the B3LYP functional significantly underestimates the ΔE which is also not unacceptable because it does not properly incorporate long-range forces.[42]

Table 2: Comparison of some selected physical properties of the D_{2d} geometry of the $(C_6F_6)_2$ dimer, obtained with various levels of theory in conjunction with the 6-311++G(d,p) basis set. [a,b]

Method[c]	r(F···F)	ΔE	ΔE (ZPV)	BSSE	(BSSE/ΔE)×100[e]	ΔE(BSSE)
MP2[d]	2.8306	–0.57	---	0.43	75.4	–0.14
M06-2X	2.8288	–0.62	–0.39	0.38	61.5	–0.24
ωB97XD	3.1666	–0.61	–0.47	0.34	56.5	–0.26
B3LYP-D	2.7825	–0.14	+0.04	0.35	260.4	+0.22
Cam-B3LYP	2.7949	–0.44	–0.30	0.34	77.8	–0.16
B3LYP	3.0603	–0.21	–0.10	0.29	136.3	+0.08
X3LYP	2.8813	–0.41	–0.28	0.33	80.8	–0.08
TPSSTPSS	3.0841	–0.39	–0.27	0.34	85.1	–0.06
PW91PW91	2.9182	–0.77	–0.64	0.36	46.4	–0.41
PBEPBE	2.9670	–0.47	–0.34	0.33	69.6	–0.14
PBE1PBE	2.9570	–0.44	–0.29	0.36	81.8	–0.08
HCTH	2.9701	–0.75	–0.61	0.31	41.9	–0.44
BHandHLYP	2.8286	–0.41	–0.25	0.35	86.2	–0.06

[a] See Fig. 1j for geometry.

[b] The properties include the F···F intermolecular bond distance (*r*/Å), the binding energy (ΔE/kcal mol^{-1}), the zero-point-vibration correction binding energy (ΔE(ZPV)/kcal mol^{-1}), the basis set superposition energy (BSSE/kcal mol^{-1}), the percentage (BSSE/ΔE ×100) and the BSSE corrected binding energy (ΔE(BSSE)/kcal mol^{-1}).

[c] See ref. 45 for details about the DFT and DFT-D functionals investigated.

[d] MP2 calculation was performed in conjunction with the 6-311G(d,p) basis set. We were unable to perform the Hessian calculation at this level because our calculation has often encountered the g_write error.

[e] Percentages (%) are estimated considering the BSSE and ΔE values upto the three decimal places.

Table 1 summarizes the basis set superposition error (BSSE) energies for all the $(C_6F_6)_2$ dimers examined, estimated using the counterpoise procedure of Boys and Bernardi[43a] with M06-2X. As can be readily seen from the data, the BSSE is as large as 2.67 kcal mol^{-1} for the most stable dimer a, and is as small as 0.33 kcal mol^{-1} for the least stable dimer l. In other words, the magnitude of the BSSE is the largest for the displaced-parallel conformations (2.23 – 2.67 kcal mol^{-1}), the intermediate for the T-shaped conformations (1.16 – 1.35 kcal mol^{-1}), and the least for the quasilinear and linear conformations of the dimer (0.33 – 0.51 kcal mol^{-1}). This may lead to a subsequent opinion that the magnitude of the BSSE does not strictly depend on the difference energies arising due to the mismatch between the basis functions of the two isolated C_6F_6 molecules and the corresponding complexed species for which the counterpoise concept was

introduced, [43a-c] but is largely controlled by the nature of the spatial arrangements (orientations) of the two C_6F_6 subunits in the equilibrium conformational geometries of the $(C_6F_6)_2$ dimer. A similar dependence of the BSSE on the conformational space was previously sought, in which case, it was demonstrated that the BSSE could become the source of error in the evaluation of the conformational stability differences of moderate-sized molecules, such as 1,2-dimethoxyethane, and therefore, an effort must be given for the careful evaluation of such energies. [46]

To see whether the BSSE energies estimated with the M06-2X functional are trusty, we have compared in Table 2 such energies estimated with MP2 and with the eleven other DFT/DFT-D functionals, all only for the $(C_6F_6)_2$ dimer j (Fig. 1). The results indicate that the BSSE is lying closely between 0.29 and 0.36 kcal mol^{-1} for all the eleven DFT/DFT-D functionals, and its value is as large as 0.43 kcal mol^{-1} with MP2, and that these are all in close consistent with the M06-2X value of 0.38 kcal mol^{-1}. Note that the BSSE is too large relative to the uncorrected binding energy of the dimer for a given computational method. For instance, the BSSE relative to the ΔE is as large as 41.9% with HCTH, 62.5% with M06-2X, 75.4% with MP2, 136.3% with B3LYP, and 260.4% with B3LYP-D (cf. Table 2). These results indicate that the BSSE must be used with caution for complexes involving weak binding energies, consistent with the suggestions of other authors.[49] Other than this, we have also examined the effect of zero-point vibration (ZPV) on the binding energy of the $(C_6F_6)_2$ dimer j. It is found that ZPV has somehow less pronounced effect on the ΔE (compared to the BSSE), evident of the ΔE(ZPV) data summarized in Table 2.

Whatever happens, the short F···F intermolecular distance found in several conformations of the $(C_6F_6)_2$ dimer is somehow greater than twice the vDW radii of the fluorine atom $rvdW_{F+F}$, 2.92 Å (rvdW(F) = 1.46 Å[30]) for most cases, expect for those in the geometries b and h-l (cf. Fig. 1), in which cases, such distances are slightly shorter than $rvdW_{F+F}$. An examination of the crystal of C_6F_6 (ref code HFBENZ[39], also see Fig. S2) has showed that a majority of the F···F distances are in the 2.945–3239 Å range, in line with our above finding. Previously, Osuna and coworkers have reported a total of twenty-three F···F contacts in the eleven $(C_6F_6)_2$ dimers examined. Of these, five were shorter, and the other eighteen were greater, than $rvdW_{F+F}$.[40] A similar conclusion can be drawn of the C···F and C···C intermolecular interactions observed in the first seven conformations of the $(C_6F_6)_2$ dimer (cf. Fig. 1a-g). These results apparently give us an impression that the recommended IUPAC feature 'In a typical halogen-bonded complex Y···X–R, the interatomic distance between X (X = halogen) and the appropriate nucleophilic atom of Y tends to be less than the sum of the van der Waals radii'[3] which may be good for medium-strong interactions, but is certainly not an effective tool for searching weakly bound interactions. This has been pointed out in similar other occasions.[5]

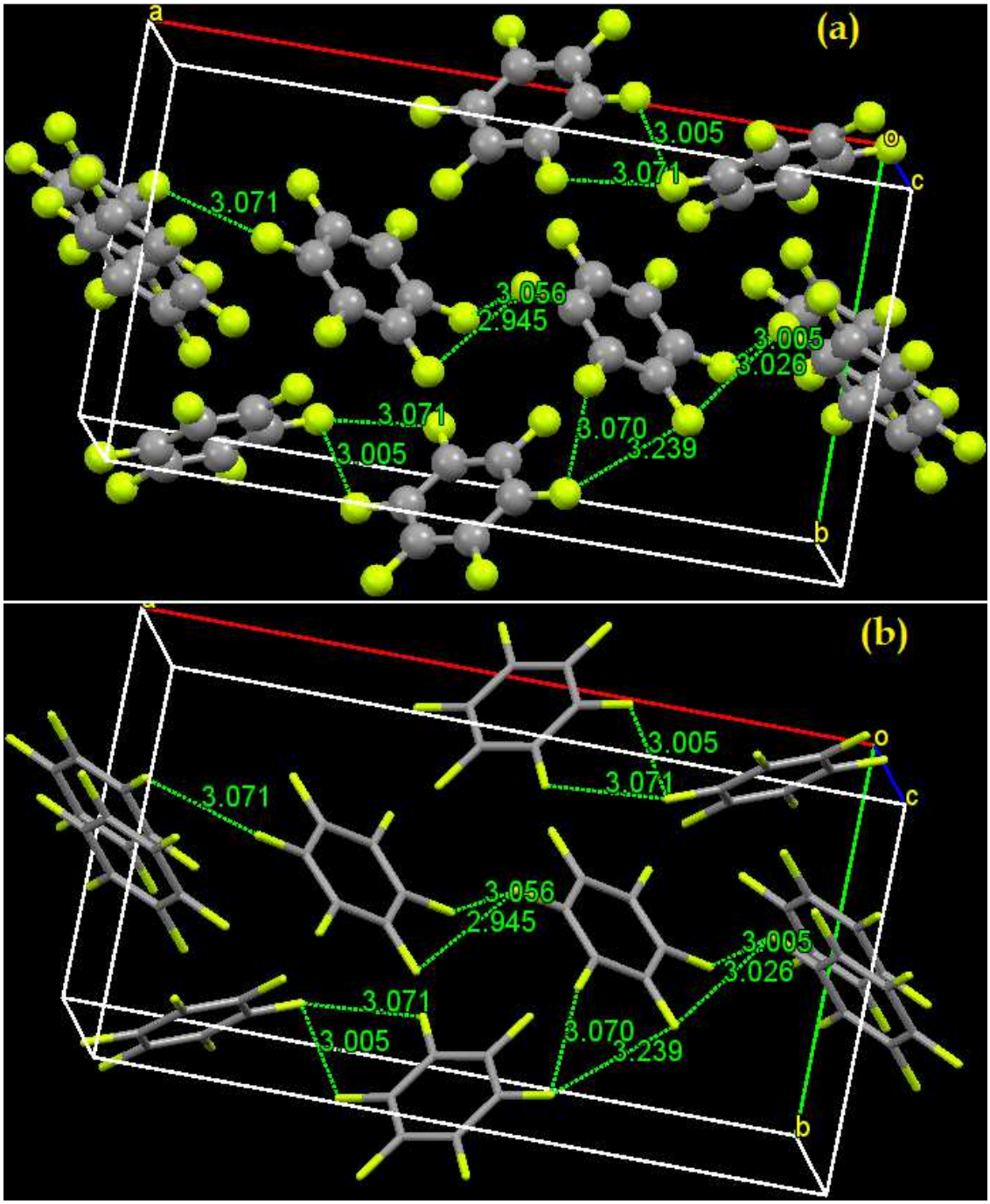

Fig S2: The crystal of perfluorobenzene C_6F_6 (refcode HFBENZ), obtained from Cambridge Structure Database (CSD). Both ball and stick (a), and crapped sticks (b) models are illustrated. Selected F···F intermolecular bond distances are given in units of Å.

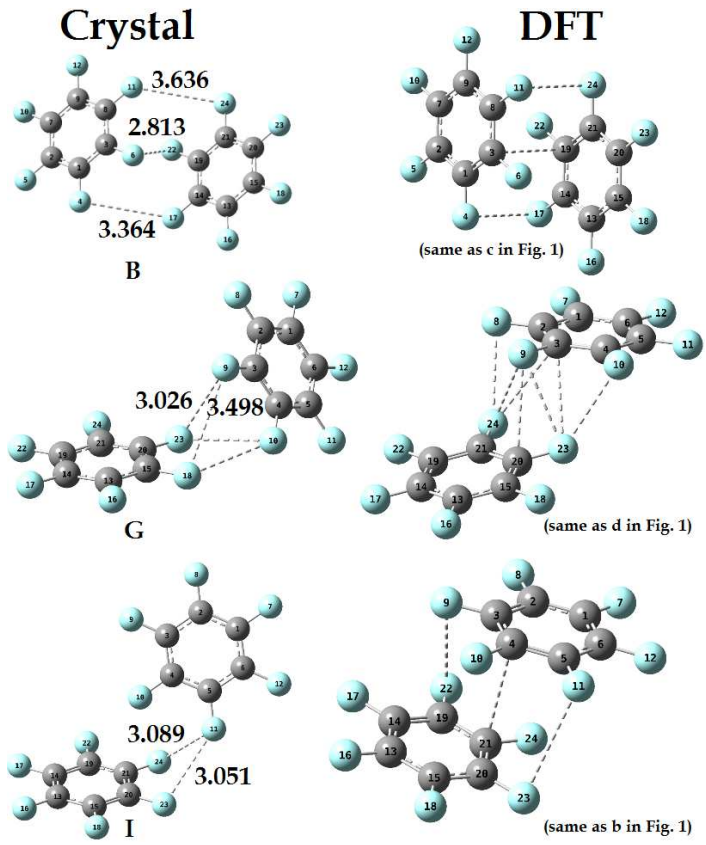

Fig. 3: Comparison of the geometries of the three symmetry non-equivalent $(C_6F_6)_2$ dimers found in the C_6F_6 crystal (ref code HFBENZ) [39] (left) with their corresponding DFT/M06-2X/6-311++G(d,p) optimized ones (right). Labeling of the dimers (B, G, and I) on the left are same as those referred in Fig. 4 of ref. 40. Selected F···F intermolecular contacts (in Å) identified in ref. 40 are illustrated; such contacts found in the optimized geometries (right) are given in Fig. 1. Atom labeling for a given system is different from the other.

The molecular electrostatic potential surfaces on the 0.001 a.u. isodensity contours of the *players* in an intermolecular interaction have often demonstrated giving a realistic view of the primary driving forces drawing the molecules together.[9] However, the tool seemingly is not very effective in unraveling the nature of the primary forces responsible for driving the fluorine atoms to form the F···F intermolecular interactions. This is doubtlessly due to the fact that the electrostatic potentials on the surfaces of the covalently bound fluorine atoms in the C_6F_6 monomers are completely negative. In the recent past, Swart et al.[38a] and Varadwaj et al.[38b] have showed that this model is a sharp failure to elucidate the nature of the X···X intramolecular halogen bonding interactions in perhalogenatedethanes (CF_3–CCl_3 and CCl_3–CCl_3, e.g.) and hexahalogenated benzene derivatives, respectively. We commend that a use of this model might be inadequate to elucidate nature of the primary driving forces responsible for the attraction between the monomers in the chelates of CHF_3 and CF_4.[33e] Our view is in line with Kawai et al.[15] who have just recently demonstrated that this model is inadequate to describe the F···F interactions responsible for assembling fully fluorinated BPEPE-F18 molecules in an ordered supramolecular layered structure.

Whilst several conformers of the $(C_6F_6)_2$ dimer were examined, we have performed BHHLYP[28] level Localized Molecular Orbital Energy Decomposition Analyses (LMO-EDA) [29] only for a few specific geometries of the $(C_6F_6)_2$ dimer, h–j (cf. Fig. 1), to provide insight into the determining energetic factors bringing the totally negative fluorine atoms together. Based on this formalism, implemented in Gamess, [20b] the interaction energy of a dimer can be written as the sum of the decomposed energies arising from electrostatics (ΔE_{es}), exchange (ΔE_{ex}), repulsion (ΔE_{rep}), polarization (ΔE_{pol}), and dispersion (ΔE_{dis}). Accordingly, the computed values associated with these five components are ca. 0.15, 0.48, 0.56, –0.95, and –1.14 kcal mol^{-1} for geometry h, respectively, and are ca. 0.00, 0.37, 0.63, –0.77, –1.04 kcal mol^{-1} for geometry i, and respectively, and are ca. 0.04, 0.23. 0.37, –0.34, and –0.63 kcal mol^{-1} for geometry j, respectively, all revealing the former three components to be repulsive and the latter two attractive. These mean the F···F interactions (irrespective of their number) in each of the three geometries are stabilized mainly by polarization and dispersive forces that contribute almost equally to the binding energy. The net interaction energies for the former dimers are calculated to be ca. –0.89 and –0.81 kcal mol^{-1}, respectively, which are well along with their M06-2X SCF binding energies of –0.94 and –0.90 kcal mol^{-1}, respectively, although that calculated for the latter dimer, –0.33 kcal mol^{-1}, was found to be inequivalent with the SCF value of –0.62 kcal mol^{-1}.

The conclusions drawn above on the fidelity of the F···F intermolecular interactions are solely based on the intermolecular geometries, electrostatic surface potential extrema, and binding energies of the $(C_6F_6)_2$ dimer. However, according to Reddy and coworkers, *X···X interactions can be of several types and that it is sometimes difficult to characterize them by using geometrical criteria only*. [27a] Thus relying on their averment we have extended our analysis of chemical bonding in the $(C_6F_6)_2$ clusters, and have discussed our QTAIM[18] and RDG[19] based topological charge density results in the following section. But before that, we would specify that Osuna et al.[40] have recently analyzed eleven symmetry unique dimers of the C_6F_6 molecule synthesized in the crystalline phase.[39] In that study they could perform first principles single point MP2/aug-cc-pVDZ calculations on several crystalline geometries of the $(C_6F_6)_2$ dimer to assess their BSSE corrected binding energies ΔE(BSSE). A range of values between –0.45 and –2.65 kcal mol^{-1} was proposed for the ΔE(BSSE) in the gas phase. However, we stress that the geometries of several of these dimers in the crystalline phase when optimized in the gas phase have resulted in different geometries in the conformal space, Fig. 3. This does not overwhelm us because the geometry of the compound stabilized in the solid state does not only controlled by the static and dynamic disorders, [47] but also influenced by several other factors, including, for example, packing forces, solvation, and counter ion effects, etc. The results manifest that the binding energies Osuna et al.[40] have reported for the $(C_6F_6)_2$ dimers might not be very meaningful.

2.3.2 QTAIM and RDG based topological charge density analyses

QTAIM rigorously provides the nature of an interaction in an atom-atom pair (whether covalent, coordinate, and/or ionic, etc.) in molecular compounds or in solids in terms of its unified charge density (ρ) topologies. [5,18,23,31] The theory in its simplest approach assumes a substantial accumulation of the charge density at the nucleus of an atom, represented by a (3, –3) nuclear attractor critical point (a local maximum). The critical bonding region between the two atoms in a molecule is represented by a (3, –1) bond critical point, bcp, a saddle point. At this point, the charge-density's first derivative is zero ($\nabla\rho = 0$), and its second derivative, called the Laplacian of the charge density $\nabla^2\rho$ ($\nabla^2\rho = \lambda_1 + \lambda_2 + \lambda_3$), is an extrema, where $\lambda_{i(i=1-3)}$ are the three eigenvalues of the Hessian matrix of the charge density at the bcp along the three principal directions. Thus when $\nabla^2\rho_b$ is a minimum at bcp (i.e., $\nabla^2\rho_b < 0$), we generally find a substantial concentration of the charge density at that bcp (as at the C=C and C–Cl covalent bcps in hexachlorobenzene, [31b] for example). When $\nabla^2\rho_b$ is a maximum at bcp (i.e., $\nabla^2\rho_b > 0$), we generally find a substantial depletion of the charge density at that bcp (as at the O···H intermolecular bcps in water (H_2O) clusters[31c]). However, for polar covalent bonds, $\nabla^2\rho_b$ at the bcps are positive, viz. the SO bond in SF_4O, for example.[31j] Note that for isolated chemical systems, such as 1-12-Difluorobenzo[c]phenantherene, a pair of two additional (3, –1) ring and (3, –3) cage critical points generally appears. In such cases, the Poincaré-Hopf relationship, n(ncp) + n(nncp) – n(bcp) + n(rcp) – n(ccp) = 1, a fundamental theorem of topology,[35a] is satisfied, where ncp, nncp, bcp, rcp, and ccp are the (3, –3) nuclear attractor critical point, (3, –3) non-nuclear attractor critical point, (3, –1) bond critical point, (3, +1) ring critical point, and (3, +3) cage critical point, respectively, and *n* refers to the number.[32b,35b,c]

According to QTAIM, the atomic basins linking each other with lines are preferential bond paths of maximal charge density, [18,31d] which are possible indicators of the presence of chemical bonding interactions. These bond paths have also been viewed as maximal exchange-correlation energy channels between bonded atomic basins according to Pendás and coworkers, [32a] and others, [32b] uncovered using Interacting Quantum Atom (IQA) model.[32c-d]

In contrary, Johnson et al.,[19a] and Contreras-García et al.,[19b-c] have recently proposed a charge density based approach, called Reduced Density Gradient (RDG), for characterizing noncovalent, coordination, and steric interactions, including halogen bonding, hydrogen bonding, σ_{hole} bonding, polar–π interactions, aromatic-aromatic (π stacking), cation–π, and metal-ligand interactions, etc. [19,33] The RDG s is a dimensionless quantity within the generalized gradient approximation of exchange-correlation term in DFT Hamiltonians,[34] and is given by Eqn. 1.

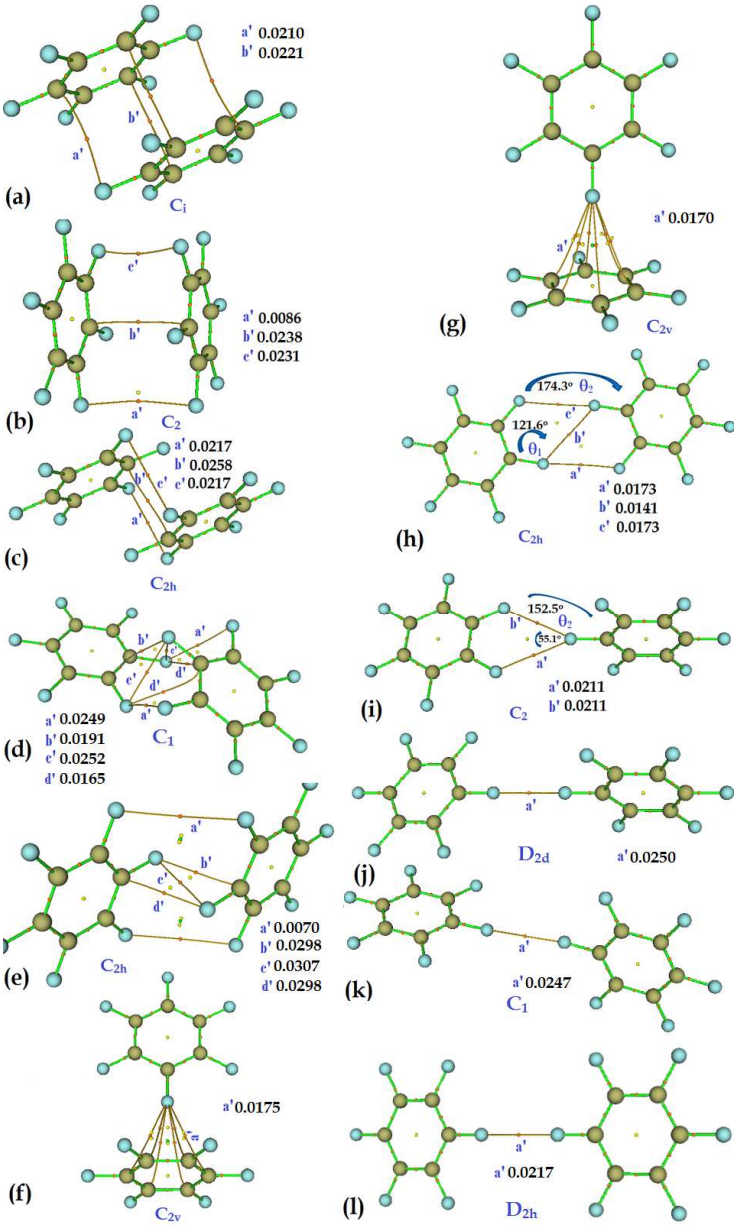

Fig. 4: Molecular graphs of the twelve conformations of the $(C_6F_6)_2$ dimer, obtained using M06-2X/6-311++G(d,p). Values of the delocalization index are listed for some selected atom pairs (in some cases, only average values are listed, viz. g), obtained within the framework of QTAIM. [36] The (3, –1) and (3, +1) bond and ring critical points are shown as tiny spheres in red and yellow, respectively. The (3, +3) critical point is shown in geen only for a few cases to avoid complications. Bond paths represent to covalent and noncovalent interactions are displayed as lines in green and dark-orange, respectively. Carbon and fluorine atoms are shown as balls in dark goldenrod and light sky blue, respectively.

Table S1: Selected QTAIM based topological properties of the charge density of all the twelve $(C_6F_6)_2$ binary complexes examined, obtained with M06-2X/6-311++G(d,p).[a],[b]

Conformation	(3,–1) bcp	ρ_b	λ_1	λ_2	λ_3	$\nabla^2\rho_b$	V_b	G_b	H_b	DI
a[c]	F17 C11	0.0064	-0.0034	-0.0031	0.0306	0.0241	-0.0042	0.0051	0.0009	0.0210
	C4 C7	0.0089	-0.0046	-0.0031	0.0335	0.0257	-0.0045	0.0055	0.0010	0.0221
b	F22 F15	0.0071	-0.0036	-0.0026	0.0424	0.0362	-0.0068	0.0079	0.0011	0.0231
	C8 C2	0.0100	-0.0071	-0.0025	0.0399	0.0304	-0.0053	0.0065	0.0011	0.0238
	F17 F20	0.0019	-0.0015	-0.0007	0.0144	0.0121	-0.0015	0.0023	0.0008	0.0086
c[c]	F16 F22	0.0055	-0.0048	-0.0040	0.0367	0.0279	-0.0051	0.0061	0.0009	0.0217
	C3 C8	0.0108	-0.0074	-0.0038	0.0449	0.0337	-0.0062	0.0073	0.0011	0.0258
d	F8 F24	0.0069	-0.0068	-0.0034	0.0454	0.0351	-0.0067	0.0077	0.0010	0.0249
	F9 C21	0.0086	-0.0072	-0.0021	0.0473	0.0380	-0.0064	0.0080	0.0016	0.0191
	F9 F23	0.0084	-0.0074	-0.0036	0.0513	0.0402	-0.0082	0.0091	0.0009	0.0252
	F9 F24	0.0084	-0.0074	-0.0036	0.0513	0.0403	-0.0082	0.0091	0.0009	0.0252
	C3 F24	0.0078	-0.0058	-0.0020	0.0425	0.0346	-0.0058	0.0072	0.0014	0.0165
	C3 F23	0.0078	-0.0058	-0.0020	0.0425	0.0346	-0.0058	0.0072	0.0014	0.0165
	F10 F23	0.0069	-0.0068	-0.0034	0.0453	0.0351	-0.0067	0.0077	0.0010	0.0249
e[c]	F7 F17	0.0014	-0.0013	-0.0012	0.0119	0.0094	-0.0010	0.0017	0.0007	0.0070
	F8 F16	0.0100	-0.0096	-0.0024	0.0612	0.0492	-0.0100	0.0112	0.0011	0.0307
	F8 C13	0.0100	-0.0081	-0.0036	0.0556	0.0440	-0.0084	0.0097	0.0013	0.0298
f[c]	F18 C8	0.0060	-0.0040	-0.0002	0.0294	0.0251	-0.0042	0.0052	0.0010	0.0175
	F18 C9	0.0060	-0.0040	-0.0001	0.0294	0.0252	-0.0042	0.0052	0.0011	0.0171
g[c]	C12 F18	0.0059	-0.0039	-0.0003	0.0289	0.0246	-0.0041	0.0051	0.0010	0.0174
	C9 F18	0.0057	-0.0038	-0.0002	0.0279	0.0240	-0.0040	0.0050	0.0010	0.0167
h[c]	F17 F19	0.0036	-0.0035	-0.0034	0.0276	0.0207	-0.0032	0.0042	0.0010	0.0141
	F17 F20	0.0039	-0.0037	-0.0036	0.0302	0.0229	-0.0037	0.0047	0.0010	0.0173
i[c]	F19 F17	0.0050	-0.0050	-0.0048	0.0370	0.0050	-0.0048	0.0058	0.0010	0.0211
j	F16 F8	0.0053	-0.0048	-0.0048	0.0399	0.0303	-0.0053	0.0064	0.0011	0.0250
k	F8 F16	0.0052	-0.0047	-0.0047	0.0393	0.0299	-0.0052	0.0064	0.0011	0.0247
l	F8 F16	0.0045	-0.0041	-0.0039	0.0344	0.0264	-0.0045	0.0055	0.0010	0.0217

[a] See Fig. 1 for details of atom labeling and conformation type. See Fig. 4 for QTAIM based molecular graph.

[b] The properties include the charge density ρ_b, the three principal eigenvalues of the Hessian of the charge density matrix $\lambda_{i\ (i=1-3)}$, the Laplacian of the charge density $\nabla^2\rho_b$, the gradient kinetic energy density G_b, the potential energy density V_b, the total energy density H_b, and .1 a.u. of ρ_b = 6.7483 eÅ^{-3}; 1 a.u. of λ_i's or $\nabla^2\rho_b$ = 24.099 eÅ^{-5}; 1 a.u. of V_b, or G_b, or H_b = 627.504 kcal mol^{-1}.

[c] Values of selected bonds are shown for symmetry reasons.

$$s = \frac{1}{[2(3\pi^2)^{\frac{1}{3}}]} \frac{|\nabla\rho|}{\rho^{\frac{4}{3}}} \quad \text{.....(1)}$$

This Eqn. envisages that as one goes far from the nuclei of a system, s will have larger values in regions where ρ(r) decays to zero exponentially, and where the $\rho(r)^{4/3}$ term tends to zero more faster than the $|\nabla\rho(r)|$ term does. At the bond critical point between two bonded atomic basins in compounds, we have $|\nabla\rho(r)| = 0$, and whence Eqn. 1 gives rise to s = 0 (the lower bound of RDG). Unequivocally, bcp is the point where one finds no difference between QTAIM and RDG.

According to Johnson et al., [19a] the supposedly stabilizing and destabilizing interactions between interatomic regions in molecules/complexes can be easy discriminated in terms of the RDG isosurface critical point, where ρ is dominated by specific noncovalent interaction (NCI), and where its gradient is nonvanishing. This critical point is a region of space characterized by either the negative or the positive sign of the second eigenvalue λ_2 ($\lambda_1 \leq \lambda_2 \leq \lambda_3$) of the Hessian matrix of the charge density. That is to say, for supposedly stabilizing interactions, $\lambda_2 < 0$, and for supposedly destabilizing interactions, $\lambda_2 > 0$, and the value of ρ determines the strength of the interaction involved. Important details on the ambiguity/unambiguity of the results of the RDG method have been discussed elsewhere.[5a-c,19, 33]

Fig. 4 collects the M06-2X/6-311++G(d,p) QTAIM molecular graphs for all the $(C_6F_6)_2$ dimers examined. In the most stable dimer, Fig. 4a, we mark four intermolecular bond paths, two C···F and two C···C. These bond paths are strained(bent), and are seemingly responsible holding the two monomers together in the dimer configuration. The ρ_b values at the C···F and C···C bcps are as small as 0.0064 and 0.0089 a.u.,respectively, which are comparable with those previously reported for various other noncovalently bonded interactions, such as H-bonds ($\rho_b \approx$ 0.0038 – 0.0325 a.u.), [31g] H—H bonds ($\rho_b \approx$ 0.0080 – 0.0168 a.u.),[31f] C···O bonds ($\rho_b \approx$ 0.0018 – 0.0029 a.u.),[5a] C···C bonds ($\rho_b \approx$ 0.0021 – 0.0034 a.u.),[5a] and F···F bonds ($\rho_b \approx$ 0.0080 – 0.0223 a.u.).[31a, e] The very small magnitude of ρ_b for the C···F and C···C bcps is indicative of the presence of closed-shell interactions. [5,18,23,31] The result is in concordance with the RDG based NCI spike and isosurface plots displayed in Fig. 5a for the corresponding dimer. As expected, it shows four attractive regions painted in green. A pair of two such regions is emanated between the four fluorine atoms, and the other pair is emanated between the four carbon atoms, both common to the two aromatic rings.

The RDG isosurface critical point features are concordant with the RDG spikes in the s vs. sign (λ_2)×ρ plot. This is not very surprising because, as expected, the $\lambda_2 < 0$ region mnemonic of stabilization unmasks two separate vertical spikes for the dimer, one for C···C and one for C···F. Similarly, the $\lambda_2 > 0$ region mnemonic of destabilization unmasks two other vertical spikes, one appears due to the (3, +1) rcps of the two aromatic rings, and one appears

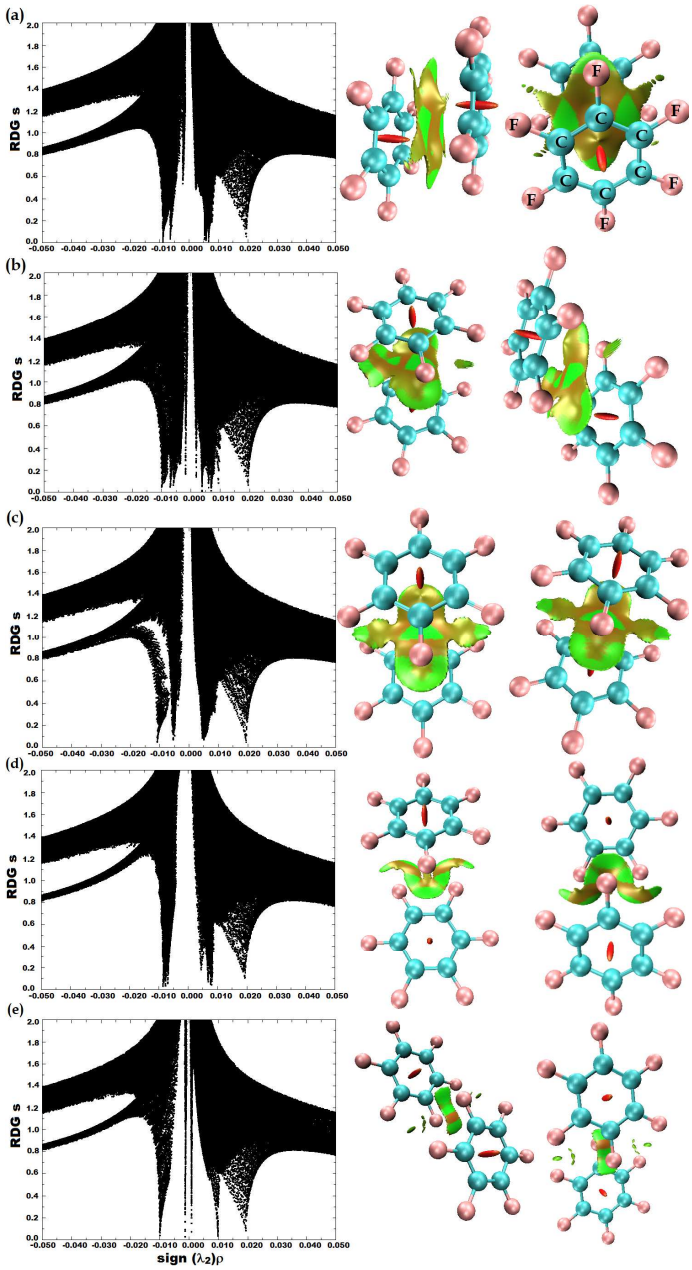

Fig. 5: M06-2X/6-311++G(d,p) calculated RDG s vs. sign(λ_2)×ρ (in a.u.) plots (left) for the first five most stable dimers of the C_6F_6 molecule (see Fig. 1a-c). The spikes in the sign(λ_2)×ρ < 0 and sign(λ_2)×ρ > 0 regions represent to the attractive and repulsive interactions, respectively. The s = 0.6 a.u. RDG isosurfaces in the ball and stick models representing to the former and latter interactions are painted in green and (brown) red, respectively (right). See Fig. 4a-e for comparision with the corresponding QTAIM molecular graphs.

due to the repulsion between the two aromatic ring surfaces of the $(C_6F_6)_2$ dimer at its

equilibrium geometry. These two repulsive aspects of chemical interaction are painted as red and brown RDG isosurfaces, respectively, see Fig. 5a. A similar comparative argument can also be made between the molecular and RDG graphs obtained for each of the four other dimers displayed in Figs. 4b-e and 5b-e, respectively. That said, there have been suggestions that the displaced-parallel arrangement between the two aromatic rings in dimers of similar varieties is a

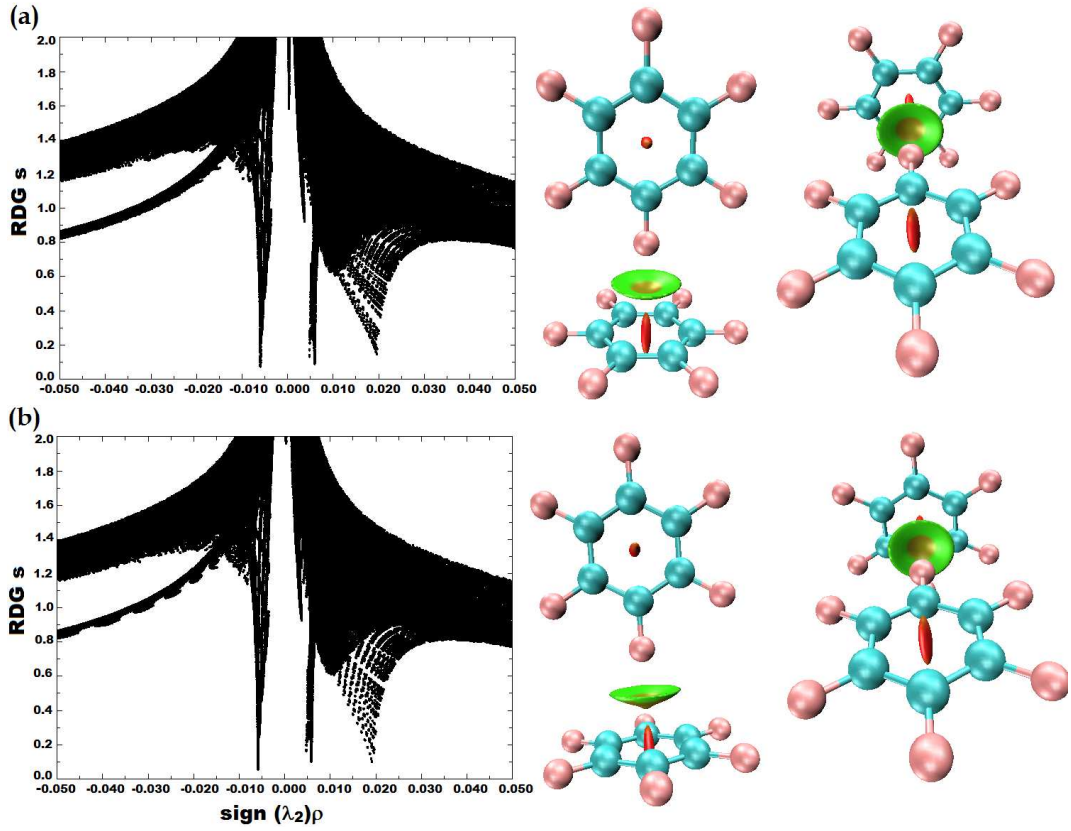

Fig 6: M06-2X/6-311++G(d,p) level RDG s versus sign(λ_2)×ρ plots (left) for the two T-shaped $(C_6F_6)_2$ dimers (values in a.u.). The spikes in the $\lambda_2 < 0$ and $\lambda_2 > 0$ regions represent to the weakly attractive and strongly repulsive regions, respectively. Shown on the right of each of these plots is the s = 0.6 a.u. RDG isosurface (ball and stick model). For clarity, two different views of the RDG isosurface are presented for each dimer. Colored isosurfaces in green and red (brown) represent to attraction and repulsion, respectively. See Figs. 1g and h for geometric details.

consequence of π—π stacking. [37] Interestingly, this is not true for the $(C_6F_6)_2$ dimers shown in Fig. 5a-e, as the attraction between the monomers in these dimers is predominantly atom-atom/atom-bond centered, evident of the discrete RDG isosurfaces in green appearing between the interacting atomic basins. In addition, neither QTAIM nor RDG does exaggerate any type of attraction between the monomers in the $(C_6F_6)_2$ dimers that can be viewed as an eventual

consequence of the alignment between the regions of positive and negative electrostatic potential, as often suggested. [37e]

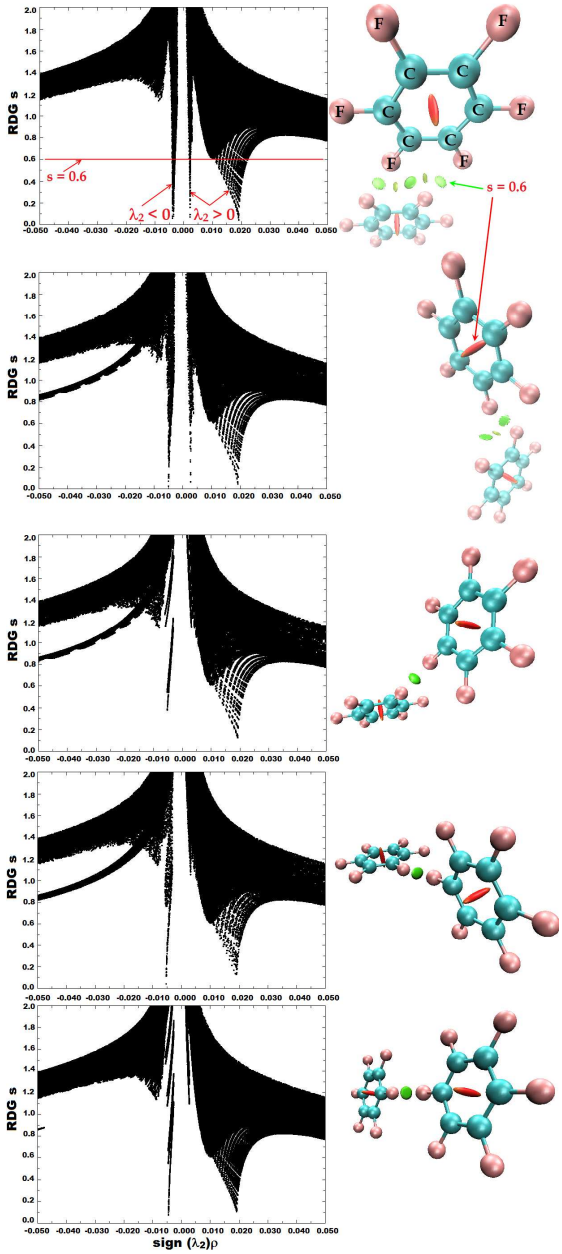

Fig. 7: M06-2X/6-311++G(d,p) level RDG s versus sign(λ_2)×ρ plots for the five high energy (least-stable) dimers (values in a.u.), see Fig. 1h-l. The spikes in the $\lambda_2 < 0$ and $\lambda_2 > 0$ regions represent to the weakly attractive and strongly repulsive regions, respectively. Shown on the right of each of these plots is the s = 0.6 a.u. RDG isosurface (ball and stick models). For each case, two different views are presented for clarification. Colored isosurfaces in green and red represent to attraction and repulsion, respectively.

The consistency between QTAIM and RDG based NCI topologies of the charge density discussed above is not quite flabbergasting.[33e] However, it is to be pointed out that the discrepancy between the results of the two methods arises, but not always, especially when the π—π interaction is the key outset of complex stabilization, as well as when the intra- and/or inter-molecular bonding region is significantly flat. To make the point more distinct, let us compare the QTAIM molecular graphs in Figs. 4b and c with the corresponding RDG isosurface graphs displayed in Fig. 5b and c, respectively. As might be immediately noticed from each of the former two graphs, QTAIM predicts three bond paths between the two C_6F_6 subunits, annunciating the possibilities of two F···F and one C···C intermolecular bonding interactions. The ρ_b and $\nabla\rho_b$ values at the bcps of such interactions in Fig. 4b are ca. 0.0071 and 0.0362 a.u., 0.0019 and 0.0121 a.u., and 0.0100 and 0.0304 a.u., respectively, while those in Fig. 4c are ca. 0.0055 and 0.0079 a.u., 0.0055 and 0.0079 a.u., and 0.0108 and 0.0337 a.u., respectively, giving the indication of the presence of closed-shell interactions.[5,31,32] Encouragingly, these links in Figs. 4b and c are indeed unraveled by NCI plots, which appear as green isosurfaces in low RDG regions between the noncovalently bonded atoms in Figs. 5b and c, respectively. In addition to these interactions, RDG predicts a few more regions of attraction appearing between the C=C π-framework of the aromatic ring in one monomer and the fluorine's lateral negative portion in the other in both the dimers, which are absent in the corresponding QTAIM predicted molecular graphs. Again, this oddity is not very uncommon because, as discussed separately by Pendás et al.[32a] and Tognetti et al.,[44] the presence or absence of bond paths between atomic basins in molecules are directly related to the competition between the primary and secondary exchange energy channels. Specifically, when no competition is present between the exchange channels, the bond path appears, and when it is present, the bond path disappears. Similarly, the bcp between the bonded atomic basins appears when the primary exchange energy channel is dominating, and disappears when the secondary exchange energy channel is more competing.[44]

Moreover, the RDG isosurfaces for the two T-shaped configurations of the $(C_6F_6)_2$ dimer, Figs. 6a and b, apprise good consistency with the QTAIM-based molecular graphs for the corresponding species, Figs. 4f and g, respectively. The latter method demonstrates the formation of the T-shaped arrangement to be due to the attraction between the fluorine's σ_{hole} in the top monomer and each of the six carbon atoms of the bottom monomer, see Fig. 4g for example. There are therefore six bond paths and six bcps in the intermolecular bonding regions, forming a cone-like topology. ρ_b at each C···F bcp is ca. 0.0060 and 0.0059 a.u. in4f and g, respectively, showing a depleted electron density profile at the bond critical point region. Similar bonding modes were previously identified for other systems, e.g., Ti bonding to the hydrocarbon frameworks, cyclopentadienyl, for example.[31h] According to Bader et al., [31h] an interaction of this type can be well described as a bonded cone-of-density rather than represented in terms of individual atom-atom interaction. The suggestion is perfectly in line with the RDG plots displayed in Figs. 6a and b for the corresponding dimers, respectively, in which, the interaction

between the fluorine and the entire C=C π-framework of the aromatic ring can be realized in terms of a cone-of-density-like isosurface. Note that the RDG isosurface between the π_{hole} (+) and the σ_{hole} (–) regions in each of these dimers is repulsive, reminiscent of the brownish circular volumes. This is in sharp disagreement with the MESP model that characterizes the interaction between fluorine and C=C π-framework as $\pi_{hole}(+)\cdots\sigma_{hole}(-)$ type. The obvious discrepancy between the results of the two computational methodologies is indeed due to the latter in which the NCI isosurfaces resulting from the low RDG regions are very much vaguer near at the (3,+1) rcps than those near at the (3,–1) bcps.[33f] According to Johnson et al.[19a] and Contreras-García et al.,[19b-c] the RDG at the former cp is always sterically repulsive. As is so, this must then mean the RDG isosurface associated with the π_{hole} of an aromatic ring will always be repulsive regardless of whether the electrostatic surface potential associated it is purely negative, or is purely positive, which, to our view, is certainly meaningless. We believe this is probably the reason that makes us no wonder why the slipped-parallel and/or T-shaped arrangements between the two C_6F_6 subunits in the $(C_6F_6)_2$ dimers produce brownish/reddish RDG domains in the midway between the two (3,+1) rcps, see Figs. 5 and 6, for examples. These results further demonstrate that the RDG reprehensibly identifies nonbonded attractions as repulsive at longer intermolecular distances, and indeed this is not in decent agreement with the previous suggestion *repulsive interactions are only recognized as such by NCI when the repulsion is very strong.*[33e]

Fig. 7 lists the NCI plots for all the other five least stable $(C_6F_6)_2$ dimers. QTAIM molecular graphs for the corresponding dimers are given in Fig. 4 from h to l. A close examination of the latter graphs indicate the presence of three F···F bonded interactions in Fig. 4h, two in Fig. 4i, and one in each of the latter three geometries in Figs. 4j-l, all inferred from the signatures of the bond path and critical point topologies.[5, 18, 23, 31] The mean charge densities at the F···F bcps are ca. 0.0058, 0.0038, 0.0053, 0.0052, and 0.0045 a.u. for the corresponding dimers, respectively (see Table S1 for the entire detail of the topological properties). Intriguingly, these bonding modes are also palpable of the plots in Fig. 7, in which, each F···F pair is accompanied with a single disk-like circular RDG volume in green in the isosurface plot, and an RDG spike in the NCI plot in the $\lambda_2 < 0$ region, both evocative of attraction.

Cormanich and coworkers have recently demonstrated that the RDG results are not always unambiguous because they unpleasantly identify nonbonded attractions as repulsive at short interatomic distances (as in CX_4 dimers, for example), and the interactions that are attractive with it do not translate into noticeable energetic stabilization.[33e] The latter characteristic can also be acknowledged from the results of this study. For example, the (stability) trend in the binding energies of the first five $(C_6F_6)_2$ dimers listed in Fig. 1 is a > b > c > d > e (see Table 1 for ΔE values). This is not sharply in consistent with the corresponding trend reflected in the vertical sizes of the RDG spike, as well as that in the peak positions of such spikes below s = 0.6 a.u. in the $\lambda_2 < 0$ region for the corresponding dimers (passing from Figs. 5a to 5e). A similar conclusion can also be released comparing the trend in the binding energies of

the three F···F bonded $(C_6F_6)_2$ dimers passing from Fig. 1j to 1l against that in their corresponding RDG spike sizes, as well as that in the peak positions of such spikes below the s = 0.6 a.u. line in red in the $\lambda_2 < 0$ region passing from Fig. 7a to 7c.

From the data in Table S1, it is unambiguous that the three eigenvalues of the Hessian of the charge density matrix are such that for all F···F/C···F/C···C bcps $\lambda_1 < 0$, $\lambda_2 < 0$, and $\lambda_3 > 0$. Because the magnitude of λ_3 is too large compared to the other two eigenvalues for these bcps, the Laplacian of the charge density, which is the mathematical sum of these three eigenvalues $\lambda_{i(i=1-3)}$ ($\nabla^2\rho_b = \lambda_1 + \lambda_2 + \lambda_3$), is positive at all such bcps, with $\nabla^2\rho_b$ values varying in the 0.0050 – 0.0492 a.u. range. Notable from Table S1 are also the kinetic energy densities (G_b) at the F···F/C···F/C···C bcps that are larger than their corresponding potential energy densities (V_b), resulting in positive total energy densities ($H_b = (V_b + G_b) > 0$) at those bcps. The diagnostics $\nabla^2\rho_b > 0$ and $H_b > 0$ synchronous with the F···F/C···F/C···C bcps are qualifications of closed-shell interactions.[5, 18, 23]

The QTAIM and RDG characterized noncovalently bonded interactions in the conformations of the $(C_6F_6)_2$ dimer are further confirmed by the analysis of the QTAIM-based delocalization index (DI), a two-electron property that has long been viewed as a measure of bond order. [36] By definition,[51] this property can be calculated for any atomic pairs regardless of whether the atoms in molecules are bonded to each other or not (i.e., whether there exist bond paths in the bonded atomic basin pairs or not). As summarized in Table S1, the DIs calculated for all the F···F, C···F, and C···C bonding interactions are in the narrow range between 0.0070 and 0.0307, which are comparable with the magnitudes previously reported for similar C···C/C···O bonded noncovalent interactions.[5a] Even so, this range is incomparable with those reported for the F···F intramolecular bonding interactions found in several polyfluoro-substituted aromatic compounds (values between 0.0374 and 0.0902), as the large DI values were predicted for very short F···F inter-nuclear separation distances ranged between 2.3 and 2.8 Å. [31a]

Now, let us look at Fig. 4a. It is apparent from this that except for the two well defined F···F interactions QTAIM's bond path and critical point topologies do not reveal the possibility of any other intermolecular bonding interactions between the other fluorine atoms in the dimer. However, the NCI plot of this the dimer in Fig. 5a gives an indication of the presence of four new F···F interactions of type-Ic. Although these interactions are too weak, they can be readily evident of the dot-like multiform domains between the fluorine atoms painted in colors ranging from light brown to green, characterized by the $F_{13}\cdots F_{20}$ (3.383 Å), $F_{15}\cdots F_{22}$ (3.382 Å), $F_{16}\cdots F_{23}$ (3.383 Å), and $F_{18}\cdots F_{19}$ (3.382 Å) interactions (see Fig. 1a for atom labeling). A DI value of 0.0073 is estimated for each of the four F···F pairs, giving an indication that these are all *representatives* of attraction.

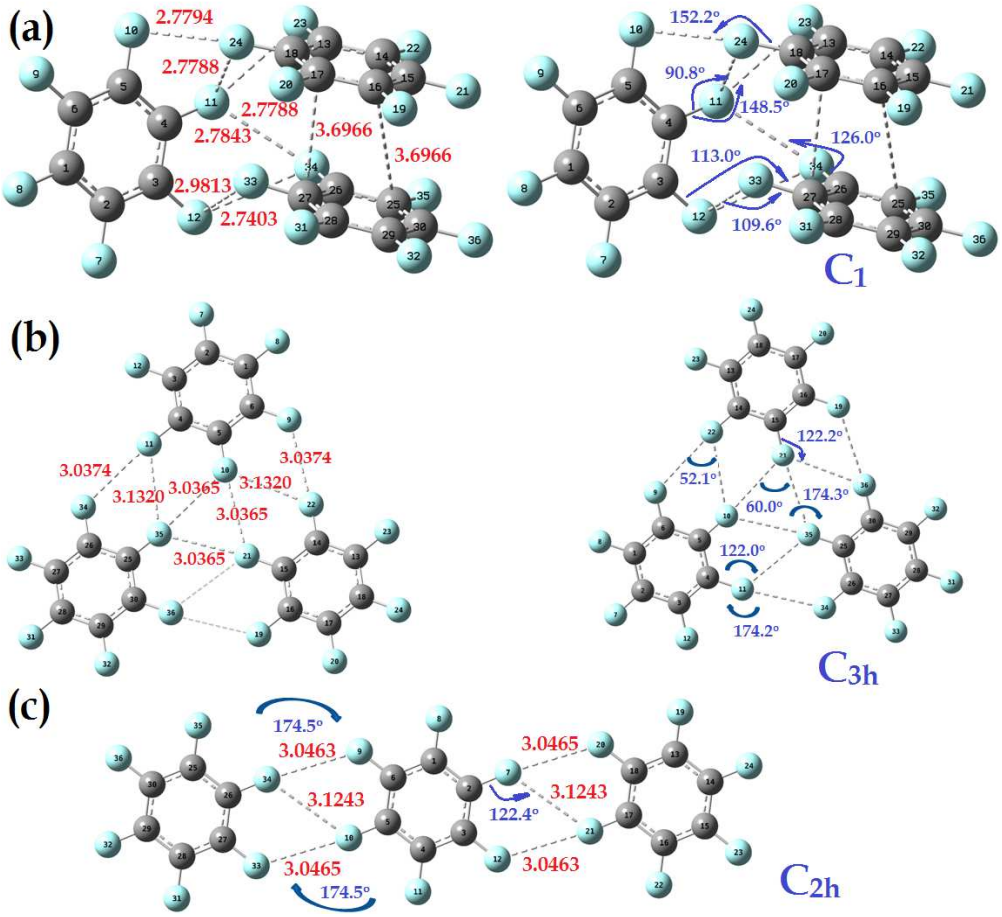

Fig. 8: The three ptimized geometries of the $(C_6F_6)_3$ trimer, obtained with M06-2X/6-311++G(d,p). Values of selected intermolecular contact distances (in Å) and bond angles (in °) are shown. For clarity, two geometries are illustrated for each of a) and b), one summarizes the intermolecular contact distances and the other the important bond angles.

2.3.3 Trimers and tetramers of C_6F_6

A specific aim of this section was to show whether the recently endorsed[15] inverted windmill geometry between the fluorine atoms in the two-dimensional supramolecular layered structure formed of the fully fluorinated BPEPE-F18 molecules is implicative of the clusters the C_6F_6 molecules. And whether such clusters are denouement of cooperative binding. In order to provide reasonable answers to these two questions, a few geometries of the conformations of the $(C_6F_6)_n$ (n = 3, 4) clusters were fully energy-minimized with M06-2X/6-311++G(d,p).

Figs. 8 and 9 illustrate the optimized geometries of the three conformations of the $(C_6F_6)_3$ trimer and of the two conformations of the $(C_6F_6)_4$ tetramer, respectively. As can be apparently seen from Fig. 8c/9b, the *planar* array of the three/four subunits of the C_6F_6 molecule results in the formation of a C_{2h} geometry for the $(C_6F_6)_3/(C_6F_6)_4$ trimer/tetramer. However, when such subunits are planerly non-arrayed, they produce geometries illustrated in Figs. 8a-b and 9a. Except for the geometry in Fig. 8a, the fluorine atoms in all the above four cases are mainly linked with each other via type-Ia and -II intermolecular topologies, Scheme 1, comparable with that found for the $(C_6F_6)_2$ dimer h (Fig. 4). Interestingly enough, the geometry in Fig. 8b, as well as that in Fig. 9a, includes windmill type geometry between the fluorine atoms, which is analogous to that reported in ref. 15. This kind of geometrical arrangement between the C_6F_6

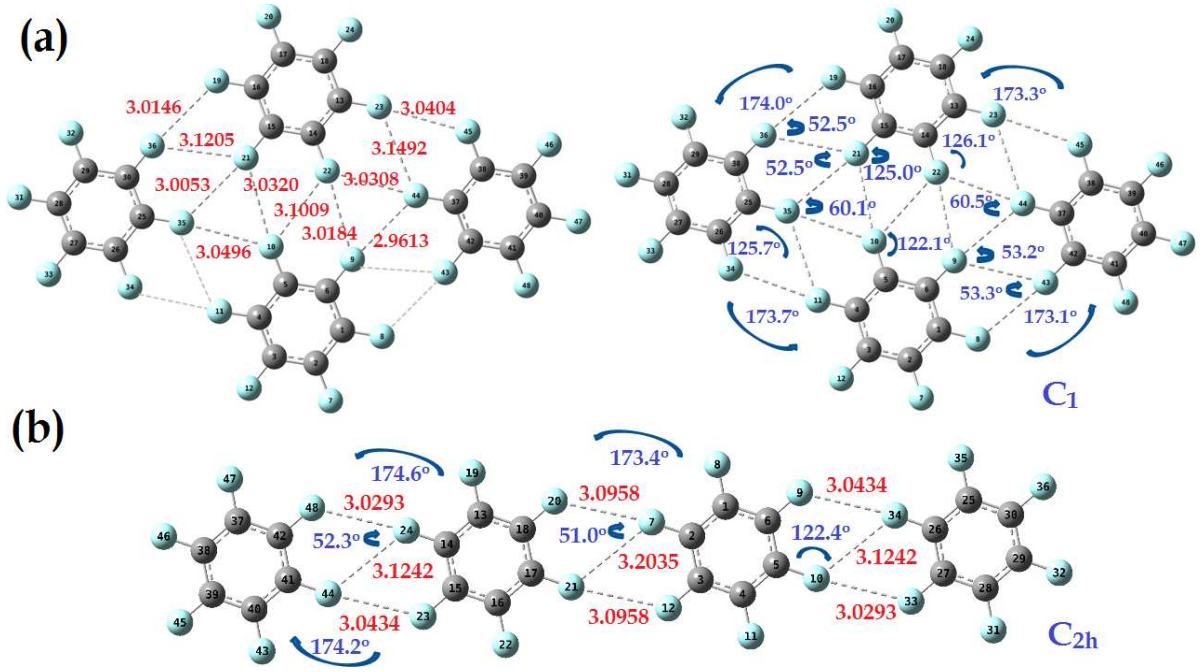

Fig. 9: Optimized geometries of the $(C_6F_6)_4$ tetramer, obtained with M06-2X/6-311++G(d,p). Values of selected intermolecular contact distances (in Å) and bond angles (in °) are shown. For clarity, two geometries are presented for a), one summarizes the intermolecular contact distances and the other the important bond angles.

subunits in $(C_6F_6)_3/(C_6F_6)_4$ is indeed a consequence of attraction between the merely negative fluorine atoms, arising mainly due to the polarization and dispersion forces, wherein electrostatics plays an important role in determining the repulsive part of the interaction (*vide supra*). It is worth mentioning that Kawai et al.[15] were not the first, but Reddy et al.[27a] were also observed similar windmill type intermolecular topologies between the halogen atoms when fully

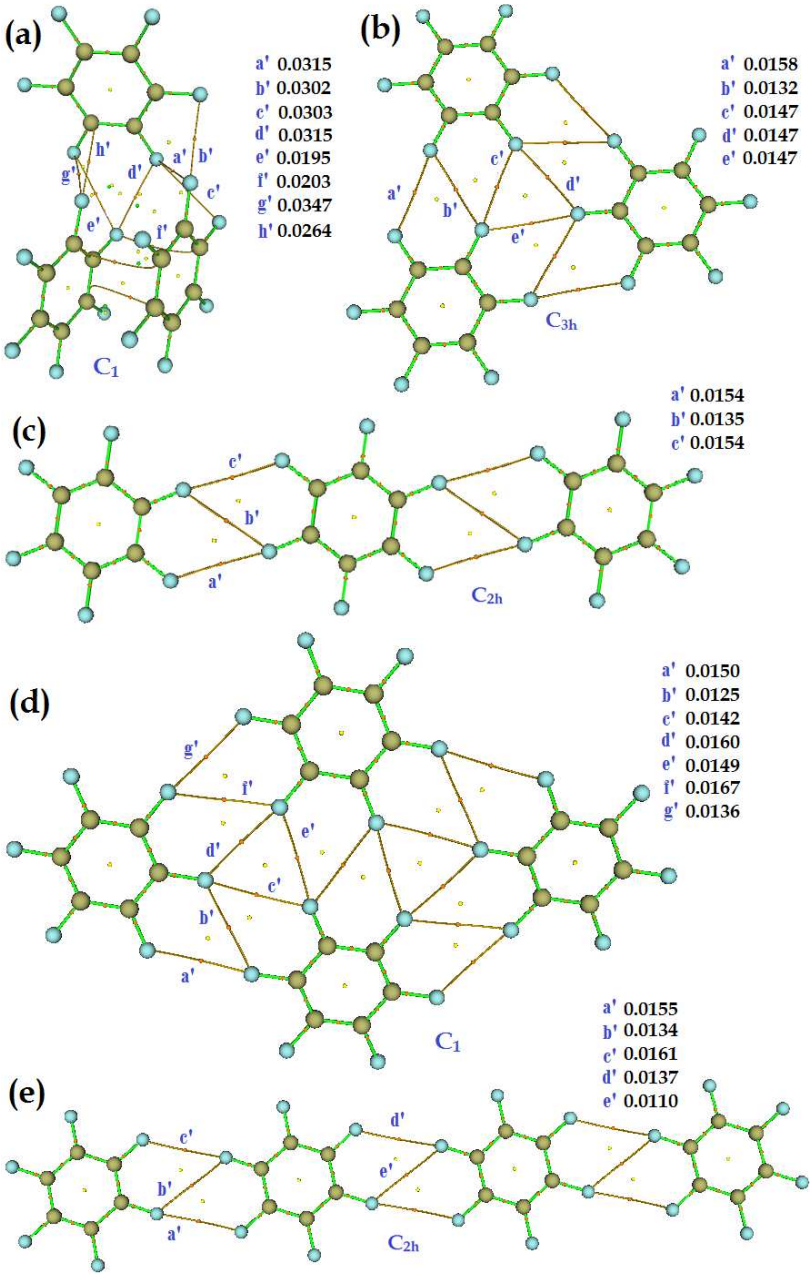

Fig. 10: Molecular graphs for some selected conformations of the $(C_6F_6)_n$ (n = 3, 4) clusters, obtained using M06-2X/6-311++G(d,p). Values of delocalization index DI are listed for selected atom pairs, obtained within the framework of QTAIM. [36] The (3, –1) and (3, +1) bond and ring critical points are shown as tiny spheres in red and yellow, respectively. The (3, +3) cage critical point is shown in green only for a few cases to avoid complications. Bond paths represent to covalent and noncovalent bonds are displayed as lines in green and dark-orange, respectively. Carbon and fluorine atoms are shown as balls in dark goldenrod and light sky blue, respectively. See Figs. 8 and 9 for details of atom numbering.

halogenated aromatic compounds were self-assembled in the solid state, with the halogens were notably of the chlorine, bromine, and iodine atoms.

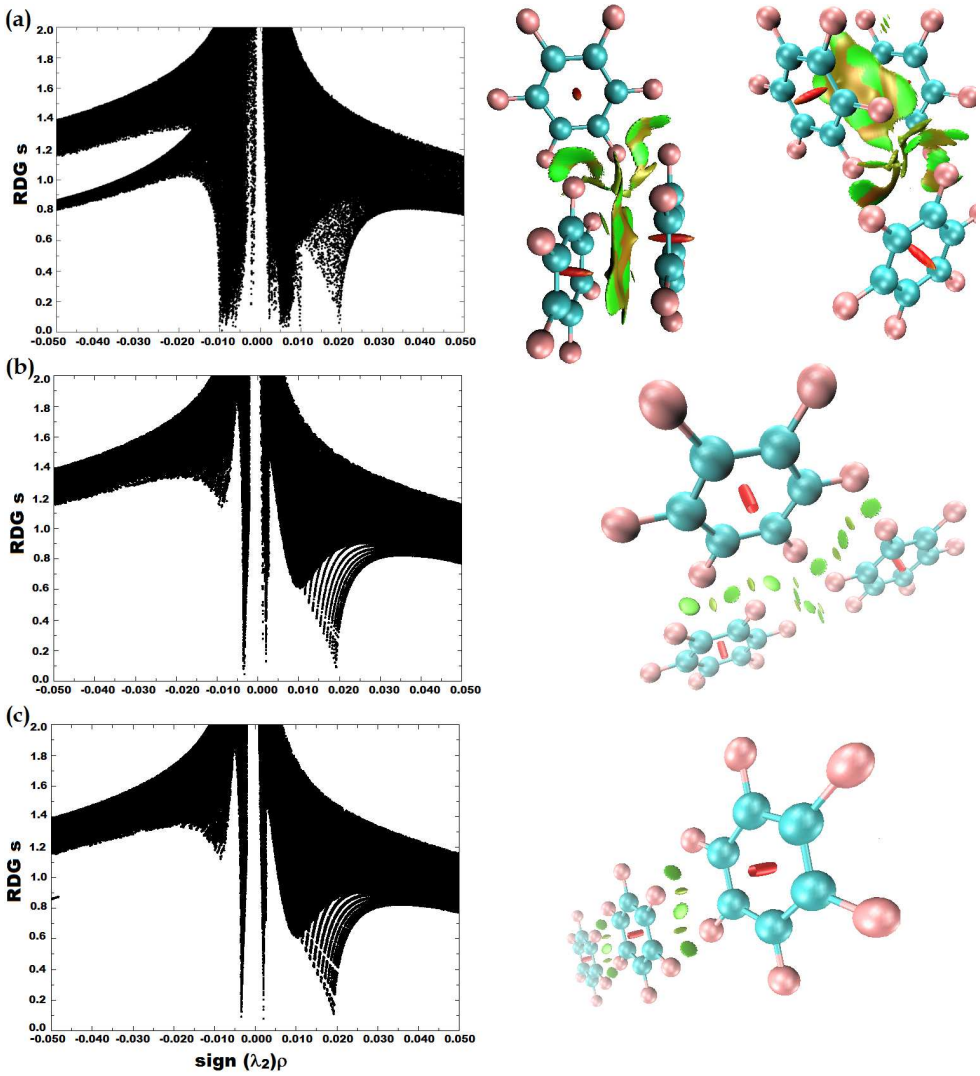

Fig. S3: RDG s vs. sign(λ_2)×ρ (in a.u.) plots for the three trimers of the C_6F_6 molecule, computed with M06-2X/6-311++G(d,p). The spikes in the sign(λ_2)×ρ < 0 and sign(λ_2)×ρ > 0 regions represent to the attractive and repulsive interactions, respectively. The s = 0.6 a.u. RDG isosurfaces in ball and stick models representing to the former and latter interactions are painted in green and red, respectively. For clarity, two different views are presented for (a). See Fig. 8 for geometric details, and Fig. 10a-c for QTAIM based molecular graphs.

Table S2: Selected QTAIM based topological properties of the charge density for the three trimers of the $(C_6F_6)_3$ complex, obtained with M06-2X/6-311++G(d,p).[a],[b]

Conformation	(3,–1) bcp	ρ_b	λ_1	λ_2	λ_3	$\nabla^2\rho_b$	V_b	G_b	H_b	DI
a	F24 F11	0.0091	-0.0089	-0.0082	0.0581	0.0410	-0.0089	0.0096	0.0007	0.0315
	F23 F11	0.0079	-0.0078	-0.0074	0.0537	0.0385	-0.0077	0.0087	0.0010	0.0303
	F34 F11	0.0082	-0.0086	-0.0080	0.0557	0.0391	-0.0079	0.0088	0.0010	0.0315
	F24 F10	0.0078	-0.0077	-0.0067	0.0531	0.0387	-0.0077	0.0087	0.0010	0.0302
	F33 F12	0.0100	-0.0096	-0.0046	0.0627	0.0485	-0.0099	0.0110	0.0011	0.0347
	F34 F12	0.0053	-0.0052	-0.0050	0.0375	0.0274	-0.0049	0.0059	0.0010	0.0195
	C13 F34	0.0067	-0.0039	-0.0024	0.0318	0.0254	-0.0044	0.0054	0.0010	0.0203
	C17 C27	0.0094	-0.0052	-0.0021	0.0351	0.0278	-0.0047	0.0058	0.0011	0.0206
	C15 C25	0.0084	-0.0038	-0.0015	0.0294	0.0241	-0.0040	0.0050	0.0010	0.0184
	F33 C3	0.0099	-0.0078	-0.0032	0.0573	0.0463	-0.0083	0.0099	0.0017	0.0264
b	F9 F22	0.0035	-0.0033	-0.0032	0.0278	0.0212	-0.0033	0.0043	0.0010	0.0158
	F10 F35	0.0035	-0.0033	-0.0032	0.0277	0.0212	-0.0033	0.0043	0.0010	0.0147
	F10 F21	0.0035	-0.0033	-0.0032	0.0277	0.0212	-0.0033	0.0043	0.0010	0.0147
	F22 F10	0.0033	-0.0032	-0.0031	0.0258	0.0195	-0.0029	0.0039	0.0010	0.0132
	F11 F35	0.0033	-0.0032	-0.0031	0.0258	0.0195	-0.0029	0.0039	0.0010	0.0132
	F11 F34	0.0035	-0.0033	-0.0032	0.0278	0.0212	-0.0033	0.0043	0.0010	0.0158
	F21 F35	0.0035	-0.0033	-0.0032	0.0277	0.0212	-0.0033	0.0043	0.0010	0.0147
	F21 F36	0.0033	-0.0032	-0.0031	0.0258	0.0195	-0.0029	0.0039	0.0010	0.0132
	F19 F36	0.0035	-0.0033	-0.0032	0.0278	0.0212	-0.0033	0.0043	0.0010	0.0058
c	F9 F34	0.0035	-0.0033	-0.0031	0.0272	0.0208	-0.0032	0.0042	0.0010	0.0154
	F10 F33	0.0035	-0.0033	-0.0031	0.0272	0.0208	-0.0032	0.0042	0.0010	0.0154
	F10 F34	0.0034	-0.0033	-0.0032	0.0263	0.0198	-0.0030	0.0040	0.0010	0.0135
	F20 F7	0.0035	-0.0033	-0.0031	0.0272	0.0208	-0.0032	0.0042	0.0010	0.0154
	F21 F7	0.0034	-0.0033	-0.0032	0.0263	0.0198	-0.0030	0.0040	0.0010	0.0135
	F21 F12	0.0035	-0.0033	-0.0031	0.0272	0.0208	-0.0032	0.0042	0.0010	0.0154

[a] See Fig. 8 for details of atom labeling and conformation type. See Fig. 10 for QTAIM based molecular graph.

[b] The properties include the charge density ρ_b, the three principal eigenvalues of the Hessian of the charge density matrix $\lambda_{i\ (i=1-3)}$, the Laplacian of the charge density $\nabla^2\rho_b$, the gradient kinetic energy density G_b, the potential energy density V_b, the total energy density H_b, and .1 a.u. of ρ_b = 6.7483 e$Å^{-3}$; 1 a.u. of λ_i's or $\nabla^2\rho_b$ = 24.099 e$Å^{-5}$; 1 a.u. of V_b, or G_b, or H_b = 627.509 kcal mol^{-1}.

Table S3: Selected QTAIM based topological properties of the charge density for the two tetramers of the $(C_6F_6)_4$ complex, obtained with M06-2X/6-311++G(d,p).[a],[b]

Conformation	(3,–1) bcp	ρ_b	λ_1	λ_2	λ_3	$\nabla^2\rho_b$	V_b	G_b	H_b	DI
a	F19 F36	0.0038	-0.0036	-0.0034	0.0292	0.0222	-0.0035	0.0046	0.0010	0.0167
	F21 F10	0.0036	-0.0034	-0.0033	0.0282	0.0215	-0.0034	0.0044	0.0010	0.0149
	F21 F35	0.0038	-0.0036	-0.0035	0.0298	0.0226	-0.0036	0.0046	0.0010	0.0160
	F21 F36	0.0034	-0.0033	-0.0032	0.0266	0.0200	-0.0030	0.0040	0.0010	0.0136
	F22 F10	0.0036	-0.0035	-0.0034	0.0277	0.0208	-0.0032	0.0042	0.0010	0.0143
	F22 F9	0.0037	-0.0035	-0.0034	0.0290	0.0221	-0.0035	0.0045	0.0010	0.0154
	F44 F22	0.0036	-0.0034	-0.0033	0.0281	0.0214	-0.0034	0.0044	0.0010	0.0149
	F23 F44	0.0031	-0.0030	-0.0030	0.0249	0.0189	-0.0028	0.0037	0.0010	0.0127
	F45 F23	0.0035	-0.0033	-0.0032	0.0276	0.0211	-0.0033	0.0043	0.0010	0.0157
	F10 F35	0.0034	-0.0032	-0.0031	0.0269	0.0206	-0.0032	0.0042	0.0010	0.0142
	F35 F11	0.0031	-0.0030	-0.0029	0.0245	0.0186	-0.0027	0.0037	0.0010	0.0125
	F11 F34	0.0033	-0.0031	-0.0030	0.0265	0.0203	-0.0031	0.0041	0.0010	0.0150
	F44 F9	0.0043	-0.0042	-0.0040	0.0330	0.0248	-0.0041	0.0052	0.0010	0.0179
	F43 F9	0.0037	-0.0036	-0.0035	0.0284	0.0213	-0.0033	0.0043	0.0010	0.0145
	F43 F8	0.0045	-0.0043	-0.0041	0.0338	0.0254	-0.0043	0.0053	0.0010	0.0196
b	F24 F48	0.0036	-0.0034	-0.0033	0.0283	0.0215	-0.0034	0.0044	0.0010	0.0161
	F24 F44	0.0034	-0.0033	-0.0032	0.0263	0.0199	-0.0030	0.0040	0.0010	0.0134
	F23 F44	0.0035	-0.0033	-0.0032	0.0274	0.0209	-0.0033	0.0042	0.0010	0.0155
	F7 F21	0.0027	-0.0026	-0.0025	0.0219	0.0168	-0.0023	0.0033	0.0009	0.0110
	F7 F20	0.0030	-0.0028	-0.0027	0.0242	0.0187	-0.0028	0.0037	0.0010	0.0137
	F12 F21	0.0030	-0.0028	-0.0027	0.0242	0.0187	-0.0028	0.0037	0.0010	0.0137
	F34 F9	0.0035	-0.0033	-0.0032	0.0274	0.0209	-0.0033	0.0042	0.0010	0.0155
	F33 F10	0.0036	-0.0034	-0.0033	0.0283	0.0215	-0.0034	0.0044	0.0010	0.0161
	F34 F10	0.0034	-0.0033	-0.0032	0.0263	0.0199	-0.0030	0.0040	0.0010	0.0134

[a] See Fig. 9 for details of atom labeling and conformation type. See Fig. 10 for QTAIM based molecular graph.

[b] The properties include the charge density ρ_b, the three principal eigenvalues of the Hessian of the charge density matrix $\lambda_{i\ (i=1\text{-}3)}$, the Laplacian of the charge density $\nabla^2\rho_b$, the gradient kinetic energy density G_b, the potential energy density V_b, the total energy density H_b, and .1 a.u. of ρ_b = 6.7483 eÅ^{-3}; 1 a.u. of λ_i's or $\nabla^2\rho_b$ = 24.099 eÅ^{-5}; 1 a.u. of V_b, or G_b, or H_b = 627.504 kcal mol^{-1}.

Whether the intermolecular bonding topologies between the fluorine atoms in the geometries of the $(C_6F_6)_n$ (n = 3, 4) clusters are persuasive of attraction (closed-shell type) are

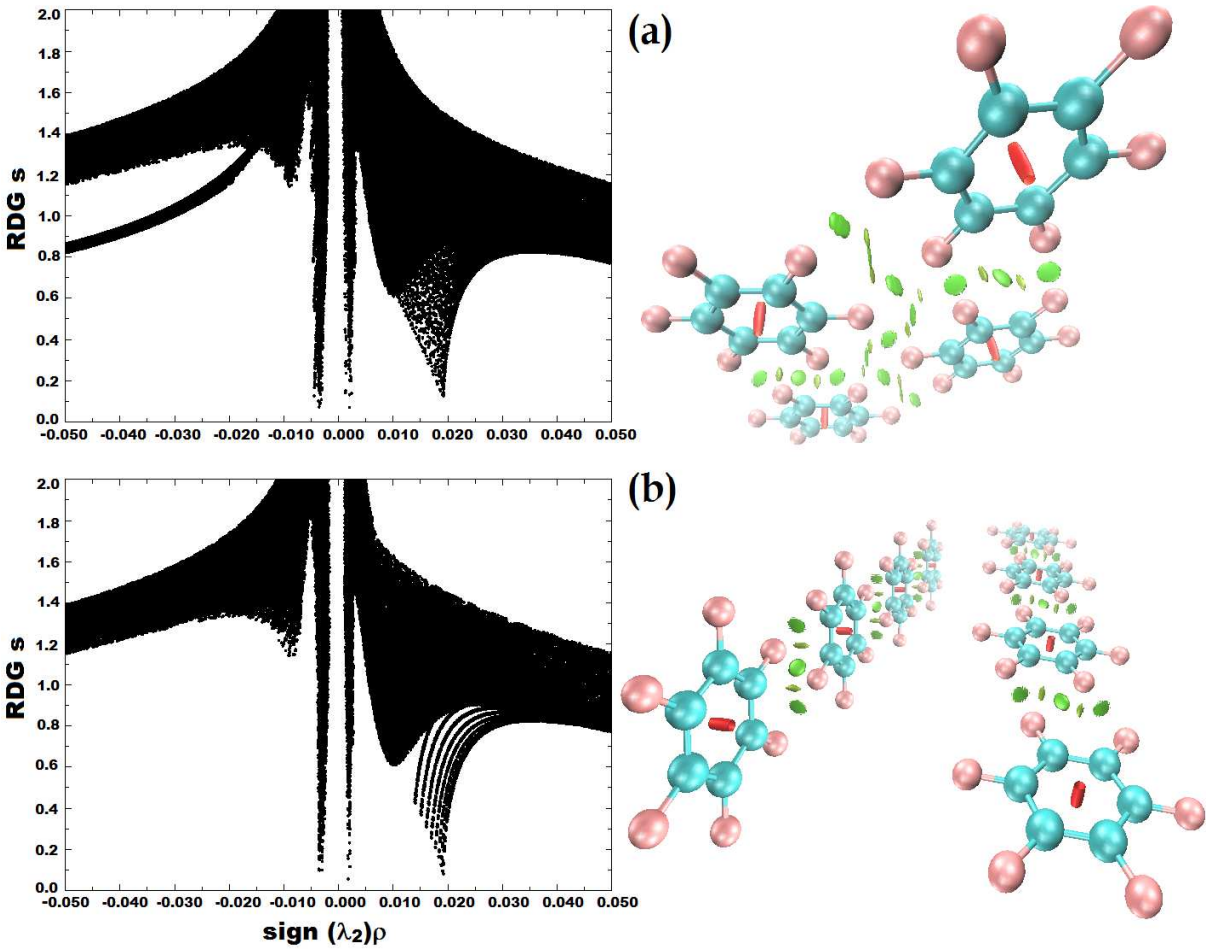

Fig. 11: RDG s vs. sign(λ_2)×ρ (in a.u.) plots for the two selected tetramers of the C_6F_6 molecule, obtained with M06-2X/6-311++G(d,p). The spikes in the sign(λ_2)×ρ < 0 and sign(λ_2)×ρ > 0 regions represent to the stabilizing and destabilizing interactions, respectively. The s = 0.6 a.u. RDG isosurfaces in the ball and stick models representing to the former and latter interactions are painted in green and red, respectively. Two different views of the isosurface of (a) are presented for clarity. See Fig. 9 for geometric details, and Fig. 10d-e for the QTAIM based molecular graphs for comparision.

inferred examining their QTAIM based molecular graphs (Fig. 10) and topological properties of the charge density (Tables S2 and S3). As can be seen from the molecular graphs, the nuclei of the bonded fluorine atoms in the F···F pairs of these clusters are evidenced by the presence of the bond path and (3, −1) bcp topologies. The charge density at such bcps is very small, all between 0.0033 and 0.0100 a.u. for the trimers, and that between 0.0027 and 0.0045 a.u. for the tetramers. The signs and magnitudes of $\nabla^2\rho_b$ and H_b at such bcps are positive and small (cf.

Tables S2 and S3 for values), revealing qualifications of closed-shell interactions. The QTAIM based delocalization indices for the F···F pairs are computed to lie between 0.0132 and 0.0315 for the trimers, and are between 0.0110 and 0.0167 for the tetramers (see detailed values in Fig. 9), which both are comparable with the corresponding values of similar contacts in the $(C_6F_6)_2$ dimers illustrated in Fig. 4. All these signatures of noncovalent bonding interactions are in fair agreement with the RDG-based spike and isosurface plots illustrated in Figs. S3 and 11 for the trimers and tetramers of the C_6F_6 molecule, respectively. To be more explicit, these latter plots each reveals expected green isosurfaces, as well as the vertical spikes, in the $\lambda_2 < 0$ region at low RDG, which are suggestive of F···F bonding interactions. A similar conclusion might also be drawn for the C···C and C···F interactions of the conformation illustrated in Fig. 8a (see Table S2 for a detailed topological properties and Fig. 10a for molecular graph).

The fluorine in the conformations of the $(C_6F_6)_2$ dimer serves as bi-, tri-, or tetra-furcating centers for F···F bond formations, Fig. 4. The particular theme is persistent with the same atom in the conformations of the $(C_6F_6)_3$ trimer and of the $(C_6F_6)_4$ tetramer. These are apparent from the QTAIM molecular graphs illustrated in 10b-e, wherein the fluorine divulges its capacity to act as tri- and tetra-furcated centers for the F···F bond formations. In the $(C_6F_6)_3$ trimer, Fig. 10a, it smartly plays its role as di-, tri-, and tetra-furcating centers. In all the above cases, it is functioning both as an electrophile and as a nucleophile for the F···F pair formation. Although the calculated F···F bond lengths and ∠F···F–C bond angles in the $(C_6F_6)_{n\ (n = 3, 4)}$ clusters in Figs. 10b-e are almost identical to those found in the geometry of the $(C_6F_6)_2$ dimer h (Fig. 4), it is eloquent that the F···F interactions marked b' are formed due to the overlapping of fluorine's negative lateral regions of identical electrostatic surface potential ($V_{s,max}$ = –6.5 kcal mol^{-1} for each, Fig. 2).

But now the question arises: what then compels the completely negative fluorine atom(s) in a C_6F_6 monomer to attract the same atom(s) in another monomer(s) at the equilibrium geometries of the $(C_6F_6)_n$ (n = 2,3,4) clusters. As discussed already above, the MESP model does not provide any straightforward answer to this question because it does not allow attraction between the two negative sites. The LMO-EDA model explains polarization and dispersion to be the main driving forces bringing the two C_6F_6 monomers together in the equilibrium cluster geometries. QTAIM's bond path topology demonstrates that the fluorine atoms in C_6F_6 would serve both as F-bond acceptor and donor for the formation of the F···F pairs in the $(C_6F_6)_n$ (n = 2,3,4) clusters. The latter two conclusions are in sharp contrast with Vallejos et al. who have suggested that the fluorine atoms are not generally polarizable and therefore not typically considered X-bond donors.[8e] Nonetheless, to provide more insight into factors that explain why the similarly negatively charged fluorine atoms in C_6F_6 are capable of forming the F···F bonding interactions, we have extended our study to perform QTAIM based source function analysis for some selected $(C_6F_6)_n$ clusters, including those illustrated in Figs. 4h, 4j-l, 8b-c, and 9a. For the geometry in Fig. 4h, each fluorine sharing the F···F interaction contributes a negative ρ value of

–0.0032 (–90.0%) a.u. to each of its two equivalent bcps marked a' and c', and of –0.0030 (–76.5%) a.u. to the bcp marked b'. Similarly, each fluorine contributes a negative ρ value of –0.0026 (–57.4%) a.u. to the $F_{16}\cdots F_{8}$ bcp in Fig. 4j (see Fig. 1j for atom numbering), of –0.0023 (–44.2%) a.u. to the same bcp in Fig. 4k, and of –0.0024 (–45.1%) a.u. to the same bcp in Fig. 4l. For the geometry in Fig. 8c, the fluorine atoms contribute negative ρ values of –0.0031 (–90.7%) and –0.0032 (–98.0%) a.u. to the $F_{9}\cdots F_{34}$ and $F_{34}\cdots F_{10}$ bcps, respectively. For the geometry in Fig. 8b, the fluorine atoms in $F_{9}\cdots F_{22}$, $F_{22}\cdots F_{10}$, and $F_{10}\cdots F_{21}$ contribute negative ρ values of –0.0031 (–85.8%), –0.0032 (–90.6%), and –0.0033 (–87.6%) a.u. to the respective bcps. And, similarly, the fluorine atoms in the geometry in Fig. 9a contribute negative ρ values of –0.0030 (–87.0%), –0.0033 (–105.3%), –0.0032 (–92.9%), –0.0032 (–88.6%), and –0.0032 (–92.3%) to the $F_{45}\cdots F_{23}$, $F_{23}\cdots F_{44}$, $F_{22}\cdots F_{10}$, $F_{22}\cdots F_{9}$, and $F_{22}\cdots F_{44}$ bcps, respectively. Our above observation is in line with Eskandari et al., [12e] who have recently concluded that in fluorine-centered noncovalent interactions the fluorine has the tendency to serve as a sink of charge density for the N···F bcps.

Whether or not the fluorine atoms of the C_6F_6 monomers in the $(C_6F_6)_n$ $(n = 3, 4)$ trimers/tetramers are bonded to each other are confirmed by estimating the uncorrected binding energies ΔE of these clusters. For this reason, we have used the relation: ΔE(trimer/tetramer) = E(trimer/tetramer) – [E(dimer/trimer) + E(C_6F_6)], where E refers to the total electronic energy of the molecular unit/subunit involved. The estimated ΔE values for the $(C_6F_6)_3$ trimers in Figs. 8c and b are ca. –1.89 and –2.76 kcal mol^{-1}, respectively, with the former is about –0.87 kcal mol^{-1} less stable than the latter one. The tendency is perpetual passing from the $(C_6F_6)_3$ trimer to the $(C_6F_6)_4$ tetramer. For instance, the ΔE for the $(C_6F_6)_4$ tetramers in Figs. 9b and a are ca. –2.81 and –4.49 kcal mol^{-1}, respectively, with the former is about –1.68 kcal mol^{-1} less stable than the latter. These results suggest that the ΔE values estimated for the planar arrayed and non-arrayed $(C_6F_6)_4$ tetramers are larger than those found for the corresponding conformations of the $(C_6F_6)_3$ trimer. And, compared to the $(C_6F_6)_2$ dimer h (Fig. 1), which has intermolecular topologies similar to those of 8b-c and 9a-b, the affinity of binding between the monomers in the $(C_6F_6)_3$ trimers, as well as in the $(C_6F_6)_4$ tetramers, increases.

The above results also indicate that the C_6F_6 subunits forming the planar arrayed geometries are relatively less stable than the corresponding planar non-arrayed ones, which is regardless of the nature of the cluster types examined. The characteristic is perspicaciously justified because the F···F intermolecular contact distances commenced between the fluorine atoms in the latter arrangement are larger in number and more tightly packed than those in the former arrangement. For example, the $(C_6F_6)_3$ geometry in Fig. 8c comprises of six F···F pairs (F···F distances vary between 3.0463 and 3.1234 Å), while that in Fig. 8b comprises of nine such pairs (F···F distances vary between 3.0374 and 3.0365 Å), which are relatively shorter. Similarly, the planarly arrayed and non-arrayed $(C_6F_6)_4$ tetramers comprise of nine and fourteen F···F pairs,

respectively, with the contacts in the former species are somehow loosely bound (cf. Fig. 8). This characteristic might explain why Kawai et al.[15] were able to observe an analogous planarly non-arrayed supramolecular layered structure formed of the BPEPE-F18 molecules on the Ag(111) surface. In any event, we have energy-minimized yet another conformation for the $(C_6F_6)_3$ trimer, Fig. 8a. Surprisingly, its binding energy is about 4.4 times larger than its other conformation in Fig. 8b (values of $\Delta E \approx -12.11$ vs. -2.76 kcal mol^{-1}), perhaps giving some evidence of the presence of synergistic binding. Such an attribute is not unexpected because the geometry of this conformation consists of a network of F···F type-Ic and -II contacts. These, along with the C···F and C···C long-ranged contacts identified, are altogether responsible for the effective stabilization of the trimer.

2.4 Conclusion

The study represented a first detailed conformational analysis of the $(C_6F_6)_2$, and to a smaller extent, $(C_6F_6)_3$ and $(C_6F_6)_4$ clusters using density functional theory. An original goal towards this investigation was intended to display the potential capacity of the C_6F_6 molecules in forming various homomolecular dimers, trimers, and tetramers, and to see whether they can be used for the emergence of self-assembled supramolecular clusters.

We showed that the geometries of several conformations of the $(C_6F_6)_2$ dimer to be stabilized by a varied number of long-ranged contacts, involving the F···F, C···F, and C···C, and in a few cases, by the π···σ_{hole} and π···lone-pair intermolecular topologies. These were found not to have dissimilar characteristics compared to what might be expected for the halogen-, hydrogen-, and other σ_{hole} interactions.

The binding energies ΔE for all the twelve $(C_6F_6)_2$ dimeric configurations ware ranged between -0.51 to -7.38 kcal mol^{-1}. The ΔE ($\Delta E \approx -7.38$ kcal mol^{-1}) for the most stable displaced-parallel arrangement (slipped but not stacked) was found to be roughly more than twice larger than that of the benzene dimer (-2.63 kcal mol^{-1}), and was somehow comparable with that of the indole···hexafluorobenzene[25a] (-7.18 kcal mol^{-1}) and benzene···hexafluorobenzene[25b,c] (-6.32 kcal mol^{-1}) π-stacked dimers. The BSSE was found to have significant effect on the nature of the conformational geometry, thus on magnitude of the ΔE.

Of significant interest was to explore the equilibrium geometries of a few of the homomolecular dimers, trimers, and tetramers of the C_6F_6 the molecule stabilized by the C–F···F–C intermolecular topologies, and which have significant geometrical similarities with the self-assembled supramolecular layered structure formed of the BPEPE-F18 molecules. Indeed, several such geometries between the C_6F_6 monomers were identified for the dimers, trimers, and tetramers. However, two geometries forming the pseudo windmill type topologies comprising of the C–F···F–C interactions were the planar $(C_6F_6)_3$ trimer (C_{3h}) and the nearly planar $(C_6F_6)_4$ tetramer (roughly C_2), in consonance with Kawai et al.'s observation.[15] Reddy et al.[27a] have also

previously reported topologically similar windmill type geometries between the hexahalogenated benzene derivatives excluding the involvement of the fluorine atom.

According to Kawai et al.'s interpretation, the F···F interactions in the supramolecular layered structure formed of the BPEPE-F18 molecules were stabilized mainly by dispersion. However, our LMO-EDA results have suggested that the formation of the F···F pair in the geometries of the $(C_6F_6)_2$ dimer is a consequence of attraction caused by the polarization and dispersive forces.

The electrostatic surface potentials on the axial and equatorial portions of the covalently bound fluorine in C_6F_6 were computed to be negatively nonequivalent, authenticating the anisotropic nature of the charge density profile around its nucleus. This has led to an immediate understanding that each fluorine in C_6F_6 accompanies a negative σ_{hole} along the outer portion of the C–F σ-axis. We have therefore made it apparent in this study that the nature of the fluorine's σ_{hole} in BPEPE-F18 could be similar to the one found in C_6F_6 given the covalently bound fluorine atoms in both these two compounds are somehow geometrically complementary, an interpretation which is against what was surmised by Kawai et al.[15]

We have showed that the totally negatively charged fluorine in isolated C_6F_6 has the potential to temper engage in directional bonding interactions with the nearest negative sites localized on the surfaces of the same atoms in other C_6F_6, despite it does not have a positive σ_{hole}. The perpetual adaptability of fluorine's directional behavior was evident in several dimeric, trimeric and tetrameric geometries of the C_6F_6 molecule, however, this was not very crystal-clear in several such geometries of the clusters that involve the F···F type-Ia/type-Ic intermolecular topologies, wherein the lateral portion of the fluorine in one C_6F_6 was involved attractively with an equivalent lateral negative portion of the same atom in other C_6F_6. Evidently, the molecular electrostatic surface potential model that was extremely useful in the past in unraveling the electrophilic and nucleophilic nature of atoms/fragments in molecules, as well as in elucidating the chemistry of noncovalent interactions, was found inadequate to provide any insightful explanation accounting for the reason why the wholly negatively charged fluorine in an isolated C_6F_6 could interact cooperatively with the same atom in another C_6F_6 to form the C–F···F–C supramolecular synthon, thereby promulgating failure of the model.

Contrariwise, the results of the QTAIM and RDG charge density based models were found to be the most remarkable. Although QTAIM, in a few instances, did not show the expected topological signatures of bonding, and RDG gave unphysical repulsive aspects of boding near the ring critical point regions, separate applications of these methodologies to the $(C_6F_6)_{n\ (n=2\text{-}4)}$ clusters could enable us confirming the attractive nature of the C–F···F–C (and other) interactions through their unified topological characteristics, reflecting superiority of these two methods over the former. Even so, QTAIM's source function analysis tool has allowed us to justify that for the formation of the F···F interactions the fluorine does not necessarily have to be a source, rather it would prefer to serve as a sink, in agreement with a recent rationale.[12e]

Finally, we would like to point out that the calculated signs and magnitudes of QTAIM charges conferred on the fluorine atoms sharing the C–F$^{\delta-}\cdots^{\delta-}$F–C interaction are identical (values approximately between –0.611 and –0.614 *e*), witnessing *like liking like*. The earmark is compatible with what was proposed some time ago for the A–H$\cdots$H–B bonding interaction.[31i] To go into a little detail of this latter interaction, it has been said that this is attractive, and is formed when both the hydrogen atoms are either electrically neutral or carry small charges which are usually of similar sign, and the A–H bond upon the formation of the A–H$\cdots$H–B interaction decreases. Notwithstanding, the aforementioned unequivocal signatures of noncovalent interactions supporting the reliability of the F$^{\delta-}\cdots^{\delta-}$F interactions formed between the two equally charged species do not come along with the previous suggestion '*halogen bonding can readily be understood as the attractive interaction between the positive outer region on the halogen and the negative site*', nor do they come along with the assertion *the negative electrostatic potential associated with a* σ_{hole} *precludes the possibility of halogen bonding–unless the electric field of the negative site is strong enough to induce a positive region on the halogen*. Thus in analogy with A–H$\cdots$H–B bonding interaction, we suggest referring the attractive interaction between the two fluorine atoms observed in the $(C_6F_6)_{n\ (n=2\text{-}4)}$ clusters to as *F$\cdots$F (or difluoride) bonding*. It is expected that this study will help others to explore the promising and hidden noncovalent chemistry of many other fluorine-based materials.

2.5 References

1. (a) P. Auffinger, F. A. Hays, E. Westho and P. Shing Ho, *Proc. Natl. Acad. Sci. U. S. A.*, 2004, 101, 16789; (b) M. R. Scholfield, C. M. V. Zanden, M. Carter and P. Shing Ho, *Protein Science*, 22, 2013, 139; (c) R. Wilcken, M. O. Zimmermann, A. Lange, A. C. Joerger and F. M. Boeckler, *J. Med. Chem.*, 2013, 56, 1363; (d) Y. Lu, T. Shi, Y. Wang, H. Yang, X. Yan, X. Luo, H. Jiang and W. Zhu, *J. Med. Chem.*, 2009, 52, 2854; (e) A. Mukherjee, S. Tothadi and G. R. Desiraju, *Acc. Chem. Res.*, 2014, 47, 2514; (f) A. Priimagi, G. Cavallo, P. Metrangolo and G. Resnati, *Acc. Chem. Res.*, 2013, 11, 2686.
2. (a) P. Metrangolo and G. Resnati, Halogen Bonding: Fundamentals and Applications, Springer-Verlag, Berlin, Heidelberg, Germany, 2008; (b) F. Meyer and P. Dubois, *Cryst. Eng. Comm*., 2013, 15, 3058.
3. G. R. Desiraju, P. Shing Ho, L. Kloo, A. C. Legon, R. Marquardt, P. Metrangolo, P. Politzer, G. Resnati and K. Rissanen, *Pure Appl. Chem.*, 2013, 85, 1711.
4. (a) G. P. Schiemenz, *Z. Naturforsch.*, 2007, 62b, 235; (b) G. A. Jeffrey and W. Saenger, Hydrogen Bonding in Biological Structures, Springer Verlag, Berlin, 1991.
5. (a) P. R. Varadwaj, A. Varadwaj and B.-Y. Jin, *Phys. Chem. Chem. Phys.*, 2014, 16, 17238; (b) P. R. Varadwaj, A. Varadwaj and B.-Y., Jin, *Phys. Chem. Chem. Phys.*, 2014, 16, 19573; (c) A. Varadwaj, P. R. Varadwaj and B.-Y. Jin, *Int. J. Quantum Chem.*, 2015, 115, 453; (d) S. J. Grabowski, *Phys. Chem. Chem. Phys.*, 2014, 16, 1824; (e) D. A. Smith, L. Brammer, C. A. Hunter and R. N. Perutz, *J. Am. Chem. Soc.*, 2014, 136, 1288.

6. (a) J. P. M. Lommerse, A. J. Stone, R. Taylor and F. H. Allen, *J. Am. Chem. Soc.*, 1996, 118, 3108; (b) B. Bankiewicz and M. Palusiak, *Struct. Chem.*, 2013, 1297; (c) J. Wang, M. Sanchez-Rosello, J. Aceña, C. del Pozo, A. E. Sorochinsky, S. Fustero, V. A. Soloshonok and H. Liu, *Chem. Rev.*, 2014, 114, 2432.
7. (a) D. O' Hagan, *J. Fluorine Chem.*, 2010, 131, 1071; (b) V. P. Reddy, Organofluorine Compounds in Biology and Medicine, Elsevier, 2015 (ISBN: 978-0-444-53748-5).
8. (a) P. Th. van Duijnen and M. Swart, *J. Phys. Chem. A*, 1998, 102, 2399; (b) P. Schwerdtfeger, Table of experimental and calculated static dipole polarizabilities for the electronic ground states of the neutral elements (in atomic units), Last Update: February 11, 2014 (available at: http://ctcp.massey.ac.nz/Tablepol2014.pdf, and at: http://ctcp.massey.ac.nz/dipole-polarizabilities); (c) A. C. Legon, *Phys. Chem. Chem. Phys.*, 2010, 12, 7736. (d) S. A. C. McDowell and J, A. Joseph, *Phys. Chem. Chem. Phys.*, 2014, 16, 10854; (e) M. J. Vallejos, P. Auffinger and P. Shing Ho, Ch 23.6. Halogen interactions in biomolecular crystal structures, *Int. Tables Cryst. F.*, Ch. 23.6, 2012 (available at: http://www-ibmc.u-strasbg.fr/arn/Westhof/publ_West/doc2011/r2011_MVallejos_Tables.pdf).
9. (a) P. Politzer, J. S. Murray and T. Clark, *Phys. Chem. Chem. Phys.*, 2010, 12, 7748; (b) P. Politzer, J. S. Murray and T. Clark, *Phys. Chem. Chem. Phys.*, 2013, 15, 11178; (c) J. S. Murray and P. Politzer, *WIREs Comput. Mol. Sci.: Overview*, 2011, 1, 153; (d) P. Politzer and J. S. Murray, *Chem. Phys. Chem.*, 2013, 14, 278; (e) P. Politzer, J. S. Murray, G. V. Janjic and S. D. Zaric, *Crystal*, 1024, 4, 12; (f) J. S. Murray, P. Lane, T. Clark, K. E. Riley and P. Politzer, *J. Mol. Model*, 2012, 18, 541.
10. (a) P. Metrangolo, J. S. Murray, T. Pilati, P. Politzer, G. Resnati and G. Terraneo, *Cryst. Growth Des.*, 2011, 11, 4238; (b) P. Metrangolo, J. S. Murray, T. Pilati, P. Politzer, G. Resnati and G. Terraneo, *Cryst. Eng. Comm.*, 2011, 13, 6593.
11. (a) T. Brinck, J. S. Murray and P. Politzer, *Int. J. Quantum Chem.*, 1992, 44, 57; (b) T. Clark, M. Hennemann, J. S. Murray and P. Politzer, *J. Mol. Model.*, 2007 13, 291; (c) T. Clark, *WIREs Comput. Mol. Sci.*, 2013, 3, 13; (d) K. E. Riley, J. S. Murray, P. Politzer, M. C. Concha and P. Hobza, *J. Chem. Theory Comput.*, 2009, 5, 155.
12. (a) J. S. Murray, P. Lane and P. Politzer, *J. Mol. Model.*, 2009, 15, 723; (b) J. S. Murray and P. Politzer, *Croat. Chem. Acta*, 2009, 82, 267; (c) W. Li, Y. Zeng, X. Zhang, S. Zheng and L. Meng, *Phys. Chem. Chem. Phys.*, 2014, 16, 19282; (d) Y. X. Lu, J.-W. Zou, Q.-S. Yu, Y.-J. Jiang and W.-N. Zhao, *Chem. Phys. Lett.*, 2007, 449, 6; (e) K. Eskandari and M. Lesan, *Chem. Eur. J.*, 2015, 21, 4739.
13. (a) M. D. Esrafili and B. Ahmadi, *Comput. Theor. Chem.*, 2012, 997,77; (b) M. D. Esrafili MD and N. Mohammadirad, *J Mol. Model*, 2013, 19, 2559; (c) M. D. Esrafili, F. Mohammadian-Sabet and M. Solimannejad, *Struct. Chem.*, 2014, 25, 1197; (d) R. Pal, G. Nagendra, M. Samarasimhareddy, V. V. Sureshbabub and T. N. Guru Row, *Chem. Commun.*, 2015, 51, 933.
14. P. Zhou, J. Zou, F. Tian and Z. Shang, *J. Chem. Inf. Model.*, 2009, 49, 2344
15. S. Kawai, A. Sadeghi, F. Xu, L. Peng, A. Orita, J. Otera, S. Goedecker and E. Meyer, *ACS Nano*, 2015, 9, 2574**.**
16. (a) Y. Zhao and D. G. Truhlar, *Theor. Chem. Acc.*, 2008, 120, 215; (b) Y. Zhao and D. G. Truhlar, *Acc. Chem. Res.*, 41, 157; (c) S. Kozuch and J. M. L. Martin, *J. Chem. Theory Comput.*, 2013, 9, 1918; (d) A. Forni, S. Rendine, S. Pieraccini and M. Sironi, *J. Mol. Graphics Model.*, 2012, 38, 31; (e) E. G. Hohenstein, S. T. Chill and C. David Sherrill, *J. Chem. Theory Comput.*, 2008, 4, 1996; (f) S. Kozuch and J. M. L. Martin, *J. Chem. Theory Comput.*, 2013, 9, 1918.
17. (a) T. Lu and F. Chen, *J. Comp. Chem.*, 2012, 33, 580; (b) T. Lu and F. Chen, *J. Mol. Graph. Model.*, 2012, 38, 314.

18. R. F. W. Bader, Atoms in Molecules - A Quantum Theory, *Oxford University Press*, Oxford, 1990.
19. (a) E. R. Johnson, S. Keinan, P. Mori-Sanchez, J. Contreras-Garcia, A J. Cohen and W. Yang, *J. Am. Chem. Soc.* 2010, 132, 6498; (b) J. R. Lane, J. Contreras-García, J. P. Piquemal, B. J. Miller and Henrik G. Kjaergaard, J. Chem. *Theory Comput.*, 2013, 9, 3263; (c) J. Contreras-Garcia, E. Johnson, S. Keinan, R. Chaudret, J.-P. Piquemal, D. Beratan and W. Yang, *J. Chem. Theor. Comp.*, 2011, 7, 625.
20. (a) Gaussian 09, Revision A.02, M. J. Frisch, G. W. Trucks, H. B. Schlegel, G. E. Scuseria, M. A. Robb, J. R. Cheeseman, G. Scalmani, V. Barone, B. Mennucci, G. A. Petersson, H. Nakatsuji, M. Caricato, X. Li, H. P. Hratchian, A. F. Izmaylov, J. Bloino, G. Zheng, J. L. Sonnenberg, M. Hada, M. Ehara, K. Toyota, R. Fukuda, J. Hasegawa, M. Ishida, T. Nakajima, Y. Honda, O. Kitao, H. Nakai, T. Vreven, J. A. Montgomery, Jr., J. E. Peralta, F. Ogliaro, M. Bearpark, J. J. Heyd, E. Brothers, K. N. Kudin, V. N. Staroverov, R. Kobayashi, J. Normand, K. Raghavachari, A. Rendell, J. C. Burant, S. S. Iyengar, J. Tomasi, M. Cossi, N. Rega, J. M. Millam, M. Klene, J. E. Knox, J. B. Cross, V. Bakken, C. Adamo, J. Jaramillo, R. Gomperts, R. E. Stratmann, O. Yazyev, A. J. Austin, R. Cammi, C. Pomelli, J. W. Ochterski, R. L. Martin, K. Morokuma, V. G. Zakrzewski, G. A. Voth, P. Salvador, J. J. Dannenberg, S. Dapprich, A. D. Daniels, Ö. Farkas, J. B. Foresman, J. V. Ortiz, J. Cioslowski, and D. J. Fox, Gaussian, Inc., Wallingford CT, 2009; (b) M.W.Schmidt, K.K.Baldridge, J.A.Boatz, S.T.Elbert, M.S.Gordon, J.H.Jensen, S.Koseki, N.Matsunaga, K.A.Nguyen, S.Su, T.L.Windus, M.Dupuis and J.A.Montgomery *J. Comput. Chem.*, 1993, 14, 1347.
21. T. A. Keith, AIMAll (Version 11.03.14), 2011. Available via DIALOG at: http://im.tkgristmill.com.
22. W. Humphrey, A. Dalke and K. Schulten, "VMD - Visual Molecular Dynamics", *J. Molec. Graphics*, 1996, 14, 33.
23. (a) P. R. Varadwaj, A. Varadwaj and G. H. Peslherbe, *J. Comput. Chem.*, 2012, 33, 2073; (b) P. R. Varadwaj, *J. Mol. Model.* 16, 2010, 965; (c) P. R. Varadwaj and H. M. Marques, *Phys. Chem. Chem. Phys.*, 2010, **12**, 2126; (d) A. Varadwaj and P. R. Varadwaj, *Chem. –Eur. J.*, 2012, 18, 15345.
24. (a) T. Janowski and P. Pulay, *Chem. Phys. Lett.*, 2007, 447, 27; (b) A. Puzder, M. Dion and D. C. Langreth, *J. Chem. Phys.*, 2006, 124, 164105; (c) W. L. Jorgensen and D. L. Severance, *J. Am. Chem. Soc.*, 1990, 11 2, 4168; (d) E. Miliordos, E. Apra and S. S. Xantheas, *J. Phys. Chem. A*, 2014, 118, 7568; (e) Y. C.Park and J. S. Lee, *J. Phys. Chem. A*, 2006, 110, 5091.
25. (a) S. Kumar and A. Das, *J. Chem. Phys.*, 2013, 139, 104311; (b) K. Pluhackova, P. Jurecka and P. Hobza, *Phys. Chem. Chem. Phys.*, 2007, 9, 755; (c) S. Tsuzuki, T. Uchimaru and M. Mikami, *J. Phys. Chem. A*, 2006, 110, 2027-2033.
26. M. R. Battaglia, A. D. Buckingham and J. H. Williams, *Chem. Phys. Lett.*, 1981, 78, 421.
27. (a) C. M. Reddy, M. T. Kirchner, R. C. Gundakaram, K. A. Padmanabhan and G. R. Desiraju, *Chem. –Eur. J.*, 2006, 12, 2222; (b) D. J. R. Duarte, N. M. Peruchena and I. Alkorta, *J. Phys. Chem. A*, 2015, 119, 3746; (c) L. Brammer, G. M. Espallargas and S. Libri, *Cryst. Eng. Comm.*, 2008, 10, 1712; (d) F. F. Awwadi, R. D. Willett, K. A. Peterson and B. Twamley, *Chem. –Eur. J.*, 2006, 12, 8952; (e) D. Chopra, *Cryst. Growth. Des.* 2012, 12, 541.
28. (a) J. P. Perdew and Y. Wang, *Phys. Rev. B*, 1992, 45, 13244; (b) A. D. Becke, *J. Chem. Phys.*, 1993, 98, 1372.
29. P. Su and H. Li, *J. Chem. Phys.*, 2009, 131, 014102.
30. S. Alvarez, *Dalton Trans.*, 2013, 42, 8617.
31. (a) C. F. Matta, N. Castillo and R. J. Boyd, *J. Phys. Chem. A*, 2005, 109, 3669; (b) E. Aubert, S. Lebègue, M. Marsman, T. T. T. Bui, C. Jelsch,. S. Dahaoui,. E. Espinosa and J. G. Angyán, *J.*

Phys. Chem. A, 2011, 115, 14484; (c) S. Jenkins, A. Restrepo, J. David, D. Yina and S. R. Kirk, *Phys. Chem. Chem. Phys.*, 2011, 13, 11644; (d) R. F. W. Bader, *J. Phys. Chem. A*, 2009, 113, 10391; (e) I. Alkorta and J. Elguero, *Struct. Chem.*, 2004, 15, 117; (f) C. F. Matta, J. Hernandez-Trujillo, T.-H. Tang and R. F. W. Bader, *Chem. –Eur. J.*, 2003, 9, 1940; (g) T.-H. Tang, E. Deretey, S. J. K. Jensen and I. G. Csizmadia, *Eur. Phys. J. D*, 2006, 37, 217; (h) R. F. W. Bader and C. F. Matta, *Inorg. Chem.*, 2001, 40, 5603; (i) J. Hernández-Trujillo and C. F. Matta, *Struct. Chem.*, 2007, 18, 849; (j) I. Love, *J. Phys. Chem. A*, 2009, 113, 2643.

32. (a) A. M. Pendás, E. Francisco, M. A. Blanco and C. Gatti, *Chem. -Eur. J.*, 2007, 13, 9362; (b) V. Tognetti and L. Joubert, *J. Chem. Phys.*, 2013, 138, 024102; (c) M. A. Blanco, A. M. Pendás and E. Francisco, *J. Chem. Theory Comput.*, 2005, 1, 1096; (d) E. Francisco, A. M. Pendás and M. A. Blanco, *J. Chem. Theory Comput.*, 2006, 2, 90.
33. (a) G. Saleh, C. Gatti, L. L. Presti and J. Contreras-Garcia, *Chem. –Eur. J.*, 2012, 18, 15523; (b) I. Cukrowski, J. H. de Lange and M. Mitoraj, *J. Phys. Chem. A*, 2014, 118, 623; (c) I. González-Veloso, J. A. Carrazana-García, D. Josa, J. Rodríguez-Otero and E. M. Cabaleiro-Lago, *Comput. Theor. Chem.*, 2013, 1053, 123; (d) M. Alonso, T. Woller, F. J. Martin-Martinez, J. Contreras-Garcia, P. Geerlings and F. De Proft, *Chem. –Eur. J.*, 2014, 20, 4845; (e) R. A. Cormanich, R. Rittner, D. O'Hagan and M. Bühl, *J. Phys. Chem. A*, 2014, 118, 7901; (f) E. V. Bartashevich, A. M. Pendás and V. G. Tsirelson, *Phys. Chem. Chem. Phys.*, 2014, 16, 16780.
34. (a) A. Zupan, J. P. Perdew, K. Burke and M. Causá, *Int. J. Qunatum Chem.*, 1997, 61, 865; (b) A. Zupan, K. Burke, E. Ernzerhof and J. P. Perdew, *J. Chem. Phys.*, 1997, 106, 10184.
35. (a) K. Collard and G. G. Hall, *Int. J. Quantum Chem.*, 1977, 12, 623; (b) *C. F. Matta*, R. J. Boyd (Eds.), "The Quantum Theory of Atoms in Molecules: From Solid State to DNA and Drug Design", Wiley-VCH, Weinheim, 2010; (c) S. Jenkins, *Int. J. Quantum Chem.*, 2013, 113, 1603.
36. (a) J. Poater, M. Solá, M. Duran and X. Fradera, *Theor. Chem. Acc.*, 2002, 107, 362; (b) X. Fradera and M. Solá, *J. Comput. Chem.*, 2002, 23, 1347; (c) C. F. Matta, J. Hernandez-Trujillo and R. F. W. Bader, *J. Phys. Chem. A*, 2002, 106, 7369; (d) C. F. Matta and J. Hernandez-Trujillo, J. Phys. Chem. A, 2003, 107, 7496; (f) *P. R. Varadwaj, A. Varadwaj, G. H. Peslherbe and H. M. Marques, J. Phys. Chem. A*, 2011, 115, 13180.
37. (a) H. Sun, K. Ye, C. Wang, H. Qi, F. Li and Y. Wang, J. Phys. Chem. A, 2006, 110, 10750; (b) M. O. Sinnokrot, E. F. Valeev and D. C. Sherrill, *J. Am. Chem. Soc.*, 2002, 124, 10887; (c) M. O. Sinnokrot and D. C. Sherrill, *J. Phys. Chem. A.*, 2004, 108, 10200; (d) S. E. Wheeler and K. N. Houk, *J. Am. Chem. Soc.*, 2008, 130, 10854; (e) S. E. Wheeler and K. N. Houk, *Mol. Phys.*, 2009, 107, 749; (f) S. E. Wheeler and K. N. Houk, *J. Chem. Theory Comput.*, 2009, 5, 2301; (g) T. Smith, L. V. Slipchenko and M. S. Gordon, *J. Phys. Chem. A*, 2008, 112, 5286; (h) E. V. Anslyn and D. A. Dougherty, Modern Physical Organic Chemistry, 1st Edn., University Science Books, Sausalito, California, 2006.
38. (a) M. P. Johansson and M. Swart, *Phys. Chem. Chem. Phys.*, 2013, 15, 11543; (b) P. R. Varadwaj, A. Varadwaj, B.–Y. Jin (manuscript submitted).
39. The Cambridge Structural Database: A quarter of a million crystal structures and rising, F. H. Allen, *Acta Cryst. B* 2002, 58, 380. CSD version 5.36 updates (Nov 2014).
40. R. M. Osuna, V. Hernández, J. T. L. Navarrete, E. Dria and J. J. Novoa, *Theor. Chem. Acc.*, 2011, 128, 541.
41. L. Goerigk, H. Kruse and S. Grimme, *Chem. Phys. Chem.*, 2011, 12, 3412.
42. (a) T. Iikura, T. Tsuneda, T. Yanai and K. Hirao, *J. Chem. Phys.*, 2001, 115, 3540; (b) T. Yanai, D. Tew and N. Handy, *Chem. Phys. Lett.*, 2004, 393, 51.
43. (a) S. F. Boys and F. Bernardai, *Mol. Phys.*, 1970, 553; (b) C. D. Sherrill, Counterpoise Correction and Basis Set Superposition Error, Created on July 21, 2010. Available at:

http://vergil.chemistry.gatech.edu/notes/cp.pdf; (c) P. Salvador, B. Paizs, M. Duran and S. Suhai, *J. Comput. Chem.*, 2001, 22, 765.
44. V. Tognetti and L. Joubert, *Phys. Chem. Chem. Phys.*, 2014, 16, 14539.
45. *The Gaussian 09 User's Reference*, available via: http://www.gaussian.com/g_tech/g_ur/k_dft.htm. Last access August 18, 2015.
46. Y.-K. Han, K. H. Kim, S.-K. Son and Y. S. Lee, *Bull. Korean Chem. Soc.*, 2002, 23, 1271.
47. C. S. Wannere, K. W. Sattelmeyer, H. F. Schaefer III and P. von R. Schleyer, *Angew. Chem.*, 2004, 116, 4296.
48. (a) D. N. Bol'shutkin, V. M. Gasan, A. I. Prokhvatilov and A. I. Erenburg, *Acta Crystallogr. Sect.B: Struct. Crystallogr. Cryst. Chem.*, 1972, 28, 3542; (b) A. N. Fitch, J. K. Cockcroft and Z.Kristallogr, 1993, 203, 29; (c) G. Pepe and J. -M. Gay, *J. Chem. Phys.*, 1989, 90, 5735.
49. (a) P. Jurečka, J. Černý, P. Hobza and D. R. Salahub, *J. Comput. Chem.*, 2007, 28, 555; (b) D. Hugas, S. Simon, and M. Duran, *Chem. Phys. Lett.*, 2004, 386, 373; (c) S. A. C. McDowell, *Chem. Phys. Lett.*, 2006, 424, 239; (d) S. A. C. McDowell, *Chem. Phys. Lett.*, 2014, 598, 1.
50. (a) S. Tsuzuki, K. Honda, T. Uchimaru, M. Mikami, K. Tanabe, *J. Am. Chem. Soc.* 2002, 124, 104; (b) S. Tsuzuki, Interaction with Aromatic Rings, in: Intermolecular Forces and Clusters I (Structure and Bonding), D. Wales, Ed., Springer-Verlag Berlin Heidelberg, *Struc. Bond.*, 2005, 115, 149; (c) P. Hobza, H. L. Selzle, E. W. Schlag, *J. Phys. Chem.* 1996, 100, 18790.
51. (a) R. F. W. Bader, M. E. Stephens, *J. Am. Chem. Soc.*, 1975, 97, 7391; (b) X. Fradera, M. A. Austen, R. F. W. Bader, *J. Phys. Chem. A*, 1999, 103, 304.

Chapter 3. Fluorine-centered Noncovalent Interactions: Attraction between Negative Sites

3.1 Introduction

Understanding the underlying physical chemistry and chemical physics of noncovalent interactions (NCIs) is rapidly expanding in recent years. [1] This is possible because there is a strong interplay between the current state-of-the-art computations and the present and past experimental observations, [2] the former approach doubtlessly sheds adequate light on elucidating many (unexplained) physical phenomena observed using the latter techniques.[3] For instance, two decades ago, it was unclear to the scientific community why the latter halogens in molecules could govern long range contacts with versatile Lewis bases in many crystallographically determined structures, even though they are negatively charged. An answer to this question, as stated by Politzer et al., [2b] was provided by Brinck et al. in 1992.[2a] In this and subsequent other studies, [2] it was demonstrated that the formation of the long ranged contact between two similarly charged halogens, as well as that between a halogen and a negative site, may not be very surprising because the halogen atoms in innumerous molecules have positive areas on the outer portions of their electrostatic surfaces.

As outlined in Cahpter 1, NCIs can be classified as hydrogen bonding (attraction of H atom in group 1 with the negative site), [1a] tetrel bonding (attraction of the Group 14 elements with the negative site), [1c] pnictogen bonding (attraction of the Group 15 elements with the negative site), [1d] chalcogen bonding (attraction of the Group 16 elements with the negative site), [1d, e] halogen bonding (attraction of the Group 17 elements engages with the negative site), [1b, d, e] and van der Waals. [43] There are similar other interactions, such as dihydrogen bonding, [44a] dihalogen bonding, [44b-d] and H—H bonding, [37] etc., that are also treated as NCI. Interests in these interactions originate not only because they occur in diverse areas of chemistry, biology, material science, and crystal engineering,[3-7] but also because they are responsible for the development of smart devices,[5b,c] as well as for the design of novel materials for applications in bio- and nanotechnologies.[5b,c] To provide examples, the presence of such interactions drives versatile chemical reactions in the solution phase,[4a-c] underpins protein folding, protein structure and molecular recognition,[4d] glues the DNA base pairs to result in functional strand like helical architectures,[4e] transforms compounds such as azopyridine derivatives into liquid crystal by combining them noncovalently with molecular halogens,[4f-g] and produces ordered layer structures through self-assemblies between molecules on *substrates*,[6] etc. Because NCIs, especially those formed between the covalently bound halogens and the negative site, for

example, play a vital role in manipulating the directional alignment between molecules, they are therefore excellent for crystals packing, [3e-f] designing drugs for *pharmacotherapeutical* use,[6] building supramolecular architectures[4h,7] (e.g., building polymeric self-assembled components, organizing macromolecular entities and templating the formation of polymers, etc.),[5c] and developing, among several other things, gel, elastic, conducting, magnetic, and photoresponsive materials.[3,5]

Owning to the profound importance of NCIs in many research fields delineated above we are particularly interested in halogen bonding, also recognized as X-bonding,[1b] which has many fundamental characteristics similarly with hydrogen bonding. [1a] It is formed when the halogen derivative in molecules with a positive region on its electrostatic surface along the outer extension of its covalent bond (called σ_{hole}) engages constructively (attractively) with the negative site present in a Lewis base.[1b] The specific feature leads to an understanding that even a negatively charged covalently bound halogen derivative can function potentially as an electrophile (i.e., an acceptor of electron density) for the nucleophile (donor of electron density) upon the formation of an X-bonding interaction. The aforesaid axially positive outer region on the covalently bound halogen is generally surrounded with a lateral belt of negative electrostatic potential, which has the ability to attract positive sites (electron deficient region) on another atom/molecule to form noncovalent/coordination bonding interactions, thereby propagandizing its amphoteric (or anisotropic) nature. [45] In any event, a halogen bond is structurally exemplified with the –Y···X– motif, where Y is the electron rich center on the Lewis base molecule (lone-pairs, π-electrons, etc.) and X is the halogen derivative notably the fluorine, chlorine, bromine, or iodine atom. The N···I motif ideally exemplifies an X-bond, and is formed when the covalently bound iodine in a molecule engages attractively with the nitrogen's electron rich region (on another molecule), with the latter comprising lone-pair electron densities. It is this interaction, which is by far most common in the thyroid hormone[3a-b] is also crystallographically observed, such as that between bis(pyridyl)oxalamides and poly(diiodobutadiyne), in which case, the pyridine groups of the host (former species) interact attractively with the iodoalkynes of the guest (latter species).[8]

The binding strength of the halogen derivative is in this order, Cl < Br < I, which is in line with the corresponding trend observed in the polarizability of the halogen in the series passing from chlorine through bromine to iodine.[2] The fluorine is not included in this trend because it is found not to be positive in innumerous occasions in molecules, for which, it has said that it cannot sustain any X-bonding engagement with the negative site due to its high electronegativity and extremely low polarizability.[2b,c,e,9] For example, the fluorine in hydrogen fluoride (HF), methyl fluoride (H_3CF), and perfluorobenzene (C_6F_6), etc., are completely negative, and may not probably halogen bond with the negative site. Even so, there are a number of molecular species, viz. FCN, F_2, FCCF, and CF_3CCF, etc., in which cases, the fluorine has boastfully displayed an area of positive electrostatic potential, the so-called fluorine's σ_{hole},[10]

which resides on the electrostatic surface of any of these molecules along the outermost extension of its covalent bond.[11,12] This positive area, which is deficient of electron density, is then encouragingly competent in forming X-bonding interactions with the nucleophiles, such as the lone pair regions of the nitrogen and oxygen atoms in ammonia (NH_3) and water (H_2O), respectively. [14a]

The early quantum chemical results of Brinck et al. have demonstrated that the fluorine atoms in tetrafluoromethane (CF_4) and H_3CF are such that they are the favorable sites only for the approach of electrophiles.[2a] A similar argument was also provided for the chlorine in chloromethane (H_3CCl), meaning that the chlorine in this compound is totally negative, and cannot halogen bond.[2] Giving an example, Ding et al. have recently demonstrated that H_3CCl can form a halogen bond with OCH_2, which is impossible according to the σ_{hole} theory because of the lack of a positive potential region around the Cl. Although all these results have been referred for over 24 years, [2b, c, e, 12, 13] it was Varadwaj et al. who have argued using their high level calculations that the above suggestions of Brinck et al.,[2a] Politzer et al.,[2b] Murray et. al.,[2d] Ding et al.,[2h] are incorrect because the fluorine and chlorine atoms in CF_4 and H_3CCl do inherently accompany electrophilic regions domiciled along the C–F and C–Cl bond ends, respectively, suggesting the fact that both the atoms in the respective molecules have the potential to cause attraction when find themselves in the close proximity to the nucleophiles.[14] And one does not therefore really need to the place a point charge at any distance from the nuclei of an atom in a given molecule to demonstrate it could induce a positive potential on the electrostatic surface of that atom through polarization. [46c]

Recently, Johansson and Swart have analyzed through quantum chemical calculations the electron density topological properties of some structurally simple perhalogenated ethanes, $X_3C–CY_3$ (X, Y = F, Cl).[15] And they have suggested in that study when one of the halogens in $X_3C–CY_3$ is the chlorine atom the calculated strength of the halogen—halogen intramolecular interaction can not only be comparable with that of hydrogen bonds, but its nature also be comparable with the unusually strong van der Waals interactions. A similar result was reported by Varadwaj et. al.,[27f] as well by Parra, [45c] on analogous systems, in which cases, the lateral negative sides of the halogen atoms were interacting with each other to form intramolecular attractive interactions. Evidently, the reliabilities of the halogen—halogen interactions in the aforesaid compounds could not be explained by the Molecular Electrostatic Surface Potential (MESP) model, as the lateral portions of the vicinal halogens in such compounds were entirely negative. And that this model does not support attraction that is consequent from two similarly charged species (or that between two species of similar site polarities), as such an arrangement is strongly repulsive according to the Coulomb's law.

Analogous to the study of Johansson and Swart[15] above, Kawai et al. have only recently made an experimental discovery using scanning tunneling and atomic force microscopy measurement techniques, in which, they were able to observe a network of $C–F^{\delta-}\cdots^{\delta-}F–C$

intermolecular interactions in an ordered two dimensional supramolecular layer formed between the fully fluorinated phenyleneethynylene (bis(2,3,5,6-tetrafluoro-4-(2,3,4,5,6-pentafluorophenylethynyl)phenyl)-ethyne (BPEPE-F18) molecules on the Ag(111) surface.[7] According to them, whereas the fluorine's σ_{hole} region in the said compound is fully described by a negative electrostatic potential, it could still temper encourage in directional bonding interaction with the same atom in its binding partner during the supramolecular self-assembly. And that dispersion is main driving force that brings the two (or more) monomers together, which is solely responsible for explaining the directional nature of the $F^{\delta-}\cdots^{\delta-}F$ interactions so-observed. Galvanized by this, we have recently attempted at investigating whether the covalently bound fluorine in C_6F_6 can set govern similar $F^{\delta-}\cdots^{\delta-}F$ attractive interactions when finds itself in the electrostatic field of the same atom in another C_6F_6.[16] Our calculated results have indeed allowed us to demonstrate that the formation of such a directional bonding interaction in dimers, trimers, and tetramers of C_6F_6 is not very surprising even though the fluorine's σ_{hole} in this molecule is entirely negative (albeit weakly). The results emerged from MESP model of that study were inadequate to explain the origin of attraction between the two entirely negative fluorine atoms. However, application of Localized Molecular Orbitals Energy Decomposition Analysis (LMO-EDA) technique could enable us to describe the aforesaid attraction between the fluorine atoms to be the consequence of polarization and dispersive forces, presumably in agreement with the Hellmann-Feynman theorem. [46c] It is worth stressing that intermolecular clusters of the above types formed between fully/partially fluorinated aromatic or non-aromatic compounds is not very rare in the solid state. [48] A previous theoretical study on some homologous dimers involving $F^{\delta-}\cdots^{\delta-}F$ intermolecular interactions can be found elsewhere.[49]

Whatever happens, an utmost interest of this Chapter is to explore whether or not the totally negatively charged fluorine atoms in fully hexafluorinated benzene, C_6F_6, do have any specific and adequate tendency to manifest attractive interactions with the Lewis bases that have negative sites of larger electrostatic potential. If an answer to this question is yes, then it might indeed be interesting to see: i) what would be the intermolecular distance range between the negative sites in the resulting heteromolecular dimers? ii) What would be the approximate binding energy range? iii) What would be the sources of interaction supposedly responsible for their effective stabilizations? And whether the strengths of these interactions can be comparable with similar dimers of the other types facilitated in the literature? To address these questions, we have selected nine Lewis bases, including water (H_2O), ammonia (NH_3), hydrogen fluoride (HF), formaldehyde (H_2CO), fluoromethane (H_3CF), and fully fluorinated pyridine (C_5F_5N), pyrimidine ($C_4F_4N_2$), pyrazine ($C_4F_4N_2$), and pyridazine ($(CF)_4N_2$) as binding partners (i.e., as Lewis bases) for C_6F_6. We have performed first principles calculations with the second-order Møller-Plesset theory MP2(full),[17] as well as that with the global density functional M06-2X,[18] both together with an affordable 6-311++G(d,p) basis set, to estimate the aforementioned equilibrium structural properties of the dimers formed of the C_6F_6 molecule upon its interaction

with each of the nine Lewis bases. For reasons discussed later, we have employed MESP model to quantitatively estimate the strengths of the various important local most positive and negative regions on the 0.001 a.u. isodensity mapped electrostatic surfaces of the monomers, and have attempted to see whether the signs and magnitudes of the electrostatic potential obtained for such regions could explain the origin of the primary driving forces that compel the similarly charged atoms, each from a given monomer, to attract each other upon the formation of each such dimer. We have also employed LMO-EDA technique to present insight into the various attractive and repulsive forces responsible causing the binding energies of the dimers to be negative. In addition, we have employed topological Quantum Theory of Atoms in Molecules (QTAIM) and Reduced Density Gradient (RDG) NCI methodologies to analyze the most important properties of the charge density at the bond critical point regions in various atomic basin pairs, and to formalize with meaningful conclusions the coordinating nature of the interatomic interactions involved in the various dimers examined.

3.2 Computational details

As mentioned above, the MP2(full) and M06-2X methods, together with the valence triple-ζ Gaussian quality 6-311++G(d,p) basis set, were employed to obtain the equilibrium geometries of all the monomers and dimers, where full denotes the inclusion of core electrons in the correlation treatment at the former level. The geometries of these compounds are belonging to different point group symmetries, e.g., C_1, C_s, $C_{\infty v}$, C_2, or C_{2v}. The Hessian second derivative calculations were performed with the same levels of theory to obtain insight into the stationary/saddle point natures of the geometries examined.

Due to limited computational resources, first-principles calculations to obtain the geometries and vibrational frequencies for the dimers were not affordable with the high level Coupled Cluster theory involving Singles, Doubles, and Triple excitations, CCSD(T).[19] Instead, we were able to perform CCSD(T)/6-311G** single points to obtain the total electronic energy for each of the monomers and dimers on their respective M06-2X/6-311++G(d,p) geometry. We did so because we were intended to calculate the CCSD(T) binding energies for the dimers, and then to compare them with the corresponding energies obtained with the low level theories, MP2(full) and M06-2X. All the calculations were carried out using GAUSSIAN 09.[20] The Gaussview 05[21] and VMD[22] packages were used for molecular visualization, and for structure and vibrational normal mode analyses.

The electron delocalization indices,[25a-e] as well as the important properties of the charge density (viz. the charge density, its Laplacian, and the second eigenvalue of its Hessian matrix, etc., at the intermolecular bond critical points)[25e-i] were evaluated using AIMAll[23] and MultiWfn[24] computer codes, both within QTAIM framework of Bader. [25j] The RDG based

topological NCI indices were obtained within the recently proposed NCI Plotting tool of Johnson et al. [26] The 0.001 a.u. (electrons/bohr^3) mapped isodensity mapped local most surface maxima and minima values ($V_{s,max}$ and $V_{s,min}$, respectively) were obtained on the electrostatic surfaces of all the monomers via MultiWfn code.[24] (We used this surface because it has been demonstrated numerous occasions[46a-e] that it reflects the specific features such as lone pairs, π electrons, strained bonds, etc., of molecules, suggested by Bader et al.[46f]) The wavefunctions obtained using M06-2X/6-311++G(d,p) geometries of the monomers and dimers were utilized for the aforesaid calculations.

3.3 Results and discussions

3.3.1 Geometries

The ball and stick models for the optimized geometries of the thirteen heteromolecular dimers examined are illustrated in Fig. 1, and the F···F, F···N, and F···O intermolecular distances are listed in Table 1. As can be immediately seen from the table, the intermolecular distances are all lie between 2.988 and 3.559 Å with M06-2X, and that between 2.889 and 3.215 Å with MP2 (full). This means, except for $H_2O\cdots F\text{–}C_6F_5$ a) and $HF\cdots F\text{–}C_6F_5$ e), the intermolecular distances obtained with the latter method compared to the former one are shorter (see diff3 values in Table 1), a feature which may not be very unusual with MP2 (full) method.[32c,d] To give an example, Varadwaj et al. have recently reported with several computational methods a range of values for the N···F intermolecular distance in $H_3N\cdots F\text{–}CF_3$, formed between the positive end of the fluorine in CF_4 and the negative nitrogen end of the NH_3 molecule. The MP2 (full) and CCSD(T)-F12 predicted N···F distance of that complex were 3.34 and 3.49 Å, respectively, which were indeed small compared to the range of values predicted between 3.34 and 3.87 Å for the same distance with several DFT and DFT-D functionals.[14a]

The fluorine in the dimers illustrated in Fig. 1 presents two types of noncovalent interaction topology for the approach of nucleophiles. In the geometries b), d), f), g), i), j), k), and l), it displays its high tendency in forming directional bonding interactions with the nucleophiles. In literature, this kind of noncovalent interaction is what is referred to as type-II interaction topology, [27] where ∠D···F–C (D = F, or N, or O) is close to 180º. In the geometries a), c), e), h), and m), the fluorine upon its coordination with the negative site in the interacting partner prefers to display the type-I intermolecular interaction topology, a topology that is largely observed between the covalently bound halogen atoms within the molecule or between molecules, as well as that between the covalently bound halogen and main group atoms, in the solid state. [27] In this latter case, as expected, ∠D···F–C (D = F, or N, or O) varies between 122

and 139°. A more geometrical detail on the aforesaid intermolecular topologies is outlined elsewhere.[16, 27f]

In majority of the dimers examined, the F···F, F··N, and F···O intermolecular distances are longer than the sum of the van der Waals radii of the respective interacting atoms (see diff1 and diff2 values, Table 1), indicating that the IUPAC recommended feature, '*In a typical R–X···Y halogen-bonded complex, the interatomic distance between X and the appropriate nucleophilic atom of Y tends to be less than the sum of the van der Waals radii*', is not sharply fulfilled for all cases, where X = halogen, R = remainder part of the molecule, and Y = Lewis base center. The oddity is not very rare.[14, 16, 27f, 28]

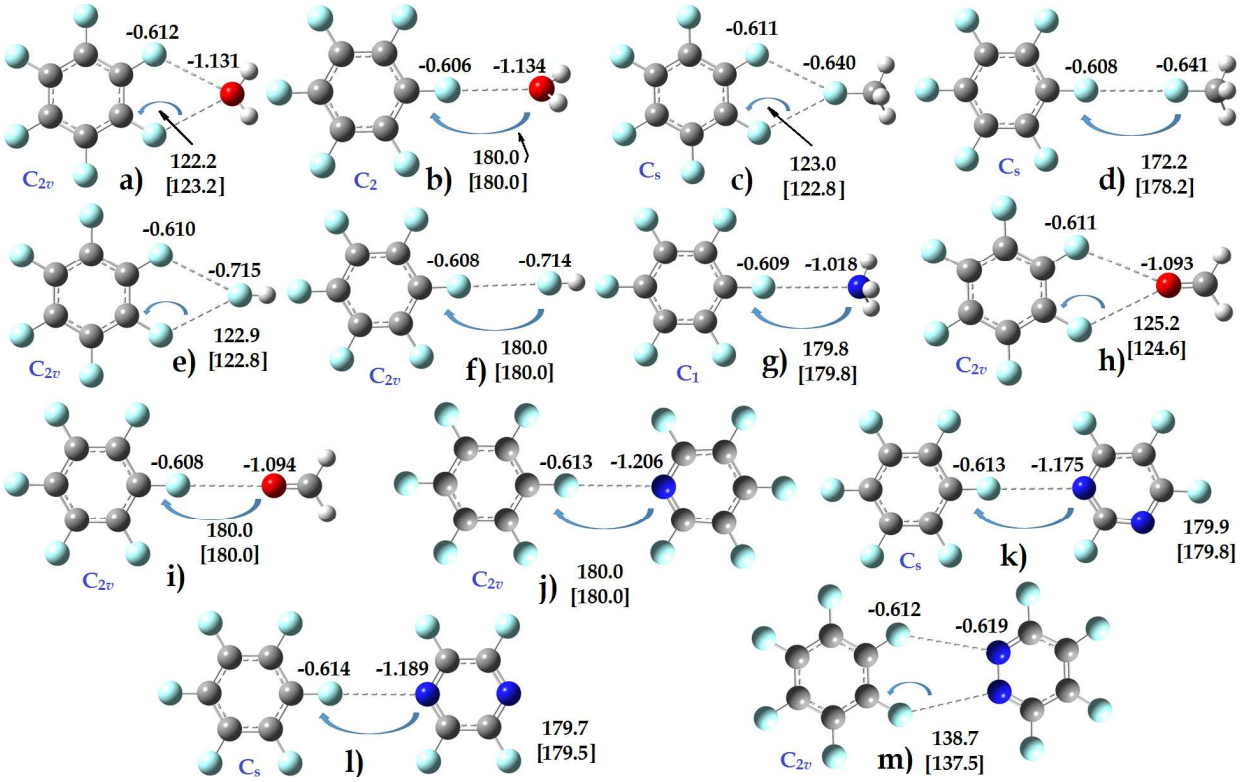

Fig. 1: M06-2X/6-311++G(d,p) dimer geometries of hexafluorobenzene (C_6F_6) with a-b) water (H_2O), c-d) fluoromethane (H_3CF), e-f) hydrogen fluoride (HF), g) ammonia (NH_3), h-i) formaldehyde ($H_2C{=}O$), j) pentafluoropyridine (C□F□N), k) tetrafluoropyrimidine ($C_4F_4N_2$), l) tetrafluropyrazine ($C_4F_4N_2$), and m) tetrafluoropyridazine ((CF)□N□). Negative values of QTAIM charges (in e) on selected atoms are displayed for each complex. The M06-2X [MP2(full)] ∠D···F–C (D = O, F, or N) angles (in °) are also displayed. The O, N, F, C, and H atoms are painted in red, deep-blue, aqua, gray, and gray-white, respectively.

Table 1: Selected structural and energetic properties of the thirteen dimers investigated. [a]

Complex [b]	vdW sum[c]	r(M06-2X)	Diff1[d]	r(MP2(full))	Diff2[e]	Diff3[f]	ΔE(M06-2X)	ΔE(MP2(full))	ratio[g]	ΔE [CCSD(T)][h]
$H_2O\cdots F–C_6F_5$ a)	2.96	2.988	0.03	3.090	0.13	0.102	–2.05	–2.77	1.4	–2.56
$H_2O\cdots F–C_6F_5$ b)	2.96	3.027	0.07	2.952	–0.01	–0.075	–0.80	–2.76	3.4	–0.44
$H_3CF\cdots F–C_6F_5$ c)	2.92	3.020	0.10	3.013	0.09	–0.007	–1.30	–2.86	2.2	–2.35
$H_3CF\cdots F–C_6F_5$ d)	2.92	3.060	0.14	2.889	–0.03	–0.171	–0.75	–3.13	4.2	–0.85
$HF\cdots F–C_6F_5$ e)	2.92	3.006	0.08	3.009	0.09	0.004	–1.26	–1.81	1.4	–1.65
$HF\cdots F–C_6F_5$ f)	2.92	3.088	0.17	2.950	0.03	–0.138	–0.57	–1.37	2.4	–0.45
$H_3N\cdots F–C_6F_5$ g)	3.12	3.330	0.21	3.187	0.07	–0.143	–0.35	–2.55	7.2	–0.66
$H_2CO\cdots F–C_6F_5$ h)	2.96	3.275	0.31	3.201	0.24	–0.074	–0.78	–2.69	3.4	–1.85
$H_2CO\cdots F–C_6F_5$ i)	2.96	3.237	0.28	3.017	0.06	–0.221	–0.42	–2.49	5.9	–0.68
$F_5C_5N\cdots F–C_6F_5$ j)	3.12	3.303	0.18	3.037	–0.08	–0.267	–1.83	–6.62	3.6	–2.06
$F_4C_4N_2\cdots F–C_6F_5$ k)	3.12	3.319	0.20	3.046	–0.07	–0.273	–1.63	–6.27	3.9	–1.93
$F_4C_4N_2\cdots F–C_6F_5$ l)	3.12	3.295	0.17	3.048	–0.07	–0.247	–1.88	–6.49	3.4	–2.10
$F_4C_4N_2\cdots F–C_6F_5$ m)	3.12	3.559	0.44	3.215	0.09	–0.344	–2.32	–7.88	3.4	–2.18

[a] Properties include van der Waals radii sums (vdW sum/Å), intermolecular bond distances (r/Å), difference bond distances (diff1, diff2, and diff3/Å), and binding energies (ΔE/kJ mol^{-1}).
[b] See Fig. 1 for configurational details.
[c] van der Waals radii for O, N, and F are ca. 1.50, 1.66, and 1.46Å, respectively.[38]
[d] Refers to the differential between the r(M06-2X) intermolecular distance and the sum of the van der Waals (vdW) radii of the noncovalently bonded atoms.
[e] Refers to the differential between the r(MP2(full)) intermolecular distance and the sum of the van der Waals (vdW) radii of the noncovalently bonded atoms (in Å).
[f] Refers to the differential, r(MP2(full)) – r(M06-2X), between the M06-2X and MP2(full) intermolecular distances.
[g] Refers to the ratio, ΔE[MP2(full)]/ ΔE[M06-2X], between the MP2(full) and M06-2X binding energies.
[h] Refers to the CCSD(T)/6-311G**//M06-2X/6-311++G(d,p) calculation.

3.3.2 Atomic charges and molecular electrostatic surface potentials

Fig. 1 also lists the QTAIM charges conferred on some selected atomic basins, especially on the ones that participate with each other to drive the two monomers to couple together in each of the dimer equilibrium geometries. Before discussing these phenomena further, we note that the signs and magnitudes of the atomic charge obtained with this method do reasonably explain the expected nature of the charge distributions on the monomers. For example, this method assigns positive and negative charges of 0.568 and −1.136 *e* to each of the two equivalent H atoms and the O atom in isolated H_2O, respectively, and of 0.342 and −1.027 *e* to each of the three equivalent H atoms and the N atom in isolated NH_3, respectively, and of 0.715 and –0.715 *e* to the H and F atoms in isolated HF, respectively. Similarly, it predicts a positive equivalent charge of 0.614 *e* for each of the C atoms and a negative equivalent charge of –0.614 *e* for each

of the F atoms in isolated C_6F_6. Evidently, the atomic charge distributions mentioned above do faithfully recover what might have expected when one deals especially with the charge neutrality feature of each of the monomers. Nevertheless, compared to the signs and magnitudes of the atomic charges in the monomers the charges on the interacting atoms sharing the intermolecular interaction(s) between them in the dimer geometries perturb very marginally (cf. Fig. 1), with the extent of this perturbation is the largest for the fluorine atom in C_6F_6 of $HF\cdots F$–C_6F_5 (value < 0.007 *e*). Conspicuously, the very marginal changes (redistributions) in the magnitudes of the charge on the atomic basins of the monomers in the dimer geometries might not necessitate any significant charge transfers, thus this cannot be treated as a factor indispensable for complex formation.

Moreover, it is also apparent from Fig. 1 that the two electronegative atoms bringing the two monomers together in each of the complex configurations are negatively charged, one with a magnitude somehow larger than that on the other, as in $H_2O^{-0.612}\cdots^{-1.131}F$–$C_6F_5$ (Fig. 1a), $H_2CO^{-0.608}\cdots^{-1.094}F$–$C_6F_5$ (Fig. 1i), and $C_4F_4N_2^{-0.613}\cdots^{-1.175}F$–$C_6F_5$ (Fig. 1k), for examples. This means the atomic charges that are of similar sign may even attract each other, thence displaying the possibility of *like liking like*. A similar phrase '*like attracting like*' was invoked some time ago to expound the term attraction that had aroused between the covalently bonded halogen derivatives, as well as that between the covalently bound main group atoms (other than the halogens) in molecules, that led to the formation of dimers. In each of such cases, the region of positive electrostatic potential (σ_{hole}) on the outermost extension of a covalently bound atom in a molecule was interacting with the region of negative electrostatic potential on the same atom in another molecule, viz., crystalline $ClCl\cdots ClCl$[29] and $ClH_2P\cdots PH_2Cl$.[30] According to Politzer et al.,[2j] in terms of global atomic charges, an interaction of the above type (i.e., between two similarly charged species) would be repulsive, because it would be "like attracting like". Interesting enough, however, for the dimers presently examined, we found no such positive regions of electrostatic potential on the highly electronegative atoms that are involved in the $O^{\delta-}\cdots F^{\delta-}$, $F^{\delta-}\cdots F^{\delta-}$, and $N^{\delta-}\cdots F^{\delta-}$ weakly bound contact pairs. For instance, the M06-2X/6-311++G(d,p) computed local most minimum of electrostatic potential, $V_{s,min}$, on the surfaces of the O, O, F and F atoms in H_2O, H_2CO, H_3CF, and C_6F_6 are calculated to be –38.3, –31.8, –26.2, and –6.5 kcal mol^{-1}, respectively, while the local most maximum of electrostatic potential, $V_{s,max}$, on the surfaces of the F, F, and F atoms in HF, H_3CF, and C_6F_6 are calculated to be –23.6, –25.8, and –4.8 kcal mol^{-1}, respectively (cf. Table 2 for details about other species). Indeed, even though the aforestated specific axial and equatorial regions on the electrostatic surface of the fluorine in isolated C_6F_6 are purely negative, it has the aptitude to favorably interact attractively with the negative sites in the other monomers to form dimers of the types illustrated in Fig. 1, a result which is consistent with what might be extracted from the atomic charge model delineated above. As a matter of fact, these results do not support a previous assertion *halogen bonding can readily be understood as the attractive interaction between the positive outer region on the*

Table 2: Selected 0.001 a.u. (electrons/bohr^3) isodensity mapped electrostatic potentials (kcal mol^{-1}) on the molecular surfaces of all the monomers examined, obtained with M06-2X in conjunction with the 6-311++G(d,p) basis set. [a]

Monomers	Atom type	$V_{s,max}$[b]	$V_{s,min}$[c]
H_2O	O lone-pair region	---	–38.3 [–37.4]
H_3N	N lone-pair region	---	–41.4 [–40.9]
HF	On F of H–F	–23.6 [–23.5]	–24.4 [–22.3]
H_2CO	On O of C–O	---	–31.8 [–29.9]
H_3CF	On F of C–F	–25.8 [–25.0]	–26.2 [–25.6]
C_6F_6	On F of C–F	–4.8 [–4.2]	–6.5 [–6.4]
Tetrafluoropyridine (C_5F_5N)	N lone-pair region	---	–20.2 [–20.7]
Tetrafluoropyrimidine ($C_4F_4N_2$)	N lone-pair region	---	–19.2 [–19.2]
Tetrafluoropyrazine ($C_4F_4N_2$)	N lone-pair region	---	–16.0 [–17.0]
Tetrafluoropyridazine ($(CF)_4N_2$)	N lone-pair region	---	–26.7 [–27.7]

[a] Square brackets represent to the [MP2(full)/6-311++G(d,p)] values.
[b] $V_{s,max}$ is the local most maximum of electrostatic potential.
[c] $V_{s,min}$ is the local most minimum of electrostatic potential.

halogen and the negative site, [2g] nor do they come along with the suggestion *the negative electrostatic potential associated with a σ_{hole} precludes the possibility of halogen bonding – unless the electric field of the negative site is strong enough to induce a positive region on the halogen.*[2b,11] Giving an example to support this latter assertion, Clark et al. have just recently demonstrated that *a charge of −0.2762*[2i] *situated 3 Å from the chlorine nucleus along the extension of the C—Cl bond in H_3C—Cl does indeed result in a positive (σ_{hole}) potential on the chlorine, which was absent on it in H_3C—Cl because the potential on the chorine prior to interaction does not reflect the polarization caused by the electric field of the oxygen in H_2CO*[46c] when both the species approach toward each other to form the $H_2CO\cdots Cl$— CH_3 dimer, as reported by Riley et al.[47a] This view is somehow in disagreement with our recent finding on the same system already outlined in the Introduction part, [14b] in agreement with an incisive view provided by others.[47b]

Let us now recall Politzer and coworkers who have advocated in several occasions that "*trying to assign a point positive or negative charge to an atom in a molecule (i.e., a monopole) is a fallacy, …., there is no rigorous basis for doing so*",[31] and have suggested the MESP model to be unique in resolving the question why the negatively charged covalently bonded halogen derivative (with a positive region on it) can attract the negative site.[2, 3,10,11,13] Clearly, this suggestion of Politzer and coworkers cannot arguably be applicable to the presently studied systems, as both the atom centered QTAIM charge and MESP models present an identical

physical picture on the overall repulsive nature of the interaction between the two negative sites that could participate bringing monomers in the complex configurations together. Note further that the chemical systems under investigation are not simply just the ones that display attraction between the entirely negative sites, but there are several dimers of the other types whereby similar attractive interactions between the negative sites can also be inferred. (Investigations on such complex systems are underway, and we report them elsewhere.) For any event, it has also been said that "like attracting like" cannot happen with tetravalent Group IV atoms, which do have entirely positive surface potentials. [31] Yet it might be interesting to see if indeed anomalies to this would appear in future investigations.

3.3.3 Binding energies and stability preference

The *binding* energy ΔE for the dimer Y···X is calculated via Eqn. 1 by subtracting the total sum of the electronic energies of the two isolated monomers [E(Y) + E(X)] from the total electronic energy E(Y···X) of the dimer.

$$\Delta E = E(Y\cdots X) - [E(Y) + E(X)] \quad \ldots\ldots(1)$$

The numerical estimates of the binding energy for all the dimers are listed in Table 1. As can be instantly seen from the data, ΔE is varying between –0.35 and –2.32 kJ mol^{-1} with M06-2X, and that between –1.37 and –7.88 kJ mol^{-1} with MP2(full), both presenting the most stable complex to be formed between C_6F_6 and $(CF)_4N_2$, Fig. 1m, wherein the two fluorine atoms in the former species are probably bonded with the two nitrogen atoms of the latter species. The ratio, ΔE[MP2(full)]/ ΔE[M06-2X], between the binding energies of the two correlated methods for each dimer is too large, values lying between 1.4 and 7.0 (cf. Table 1), with the smallest and the largest of it correspond to the dimers of C_6F_6 with NH_3 and that with H_2O and HF, respectively. Such large ratios obtained between the ΔE values of the two computational methods might give us the impression that dispersion is probably one of the major driving forces responsible for the stabilization of the dimers, as MP2(full), compared to any other DFT functionals, accounts for such an effect to some reasonable extent. Note that it must be kept in mind that whilst MP2 is robust, but there are many other chemical systems, organosilicon aromatic compounds, as well as other systems that involve stacked π interactions, [42a] for examples, wherein it dramatically fails to produce the expected results.

Moreover, the MP2(full) trend in the ΔE values for the thirteen dimers noticeable from the data in Table 1 is in this order: m) > j) > l) > k) > d) > c) > a) > b) > h) > g) > i) > e) > f). This is in sharp disagreement with that found with M06-2X, i.e., m) > a) > l) > j) > k) > c) > e) > b) > h) > d) > f) > i) > g). The apparent discrepancy between the trends in the MP2(full) and DFT(M06-2X) energies might not be very atypical since the electron-electron correlation energy

(London dispersion energy) accounted for by the former method is known to be generally too high, which is assuredly one of the reasons that might explain why MP2(full) binding energies listed in Table 1 are relatively large, and why there is an alternation in the stability preference. [32, 42] Thus considering the above mismatch between the trends in the ΔE values could be due to the MP2 (full), we have performed high level CCSD(T)/6-311G** single points on the M06-2X/6-311++G(d,p) optimized geometries for both the monomers and dimers. The ΔE values calculated for the all the thirteen dimers with this method and listed in Table 1 readily enable us to comment that the magnitudes such energies are not only pretty close to those of M06-2X for all dimers, but indeed also very small compared to those of MP2(full). Furthermore, the corresponding CCSD(T) trend in the ΔE values for the dimers is: a) > c) > m) > l) > j) > k) > h) > e) > d) > i) > g) > f) ≈ b), which is, again, no similar with either of the aforementioned trends discussed above. Although the three different trends found for the binding energy with three different computational approaches are dissimilar with each other, this could not hinder the monomers from forming the weakly found dimers illustrated in Fig. 1.

Nevertheless, the interaction strengths for the dimers of C_6F_6 with the nine Lewis bases are computed to be all very weak. Their binding energies are comparable with what have already been reported for numerous other dimers formed of the carbon bound halogens notably of the chlorine, bromine, and iodine atoms with the negative site. For instance, the previously reported binding energy was –9.24 kJ mol^{-1} for $C_6H_5Br\cdots NH_3$ with MP2/aug-cc-PVTZ, [33] and –12.30 kJ mol^{-1} for $C_6H_5I\cdots NH_3$ with MP2(full)/Lanl2DZ*,[34] wherein the positive σ_{hole} on the halogen atom in a monomer was interacting with the negative nitrogen on the other. Varadwaj et al. have recently reported comparable binding energies of –1.92, –2.95, –2.36, –2.38, and –3.96 kJ mol^{-1} for the fluorine bonded CF_4 complexes of NH_3, HCN, HF, H_2O, and $H_2C=O$, respectively, in which cases, the positive σ_{hole} on the fluorine atom in CF_4 was halogen bonded with the negative sites N, N, F, O and O in NH_3, HCN, HF, H_2O, and H_2CO, respectively.[14a] Similarly, Mani and Arunan have recently reported several carbon centered σ_{hole} bonded dimers, wherein the basis set superposition error (BSSE) corrected binding energies were turn out to be positive, and again, this was interestingly regardless of the nature of the dimers investigated. For instance, the binding energies reported by these latter authors were in the 2.6 – 15.9, 3.6 – 16.8, and 2.8 – 16.7 kJ mol^{-1} ranges for the dimers of CH_3F with several Lewis bases with MP2/6-311++G(3df,2p), MP2/Aug-cc-pVTZ, and CCSD(T)/6-311++G(3df,2p), respectively, and were in the 2.4 – 9.0, 2.9 – 9.7, and 2.2 – 9.7 kJ mol^{-1} ranges for the dimers of CH_3OH with several similar Lewis bases with the corresponding computational methods, respectively.[35] There are analogous studies reported elsewhere that have discussed comparable magnitudes of the binding energy for other dimers.[25g, 36] It is worth mentioning that the BSSE corrected binding energies reported by Mani and Arunan for the dimers just mentioned above were positive, which, we trust, were probably due to the transformation of the negative sign to positive ones after inclusion of the BSSE.

Because of this, as well for reasons discussed elsewhere, [14b, 16] we avoid to estimate and include the effect of BSSE for the presently studied dimers.

Yet it would be interesting to scrutinize the primary forces that are responsible bringing the entirely negatively charged atoms of the two monomers together in the equilibrium configurations of the dimers. Towards this end, we have analyzed the energetic components of a few randomly selected dimers. This was obtained using LMO-EDA with M06-2X/6-311++G(d,p). Based on this model, the total interaction energy of a dimer is the sum of the energies arising from contributions due to electrostatics (ΔE_{es}), exchange (ΔE_{ex}), repulsion (ΔE_{rep}), polarization (ΔE_{pol}), and dispersion (ΔE_{dis}). Accordingly, such component energies were calculated using GAMESS[50] to be +1.13, +1.34, +4.90, –4.64, –5.52 kJ mol^{-1} for the configuration in Fig. 1a ($H_2O\cdots F\text{–}C_6F_5$), and that to be +1.51, +1.42, +1.76, –3.26, and –3.43 kJ mol^{-1} for the configuration in Fig. 1c ($H_3CF\cdots F\text{–}C_6F_5$), and that to be +1.30, +0.63, +0.46, –1.39, –1.30 kJ mol^{-1} for the configuration in Fig. 1d ($H_3CF\cdots F\text{–}C_6F_5$), and that to be +1.51, +1.46, +1.78, –3.18, –3.51 kJ mol^{-1} for the configuration in Fig. 1e ($HF\cdots F\text{–}C_6F_5$) (–1.94 kJ mol^{-1}). Translucently, the total interaction energies for these four dimers are ca. –2.79, –2.01, –0.30, and –1.94 kJ mol^{-1}, respectively. Indeed, these values are comparable qualitatively with the M06-2X SCF binding energies of –2.05, –1.30, –0.75, and –1.26 kJ mol^{-1} for the corresponding dimers, respectively (cf. Table 1). These impressive results sonorously allow us to comprehend that polarization and dispersion are the main attractive sources contributing totally to the overall stability of the dimers, even though the Coulomb's law of electrostatics does not recognize such a possibility of attraction between the similarly negatively charged species.

3.3.4 QTAIM, RDG and delocalization indices

Before proceeding to discuss the topological results of the charge density, it is probably crucial to raise the question: does it likely that the highly electronegative similarly charged atoms in each of the nine monomers bearing areas of entirely negative electrostatic potential interact attractively with the completely negative fluorine in C_6F_6 to form the thirteen dimers examined? To provide a reasonable answer to the question further, we firstly note that the most popular MESP model did not support the aforesaid possibility of attraction between the entirely negative sites. Secondly, we call on the criterion proposed some years ago for identifying H···H interactions between two similar H atoms in molecules or in complexes, for example, biphenyl.[37] According to this, [37] the H···H interaction is attractive, and is formed when both the H atoms participating with each other are either electrically neutral or carry small charges of similar sign. In analogy with this, it is indeed evident form Fig. 1 that both the atoms in the O···F, or N···F, or F···F pair carry charges of similar polarity. Thus, in line with Hernández-Trujillo et al., [37] the interaction involved in each of these pairs might be treated as noncovalent.

Table 3: The intermolecular (3, −1) bond critical point properties of the charge density (in a.u.) for the thirteen dimers formed of the C_6F_6 monomer with the negative site localized on each of the nine Lewis bases, obtained through QTAIM analysis with M06-2X/6-311++G(d,p). Included are also the delocalization indices for the weakly bonded interactions involved. [a]

Complex [b]	ρ_b	λ_2	$\nabla^2\rho_b$	δ
$H_2O\cdots F\text{–}C_6F_5$ a)	0.0060	–0.0049	0.0271	0.0306
$H_2O\cdots F\text{–}C_6F_5$ b)	0.0048	–0.0037	0.0239	0.0269
$H_3CF\cdots F\text{–}C_6F_5$ c)	0.0042	–0.0038	0.0234	0.0189
$H_3CF\cdots F\text{–}C_6F_5$ d)	0.0030	–0.0025	0.0186	0.0159
$HF\cdots F\text{–}C_6F_5$ e)	0.0042	–0.0038	0.0239	0.0194
$HF\cdots F\text{–}C_6F_5$ f)	0.0027	–0.0022	0.0173	0.0146
$H_3N\cdots F\text{–}C_6F_5$ g)	0.0037	–0.0028	0.0162	0.0261
$H_2CO\cdots F\text{–}C_6F_5$ h)	0.0028	–0.0024	0.0149	0.0147
$H_2CO\cdots F\text{–}C_6F_5$ i)	0.0025	–0.0018	0.0141	0.0149
$F_5C_5N\cdots F\text{–}C_6F_5$ j)	0.0032	–0.0024	0.0149	0.0201
$F_4C_4NN\cdots F\text{–}C_6F_5$ m)	0.0031	–0.0023	0.0145	0.0194
$F_4NC_4N\cdots F\text{–}C_6F_5$ l)	0.0033	–0.0025	0.0152	0.0204
$(CF)_4N_2\cdots F\text{–}C_6F_5$ k)	0.0019	–0.0014	0.0095	0.0116

[a] The properties include the charge density (ρ_b), the second eigenvalue of the Hessian of charge density (λ_2), the Laplacian of the charge density ($\nabla^2\rho_b$), and the delocalization index (δ).

[b] See Fig. 2 for molecular graphs and Fig. 1 for configurational details.

[c] For the geometries in a), c), e), and h) involving two equivalent noncovalently bonded interactions, the mean values are listed.

Other than the characteristics outlined just above, we have performed QTAIM and RDG analyses to briefly explore the interaction topologies of the charge density involved between the interacting atoms in each dimer. The theoretical details of these approaches have discussed several times previously, [25, 26] and we therefore do not elaborate them here. The results obtained through applications of these methodologies on the DFT/M06-2X optimized dimer geometries are shown in Fig. 2, with the QTAIM molecular graph for each system is depicted on the left and the corresponding RDG-based NCI isosurface critical point graph belonging to the low-density and –gradient regions is on the right. As can be grandiloquently seen, the former graphs illustrate the desired bond paths and (3, −1) bond critical points (bcps) between the covalently bonded atoms, as well as those between the atoms that are noncovalently bonded. The results are in excellent agreement with the RDG analysis, in which, the critical bonding region between any two atoms in a given noncovalently bonded pair, such as O···F, N···F, and F···F, etc., is favorably described by an approximate disk-shaped circular isosurface in green. For instance, there are two such isosurface critical points between the interacting O and F atoms in geometry Fig. 2a ($H_2O\cdots FC_6F_5$), and that between the two interacting F atoms in geometry Fig. 2e

(HF···FC$_6$F$_5$), and that between the O and F atoms in geometry Fig. 2h (H$_2$CO···FC$_6$F$_5$). And for each of the all other complexes (viz. b, d, e, h, and i-l of Fig. 2) the intermolecular region is described by a singular isosurface critical point, all reminiscent of closed-shell structures.[25, 26] It is worth noting that the presence and strength of the abovementioned interactions between the negatively charged atoms of the dimers can also be graphically realized by inspecting the RDG vs. Sign(λ_2)×ρ plots provided in the supplementary information (Figs S1-S3). In these plots, one might prominently see that the region where the second eigenvalue of the Hessian of the charge density λ_2 is negative ($\lambda_2 < 0$) there appears a spike that is representative of bonding. And that where λ_2 is positive ($\lambda_2 > 0$) there appears another spike(s) representative of non-bonding and/or repulsive interactions (e.g., steric clashes). For each of these two regions, ρ determines the interaction strength.[26a] (Table 3 lists the λ_2 values for all types noncovalently bonded (attractive) interactions revealed, which, as just indicated above, are small and negative.)

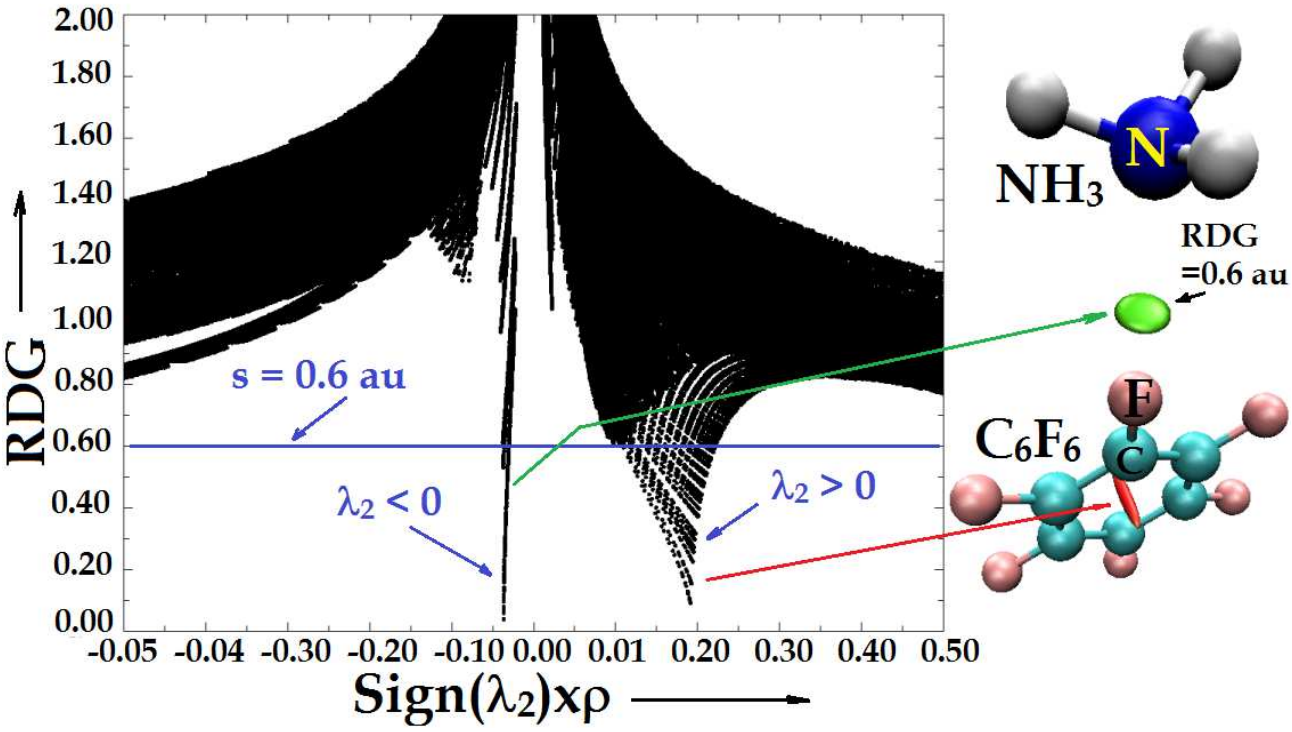

Fig. S1: RDG vs. Sign(λ_2)×ρ NCI (left) and RDG = 0.6 a.u. isosurface (right) graphical plots for H$_3$N···FC$_6$F$_5$. The spikes in the $\lambda_2 < 0$ and $\lambda_2 > 0$ regions represent to the bonded (attractive) and non-bonded (repulsive) interactions (see Figs. 1g and 2g for the optimized geometry and QTAIM molecular graph for the same dimer).

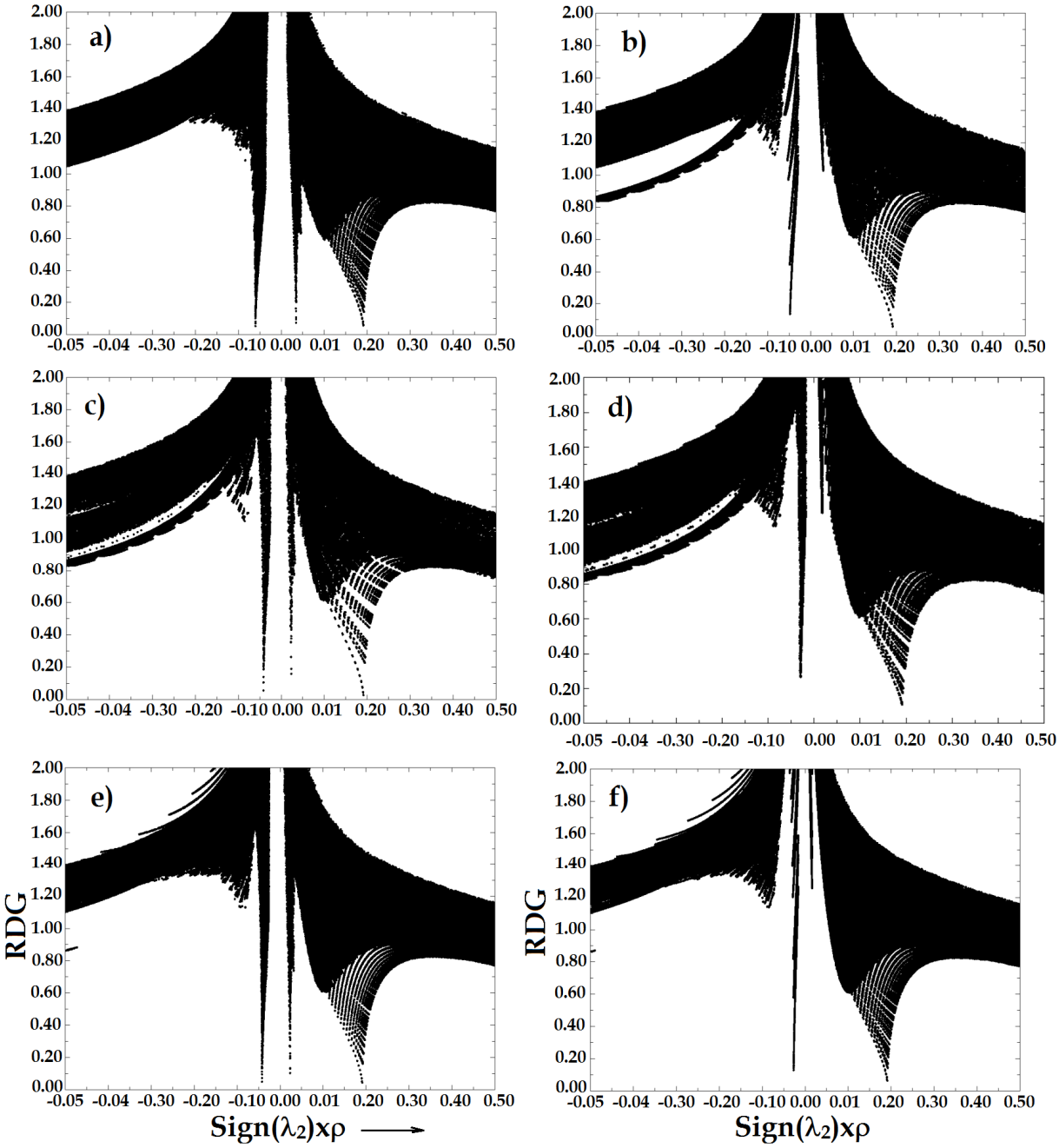

Fig. S2: RDG vs. Sign(λ_2)×ρ plot for $H_2O\cdots FC_6F_5$ a), $H_2O\cdots FC_6F_5$ b), $H_3CF\cdots FC_6F_5$ c), $H_3CF\cdots FC_6F_5$ d), $HF\cdots FC_6F_5$ e) and $HF\cdots FC_6F_5$ f) (values in a.u.). The spikes in the $\lambda_2 < 0$ and $\lambda_2 > 0$ regions represent to the bonded (attractive) and non-bonded (repulsive) interactions. The respective s = 0.6 a.u. RDG isosurfaces painted in green and red are depicted in Fig. 2 (see the ball and stick models). See Fig. 1 for conformational details.

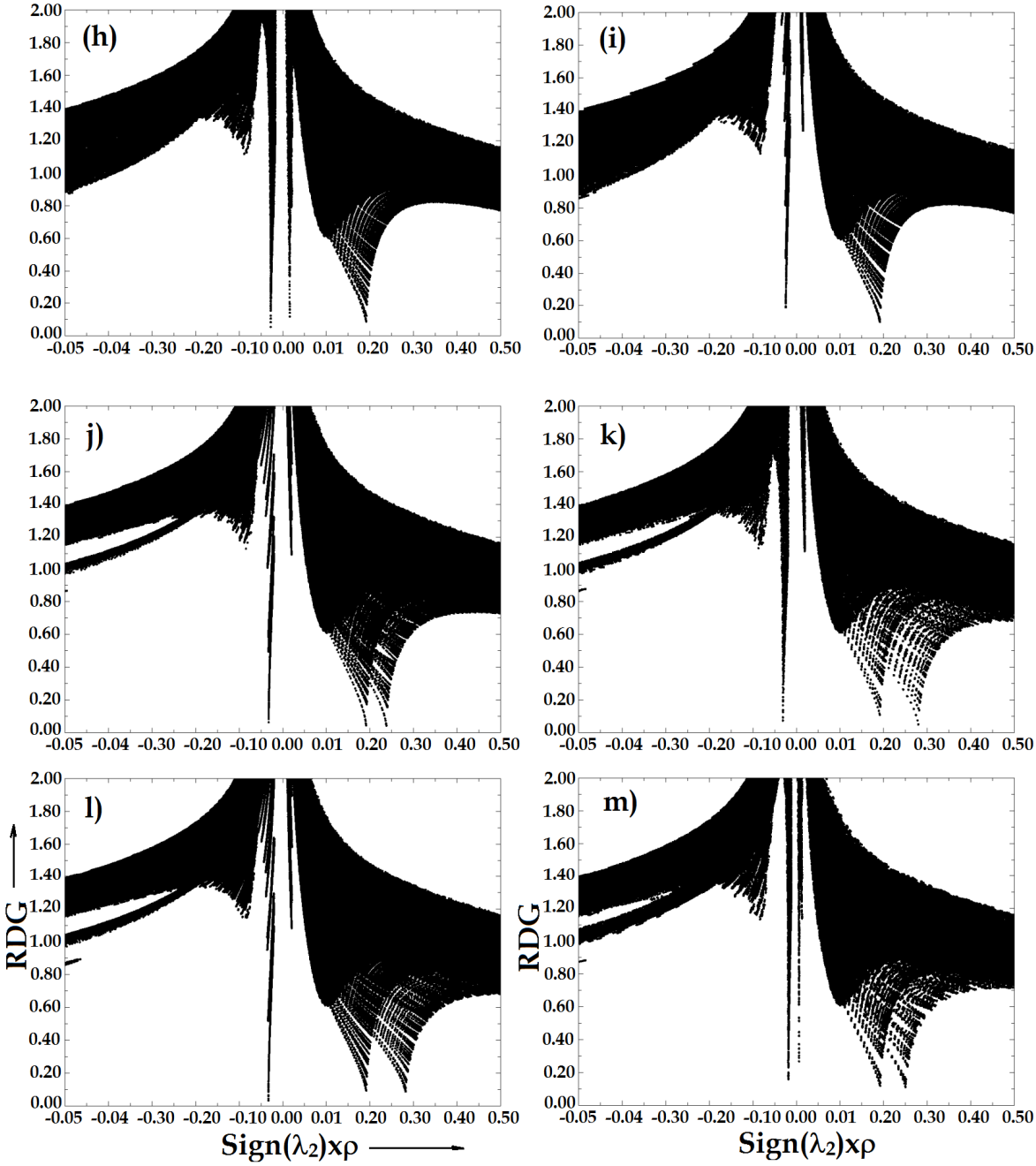

Fig. S3: RDG vs. Sign(λ_2)×ρ plot for $H_2CO\cdots FC_6F_5$ h), $H_2CO\cdots FC_6F_5$ i), $C_5F_5N\cdots FC_6F_5$ j), $C_4F_4N_2\cdots FC_6F_5$ k), $C_4F_4N_2\cdots FC_6F_5$ l), and $(CF)_4N_2\cdots FC_6F_5$ m) (values in a.u.). The spikes in the $\lambda_2 < 0$ and $\lambda_2 > 0$ regions represent to the bonded (attractive) and non-bonded (repulsive) interactions. The respective s = 0.6 a.u. RDG isosurfaces painted in green and red are depicted in Fig. 2 (see the ball and stick models). See Fig. 1 for conformational details.

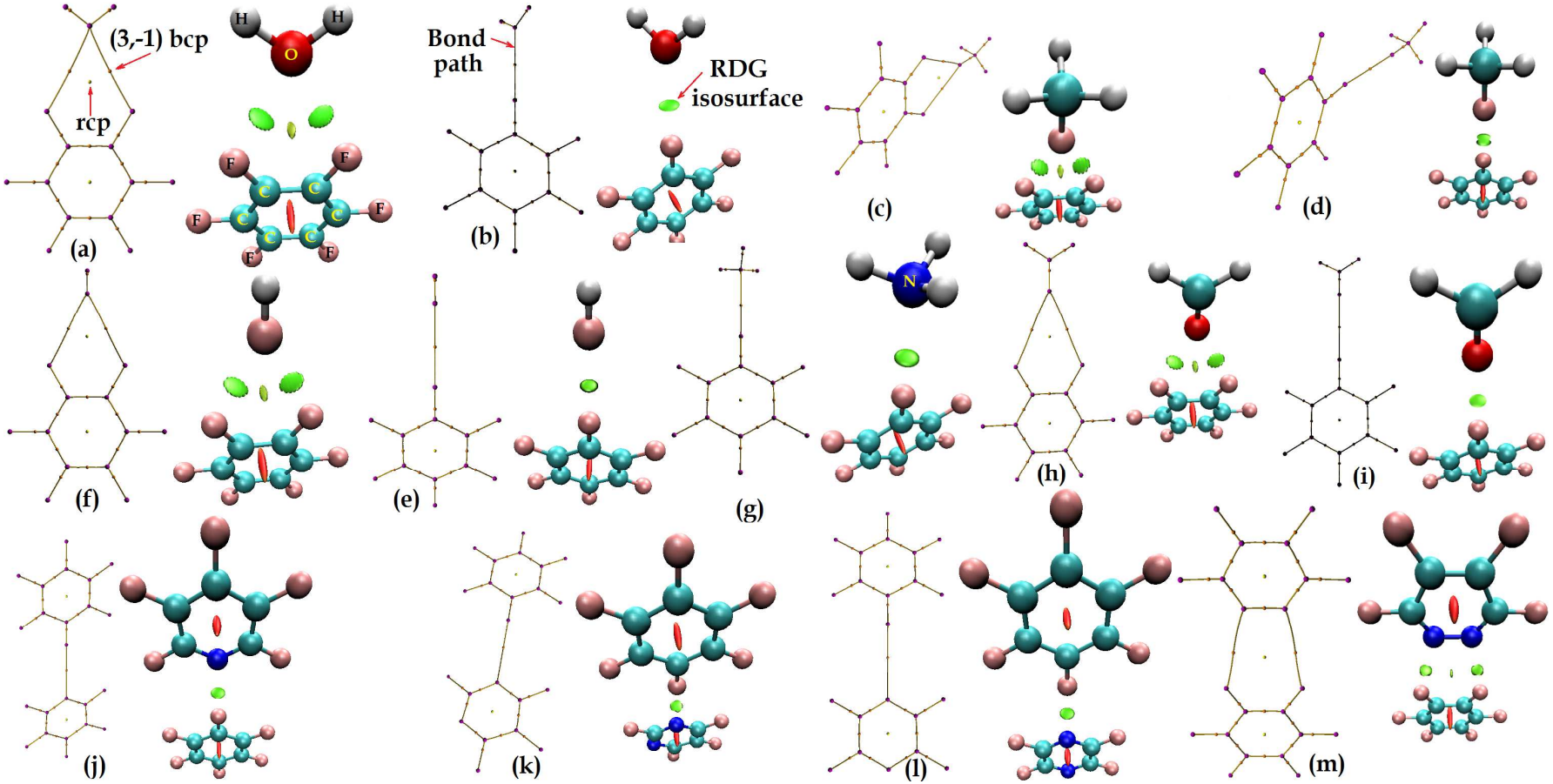

Fig 2: QTAIM based molecular graphs for the dimers of hexafluorobenzene (C_6F_6) with a-b) water (H_2O), c-d) fluoromethane (H_3CF), e-f) hydrogen fluoride (HF), g) ammonia (NH_3), h-i) formaldehyde ($H_2C=O$), j) pentafluoropyridine (C_5F_5N), k) tetrafluropyrimidine ($C_4F_4N_2$), l) tetrafluropyrazine ($C_4F_4N_2$), and m) tetrafluoropyridazine ($(CF)_4N_2$). Each dot at the center of the six-membered fluoro-substituted benzene ring represents the (3,+1) ring critical point (rcp), and that between each bonded pair of two atomic basins to the (3,–1) bond critical point. The RDG = 0.6 a.u. isosurface critical point plots (green circular volumes between noncovalently bonded atoms) for the corresponding complexes are also displayed (ball and stick models). The red RDG isosurface at the center of each 6-membered delocalized ring is a consequence of repulsion (characterized by $\lambda_2 > 0$), while green ones between the molecules are resulting from attraction (characterized by $\lambda_2 < 0$). The O, N, F, C, and H atoms are painted in red (as in a), deep-blue (as in g), light-pink (as in a), light-blue (as in a), and gray-white (as in a), respectively.

The calculated charge densities ρ_b at the O···F, N···F, and F···F bcps of the dimers illustrated in Fig. 2 are found to lie between 0.0019 and 0.0060 a.u. (cf. Table 3 for details). These values are somehow comparable with the corresponding values of 0.0038 – 0.0325 a.u. for H-bonds, [39a] of 0.0080 – 0.0168 a.u. for H···H bonds,[39b] of 0.0018 – 0.0029 a.u. for C···O bonds,[28a] of 0.0021 – 0.0034 a.u. for C···C bonds,[28a] and of 0.0080 – 0.0223 a.u. for F···F bonds.[39a, c] The Laplacian of the charge densities at the bcps, $\nabla^2\rho_b$, of the corresponding atom pairs are computed to lie in the range from 0.0095 to 0.0271 a.u. (cf. Table 3). Because its magnitude is very small, and its sign is positive for all such interactions, one could therefore recognize the O···F, or N···F, or F···F pair to be closed-shell type.[14, 16,25c-j]

Over and over again, the delocalization index, δ, a measure of the number of electron pairs exchanged between a pair two atomic basins in molecules, is calculated for all possible atom pairs in each dimer within the framework of QTAIM,[25a-b] and the results summarized in Table 3 are only for the O···F, N···F and F···F diatomic pairs. Encouragingly, the value of δ is calculated precisely between 0.0116 and 0.0306 for all such interactions, which are well along with the corresponding values reported previously for various noncovalently bonded interactions in diverse dimers (for examples, δ were between 0.063 (H_3P···HSH) and 0.213 (H_3N···HCl)) for H-bonds,[40a] and that between 0.0236 (H_2BH···HBr) – 0.1780 (NaH···HF) for H···H bonds,[40b] etc.).

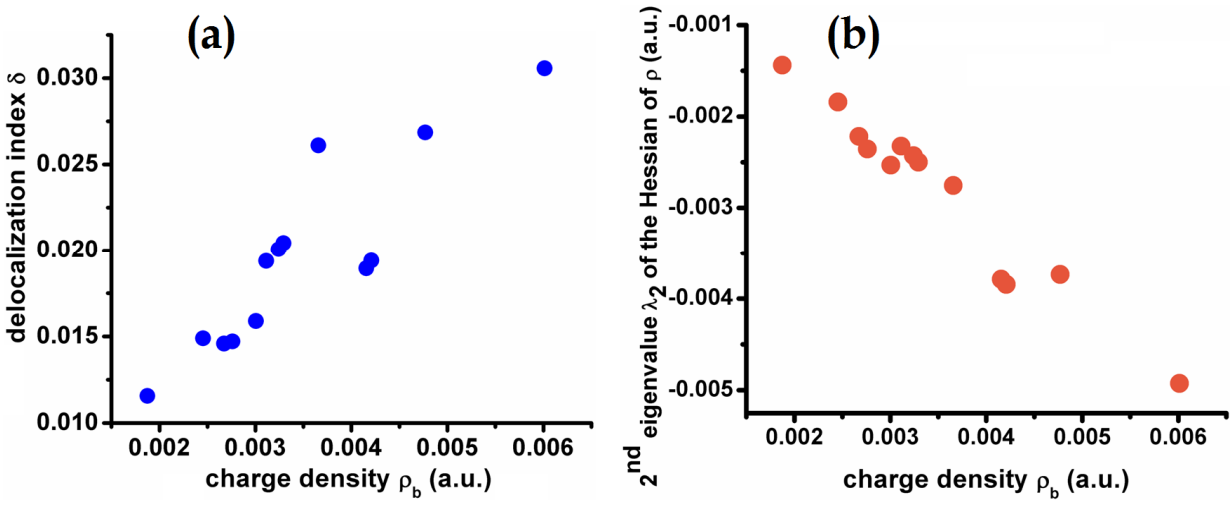

Fig. 3: Relationship between delocalization index δ and the (3,–1) bond critical point charge density ρ_b (a), and that between the latter property and the second eigenvalue λ_2 of the Hessian of the charge density (b) for the O···F, F···F, and N···F weakly bonded interactions found in all the thirteen dimers investigated.

Fig. 3a manifests the dependence, though not very perfect, of the delocalization index δ on the charge density ρ_b, while Fig. 3b manifests that of the second eigenvalue λ_2 of the Hessian of the charge density on the latter property for the D···F interactions, where D = F, N, and O. Similar dependencies have been discussed for other systems elsewhere. [14b, 51]

3.4 Conclusions

This paper theoretically presented for the first time using first-principles calculations the possibility of attractive intermolecular interactions between the entirely negative fluorine in perfluorobenzene and the various negative site(s) feasible in a series of nine different Lewis bases. Towards this end, firstly, it showed that the $O^{\delta-}\cdots F^{\delta-}$, $F^{\delta-}\cdots F^{\delta-}$, and $N^{\delta-}\cdots F^{\delta-}$ intermolecular distances computed for all the thirteen dimers examined are either close to or slightly smaller (or larger) than the sum of the van der Waals radii of the interacting atoms, unsurprisingly presenting an attainment or a failure of the IUPAC geometric criterion, thereby promulgating the fact that the use of this criterion may not be suitable to look for weakly bound noncovalent interactions in intermolecular complexes.

Secondly, the directional preference of bonding was shown evident in several geometries of the dimers of C_6F_6 with eight Lewis bases, meaning that the type-II interaction topology (with $\angle$D···F–C (D = F, N, and O) close to 180°) was sharply reflected between the noncovalently bonded atoms in such complexes. However, for a few other dimers of the C_6F_6, where the solely negatively charged atoms in the Lewis bases, e.g., the O, O and F atoms in H_2O, H_2CO, and HF, for examples, were involved to serve as bifurcated acceptors (three-centered), the appearance of the type-I interaction topology was not very surprising (herein $\angle$D···F–C (D = F, or N, or O) varies between 122 and 139°, determined depending on the nature of Lewis base molecule interacting with the equatorial sites of the fluorine in C_6F_6).

Thirdly, it showed that the binding energies for all the dimers computed with M06-2X to be very weakly, about a factor of 1.4 to 7.2 times smaller than those obtained with MP2(full). The smallest and largest values of ΔE obtained with the later method were lying between −1.37 (for HF···FC_6F_5) and −7.88 kJ mol^{-1} ($(CF)_4N_2$)···FC_6F_5). Interestingly, this energy range was found to be substantially larger than that evaluated with [CCSD(T)] for the corresponding dimers, which is not unexpected because MP2(full) largely overestimates the correlated energies. In any case, both the M06-2X and CCSD(T) calculated binding energies for the presently studied dimers are comparable with the previously reported dissociation energy of 1.3 kJ mol^{-1} for the methane dimer, as well as with that of the range, 0.52 – 12.38 kJ mol^{-1}, reported for the

H···H bonded dimers of alkanes and polyhedranes.[36] Thus, in analogy with the interpretations of Echeverría et al.,[36] one may now conclude that one of the main driving forces, in addition to the London forces, that causes the attraction between the completely negative sites may be attributed to the polarizabilities of the interacting atoms in the monomers of the dimers, which has the $1/r^6$ dependence, where r is the intermolecular distance.

Indeed, the aforementioned claim is somehow in agreement with the LMO-EDA results, in which, it is found that whereas electrostatic energy due to the Coulomb force between the negatively charged species is repulsive, polarization and dispersion are the main ruling forces that bring such negatively charged species together in the equilibrium configurations of the dimers investigated.

Fourthly, using the topological properties of the electron density and the electron delocalization indices we have demonstrated that the $O^{\delta-}\cdots F^{\delta-}$, $F^{\delta-}\cdots F^{\delta-}$, and $N^{\delta-}\cdots F^{\delta-}$ intermolecular contacts are predominantly of closed-shell type, in excellent agreement with the results of the RDG based NCI analysis. Even so, the molecular electrostatic surface potential model did not allow us to recognize the possibility of such interaction types. This is obviously due to the fact that application of the latter model to the presently studied systems does not return the favor of likeness (attraction) between similarly negatively charged species, in agreement with the Coulomb's inverse square force law of electrostatics. Again, this feature is not very surprising as this model is good to explore noncovalent interactions in intermolecular complexes that are predominately stabilized by electrostatics,[2b, 41, 46c] wherein attractive forces such as dispersion, polarization, charge transfer, and induction play a minor role.

3.5 References

1. (a) G. R. Desiraju, Angew. Chem. Int. Ed., 2011, 50, 52; (b) G. R. Desiraju, P. Shing Ho, L. Kloo, A. C. Legon, R. Marquardt, P. Metrangolo, P. Politzer, G. Resnati and K. Rissanen, Pure Appl. Chem., 2013, 85, 1711; (c) A. Bauzá, T. J. Mooibroek and A. Frontera, Angew. Chem. Int. Ed., 2013, 52, 12317; (d) *J. George, V. L. Deringer and R. Dronskowski, J. Phys. Chem. A,* 2014, 118, 3193; (e) *W. Wang, B. Ji and Y. Zhang, J. Phys. Chem. A,* 2009, 113, 8132.
2. (a) T. Brinck, J. S. Murray and P. Politzer, Int. J. Quantum Chem., 1992, 19, 57; (b) P. Politzer, J. S. Murray and T. Clark, Phys. Chem. Chem. Phys., 2010, 12, 7748; (c) P. Politzer, J. S. Murray and T. Clark, Phys. Chem. Chem. Phys., 2013, 15, 11178; (d) J. S. Murray and P. Politzer, WIREs Comput. Mol. Sci.: Overview 2011, 1, 153; (e) P. Politzer and J. S. Murray, Chem. Phys. Chem,, 2013, 14, 278; (f) P. Politzer, J. S. Murray, G. V. Janjic and S. D. Zaric, Crystal, 1024, 4, 12; (g) J. S. Murray, P. Lane, T. Clark, K. E. Riley and P. Plitzer, J. Mol. Model, 2012, 18, 541; (h) X. Ding, M. Tuikka and M. Haukka, Halogen Bonding in Crystal Engineering, Recent Advances in Crystallography. In Jason BB,

ed.; 2012, ISBN: 978-953-51-0754-5, InTech, doi: 10.5772/48592. Available from: http://www.intechopen.com/books/recent-advances-in crystallography/halogen-bonding-in-crystal-engineering; (i) J. S. Murray, K. E. Riley, P. Politzer and T. Clark, Aust. J. Chem., 2010, 63, 1598.

3. P. Auffinger, F. A. Hays, E. Westhof and P. Shing Ho, Proc. Natl. Acad. Sci. U. S. A., 2004, 101, 16789; (b) M. R. Scholfield, C. M. V. Zanden, M. Carter and P. Shing Ho, Protein Science, 22, 2013, 139; (c) R. Wilcken, M. O. Zimmermann, A. Lange, A. C. Joerger and F. M. Boeckler, J. Med. Chem., 2013, 56, 1363; (d) Y. Lu, T. Shi, Y. Wang, H. Yang, X. Yan, X. Luo, H. Jiang and W. Zhu, J. Med. Chem., 2009, 52, 2854; (e) A. Mukherjee, S. Tothadi and G. R. Desiraju, Acc. Chem. Res., 2014, 47, 2514; (f) A. Priimagi, G. Cavallo, P. Metrangolo and G. Resnati, Acc. Chem. Res., 2013, 11, 2686.
4. (a) M. Boero, T. Ikeshoji, C. C. Liew, K. Terakura and M. Parrinello, J. Am. Chem. Soc., 2004, 126, 6280; (b) J. M. Berg, J. L. Tymoczko and L. Stryer, Biochemistry, 5th Edn., New York: W H Freeman, 2002; (c) S. V. Rosokha and M. K. Vinakos, Phys. Chem. Chem. Phys., 2014, 16, 1809; (d) R. E. Hubbard and M. K. Haider, (February 2010) Hydrogen Bonds in Proteins: Role and Strength. In: Encyclopedia of Life Sciences (ELS). John Wiley & Sons, Ltd: Chichester. DOI: 10.1002/9780470015902.a0003011.pub2; (e) C. F. Guerra, F. M. Bickelhaupt, J. G. Snijders, and E. J. Baerends, J. Am. Chem. Soc., 2000, 122, 4117; (f) H. L. Nguyen, P. N. Horton, M. B. Hursthouse, A. C. Legon and D. W. Bruce, *J. Am. Chem. Soc.*, 2004, 126, 16; (g) Y. Chen, H. Yu, L. Zhang, H. Yang and Y. Lu, Chem. Commun., 2014, 50, 9647; (h) R. Gutzler, C. Fu, A. Dadvand, Y. Hua, J. M. MacLeod, F. Rosei and D. F. Perepichka, Nanoscale, 2012,4, 5965.
5. (a) P. Metrangolo and G. Resnati, Halogen Bonding: Fundamentals and Applications, Springer-Verlag, Berlin, Heidelberg, Germany, 2008; (b) F. Meyer and P. Dubois, Cryst. Eng. Comm., 2013, 15, 3058; (c) G. Berger, J. Soubhye and F. Meyer, Polym. Chem., 2015, 6, 3559.
6. *(a) Y. Lu, T. Shi, Y. Wang, H. Yang, X. Yan, X. Luo, H. Jiang and W. Zhu, J. Med. Chem., 2*009, 52, 2854; (b) *S. Sirimulla, J. B. Bailey, R. Vegesna and M. Narayan, J. Chem. Inf. Model.*, 2013, 53, 2781; (c) Y. Lu, Y. Liu, Z. Xu, H. Li, H. Liu and W. Zhu, Expert Opin. Drug. Discov. 2012, 7, 375.
7. S. Kawai, A. Sadeghi, F. Xu, L. Peng, A. Orita, J. Otera, S. Goedecker and E. Meyer, ACS Nano, 2015, 9, 2574.
8. (a) H. Jin, A. M. Plonka, J. B. Parise and N. S. Goroff, Cryst. Eng. Comm,, 2013, 15, 3106; (b) A. W. Sun, J. W. Lauher and N. S. Goroff, Science, 2006, 312, 1030; (c) C. Wilhelm, S. A. Boyd, S. Chawda, F. W. Fowler, N. S. Goroff, G. P. Halada, C. P. Grey, J. W. Lauher, L. Luo, C. D. Martin, J. B. Parise, C. Tarabrella and J. A. Webb, J. Am. Chem. Soc., 2008, 130, 4415; (d) N. S. Goroff, S. M. Curtis, J. A. Webb, F. W. Fowler and J. W. Lauher, Org. Lett., 2005, 7, 1891.
9. M. J. Vallejos, P. Auffinger, P. Shing Ho, In: D. M. Himmel, M. G. Rossman, editors. Hoboken, NJ: Wiley; 2012. Halogen interactions in biomolecular crystal structures, in: *International Tables* of *Crystallography*, Volume *F*, 2nd ed., *Ch 23.6*, 2012 (available at: http://www-ibmc.u-strasbg.fr/arn/Westhof/publ_West/doc2011/r2011_MVallejos_Tables.pdf).
10. T. Clark, M. Hennemann, J. S. Murray and P. Politzer, J. Mol. Model., 2007 13, 291.
11. (a) P. Metrangolo, J. S. Murray, T. Pilati, P. Politzer, G. Resnati and G. Terraneo, Cryst. Growth Des. 2011, 11, 4238; (b) P. Metrangolo, J. S. Murray, T. Pilati, P. Politzer, G. Resnati and G. Terraneo, Cryst. Eng. Comm. 2011, 13, 6593.
12. K. Eskandari and M. Lesan, Chem. –Eur. J., 2015, 21, 4739.
13. T. Clark, WIREs Comput. Mol. Sci., 2013, 3, 13.

14. (a) A. Varadwaj, P. R. Varadwaj and B.-Y. Jin, Int. J. Quantum Chem., 2015, 115, 453; (b) P. R. Varadwaj, A. Varadwaj and B.-Y. Jin, Phys. Chem. Chem. Phys., 2014, 16, 19573.
15. M. P. Johansson and M. Swart, Phys. Chem. Chem. Phys., 2013, 15, 11543.
16. P. R. Varadwaj, A. Varadwaj and B.–Y. Jin, Phys. Chem. Chem. Phys., 2015, DOI: 10.1039/C5CP03209A.
17. M. Head-Gordon and T. Head-Gordon, Chem. Phys. Lett., 1994, 220, 122.
18. (a) Y. Zhao and D. G. Truhlar, Theor. Chem. Acc., 2008, 120, 215; (b) Y. Zhao and D. G. Truhlar, Acc. Chem. Res. 2008, 41, 157.
19. J. A. Pople, M. Head-Gordon and K. Raghavachari, J. Chem. Phys., 1987, 87, 5968.
20. (a) Gaussian 09, Revision A.02, M. J. Frisch, G. W. Trucks, H. B. Schlegel, G. E. Scuseria, M. A. Robb, J. R. Cheeseman, G. Scalmani, V. Barone, B. Mennucci, G. A. Petersson, H. Nakatsuji, M. Caricato, X. Li, H. P. Hratchian, A. F. Izmaylov, J. Bloino, G. Zheng, J. L. Sonnenberg, M. Hada, M. Ehara, K. Toyota, R. Fukuda, J. Hasegawa, M. Ishida, T. Nakajima, Y. Honda, O. Kitao, H. Nakai, T. Vreven, J. A. Montgomery, Jr., J. E. Peralta, F. Ogliaro, M. Bearpark, J. J. Heyd, E. Brothers, K. N. Kudin, V. N. Staroverov, R. Kobayashi, J. Normand, K. Raghavachari, A. Rendell, J. C. Burant, S. S. Iyengar, J. Tomasi, M. Cossi, N. Rega, J. M. Millam, M. Klene, J. E. Knox, J. B. Cross, V. Bakken, C. Adamo, J. Jaramillo, R. Gomperts, R. E. Stratmann, O. Yazyev, A. J. Austin, R. Cammi, C. Pomelli, J. W. Ochterski, R. L. Martin, K. Morokuma, V. G. Zakrzewski, G. A. Voth, P. Salvador, J. J. Dannenberg, S. Dapprich, A. D. Daniels, Ö. Farkas, J. B. Foresman, J. V. Ortiz, J. Cioslowski, and D. J. Fox, Gaussian, Inc., Wallingford CT, 2009; (b) M.W.Schmidt, K.K.Baldridge, J.A.Boatz, S.T.Elbert, M.S.Gordon, J.H.Jensen, S.Koseki, N.Matsunaga, K.A.Nguyen, S.Su, T.L.Windus, M.Dupuis and J.A.Montgomery J. Comput. Chem., 1993, 14, 1347.
21. GaussView, Version 5, R. Dennington, T. Keith and J. Millam, *Semichem Inc.*, Shawnee Mission, KS, 2009.
22. T. A. Keith, AIMAll (Version 11.03.14), 2011. Available via DIALOG at: http://im.tkgristmill.com.
23. (a) T. Lu and F. Chen, J. Comp. Chem. 2012, 33, 580; (b) T. Lu and F. Chen, J. Mol. Graph. Model. 2012, 38, 314.
24. W. Humphrey, A. Dalke, K. Schulten, "VMD - Visual Molecular Dynamics", J. Molec. Graphics, 1996, 14, 33.
25. (a) J. Poater, M. Solá, and M. Duran, X. Fradera, Theor. Chem. Acc., 2002, 107, 362; (b) X. Fradera and M. Solá, J. Comput. Chem., 2002, 23, 1347; (c) C. F. Matta, J. Hernandez-Trujillo and R. F. W. Bader, J. Phys. Chem. A, 2002, 106, 7369; (d) C. F. Matta and J. Hernandez-Trujillo, J. Phys. Chem. A, 2003, 107, 7496; (e) P. R. Varadwaj, A. Varadwaj, G. H. Peslherbe and H. M. Marques, J. Phys. Chem. A, 2011, 115, 13180; (f) P. R. Varadwaj, J. Mol. Model., 2010, 16, 965; (g) P. R. Varadwaj and H. M. Marques, Phys. Chem. Chem. Phys., 2010, 12, 2126; (h) A. Varadwaj and P. R. Varadwaj, Chem. –Eur. J., 2012, 18, 15345; (i) P. R. Varadwaj, A. Varadwaj and B. –Y. Jin, Phys. Chem. Chem. Phys., 2015, 17, 805; (j) R. F. W. Bader, Atoms in Molecules - A Quantum Theory, *Oxford University Press*, Oxford, 1990.
26. (a) E. R. Johnson, S. Keinan, P. Mori-Sanchez, J. Contreras-Garcia, A J. Cohen and W. Yang, J. Am. Chem. Soc., 2010, 132, 6498; (b) J. R. Lane, J. Contreras-García, J. P. Piquemal, B. J. Miller and H. G. Kjaergaard, J. Chem. Theory Comput., 2013, 9, 3263; (c) J. Contreras-Garcia, E. Johnson, S. Keinan, R. Chaudret, J.-P. Piquemal, D. Beratan and W. Yang, J. Chem. Theor. Comp., 2011, 7, 625.
27. (a) L. Brammer, G. M. Espallargas and S. Libri, Cryst. Eng. Comm., 2008, 10, 1712; (b) F. F. Awwadi, R. D. Willett, K. A. Peterson and B. Twamley, Chem. –Eur. J., 2006, 12, 8952; (c) D. Chopra, Cryst. Growth. Des. 2012, 12, 541; (d) S. M. Walter, F. Kniep, E. Herdtweck and

S. M. Huber, Angew. Chem. Int. Ed., 2011, 50, 7187; (e) C. M. Reddy, M. T. Kirchner, R. C. Gundakaram, K. A. Padmanabhan and G. R. Desiraju, Chem. –Eur. J., 2006, 12, 2222; (f) P. R. Varadwaj, A. Varadwaj and B.-Y. Jin. J. Comput. Chem., 2015, DOI: 10.1002/jcc.24211; (g) R. A. Cormanich, R. Rittner, D. O'Hagan and M. Bühl, J. Phys. Chem. A, 2014, 118, 7901.

28. (a) P. R. Varadwaj, A. Varadwaj and B.-Y. Jin, Phys. Chem. Chem. Phys., 2014, 16, 17238; (b) S. J. Grabowski, Phys. Chem. Chem. Phys., 2014, 16, 1824; (c) D. A. Smith, L. Brammer, C. A. Hunter and R. N. Perutz, J. Am. Chem. Soc., 2014, 136, 1288.
29. V. G. Tsirelson, P. F. Zou, T. –H. Tang and R. F. W. Bader, 1995, Acta Cryst. A 1995, 51, 143.
30. P. Politzer and J. S. Murray, Molecular electrostatic potentials: some observations. In: K. Ghosh K, P. Chattaraj (eds) Concepts and methods in modern theoretical chemistry, vol. 1: electronic structure and reactivity. Taylor & Francis, New York, pp 181–199, 2013.
31. P. Politzer, J. S. Murray and T. Clark, Top. Curr. Chem., 2015, 358, 19.
32. (a) P. R. Varadwaj and H. M. Marques, Theor. Chem. Acc., 2010, 127, 711; (b) B. Sutay, A. Tekin and M. Yurtsever, Theor. Chem. Acc., 2012, 131, 1120; (c) P. Hobza and K. Müller-Dethlefs, Characteristics of Non-covalent Complexes and Their Determination by Theoretical and Experimental Techniques (Chapter 2), in: Non-Covalent Interactions: Theory and Experiment, RSC Theoretical and Computational Chemistry Series No. 2., DOI:10.1039/9781847559906, 2010; (d) I. Dabowska, P. Jurecka and P. Hobza, J. Chem. Phys., 2005, 122, 204322.
33. Y.-X. Lu, J.-W. Zou, Y.-H. Wang, Y.-J. Jiang and Q.-S. Yu, J. Phys. Chem. A, 2007, 111, 10781.
34. J.-W. Zou,Y.-J. Jiang, M. Guo, G.-X. Hu, B. Zhang, H.-C. Liu and Q.-S. Yu, Chem. –Eur. J., 2005, 11, 740.
35. D. Mani and E. Arunan, Phys. Chem. Chem. Phys., 2013, 15, 14377.
36. J. Echeverría, G. Alullón, D. Danovich, S. Shaik and S. Alvarez, Nat. Chem., 2011, 3, 323.
37. J. Hernández-Trujillo and C. F. Matta, Struct. Chem., 2007, 18, 849.
38. S. Alvarez, Dalton Trans., 2013, 42, 8617.
39. (a) C. F. Matta, N. Castillo and R. J. Boyd, J. Phys. Chem. A, 2005, 109, 3669; (b) C. F. Matta, J. Hernandez-Trujillo, T.-H. Tang and R. F. W. Bader, Chem. –Eur. J., 2003, 9, 1940; (c) I. Alkorta and J. Elguero, Struct. Chem., 2004, 15, 117.
40. (a) J. Poater, M. Solá and F. M. Bickelhaupt, Chem. –Eur. J., 2006, 12, 2889; (b) D. Hugas, L. Guillaumes, M. Duran and S. Simon, Comput. Thoer. Chem., 2012, 998, 113.
41. (a) P. Politzer, J. S. Murray and Z. Peralta-Inga, Int. J. Quantum Chem., 2001, 86, 676; (b) A. J. Stone, *J. Am. Chem. Soc.*, 2013, 135, 7005.
42. (a) T. Janowski and P. Pulay, J Am Chem Soc., 2012, 134, 17520; (b) I. C. Gerber and J. G. Ángyán, J. Chem. Phys., 2007, 126, 044103.
43. (a) J. P. P. Ramalho, J. R. B. Gomes and F. Illas, RSC Adv., 2013,3, 13085; (b) J. Klimes and A. Michaelides, J. Chem. Phys., 2012, 137, 120901; (c) B. I. Lundqvist, Y. Andersson, H. Shao, S. Chan and D. C. Langret, Int. J. Quantum Chem., 1995, 56, 247.
44. (a) P. L. A. Popelier, *J. Phys. Chem. A*, 1998, 102,1873; (b) V. R. Hathwar, S. M. Roopan, R. Subashini, F. N. Khan and T. N. Guru Row, J. Chem. Sci., 2010, 122, 677; (c) M. Yahia-Ouahmed, V. Tognetti and L. Joubert, Comput. Theor. Chem., 2015, 1053, 254; (d) S. J. Grabowski, Theor. Chem. Acc., 2013, 132, 1347.
45. (a) Y. V. Nelyubina, M. Yu. Antipin, D. S. Dunin, V. Yu. Kotov and K. A. Lyssenko, Chem. Commun., 2010, 46, 5325; (b) A. G. Dikundwar and T. N. G. Row, *Cryst. Growth Des.*, 2012, 12, 1713; (c) R. D. Parra, Molecules, 2014, *19*, 1069.

46. (a) J. S. Murray, P. Lane and P. Politzer, J. Mol. Model., 2009, 15, 723; (b) P. Politzer and J. S. Murray, Cryst. Growth Des., 2015, 15, 3767; (c) T. Clark, P. Politzer and J. S. Murray, WIREs Comput. Mol. Sci., 2015, 5, 169; (d) P. Politzer, J. S. Murray and T. Clark, J. Mol. Model. 2015, 21, 52; (e) P. Politzer, J. S. Murray, D. Yepes and P. Jaque, J. Mol. Model., 2014, 20, 2351; (f) R. F. W. Bader, M. T. Carroll, J. R. Cheeseman and C. Chang, J. Am. Chem. Soc., 1987, 109, 7968.
47. (a) K. E. Riley and P. Hobza, J. Chem. Theory Comput., 2008, 4, 232; (b) M. Kolář and P. Hobza, J. Chem. Theory Comput., 2012, 8, 1325.
48. (a) D. N. Bol'shutkin, V. M. Gasan, A. I. Prokhvatilov and A. I. Erenburg, Acta Crystallogr., Sect. B: Struct. Crystallogr. Cryst. Chem., 1972, 28, 3542; (b) A. N. Fitch, J. K. Cockcroft and Z. Kristallogr., 1993, 203, 29; (c) G. Pepe and J.-M. Gay, J. Chem. Phys., 1989, 90, 5735.
49. R. M. Osuna, V. Hernández, J. T. L. Navarrete, E. Dria and J. J. Novoa, Theor. Chem. Acc., 2011, 128, 541.
50. General Atomic and Molecular Electronic Structure System (GAMESS). M. W. Schmidt, K. K. Baldridge, J. A. Boatz, S. T. Elbert, M. S. Gordon, J. H. Jensen, S. Koseki, N. Matsunaga, K. A. Nguyen, S. Su, T. L. Windus, M. Dupuis, J. A. Montgomery J. Comput. Chem., 1993 14, 1347.
51. C. F. Matta and J. Hernandez-Trujillo, J. Phys. Chem. A, 2003, 107, 7496.

Chapter 4. Electronic Structure Studies of Molecular Methylammonium Lead Triiodide Perovskite

4.1 Introduction

Designing high-performance photoresponsive visible-light-driven materials for solar cells is cutting-edge research.[1] Among others,[2] hybrid organic–inorganic lead/tin/germanium trihalide perovskite systems are a special class of novel materials that have created historical *breakthroughs* in photovoltaic technology.[3] Even though perovskite compounds have been known to the scientific community for over a century,[4] they have only recently evoked renewed interest.[1] This was made possible by Kojima *et al.*,[5] who reported the photon-to-electricity power conversion efficiency (PCE) of the methylammonium lead(II) tribromide ($CH_3NH_3PbBr_3$) perovskite as 2.2% in 2006,[5a)] and of methylammonium lead(II) triiodide ($CH_3NH_3PbI_3$, or $MAPbI_3$, or $[CH_3NH_3{\bullet\bullet\bullet}I_3Pb]$) perovskite as 3.8% in 2009.[5b)] These two fundamental studies were assumedly sufficient to inspire the solar energy community to carry out further researches on these,[1,6] as well as on analogous systems,[7] for further development of the PCE value of these materials with variable experimental settings.[6a),b)]

Over 2000 articles have already been published addressing various aspects of the trihalide perovskite solar cell materials. Interestingly, this was achieved within the very short period between 2012 and 2017.[8,9] Although versatile trihalide perovskites have been experimentally synthesized, many of them are reported to be in two and three dimensions.[10] However, $CH_3NH_3PbI_3$ is the only system that has displayed very high semiconducting performance due to a number of its specialized characteristics.[11a)] Some of them, for example, include very high light absorbing potential, giant photoinduced dielectric constant,[11b)] very small excitation binding energy (<<16 meV at room temperature),[11c)] very small excitonic reduced effective mass ($\approx 0.104m_e$, where m_e is the electron mass),[11c)] and large effective diffusion lengths – about 100 nm for both electrons and holes (meaning large diffusion lengths for excitons as well).[11e)–f)] Because of these specific features, studies on the $CH_3NH_3PbI_3$ perovskite system, as well as on analogous derivatives, have been seriously focused on by a wide range of scientists,[1–2,5-6,11-13] leading to a National Renewable Energy Laboratory (NREL) certified PCE value of 22.1% reported early last year.[3,13] Grancini *et al.* have just recently provided experimental evidence of one-year stable perovskite solar cells by 2D/3D interface engineering comprising the $CH_3NH_3PbI_3$ system.[14]

Discovery of air- and moisture-stable perovskite solar cell materials with long-term device stability is one of the main concerns of the current solar cell research.[15] Therefore, serious attention has been given to developing low-bandgap trihalide-based photovoltaic

perovskite materials, which are of different varieties.[16] This is unsurprising because materials of these kinds have proven beneficial for the development of powerful ambipolar carrier transport devices,[11d)] e.g., transistors and light-emitting diodes. These devices work both in accumulation (p-type) and inversion (n-type) modes.[17a)]

Another distinct advantage of these kinds of single-crystalline trihalide perovskite materials is that the maximum efficiency of photon conversion into electrical energy can boost photovoltaic device PCE up to 25%, or even up to 35%.[17b)] Quan *et al.* have claimed that they were the first to report certified hysteresis-free solar power conversion in a planar perovskite solar cell, in which the certified PCE was about 15.3%.[17c)]

Trihalide perovskites have the general chemical formula BMY_3, where B is an inorganic/organic cation with +1 oxidation state (e.g., $Cs^+/CH_3NH_3^+$), M is a metal ion with +2 oxidation state (e.g., $Pb^{2+}/Sn^{2+}/Ge^{2+}$), and Y is a halogen derivative with an oxidation state of –1 (namely $Cl^-/Br^-/I^-$). The formula is derived from $CaTiO_3$, a mineral that was discovered by Gustov Rose in 1839, and honors the Russian mineralogist Lev Aleksevich von Perovski.[18a] This is the reason compounds such as $SrTiO_3$, $BiFeO_3$, and $Pb[Zr_xTi_{1-x}]O_3$ ($0 \leq x \leq 1$), *etc.*, having geometrical topologies identical to $CaTiO_3$ are called perovskites.[18b] When the halogen derivative Y in the formula BMY_3 refers to the monovalent iodide anion I^-, the symbol M to the Pb^{2+} divalent cation, and B to the methylammonium $CH_3NH_3^+$ (also called MA) monovalent organic cation, the resulting species is methylammonium lead(II) triiodide ($CH_3NH_3PbI_3$), an organic–inorganic hybrid perovskite.[18c-d] It is experimentally known to be structurally viable in three major temperature phases, such as orthorhombic (stable below T ≈ 165 K), tetragonal (stable in

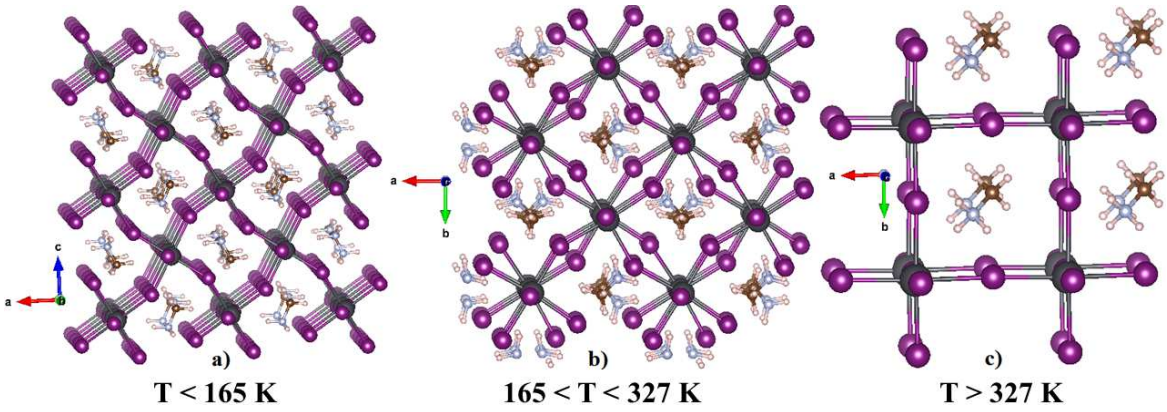

Scheme 1: The 2×2×2 supercell models representing the a) orthorhombic, b) tetragonal, and c) pseudocubic geometries of the hybrid organic-inorganic $CH_3NH_3PbI_3$ perovskite system. The symbol T represents the temperature at which these geometries are stable. In the ball and stick models, iodine: purple, carbon: reddish-brown, nitrogen: light-blue, hydrogen: grey-white. The geometrical views are presented along ac and ab planes for a) and b)–c), respectively.

the range 165 < T < 327 K), and pseudocubic (stable above T ≈ 327 K), Scheme 1.[18e-h]

$CH_3NH_3PbI_3$ with appropriate tandem technology is also efficient for photocatalytic water splitting.[19] The bandgap of this kind of perovskite materials is determined by the supramolecular dimension. For example, the dimensional reduction from 3D to 2D causes the bandgap of the material to increase. Chang *et al.* showed that the 2D quantum well perovskite structure has a bandgap of 1.86 eV, which is larger than that of its corresponding 3D analogue (1.17 eV).[20] Similarly, increasing the number of lead-halide layers in the 2D quantum well structure decreases the bandgap from 1.86 eV (one layer) through 1.59 eV (two layers) to 1.44 eV (three layers). The change was suggested to be due to the carrier confinement in the lead-based halide perovskites unperturbed by the organic cation.

The study is mainly focused on the $CH_3NH_3PbI_3$ perovskite bulk when it is visualized as a supermolecule. It is doable only when the bulk is seen as a binary complex/cluster (in zero-dimension), which is possible when no periodic boundary condition is employed to it. The characteristic features of the building block may in some way be similar to what might be expected for other hydrogen bonded clusters.[21a-e] The main difference between the former and latter systems lies in the fact that $CH_3NH_3PbI_3$ may be electrically neutral analogously as Na^+Cl^- (wherein charge-charge type Coulombic interaction plays a major role), while the stability of the latter ones may or may not have the same electrostatic origin.[21e]

Molecular $CH_3NH_3PbI_3$ may be assumed to be a by-product of two subunits, the PbI_3^- anion and the $CH_3NH_3^+$ cation, driven by electrostatics. The attractive intermolecular interaction between the monomers forming this hetero-molecular cluster is not unusual because the triangular face formed by the three I^- ions in PbI_3^- is electron rich, meaning it is highly nucleophilic, which is hence an ideal platform to accommodate the electron-deficient H atoms of the $–NH_3/–CH_3$ group in $CH_3NH_3^+$. This is perhaps the general understanding of many scientists, which has appeared in many research articles.[8,22]

Fang and Jena have recently studied molecular $CH_3NH_3PbY_3$ (Y = halogen derivative) and some of the substituted derivatives that replace Y by the superhalogens BH_4^- or $HCOO^-$, Pb^{2+} by Sn^{2+} or Ge^{2+}, and $CH_3NH_3^+$ by $HC\text{-}(NH_2)_2^+$, as fundamental building blocks.[23a] They have concluded that the properties of the organic–inorganic hybrid perovskites such as the fundamental bandgap, the gap deformation potential, the exciton binding energy, and the hygroscopicity, all originate from their corresponding molecular moieties. In addition, they have recommended adopting simple molecular models similarly as they have employed, together with Goldschmidt's tolerance factor as an important combination, to make quick estimations for the stability and functional properties of new hybrid perovskite materials, which can serve as a preliminary screening process before accurate bulk calculations.

This Chapter is focused to investigate theoretically the physical and electronic properties of parent $CH_3NH_3PbI_3$, and its possible conformers using density functional theory (DFT).[24] The primary interest is to understand if the $CH_3NH_3PbI_3$ perovskite blocks are stable in the gas phase, and whether there is any connection between the gas and solid-state geometrical features, the latter evaluated/reported using periodic DFT calculations. The secondary interest is to uncover the binding strengths of the intermolecular interactions formed between PbI_3^- and $CH_3NH_3^+$, and to examine whether these strengths can be comparable with noncovalent interactions of any such kind viable in the wide literature as very strong, strong, moderate, weak and van der Waals.[25] One of the most important concerns toward this end is to investigate whether the intermolecular interactions in $CH_3NH_3PbI_3$ do involve in any kind of proton-transfer features? Another concern is to see whether such interactions can be regarded as purely electrostatic, or whether one can recognize them as largely covalent, or a mixture of the two? The final aim is to employ various current state-of-the-art modeling tools (e.g., Natural Bond Orbital (NBO)'s second-order hyperconjugative analysis,[26] the quantum theory of atoms in molecules (QTAIM) topological analysis,[27] and the reduced density gradient noncovalent interaction (RDG-NCI) analysis[28] to examine and to unravel the nature of the various chemical bonding interactions responsible for unitizing the monomeric fragments PbI_3^- and $CH_3NH_3^+$ into clustered configurations.

4.2 Computational details

The Gaussian 09 code[29] was utilized for the calculations of the geometries and electronic properties of the most stable $CH_3NH_3PbI_3$, and its possible conformations. The DFT-M06-2X[30] functional, in conjunction with an augmented all-electron double-ζ ADZP basis set,[31] was employed to calculate the first derivative of the energy with respect to the atom fixed nuclear coordinates, and one-electron properties of all the clusters examined. The choice of the DFT functional is obviously due to the fact that it has been recommended as a global hybrid, and that it is suitable for applications involving main-group thermochemistry, kinetics, noncovalent interactions, and electronic excitation energies to valence and Rydberg states.[30]

Frequency calculation was performed for each of the optimized conformational geometries of the $CH_3NH_3PbI_3$. The eigenvalues of the Hessian second derivative matrix were found to be real for all cases, meaning the conformer geometries are all minimum with respect to the current level of theory.

In most of the experimental studies[18e,18g,22e] identification of the intermolecular noncovalent interactions in the various geometries of $CH_3NH_3PbI_3$ was accomplished using the intermolecular distance as a metric. However, as demonstrated previously on several occasions, characterizing this attribute only through the distance criterion is not standalone, as is not suitable alone for identifying intermolecular interactions that are

weak.[33,34] To this end, QTAIM[27a] implemented in AIMAll[27b] was employed to the $CH_3NH_3PbI_3$ blocks for insight into the various chemical bonding interaction topologies involved to unite the monomeric fragments PbI_3^- and $CH_3NH_3^+$ together in binary configurations. This approach also allows us to quantify the intermolecular interaction strengths in terms of charge density and other topological descriptors, including for example, the Laplacian of the charge density, the kinetic (G_b), potential (V_b), and total energy ($H_b = G_b + V_b$) densities. RDG-NCI[28] is employed to examine the extent to which it recovers the topology of bonding interactions that are identified and characterized by QTAIM.[27a] Through this, one can demonstrate further the efficacy of the latter method in unraveling the genuineness of the physical chemistry it presents to the scientific community.

Geometry relaxation and bandgap calculations using periodic DFT were performed using VASP.[35b–e] The Perdew–Burke–Ernzerhof (PBE) exchange-correlation functional, together with the projector augmented wave (PAW) potentials for all atoms, the cut-off energy for the plane wave basis set of 520 eV, and a 6 × 6 × 6 Γ-centered *k*-point sampling of the Brillouin zone were set for the periodic relaxation of the geometry of the $CH_3NH_3PbI_3$ bulk that corresponds to the high temperature pseudocubic phase, as well as for bandgap calculation. The tetrahedron method with Blöchl corrections for the Brillouin-zone integrations was utilized for this purpose.[35f]

In addition, NBO[26] was employed to examine whether the orbital chemistry gleaned with this approach can be comparable with those emanated with the aforesaid charge density approaches.[27a,28] Specifically, our interest was to examine if the reliabilities of the bond paths developed between the various atomic basins constituting the triiodide perovskite clusters have any consistency with the second-order perturbative estimates of donor–acceptor (bond–antibond) interactions in the NBO basis, which are consequences of charge-transfer delocalization (hyperconjugation).[26a] According to this method, for a given set of donor NBO (i) and acceptor NBO (j), the stabilization energy $E^{(2)}$ for a given interaction type associated with delocalization $i \rightarrow j$ can be estimated with Eqn 1, where q_i is the donor orbital occupancy, ε_i and ε_j are orbital energies (diagonal elements), and $F(i, j)$ is the off-diagonal NBO Fock matrix element.[26a]

$$E^{(2)} = \Delta E_{ij} = q_i \frac{|F(i,j)|^2}{\varepsilon_i - \varepsilon_i} \quad \text{.....1)}$$

For the calculation of the binding energy, ΔE, the sum of the total electronic energies of the two monomeric fragments $CH_3NH_3^+$ and PbI_3^- ($\sum_{Monomers} E_T(CH_3NH_3^+, PbI_3^-)$) was subtracted from the total electronic energy $E_T(CH_3NH_3^+ \bullet\bullet\bullet PbI_3^-)$ of a given $CH_3NH_3PbI_3$ conformer (Eqn. 2)); this is a standard procedure [36-38] that we have employed previously to calculate binding energy.[39]

For calculating the change in the Gibb's free energy ΔG^0, the sum of the total Gibb's free energies of the two monomers ($\sum_{Monomers} G(CH_3NH_3^+, PbI_3^-)$) was subtracted from the total Gibb's free energy $G_T(CH_3NH_3^+ \bullet\bullet\bullet PbI_3^-)$) of a given $CH_3NH_3PbI_3$ conformer (Eqn. 3)). Ref.[40] gives full detail of the enthalpic and entropic terms involved in the calculation of free energy *G*.

$$\Delta E = E_T(CH_3NH_3^+ \bullet\bullet\bullet PbI_3^-) - \sum_{Monomers} E_T(CH_3NH_3^+, PbI_3^-) \quad \text{.....2)}$$

$$\Delta G^0 = G_T(CH_3NH_3^+ \bullet\bullet\bullet PbI_3^-) - \sum_{Monomers} G(CH_3NH_3^+, PbI_3^-) \quad \text{.....3)}$$

No basis set superposition error is considered since the basis set used to study the $MAPbI_3$ conformers is of double-ζ valence quality, and the energy correction can be erroneous.[41]

4.3 Results and Discussion

4.3.1 What does the organic cation do in $CH_3NH_3PbI_3$?

An important consideration of this study is to provide a judgement on what causes octahedral tilting observed in the low-temperature orthorhombic geometry of $CH_3NH_3PbI_3$ in 3D (hereafter o-$MAPbI_3$) [18g,18f,42]? Answers to this question were provided by several authors in the past in studies that have involved bulk calculations and others.[42-46] However, to us, these are not sufficient to fully understand both static and dynamic natures of the coupling between the inorganic and organic frameworks in $CH_3NH_3PbI_3$.

According to Fang and Jena, [23a] the physical/chemical stability of $CH_3NH_3PbI_3$ stems from respective molecular motifs PbI_3^- and $CH_3NH_3^+$. Motta *et al.* have suggested that the role of the molecular cation is just only to dance.[47] Although this is against common chemical intuition, there are several reports suggesting that the organic cation does not do anything for the development of the electronic structure of the $CH_3NH_3PbI_3$ system. [22e,48-59] For instance, Whalley *et al* have asserted that "In the static picture (as in the case of an electronic band structure calculated for a single ionic snapshot), MA plays no direct role in optoelectronic properties of the material as the molecular electronic levels lie below that of the inorganic framework …".[49] In contrary, Wang *et al.* have observed that MA can serve as an additive in the solution of $CH_3NH_3PbI_3$, which plays a key role in the film-forming process.[51] Salado *et al.* have demonstrated that the organic cation part in the perovskite plays an important role in terms of crystal structure tuning from tetragonal to trigonal or pseudocubic or vice versa depending on the organic cations used, while it also

displays different microstructure.[52] In fact, there are versatile views that have been presented about the role of the organic cation. For instance, i) Mosconi *et al.* have shown that the organic cations play an important role in determining the structural, electronic, and optical properties of organometallic perovskites;[53-54] ii) Brivio *et al.* have proposed that due to the permanent electric dipole of MA, a photoferroic effect may be accessible, which could enhance carrier collection;[50] iii) Leguy *et al.* have shown that the charged nature of the organic molecules can also contribute to the superior solar conversion efficiency of lead halide perovskites; [55] iv) Berry *et al.* have urged that the nature and density of these bulk and surface defects, and the role of the organic cations, beyond insuring charge balance, are still mostly unknown; [56] v) Zheng *et al.* have argued that other than serving as a large B-site cation to maintain the BMX_3 perovskite structure, the role of the organic cations in defect tolerance is still mostly unknown;[57] vi) Berdiyorov *et al.* have concluded that despite recent extensive research, the role of organic cations in defining the excellent photovoltaic performance of these materials is not fully understood; [58] vii) Chen *et al* have provided a microscopic understanding of the structural energy landscape and have shown that the entropy contribution of the organic cation to the Gibbs free energy plays a crucial role in the selection of structure and stability of the hybrid organic-inorganic perovskite.[59] Clearly, from a variety of controversial discussions/suggestions presented by various authors, it is hard to judge what is then the role of the organic cation?

However, it should be kept in mind that either the PbI_3^- or the $CH_3NH_3^+$ isolated species that are participating attractively to form the $CH_3NH_3PbI_3$ system do not individually have any real physical existence during the absence of either of them. In this respect, the electronic structure and optical properties emanated of the $CH_3NH_3PbI_3$ perovskite system can be represented as collective. Otherwise, if these two isolated subunits could individually produce all sorts of functional optoelectronic properties, why then does one essentially invoke the organic part ($CH_3NH_3^+$) to push it to couple with the inorganic part (PbI_3^-) to demonstrate the chemical/physical stability of the entire $CH_3NH_3PbI_3$ bulk and its supramolecular framework? And, the opinion "the organic cation only dance"[47] has been provided because it is perhaps difficult to accurately probe the individual optoelectronic contribution of the organic and inorganic ions leading to the formation of the $CH_3NH_3PbI_3$ perovskite system. This view may be in line with a recent demonstration of Kieslich and Goodwin.[60]

Does the organic cation responsible for octahedral tilting in o-$MAPbI_3$? We address this problem in 4.3.8.

4.3.2 Conformations and analogies with the solid state analogues

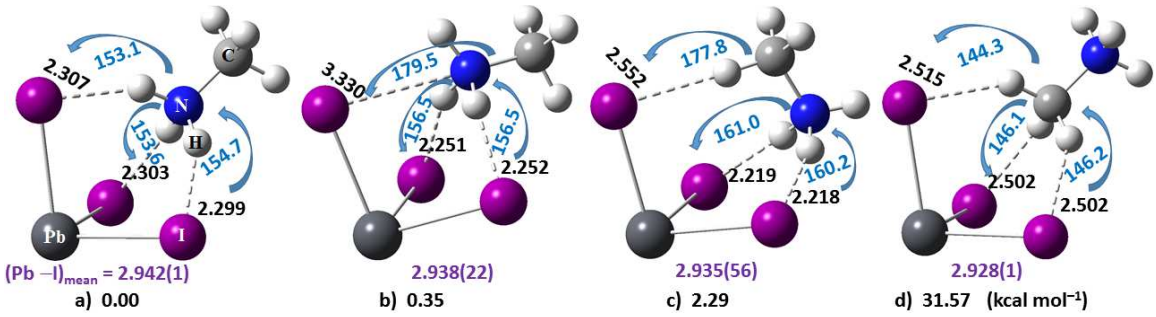

Fig. 1: a)–d) Minimum-energy conformations of $CH_3NH_3PbI_3$, identified with M06-2X/ADZP. Illustrated are the relative energies (from 0.00 to 31.57 kcal mol^{-1}), selected intermolecular bond distances (in Å) and bond angles (in °) respectively). The mean Pb–I bond distances (in Å) are also shown in each case (purple). The solid lines between atoms in a)–d) represent covalent/coordinate bonds, while the dashed lines represent tentative intermolecular interactions (see text for discussion).

Results of gas phase calculations are always fascinating since the chemical system under investigation is fully isolated and uninfluenced by the (external) surrounding agencies such as those arising from the crystal field, solvation and packing, among other

Table 1: Selected physical properties of $CH_3NH_3^+\bullet\bullet\bullet{}^-I_3Pb$, obtained with M06-2X/ADZP. [a]

Conformer	Rel. Stab.	ΔE	$\Delta E(zpe)$	ΔG^0	r(I•••H–N)	R(I•••H–C)	cis-∠(I-M-I)	∠(I…H-N)	∠(I…H-C)
Fig. 1a)	0.00	-125.11	-125.06	-114.24	2.303(4)	---	90.9(0)	153.8(8)	---
Fig. 1b)	0.35	-124.76	-124.52	-113.52	2.251(0)	3.330[b]	90.2(1)	156.5(0)	---
Fig. 1c)	2.29	-122.81	-122.21	-110.93	2.218(1)	2.552	92.3(9)	160.6(6)	177.8
Fig. 1d)	31.57	-93.53	-92.08	-81.64	---	2.506(7)	94.0(1)	---	145.5

[a] The properties include the relative stability (Rel. Stab. / kcal mol^{-1}), the binding energy (ΔE/ kcal mol^{-1}), the zero-point corrected binding energy (ΔE *(zpe)* / kcal mol^{-1}), the change in the Gibb's free energy (ΔG^0 / kcal mol^{-1}), the bond distances (r / Å) and selected bond angles (∠ / °).

things. For the present case, such calculations have enabled us to identify a few geometries for $CH_3NH_3PbI_3$. These are illustrated in Fig. 1, which can be regarded as four possible conformations. These are geometrically stable, and are obtained by optimizing several initial (trial) geometries of $CH_3NH_3PbI_3$ prepared manually by rotating $CH_3NH_3^+$ around the outer surface of the triangular I_3 face of the inorganic PbI_3^- core.

The real $CH_3NH_3PbI_3$ solar cell semiconductor (infinite crystal) would be different from the small cluster models presented in Fig. 1. However, calculations on these models do assist to grasp what happens in the solid state. Studies of Fang *et al.*, [23] and others,[22e, 62,63] are examples this kind.

Should these be treated as witness for the inappropriateness of the modelization? No, these should not be. It must be understood that an embedded cluster model mimics the real interaction between the fragments. Accordingly, the cluster models used in this study are adequate to some extent to capture the nature of the intermolecular interaction between the organic and inorganic fragments observed in the solid state.

This can be readily understood by comparing conformations of Fig. 1 and the local relaxed geometries of the $CH_3NH_3PbI_3$ bulks[61] illustrated in Figs. S1–S3. The comparison indicates that the modes of intermolecular interaction identified in the gas phase geometries are likely in the bulk and supercell geometries. Also, the gas phase results are in good agreement with Leguy *et al.*, [55] who have used quasielastic neutron scattering and molecular dynamics simulation data to show that the $CH_3NH_3^+$ dipolar ions reorientate between the faces, corners or edges of the pseudocubic lattice cages in the $CH_3NH_3PbI_3$ crystals with a room temperature residence time of ~14 ps, and where free rotation, π-flips and ionic diffusion are ruled out within a 1–200 ps time window. Similarly, Ren *et al.*,[42] based on their high temperature measurements, have showed that

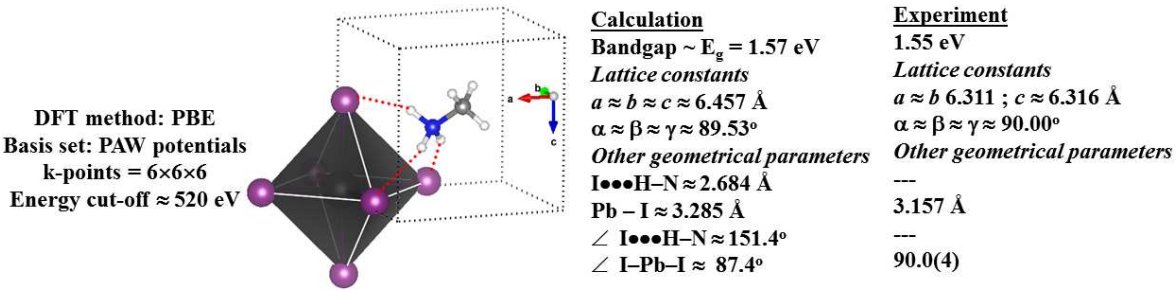

Fig. 2: The pseudocubic geometry of the $CH_3NH_3PbI_3$ bulk, obtained using spin-projected DFT-PBE calculation employing periodic boundary condition. It is analogous with the corresponding geometry discussed by Motta *et al.*,[22c] in which, the location of the $CH_3NH_3^+$ ion inside the cell with the CN bond aligned along the [111] direction. Available experimental properties[18e)] are listed for comparison.

for the pseudocubic structure the organic cation aligns along the [111] (diagonal), the [011] (edge), and the [100] (face) directions of the unit cell. Encouragingly, this result of Ren *et al.* is consistent with the orientations of MA found in the conformers a), b) and c) of $CH_3NH_3PbI_3$, respectively.

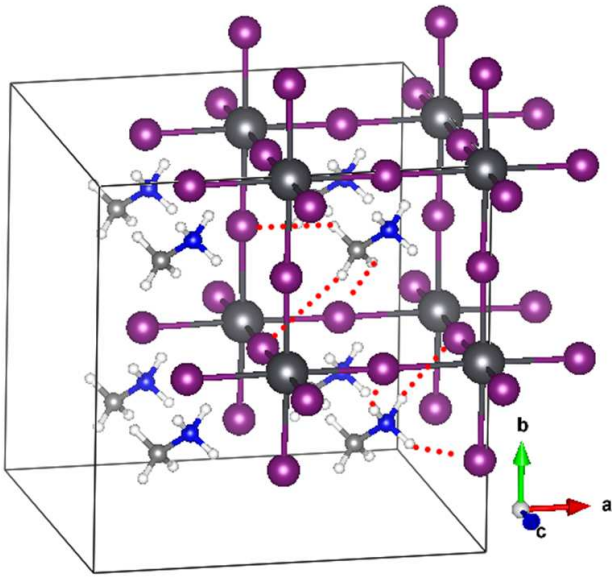

a)

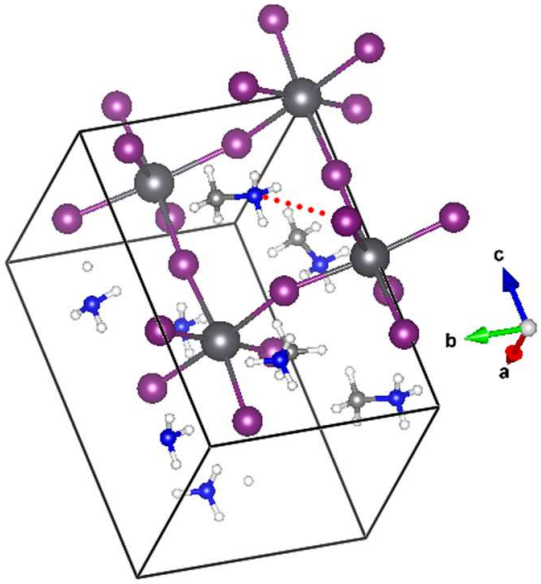

b)

Fig. S1: a) The 2×2×2 super cell of the $CH_3NH_3PbI_3$ perovskite system representing to the pseudo-cubic phase (space group *Pm3m*), showing the I•••H–N and I•••H–C intermolecular hydrogen bonding interactions found as in conformer a) & d) of Fig. 1, respectively (the bulk analogue is shown in Fig. 2). The monoclinic (space group *Cc*, Materials Project ref. ID: mp-995227) unit cell geometry of the $CH_3NH_3PbI_3$ system shown in b) illustrates the possibility of the I•••N(–C) noncovalent interaction found as in conformer b) of Fig. 1.

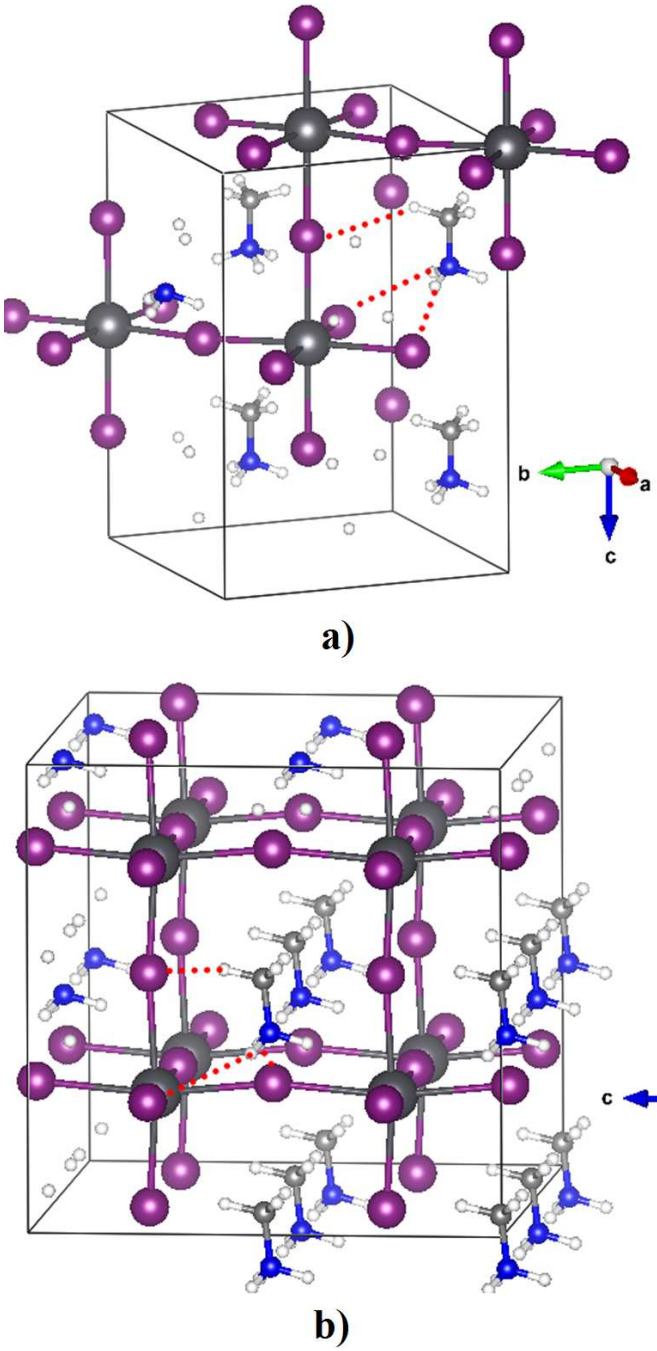

Fig. S2: a) The triclinic (space group *P1*, Materials Project ref. ID: mp-990432[1]) and b) the 2×2×2 monoclinic (space group *Pm*, Materials Project ref. ID: mp-977013) super cell of the $CH_3NH_3PbI_3$ perovskite system, showing the I•••H–N and I•••H–C intermolecular interactions found as in conformer c) of Fig. 1.

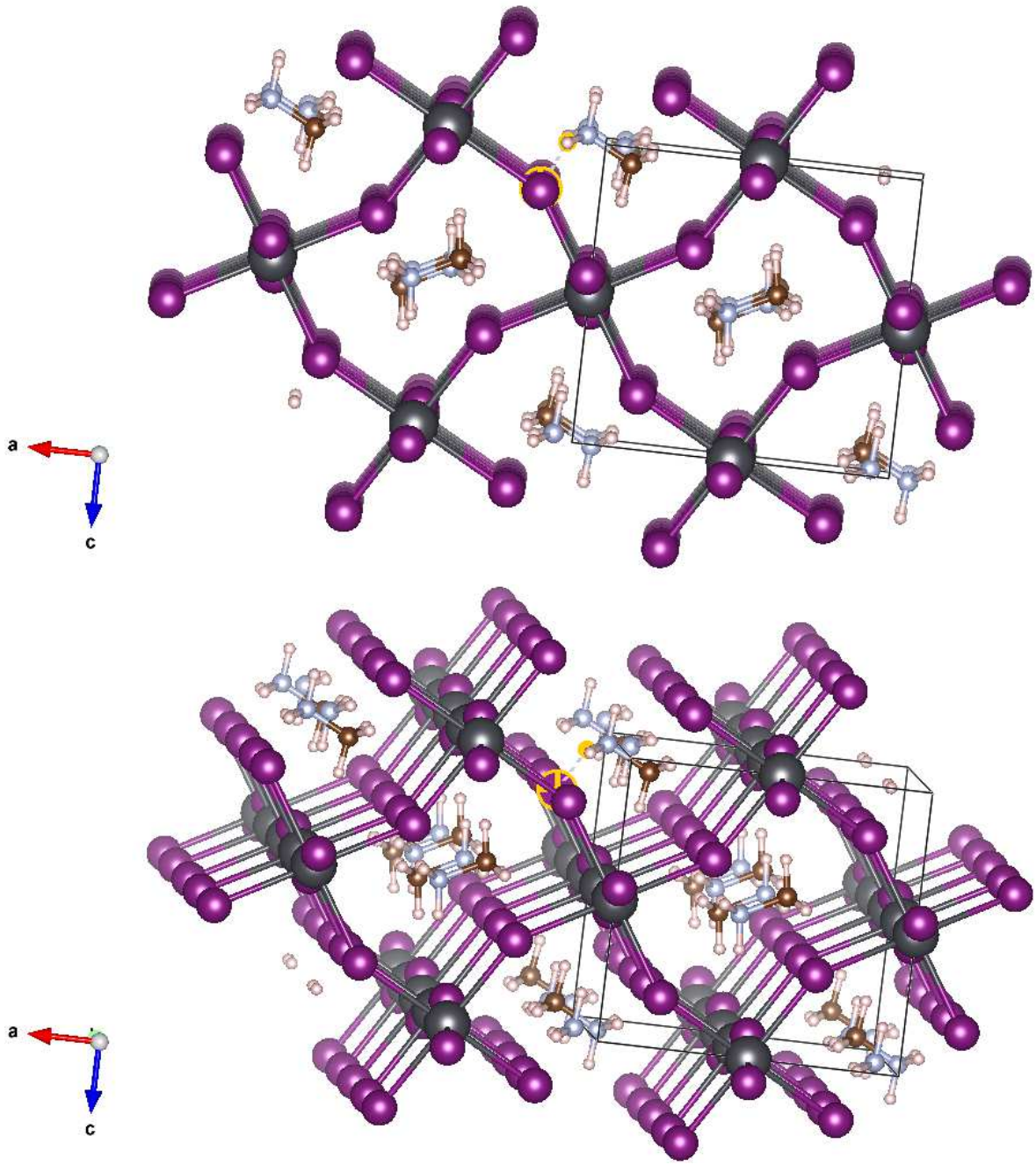

Fig. S3: Two views of the 2×2×2 low-temperature orthorhombic phase of the $CH_3NH_3PbI_3$ perovskite system (space group *Pnma*, Materials Project ref. ID: mp-995214[1]), showing an I•••H–N intermolecular interaction.

The relative energy difference between the most and least stable conformers of $CH_3NH_3PbI_3$ is approximately 31.57 kcal mol^{-1}, Table 1. The former is analogous with the pseudocubic geometry of the $CH_3NH_3PbI_3$ bulk stable at temperatures > 327 K, predicted using periodic DFT calculation, Fig. 2. A similar bulk configuration was reported in previous studies.[22e,47, 62-63]

4.3.3 Potential energy surface

Fig. 3 presents the relaxed potential energy surface (PES) of $CH_3NH_3^+ \bullet\bullet\bullet^- PbI_3$, obtained using five correlated levels of theory, B3LYP, CAM-B3LYP, X3LYP, PBEPBE, and MP2(fc), where fc represents the frozen-core treatment. A DZP basis set retrieved from the EMSL basis set library was used for this purpose.[31]

The minimum on the PES curve is appearing around the Pb•••N distance of 3.9 Å. The overall geometry of the system at this point is same as that of the most stable conformer illustrated in Fig. 1a.

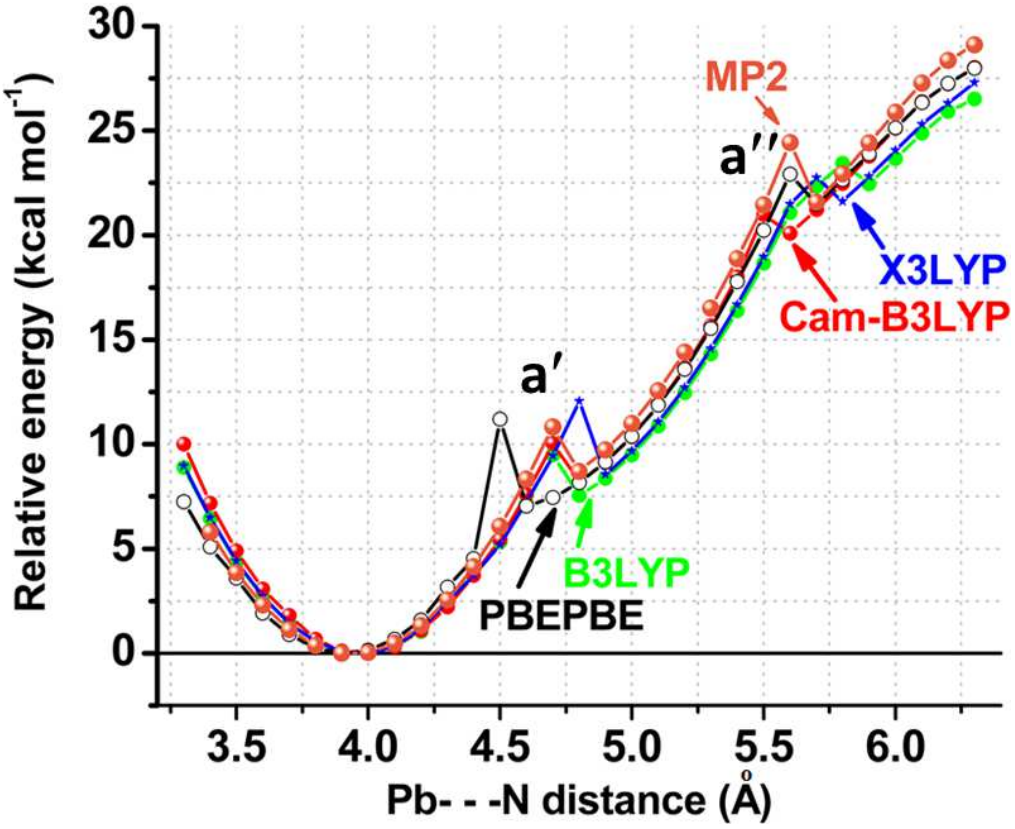

Fig. 3: Relaxed potential energy surface of the most stable $CH_3NH_3^+ \bullet\bullet\bullet^- PbI_3$. In this scan, the Pb•••N intermolecular distance was constrained with step size of 0.1 Å for about 35 steps keeping all the other geometrical degrees of freedom to vary.

The PES curve is nearly a single well and slightly asymmetric. There are two artifactual regions on the curve, marked by a′ and a″. One is appearing in the 4.5 – 4.8 Å region, and the other is in the 5.5 – 5.8 Å region. While these appear persistently regardless of the computational methods applied, these do not exemplify any real local minima. These represent abrupt changes in the potential energy curve caused by the movement of the CH_3NH_3+ species during the energy-minimization process.

Since the five different levels of theory give similar sort of information on the nature of the PES curve, this leads to a meaning that the stabilization energy associated with intermolecular interactions forming $CH_3NH_3^+$•••$^-PbI_3$ may be a little affected by the nature of the correlated functionals when examined with the same basis set. Whether or not this is the case is currently the subject of another benchmark study that includes several tens of correlated functionals and a few basis sets. [64]

4.3.4 Geometrical characterization of noncovalent interactions

Are the short I•••H intermolecular distances illustrated in Fig. 1 for $CH_3NH_3PbI_3$ reminiscent of hydrogen bonding,[65-66] or these should be recognized as halogen bonding interactions?[67] The I•••H motif is not a consequence of halogen bonding,[67-71] as the electrostatic surface of the Pb-bound iodine is entirely negative and it does not involve in bonding with any positive site on another halogen.

For characterizing whether the I•••H contact can be regarded as hydrogen bonding, we review the literature in a nut-shell by asking the question, what is a hydrogen bond? A hydrogen bond, historically represented by the motif A•••H–D, is simply an energy of attraction between a positively charged covalently bound hydrogen and an electron rich site (viz. a Lewis base). In A•••H–D, the H atom is shared between two electronegative species A and D (as in H_2O•••H–OH, for example), which are called as hydrogen bond acceptor and donor fragments, respectively. It may be stressed that there have been a number of definitions and characteristic features proposed for hydrogen bonding (more than 50[65]), starting from the first one probably provided by Huggins in 1922.[66,72] It was only in 2011 IUPAC has recommended a refined definition for it.[65] It is accompanied by a list of six criteria, E1–E6, five characteristics, C1–C5, and nine footnotes, F1–F9; each may be evoked as a *signature to identify the presence of hydrogen bonding interactions in molecules, in molecular clusters, and/or in solids*. According to the latest definition, [65] *a typical hydrogen bond may be depicted as D–H•••A–Z, where the three dots denote the bond, and D–H represents the hydrogen bond donor. The acceptor may be an atom or an anion A, or a fragment or a molecule A–Z, where A is bonded covalently to Z. In more specific cases, D and A can be the same with both D–H and A–H are the same as well leading to symmetric hydrogen bonds* (the acceptor as an electron-rich region such as, but not limited to, a lone pair in A or a π-bonded pair in A–Z).

Desiraju, on the other hand, has suggested that *to define a hydrogen bond one must have a minimum of four atoms, D, H, A and Z (or groups of atoms because a group of atoms can also constitute a valid acceptor fragment).*[73] *The entire motif D–H•••A–Z is properly considered as the hydrogen bond because each part (D–H, H•••A and A–Z) affects the other parts and is likewise affected by them. It is misleading to think that only the H•••A part constitutes the hydrogen bond.* To this end, let us consider the attractive interaction between X^- (X = I, Cl, Br) and H_2O. A question now arises: can we call the three dots in X^-•••H–O(H) a hydrogen bond? This question is immediate because the X^-•••H–O motif does not include a minimum of four atoms. And an answer is "yes", one can call this as a hydrogen bond based on the other characteristics of IUPAC. [65]

To our view, unless and otherwise the chemical environment is extremely complicated, one does not need a minimum of four atoms to define either a hydrogen bond or any other noncovalent interaction, or their directionalities. For the latter attribute, only three atoms are required, that is, three atoms are required to define the angle of approach of the electrophile. In the example given above, the three atoms X, H and O are more than sufficient to define both the X^-•••H–O hydrogen bond and its directionality. If one does not consider the directionality feature into account, then even three atoms are not needed to define a hydrogen bond. This is because a hydrogen bond is generally occurred between the nuclei of *two* atomic basins that are bonded with each other. This is perhaps the reason the geometric feature "less than the sum of the van der Waals radii of *two* atoms (but not three or more)" has been introduced for identifying noncovalent interactions in complex systems, [67] even though arguments opposite to this recommendation are not very rare in the literature.[33-34,66,68-71,74] The current state-of-the-art computational approaches such as molecular electrostatic surface potential (MESP),[68-69,75-79] QTAIM,[80-82,27a] RDG-NCI,[28] and density overlap region index (DORI),[84] and others, consider two atomic basins (or regions) to determine whether or not there is a noncovalent bonding interaction between them.

Considering the above discussions into account, it can be said that the suggestion of Desiraju might make some sense for systems that comprise both the fragments D–H and A–Y, but there are many occasions wherein the requirement Desiraju suggested for hydrogen bonding[73]cannot be fulfilled. The oversimplified yet standalone adoption of the textbook level definition provided at the beginning of this subsection is adequate to identify any moderate to strong hydrogen bonded interactions in chemical systems, no matter, whether the interaction involved is intermolecular or intramolecular. It should be kept in mind that the various definitions known to us today are nothing but man-made constructs based on some theoretical/experimental observations on some specific chemical systems. There is no guarantee that the definition/statement provided by a scientist can always be universal. It may work well on some systems, and may be a

failure on the other. Counterintuitive examples supporting our claim can be found elsewhere.[85-89]

Following the simplified definition provided at the beginning of this section, it seems to us that the $CH_3NH_3PbI_3$ conformer a) in Fig. 1 conceives three I•••H–N hydrogen bonding interactions, of b) two I•••H–N, of c) two I•••H–N and one I•••H–C, and of d) three I•••H–C hydrogen bonding interactions, respectively. The calculated mean I•••H(–C/N) distances are ca. 2.303, 2.251, 2.218, and 2.506 Å for the four conformers a), b), c), and d), respectively. Clearly, each of these is significantly smaller than the sum of the van der Waals radii, 3.24 Å, of the I and H atoms (2.04 and 1.20 Å,[90] respectively), satisfying a criterion of IUPAC.[67] The specific feature is not only evident of the intermolecular contacts identified for the four gas phase conformers, but also valid for that found for the geometry of the $CH_3NH_3PbI_3$ bulk illustrated in Fig. 2 (values 2.684 Å vs. 3.24 Å). The satisfaction of less than the sum of the van der Waals radii criterion signifies significant mutual penetration between the radii of the I and H atoms, promoting the formation of the I•••H hydrogen bonding interactions. This indicates possibility of marginal proton transfers from the $–NH_3$ group (or from the $–CH_3$ group) in $CH_3NH_3^+$ to the coordinated I atoms of the inorganic PbI_3^- core.

The marked difference between the I•••H distances of the gas and bulk geometries suggests that the intermolecular hydrogen bonding interactions in $CH_3NH_3PbI_3$ are probably stronger in the gas phase compared to those of the latter phase. However, no direct comparison can be made between the strengths of these interactions identified for the two phases since the binding energies for these in the latter phase are unavailable.

4.3.5 Are the hydrogen bonding interactions in $CH_3NH_3PbI_3$ directional?

Perhaps yes. The three atoms are generally used to define directionality in noncovalent interactions. As such, the A•••H–D motif is said to be directional when the angle formed by the three atoms A, H and D (∠A•••H–D) lies in the range 160–180°.[65-66,91] In addition, there are discussions in the literature suggesting that intermolecular interactions with the angle of approach in the 140–160° range can be regarded as the consequence of directional bonding.[91-95] For $CH_3NH_3PbI_3$, the ∠I•••H–N (or the ∠I•••H–C) formed by the three atoms I, H, and N (or I, H, and C) defines the directionality of hydrogen bonding. The mean values of ∠I•••H–N are 153.8 ± 0.8°, 156.5 ± 0.0° and 160.6 ± 0.6° for conformers a), b) and c), respectively, where ± refers to the standard deviations. Similarly, the mean values of the ∠I•••H–C are ca. 177.8 ± 0.0° and 145.5 ± 1.1° for conformers c) and d), respectively, Fig. 1 and Table 1.

As clarified in 4.3.12, as well as in Table S3 (NBO second-order perturbation analysis results), we have identified another intermolecular interaction between an iodine atom in PbI_3^- and the N atom of the $–NH_3$ group in $CH_3NH_3^+$ in conformer b). It concerns

the I•••N interaction. It is weak and directional. We have identified this based on the I•••N intermolecular distance of 3.330 Å, which is less than the sum of van der Waals radii of the I and N atoms, 3.54 Å. This interaction is directional, with ∠I•••N–C ≈ 179.5 ± 0.0°.

Lee *et al.* have argued that $MAPbI_3$ in its orthorhombic phase shows an identical tilt pattern to many inorganic oxide perovskites, being driven instead by a particular pattern of highly directional hydrogen bonds.[32c] Our analysis of the geometry in Scheme 2 gave the ∠I•••H–C angle lying between 138 and 147.8º, whereas the ∠I•••H–N angle lying between 123.3 and 153.3º. There is another orthorhombic geometry catalogued in the Materials Project database (ref. code: mp-995214 (*Pnma*)), in which case, the former angle varies between 152.8 and 165º, whereas the latter angle varies between 160.5 and 179.6º.

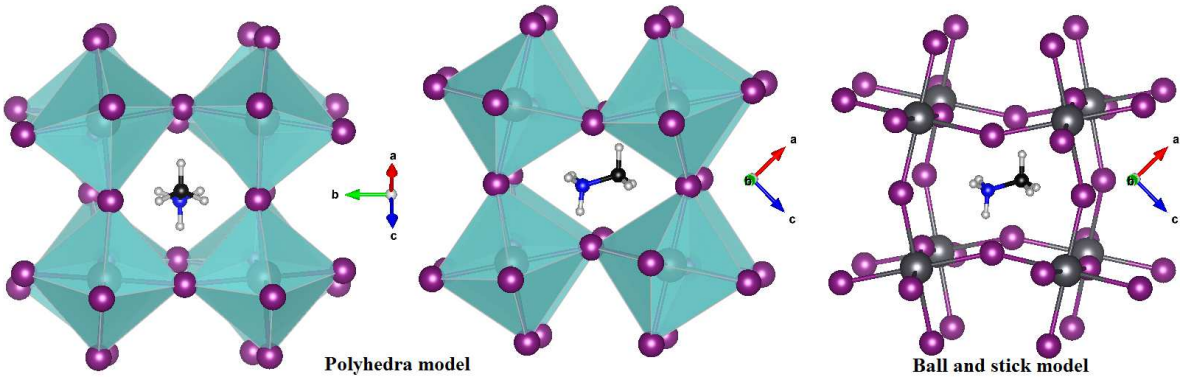

Scheme 2: Polyhedral and ball-and-stick model views of the DFT relaxed *Pnma* geometry of o-$CH_3NH_3PbI_3$ (Materials Project[61] ref. code: mp-995203).

The directional nature of the intermolecular interactions in $CH_3NH_3PbI_3$ indicates that it is probably an important characteristic for designing functional materials.

4.3.6 Energetic landscape and stability

The four conformers of the $CH_3NH_3PbI_3$ block illustrated in Fig. 1 are not only stable in the gas phase at 0 K, but also thermodynamically stable at 298.15 K. The former feature is evident of the binding energies ΔE that are predicted to be negative for all the conformers, while the latter is reminiscent of the changes in the free energies ΔG^0 that are negative, Table 1.

The magnitudes of the ΔE are unusually large. For instance, the ΔE are ca. –125.11, –124.76, –122.81, and –93.53 for conformers a), b), c) and d), respectively. Similarly, the

ΔG^0 are also large. These are ca. –114.24, –113.52, –110.93, and –81.64 kcal mol^{-1} for the corresponding conformers, respectively. The zero-point vibration has a very small effect on the magnitude of ΔE for the most stable conformer, although it is not so for the other three (see ΔE *(zpe)* values in Table 1).

For comparison, we cite *Lee et al.* who have shown that the distinct strengths of the intermolecular hydrogen bonding interaction between the metal-organic (host) framework and the organic cation (guest) in certain host-guest perovskite architectures can assist in tuning the Young's moduli and hardness. [96] Specifically, it was shown that the guanidinium and formamidinium organic cations bind to the metal organic frameworks such that the ΔE varies between –69.41 and –106.77 kcal mol^{-1} for $[(NH_3)_3)][Mn(HCOO)_3]$ and $[(CH_3)_2NH_2)][Mn(HCOO)_3]$, respectively. An editorial of the *J. Am. Chem. Soc.* has spotlighted this remarkable finding as "Small Bonds a Big Deal in Perovskite Cells". [97] From all these discussions, it is obvious that the intermolecular hydrogen bonding interactions observed for the triiodide perovskite blocks are certainly specific and distinguished, which are a kind of glue-like sticky adhesives that are essentially required for the rational design of novel soft nanomaterials. Ostensibly, it might now be understood that these *ultra-strong* interactions in $CH_3NH_3PbI_3$, as well as those in analogous derivatives falling into the same category, deserve extensive theoretical exploration for the fundamental understanding of the underlying physical chemistry involved.

The massively large ΔE obtained for the four $CH_3NH_3PbI_3$ conformers (Table 1) are not comparable with the corresponding ones reported for very strong, strong-, moderate- and weak-strength interactions, Tables 2 and S1. From the various classification schemes already documented on hydrogen bonding, [25, 98-108] it could be understood that very strong interactions comprise increasingly more covalent component than being electrostatic, with $-15 < \Delta E \leq -40$ kcal mol^{-1} (covalent limit, –40 kcal mol^{-1}), whereas strong interactions comprise large electrostatic component with appreciable covalency, with $-4 < \Delta E < -15$ kcal mol^{-1} (electrostatic limit, –15 kcal mol^{-1}). However, very weak interactions are seemingly not just dispersive but include some electrostatic components with $-4 < \Delta E \leq -0.25$ kcal mol^{-1} (van der Waals limit, –0.25 kcal mol^{-1}) and the interactions that are having bond energies around (or below) –0.25 kcal mol^{-1} can probably be recognized as predominantly dispersive with marginal contribution from electrostatics (what are generally called as van der Waals). While Desiraju has divided the intermolecular interactions into four categories (very strong, strong, very weak and van der Waals), there is no compact list of characteristic properties viable in literature that can isolate the latter two. One might therefore visualize the latter two interaction types to have somehow similar characteristic properties, even though they are separated by an energy boundary existing at –0.25 kcal mol^{-1}.

Table 2: Comparison of the characteristic properties of the *ultra-strong* hydrogen bonding interactions emanated of this work with those already recommended for the strong, moderate and weak hydrogen bonding interactions (Steiner, [102] and Jeffery[100-101]).

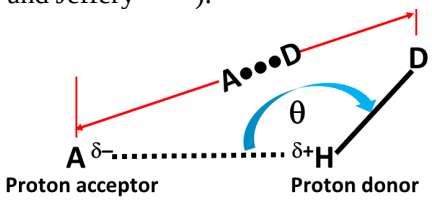

Property	Ultra-strong	Strong [a-c]	Moderate [a-c]	Weak [a-c]	van der Waals [d]
	Pronouncedly Covalent and Electrostatic	Strongly Covalent	Mostly Electrostatic	Electrostatic/ dispersion	Dispersion dominant
A•••H(Å)	2.0 – 2.7	1.2 – 1.5	1.5 – 2.2	> 2.2	> 2.2
Lengthening of (H–D) (Å)	0.01 – 0.02	0.08 – 0.025	0.02 – 0.08	< 0.02	<< 0.02
H–D *vs.* A•••H	H–D << A•••H	H–D ≈ A•••H	H–D < A•••H	H–D << A•••H	H–D << A•••H
A•••D length range (Å)	3.0 – 3.7	2.2 – 2.5	2.5 – 3.2	> 3.2	> 3.2
Directionality	Moderate-to-strong	Strong	Moderate	Weak	---
Bond angles (°)	> 130	170 – 180	> 130	> 90	90 – 180[e,f]
Bond energy (–kJ mol^{-1})	>>> 167	63 – 167	17 – 63	4 – 17	≤ 4
(–kcal mol^{-1})	>>> 40	15 – 40	4 – 15	0.25 – 4.0	≤ 0.25
IR shift (cm^{-1})	---	25%	10 – 25%	< 10%	
^{1}H shift (ppm)	---	14 – 22	< 14	- - -	
		QTAIM Characteristics			
Charge density (ρ_b)	$\rho_b > 0$	$\rho_b > 0$	$\rho_b > 0$	$\rho_b > 0$	$\rho_b > 0$
Sign of the Laplacian of the charge density ($\nabla^2\rho_b$)	$\nabla^2\rho_b > 0$	$\nabla^2\rho_b > 0$	$\nabla^2\rho_b > 0$	$\nabla^2\rho_b > 0$	$\nabla^2\rho_b > 0$
Sign of total energy density (H_b)	$H_b < 0$	$H_b < 0$	$H_b < 0/H_b > 0$	$H_b > 0$	$H_b > 0$

[a] Desiraju has classified the last four interaction types as very strong, strong, very weak and van der Waals. In this scheme, the very weak interactions were separated from van der Waals by an energy barrier at ≈ –0.25 kcal mol^{-1} (see Fig. S4 and Table S1). [98-99]

[b] See the recent paper of Hunt *et al.* for more discussion about classification of intermolecular interactions.[25a]

[c] Szatyłowicz has divided these latter four interactions as very strong, strong, moderate and weak (see text for discussion).[106]

[d] As indicated in the text, there are no such well-defined characteristic properties reported for van der Waals. These, in many occasions, would display characteristics that can be reminiscent of weak interactions.

[e] There is no specific directional preference for van der Waals, since the angle of interaction can vary between 90 and 180°.

[f] Ref. 25b. Ref. 113.

The classification scheme provided by Desiraju[98-99] is not same as those have been individually provided by Jeffery et al.,[100-101] Steiner,[102] and others,[103-108] Tables 2

and S1.

Szatyłowicz has classified hydrogen bonding interactions as very strong, strong, moderate and weak, with (negative) stabilization energies of 30–40, 15–30, 4–15 and 0.25–4 kcal mol^{-1}, respectively.[106] The very strong interactions were proposed to have either low-barrier, or single-well characteristics. This may be consistent with the characteristic revealed for $CH_3NH_3PbI_3$, Fig. 3.

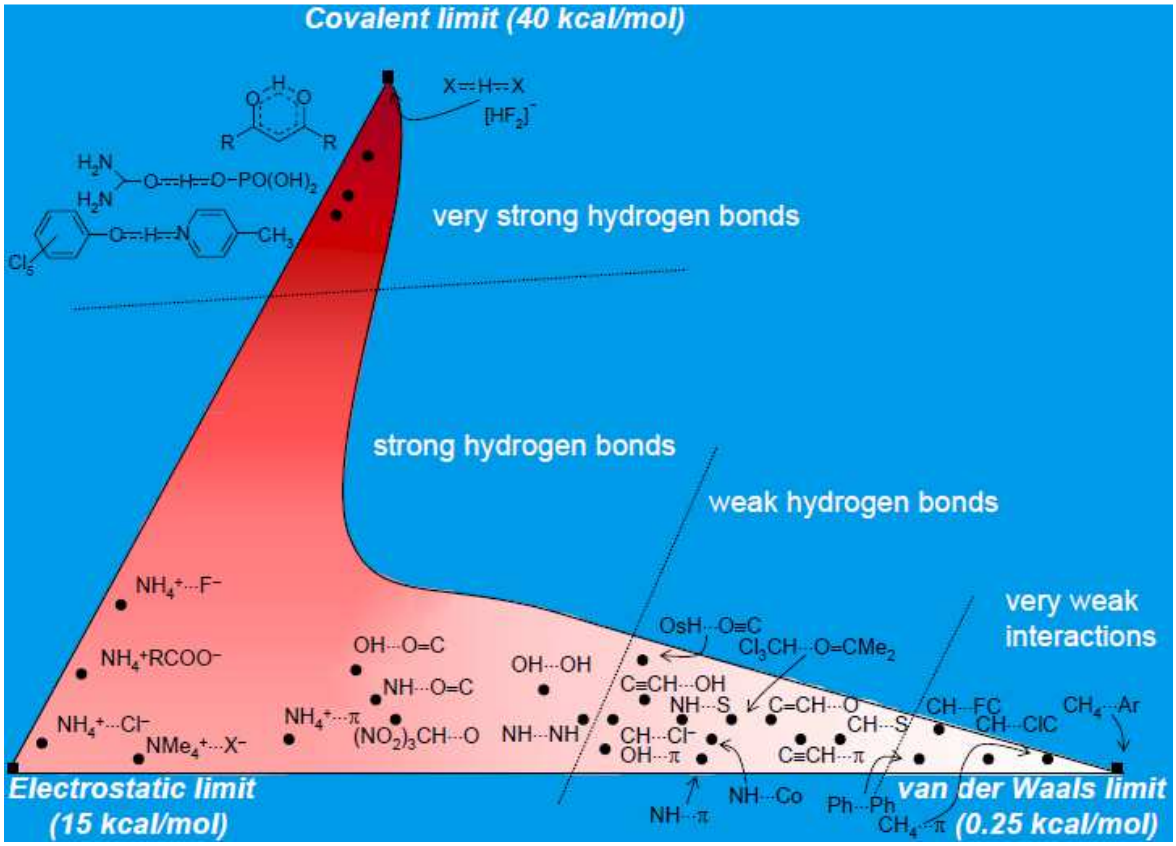

Fig. S4: A tentative classification of hydrogen bonding interaction proposed by Desiraju. [2] The composite nature (electrostatic, dispersive and covalent character, etc.) of the interaction is highlighted by the three extreme situations of widely differing energies. The sketch is not strictly quantitative but the coloring attempts to provide a visual scale of energies. The figure serves as a rough guide to the balance of electrostatics, van der Waals nature, and covalency in any A•••H–D interaction. For the weak interactions, the covalent character is very small and may be interpreted as charge transfer. A van der Waals interaction is considered to have dispersive and repulsive components. [3]

The traditional classification of noncovalent interactions into three major groups (strong, moderate and weak) was possible based on the availability of various experimental and theoretical data on gas and solid state systems. The [F•••H–F]$^-$

classical system is the one among a few strongly bound systems that has been invoked numerously to represent a strongly bound interaction, with $\Delta E \approx -40$ kcal mol^{-1}, Fig. S4.[98-108] Similarly, van der Waals are dispersion driven since these can be readily understood as having stabilization energies ≈ -0.25 kcal mol^{-1}.[98-99,108] An anonymous reviewer has just recently argued that one would suspect whether a weak intermolecular attraction with this magnitude that merely arises from a universal intermolecular dispersion, as would hold together any pair of molecules, with or without noncovalent bonding, which would be either reinforced or opposed by a Coulombic force that is too weak to fully oppose the latter attraction.

Now the question arises: how to recognize noncovalent interactions that are beyond the covalent limit, –40 kcal mol^{-1}? Should these be called as purely covalent (or pronouncedly covalent), analogously as how binary complexes with bond energy $\Delta E \approx -0.25$ kcal mol^{-1} have been regarded as van der Waals[98-99,108]? Should not it be sagacious to put the high-strength interactions found for the perovskite systems into another class?

Apparently yes, these should be separated into another class, analogously as the interaction in the $[F\bullet\bullet\bullet HF]^-$ ionic system has been identified as "very strong", whereas those in the $NH_4^+\bullet\bullet\bullet^-X$ (X = F, Cl) ion-pairs as "strong". We suggest this because $CH_3NH_3PbI_3$ is accompanied with a set of distinct characteristic properties that are not comparable with any set of properties prescribed for either of the four major types of intermolecular hydrogen bonding interactions summarized in Table 2?

The properties of hydrogen bonding emanated for BMY_3 do not appropriately match with those proposed by Desiraju and coworkers,[98-99] as well as by others. [100-108] Table 2 summarizes the difference, and S1 clarifies it in detail. These properties for BMY_3 are obtained both with RCCSD/cc-pVTZ and PBEPBE/aug-cc-PVTZ (pseudo potentials used for Pb and I), in addition to M06-2X/ADZP. These characteristic properties in Table 2 are applicable not only to the conformers of $CH_3NH_3PbI_3$, but also to another twenty-nine BMY_3 perovskite blocks. The metal ions included in the analysis were mainly of Pb, Sn and Ge; the Y-site anions were of the latter three halogen derivatives Y (Y = Cl, Br and I); and the B-site cation was $CH_3NH_3^+$ and so on.

The following six points clarify the reason for which one might wish to put the presently observed intermolecular hydrogen bonding interactions into a separate category.

1- The A•••H intermolecular bond distances for strong, moderate and weak interactions have been proposed to be 1.2–1.5, 1.5–2.2 and > 2.2 Å, respectively. For the BMY_3 systems, the corresponding distance (Y(Y=Cl, Br, I)•••H) lies between 2.0 and 2.7 Å. Clearly, this range is not comparable with those recommended for either the moderate/strong strength interactions or the van der Waals (Tables 2 and S1).

2- Desiraju and Steiner have proposed the lengthening of the H–D bond to be such that it would be in the 0.05 – 0.2 Å range for very strong interactions, 0.01 – 0.02 Å for strong interactions, and < 0.01 Å for weak interactions (Table S1).[4] The former range is fully inconsistent with the range observed with the lengthening of the N–H bonds for the BMY_3 systems, which lies between 0.01 and 0.02 Å (Table 2).

3- The A•••D separation distances (i.e., the Y•••N separation distances) between the electronegative atoms sharing the hydrogens in the BMY_3 perovskites are found to lie between 3.0 and 3.7 Å. These values signify that the strengths of the intermolecular interactions in the BMY_3 systems may not be comparable with those recommended for the moderate and weakly bound interactions (2.5–3.2 and 3.2 Å, respectively).

4- The A•••H intermolecular bond distance and the H–D proton donor bond distance are recommended to be such that H–D ≈ A•••H for strong interactions, H–D < A•••H for moderate interactions, and H–D << A•••H for weak interactions. However, for BMY_3, the H–D bond distance is found to be too small compared to the A•••H intermolecular bond distance (i.e., H–N << Y•••H). While this latter feature matches with the corresponding characteristic of the weakly bound interaction, one cannot call the BMY_3 as weakly bound.

5- Strong and very strong hydrogen bonding interactions are generally highly directional, with the angle of approach θ close to 180^o (see Table 2). For moderate interactions, this angle is comparatively smaller, with θ > 130^o. However, for the BMY_3 systems, a majority of this angle (θ = ∠Y•••H–N) were calculated to be in the 140 and 155^o range, showing that the Y•••H hydrogen bonding interactions are not strongly directional. The above comparison signifies that the A•••H interactions in BMY_3 systems are of moderate strength.

6- The bond energies between the A and H-sites in BMY_3 are calculated to vary between –70 and –140 kcal mol^{-1}. These are substantially larger than the energy range already proposed for very strong and strong hydrogen bonds, with the $-\Delta E$ values lying between 15–40 and 4–15 kcal mol^{-1}, respectively (covalent limit, –40 kcal mol^{-1}). Evidently, this comparison suggests that the A•••H hydrogen bonding interactions in the BMY_3 building blocks cannot be regarded as either weak, or moderate, or even strong/very strong, thereby they should be grouped into another class. We therefore propose to call them as *ultra-strong*.

Table S1: Some characteristic properties of very strong, strong, and weak hydrogen bonds proposed by Desiraju and Steiner.[a,b]

Property	Very strong	Strong	Weak
Bond energy (-kcal mol^{-1})	15 – 40	4 – 15	< 4
Examples	[F•••H•••F]$^-$ [N•••H.•••N]$^+$ P–OH•••O=P	O–H•••O=C N–H•••=C O–H•••O– H	C–H..O O–H.•••π Os–H•••O
IR Vs relative shift	25%	5 – 25%	< 5%
Bond lengths	H–A ≈ D–H	H•••A > D–H	H•••A >> D–H
Lengthening of D–H (Å)	0.05 – 0.02	0.01 – 0.05	< 0.01
***r*(D•••A) range (Å)**	2.2 – 2.5	2.5 – 2.2	2.0 – 3.0
d(A•••H) range (Å)	1.2 – 1.5	1.5 – 2.2	2.0 – 3.0
Bonds shorter than vdW	100%	Almost 100%	30 – 80%
θ(A•••H–X) range (º)	175 – 180	130 – 180	90 – 180
***k*T (at room temperature)**	> 25	> 7 – 25	> 7
Effect of crystal packing	Strong	Distinctive	Variable
Utility of crystal engineering	Unknown	Useful	Partly useful
Covalency	Pronounced	Weak	Vanishing
Electrostatics	Significant	Dominant	Moderate

[a] Ref. 98-99.

[b] According to Desiraju and Steiner, different terminologies have been employed by them to classify hydrogen bonds. Jeffrey and Saenger (1991) have classified hydrogen bonds as 'strong' and 'weak' while Jeffrey (1997) has elaborated this further to 'strong', 'moderate' and 'weak'. The reader will note that there is a near correspondence between the category we term 'strong' and Jeffrey calls 'moderate'. Jeffrey's terminology is in keeping with the biological literature where bonds such as O–H•••O–H, and especially O_w–H•••O_w–H, are not taken to be particularly 'strong', and N–H•••O definitely veers towards what is understood as 'weak'. The reason Desiraju and Steiner refer to the middle category as 'strong' originates from supramolecular considerations. By 'strong' they mean hydrogen bonds that are able to control crystal and supramolecular structure effectively. This certainly includes O–H•••O=C, N–H•••O=C and O–H•••O–H. By weak' we mean hydrogen bonds whose influence on crystal structure and packing is variable. In this sense, a strong hydrogen bond is one which is much stronger than a van der Waals interaction while a weak hydrogen bond is one which is not. In the end though, these discussions are semantic in nature. Still, terminologies are necessary even if they are subjective and it is necessary for the reader to know at an early stage what they mean by the terms strong and weak.

4.3.7 Approximate origin of large binding energy

The unusually large *ΔE* can be thought to arise largely from charge–charge Coulombic attraction because the two ions PbI_3^- and $CH_3NH_3^+$ interacting with each other have opposite charge polarities. In addition to this, charge–dipole and dipole–dipole electrostatic interactions are also expected to contribute prominently to the *ΔE* because both PbI_3^- and $CH_3NH_3^+$ possess dipole moments μ of 2.89 and 2.29 Debye, respectively; the latter properties were calculated by considering the origin at the center of the mass.

In addition to the electrostatic contribution, induction (polarization) and dispersion are expected to contribute to the *ΔE*, arising from various higher order effects. To provide evidence in support of this argument, we cite a recent study of one of us (PRV), who, has carried out an energy decomposition analysis for an analogous Sn-based perovskite system, $CH_3NH_3SnI_3$. With the SAPT2+3/TZP level of truncation, where SAPT represents the symmetry adapted perturbation theory, [109,110] it was found that the electrostatic, polarization and dispersion energy component contributions to the net interaction energy of the system can be as large as –99.38, –26.61 and –11.95 kcal mol^{-1}, respectively. The very large polarization (and dispersion) contributions may demand that the I•••H–N (and I•••H–C) intermolecular hydrogen bonding interactions in $CH_3NH_3SnI_3$ are considerably covalent with predominant contribution from electrostatic.

This view may be line with the recommended IUPAC criterion E1, "*For a hydrogen bond A–H•••D–Z, the forces involved in the formation of a hydrogen bond include those of an electrostatic origin, those arising from charge transfer between the donor and acceptor leading to partial covalent bond formation between H and D, and those originating from dispersion*."[65] Refs[111-112] provide additional insight into covalency in hydrogen bonding.

4.3.8 Octahedral tilting

The geometry of o-$CH_3NH_3PbI_3$ corresponding to the *Pnma* space group accompanies a particular pattern of rotations of the PbI_6^{4-} octahedra. It involves either in-phase or out-of-phase rotations around the three I–Pb–I axes.[18e,18g,42] The tilting pattern in Glazer notation[83a] can be described by $a^-b^+a^-$, and is not indifferent from what can be expected for the corresponding system with (*Pm3m*) cubic symmetry ($a^0b^0c^0$).

Lee *et al.* have recently reported a first-principles study that has used hydrogen bonding to rationalize octahedral tilting in $CH_3NH_3PbI_3$.[32a] The same authors and additional coworkers in another study have attempted to resolve the physical origin of octahedral tilting in halide perovskites in general.[32c] According to them, relatively little progress has been made in the understanding of the role played by the intermolecular

hydrogen bonding interaction in the structural evolution of trihalide perovskites. So, they have suggested that their calculations have revealed the presence of I•••H–N and I•••H–C hydrogen bonding interactions in $CH_3NH_3PbI_3$. The strength of these interactions was inferred based on the magnitude of the intermolecular distances, as well as that with hydrogen bond index introduced sometime ago by Li *et al.*.[83b]

According to Lee *et al.*,[32a] "*The N•••I distances are much shorter than those of I•••C and also the angle of* I•••H–C *is smaller than that of* I•••H–N. *Accordingly, the hydrogen-bond interactions mainly originate from H atoms on nitrogen.*" Based on this criterion (ie., I•••H < 3 Å), and assuming that the I•••H–C interactions are too weak, and are unimportant, the authors were able to recognize only three I•••H–N hydrogen bonding interactions between the protons of the $–NH_3$ fragment in MA and the iodine atoms of the Pb–I cage interior. They then have interpreted that these are the only interactions that can account for the pronounced octahedral tilting observed in the o-$CH_3NH_3PbI_3$ geometry since the I•••H–N hydrogen bonds in the perovskite cage are controlled by both the particular inorganic $a^-b^+a^-$ tilt pattern and the organic MA conformation.

In fact, it is not very surprising that the N•••I distances will not be shorter than those of I•••C given there is a clear difference between the van der Waals radii of the C and N atoms (1.77 vs. 1.66 Å[90]). Also, the assumption that "weak interactions do not contribute" do not match with numerous other observations for non-perovskite systems that demonstrate weak interactions > 3 Å can be powerful in the design of ordered supramolecular materials.[87,113-115] In some of these latter studies the sum of the van der Waals radii of interacting atoms was either close to, or larger than, the intermolecular distance between the bonded atomic basins.

Our study indicates that the above assumption “the weak interactions are not responsible for the octahedral tilting of o-$MAPbI_3$” is incorrect, and the view provided is incomplete. In fact, the I•••H–N contacts are indeed stronger than the I•••H–C contacts if judged based on the I•••H intermolecular distances. However, from the charge density analysis, we found that the protons of both the ammonium and methyl groups of MA generate almost an identical number of I•••H contacts. For instance, in the geometry shown in Scheme 2, there are nine I•••H–N and nine I•••H–C contacts (not shown). This provides us with an understanding that there is a strong competition between the protons of these two groups of MA aggrandizing the formation of both I•••H–N and I•••H–C hydrogen bonds. This is perhaps one of the reasons for which coordinated iodine atoms could have enforced to be pulled toward the interior of the perovskite cage in the orthorhombic phase, causing significant Pb–I–Pb tilting of the corner sharing PbI_6^{4-} octahedra. This explains why the geometry of the o-$CH_3NH_3PbI_3$ system is

significantly distorted from the cubic symmetry.[18e,42] It also explains the reason for which the centroid of the MA lies near the center of the perovskite cage in the orthorhombic geometry, [18g] whereas it is off-center in the high-temperature tetragonal and pseudocubic geometries. For instance, Ren *et al.*[42] have asserted that *for both the tetragonal and cubic geometries measured at 295 and 350 K, respectively, the middle point of the C−N bond being located slightly off the body-center position from the high symmetry sites in the crystal structure, induced by the formation of hydrogen bond-like interactions between the $-NH_3^+$ substituent of the organic cation and the iodine atoms of [PbI_6] octahedra*.

From the discussions given above, it is apparent that the prominent octahedral tilting in o-$CH_3NH_3PbI_3$ is caused by the organic cation, which plays a major role in determining the low-bandgap for the material.

4.3.9 QTAIM topology of chemical bonding

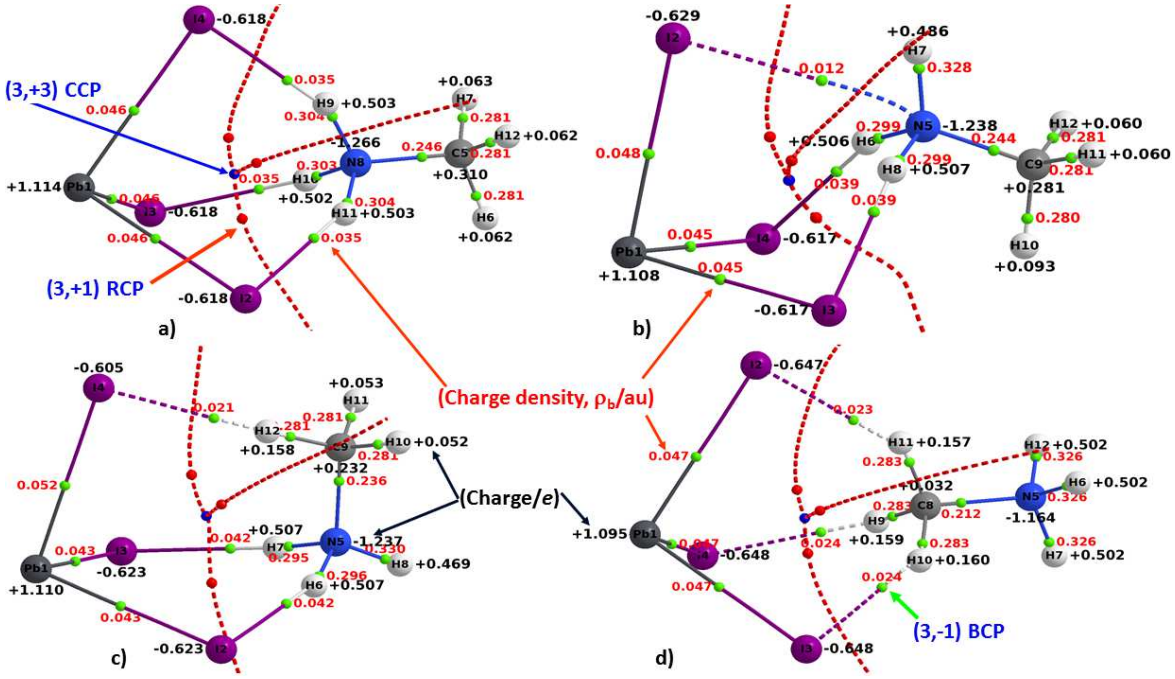

Fig. 4: M06-2X/ADZP level QTAIM molecular graphs for $CH_3NH_3^+$•••$^-PbI_3$. In a)–d), the iodine and lead atoms are displayed as large spheres in purple and dark gray, respectively, while the nitrogen and carbon atoms as medium spheres in blue and light gray, respectively, and the hydrogen atoms as tiny spheres in white-gray. The solid and dashed lines between atomic basins in atom color represent the bond paths, which each is a line of maximum charge density in accord with the connotation of Bader. [118,119] The RCP attractor paths are illustrated by dashed lines in red. Tiny spheres in green, red, and blue represent the (3,–1) bond critical points (BCPs), (3,+1) ring critical points (RCPs), and (3,+3) cage critical points (CCPs), respectively. The charge density (ρ_b/au) at each bond critical point is shown in red, while the charges (in *e*) conferred on atoms are shown in black. Each molecular graph associates one CCP, three RCPs, and thirteen BCPs such that they all together satisfy the *Poincaré–Hopf* relationship, n + b + r + c = 1, where n, b, r, and c are the numbers of NACPs (number of nuclear attractor critical points), BCPs, RCPs, and CCPs, respectively.

The theoretical details of QTAIM have numerously been discussed. [27a,116] Its application to the $CH_3NH_3PbI_3$ molecular blocks have resulted in molecular graphs that are illustrated in Fig. 4. These graphs are approximate chemical representations of detailed bonding interactions, giving rise to molecular structures that might be gleaned from chemical intuitions.

Table S2: Topological charge density properties of the $CH_3NH_3PbI_3$ nanoclusters, obtained with M06-2X/ADZP.[a, b]

	Bond Type	ρ_b	λ_1	λ_2	λ_3	$\nabla^2\rho$	ε_b	V_b	G_b	H_b
a)	Pb1—I2	0.0460	-0.0330	-0.0329	0.1423	0.0764	0.01	-0.0381	0.0286	-0.0095
	Pb1—I3	0.0459	-0.0329	-0.0327	0.1419	0.0763	0.01	-0.0379	0.0285	-0.0094
	Pb1—I4	0.0460	-0.0330	-0.0328	0.1422	0.0764	0.01	-0.0380	0.0286	-0.0095
	I2•••H11	0.0349	-0.0382	-0.0382	0.1351	0.0588	0.00	-0.0234	0.0191	-0.0044
	I3•••H10	0.0354	-0.0390	-0.0389	0.1366	0.0587	0.00	-0.0238	0.0193	-0.0046
	I4•••H9	0.0352	-0.0386	-0.0386	0.1360	0.0588	0.00	-0.0237	0.0192	-0.0045
b)	Pb1—I2	0.0484	-0.0349	-0.0347	0.1461	0.0764	0.01	-0.0408	0.0299	-0.0108
	Pb1—I3	0.0451	-0.0324	-0.0322	0.1410	0.0764	0.01	-0.0372	0.0281	-0.0091
	Pb1—I4	0.0451	-0.0324	-0.0322	0.1410	0.0764	0.01	-0.0372	0.0281	-0.0091
	I2•••N5	0.0124	-0.0074	-0.0031	0.0589	0.0484	1.39	-0.0078	0.0100	0.0021
	I3•••H8	0.0392	-0.0448	-0.0441	0.1478	0.0588	0.02	-0.0272	0.0210	-0.0062
	I4•••H6	0.0392	-0.0449	-0.0442	0.1479	0.0588	0.02	-0.0272	0.0210	-0.0063
c)	Pb1—I2	0.0435	-0.0311	-0.0308	0.1383	0.0764	0.01	-0.0355	0.0273	-0.0082
	Pb1—I3	0.0434	-0.0311	-0.0307	0.1381	0.0763	0.01	-0.0354	0.0272	-0.0082
	Pb1—I4	0.0522	-0.0379	-0.0375	0.1544	0.0790	0.01	-0.0455	0.0327	-0.0129
	I2•••H6	0.0417	-0.0487	-0.0482	0.1548	0.0579	0.01	-0.0293	0.0219	-0.0074
	I3•••H7	0.0418	-0.0488	-0.0483	0.1549	0.0578	0.01	-0.0293	0.0219	-0.0074
	I4•••H12	0.0209	-0.0200	-0.0198	0.0898	0.0500	0.01	-0.0129	0.0127	-0.0002
d)	Pb1—I2	0.0468	-0.0336	-0.0332	0.1445	0.0776	0.01	-0.0392	0.0293	-0.0099
	Pb1—I3	0.0467	-0.0335	-0.0332	0.1443	0.0776	0.01	-0.0391	0.0292	-0.0099
	Pb1—I4	0.0467	-0.0336	-0.0332	0.1444	0.0776	0.01	-0.0392	0.0293	-0.0099
	I2•••H11	0.0232	-0.0220	-0.0213	0.0998	0.0565	0.03	-0.0152	0.0147	-0.0005
	I3•••H10	0.0237	-0.0226	-0.0220	0.1016	0.0569	0.03	-0.0156	0.0149	-0.0007
	I4•••H9	0.0237	-0.0226	-0.0220	0.1015	0.0569	0.03	-0.0156	0.0149	-0.0007

[a] See Fig. 1, as well as the ball and stick models in Table S3, for conformational and atomic labeling details.
[b] Properties include the charge density (ρ_b/au), the three principal eigenvalues of the charge density matrix ($\lambda_{i=1-3}$/au), the Laplacian of the charge density ($\nabla^2\rho_b$ /au), the ellipticity (ε_b), the potential energy density (V_b/au), the kinetic energy density (G_b/au), total energy density ($H_b = V_b + G_b$/au). ε_b is unitless.

The $CH_3NH_3PbI_3$ system is topologically interesting. No matter what is the orientation of the organic cation, each of the four conformations displays a topology that comprises an identical number of critical points of the charge density, Fig. 4. For instance, each conformer accompanies three ring critical points RCPs (characteristic of ring surfaces) such that their combination produces a cage-like structure characterized by

a cage critical point CCP. Norberto, Matta and Boyd have previously discussed a CCP containing topology in another molecular system.[117]

Table S2 summarizes the various topological descriptors of the charge density for all the four $CH_3NH_3^+$•••$^-PbI_3$ conformers. These include the charge density at BCP (ρ_b), the three principal eigenvalues of the Hessian of the charge density matrix ($\lambda_{i\,=\,1–3}$), the

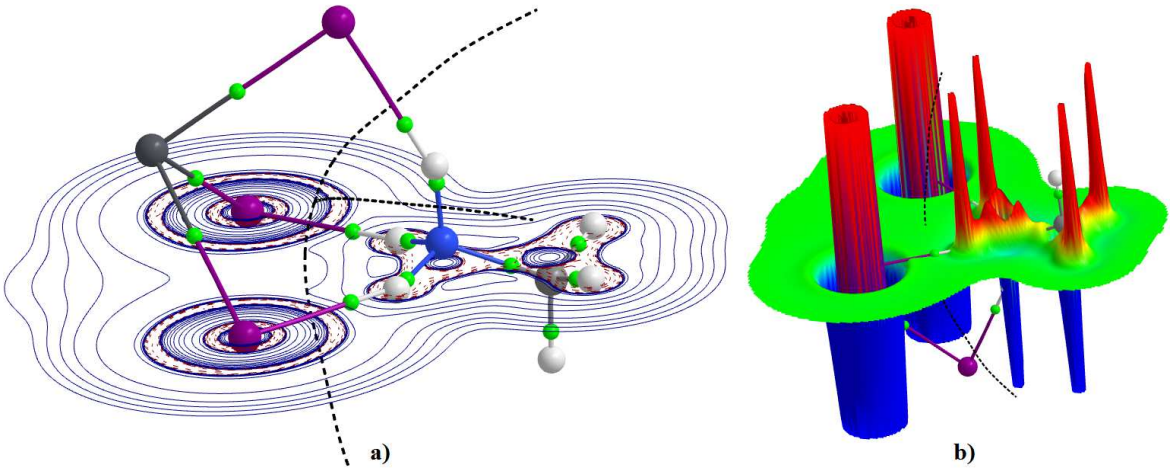

Fig. S5: a) 2D contour plot of the Laplacian of the charge density for the most stable $CH_3NH_3^+$•••$^-PbI_3$, obtained in the I–I–H plane. The dashed contour lines in red and the solid contour lines in blue represent regions of charge concentration ($\nabla\rho_b < 0$) and depletion ($\nabla\rho_b > 0$), respectively. b) The relief map of the Laplacian of the charge density, truncated at a maximum height of 7.0 au.

ellipticity ($\varepsilon_b = \lambda_2/\lambda_1 – 1$), the Laplacian of the charge density ($\nabla^2\rho_b = \lambda_1 + \lambda_2 + \lambda_3$, $\lambda_1 < \lambda_2 < \lambda_3$), the gradient kinetic (G_b), potential (V_b), and total energy densities (H_b, $H_b = G_b + V_b$). Both from Table S2 and Fig. 4, it is obvious that ρ_b lies in the 0.021–0.042 a.u. range for the I•••H–N and I•••H–C hydrogen bonds, with the former are stronger than the latter. If one compares the mean charge densities calculated for the I•••H–N and I•••H–C BCPs of the two symmetric structures a) and d), respectively, it can be said that the former interaction is roughly about two times stronger than the later one.

For I•••N–C (Fig. 4b), $\rho_b \approx 0.012$ a.u. This suggests that the I•••H–C and I•••H–N interactions are about 2-to-3 times stronger than this interaction.

The ρ_b calculated for the BCPs of all kinds of noncovalent interactions in $CH_3NH_3^+$•••$^-PbI_3$ are found to be smaller than the corresponding range of values, 0.043–0.052 a.u., calculated for the Pb–I coordinate bonds in $CH_3NH_3PbI_3$. This is not very surprising because the latter interactions are more covalent and ionic than the former ones. The specific attribute can be grasped looking at the signs and magnitudes of both $\nabla^2\rho_b$ and H_b, Table S2. For example, except for the I•••N–C, the I•••H–N and I•••H–C interactions are characterized by $\nabla^2\rho_b > 0$ and $H_b < 0$. The former characteristic is

indicative of closed-shell interaction,[27a,80] while the latter is indicative of the presence of covalency.[120-121] Fig. S5 illustrates both the contour plot and relief map of the Laplacian of the charge density, illustrating the nature of the charge concentration and depletion in the most stable $CH_3NH_3PbI_3$ system.

Note that covalency both in hydrogen and coordinate-bonding interactions is generally expected when the potential energy density V_b dominates over the gradient kinetic energy density G_b of the electrons. As a result, the total energy density H_b ($H_b = V_b + G_b$) in those regions of space also dominates, indicative of significant concentration of charge density.[120-121] This is possible especially when $G_b > 0$, $V_b < 0$, $|G_b| << |V_b|$, $H_b < 0$.

For the I•••N–C interaction in Fig. 4b, $\nabla^2\rho_b \approx 0.0484$ a.u. and $H_b \approx 0.0021$ a.u. These show that the $\nabla^2\rho_b$ and H_b are both positive for this interaction. The former signature is indifferent in characteristic from the hydrogen bonded interactions already discussed above, but is predominantly electrostatic because both $\nabla^2\rho_b > 0$ and $H_b > 0$.[80] The positive $\nabla^2\rho_b$ is mainly due to the eigenvalue λ_3 along the bond path direction. Its magnitude is substantially larger than the sum of the other two eigenvalues λ_1 and λ_2 (associated with the other two perpendicular directions), Table S2.

Except for I•••N–C, the ε_b for all Pb•••I, I•••H–N and I•••H–C interactions in $CH_3NH_3^+$•••$^-PbI_3$ is close to 0.03, meaning that coordinate and intermolecular bonding interactions are all singular and there is no involvement of π-character. For the former case, $\varepsilon_b \sim 1.36$. The large ε_b may be a signature of annihilation of the bond, which is not very surprising during the vibrational motion since the BCP and RCP are in close proximity.

The charge density at the RCPs and CCPs are calculated to be very small for all the conformers of $CH_3NH_3PbI_3$. Among all the three types of critical points, it follows the conventional trend, $\rho_b > \rho_r > \rho_c$, for each conformer. The same trend is found for each of the properties $\nabla^2\rho$, G, V, and H when all the three types of critical points are compared.

QTAIM results are in consistent with those of RDG-NCI isosurface and NBO second order perturbative lowering energy analyses (S2 and S3, respectively).

4.3.10 Charge transfer

The utility of partial atomic charge to understand various chemical phenomena is constructive, [85-87,122] even though some scientists question on its reliability.[123-125] Atomic charge is not only experimentally determined, but also easily quantified theoretically using various population schemes, e.g., Mulliken, Hirshfield, QTAIM, NPA, CHELPG and APT, *etc*.[126]

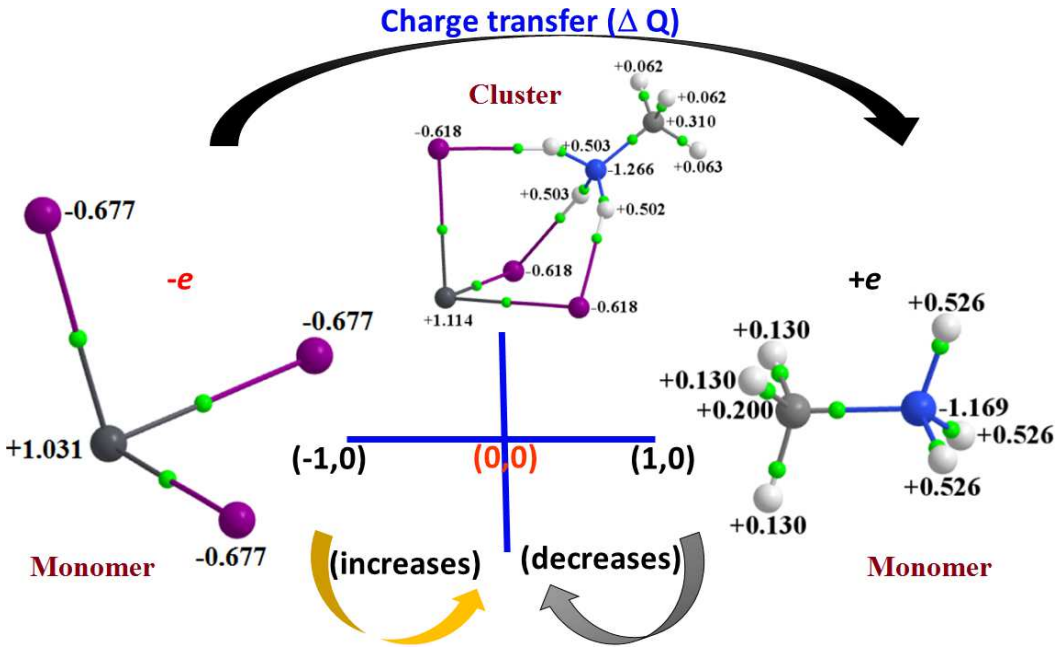

Fig. 5: Schematic diagram for the transfer of charge ΔQ between PbI_3^- and $CH_3NH_3^+$ upon the formation of the $CH_3NH_3^+$•••^-I_3Pb block; the black arrow indicates the direction of charge transfer. Shown are the M06-2X/ADZP level QTAIM charges (in *e*) on atoms in isolated PbI_3^- and $CH_3NH_3^+$.

The rearrangement of partial charges on atoms is a common feature that has seen in the past to assist in the fundamental understanding of the formation of supramolecular complex systems.[127-129] The same feature may be evident for the $CH_3NH_3^+$•••^-I_3Pb conformers. To exploit this, it should be understood that the fragment PbI_3^- in its formal isolated state carries a net electronic charge of –1.0, and the $CH_3NH_3^+$ fragment a net electronic charge of +1.0. However, as shown in Fig. 5, the formation of the most stable $CH_3NH_3^+$•••^-I_3Pb conformer is accompanied with the significant rearrangement of partial atomic charges. As expected, the –1.00 electronic charge on PbI_3^- is increased to –0.74, and the +1.0 of electronic charge on $CH_3NH_3^+$ is decreased to +0.74. This means the net electronic charge on the PbI_3^- fragment in $CH_3NH_3^+$•••^-I_3Pb is progressively becoming more positive, while that on the $CH_3NH_3^+$ subunit is becoming less positive, both compared with the net charges conferred on each isolated counterpart. Similar results were also obtained for the other three conformers, as well as with the Hirshfield population scheme[130] (values not given).

According to Politzer and others,[124] Clark and coworkers,[131] "it is increasingly being recognized that charge transfer theory is a mathematical attempt to represent a physical process, which is the mutual polarization of the interacting molecules, the so-called

"donor" and "acceptor". Thus it is redundant to cite both charge transfer and polarization as separate factors in noncovalent interactions."

The charge transfer (ΔQ) between PbI_3^- and $CH_3NH_3^+$ is calculated for all conformers is listed in Table 3. The largest of ΔQ is found for conformer a) compared to those of the three high-energy conformers. That is, ΔQ is the largest of 0.26 *e* for the most stable conformer, and the least of 0.15 *e* for the least stable conformer of the $CH_3NH_3^+$•••^-I_3Pb system (see Fig. 1 for conformer type and Table 3 for ΔQ values). In each case, it occurs in a direction from the PbI_3^- fragment to the $CH_3NH_3^+$ fragment. This mechanism is perhaps analogous to the way an electron is transferred from ^{11}Na to ^{17}Cl to form the Na^+Cl^- diatomic molecule.

The trend in ΔQ by some means, though not very perfect, shows a close match with the trend found for the *ΔE* for the $CH_3NH_3^+$•••^-I_3Pb conformers. Interestingly, the nature and direction of charge transfer found in this study for $CH_3NH_3^+$•••^-I_3Pb, Fig. 5, are qualitatively in good agreement with a recent study of Madjet *et al.*[122c)]

Table 3: M06-2X/ADZP estimates of charge transfer (ΔQ/*e*) between the fragments PbI_3^- and $CH_3NH_3^+$ at the $CH_3NH_3^+$•••^-I_3Pb equilibrium geometries. [a]

Fig. 3	ΔQ(QTAIM)	ΔQ(Hirshfield)
Conformer a)	0.260	0.463
Conformer b)	0.246	0.429
Conformer c)	0.259	0.455
Conformer d)	0.151	0.270

[a] See Fig. 5 for the direction of charge transfer

4.3.11 Reduced Density Gradient Noncovalent Interaction Approach

According to Jonson *et al.*,[6] the sign of second eigenvalue of the Hessian of the charge density matrix λ_2 determines the nature of an interaction and the value of ρ determines the strength. This view may not be very surprising because at a nuclear position, ρ is a maximum and the eigenvalues $\lambda_{i=1-3}$ are all negative. At the cage or ring critical points, it is a minimum and the eigenvalues $\lambda_{i=1-3}$ are all positive. The remaining regions of space can thus be characterized by a negative λ_1 ($\lambda_1 < 0$), a positive λ_3 ($\lambda_3 > 0$), and in this case, the sign of the second greatest eigenvalue λ_2 can either be positive ($\lambda_2 > 0$) or negative ($\lambda_2 < 0$). Apparently, this is the reason the sign of λ_2 has been

regarded as a potential indicator to discriminate attractive interactions (λ_2 negative ($\lambda_2 < 0$)) from repulsive ones (λ_2 positive ($\lambda_2 > 0$)).

The RDG $s(r)$ is related to the charge density ρ, and its gradient $\nabla\rho$ by Eqn. 1′.

$$RDG(r) = s(r) = \frac{1}{2(3\pi^2)^{\frac{1}{3}}} \frac{|\nabla\rho(r)|}{\rho(r)^{\frac{4}{3}}} \quad \ldots\ldots\ldots\ldots\ldots\ldots\ldots\ldots\ldots\ldots\ldots\ldots\ldots\ldots\ldots\ldots 1')$$

Fig. S6 illustrates the 2D plot of *s* against $\rho \times$ sign (λ_2) that uncovers the repulsive and attractive (noncovalent) interactions the $CH_3NH_3^+$•••^-I_3Pb chemical system comprises. It also illustrates the 3D isosurface plots corresponding to these two types of interactions. These are shown as the top and bottom graphics in each panel, respectively. The disc-like surfaces in deep-blue between the Pb^{2+} and I^- ions in a) indicate that the charge density is largely accumulated in the bonding regions. A similar information can be gained from the isosurfaces found between H atoms of the $–NH_3$ fragment in the organic cation and the I^- ions. However, and as expected, the disc-like isosurfaces associated with the latter interactions are not markedly blue compared to those feasible between the Pb and I atoms because of the appreciable difference in the charge density in the bonding regions.

It is apparent from Fig. S6 that I•••H–C hydrogen bonding interactions in c) and d), as well as the I•••N–C noncovalent interaction in b), are all characterized by green-like isosurfaces, with the latter one somehow more subtle. This result indicates that the charge density at the bonding regions of these interactions are significantly depleted compared to those found for the I•••H–N hydrogen bonding interactions viable in a), b) and c). All the features are also evident of the *s* against $\rho \times$ sign (λ_2) 2D plots in the $\lambda_2 < 0$ regions, which appear as spikes. The peak locations of these spikes refer to the strengths of the intermolecular noncovalent interactions revealed.

All these results clearly enable us to conclude that the chemical bonding topologies unraveled using QTAIM for $CH_3NH_3PbI_3$ are in decent agreement with those originated from RDG-NCI (S2) and NBO analysis (S2 and Table S3).

4.3.12 NBO second order perturbation theory analysis

According to second order perturbation theory analysis of Fock matrix in NBO basis,[7] the formation of the $CH_3NH_3^+$•••^-I_3Pb cluster may be understood as a result of hyperconjugation (charge transfer delocalization) between the PbI_3^- and $CH_3NH_3^+$ species. As such, this analysis dictates predominant charge transfer delocalization between the interacting monomers.

For the most stable conformer illustrated in Fig. 1a), it is occurring from the lone-pair (LP) electron donating orbitals of the three iodide atoms of the PbI_3^- subunit (i.e., LP(3) I in PbI_3^-) to the σ* antibonding orbitals of the N–H bond(s) (i.e., σ*(N–H)) of the

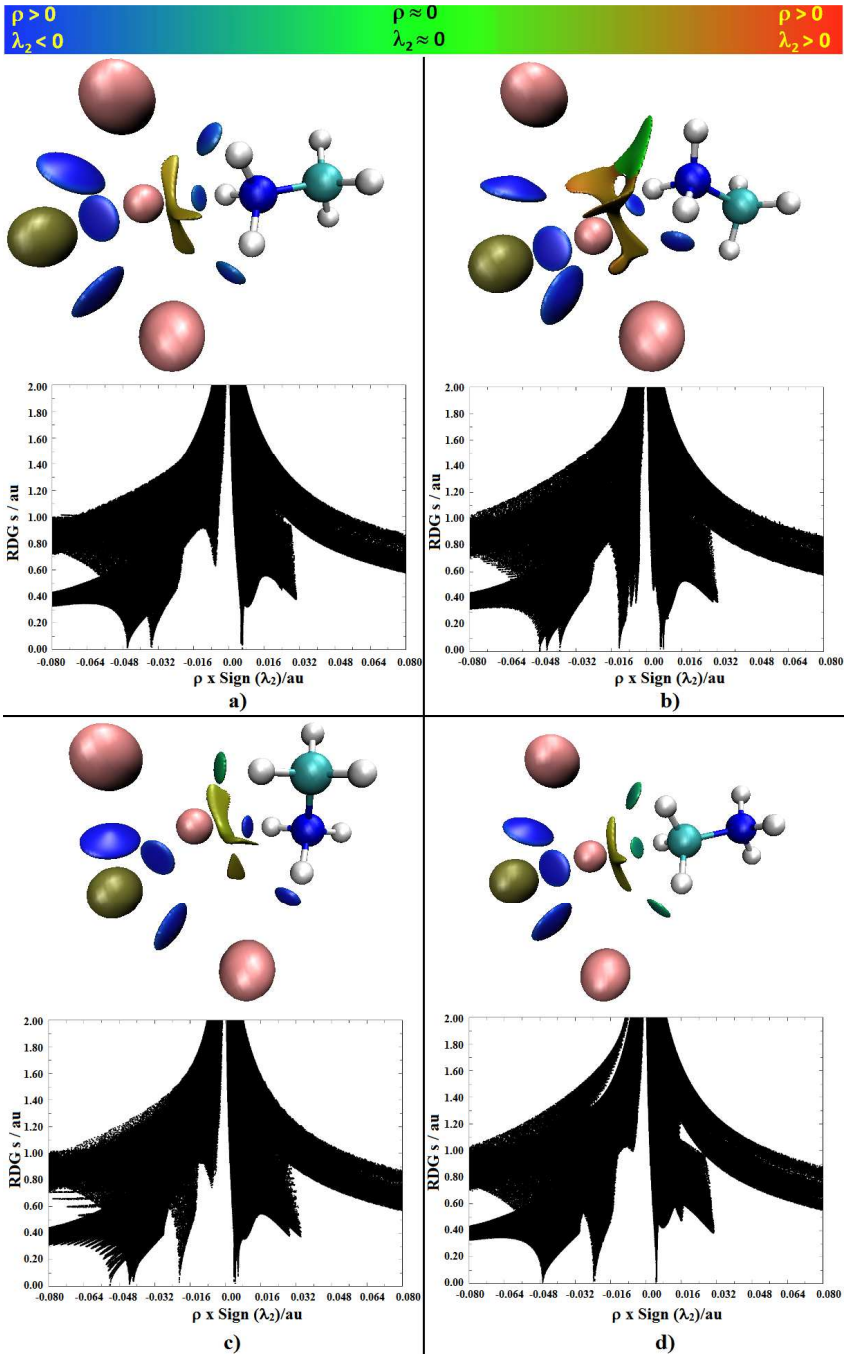

Fig. S6: The M06-2X/ADZP RDG 0.3 a.u. isosurface plots in 3D (top) and the s against $\rho \times$ sign (λ_2) plots 2D (bottom) for each conformer of the $CH_3NH_3^+$•••^-I_3Pb nanocluster.

$CH_3NH_3^+$ subunit, i.e., LP(3) I $\rightarrow$ σ*(N–H), where (3) denotes the third LP orbital. For conformation d), such predominant charge transfer interactions occur between the LP of the electron donating orbitals of the three iodine atoms in PbI_3^- and the σ* antibonding

orbitals of the C–H bond(s) of the $CH_3NH_3^+$ subunit, i.e., LP(3) I → σ*(C–H). The strengths of the respective hyperconjugative interactions quantified with $E^{(2)}$ are close to 40.0 and 15.0 kcal mol^{-1} for conformations a) and d), respectively. Additional hyperconjugative interactions between various bonding and antibonding orbitals associated with the PbI_3^- and $CH_3NH_3^+$ species are detailed in Table S3. These are having $E^{(2)}$ > 2.0 kcal mol^{-1} in a) and ≈ 0.50 kcal mol^{-1} in d), which include the [σ(Pb—I) → σ*(N–H)] and [σ(Pb—I) → σ*(C–H)] delocalizations, respectively, showing the involvement of the σ-type Pb—I coordination bonds in hyperconjugation. All these delocalizations are collectively liable for strengthening the stabilities of the $CH_3NH_3^+$•••^-I_3Pb system.

For conformation b), two types of hyperconjugative interactions are evident. In it, one of them is LP(3) I → σ*(N–H) (for I•••H–N), which is relatively stronger than the weak one LP(3) I2 → σ*(1)N5—C9 (for I•••N–C), with $E^{(2)}$ for these 45.62 *vs.* 0.91 kcal mol^{-1}, Table S3. Interestingly, these interactions were also identified with QTAIM (Fig. 3b) and RDG-NCI, Fig. S6. QTAIM predicts the latter interaction to be accompanied with a curved bond path (strained), whereas RDG-NCI identifies it through a green isosurface appeared between the two nuclei of bonded atomic basins. The attraction between the I and N atoms that leads to development of the I•••N–C is due to the joint influence of three adjacent hydrogen atoms in $–NH_3$ of $CH_3NH_3^+$ that show hyperconjugative interactions with the same iodide atom. Such hyperconjugations are described by LP (3) I2 → σ*(1) N5—H6, LP (3) I2 → σ*(1) N5—H7, and LP (3) I2 → σ*(1) N5—H8, with $E^{(2)}$ for these three lie between 0.8 and 1.1 kcal mol^{-1}.

For conformer c), the I•••H–N and I•••H–C are described by LP(3) I → σ*(N–H) and LP(3) I → σ*(C–H) hyperconjugative interactions, respectively, with the strength of the former being substantially stronger than the latter. This is evocative of the magnitude of $E^{(2)}$. For instance, $E^{(2)}$ amounts to 53.26 and 53.66 kcal mol^{-1} for the two I•••H–N interactions, and that to 13.94 kcal mol^{-1} for the I•••H–C, Table S3.

In summary, the NBO results are found to be in excellent agreement with those found with QTAIM and RDG analyses, thereby recommending the fact that the employment of any of these three approaches can be advantageous in generating similar information about the topologies of chemical bonding interactions involved in the conformers of the $CH_3NH_3^+$•••$^-PbI_3$ system, as well as in analogous derivatives of trihalide perovskite.

Table S3: Second order hyperconjugation interaction energies $E^{(2)}$ associated with various important electron delocalizations between the donor NBOs (i) and acceptor NBOs (j) for the $CH_3NH_3^+ \bullet\bullet\bullet ^-PbI_3$ clusters. [a]

Donor NBO (i)		Acceptor NBO (j)	$E^{(2)}$/ kcal mol^{-1} [b]
Conformer a)			
LP (3) I2	→	σ*(1) N8—H11	38.57
LP (3) I3	→	σ*(1) N8—H10	39.95
LP (3)I4	→	σ*(1) N8—H9	39.28
BD (1)Pb1—I2	→	σ*(1) N8—H11	2.14
BD (1)Pb1—I3	→	σ*(1) N8—H10	2.43
BD (1)Pb1—I4	→	σ*(1) N8—H9	2.25
Conformer b)			
LP (3) I2	→	σ*(1) N5—H6	0.80
LP (3) I2	→	σ*(1) N5—H7	1.08
LP (3) I2	→	σ*(1) N5—H8	0.80
LP (3) I2	→	σ*(1) N5—C9	0.91
LP (3) I3	→	σ*(1) N5—H8	45.62
LP (3) I4	→	σ*(1) N5—H6	45.72
LP (1) I3	→	σ*(1) N5—H8	4.84
LP (1) I4	→	σ*(1) N5—H6	4.85
BD(1)Pb1—I3	→	σ*(1) N —H8	6.27
BD(1)Pb1—I4	→	σ*(1) N5—H6	6.29
Conformer c)			
LP (3) I2	→	σ*(1) N5—H6	53.26
LP (1) I2	→	σ*(1) N5—H6	5.02
BD(1)Pb1—I2	→	σ*(1) N5—H6	1.65
LP (3)I3	→	σ*(1) N5—H7	53.66
LP (1) I3	→	σ*(1) N5—H7	5.04
BD(1)Pb1—I3	→	σ*(1) N5—H7	1.67
LP (3)I4	→	σ*(1) C9—H12	13.94
BD(1)Pb1—I4	→	σ*(1) C9—H12	1.05
Conformer d)			
LP (3) I2	→	σ*(1) C8—H11	14.22
BD (1)Pb1—I2	→	σ*(1) C8—H11	0.49
LP (3) I3	→	σ*(1) C8—H10	15.16
BD (1)Pb1—I3	→	σ*(1) C8—H10	0.59
LP (3)I4	→	σ*(1) C8—H9	15.16
BD (1)Pb1—I4	→	σ*(1) C8—H9	0.60

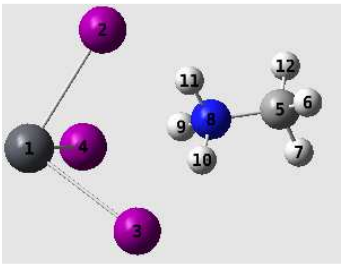
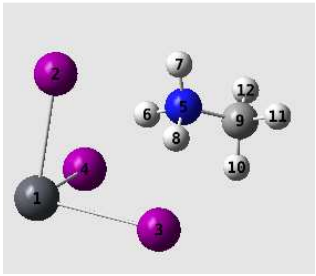
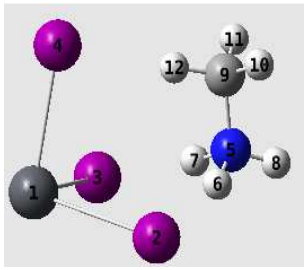
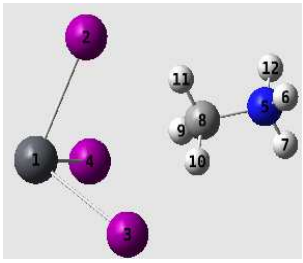

[a] LP, BD, and σ*, represent the lone-pair, bonding, and anti-bonding natural orbitals involved, respectively.
[b] See Eqn 1) for $E^{(2)}$.

4.3.13 Is molecular $CH_3NH_3^+ \bullet\bullet\bullet^- PbI_3$ a Mulliken inner complex?

Perhaps yes. According to Mulliken and Person,[128] interactions based on the degree of charge transfer between the donor and acceptor molecules can be classified as Mulliken outer and inner complexes. For example, a typical hydrogen bond D•••H–A, predominantly of electrostatic origin, which is accompanied with a little amount of ΔQ, can be regarded as an outer complex. An inner complex is more strongly bound, and is generally identified in the form of an ion-pair, $[D–H]^-\bullet\bullet\bullet A^+$. According to Hill[21c)] and Shaw *et al.*,[21d)] the physical notion of an inner complex should not be taken as a requirement of a complete transfer of H^+, or X^+ (X = halogen derivative), but simply to signify significant charge transfer on complex formation. Typically, the ΔQ is less than 0.1*e* for (weaker) outer complexes, and those are accompanied with large ΔQ can be regarded as Mulliken inner complexes. For example, thiirane•••ClF and H_3P•••ICl are examples of Mulliken inner complexes because they involve ΔQ as large as 0.279 and 0.144 *e*, respectively, whereas the thiirane•••HCl, oxirane•••HCl, NH_3•••Cl and H_3N•••XY (X, Y = halogen derivative) hydrogen- and halogen-bonded complexes are good examples of Mulliken outer complexes. Considering these, as well as the interpretations provided by others for homologous systems, [129] it is obvious that $CH_3NH_3^+\bullet\bullet\bullet^- PbI_3$ is an inner-type Mulliken complex due to several reasons. Some of these include: i) the unusually large binding energies, ii) the short I•••H intermolecular distances of separation, and iii) the large amount of transfer of charge between the interacting partners, ΔQ >> 0.14 *e*. In addition, and in agreement with iii), the NBO's second-order perturbation analysis has provided evidence about the large charge transfer delocalizations between the coordinated iodide lone-pair orbitals of the PbI_3^- and the antibonding σ*(N–H) orbitals of the $CH_3NH_3^+$ ($E^{(2)}$ lies between 13.95 and 53.66 kcal mol^{-1}, Table S3).

4.4 Conclusions

In this study, we have performed M06-2X level DFT calculations using an all-electron double-ξ ADZP basis set to study the geometrical and energetic stabilities, and the electronic and orbital properties of the numerously studied $CH_3NH_3PbI_3$ system in the gas phase. The non-periodic computational results obtained are compared with those reported experimentally in the solid state, as well with those are obtained from this calculation employing periodic DFT. Among several other things, the study has identified four stable conformers for $CH_3NH_3PbI_3$. These can be regarded as representative models for the understanding of intermolecular interactions in the various phases of the corresponding system in the crystalline phase. The result is by some means is in

appealing agreement with the theoretical[55] and experimental[18g,42,55] results reported by others.

Based on the nature of various characteristic properties such as the unusually large binding energy, charge transfer, short intermolecular bond distance, and a few others, we have suggested the $CH_3NH_3PbI_3$ molecular blocks to be referred to as Mulliken inner complexes, whose solid state analogues have adequate implications in the design of advanced functional nanomaterials and optoelectronic devices. This view might be in agreement with Hill *et al.*, [21d] who have asserted that interactions involving Mulliken inner type have desirable implications for fields such as crystal engineering and nanomaterials, where highly directional and strong interactions can be exploited for fine-control of the overall structure and properties. It is also in line with an anonymous reviewer who has pointed out that the gas phase molecular conformations could be considered as embryos for the understanding of the subsequent growth of solid state $CH_3NH_3PbI_3$. In this context the inclusion of a second, third, or fourth, *etc.*, building block of the $CH_3NH_3PbI_3$ system in the calculation can lead to the development of any supramolecular system whose physical properties can be of interest to researchers performing physical vapor deposition experiments to produce good quality $CH_3NH_3PbI_3$ thin-films.[132] Since hydrogen bonding controls the tilting of the octahedra of the halide based perovskite systems especially in the low temperature phase, in which, the latter controls band gaps and carrier masses,[32c] the study is line with a perspective of Lee *et al.* in a sense that engineering the strength and direction of the hydrogen bonding between the organic and inorganic frameworks might be considered as a future avenue for optimizing solar cell photovoltaic efficiency. The computational results discussed in light of the *ultra-strong* nature of the intermolecular hydrogen bonding interactions in $CH_3NH_3PbI_3$ will benefit researchers who are working on the future development of such highly valued functional materials for device applications, and beyond.

4.5 References

1. M. M. Lee, J. Teuscher, T. Miyasaka, T. N. Murakami, H. J. Snaith, *Efficient hybrid solar cells based on meso-superstructured organometal halide perovskites, Science* 2012, 338, 643–647.
2. a) Y. Hinuma, A. Grüneis, G. Kresse, F. Oba, Band alignment of semiconductors from density-functional theory and many-body perturbation theory, *Phys. Rev. B* 2014, 90, 155405; b) Y. Zhao, D. G. Truhlar, Calculation of semiconductor band gaps with the M06-L density functional, *J. Chem. Phys.* 2009, 130, 074103; c) Y. Wu, M. K. Y. Chan, G. Ceder, Prediction of semiconductor band edge positions in aqueous environments from first principles, *Phys. Rev. B* 2011, 83, 235301.
3. National Renewable Energy Laboratory (NREL) Best Research-Cell Efficiency chart. http://www.nrel.gov/ncpv/images/efficiency_chart.jpg (2016).

4. O. B. Boggild, Crystalline form and twin formations of cryolite, perovskite and boracite, ZEITSCHRIFT FUR KRYSTALLOGRAPHIE UND MINERALOGIE 1911, 50, 349-429.
5. a) A. Kojima, K. Teshima, T. Miyasaka, Y. Shirai, Novel photoelectrochemical cell with mesoscopic electrodes sensitized by lead-halide compounds, In *Proc. 210th ECS Meeting* (ECS, 2006); b) K. Kojima, Y. Teshima, Y. Shirai, T. Miyasaka, Organometal halide perovskites as visible-light sensitizers for photovoltaic cells, *J. Am. Chem. Soc.* 2009, 131, 6050-6051.
6. S. D. Stranks, H. J. Snaith, Metal-halide perovskites for photovoltaic and light-emitting devices, *Nat. Nanotech.* 2015, 10, 391–402.
7. H. S. Kim, C. R. Lee, J. H. Im, K. B. Lee, T. Moehl, A. Marchioro, S. J. Moon, R. Humphry-Baker, J. H. Yum, J. E. Moser, M. Grätzel, N. G. Park, Lead iodide perovskite sensitized all-solid-state submicron thin film mesoscopic solar cell with efficiency exceeding 9%, *Sci. Rep.* 2012, **2**, 591.
8. P. R. Varadwaj, Methylammonium lead trihalide perovskite solar cell semiconductors are not organometallic: A perspective, *Helv. Chim. Acta* 2017, DOI: 10.1002/hlca.201700090.
9. Thomson Reuters Web of Science, The most comprehensive and versatile research platform. This is available at: https://webofknowledge.com/
10. The Cambridge Structural Database, CSD version 5.37 updates (Feb 2016), C. R. Groom, I. J. Bruno, M. P. Lightfoot and S. C. Ward, *Acta Cryst.* 2016, B72, 171-179.
11. a) C. C. Stoumpos, M. G. Kanatzidis, Halide perovskites: Poor man's high-performance semiconductors, *Adv. Mat.* 2016, 28, 5778–5793; b) E. J. Juarez-Perez, *et al.*, Photoinduced giant dielectric constant in lead halide perovskite solar cells, *J. Phys. Chem. Lett.* 2014, 5, 2390–2394; c) A. Miyata, *et al.*, Direct measurement of the exciton binding energy and effective masses for charge carriers in organic–inorganic tri-halide perovskites, *Nat. Phys.* 2015, 11, 582–587; d) G. Georgi, J.-I. Fujisawa, H. Segawa, K. Yamashita, Small photocarrier effective masses featuring ambipolar transport in methylammonium lead iodide perovskite: A density functional analysis, *J. Phys. Chem. Lett.* 2013, 4, 4213–4216; e) G. C. Xing, N. Mathews, S. Y. Sun, S. S. Lim, Y. M. Lam, M. Gratzel, S. Mhaisalkar, T. C. Sum, Long-range balanced electron- and hole-transport lengths in organic-inorganic $CH_3NH_3PbI_3$, *Science* 2013, 342, 344–347; f) Z. Gevorkian, V. Gasparian, Y. Lozovik, Large diffusion lengths of excitons in perovskite and TiO_2 heterojunction, *Appl. Phys. Lett.* 2016, 108, 051109.
12. a) A. K. Chilvery, *et al.*, Perovskites: transforming photovoltaics, a mini-review, *J. Photon. Energy.* 2015, 5, 057402; b) P. P. Boix, S. Agarwala, T. M. Koh, N. Mathews, S. G. Mhaisalkar, Perovskite solar cells: Beyond methylammonium lead iodide, *J. Phys. Chem. Lett.* 2015, 6, 898–907.
13. J.-W. Lee, H.-S. Kim, H. Shin, H. S. Jung, P. J. Yoo, J. H. Park, D.-Y. Jung, N.-G. Park, A Sharp focus on perovskite solar cells at Sungkyun International Solar Forum (SISF), *ACS Energy Lett.* 2016, 1, 500−502.
14. G. Grancini, C. Roldán-Carmona, I. Zimmermann, E. Mosconi, X. Lee, D. Martineau, S. Narbey, F. Oswald, F. De Angelis, M. Graetzel, M. Khaja Nazeeruddin, One-Year stable perovskite solar cells by 2D/3D interface engineering, *Nat. Commun*. 2017, 8, 15684.
15. a) T. Singh, J. Singh, T. Miyasaka, Role of metal oxide electron-transport layer modification on the stability of high performing perovskite solar cells, *Chem. Sus. Chem.* 2016, 9, 2559–2566; b) M. K. Nazeeruddin, Perovskite solar cells and devices, *Chem. Sus. Chem.* 2016, 9, 2516–2714; c)

P.-P. Sun, W.-J. Chi, Z.-S. Li, Effects of water molecules on the chemical stability of $MAGeI_3$ perovskite explored from a theoretical viewpoint, Phys. Chem. Chem. Phys. 2016, 18, 24526-24536; d) C. Clegg, I. G. Hill, Systematic study on the impact of water on the performance and stability of perovskite solar cells, *RSC Adv.* 2016, 6, 52448-52458; e) Z. Song, A. Abate, S. C. Watthage, G. K. Liyanage, A. B. Phillips, U. Steiner, M. Graetzel, M. J. Heben, Perovskite solar cell stability in humid air: Partially reversible phase transitions in the PbI_2-CH_3NH_3I-H_2O system, *Adv. Energy Mater.* 2016, 1, DOI: 10.1002/aenm.201600846; f) J. M. Frost, K. T. Butler, F. Brivio, C. H. Hendon, M. van Schilfgaarde, A. Walsh, Atomistic origins of high-performance in hybrid halide perovskite solar cells, *Nano Lett.* 2014, 14, 2584− 2590.

16. a) F. Giustino, H. J. Snaith, Toward lead-free perovskite solar cells, ACS Energy Lett. 2016, 1, 1233–1240; b) Y.-Y. Sun, J. Shi, J. Lian, W. Gao, M. L. Agiorgousis, P. Zhangde, S. Zhang, Discovering lead-free perovskite solar materials with a split-anion approach, Nanoscale, 2016,8, 6284-6289; c) F. Hao, C. C. Stoumpos, D. H. Cao, R. P. H. Chang, M. G. Kanatzidis, Lead-free solid-state organic–inorganic halide perovskite solar cells, Nat. Photon. 2014, 8, 489–494; d) S. Gupta, T. Bendikov, G. Hodes, D. Cahen, $CsSnBr_3$, A lead-free halide perovskite for long-term solar cell application: Insights on SnF_2 dddition, *ACS Energy Lett.* 2016, 1, 1028–1033; e) F. Wei, *et al.*, The synthesis, structure and electronic properties of a lead-free hybrid inorganic–organic double perovskite $(MA)_2KBiCl_6$ (MA = methylammonium), *Mater. Horiz.* 2016, 3, 328-332; f) G. Volonakis, *et al.*, $Cs_2InAgCl_6$: A new lead-free halide double perovskite with direct band gap, https://arxiv.org/ftp/arxiv/papers/1611/1611.05426.pdf (last retrieved on 1 February 2017).
17. a) F. Li, *et al.*, Ambipolar solution-processed hybrid perovskite phototransistor, *Nat. Commun.* 2015, 6, 8238, doi:10.1038/ncomms9238; b) X. Y. Chin, *et al.*, Lead iodide perovskite light-emitting field-effect transistor, *Nat. Commun.* 2015, 6, 7383, doi:10.1038/ncomms8383; c) L. N. Quan, *et al.*, Ligand-stabilized reduced-dimensionality perovskites, *J. Am. Chem. Soc.* 2016, 138, 2649–2655.
18. a) A documentary on perovskite, this is available via: https://en.wikipedia.org/wiki/Perovskite#cite_note-Webmin-2; b) Strontium titanate, this is available via: https://en.wikipedia.org/wiki/Strontium_titanate (last retried on 1 February 2017); c) B. Saparov, D. B. Mitzi, Organic–inorganic perovskites: Structural versatility for functional materials design, *Chem. Rev.* 2016, 116, 4458; d) J. S. Manser, M. I. Saidaminov, J. A. Christians, O. M. Bakr, P. V. Kamat, Making and breaking of lead halide perovskites, *Acc. Chem. Res.* 2016, 49, 330-8; e) C. C. Stoumpos, C. D. Malliakas, M.i G. Kanatzidis, Semiconducting tin and lead iodide perovskites with organic cations: Phase transitions, high mobilities, and near-infrared photoluminescent properties, *Inorg. Chem.* 2013, 52, 9019–9038; f) A. Wakamiya, M. Endo, T. Sasamori, N. Tokitoh, Y. Ogomi, S. Hayase, Y. Murata, Reproducible fabrication of efficient perovskite-based solar cells: X-ray crystallographic studies on the formation of $CH_3NH_3PbI_3$ layers, *Chem. Lett.* 2014, 43, 711 – 713; g) M. T. Weller, O. J. Weber, P. F. Henry, A. M. Di Pumpo, T. C. Hansen, Complete structure and cation orientation in the perovskite photovoltaic methylammonium lead iodide between 100 and 352 K *Chem. Commun.* 2015, 51, 4180; h) T. Baikie, Y. Fang, J. M. Kadro, M. Schreyer, F. Wei, S. G. Mhaisalkar, M. Graetzeld, T. J. White, Synthesis and crystal chemistry of the hybrid perovskite $(CH_3NH_3)PbI_3$ for solid-state sensitised solar cell applications, J. Mater. Chem. A, 2013,1, 5628-5641.

19. a) A. R. Bin, M. Yusoff, J. Jang, Highly efficient photoelectrochemical water splitting by a hybrid tandem perovskite solar cell, *Chem. Commun.* 2016,52, 5824-5827; b) M. Crespo-Quesada, L. M. Pazos-Outón, J. Warnan, M. F. Kuehnel, R. H. Friend, E. Reisner, Metal-encapsulated organolead halide perovskite photocathode for solar-driven hydrogen evolution in water, *Nat. Commun*. 2016, 7, doi:10.1038/ncomms12555.
20. Y. H. Chang, C. H. Park, K. Matsuishi, First-principles study of the structural and the electronic properties of the lead-halide-based inorganic-organic perovskites $(CH_3NH_3)PbX_3$ and $CsPbX_3$ (X = Cl, Br, I), *J. Korean Phys. Soc.* 2004, 44, 889-893.
21. a) J. W. Larson, T. B. McMahon, Strong hydrogen bonding in gas-phase anions. An ion cyclotron resonance determination of fluoride binding energetics to Broensted acids from gas-phase fluoride exchange equilibrium measurements, *J. Am. Chem. Soc*. 1983, 105, 2944–2950; b) Emiliana D'Oria, Juan J. Novoa, Cation–anion hydrogen bonds: A new class of hydrogen bonds that extends their strength beyond the covalent limit: A theoretical characterization, *J. Phys. Chem. A* 2011, 115, 13114–13123; c) R. A. Shaw, J. G. Hill, A. C. Legon, Halogen bonding with phosphine: Evidence for Mulliken inner complexes and the importance of relaxation energy, *J. Phys. Chem. A* 2016, 120, 8461–8468; d) G. H. Hill, The halogen bond in thiirane···ClF: an example of a Mulliken inner complex, *Phys. Chem. Chem. Phys.* 2014, 16, 19137-19140; e) S. Scheiner (ed.), Noncovalent Forces, Challenges and Advances in Computational Chemistry and Physics 2015, 19, Springer, ISBN 978-3-319-14162-6 ISBN 978-3-319-14163-3 (eBook), DOI 10.1007/978-3-319-14163-3.
22. a) I. Borriello, G. Cantele, D. Ninno, Ab initio investigation of hybrid organic–inorganic perovskites based on tin halides. *Phys. Rev. B* 2008, 77, 235214; b) W.-J. Yin, T. Shi, Y. Yan, Unusual defect physics in $CH_3NH_3PbI_3$ perovskite solar cell absorber, *Appl. Phys. Lett.* 2014, 104, 063903; c) F. Brivio, K. T., Butler, A. Walsh, M. van Schilfgaarde, Relativistic quasiparticle self-consistent electronic structure of hybrid halide perovskite photovoltaic absorbers. *Phys. Rev. B* 2014, 89, 155204; d) P. Umari, E. Mosconi, F. De Angelis, Relativistic gw calculations on $CH_3NH_3PbI_3$ and $CH_3NH_3SnI_3$ perovskites for solar cell applications, *Sci. Rep.* 2014, 4, 4467; e) C. Motta, F. El-Mellouhi, S. Kais, N. Tabet, F. Alharbi, S. Sanvito, Revealing the role of organic cations in hybrid halide perovskite $CH_3NH_3PbI_3$, *Nat. Commun.* 2015, 6, 7026, doi:10.1038/ncomms8026.
23. a) H. Fang, P. Jena, Molecular origin of properties of organic–inorganic hybrid perovskites: The big picture from small clusters, *J. Phys. Chem. Lett.* 2016, 7, 1596–1603; b) Q. Yao, H. Fang, K. Deng, E. Kan, P. Jena, Superhalogens as building blocks of two-dimensional organic–inorganic hybrid perovskites for optoelectronics applications, *Nanoscale* 2016, 8, 17836-17842; c) H. Fang, P. Jena, Super-ion inspired colorful hybrid perovskite solar cells, *J. Mater. Chem. A* 2016, 4, 4728.
24. W. Kohn, L. J. Sham, Self-consistent equations including exchange and correlation effects, *Phys. Rev.* 1965, 140, A1133.
25. a) H. Hunt, e*t al.*, Hydrogen bonding in ionic liquids, *Chem. Soc. Rev.* 2015, 44, 1257-1288; b) T. Steiner, G. R. Desiraju, Distinction between the weak hydrogen bond and the van der Waals interaction Chem. Commun. 1998, 891.
26. a) NBO 6.0 Program Manual Natural Bond Orbital Analysis Programs, Ed. F. Weinhold, E. D. Glendening. This document is available via: http://nbo6.chem.wisc.edu/nboman.pdf; b) F.

Weinhold, Natural bond orbital analysis: A critical overview of relationships to alternative bonding perspectives, *J. Comput. Chem.* 2012, 33, 2363–2379; c) F. Weinhold, Natural bond critical point analysis: Quantitative relationships between natural bond orbital-based and QTAIM-based topological descriptors of chemical bonding, *J. Comput. Chem.* 2012, 33, 2440–2449.

27. a) R. F. W. Bader, Atoms in Molecules: A Quantum Theory, Oxford University Press, Oxford, 1990; b) AIMAll (Version 16.10.31), Todd A. Keith, TK Gristmill Software, Overland Park KS, USA, 2016 (aim.tkgristmill.com).
28. a) E. R. Johnson, S. Keinan, P. Mori-Sanchez, J. Contreras-Garcia, A. J. Cohen, W. Yang, Revealing noncovalent interactions, *J. Am. Chem. Soc.* 2010, 132, 6498-6506; b) J. Contreras-Garcia, E. R. Johnson, S. Keinan, R. Chaudret, J-P. Piquemal, D. N. Beratan, W. Yang, NCIPLOT: a program for plotting non-covalent interaction regions, *J. Chem. Theory Comput.* 2011, 7, 625-632.
29. Gaussian 09, Revision C.01, M. J. Frisch, G. W. Trucks, H. B. Schlegel, G. E. Scuseria, M. A. Robb, J. R. Cheeseman, G. Scalmani, V. Barone, B. Mennucci, G. A. Petersson, H. Nakatsuji, M. Caricato, X. Li, H. P. Hratchian, A. F. Izmaylov, J. Bloino, G. Zheng, J. L. Sonnenberg, M. Hada, M. Ehara, K. Toyota, R. Fukuda, J. Hasegawa, M. Ishida, T. Nakajima, Y. Honda, O. Kitao, H. Nakai, T. Vreven, J. A. Montgomery, Jr., J. E. Peralta, F. Ogliaro, M. Bearpark, J. J. Heyd, E. Brothers, K. N. Kudin, V. N. Staroverov, R. Kobayashi, J. Normand, K. Raghavachari, A. Rendell, J. C. Burant, S. S. Iyengar, J. Tomasi, M. Cossi, N. Rega, J. M. Millam, M. Klene, J. E. Knox, J. B. Cross, V. Bakken, C. Adamo, J. Jaramillo, R. Gomperts, R. E. Stratmann, O. Yazyev, A. J. Austin, R. Cammi, C. Pomelli, J. W. Ochterski, R. L. Martin, K. Morokuma, V. G. Zakrzewski, G. A. Voth, P. Salvador, J. J. Dannenberg, S. Dapprich, A. D. Daniels, Ö. Farkas, J. B. Foresman, J. V. Ortiz, J. Cioslowski, and D. J. Fox, Gaussian, Inc., Wallingford CT, 2009.
30. Y. Zhao, D. G. Truhlar, The M06 suite of density functionals for main group thermochemistry, thermochemical kinetics, noncovalent interactions, excited states, and transition elements: two new functionals and systematic testing of four M06-class functionals and 12 other functionals, *Theor. Chem. Account.* 2008, 120: 215. doi:10.1007/s00214-007-0310-x.
31. EMSL basis set library. This is available via: https://bse.pnl.gov/bse/portal (last retrieved 30 June 2016).
32. a) J.-H. Lee, N. C. Bristowe, P. D. Bristowe, A. K. Cheetham, Role of hydrogenbonding and its interplay with octahedral tilting in $CH_3NH_3PbI_3$, *Chem. Commun.* 2015, 51, 6434; b) A. Arakcheeva, D. Chernyshov, M. Spina, L. Forró, E. Horváth, $CH_3NH_3PbI_3$: precise structural consequences of water absorption at ambient conditions, *Acta Cryst.* 2016. B72, 716-722; c) J. -H. Lee, N. C. Bristowe, J. H. Lee, S. -H. Lee, P. D. Bristowe, A. K. Cheetham, H. M. Jang, Resolving the physical origin of octahedral tilting in halide perovskites, *Chem. Mater.* 2016, 28, 4259–4266.; d) J.H. Lee, J.-H. Lee, E.-H. Kong, H. M. Jang, The nature of hydrogen bonding interaction in the prototypic hybrid halide perovskite, tetragonal $CH_3NH_3PbI_3$, *Sci. Rep.* 2016, 6, 21687, doi:10.1038/srep21687; e) J. H. Lee, J.-H. Lee, E.-H. Kong, H. M. Jang, Two distinct modes of hydrogen bonding interaction in the prototypic hybrid halide perovskite, tetragonal $CH_3NH_3PbI_3$, arXiv:1511.02643 [cond-mat.mtrl-sci]; the document is available via: https://arxiv.org/abs/1511.02643;
33. a) V. I. Bakhmutov, Dihydrogen Bond: Principles, Experiments, and Applications, Ch. 12, pp. 117, Wiley-Interscience, Joh Wiley and Sons, Inc., 2008, ISBN 978-0-470-18096-9; b) J.-W.

Zou, M. Huang, G.-X. Hu, Y.-J. Jiang, Toward a uniform description of hydrogen bonds and halogen bonds: correlations of interaction energies with various geometric, electronic and topological parameters† *RSC Adv*. 2017, 7, 10295-10305; c) D. Kaur, S. Khanna, Hydrogen bonding of formamide, urea, urea monoxide and their thio-analogs with water and homodimers, *J. Chem. Sci*. 2014, 126, 1815–1829; d) B. Lakshmi, A. G. Samuelson, K. V. J. Jose, S. R. Gadre, E. Arunan, Is there a hydrogen bond radius? Evidence from microwave spectroscopy, neutron scattering and X-ray diffraction results, *New J. Chem*. 2005, 2 9, 371–377.

34. a) P. Ganguly, G. R. Desiraju, Van der Waals and polar intermolecular contact distances: Quantifying supramolecular synthons, *Chem. Asian J*. 2008, 3, 868-80; b) V. R. Hathwar, M. Sist, M. R. V. Jørgensen, A. H. Mamakhel, X. Wang, C. M. Hoffmann, K. Sugimoto, J. Overgaard, B. B. Iversena, Quantitative analysis of intermolecular interactions in orthorhombic rubrene, *IUCrJ*. 2015, 2, 563–574; c) J. Echeverría, G. Aullón, S. Alvarez, Dihydrogen intermolecular contacts in group 13 compounds: H···H or E···H (E = B, Al, Ga) interactions? *Dalton Trans.* 2017, 46, 2844-2854.
35. a) G. Kresse, J. Hafner, Ab initio molecular dynamics for liquid metals, *Phys. Rev. B* 1993, 47, 558; b) G. Kresse, J. Hafner, Ab initio molecular-dynamics simulation of the liquid-metal-amorphous-semiconductor transition in germanium, *Phys. Rev. B* 1994, 49, 14251; c) G. Kresse, J. Furthmüller, Efficiency of ab-initio total energy calculations for metals and semiconductors using a plane-wave basis set, *Comput. Mat. Sci.* 1996, 6, 15; d) G. Kresse, J. Furthmüller, Efficient iterative schemes for ab initio total-energy calculations using a plane-wave basis set, *Phys. Rev. B* 1996, 54:11169; e) P. E. Blöchl, O. Jepsen, O. K. Andersen, Improved tetrahedron method for Brillouin-zone integrations, *Phys. Rev. B* 1994, 49, 16223–16233.
36. P. R. Varadwaj, H. M. Marques, The physical chemistry of coordinated aqua-, ammine-, and mixed-ligand Co^{2+} complexes: DFT studies on the structure, energetics, and topological properties of the electron density, *Phys.Chem. Chem. Phys*. 2010, 12, 2126-2138.
37. A. Varadwaj, P. R. Varadwaj, Can a Single Molecule of Water be Completely Isolated Within the Subnano□Space Inside the Fullerene C60 Cage? A Quantum Chemical Prospective, *Chem. Euro. J*. 2012, 18, 15345-15360.
38. P. R. Varadwaj, A. Varadwaj, H. M. Marques, DFT-B3LYP, NPA-, and QTAIM-based study of the physical properties of [M (II)(H2O) 2 (15-crown-5)](M= Mn, Fe, Co, Ni, Cu, Zn) complexes, *J. Phys. Chem. A* 2011, 115, 5592-5601.
39. J. A. Pople, The Lennard-Jones lecture. Intermolecular binding, *Faraday Discuss* 1982, 73, 7 – 17.
40. J. W. Ochterski, Thermochemistry in Gaussian, 2000; this document is available via: http://web.thu.edu.tw/ghliu/www/pdf/thermo.pdf
41. Ł. M. Mentel, E. J. Baerends, Can the Counterpoise Correction for Basis Set Superposition Effect Be Justified? *J. Chem. Theory Comput*. 2014, 10, 252–267.
42. Y. Ren, I. W. H. Oswald, X. Wang, G. T. McCandless, J. Y. Chan, Orientation of organic cations in hybrid inorganic-organic perovskite $CH_3NH_3PbI_3$ from subatomic resolution single crystal neutron diffraction structural studies. *Cryst. Growth Design*, 2016, 16, 2945-2951.
43. C. Quarti, E. Mosconi, J. M. Ball, V. D'Innocenzo, C. Tao, S. Pathak, H. J. Snaith, A. Petrozza, F. De Angelis, Structural and optical properties of methylammonium lead iodide across the

tetragonal to cubic phase transition: implications for perovskite solar cells, *Energy Environ. Sci.*, 2016, 9, 155.

44. F. Brivio, J. M. Frost, J. M. Skelton, A. J. Jackson, O. J. Weber, M. T. Weller, A. R. Goni, A. M. A. Leguy, P. R. F. Barnes, A. Walsh, Lattice dynamics and vibrational spectra of the orthorhombic, tetragonal, and cubic phases of methylammonium lead iodide, *Phys. Rev. B* 2015, 92, 144308.
45. A. Bernasconi, L. Malavasi, Direct evidence of permanent octahedra distortion in $MAPbBr_3$ hybrid perovskite, *ACS Energy Lett.*, 2017, 2, 863–868.
46. L. Z. Tan , Fan Zheng, and Andrew M. Rappe, Intermolecular interactions in hybrid perovskites understood from a combined density functional theory and effective hamiltonian approach, *ACS Energy Lett*., 2017, 2, 937–942
47. S. Sanvito, C. Motta, F. El-Mellouhi, Waltzing molecules for high-efficiency photovoltaics, *SPIE Newsroom*, 2015, DOI: 10.1117/2.1201509.006060.
48. I. Borriello, G. Cantele, D. Ninno, Ab initio investigation of hybrid organic-inorganic perovskites based on tin halides, *Phys. Rev. B*, 2008, 77, 235214.
49. L. D. Whalley, J. M. Frost, Y.-K. Jung, A. Walsh, Perspective: Theory and simulation of hybrid halide perovskites, *J. Chem. Phys*. 2017 146, 220901.
50. F. Brivio, A. B. Walker, A. Walsh, Structural and electronic properties of hybrid perovskites for high-efficiency thin-film photovoltaics from first-principles, *APL Mater*. 2013, 1, 042111.
51. Y. Wang, N. Song, L. Feng, X. Deng, Effects of Organic Cation Additives on the Fast Growth of Perovskite Thin Films for Efficient Planar Heterojunction Solar Cells, *ACS Appl. Mater. Interfaces* 2016, 8, 24703–24711.
52. M. Salado, L. Calio, R. Berger, S. Kazim, S. Ahmad, Influence of the mixed organic cation ratio in lead iodide based perovskite on the performance of solar cells, *Phys Chem Chem Phys*. 2016 18, 27148-27157.
53. E. Mosconi, A. Amat, Md. K. Nazeeruddin, M. Grätzel, F. De Angelis, First-Principles Modeling of Mixed Halide Organometal Perovskites for Photovoltaic Applications, *J. Phys. Chem. C*, 2013, 117, 13902–13913.
54. E. Mosconi, C. Quarti, T. Ivanovska, G. Ruani, F. De Angelis, Structural and electronic properties of organo-halide lead perovskites: a combined IR-spectroscopy and ab initio molecular dynamics investigation, *Phys. Chem. Chem. Phys.*, 2014,16, 16137-16144.
55. A. M. A. Leguy, *et al.*, The dynamics of methylammonium ions in hybrid organic–inorganic perovskite solar cells, *Nat.Commun.* 2015, 6, 7124, doi:10.1038/ncomms8124.
56. J. Berry, *et al.*, Hybrid Organic–Inorganic Perovskites (HOIPs): Opportunities and Challenges, *Adv. Mater*. 2015, 27, 5102–5112.
57. F. Zheng, D. Saldana-Greco, S. Liu, A. M. Rappe, Material Innovation in Advancing Organometal Halide Perovskite Functionality, *J. Phys. Chem. Lett.*, 2015, 6, 4862–4872.
58. G. R. Berdiyorov, F. El-Mellouhi, M. E. Madjet, F. H. Alharbi, S. N. Rashkeev, Electronic transport in organometallic perovskite $CH_3NH_3PbI_3$: The role of organic cation orientations, *Appl. Phys. Lett.* 2016, 108, 053901.
59. T. Chen, B. J. Foley, C. Park, C. M. Brown, L. W. Harriger, J. Lee, J. Ruff, M. Yoon, J. J. Choi, S.-H. Lee, Entropy-driven structural transition and kinetic trapping in formamidinium lead iodide perovskite, *Sci. Adv.*, 2016, 2, e1601650 DOI: 10.1126/sciadv.1601650.

60. G. Kieslich, A. L. Goodwin, The same and not the same: molecular perovskites and their solid-state analogues, *Mater. Horiz.* 2017, 4, 362-366.
61. A. Jain, S.P. Ong, G. Hautier, W. Chen, W.D. Richards, S. Dacek, S. Cholia, D. Gunter, D. Skinner, G. Ceder, K.A. Persson, The Materials Project: A materials genome approach to accelerating materials innovation, *APL Materials*, 2013, 1, 011002.
62. G. Giorgi, J.-I. Fujisawa, H. Segawa, K. Yamashita, Cation Role in Structural and Electronic Properties of 3D Organic–Inorganic Halide Perovskites: A DFT Analysis, *J. Phys. Chem. C*, 2014, 118, 12176–12183.
63. A. Walsh, Principles of Chemical Bonding and Band Gap Engineering in Hybrid Organic–Inorganic Halide Perovskites, *J. Phys. Chem. C*, 2015, 119, 5755–5760.
64. A. Varadwaj, P. R. Varadwaj, K. Yamashita, On the ability of density functionals in predicting the physical properties of the $CH_3NH_3PbI_3$ perovskite nanoclusters, 2017 (To be submitted soon).
65. E. Arunan, *et al.*, Definition of the hydrogen bond (IUPAC Recommendations 2011), *Pure Appl. Chem.* 2011, 83, 1637–1641.
66. E. Arunan, Definitions of a hydrogen bond. This is available via: http://ipc.iisc.ernet.in/~arunan/iupac/iupac/Definition_of_HydrogenBond.pdf (last retrieved on June 19, 2017); References therein.
67. G. R. Desiraju, *et al.*, Definition of the halogen bond (IUPAC Recommendations 2013), *Pure Appl. Chem.* 2013, 85, 1711-1713.
68. A. Varadwaj, P.R. Varadwaj, B.-Y Jin, Fluorines in tetrafluoromethane as halogen bond donors: Revisiting address the nature of the fluorine's σ_{hole}, *Int. J. Quantum Chem.* 2015, 115, 453-470.
69. P.R. Varadwaj, A. Varadwaj, B.-Y. Jin, Halogen bonding interaction of chloromethane with several nitrogen donating molecules: addressing the nature of the chlorine surface σ-hole, *Phys. Chem. Chem. Phys.* 2014, 16, 19573-19589.
70. P. R. Varadwaj, A. Varadwaj, B.-Y. Jin, Unusual bonding modes of perfluorobenzene in its polymeric (dimeric, trimeric and tetrameric) forms: entirely negative fluorine interacting cooperatively with entirely negative fluorine, *Phys. Chem. Chem. Phys.* 2015, 17, 31624-31645.
71. A. Varadwaj, P.R. Varadwaj, B.-Y Jin, Can an entirely negative fluorine in a molecule, viz. perfluorobenzene, interact attractively with the entirely negative site (s) on another molecule (s)? Like liking like! *RSC Adv.* 2016, 6, 19098-19110.
72. M. L. Huggins, Electronic Structures of Atoms, *J. Phys. Chem.*, 1922, 26, 601–625.
73. G. R. Desiraju, A bond by any other names, *Angew. Chem. Int. Ed.* 2011, 50, 52–59.
74. G. P. Schiemenz, The Sum of van der Waals Radii – A Pitfall in the Search for Bonding, Z. *Naturforsch.* 2007, 62b, 235 – 243.
75. P. Politzer, P. R. Laurence, K. Jayasuriya, Molecular electrostatic potentials: an effective tool for the elucidation of biochemical phenomena, *Environ Health Perspect* 1985, 61, 191–202.
76. P. Politzer, J. S. Murray, T. Clark, Halogen bonding and other σ-hole interactions: A perspective, *Phys. Chem. Chem. Phys*. 2013, *15*, 11178–11189.
77. P. Politzer, J. S. Murray, T. Clark, Halogen bonding: An electrostatically-driven highly directional noncovalent interaction, *Phys. Chem. Chem. Phys.* 2010, 12, 7748–7757.
78. P. Politzer, J. S. Murray, Halogen bonding: An interim discussion. *Chem. Phys. Chem.* 2013, 14, 278–294.

79. T. Clark, M. Hennemann, J. S. Murray, P. Politzer, Halogen bonding: The σ-hole. *J. Mol. Model*. 2007, *13*, 291–296.
80. a) G. V. Gibbs, O. Tamada, M. B. Boisen Jr., F. C. Hill, Laplacian and bond critical point properties of the electron density distributions of sulfide bonds: A comparison with oxide bonds, *Am. Mineralog.* 1999, 4, 435–446; b) C. F. Matta, A. A. Arabi, Electron-density descriptors as predictors in quantitative structure--activity/property relationships and drug design, *Future. Med. Chem.* 2011, 969-94.
81. R. F. W. Bader, T. T. Nguyen-Dang, and Y. Tal, A *topological theory* of molecular structure, *Rep. Prog. Phys.* 1981, 44, 893 948.
82. R. F. W. Bader, Atoms in Molecules, http://www.wiley.com/legacy/wileychi/ecc/samples/sample02.pdf.
83. a) The classification of tilted octahedra in perovskites A. M. Glazer, *Acta Cryst*. 1972, B28, 3384-3392; b) X.-Z. Li, B. Walker, A. Michaelides, Quantum nature of the hydrogen bond, *Proc. Natl. Acad. Sci. USA*. 2011, 108, 6369–6373.
84. P. de Silva, C. Corminboeuf, Simultaneous Visualization of Covalent and Noncovalent Interactions Using Regions of Density Overlap, *J. Chem. Theory Comput.*, 2014, 10, 3745–3756.
85. J. Lekner, Electrostatics of two charged conducting spheres, *Proc. R. Soc. A* 2012, 468, 2829–2848.
86. P. Ball, Like attracts like? Everything you thought you knew about electrostatics is probably wrong, *Nature* doi:10.1038/nature.2012.10698.
87. S. Kawai, A. Sadeghi, F. Xu, L. Peng, A. Orita, J. Otera, S. Goedecker, E. Meyer, Extended Halogen Bonding between Fully Fluorinated Aromatic Molecules, *ACS Nano* 2015, 9, 2574–2583.
88. H. Fang P. Jena, $B_{12}(SCN)_{12}^{-}$: An ultrastable weakly coordinating dianion, *J. Phys. Chem. C*, 2017, 121, 7697–7702.
89. T. Zhao, J. Zhou, Q. Wang, P. Jena, Like Charges Attract? *J. Phys. Chem. Lett.* 2016, 7, 2689–2695.
90. S. Alvarez, A cartography of the van der Waals territories, *Dalton Trans.* 2013, 42, 8617-8636.
91. P. A. Kollman, Theory of hydrogen bond directionality, *J. Am. Chem. Soc.*, 1972, 94, 6, 1837–1842.
92. M. R Scholfield, C. M V. Zanden, M. Carter, P Shing Ho, Halogen bonding (X-bonding): A biological perspective *Protein Sci*. 2013 Feb; 22(2): 139–152.
93. S. Z.Borozana, S. Stojanovic, Halogen bonding in complexes of proteins and non-natural amino acids, *Computat. Bio. Chem*. 2013, 47, 231.
94. G. Cavallo, P. Metrangolo, R. Milani, T. Pilati, A. Priimagi, G. Resnati, G. Terraneo, The halogen bond, *Chem. Rev.* 2016, 116, 2478–2601.
95. S. W.L. Hogan, T. van Mourik, Competition between hydrogen and halogen bonding in halogenated 1- methyluracil:water systems, *J. Comput. Chem.* 2016, 37, 763 – 770.
96. A. Wei Li, A. Thirumurugan, P. T. Barton, Z. Lin, S. Henke, H. H.-M. Yeung, M. T. Wharmby, E. G. Bithell, C. J. Howard, A. K. Cheetham, Mechanical Tunability via Hydrogen Bonding in Metal–Organic Frameworks with the Perovskite, *J. Am. Chem. Soc.* 2014, 136, 7801–7804.
97. L. K. Boerner, Spotlights on Recent JACS Publications, *J. Am. Chem. Soc*. 2014, 136, 7783−7784.

98. G. R. Desiraju, T. Steiner, The weak hydrogen bond: In structural chemistry and biology, Oxford University Press: Oxford and New York. 1999.
99. G. R. Desiraju, Hydrogen Bridges in Crystal Engineering: Interactions without Borders, *Acc. Chem. Res*. 2002, 35, 565–573.
100. G. A. Jeffrey, W. Saenger, Hydrogen Bonding in Biological Structures; Springer: Berlin, Germany, 1991.
101. G. A. Jeffrey, An introduction to hydrogen bonding, Oxford University Press: New York, 1997.
102. T. Steiner, The Hydrogen Bond in the Solid State, *Angew Chem. Int. Edn*. 2002, 41, 48 – 76.
103. G. Gilli, P. Gilli, The Nature of the Hydrogen Bond; Oxford University Press Inc.: New York, NY, USA, 2009.
104. S. Scheiner, Hydrogen Bonding a Theoretical Perspective; Oxford University Press Inc.: New York, NY, USA, 1997.
105. S. J. Grabowski, Ed.; Hydrogen Bonding—New Insights; Springer: Dordrecht, The Netherlands, 2006.
106. H. Szatyłowicz, Structural aspects of the intermolecularhydrogen bond strength: H-bondedcomplexes of aniline, phenol andpyridine derivatives, *J. Phys. Org. Chem*.2008, 21 897–914.
107. R. Parthasarathi, V. Subramanian, N. Sathyamurthy, Hydrogen Bonding without Borders: An Atoms-in-Molecules Perspective *J. Phys. Chem. A*, 2006, 110, 3349–3351.
108. A. V. Afonin, A. V. Vashchenkoa, M. V. Sigalov, Estimating the energy of intramolecular hydrogen bonds from 1H NMR and QTAIM calculations, *Org. Biomol. Chem.*, 2016, 14, 11199-11211.
109. SAPT: SYMMETRY-ADAPTED PERTURBATION THEORY, http://www.psicode.org/psi4manual/master/sapt.html (last retrieved on June 20, 2017).
110. Psi4: An open-source *ab initio* electronic structure program," J. M. Turney, A. C. Simmonett, R. M. Parrish, E. G. Hohenstein, F. Evangelista, J. T. Fermann, B. J. Mintz, L. A. Burns, J. J. Wilke, M. L. Abrams, N. J. Russ, M. L. Leininger, C. L. Janssen, E. T. Seidl, W. D. Allen, H. F. Schaefer, R. A. King, E. F. Valeev, C. D. Sherrill, and T. D. Crawford, *WIREs Comput. Mol. Sci.* 2012, **2**, 556.
111. a) B. Wang, W. Jiang, X. Dai, Y. Gao, Z. Wang, R.-Q. Zhang, Molecular orbital analysis of the hydrogen bonded water dimer, *Sci. Rep.* 2016, 6, 22099; b) V. L. Deringer, U. Englert, R. Dronskowski, Covalency of hydrogen bonds in solids revisited, *Chem. Commun*., 2014,50, 11547-11549.
112. H. Elgabarty, R. Z. Khaliullin, T. D. Kühnea, Covalency of hydrogen bonds in liquid water can be probed by proton nuclear magnetic resonance experiments, *Nat. Commun.* **2015**, 6, 8318.
113. Shigeki Kawai, Tomohiko Nishiuchi, Takuya Kodama, Peter Spijker, Rémy Pawlak, Tobias Meier, John Tracey, Takashi Kubo, Ernst Meyer, Adam S. Foster. Direct quantitative measurement of the C═O···H–C bond by atomic force microscopy, *Sci. Adv.* 2017, 3, e1603258.
114. G. R. Desiraju, The C−H···O Hydrogen Bond: Structural Implications and Supramolecular Design, *Acc. Chem. Res*., 1996, 29, 441–449.

115. P. Baillargeon, É. Caron-Duval, É. Pellerin, S. Gagné, Y. L. Dory, Isomorphous Crystals from Diynes and Bromodiynes Involved in Hydrogen and Halogen Bonds, *Crystals* 2016, 6, 37.
116. C. F. Matta, R. J. Boyd, The Quantum Theory of Atoms in Molecules: From Solid State to DNA and Drug Design, 2007 Wiley-VCH Verlag GmbH & Co. KGaA.
117. N. Castillo, C. F. Matta, R. J. Boyd, The first example of a cage critical point in a single ring: A novel twisted [alpha]-helical ring topology, *Chem. Phys. Lett*. 2005, 409, 265-269.
118. R. F. W. Bader, A Bond Path: A Universal Indicator of Bonded Interactions Department of Chemistry, *J. Phys. Chem. A*, 1998, 102, 7314–7323.
119. R. F. W. Bader, Bond Paths Are Not Chemical Bonds *J. Phys. Chem. A*, 2009, 113, 10391–10396.
120. M. A. Blanco, A. M. Pendás, E. Francisco, Interacting, Quantum Atoms: A Correlated Energy Decomposition Scheme Based on the Quantum Theory of Atoms in Molecules, *J. Chem. Theory Comput.* 2005, 1, 1096–1109.
121. S. J. Grabowski, What Is the Covalency of Hydrogen Bonding? *Chem. Rev*., 2011, 111, 2597–2625.
122. a) V. Tognetti, L. Joubert, On the use of Bader's atomic charges for the evaluation of charge transfers between ground and excited states, *Chem. Phys. Lett.* 2013, 557, 150 – 153; b) R. F. W. Bader, C. F. Matta, Atomic charges are measurable quantum expectation values: A rebuttal of criticisms of QTAIM charges, *J. Phys. Chem. A* 2004, 108, 8385–8394; c) M. E. Madjet, F. El-Mellouhi, M. A. Carignano, G. R. Berdiyorov, Atomic partial charges on $CH_3NH_3PbI_3$ from first-principles electronic structure calculations, *J. Chem. Phys.* 2016, 119, 165501.
123. Mutual polarization of monomer charge distribution in $(HCN)_2$, $(HCN)_3$, and $(HCN)_\infty$ (HW, R. S. Ruof *J. Chem. Phys*. 1991, 94, 2717.
124. P. Politzer, J. S. Murray, A unified view of halogen Bonding, hydrogen bonding and other σ-hole interactions, in: S. Scheiner (ed.), Noncovalent Forces, Challenges and Advances in Computational Chemistry and Physics 2015, 19, DOI 10.1007/978-3-319-14163-3_10.
125. P. Politzer, J. S. Murray, M. C. Concha, Sigma-hole bonding between like atoms; a fallacy of atomic charges, *J. Mol. Model.* 2008, 14, 659-65.
126. Partial atomic charge. A documentation in Wiki, available at: https://en.wikipedia.org/wiki/Partial_charge (last retrieved on June 21, 2017).
127. a) S. Shan, D. Herschlag, The change in hydrogen bond strength accompanying charge rearrangement: Implications for enzymatic catalysis, *Proc. Natl. Acad. Sci. USA.* 1996, 93, 14474–14479; b) A. C. Legon, Nature of complexes B … ClF in the gas phase: Conclusions from systematic variation of the Lewis base B and a comparison of the B … ClF/B … HCl series, *Chem. Phys. Lett*. 1997, 279, 55 – 64.
128. R. S. Mulliken, W. B. Person, Molecular complexes, a lecture and reprint volume, Wiley, New York, 1969.
129. Electron-driven acid-base chemistry: Proton transfer from hydrogen chloride to ammonia, *Science* 2008, 319, 936-939.
130. F. L. Hirshfeld, Bonded-atom fragments for describing molecular charge densities, *Theor. Chim. Acta.* 1977, 44, 129.
131. a) T. Clark, J. S. Murray, P. Politzer, Role of polarization in halogen bonds, *Aust. J. Chem.* 2014, 67, 451–456; b) T. Clark, J. S. Murray, P. Politzer, Correct electrostatic treatment of

noncovalent interactions: the importance of polarization, *WIREs Comp. Mol. Sci.* 2015, DOI: 10.1002/wcms.1210.
L. She, M. Liu, D. Zhong, Atomic Structures of $CH_3NH_3PbI_3$ (001) Surfaces, *ACS Nano*, 2016, 10, 1126–1131.

Chapter 5. The Chemistry of the Organic Cation in $CH_3NH_3PbI_3$

5.1 Introduction

Hybrid organic-inorganic methylammonium lead triiodide (hereafter $CH_3NH_3PbI_3$, or $MAPbI_3$) is one of the massively studied composite systems within the last four years (from 2013 to 2017).[1] It is believed to be a rising star for making highly efficient photovoltaic solar cells.[2] This believe lies in its strong ability to convert the photonic energy into electricity.[3] Because of this, it has often been demonstrated that it has created an outstanding record of its power conversion efficiency compared to numerous other photovoltaic semiconductors.[4] Despite the material is very sensitive to the environmental ingredients,[5] experimentalists hope and are trying their levels best to develop technology-based strategies to commercialize the $MAPbI_3$ system as an efficient future semiconductor device for energy conversion from the renewable (sun light).[6]

Innumerous experimental studies have already been performed for the $CH_3NH_3PbI_3$ system and for its other halogen derivatives comprising Cl and Br.[7-8] These studies have revealed various specialized properties for these materials, [9] excellent for photovoltaic applications.[10-11] Apart from their low bandgaps covering the visible region,[10] a few of these special properties include the small exciton binding energy (~ 16 meV),[11] small effective electron and hole masses,[12] high charge carrier mobilities (mobility of electrons to be in the range 5–10 $cm^2V^{-1}s^{-1}$ and that for holes to be in the range 1–5 $cm^2V^{-1}s^{-1}$),[13] abnormally low bimolecular recombination,[14] the giant dielectric constant,[15] and so on. Many of these properties were also theoretically examined for $CH_3NH_3PbX_3$ (X = Cl, Br, I), including the mixed trihalide analogues. Additional physical insights into the electronic structures of these materials have also gained by scrutinizing their band structures, the DOS spectra and various other optoelectronic properties. [16] Although these calculations are not very expensive for the bulk, they are computationally very demanding when the bulks are used for the construction of supercell models comprising a few hundreds of atoms.[16]

Among the known trihalide perovskites, $CH_3NH_3PbI_3$ has the ability in making efficient and cheap photovoltaic devices. It has generated numerous attention due to the fact that its geometry experiences both first and second order phase transitions with respect to the change of the temperature.[17-18] For instance, its geometry is stable below 162 K that belongs to the orthorhombic phase (space group symmetry, *Pnma*). Beyond this temperature, first order phase transition occurs. In this phase, its geometry is tetragonal, which remains stable in the temperature 162 – 327 K range (space group symmetry, *I4/mcm*). With further increase of the temperature (> 327 K), second order

phase transition occurs. It then adopts a pseudocubic geometry with *Pm3̄m* space group symmetry.[17-18]

Nevertheless, with a view to understand the physical chemistry and optical physics of the hybrid organic-inorganic perovskite bulk systems from their corresponding molecular building blocks, Fang *et al.* have performed first-principles exploration for over forty perovskite blocks in zero-dimension.[19] They have demonstrated that the electronic properties, including the bandgap, the gap deformation potential, and the exciton binding energy as well as the chemical stability of organic–inorganic hybrid perovskites can be traced back to their corresponding molecular motifs. Also, the study has shown that when the halogen atoms (*e.g.* I) are sequentially replaced with superhalogen (*e.g.* BH_4) the bandgap and exciton binding energy increase monotonically with the superhalogen content, with the exciton binding energy of the $(C_4H_9NH_3)_2Pb(BH_4)_4$ system approaching the value close to that expected for the monolayer black phosphorus. The corresponding lead-free admixtures $(C_4H_9NH_3)_2MI_{4-x}(BH_4)_x$ (M = Sn and Ge; x = 0–4) have also displayed the same feature. From these findings, it has thus been concluded that a combination of quantum confinement and compositional change can be used as an effective strategy to tailor the bandgap and the exciton binding energy of two-dimensional hybrid perovskites, making them promising candidates for optoelectronic applications.[19b)] Theoretical studies on similar perovskite systems, but with different research objectives have been reported recently. [19c,20]

According to Green *et al.*, [6b] *photon conversion efficiency over 22% was confirmed in early 2016 for* $MAPbI_3$*. However, it should not be forgotten that some of these record devices will maintain their record-breaking performance for periods that may be as short as 10 min. Good progress on the efficiency front since then has been made with both all perovskite and perovskite/silicon tandem cells, with confirmed efficiencies of 23.6% demonstrated for the latter*.

From a recent conversation of Grätzel with the Editors of *ACS Energy Letters*, [6c] it has been apparent that perovskite systems as light-harvesters are very promising. According to him, a pretty long testing period is ahead of us, and perhaps in next 5 years we will have mature perovskite systems that can be put on the market.

In this study, we have performed first-principles density functional theory calculations with a pure-GGA type functional, PBEPBE, to explore the electronic structures of the $CH_3NH_3PbI_3$ molecular building block in zero-dimension and the $[MAPbI_3]_{n=2-15}$ chain-like systems in one-dimension. Toward these calculations, we have aimed at answering four fundamentally important questions for the simplistic physical understanding of the topological aspects of $CH_3NH_3PbI_3$. Q1: Can $CH_3NH_3PbI_3$ in its molecular/complex form be comparable with any of its solid state analogues? Q2: What is the role of the methylammonium organic cation (hereafter MA, or $CH_3NH_3^+$) in the design of the supramolecular $CH_3NH_3PbI_3$ system? Q3: What physical principle of operation would drive the molecular building blocks to self-assemble together, leading to the formation of the $CH_3NH_3PbI_3$ chain-like architectures in 1D and so on? Q4: Can there

be any structure-property relationship anticipated between the electronic structures of the $[MAPbI_3]_{n=1-15}$ systems and their corresponding energetic, electronic and orbital properties?

5.2 Computational details

Gaussian 09[21] and Gaussview 05[22] codes were utilized for the electronic structure calculations and visualizations of the geometries and vibrational normal mode frequencies of the zero- and one-dimensional clusters of $CH_3NH_3PbI_3$, respectively. Both tight convergence and ultrafine integration grid were invoked. The combination of the PBEPBE functional with the DZP basis set was employed for the all electronic structure calculations conducted. The selection of the basis set is due to the fact that i) it is a good compromise between time and accuracy of results obtained, ii) it is one among a few *all-electron* correlation consistent basis sets available in the EMSL basis set exchange library, [23] and our current exploration suggests that iii) its combination with the PBEPBE functional produces relatively smaller HOMO-LUMO fundamental gap for $[MAPbI_3]$ compared to those produced by several other basis sets,[24] where the terms HOMO and LUMO represents to the highest occupied and lowest unoccupied molecular orbitals, respectively.

5.3 Results and Discussions

5.3.1 The geometries

Fig. 1a illustrates the molecular building block of $[MAPbI_3]$ in 0D. It is the consequence of the attractive engagement between PbI_3^- and MA. It is the same stable 0D dimer exploited previously using M06-2X/ADZP. [20c] This is recently shown to be predominantly stabilized by Coulomb-type electrostatic attraction, which is strong enough to overcome the repulsive effect arising from exchange repulsion. The energy contributions arising from polarization and dispersion are shown to be additive, [26] enhancing substantially the overall energy of stabilization for this system. This was perhaps the reason, for which, it was claimed that the intermolecular hydrogen bonding interaction between organic and inorganic fragments conceives significant covalent component in addition to the inherent contribution from electrostatics.

The bulk form of $[MAPbI_3]$ is depicted in Fig. 2a. As indicated in Introduction, the bulk has indeed assisted us to construct various size-constricted $1\times1\times n$ (n = 2–15) chain models in 1D through periodic boundary condition.[25] Figs. 2b-c, for example, represent the $(1\times1\times5)$ nanowire of $MAPbI_3$ in 1D. For these, the Pb–I–Pb angles are almost linear ($\angle$Pb–I–Pb $\approx 180^o$) since there is negligible octahedral tilting. [35]

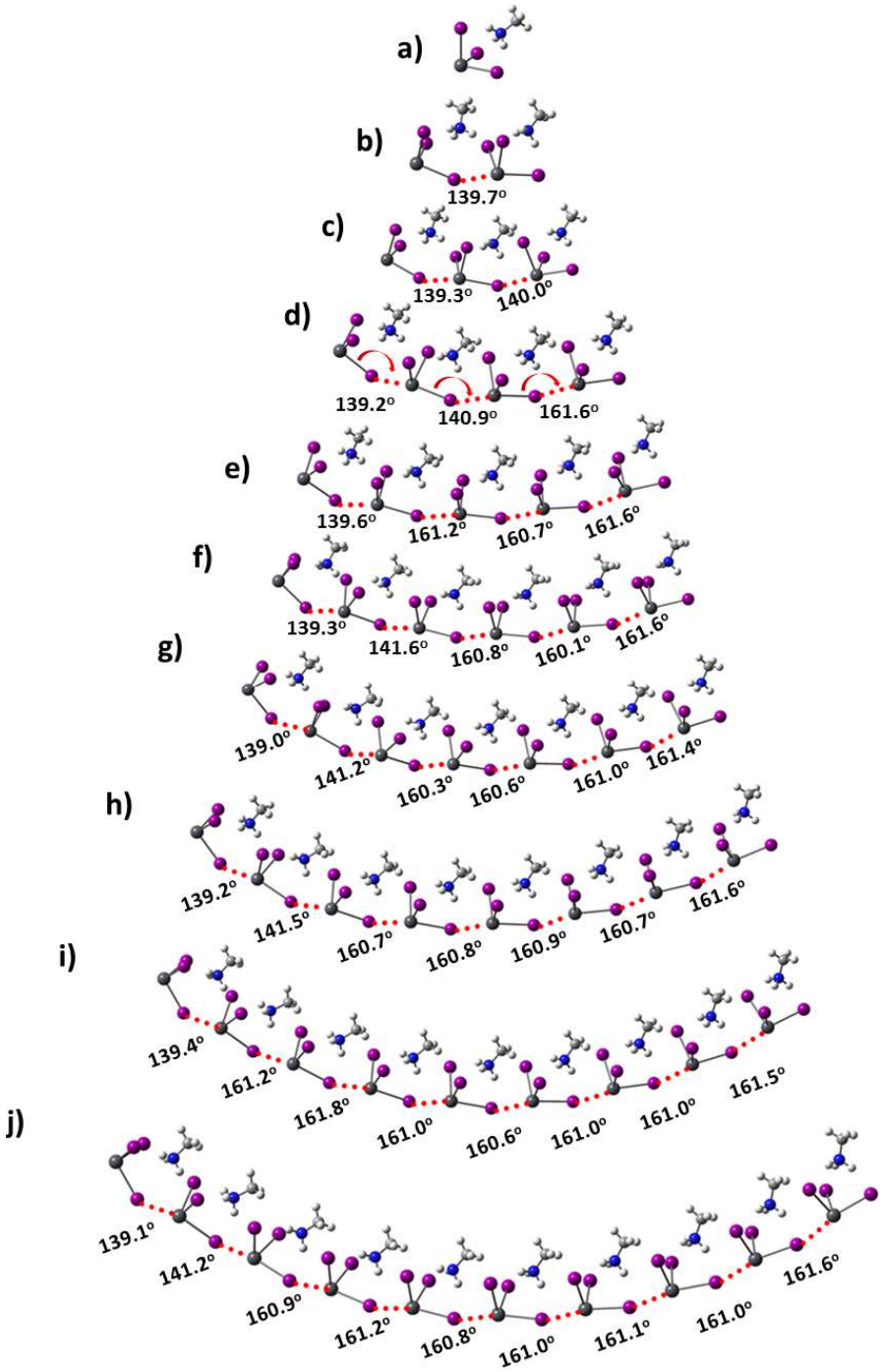

Fig. 1: PBEPBE/DZP energy-minimized geometries for $[MAPbI_3]_{n=1–10}$. Except for a), the Pb–I–Pb tilting angles are shown for the remaining geometries. The dotted line in red represents the link between the $MAPbI_3$ subunits in each cluster. The Pb–I bond distances are all computed to lie in the 3.00 – 3.46 Å range, in agreement with the experimental range of values lying between 3.00 and 3.330 Å. [18,39]

The geometries of $[MAPbI_3]_{n=2-15}$ energy-minimized with PBEPBE/DZP are illustrated in Figs. 1b-j. For each $[MAPbI_3]_{n\ =\ 2-15}$, the $CH_3NH_3^+$ cation is in its staggered form, similarly as found experimentally. [35b, 36] In all these cases, the $–NH_3$ group in MA is pointing towards the triangular face formed by the three coordinated iodides of the corner sharing PbI_3^- anion. The orientation of $CH_3NH_3^+$ ion inside the cell is such that the CN bond coincides with the [111] direction. Ren *et al.*,[39a] based on their high temperature measurements, have showed that for the pseudocubic structure the $CH_3NH_3^+$ aligns along the [111] (diagonal), the [011] (edge), and the [100] (face) directions of the unit cell, answering Q1.

Fig. 3 illustrates schematics for the crystallographic geometries of the three major phases of $MAPbI_3$. These are referred to as orthorhombic, tetragonal and pseudocubic.

The mean Pb–I bond distances in $MAPbI_3$ were experimentally reported to be 3.176(3) (orthorhombic, CSD ref code MAPBTI01), 3.174(0) (tetragonal, CSD ref code MAPBTI05), 3.161 (22) (tetragonal, CSD ref code MAPBTI03), 3.162 (2) (tetragonal, CSD ref code MAPBTI04), and 3.157(35) Å (pseudocubic, CSD ref code MAPBTI01). [29]

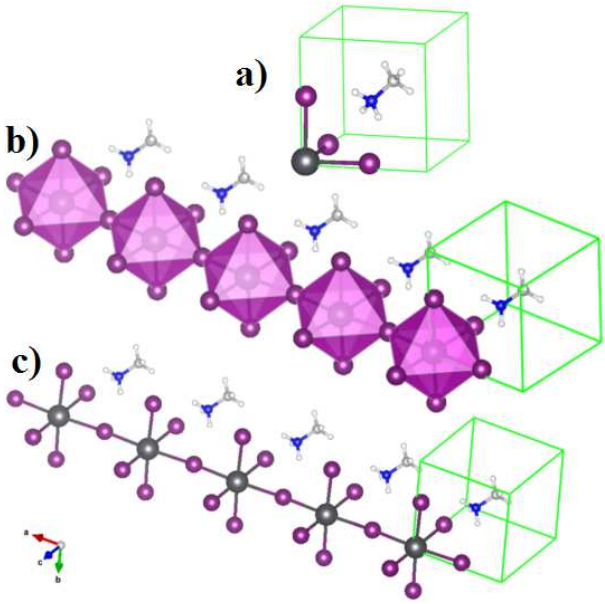

Fig. 2: a) The PBE/PAW relaxed geometry of the $MAPbI_3$ perovskite bulk in the pseudocubic phase (k-points: 6×6×6; cut-off energy 520 eV), obtained using VASP.[25] The polyhedra model in b) and the ball and stick model in c) represent to the same 1×1×5 nanowire system of $MAPbI_3$ in 1D, constructed using the bulk presented in a).

The calculated mean of the Pb–I coordinate bonds in $[MAPbI_3]$ block illustrated in Fig. 1a is ca. 3.011 Å. This is about 0.274 (0.146 Å) smaller than the corresponding value of 3.285 (3.157 Å) calculated (experimental) for the cubic geometry of the $MAPbI_3$ bulk. The discrepancy between these geometries is not very surprising.[27a-b] In the remaining $[MAPbI_3]_{n=2-15}$ systems, the computed mean Pb–I bond distance is somehow elongated compared to that found for the corresponding molecular building block. The values of these bond distances lie between 3.007 and 3.456 Å for all these systems, which are consequences of competitive hydrogen bonding environment.

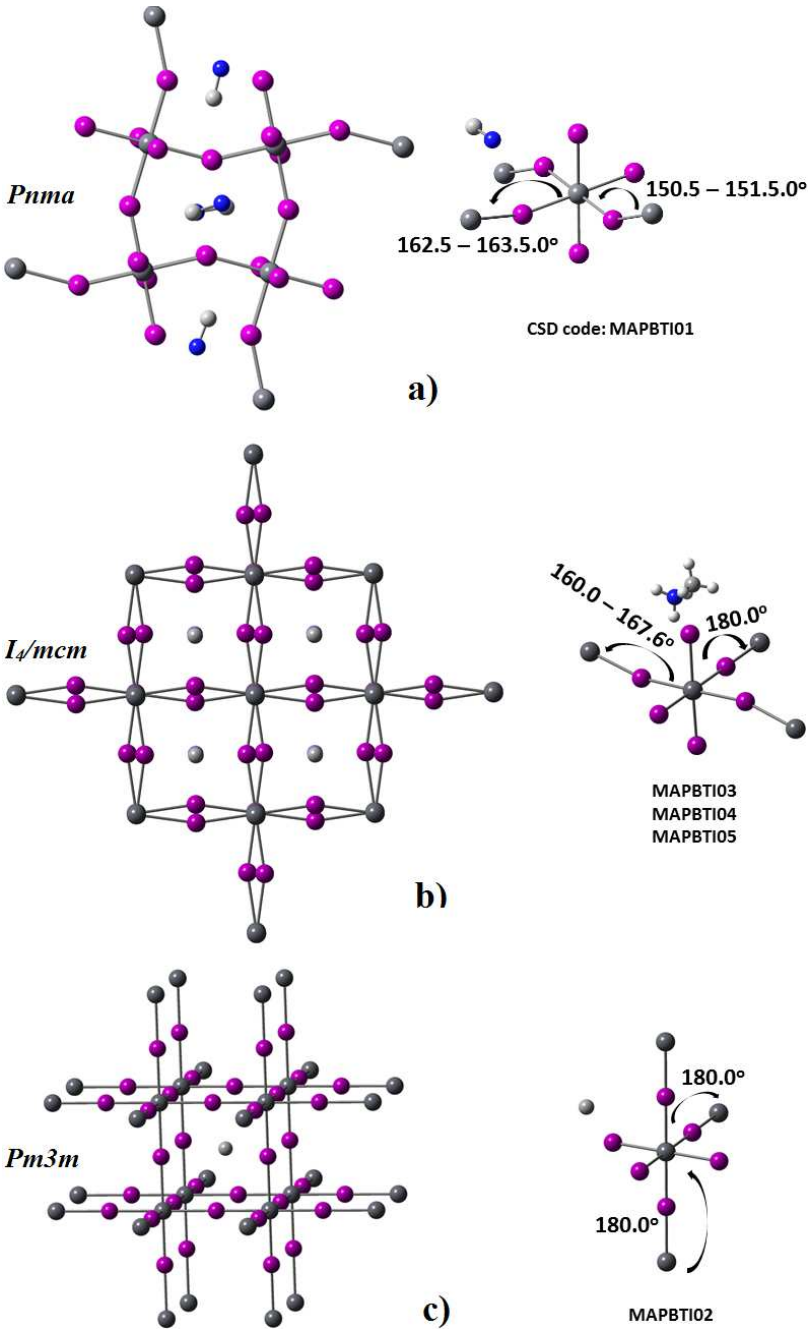

Fig. 3: Crystal geometries of the three major phases of $MAPbI_3$. a) Orthorhombic (< 162 K); b) Tetragonal (162 < T < 327 K); and c) Cubic (T > 327 K). The space group (left) and ∠Pb–I–Pb (right) are shown for each case. For clarity, the H atoms on the organic cation MA are not shown for cases. The reference codes catalogued in the Cambridge Structural Database (CSD) are displayed.[29]

The $[MAPbI_3]_2$ dimer was formed when two units of $[MAPbI_3]$ were in close

proximity, Fig. 1b. Its equilibrium geometry conceives the Pb–I•••Pb–I chain-like motif. The length of this motif is approximately 9.544 Å. The corner-sharing Pb–I•••Pb angle, which was absent in the [$MAPbI_3$] block geometry, is now developed. While it is linear in the 1×1×*2* supercell geometry of $MAPbI_3$, it is largely deviated from linearity in $[MAPbI_3]_2$. For instance, compared to the value of 180.0° for ∠Pb–I•••Pb in the 1×1×*5* perovskite geometry in 1D, it is roughly 40.0° reduced in the $[MAPbI_3]_2$ dimer. As a result, the ∠Pb–I•••Pb became bent, illustrating a clear distinction between cluster and supercell phenomena.

The Pb–I•••Pb angle in the orthorhombic and tetragonal phase geometries of $MAPbI_3$ observed in the solids state were also found to be titled. [17-18,39] However, it was pronounced in the former than in the latter phase. [39] For instance, at low temperature, the $CH_3NH_3^+$ cation was oriented in a particular direction in orthorhombic $CH_3NH_3PbI_3$, and this was confirmed by both experiment and calculation. The deviation of the ∠Pb–I•••Pb from linearity was attributed to what has been called as octahedral tilting, which can be understood by means of Glazer notation, [49] $a^-b^+a^-$. This is not indifferent from that can be expected for the corresponding system with (*Pm3m*) cubic symmetry ($a^0b^0c^0$) since in this latter case the corner-shared PbI_6^{4-} octahedra does not show any such tilting along the three directions, *a*, *b*, and *c*. In contrary, in the room-temperature tetragonal phase geometry of the system (*I4/mcm* space group) the PbI_6^{4-} octahedra do not show any such alternative tilting along the *a*- and *b*-axes as found for orthorhombic phase, but show out-of-phase tilting along the *c*-axis; in the Glazer's notation, this is in line with the $a^0a^0c^-$ tilt pattern.[35]

The successive additions of three, four, five, etc., blocks of $MAPbI_3$ around the $[MAPbI_3]_2$ dimer can lead to clustered geometries of various kinds. However, it is not possible to study everything in a single sort. As clarified in Introduction, we have focused only on a specific type of configuration that can be comparable with a similar configuration reported in the solid state. As such, we have centered only on the chain-like geometries of the $[MAPbI_3]_{n=2-15}$ in 1D, Fig. 1.

From Fig. 1, it is clear that as the size *n* in $[MAPbI_3]_n$ increases the overall length of the •••Pb–I•••Pb–I••• chain increases. Also, at the same time, the Pb–I•••Pb angle increases from a value of 139° to a value of 162°. For instance, for $[MAPbI_3]_2$, ∠Pb–I•••Pb ≈ 139.7°, Fig. 1b. As the size increases from *n* = 2 to *n* = 3, $[MAPbI_3]_3$ is formed. It accompanies with two ∠Pb–I•••Pb angles, one 139.3° and one 140.0°. A further increase of *n* from *n* = 3 to *n* = 4 has enabled the formation of the $[MAPbI_3]_4$ tetramer, Fig. 1d. It is accompanied with three ∠Pb–I•••Pb angles, 139.2, 140.9 and 161.6°. And, in the largest system examined, $[MAPbI_3]_{15}$, the first two Pb–I•••Pb angles (from left) are 139.0 and 140.8°, and the remaining twelve angles are varied between 160.2 and 161.7°. This pattern is actually evident of most of the long-chain $[MAPbI_3]_n$ systems,

with $5 < n \leq 15$. Clearly, the large variation between the Pb–I–Pb angles within the same chain system is due to the fact that this angle does dependent not only on the PbI_6^{4-} octahedra (missing in all clusters), but also on the nature of the local network of intermolecular hydrogen bonding interactions between the organic and inorganic fragments. This result also demonstrates that octahedral tilting is not just a solid state effect as often understood, rather it is a low-temperature effect that can be very distinct in the gas phase geometry. Knutson *et al.* have hypothesized that the titling angle is the dominant structural factor that controls the bandgap for the $[R–NH_3]SnI_4$ perovskite crystals, enabling the material for photovoltaic applications.[28] This perspective is in line with Lee *at al*.,[35a] who have enunciated that hydrogen bonding essentially plays a critical role in stabilizing octahedral tilts in hybrid perovskites such as $MAPbI_3$, which affects both bandgap and carrier masses, thereby a vital component for optimizing solar cell efficiency.

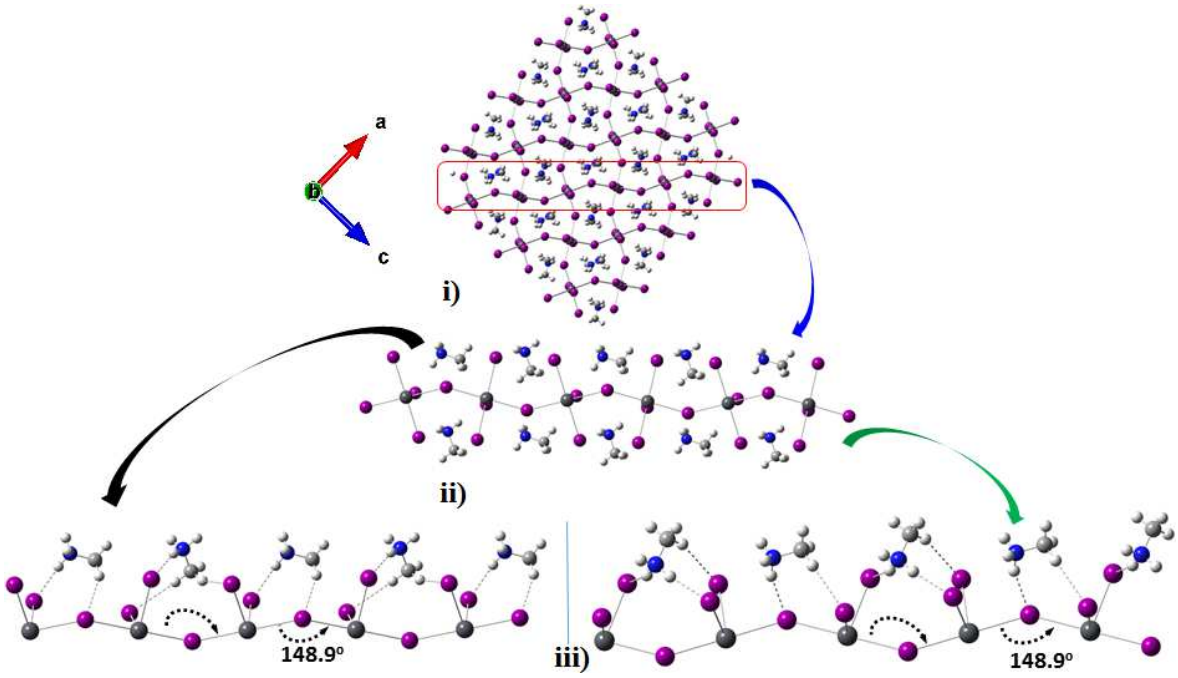

Fig 4: i) A view 3×2×3 supercell model for the orthorhombic (*Pnma*) relaxed geometry of $MAPbI_3$, with the unit cell geometry obtained from the materials project database. [30] Shown in ii) is the part of i) enclosed by the red rectangle. Shown in iii) are the neutral $[MAPbI_3]_5$, emerged from ii) through cuts.

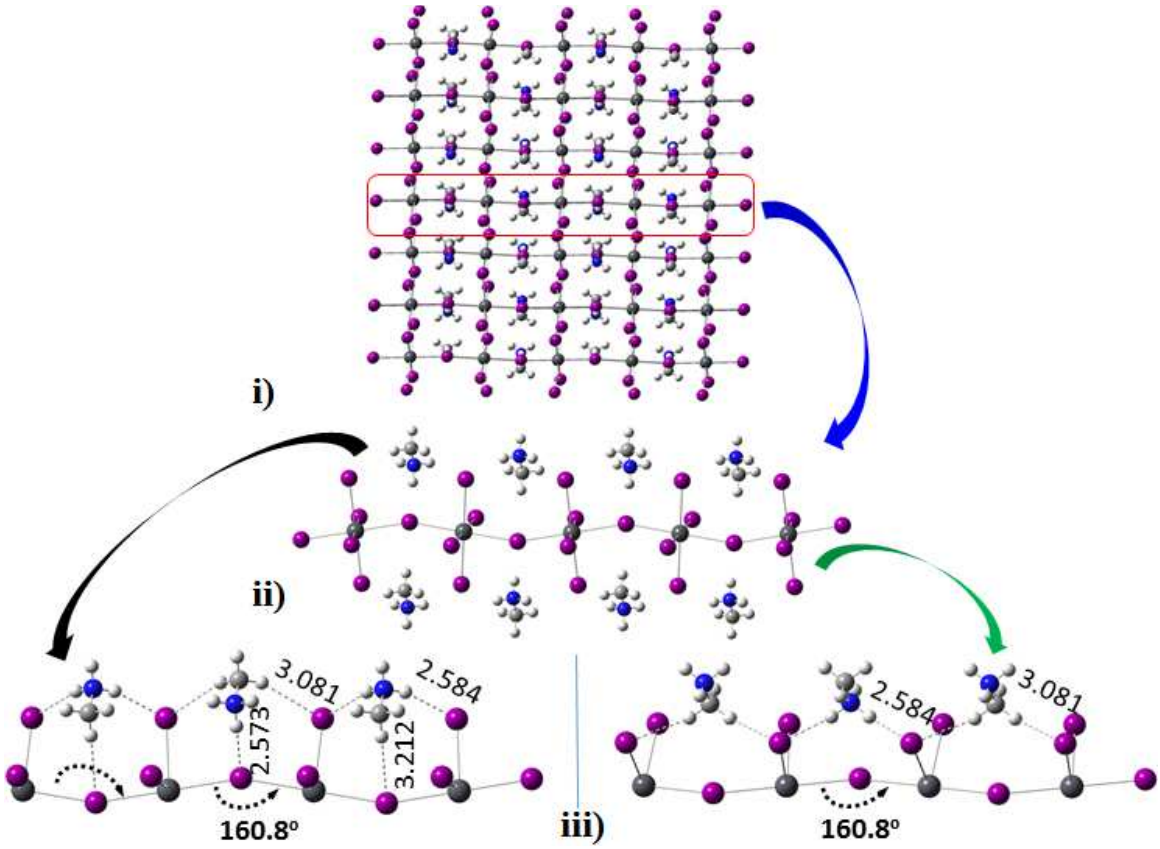

Fig 5: Another view 3×2×3 supercell model for the orthorhombic (*Pnma*) relaxed geometry of $MAPbI_3$, with the unit cell geometry obtained from the materials project database. [30] Shown in ii) is the part of i) enclosed by the red rectangle. Shown in iii) are the neutral $[MAPbI_3]_5$, emerged from ii) through cuts.

Apart from these, the apparent deviations of the Pb–I–Pb angles between orthorhombic $MAPbI_3$ and $[MAPbI_3]_{n=2–15}$ can be realized by comparing the geometries shown in Fig. 3a and 1. Note that there are two types of ∠Pb–I–Pb angles in the experimental geometry of $MAPbI_3$ illustrated in Fig. 3a. One of it lies in the 162.5 – 163.5° range, and the other lies the 151.5 – 152.5° range. These two angles in the periodic DFT relaxed geometry of $MAPbI_3$ were reported to be 160.8 and 148.9°, respectively. [30] Evidently, this former angle both in the experimental and calculated geometries correlates with the ones illustrated in the gas phase geometries, values lying between 160 and 162°. Such a correspondence between the gas and solid phase is reasonable because the gas

phase calculations were carried out at low temperature, 0 K, giving further insight into Q1.

It was experimentally observed that the organic cation reorients, as well as rotates inside the tetragonal and pseudocubic cages upon raising the temperature beyond 162 K. It is thus not surprising to believe that the molecular ion would experience various modes of intermolecular interactions with the coordinated iodides of the inorganic cage. Although there can be several of these, two such immediate interacting modes of the molecular organic cation in the orthorhombic phase (other than the ones illustrated in Fig. 1) are exemplified in Figs. 4 and 5. In both cases, the various cuts in 1D produce clusters of variable sizes, giving evidences for the significant possiblity of the formation of two types of intermolecular interactions in the vapor phase as well, I•••H–N and I•••H–C (the former relatively stronger than the latter). A complete exploration of the physical chemistry of these interactions, including the structural diversities in the conformational space, is currently underway, and this will be reported elsewhere.

5.3.2 Energy landscapes and cooperativity

One of the most crucial properties often invoked to understand noncovalent interactions in molecular clusters is the binding energy, ΔE. It is experimentally measurable by quantum mechanics. Previous studies of Legon *et al.* provide experimental evidence for the determination of ΔE for hydrogen bonded systems. [31]

Discussed below are two approaches that are adopted for the calculation of ΔE for $[MAPbI_3]_{n=1–15}$.

In the first approach, MA and PbI_3^- were considered as the two monomeric fragments of the $[MAPbI_3]$ molecular block. Then the overall and stepwise binding energies (ΔE(overall) and ΔE(stepwise), respectively) for $[MAPbI_3]_{n=1–15}$ were calculated using Eqns 1 and 2, respectively, where E is the total electronic energy of the individual species involved.

$$\Delta E(\text{overall}) = E([MAPbI_3]_{n=1–15}) - n \times E([MA]) - n \times E([PbI_3^-]) \quad \text{……..…1}$$

$$\Delta E(\text{stepwise}) = E([MAPbI_3]_{n=2–15}) - E([MAPbI_3]_{n-1}) - E[MA] - E([PbI_3^-]) \text{…....2}$$

Both ΔE(overall) and ΔE(stepwise) for $[MAPbI_3]_{n=1–15}$ are listed in Table 1. The data show that the ΔE(overall) for $[MAPbI_3]$ block is ca. –114.9 kcal mol^{-1}, predicting a substantial energy of stabilization for its geometry. This energy is about 2.87 times (nearly thrice) larger than the covalent limit, –40.0 kcal mol^{-1}.[32] The result indicates that the intermolecular hydrogen bonding interactions formed between $CH_3NH_3^+$ and PbI_3^- in $[MAPbI_3]$ contain non-negligible amount of covalency.

From Table 1, it is also obvious that as the size *n* in $[MAPbI_3]_n$ increases, the ΔE(overall) also increases monotonically. For example, the ΔE(overall) for $[MAPbI_3]_2$ is calculated to be –245.9 kcal mol^{-1}, which is much larger than that found for the corresponding block. In fact, this value is about –16.1 kcal mol^{-1} larger than the value of –229.8 kcal mol^{-1} (twice the ΔE(overall) of the $[MAPbI_3]$ block). Similarly, for the $[MAPbI_3]_3$ trimer, $[MAPbI_3]_4$ tetramer and $[MAPbI_3]_5$ pentamer, for instances, the ΔE(overall) are calculated to be –376.4, –506.8 and –636.9 kcal mol^{-1}, respectively.

Table 1: Selected physical properties of $[MAPbI_3]_{n = 1–15}$, computed with PBEPBE/DZP.[a]

n	Cluster	ΔE(overall) / kcal mol^{-1} [b]	ΔE(stepwise) / kcal mol^{-1} [c]	ΔE′(overall) / kcal mol^{-1} [d]	ΔE′(stepwise) / kcal mol^{-1} [e]	μ / Debye	HOMO/eV	LUMO/eV	E_g/eV	α /au
1	$(MAPbI_3)_1$	-114.9	0.0	0.0	0.0	4.5	-5.79	-2.12	3.67	152.38
2	$(MAPbI_3)_2$	-245.9	-131.0	-16.0	-16.0	7.9	-5.44	-2.47	2.97	338.72
3	$(MAPbI_3)_3$	-376.4	-130.5	-31.6	-15.6	9.7	-5.36	-2.63	2.73	551.39
4	$(MAPbI_3)_4$	-506.8	-130.4	-47.0	-15.4	11.3	-5.23	-2.77	2.46	803.39
5	$(MAPbI_3)_5$	-636.9	-130.1	-62.2	-15.2	12.9	-5.14	-2.92	2.22	1126.04
6	$(MAPbI_3)_6$	-767.7	-130.8	-78.1	-15.9	14.7	-5.07	-2.97	2.10	1386.70
7	$(MAPbI_3)_7$	-898.3	-130.6	-93.7	-15.6	17.0	-5.01	-3.03	1.98	1695.15
8	$(MAPbI_3)_8$	-1028.9	-130.6	-109.4	-15.7	19.6	-4.98	-3.09	1.89	2009.29
9	$(MAPbI_3)_9$	-1159.1	-130.3	-124.8	-15.3	22.9	-4.94	-3.18	1.77	2389.36
10	$(MAPbI_3)_{10}$	-1290.2	-131.0	-140.9	-16.1	26.6	-4.91	-3.18	1.68	2662.01
11	$(MAPbI_3)_{11}$	-1420.5	-130.3	-156.2	-15.4	30.7	-4.88	-3.25	1.64	3051.00
12	$(MAPbI_3)_{12}$	-1551.6	-131.1	-172.4	-16.2	34.8	-4.86	-3.23	1.60	3309.77
13	$(MAPbI_3)_{13}$	-1681.9	-130.3	-187.8	-15.4	39.0	-4.85	-3.30	1.55	3698.24
14	$(MAPbI_3)_{14}$	-1812.7	-130.8	-203.7	-15.8	43.6	-4.84	-3.32	1.53	4019.50
15	$(MAPbI_3)_{15}$	-1943.9	-131.2	-219.9	-16.2	47.8	-4.82	-3.29	1.52	4278.29

[a] Properties include the number *n* of $MAPbI_3$ in $[MAPbI_3]n$, the overall binding energies (ΔE(overall) and ΔE′(overall)), the stepwise binding energies (ΔE(stepwise) and ΔE′(stepwise)), the dipole moment (μ), the HOMO, the LUMO, the HOMO-LUMO fundamental gap (E_g), and the mean polarizability (α).
[b] Eqn 1; [c] Eqn. 2; [d] Eqn 3; [e] Eqn. 4.

These are about –31.7, –47.2 and –62.4 kcal mol^{-1} larger than thrice, quarce and quince the ΔE(overall) of the $[MAPbI_3]$ block.

$[MAPbI_3]_{15}$ is found to be the most stable among all the fifteen systems examined. The ΔE(overall) for this chain is calculated to be as large as –1943.9 kcal mol^{-1}, which is about –220.4 kcal mol^{-1} larger than the value of fifteen-times the ΔE(overall) of the $[MAPbI_3]$ block, giving further evidence of synergistic binding. This manifests that the supramolecular analogues of $[MAPbI_3]$ would be increasingly more stable than the corresponding small clusters.

The above results promise a specific type of physical principle of operation that drives the molecular building blocks, MA and PbI_3^-, to self-assemble, leading to the emergence of the $[MAPbI_3]_n$ architectures in 1D, answering Q3. The same argument can

be applicable to the large-scale supramolecular derivatives of $MAPbI_3$ in 2 and 3D. This also means I•••H–N intermolecular hydrogen bonding interactions largely responsible for the formation of $[MAPbI_3]_n$ are consequences of the physical principle of operation called non-additive cooperativity, which are strongly synergistic. The concept of cooperativity in hydrogen bonding has previously been exploited to understand a number of different chemical systems comprising hydrogen bonding interactions. [38]

While the ΔE(overall) for $[MAPbI_3]_n$ increases by increasing the number *n* of building blocks, the ΔE(stepwise) are calculated to be nearly constant. The latter lies between –130.1 and – 131.2 kcal mol^{-1}, showing the variation to be within 1.1 kcal mol^{-1}, Table 1. To make this latter feature apparent, the ΔE(stepwise) between $[MAPbI_3]$ and $[MAPbI_3]_2$, $[MAPbI_3]_2$ and $[MAPbI_3]_3$, $[MAPbI_3]_3$ and $[MAPbI_3]_4$, and $[MAPbI_3]_5$ and $[MAPbI_3]_5$ are ca. –130.9, –130.5, –130.4 and –130.1 kcal mol^{-1}, respectively. This further signifies that both the interacting monomers PbI_3^- and MA play their roles as additives for the large scale emergence of the $[MAPbI_3]_n$ supramolecular cluster chains, and the binding between them is indeed cooperative, providing stability to the resulting system. This concerns the second question, Q2, addressing what role the $CH_3NH_3^+$ cation plays for the supramolecular design of the $CH_3NH_3PbI_3$ perovskite solar cell.

The second approach utilizes Eqns. 3 and 4 to calculate the overall and stepwise binding energies (ΔE′(overall) and ΔE′(stepwise)) for $[MAPbI_3]_{n=2–15}$, respectively. In this case, the $[MAPbI_3]$ block was assumed as a monomer, and E′ refers to the total electronic energy of the individual species involved.

$$\Delta E'(\text{overall}) = E'([MAPbI_3]_{n=2–15}) - n \times E'([MAPbI_3]) \quad \text{……..……3}$$

$$\Delta E'(\text{stepwise}) = E'([MAPbI_3]_{n=2–15}) - E'([MAPbI_3]_{n-1}) - E'([MAPbI_3]) \text{…...……4}$$

The calculated ΔE′(overall) and ΔE′(stepwise) for $[MAPbI_3]_{n=2–15}$ are summarized in Table 1. It may be kept in mind that the ΔE′(overall) for $[MAPbI_3]_n$ actually involve the estimation of the binding energies associated with the coordinate interactions between the $MAPbI_3$ monomers. The dotted lines in red in each $[MAPbI_3]_n$ in Fig. 1 refers to the dative coordinate bonding interaction between the $MAPbI_3$ monomers. To make the understanding simple, let us now consider the $[MAPbI_3]_2$ dimer displayed in Fig. 1b). In it, there is only one such coordinate bonding interaction between the two $MAPbI_3$ monomers, and the ΔE′(overall) for this interaction calculated with Eqn. 3 is approximately –16.0 kcal mol^{-1}.

The $[MAPbI_3]$ block is stabilized by three equivalent I•••H–N intermolecular hydrogen bonding interactions. These are reflected in the molecular graph illustrated in Fig. 6a. These appear as solid lines between MA and PbI_3^-, emanated through application of quantum theory of atoms in molecules. [33] A related point to consider is whether the same topology of bonding is evident in $[MAPbI_3]_n$. To shed some light on this, let us look

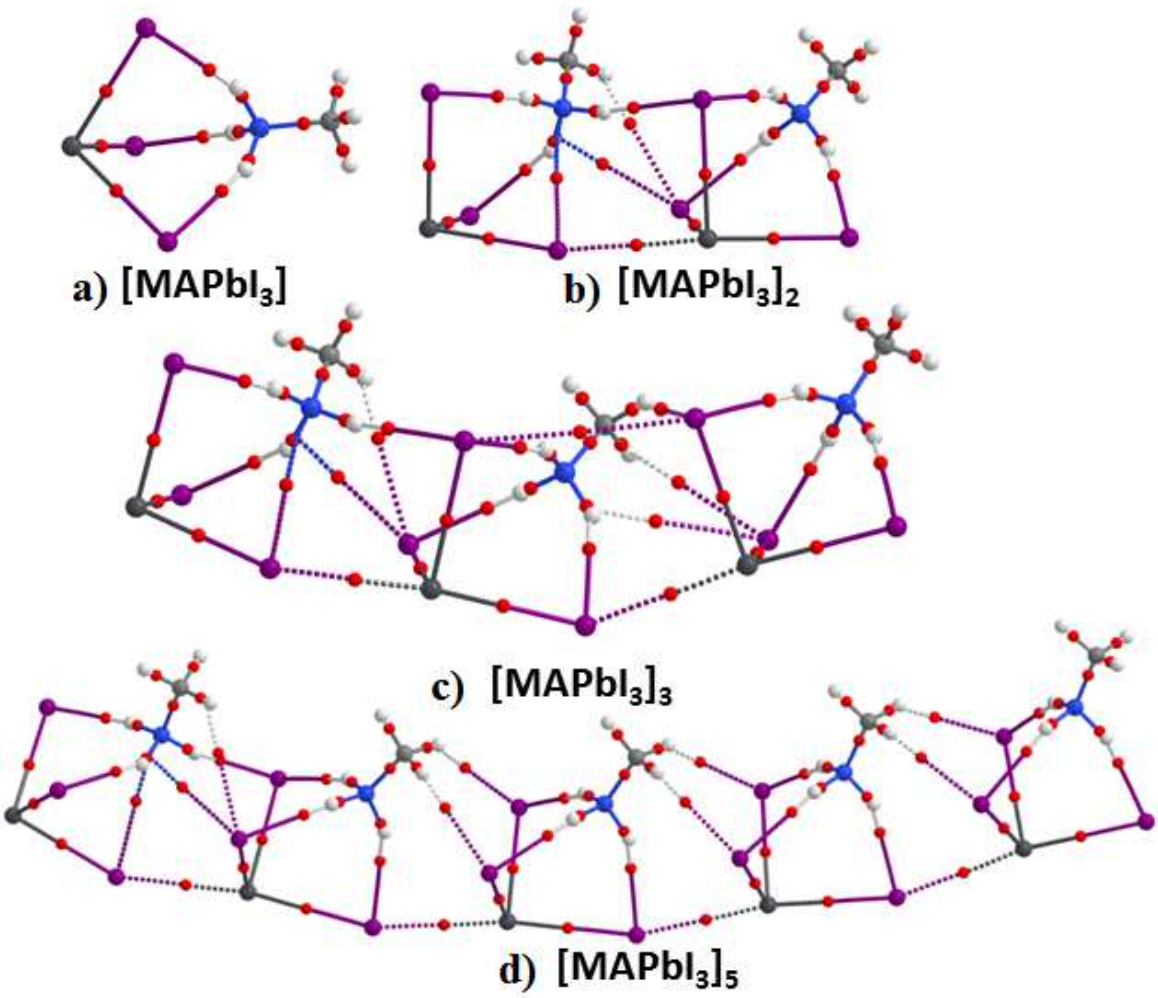

Fig. 6: Selected molecular graphs for a) $[MAPbI_3]$, b) $[MAPbI_3]_2$, c) $[MAPbI_3]_3$ and d) $[MAPbI_3]_5$, obtained using quantum theory of atoms in molecules. [33] The solid and dotted lines between Pb and I in atom color represent intra- and inter-molecular coordinate bonding interactions, respectively. The dotted lines in atom color between the H atoms of the ammonium and methyl groups of MA and the I atoms of the PbI_3^- species refers to bond paths, which are indicative of possible intermolecular hydrogen bonding interactions. The bond critical points are displayed as small red spheres between atoms basins, wherein $\nabla\rho(r_s)\cdot n(r_s) = 0$, for every point r_s on the surface $S(r_s)$, where $n(r_s)$ is the unit vector normal to the surface at r_s.

at the molecular graph of the $[MAPbI_3]_2$ dimer (Fig. 6b). In addition to the I•••H–N hydrogen bonding interactions similarly as found for Fig. 6a, it accompanies a Pb•••I type coordinate dative bonding interaction. At the same time, it also gives information about the development of some secondary intermolecular hydrogen bonding interactions,

such as weakly bound I•••H–N and I•••H–C. This means that the $[MAPbI_3]_n$ multimers are formed not only through the I•••Pb type coordinate bonding interactions that connect the $[MAPbI_3]$ monomers together, but also simultaneously through the joint effort of a few other I•••H–N and I•••H–C intermolecular hydrogen bonding interactions. Examples of similar coordination and intermolecular hydrogen bonding interactions in $[MAPbI_3]_3$ and $[MAPbI_3]_5$ are illustrated in Figs. 6c and d, respectively. This means that the $\Delta E'$(overall) of –16.0 kcal mol^{-1} calculated for $[MAPbI_3]_2$ is a collective contribution arising predominantly due to the formation of the Pb•••I coordinate bonding interaction, and partially due to the I•••H–N and I•••H–C secondary intermolecular hydrogen bonding interactions and so on.

Again, the data in Column 6 of Table 1 indicate that the $\Delta E'$(stepwise) are nearly constant, with values fluctuating between –15.2 and –16.2 kcal mol^{-1} (all within 1 kcal mol^{-1}). This means that the successive addition of a single unit of the $MAPbI_3$ block to the dimer, or that to the trimer, or that to the tetramer, and so on, increases the stepwise binding energy by ~ 15–16 kcal mol^{-1}. This conveys us further with a notion that the $[MAPbI_3]$ molecular block plays the role as an additive for the large-scale supramolecular emergence of the corresponding system in 1D.

5.3.3 Structure-property relationships

Of significant interest in materials science and organic reactive chemistry is the determination of the HOMO-LUMO fundamental gap, E_g. It is so, as it assists to explain manifold physical effects. For instance, it helps to characterize the color, the *non-linear optical responses and the* photovoltaic abilities of chemical compounds. When the HOMO of a nucleophile interacts constructively with the LUMO of an electrophile, and both are somehow closer in energies, then the attractive interaction between them is stronger. The importance of HOMO-LUMO gap is recently detailed in ref. [34] Its solid state analogue of HOMO-LUMO gap is called bandgap.

Table 1 summarizes the energies of the HOMO, LUMO and HOMO-LUMO gap for $[MAPbI_3]_{n=1–15}$. For the perovskite block, E_g is ca. 3.67 eV. This is very large compared to the solid state thin film bandgap of $MAPbI_3$ (experimental values range between 1.50 – 1.73 eV). For instance, the experimental bandgap was reported to be 1.65 eV for the orthorhombic geometry, 1.61 eV for the tetragonal geometry, and 1.69 eV for the pseudocubic geometry of $MAPbI_3$. [37] The above discrepancy between the gas and solid state E_g values is not very surprising because packing and counter ion effects, and solvation, among many other things, are fully ignored in the gas phase calculation. Moreover, from our recent benchmark investigation involving hundred DFT functionals on $MAPbI_3$, it is found that the HOMO-LUMO gap can be controlled in a specific range

by changing the percentage of the Hartree-Fock (HF) exchange in the DFT functional. In particular, the DFT functionals (viz. PBEPBE) that account for 0% HF exchange and least amount of electron-electron correlation effects gave small HOMO-LUMO gap for $MAPbI_3$ compared to those containing high percentage of HF. The RHF and CCSD approaches, on the other hand, have produced E_g for $MAPbI_3$ to be as large as 9.5 eV.

The HOMO and LUMO values for $[MAPbI_3]_{n=1–15}$ are all calculated to be large and negative. As the number n in $[MAPbI_3]_n$ increases passing from 1 to 15, the magnitude of the HOMO energy decreases, Table 1. At the same time, the magnitude of the LUMO energy increases. The decrease of the HOMO energy is seemingly not very systematic. It is evident of Table 1, which shows that the trend in the decrease in the HOMO energy is faster for $[MAPbI_3]_n$ from n = 1 up to n = 6, and then remarkably slower for the remaining cluster systems (for n > 6). An opposite feature can be noticeable with the trend found for the increase in the LUMO energy for the corresponding systems. The decrease and increase in the HOMO and LUMO energies can account for the gap calculated between them, which is found to be continuously decreasing as n in $[MAPbI_3]_n$ increases.

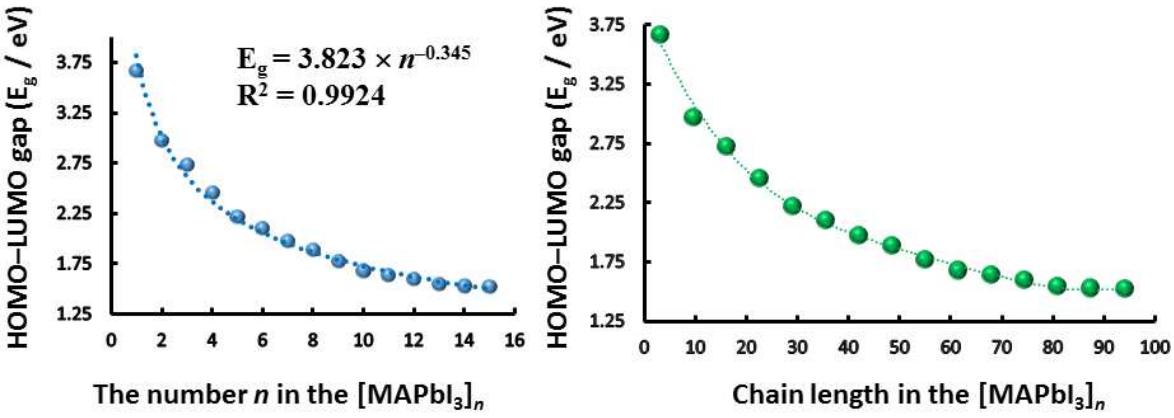

Fig 7: Dependence of HOMO-LUMO gap (E_g) on the number n (left) and that of the former on the chain length (right) for $[MAPbI_3]_{n = 1–15}$. The data for the $MAPbI_3$ block is included in both plots.

The first graph on the left of Fig. 7 presents the actual dependency of E_g on n for $[MAPbI_3]_n$, showing near convergence of E_g when n > 13. The second graph on the right presents the dependence of E_g on the chain length for the corresponding complex systems.

For $[MAPbI_3]_{15}$, a HOMO-LUMO gap of 1.52 eV is calculated. It is about 41.64% reduced compared to that calculated for the block. The reduction in E_g is indeed

very large. But, encouragingly, it is comparable with the experimental bandgap of 1.53 eV reported for the tetragonal phase of the $MAPbI_3$ thin film semiconductor. [37c]

Lin *et al.* have recently designed a series of superalkali-doped $Si_{12}C_{12}$ nanocage $M_3O@Si_{12}C_{12}$ (M = Li, Na, K) with donor–acceptor framework and studied them using DFT.[42a] It was observed in the study that the HOMO–LUMO gap is conspicuously narrowed with the increase of atomic number of the alkali metal in these systems. In specific, it was found that the E_g can decrease from a value of 5.452 eV of pure $Si_{12}C_{12}$ nanocage to values of 3.750, 2.984, and 2.634 eV for $Li_3O@Si_{12}C_{12}$, $Na_3O@Si_{12}C_{12}$, and $K_3O@Si_{12}C_{12}$, respectively. Because of this and other reasons, the authors have suggested that the pristine $Si_{12}C_{12}$ cluster could be transformed to n-type semiconductor by introduction of the superalkali M_3O. While the aforementioned gap was significantly affected with the change of the metal system, the trend they observed for the gap for their systems is qualitatively in consistent with that we observed for $[MAPbI_3]_n$, Fig. 7.

Fig. 8 presents two plots. The first one on the left describes the dependency between E_g and $\Delta E'$(overall). The second one on the right describes the dependency between E_g and ΔE (overall). Both these graphs show that as $[MAPbI_3]_n$ becomes relatively more stable with increasing *n* (*cause*), the energy gap between the HOMO and LUMO decreases (*effect*). An exactly similar feature was observed previously for the corresponding solid state system. That is, the bandgap was shown to be decreased as the dimensionality of the perovskite material increased from 2D to 3D.[41] For 2D perovskite structures, a decrease of bandgap was observed upon the increase of the number of

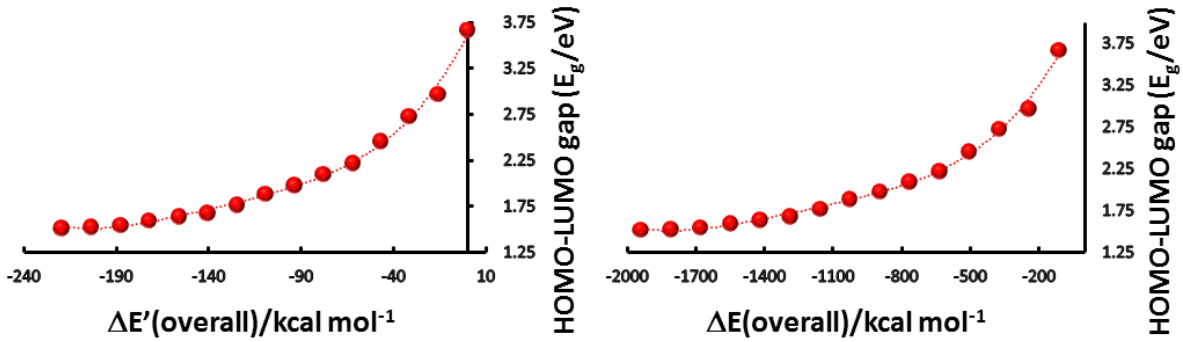

Fig: 8: Dependence of HOMO-LUMO gap (E_g) on the $\Delta E'$(overall) (left), as well as that on the ΔE(overall) (right) for $[MAPbI_3]_{n = 1–15}$.

stacked perovskite layers. [41f] This was demonstrated to be due to the effect of carrier confinement. The particular attribute is often cited to be beneficial for solar cell photovoltaic applications since it is a very important material property.[41a]

In addition to other properties, [42] the two most important properties that many functional materials possess are the dipole moment μ and the response electric property such as the static dipole polarizability α. For instance, Carsten *et al.* have demonstrated that that not only the energetics but the dipole moments are also responsible for the construction of high power conversion efficiency solar cell device made from the PTB series of low band gap copolymers. [43] Accordingly, we have calculated μ and α for $[MAPbI_3]_n$, and the results are listed in Table 1. As such, the block form of $[MAPbI_3]$ is polar. Compared to the two isolated species MA and PbI_3^-, the charge asymmetry in $[MAPbI_3]$ is large. This can be realized by inspecting the calculated dipole moments for the corresponding species: μ ~ 2.3 D for MA; ~ 3.0 D for PbI_3^-; and ~4.5 D for $[MAPbI_3]$.

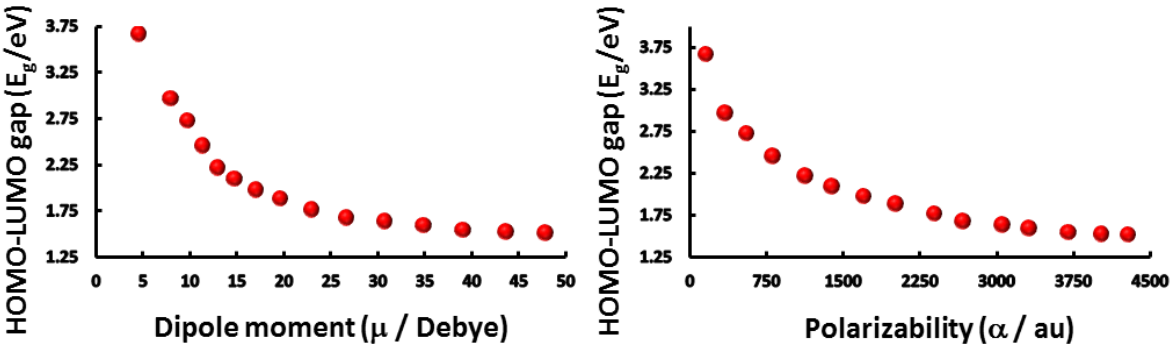

Fig: 9: Dependence of HOMO-LUMO gap E_g on dipole moment (left) and that on polarizability α for $[MAPbI_3]_n$. The data for the $MAPbI_3$ block is included in plots.

In reality, perovskite thin films are centrosymmetric. This view is probably in line with a most recent study of Sharada *et al*., [44] who have attempted to shed some light on the continued controversy concerning the polar/nonpolar nature of the $MAPbI_3$ using the results of temperature dependent single crystal X-ray diffraction and P–E loop measurements. According to them, $MAPbI_3$ is centrosymmetric, nonpolar, structure for this compound in all three phases, namely the high temperature cubic phase, the intermediate temperature tetragonal phase and the low temperature orthorhombic phase. In our view, this observation is not very surprising because the net dipole moment of the PbI_6 inorganic core is locally cancelled out by the dipolar effects of the surrounding

molecular organic cations, thereby enforcing the net dipole moment of the entire system to become zero. While these and other researches question on the polarity, [44-45] others suggested it is a necessary requirement for the observed ferroelectricity in $MAPbI_3$. [46-47]

Furthermore, the size of $[MAPbI_3]_n$ increases as *n* increases. Concomitant with this is the increase in the degree of charge asymmetry. This is understood by looking at the μ values of $[MAPbI_3]_n$, Table 1. The data suggests that as *n* increases μ increases systematically for $[MAPbI_3]_n$. This is the reason the larger systems such as $[MAPbI_3]_{13}$, $[MAPbI_3]_{14}$ and $[MAPbI_3]_{15}$ are accompanied with very large dipole moments of 39.0, 43.6 and 47.8 D, respectively. Fig. 9 (left) displays the actual dependency of HOMO-LUMO gap on μ, as well as of that on α (right) for $[MAPbI_3]_n$. Both these dependencies illustrate that the relationship between these properties are nonlinear. However, when μ was plotted against α, as well as that against *n* for $[MAPbI_3]_n$, a linear relationship was found. Nevertheless, all these relationships between structure and properties (energetic, electronic and orbital properties) for $[MAPbI_3]_n$ may address the reason for the observed functionality of $MAPbI_3$, especially as a light responsive material, for which, it has been recognized as an efficient semiconductor, thereby addressing Q4.

Finally, we aim to shed some light on the question: is $CH_3NH_3PbI_3$ polar? [44] In order to do so, we first aim to ask: is benzene polar? The simplistic answer to this latter question is "no", it is not. This answer is generally attributed to the high structural symmetry of the molecule. However, according to Anslyn and Dougherty, *the most sensible answer to this question is "yes"*, benzene is polar; it is quadrupolar rather than dipolar. To support this claim, these authors have provided this argument: "Water binds cations electrostatically by aligning its large permanent dipole moment appropriately, as like as benzene binds cations electrostatically by aligning its large permanent quadrupole moment appropriately." Also, it should not be confused with the fact that benzene is a nonpolar solvent, and in this sense, it is hydrophobic, discriminating between molecular phenomena and bulk.

When does a chemical system call polar? Typically, as already outlined above, a chemical system is called polar when it has a permanent dipole moment. If a molecule can bind ions strongly through a predominantly electrostatic interaction, it should be considered to be polar. To this end, the $CH_3NH_3PbI_3$ material has shown in many instances to be attracted electrostatically toward H_2O, thereby forming strong hydrogen bonding interactions. This means $CH_3NH_3PbI_3$ is a polar material. This also means that $CH_3NH_3PbI_3$ is not hydrophobic; it is rather hydrophilic. It is true that the $CH_3NH_3PbI_3$ system has an overall vanishing dipole moment due to the structural symmetry, but is a polar material.

5.4 Conclusion

The study has presented the fundamental gas phase chemistry of $[MAPbI_3]_{n=1–15}$ both in zero- and one-dimensions using DFT. It has drawn the following conclusions.

i) The solid state orthorhombic geometry of $MAPbI_3$ is likely to be stable in the gas phase, and octahedral tilting is not a solid state effect as generally understood.

ii) Considering MA and PbI_3^- as two monomeric fragments, the binding energies for $[MAPbI_3]_{n=1–15}$ have lied between –114.9 and –1943.9 kcal mol^{-1}.

iii) Passing from the $[MAPbI_3]$ block to the $[MAPbI_3]_2$ dimer, the overall binding energy has increased significantly. This increase is twice larger than the binding energy of the $[MAPbI_3]$ block. Similar results were also obtained for the remaining $[MAPbI_3]_{n=3–15}$ systems in 1D, displaying the emergence of non-additive cooperative binding phenomena.

iv) Increasing the number n in $[MAPbI_3]_n$ increases the stepwise binding energy significantly, with values between 130.0 – 131.1 kcal mol^{-1}, suggesting both MA and PbI_3^- to play as additives in the rationale design.

v) A comparison of the energy range mentioned in ii) with the experimental bond dissociation energies of Na–H (48.04 kcal mol^{-1}), Na–F (114.96 kcal mol^{-1}), Na–Cl (97.99 kcal mol^{-1}), Na–Br (88.43 kcal mol^{-1}), and Na–I (71.94 kcal mol^{-1})[40] has indicated that the strength of the intermolecular hydrogen bonding interactions in $[MAPbI_3]$, as well as those in $[MAPbI_3]_n$, are unusually stronger. This gives unequivocal evidence about the fact that the intermolecular interactions in $[MAPbI_3]_n$ are very special, which do not only contain significant ionic components but also appreciable amount of covalent components, essentially required for the sophisticated design of functional soft materials.

vi) Considering $[MAPbI_3]$ as a monomer, and passing from it to the dimer $[MAPbI_3]_2$, as well as from the latter to the next multimer and so on, the binding energies have increased constantly in the 15.2 – 16.2 kcal mol^{-1} range, giving further evidence about the additive nature of $MAPbI_3$.

vii) The HOMO-LUMO fundamental gap for $[MAPbI_3]$ in 0D is predicted to be large. Even so, the study has shown that increasing the cluster size can recover the bandgap of the thin film material.

viii) The dipole moment and polarizability of $[MAPbI_3]_n$ have increased significantly with increasing n. Concomitant with these, the HOMO-LUMO gap has decreased. Evidently, these fascinating attributes might

explain why $MAPbI_3$ has been identified as one of the most remarkable materials for applications in photovoltaics.

The results presented would be of interest to researchers performing physical vapor deposition experiments to produce good quality $CH_3NH_3PbI_3$ thin-films.[50] These have also improved the fundamental understanding of the physical chemistry and chemical physics of $MAPbI_3$, and have opened challenges encouraging computational chemists to model large-scale functional materials using density functional theory.

5.5 References

1. a) W. Zhang, G. E. Eperon, H. J. Snaith, halide perovskites for energy applications, *Nat. Energy* 2016, 1, 16048; b) S. D. Stranks, H. J. Snaith, Metal-halide perovskites for photovoltaic and light-emitting devices, *Nat. Nanotech.* 2015, 10, 391–402.
2. a) R. Fang, *et al.*, The rising star in photovoltaics-perovskite solar cells: The past, present and future, *Sci. China Technol. Sci.* 2016, 59: 989; b) M. Namatame1, M. Yabusaki, T. Watanabe, Y. Ogomi, S. Hayase, Direct observation of dramatically enhanced hole formation in a perovskite-solar-cell material spiro-OMeTAD by Li-TFSI doping, *Appl. Phys. Lett.* 2017, 110, 123904.
3. S. S. Shin, *et al*., Colloidally prepared La-doped BaSnOelectrodes for efficient, photostable perovskite solar cells, *Science* 2017, DOI: 10.1126/science.aam6620.
4. Research Cell Record Efficiency Chart, see at: https://www.nrel.gov/pv/assets/images/efficiency-chart.png.
5. A. B. Berthe, *et al.*, Organometal halide perovskite solar cells: degradation and stability, *Energy Environ. Sci.* 2016, 9, 323-356.
6. a) R F. Service, Perovskite solar cells gear up to go commercial, *Science* 2016, 354, 1214-1215; b) M. A. Green, A. Ho-Baillie, Perovskite solar cells: The birth of a new era in photovoltaics, ACS Energy Lett. 2017, 2, 822−830; c) F. De Angelis, P. Kamat, A conversation with Michael Grätzel, *ACS Energy Lett.* 2017, 2, 1674–1676.
7. W. Nie, *et al.*, High-efficiency solution-processed perovskite solar cells with millimeter-scale grains, *Science* 2015, 347, 522-525.
8. S. Colella, *et al.*, $MAPbI_{3-x}Cl_x$ mixed halide perovskite for hybrid solar cells: The role of chloride as dopant on the transport and structural properties, *Chem. Mater.* 2013, 25, 4613–4618.
9. A. Miyata, *et al.*, Direct measurement of the exciton binding energy and effective masses for charge carriers in organic–inorganic tri-halide perovskites, Nat. Phys. 2015, 11, 582–587.
10. F. Hoefler, G. Trimmel, T. Rath, Progress on lead-free metal halide perovskites for photovoltaic applications: a review Sebastian, Monatsh Chem. 2017, DOI 10.1007/s00706-017-1933-9.
11. Valerio D'Innocenzo, *et al.*, Excitons versus free charges in organo-lead tri-halide perovskites, Nat. Commun. 2014, 5, 3586.
12. K. Galkowski, *et al.*, Determination of the exciton binding energy and effective masses for methylammonium and formamidinium lead tri-halide perovskite semiconductors, *Energy Environ. Sci.* 2016, 9, 962-970.
13. C. Motta, F. El-Mellouhi, S. Sanvito, Charge carrier mobility in hybrid halide perovskites, Sci. Rep. 2015, 5, 12746.

14. C. Wehrenfennig, *et al.*, High charge carrier mobilities and lifetimes in organolead trihalide perovskites, *Adv. Mater.* 2014, 26, 1584–1589.
15. E. J. Juarez-Perez, *et al.*, Photoinduced giant dielectric constant in lead halide perovskite solar cells, *J. Phys. Chem. Lett.* 2014, 5, 2390–2394.
16. a) E. Mosconi, *et al.*, Electronic and optical properties of $MAPbX_3$ perovskites (X = I, Br, Cl): a unified DFT and GW theoretical analysis, *Phys. Chem. Chem. Phys.* 2016, 18, 27158-27164; b) A. M. A. Leguy, *et al.*, Experimental and theoretical optical properties of methylammonium lead halide perovskites, *Nanoscale* 2016, 8, 6317-6327; c) C. Eames, et al., Ionic transport in hybrid lead iodide perovskite solar cells, *Nat. Commun.* 2015, 6, 7497; d) A. Mattoni, *et al.*, Methylammonium rotational dynamics in lead halide perovskite by classical molecular dynamics: The Role of temperature, *J. Phys. Chem. C* 2015, 119, 17421–17428; e) Charge carrier trapping at surface defects of perovskite solar cell absorbers: A first-principles study H. Uratani, Koichi Yamashita, *J. Phys. Chem. Lett.* 2017, 8, 742−746.
17. a) R. G. Niemann, *et al.*, Halogen effects on ordering and bonding of $CH_3NH_3^+$ in $CH_3NH_3PbX_3$ (X = Cl, Br, I) hybrid perovskites: A vibrational spectroscopic study, *J. Phys. Chem. C* 2016, 120, 2509-2519; M. T. Weller, O. J. Weber, P. F. Henry, A. M. Di Pumpo, T. C. Hansen, Complete structure and cation orientation in the perovskite photovoltaic methylammonium lead iodide between 100 and 352 K *Chem. Commun.* 2015, 51, 4180; h) T. Baikie, Y. Fang, J. M. Kadro, M. Schreyer, F. Wei, S. G. Mhaisalkar, M. Graetzeld, T. J. White, Synthesis and crystal chemistry of the hybrid perovskite $(CH_3NH_3)PbI_3$ for solid-state sensitised solar cell applications, J. Mater. Chem. A, 2013,1, 5628-5641.
18. a) C. C. Stoumpos, C. D. Malliakas, M.i G. Kanatzidis, Semiconducting tin and lead iodide perovskites with organic cations: Phase transitions, high mobilities, and near-infrared photoluminescent properties, *Inorg. Chem.* 2013, 52, 9019–9038; b) A. Wakamiya, M. Endo, T. Sasamori, N. Tokitoh, Y. Ogomi, S. Hayase, Y. Murata, Reproducible fabrication of efficient perovskite-based solar cells: X-ray crystallographic studies on the formation of $CH_3NH_3PbI_3$ layers, *Chem. Lett.* 2014, 43, 711 – 713; c) K. P. Ong, *et al.*, Structural evolution in methylammonium lead iodide $CH_3NH_3PbI_3$, *J. Phys. Chem. A* 2015, 119, 11033–11038.
19. a) H. Fang, P. Jena, Molecular origin of properties of organic–inorganic hybrid perovskites: The big picture from small clusters, *J. Phys. Chem. Lett.* 2016, 7, 1596–1603; b) Q. Yao, H. Fang, K. Deng, E. Kan, P. Jena, Superhalogens as building blocks of two-dimensional organic–inorganic hybrid perovskites for optoelectronics applications, *Nanoscale* 2016, 8, 17836-17842; c) H. Fang, P. Jena, Super-ion inspired colorful hybrid perovskite solar cells, *J. Mater. Chem. A* 2016, 4, 4728.
20. a) G Giorgi, T. Yoshihara, K. Yamashita, Structural and electronic features of small hybrid organic–inorganic halide perovskite clusters: a theoretical analysis, *Phys. Chem. Chem. Phys.* 2016,18, 27124-27132; b) G. Giorgi, K. Yamashita, Zero-dimensional hybrid organic−inorganic halide perovskite modeling: Insights from first principles, *J. Phys. Chem. Lett.* 2016, 7, 888−899; c) A. Varadwaj, P. R. Varadwaj, K. Yamashita, Hybrid organic-inorganic $CH_3NH_3PbI_3$ perovskite building blocks: Revealing ultra-strong hydrogen bonding and Mulliken inner complexes and their implication in materials design, 2017, https://arxiv.org/abs/1703.10286.
21. Gaussian 09, Revision C.01, M. J. Frisch, *et al.*, Gaussian, Inc., Wallingford CT, 2016.
22. GaussView, Version 5, Roy Dennington, Todd Keith, and John Millam, Semichem Inc., Shawnee Mission, KS, 2009.

23. D. Feller, The Role of Databases in Support of Computational Chemistry Calculations, *J. Comp. Chem.* 1996 17, 1571-1586; b) K. L. Schuchardt, Basis set exchange: A community database for computational sciences, *J. Chem. Inf. Model.* 2007, 47, 1045-1052.
24. A. Varadwaj, P. R. Varadwaj, K. Yamashita, On the accuracy of density functionals in predicting the bandgap and binding energy of the methylammonium lead triiodide perovskite solar cell nanocluster, 2017, (To be submitted soon).
25. a) G. Kresse, J. Hafner, Ab initio molecular dynamics for liquid metals, *Phys. Rev. B* 1993, 47, 558; b) G. Kresse, J. Hafner, Ab initio molecular-dynamics simulation of the liquid-metal-amorphous-semiconductor transition in germanium, *Phys. Rev. B* 1994, 49, 14251; c) G. Kresse, J. Furthmüller, Efficiency of ab-initio total energy calculations for metals and semiconductors using a plane-wave basis set, *Comput. Mat. Sci.* 1996, 6, 15; d) G. Kresse, J. Furthmüller. Efficient iterative schemes for ab initio total-energy calculations using a plane-wave basis set, *Phys. Rev. B* 1996, 54:11169; e) P. E. Blöchl, O. Jepsen, O. K. Andersen, Improved tetrahedron method for Brillouin-zone integrations, *Phys. Rev. B* 1994, 49, 16223–16233.
26. P. R. Varadwaj, Methylammonium lead trihalide perovskite solar cell semiconductors are not organometallic: A perspective, *Helv. Chim. Acta* 2017, DOI: 10.1002/hlca.201700090.
27. a) P. J. Hasnip, Density functional theory in the solid state, Philos Trans A Math Phys Eng Sci. 2014, 372, 20130270; b) G. Kieslich, Goodwin, The same and not the same: molecular perovskites and their solid-state analogues, *Mater. Horiz.* 2017, 10.1039/C7MH00107J.
28. J. L. Knutson, *et al.*, Tuning the band gap in hybrid tin iodide perovskite semiconductors using structural templating, *Inorg. Chem.* 2005, 44, 4699.
29. C. R. Groom, I. J. Bruno, M. P. Lightfoot and S. C. Ward, The Cambridge Structural Database, *Acta Cryst.* 2016, B72, 171-179.
30. A. Jain, S.P. Ong, G. Hautier, W. Chen, W.D. Richards, S. Dacek, S. Cholia, D. Gunter, D. Skinner, G. Ceder, K.A. Persson, The Materials Project: A materials genome approach to accelerating materials innovation, *APL Materials* 2013, 1, 011002.
31. A. C. Legon and D. J. Millen, Gas-phase spectroscopy and the properties of hydrogen-bonded dimers: HCN…HF as the spectroscopic prototype, *Chem. Rev.* 1986, 86, 635-57.
32. H. Hunt, e*t al.*, Hydrogen bonding in ionic liquids, *Chem. Soc. Rev.* 2015, 44, 1257-1288.
33. a) R.F.W. Bader, Atoms in Molecules: A Quantum Theory, Oxford University Press, Oxford, 1990; b) AIMAll (Version 16.10.31), Todd A. Keith, TK Gristmill Software, Overland Park KS, USA, 2016 (aim.tkgristmill.com).
34. E. J. Baerends, The Kohn-Sham gap, the fundamental gap and the optical gap: the physical meaning of occupied and virtual Kohn-Sham orbital energies, *Phys. Chem. Chem. Phys.* 2013, 15, 16408-25.
35. a) J.-H. Lee, *et al.*, Resolving the physical origin of octahedral tilting in halide perovskites, *Chem. Mater.* 2016, 28, 4259−4266; b) J.-H. Lee, *et al.*, Role of hydrogen-bonding and its interplay with octahedral tilting in $CH_3NH_3PbI_3$, *Chem. Commun.* 2015, 51, 6434-6437.
36. Q. Chen, *et al.*, Under the spotlight: The organic–inorganic hybrid halide perovskite for optoelectronic applications, *nanotoday*, 2015, 10, 335.
37. a) C. Quarti, E. Mosconi, J. M. Ball, V. D'Innocenzo, C. Tao, S. Pathak, H. J. Snaith, A. Petrozza, F. D. Angelis, Structural and optical properties of methylammonium lead iodide across the tetragonal to cubic phase transition: implications for perovskite solar cells, *Cryst. Growth Des.* 2016, 16, 2945−2951; b) C. Quarti, E. Mosconi, J. M. Ball, V.

D'Innocenzo, C. Tao, S. Pathak, H. J. Snaith, A. Petrozza, F. D. Angelis, Structural and optical properties of methylammonium lead iodide across the tetragonal to cubic phase transition: implications for perovskite solar cells, *Energy Environ. Sci.* 2016, 9, 155; c) A. Suzuki, H. Okada, T. Oku, Fabrication and characterization of $CH_3NH_3PbI_{3-x-y}Br_xCl_y$ perovskite solar cells, *Energies* 2016, 9, 376.

38. a) R.D. Parra, J. Ohlssen, Cooperativity in intramolecular bifurcated hydrogen bonds: An ab initio study, *J. Phys. Chem. A* 2008, 112, 3492; b) T. van Mourik, A. J. Dingley, Characterizing the cooperativity in H-bonded amino structures, J. *Phys. Chem. A* 2007 111, 11350-11358; c) H.-J. Song, *et al.*, Density functional theory study of the properties of N−H···N, Noncooperativities, and intermolecular interactions in linear trans-diazene clusters up to ten molecules, *J. Phys. Chem. A* 2006 110, 6178-6183; d) A. N. Petelski, et al., Intermolecular perturbation in the self-assembly of melamine, *Theor. Chem. Acc.* 2016, *135*, 65; e) A. S. Mahadevi, G. N. Sastry, Cooperativity in noncovalent interactions, *Chem. Rev.* 2016, 116, 2775–2825.
39. a) Y. Ren, *et al.*, Orientation of organic cations in hybrid inorganic–organic perovskite $CH_3NH_3PbI_3$ from subatomic resolution single crystal neutron diffraction structural studies, *Cryst. Growth Des.* 2016 16, 2945–2951; b) A. Poglitsch, D. Weber, Dynamic disorder in methylammoniumtrihalogenoplumbates (II) observed by millimeterwave spectroscopy, *J. Chem. Phys.* 1987, 87, 6373–6378; c) N. Onoda-Yamamuro, T. Matsuo and H. Suga, Calorimetric and IR spectroscopic studies of phase transitions in methylammonium trihalogenplumbates (II), *J. Phys. Chem. Solids* 1990, 51, 1383–1395; d) O. Knop, R. E. Wasylishen, M. A. White, T. S. Cameron and M. J. M. Van Voort, Alkylammonium lead halides. Part 2. $CH_3NH_3PbX_3$ (X = C1, Br, I) perovskites: cuboctahedral halide cages with isotropic cation reorientation1, *Can. J. Chem.* 1990, 68, 412–422.
40. a) T. L. Cottrell, The Strengths of Chemical Bonds, 2d ed., Butterworth, London, 1958; b) B. deB. Darwent, National Standard Reference Data Series, National Bureau of Standards, no. 31, Washington, 1970; c) S. W. Benson, J. Chem. Educ. 42:502 (1965); d) J. A. Kerr, *Chem. Rev.* 66:465 (1966); e) The properties can be also available via: https://labs.chem.ucsb.edu/zakarian/armen/11---bonddissociationenergy.pdf (last retrieved on June 27, 2017).
41. a) N.-G. Park, Perovskite solar cells: an emerging photovoltaic technology, *materialstoday* 2015, 18, 65-72; b) D.B. Mitzi, et al., *Nature* 1994, 369, 467-469; c) Y. Takeoka, K. Asai, M. Rikukawa, K. Sanui, Systematic studies on chain lengths, halide species, and well thicknesses for lead halide layered perovskite thin films, *Bull. Chem. Soc. Japan* 2006, 79, 1607–1613; d) M. I. Ahmed, A. Habib, S. Saad, Javaid, Perovskite solar cells: Potentials, challenges, and opportunities, *Int. J. Photoenergy* 2015, 2015, 592308, http://dx.doi.org/10.1155/2015/592308; e) C.-J. Que, C.-J. Mo, Z.-Q. Li, G.-L. Zhang, Q.-Y. Zhu, J. Dai, Perovskite-Like Organic–Inorganic Hybrid Lead Iodide with a Large Organic Cation Incorporated within the Layers, *Inorg. Chem.* 2017, 56, 2467–2472; f) Q. Chen, et al., Under the spotlight: The organic–inorganic hybrid halide perovskite for optoelectronic applications, *nanotoday* 2015, 10, 355-396.
42. a) Z. Lin, T. Lu, X. -L. Ding, A theoretical investigation on doping superalkali for triggering considerable nonlinear optical properties of $Si_{12}C_{12}$ nanostructure, *J. Comput. Chem.* 2017, 38, 1574–1582; b) A. J. Moad, C. W. Moad, J. M. Perry, R. D. Wampler, G. S. Goeken, N. J. Begue, T. Shen, R. Heiland, G. J. Simpson, NLOPredict: visualization and data analysis software for nonlinear optics, J. Comput. Chem. 2007, 28, 1996-2002.
43. B. Carsten, J. M. Szarko, H. Jung Son, W. Wang, L. Lu, F. He, B. S. Rolczynski, S. J. Lou, L. X. Chen, L. Yu, Examining the effect of the dipole moment on charge separation

in donor–acceptor polymers for organic photovoltaic applications, *J. Am. Chem. Soc.* 2011, 133, 20468–20475.
44. G. Sharada, P. Mahale, B. P. Kore, S. Mukherjee, M. S. Pavan, C. De, S. Ghara, A. Sundaresan, A. Pandey, T. N. G. Row, D. D. Sarma, Is $CH_3NH_3PbI_3$ polar? J. Phys. Chem. Lett. 2016, 7, 2412–2419.
45. Y. Dang, Y. Liu, Y. Sun, D. Yuan, X. Liu, W. Lu, G. Liu, H. Xia, X. Tao, Bulk crystal growth of hybrid perovskite material $CH_3NH_3PbI_3$, CrystEngComm 2015, 17, 665–670.
46. E. Strelcov, Q. Dong, T. Li, J. Chae, Y. Shao, Y. Deng, A. Gruverman, J. Huang, A. Centrone, $CH_3NH_3PbI_3$ perovskites: Ferroelasticity revealed, Sci. Adv. 2017, 3, e1602165
47. J. Beilsten-Edmands, G. E. Eperon, R. D. Johnson, H. J. Snaith, P. G. Radaelli, Nonferroelectric nature of the conductance hysteresis in $CH_3NH_3PbI_3$ perovskite-based photovoltaic devices. Appl. Phys. Lett. 2015, 106, 173502.
48. E. V. Anslyn, D. A. Dougherty, Modern Physical Organic Chemistry, University Science Books Sausalito, California, 2005, ISBN 1–891389–31–9.
49. A. M. Glazer, The classification of tilted octahedra in perovskites, *Acta Cryst.* 1972, B28, 3384-3392.
50. L. She, M. Liu, D. Zhong, Atomic structures of $CH_3NH_3PbI_3$ (001) surfaces, *ACS Nano* 2016, 10, 1126–1131.

Chapter 6. The Natures of Charge Transfer in $CH_3NH_3PbI_3$ and $CsPbI_3$

6.1 Introduction

A great number of studies were conducted recently on hybrid organic–inorganic lead trihalide perovskites, especially on the methylammonium lead trihalide perovskites $CH_3NH_3PbY_3$, where Y = $I_{(3-x)}Br_{x=1-3}$, $I_{(3-x)}Cl_{x=1-3}$, $Br_{(3-x)}Cl_{x=1-3}$, and IBrCl.[1-5] These can be grouped into the broad class with generic formula BMY_3, where B is the organic/inorganic cation (viz. $CH_3NH_3^+/Cs^+$), M is the metal cation (viz. Sn^{2+}/Ge^{2+}), and Y is the inorganic/organic anion (viz. X^-(X = Cl, Br, I)/$HCOO^-$). An obvious reason for such an upsurge of scientific interest lies in their important application in photovoltaics, especially as single-junction solar cell absorbers.[6] The bandgap E_g for the $CH_3NH_3PbY_3$ materials is tunable in the visible region of the electromagnetic spectrum by changing the constituent halogen concentrations, with E_g varying between 1.5 and 3.1 eV.[1] These materials are highly sensitive to the environmental ingredients, experiencing degradation by photoinduction, water and O_2 exposures, and several others.[7] Thermal degradation is a major factor that does not allow the material to stand within the time scales of the processing and operational window, thereby making these materials not yet ready for their immediate commercialization.[8] Development of new technologies to drive these and lead-free hybrid materials for outdoor activities is actively on-going.[9]

Methylammonium in $CH_3NH_3PbY_3$ is volatile. This can be replaced by any other volatile or nonvolatile species to design materials that can have similar or even better geometrical stability. Thus when MA is replaced by the cesium ion in $CH_3NH_3PbY_3$, the resulting $CsPbY_3$ absorbers are an inorganic hybrid material with improved optical and thermal stability. A stabilized photo power conversion efficiency (PCE) of 6.5%, and a bandgap of 1.9 eV have reported for the most efficient member of the series called $CsPbI_3$.[8] Similarly, $CsPbI_2Br$ is employed in a planar architecture device resulting in 9.8% PCE and over 5% stabilized power output.[10] The $CsPb(Br_xI_{1-x})_3$ perovskites are demonstrated to be thermodynamically favorable at room temperature, presumably due to the mixed halide content.[11] Studies on other derivatives of this family can be found elsewhere.[2-5]

Both $CH_3NH_3PbY_3$ and $CsPbY_3$ are important and interesting candidates for studies, both from experimental and theoretical point of views. These compounds can be synthesized easily using a number of experimental synthetic technologies. One of them is the two-step method, which is based on the transformation of lead(II) iodide (PbI_2), lead(II) bromide ($PbBr_2$) and lead(II) chloride ($PbCl_2$) salts into $MAPbBr_3$ perovskite after dipping in a methylammonium bromide (MABr) solution. Such a process can assist in the preparation of

the methylammonium lead tribromide ($MAPbBr_3$) thin film. [12] It is generally observed that $CsPbI_3$ is yellow and adopts non-perovskite phase at room temperature. However, by careful processing control and development of a low-temperature phase transition route can transform the material as colored black.[10]

Nevertheless, each compound $CH_3NH_3PbY_3$ is assumed to be the mixture of an organic and an inorganic species, $CH_3NH_3^+$ and PbY_3^-.[13,14] For the $CsPbY_3$ series, the two constituent mixtures are inorganic, Cs^+ and PbI_3^-. Depending on the concentration of PbY_3^- in solution, whether higher or lower, the formation of a given type of perovskite system is likely. For instance, it was shown that concentration of PbI_3^- in solution is higher for PbI_2 + MAI than for $PbCl_2$ + MAI, [15] which is good for the formation of $MAPbI_3$ species. According to Stamplecoskie *et al.*, [16] thin films obtained from the deposition of solutions containing lead halides and the $CH_3NH_3^+$ organic cation are known to yield the $CH_3NH_3PbI_3$ perovskite structure upon annealing. Their spectroscopic investigation indicate that $CH_3NH_3PbI_3$ films reveal two different excited state behaviors, viz. charge separated state ($CH_3NH_3PbI_3 + h\nu \rightarrow CH_3NH_3PbI_3$ (e-h)$\rightarrow CH_3NH_3PbI_3$) and an excited charge transfer state ($CH_3NH_3PbI_3 + h\nu \rightarrow [CH_3NH_3PbI{\bullet\bullet\bullet}I_2]$). These two states remain coupled to form a dual excited state. However, when both these states undergo charge recombination they regenerate the ground state. [16]

In this Chapter, I am keen at giving solutions to two fundamentally important problems. Firstly, I aimed at answering whether the zero-dimensional [$MAPbI_3$] and [$CsPbI_3$] molecular building blocks can be regarded as charge transfer complexes in their respective ground electronic states. I focused at investigating this feature theoretically with the aid of a simple charge rearrangement model which allows the assessment of the details of the nature of both intra- and intermolecular charge transfers accompanying the formation of the perovskite blocks [$MAPbI_3$] and [$CsPbI_3$] in zero-dimension, as well as of the $[MAPbI_3]_{n=2–15}$ and $[CsPbI_3]_{n=2–10}$ nanocluster chains in one-dimension, all in their respective ground electronic states. Secondly, we intended at examining the extent to which this charge transfer is dependent on the bond distances. That is, to see how large is the effect of the charge transfers on the chain lengths for both the $[MAPbI_3]_{n=1–15}$ and $[CsPbI_3]_{n=1–10}$ series.

6.2 Computational details

The Pb and I atoms are very heavy, and their occupancies increase by increasing the number of the building blocks in the $[MAPbI_3]_{n=1–15}$ and $[CsPbI_3]_{n=1–10}$ clusters. Given there are very rare all-electron correlation consistent basis sets viable for these atoms, and given the sizes of the perovskite clusters examined in this study are very large, a standard all-electron DZP basis set was a reasonable choice for holding the compromise between time and chemical accuracy. The DZP basis set was retrieved from the EMSL basis set library.[19]

We have performed density functional theory calculations with PBEPBE method[17] to determine the equilibrium geometries of the $[MAPbI_3]_{n=1–15}$ and $[CsPbI_3]_{n=1–10}$ cluster series in their respective electronic ground states. The resulting Pb–I–Pb skeletal backbones of these

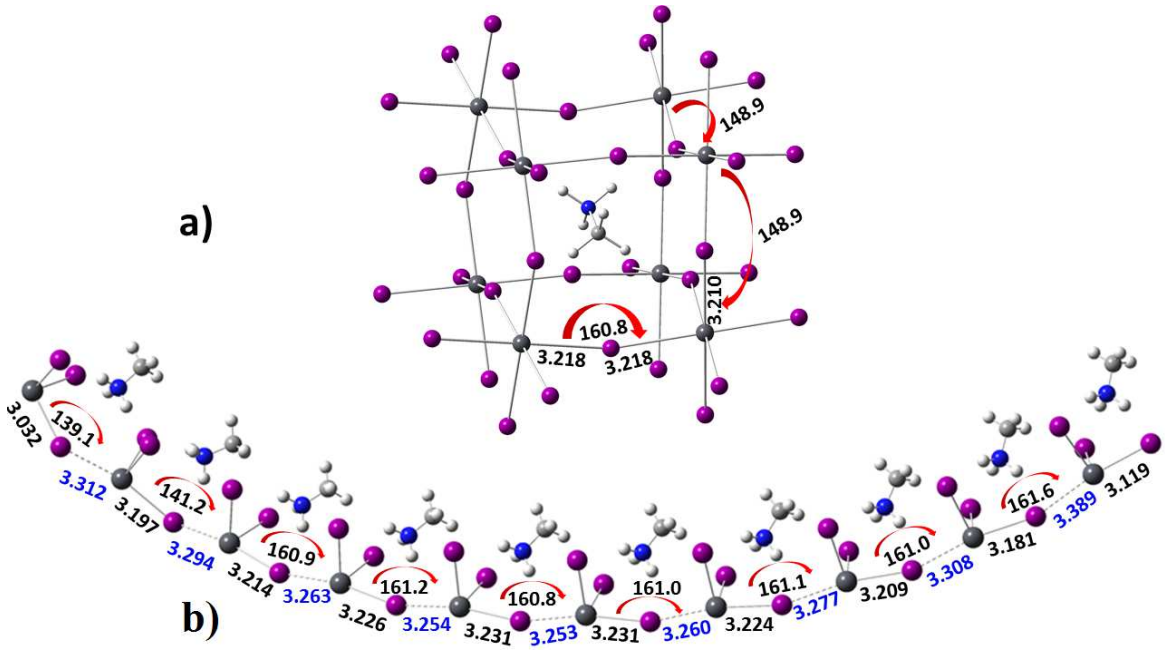

Fig. 1: a) Schematic for the orthorhombic *Pnma* relaxed geometry of $MAPbI_3$, showing some selected Pb–I coordinate bond distances and the Pb–I–Pb tilting angles.[43] b) The gas phase energy-minimized geometry of the $[MAPbI_3]_{10}$ nanowire in 1D, showing some selected Pb–I coordinate bond distances and the Pb–I–Pb tilting angles. Bond-lengths and -angles are given in Å and °, respectively.

energy-minimized systems for both the series are partially analogous to their corresponding crystal geometries reported in the low-temperature orthorhombic phase, showing that the model systems exploited can capture the intermolecular interactions expected of the low temperature crystalline geometries.[18]

Fig. 1a illustrates, for example, the schematic for the periodic DFT relaxed orthorhombic *Pnma* geometry for the $MAPbI_3$, [43] which is observed as the low-temperature geometry of the material in the solid state. Fig. 1b represents to the gas phase energy-minimized structure of the $[MAPbI_3]_{10}$ nanowire in 1D. It is analogous with the local geometry a) in a given direction. This can be figured out from the selected solid state geometrical parameters that are shown for both the structures. The first two Pb–I–Pb titling

angles in the gas phase geometry (see from left) are significantly different from those of the other seven angles since the nearest neighboring coordinated iodide is missing in the first block of the cluster. However, this angular mismatch problem compared to that observed in the geometry in the crystalline phase was eventually resolved after adding one more molecular block to the chain and so on. Nonetheless, a similar result is also obtained for the $[CsPbI_3]_{n=2–10}$ clusters when their geometrical properties were compared against the corresponding ones obtained for the *Pnma* orthorhombic geometry of the $CsPbI_3$ perovskite (not shown).

Quantum theory of atoms in molecules (QTAIM),[20a] Mulliken,[20b] Hirshfeld,[20c] Voronoi deformation density (VDD), [20d] Natural Population Analysis (NPA),[42] and Becke atomic charge with atomic dipole moment correction[20e] level population analyses were performed to determine the net atomic charges conferred on various atoms constituting the isolated fragments PbI_3^-, $CH_3NH_3^+$ and Cs^+, as well as the $[MAPbI_3]_{n=1–15}$ and $[CsPbI_3]_{n=1–10}$ systems. The Gaussian 09 code[21] was employed for electronic structure calculations, and for calculations of the Mulliken and NPA charges, whereas the AIMAll[22] and MultiWfn[23] codes were employed for the calculations of the QTAIM and other charges (Hirshfeld, VDD and Becke), respectively.

Hereafter, methylammonium lead triiodide perovskite will be referred to as either $[MAPbI_3]$ or $CH_3NH_3PbI_3$, or $[PbI_3{\bullet\bullet\bullet}H_3NCH_3]$, etc.

6.3 Results and discussions

6.3.1 Nature of charge transfer

Analysis of the calculated QTAIM charges suggests that for the formation of the $[MAPbI_3]$ and $[CsPbI_3]$ molecular building blocks in 0D, as well as of the $[MAPbI_3]_{n=2–15}$ and $[CsPbI_3]_{n=2–10}$ nanowire cluster series in 1D, three types of charge transfer interactions are essentially needed to be involved; two are direct and one is indirect.

The schematics for all the three types of charge transfer process are presented in Scheme 1. The first (indirect) mechanism of charge transfer involves the formation of the isolated PbI_3^- species. It is a result of significant interatomic charge transfers between the Pb^{2+} cation and the three I^- anions. The same mechanism that involves the formation of the PbI_3^- ion is likely in solution. [15]

For the formation of the isolated PbI_3^-, each iodide with its formal –1 charge transfers approximately 0.380 *e* to the Pb^{2+} ion core, evaluated with QTAIM. This suggests a total charge of 1.14 *e* is transferred from the three I^- ions to the Pb core upon the formation of the isolated PbI_3^- ion. Concomitant with this, the formal +2 charge of the Pb ion core reduces to a value of +0.860 *e* in PbI_3^-. This is pictorially shown in a) of Scheme 1.

The QTAIM integrated charges for the $MAPbI_3$ molecular building block are illustrated in Fig. 2a. From these, it is found that a net charge of +0.278 e is to be transferred from the entire PbI_3^- subunit to the $CH_3NH_3^+$ cation when both are in the equilibrium

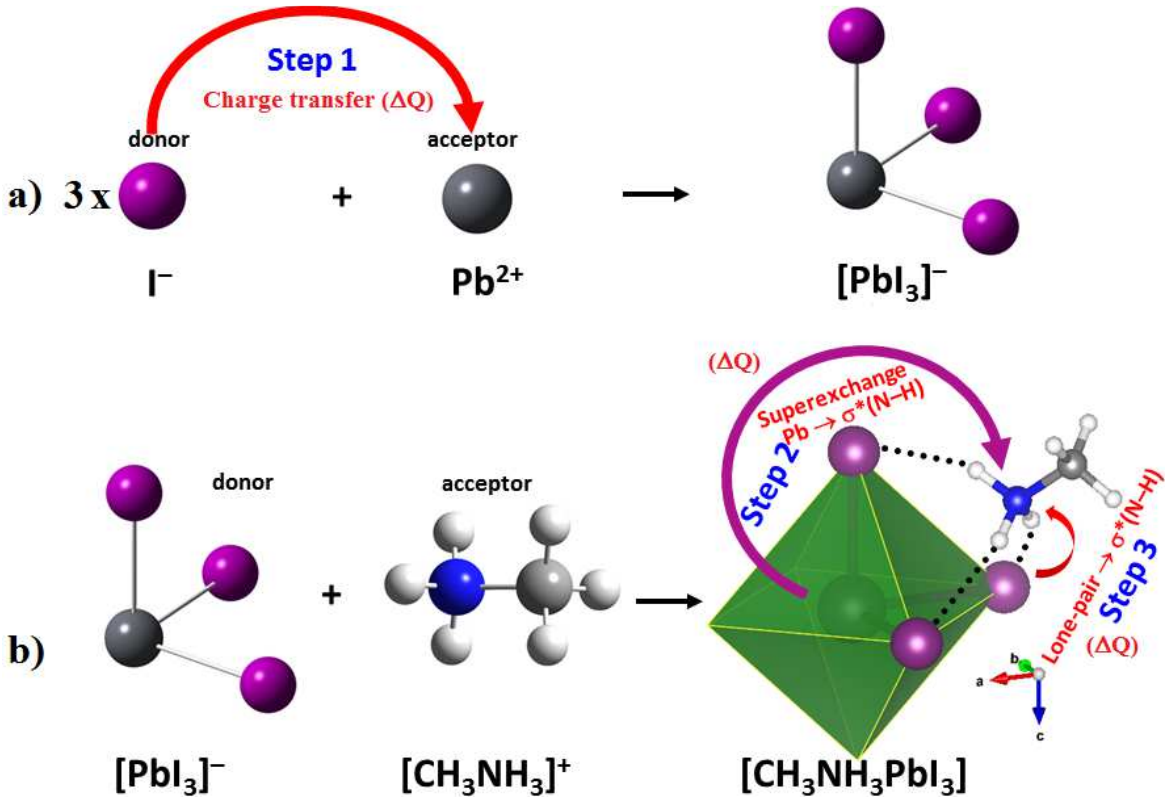

Scheme 1: Schematic representation of possible charge transfer pathways for the formation of the $[CH_3NH_3PbI_3]$ system. In a) the iodide ions transfer charge to the valence-accepting orbitals of the Pb^{2+} ion core, leading to the formation of the PbI_3^- anion (step 1). b) The interaction between PbI_3^- and $CH_3NH_3^+$ enables charge transfer from the Pb ion core to the $CH_3NH_3^+$ subunit through a superexchange mechanism (step 2), and that from the lone-pair bonding orbitals of the coordinated iodides in PbI_3^- to the σ*(N–H) antibonding orbitals of the $CH_3NH_3^+$ organic cation (step 3). Black dots between atoms in b) in the pseudo-polyhedron represent the N•••H–N intermolecular hydrogen bonding interactions. The terms donor and acceptor represent to electron-donor and -acceptor, respectively, and the ΔQ represents the charge transfer. For details, see text.

geometry of the $MAPbI_3$ cluster. A question now arises: what is the extent of this charge transfer from the individual fragments of the inorganic PbI_3^- species to the organic $CH_3NH_3^+$ cation at equilibrium? Is there any charge to be transferred from the Pb core to the $CH_3NH_3^+$ organic ion? Can this be described by hoping, or by super-exchange mechanism? Are there any charge transfer transferred between the electron rich orbitals of the coordinated iodides and the electron-accepting orbitals of the organic cation? Answers to these questions have provided below.

The second type of charge transfer is auxiliary. It is schematic of step 2 of Scheme 1. It can be identified by inspecting the nature of the charge distributions on the atoms

constituting both the interacting monomers, and those constituting the $MAPbI_3$ and/or $[MAPbI_3]_{n = 2–15}$ systems. To make this understanding unambiguous, we cite that a net partial charge of +0.924 *e* is conferred on the Pb core of the PbI_3^- fragment of the $[PbI_3 \bullet\bullet\bullet H_3NCH_3]$ cluster at equilibrium (cf. Fig. 1a). This is different from that of +0.860 *e* calculated for the corresponding atom in isolated PbI_3^-. This shows that the charge on the Pb core in $[MAPbI_3]$ relative to that on it in isolated PbI_3^- is increased by 0.064 *e*. This gives an evidence about the fact that some fractional charge densities are certainly transferred from the Pb core in isolated PbI_3^- to an atomic/molecular fragment $[MAPbI_3]$ to which is it directly/indirectly bonded.

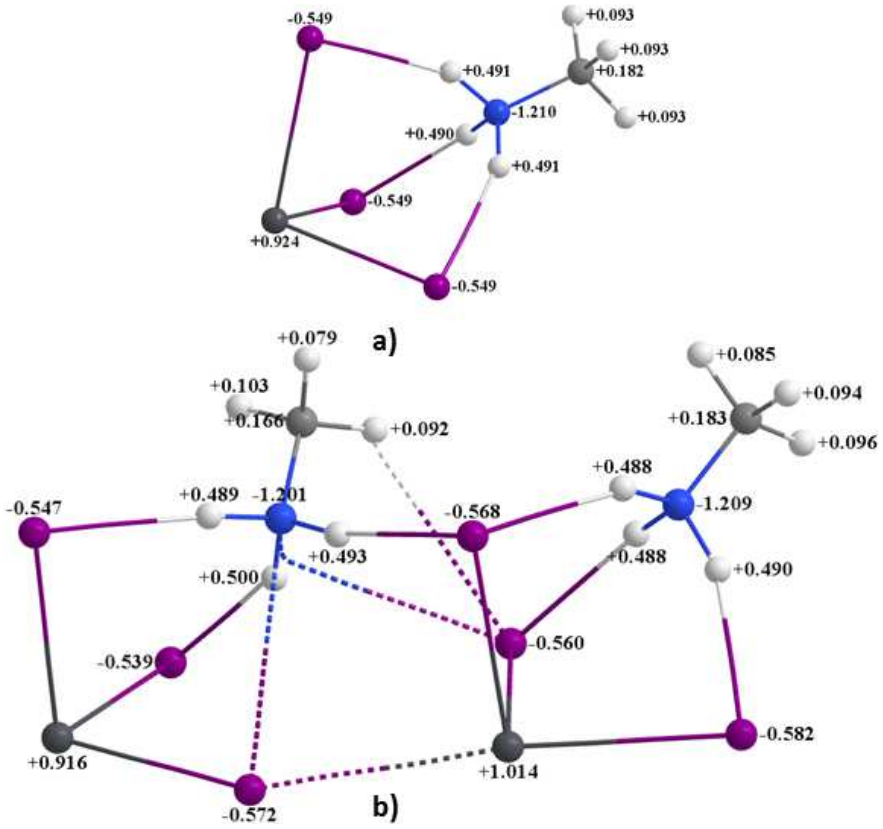

Fig 2: Examples illustrating the integrated QTAIM charges (in *e*) for a) $[MAPbI_3]$ and b) $[MAPbI_3]_2$, obtained with PBEPBE/DZP. The solid and dotted lines represent the bond paths, originated through QTAIM analyses.

Our next aim is to find out whether this charge transfer is from the Pb atom in PbI_3^- to the iodides to which it is datively bonded, or whether it is transferred to the neighboring LUMO of the $CH_3NH_3^+$ cation to which it is not at all linked through any

chemical bond, where the term LUMO is the lowest unoccupied molecular orbital. Before addressing this question, we first discuss below the third mechanism of charge transfer, which is occurring between the PbI_3^- and $CH_3NH_3^+$ fragments in $[PbI_3 \bullet\bullet\bullet H_3NCH_3]$.

The integrated QTAIM charge on each iodide in isolated PbI_3^- is ca. –0.620 *e*, Fig. 2a. The corresponding charge on the same atom in the same fragment in $[MAPbI_3]$ is ca. –0.549 *e*. Apparently, there is a difference of 0.071 *e* between the magnitudes of the charges conferred on the I atoms of the same fragment belonging to these two molecular domains. This provides further evidence about a net transfer of charge to its neighboring species during the formation of the $[MAPbI_3]$ molecular cluster. Since each coordinated iodide transfers an equivalent amount of charge, then this leads to a conclusion that a total charge of 0.213 *e* to be transferred from the three coordinated iodides to the neighboring species. Where does this transfer exactly occur? Which neighboring species are involved? Whether the charge is to be transferred to the coordinated Pb, or whether it is transferred to the $CH_3NH_3^+$ organic cation?

The charge from the coordinate iodides cannot be transferred to the lead core at the equilibrium geometry of the $[MAPbI_3]$ building block. This is because the charge on the $Pb^{+0.860}$ in isolated PbI_3^- is found to be less positive than that of it ($Pb^{+0.924}$) in the $MAPbI_3$ molecular block (*vide supra*). The transformation of the charge on the Pb core passing from the former to the latter species is possible only when the Pb core in the latter species transfers charge (or equivalently the core accepts some electron density in the former species), thereby becoming relatively more positive in $MAPbI_3$ than it was in isolated PbI_3^-. (This may be analogous to the way the ^{11}Na atom transfers an electron and becoming $^{10}Na^+$, and the ^{17}Cl receives an electron and becoming $^{18}Cl^-$, and their combination leads the formation of the Na^+Cl^- diatomic molecule.) Thus, the answer to the last questions above is apparently the latter. That is, the charges on the coordinated iodides are to be transferred to the $CH_3NH_3^+$ organic cation. Why?

As will be clearer later, this is reasonable because the $[PbI_3^- \bullet\bullet\bullet {}^+H_3NCH_3]$ ion-pair involves the formation of strong I•••H–N intermolecular hydrogen bonding interactions. This kind of arrangement requires at least some transfer of charge between the interacting partners. [38] This charge is found to be transferred from the lone-pair electron rich orbitals of the coordinated iodides in the PbI_3^- subunit to the σ*(N–H) antibonding orbitals of the $CH_3NH_3^+$ cation (*vide infra*).

From the results discussed above, it is now clear that a total of 0.213 *e* from the three I atoms of the isolated PbI_3^- species is transferred to the $CH_3NH_3^+$ cation in the $[PbI_3^- \bullet\bullet\bullet {}^+H_3NCH_3]$ block. It is also obvious at the same time that a net charge of 0.064 *e* is transferred from the Pb atom to the neighboring species with which it is directly/indirectly linked. Evidently, when these two quantities are summed over, a value of +0.277 *e* is resulted. This value is actually the net calculated charge transferred

(+0.278 *e*) from the PbI_3^- anion to the $CH_3NH_3^+$ cation, thereby accompanying the formation of the [$MAPbI_3$] block. (The difference between these latter two quantities of charge transfer, ≈ 0.001 *e*, can be attributed to the integration error.)

From the discussions above, it is probably clear that there is no direct bonding interaction observed between the Pb core of PbI_3^- and the ammonium fragment of $CH_3NH_3^+$ in [PbI_3^-•••$^+H_3NCH_3$]. Because of this, the [$MAPbI_3$] molecular cluster or its solid state bulk analogue should not be called as organometallic, [39] as numerously cited. [40] Since the Pb core donates charge, and is reflected only on the organic cation through the net amount of charge transferred, there is therefore no doubt that this charge transfer between the Pb^{2+} core and the $CH_3NH_3^+$ cation is supposedly carried out by a *superexchange* (or tunneling) mechanism since it is taking place between the two cations via the intermediate iodide anions. This should be through the three Pb—I coordinate bonds. The result clarifies the question raised above, that is, whether the charge on the Pb core in PbI_3^- is to be transferred to the coordinated iodides, or whether it is to be transferred to the $CH_3NH_3^+$ cation. (A discussion of the underlying concept of *superexchange* between two cations via an intermediate anion can be found elsewhere. [37a] Similar discussions can be found elsewhere.[37b-e])

QTAIM does not provide the details of the charge transfer between the atomic and/or molecular orbitals involved. In order to gain insight into the orbital origins of charge transfer between Pb and $CH_3NH_3^+$, NBO's second order perturbative theory analysis of Fock matrix in NBO basis is one of the most promising approaches. [42] An application of this at the PBEPBE/DZP level to the currently studied systems gave direct evidence of the charge transfer delocalization between electron donor and acceptor natural bond orbitals. Accordingly, our analysis shows that the transfer of charge (second type, see above) will be taking place from each of the three Pb–I bonding orbitals of the PbI_3^- subunit to the σ*(N–H) antibonding orbitals of the $CH_3NH_3^+$ fragment. The second order energies $E^{(2)}$ associated with these charge transfer delocalizations accompanying the formation of the [$MAPbI_3$] building block are ca. 1.48, 1.50 and 1.46 kcal mol^{-1} for σ(Pb–I) → σ*(N–H_9), σ(Pb–I) → σ*(N–H_{10}) and σ(Pb–I) → σ*(N–H_{11}), respectively. Similar arguments can be applicable to the other $[MAPbI_3]_{n=2–15}$ clusters in 1D.

The third type of charge transfer is also revealed by the NBO analysis, which can be described by the n(I) → σ*(N–H) hyperconjugative delocalizations, where n is the lone-pair orbital of the coordinated iodides. However, in this latter case, the $E^{(2)}$ are substantially larger ($E^{(2)}$ ~ 36.85 kcal mol^{-1}).

The natural electronic configuration analysis shows that the electronic occupancies for the 6s and 6p natural orbitals of Pb are ca. 1.90 and 1.43 electrons, respectively, whereas the electronic occupancies of the 5s and 5p orbitals of each I atom are ca. 1.94 and 5.48, respectively. This shows the p-orbitals of both Pb and I in [$MAPbI_3$] are not empty, and are occupied with 1.43 and 0.48 electrons, respectively.

According to the previously reported periodic DFT calculations, [35] the conduction band minimum (CBM) for the $MAPbI_3$ system is built mainly from the overlap of the p-states of Pb, while the valence band maximum (VBM) is built through the combination of the Pb's s- and I's p orbital characters. Due to the strong Pb(s)−I(p) antibonding coupling, the VBM is above the I's p atomic orbital. The view is in line with the reported DOS and partial charge density plots that suggested the VBM as a mixture of Pb's s and I's p antibonding characters, whereas the CBM is contributed from the Pb's p character, reflecting the dual nature (ionic and covalent) of halide perovskites' electronic structures. Moreover, these results suggest that the organic cation does not contribute to the development of either of the two bands, meaning it plays no role for the development of the electronic band structure of the $MAPbI_3$ solar cell semiconductor. [41] This result is not in agreement with the QTAIM and NBO rationalizations provided above.

Motta and coworkers [36] have argued that the $CH_3NH_3^+$ cation does not play any role in the optical and electronic response of the $MAPbI_3$ materials. Rather, it does contribute only to the structural cohesion of the overall perovskite geometry. In contrary, the same authors have further stated in the same study that the there is a small contribution ~0.5 eV below the VBM attributable to the organic cations. This chemically intuitive result was revealed through a careful analysis of the DOS projected on the various atoms. It is in agreement with the QTAIM and NBO results discussed above in a sense that the organic cation contributes positively to the development of the entire electronic structure of the perovskite for which $MAPbI_3$ has its own stability, shape and functionality.

In a recent frontier article of Materials Horizons, [44] which cites the study of Butlet *et al.*, [45] it has rationalized that the coupling between the inorganic and organic moieties appears to originate from hydrogen bonding interactions. It has further asserted that the $CH_3NH_3^+$ cation has no contributions to the band edges of the material, while coupling might contribute to the dynamics of the PbI_3^- lattice and therewith to a rather dynamic band structure as suggested by molecular dynamic simulations. [46] It is clear that these two statements contain some controversy, and the chemistry of intermolecular hydrogen bonding interactions in the rational design of perovskite materials is yet to be understood. This view might be in line with the authors of the above study, who have concluded that the phenomena associated with factors "dynamics and coupling" drive the photovoltaic properties of these systems. However, the precise mechanism that can explain these is open for challenging discussions. [44]

Table 1 lists the intermolecular charge transferred (ΔQ) between the interacting partners for the $[MAPbI_3]_{n = 1–15}$ series of clusters, evaluated using six population schemes employed. As can be seen from the data, QTAIM has predicted the preferential dominant charge transfer channel for the direction of the ΔQ to be from the PbI_3^- anion(s) to the $CH_3NH_3^+$ cation(s) for each member of the series. The ΔQ for each $[MAPbI_3]_{n = 1–15}$ is

evaluated by subtracting the formal net –1 charge of the isolated PbI_3^- species from the net charge on the same fragment in the energy-minimized geometry of the same cluster. An identical result can also be extracted by subtracting the net formal +1 charge of the isolated $CH_3NH_3^+$ from the net charge of the corresponding fragment viable in the same energy-minimized cluster. For instance, the ΔQ of –0.278 *e* for the [$MAPbI_3$] block is calculated by subtracting the net formal +1.000 charge on isolated $CH_3NH_3^+$ from the value of +0.722 *e* conferred on the same fragment in the corresponding block. Similarly, it should be understood that $[MAPbI_3]_2$ dimer is formed due to the assembly between two PbI_3^- anion(s) and two $CH_3NH_3^+$ cation(s). Thus, for it, the +2 formal charges on the two $CH_3NH_3^+$ cations were subtracted from the value of +1.437 e conferred on the two MA species in the corresponding dimer geometry (see Fig. 1b for details), resulting in a value of –0.563 *e* for the ΔQ, and so forth. All these results suggest that the charges on the MA species are to be decreased compared to its formal +1 charge, meaning that it is to be less electropositive by accepting fractional electron densities from the electron donor fragment PbI_3^-. In contrary, and at the same time, the net charge on the PbI_3^- anion(s) is to be increased, meaning it has to become more electropositive by losing some of the electron densities. This result gives solid evidence about the fact that ΔQ is indeed a consequence of charge rearrangement during complex formation. The physically meaningful scenario is not impossible since electrostatic polarization plays an important role for the stabilization of the [$MAPbI_3$] building block and its derivatives. Evidently, the result further rationalizes the fact that the [$MAPbI_3$] is indeed an

Table 1: Charge transfer (ΔQ/*e*) for the $[MAPbI_3]_{n=1–15}$ systems, obtained with M06-2X/DZP level of theory using six population schemes employed. Included is the chain length (length/Å) for all these systems.

n	Cluster	QTAIM	NPA	Becke	Mulliken	VDD	Hirshfeld	Length
1	$[MAPbI_3]_1$	0.278	0.390	0.376	0.472	0.506	0.528	3.011
2	$[MAPbI_3]_2$	0.563	0.611	0.705	0.988	1.021	1.115	9.544
3	$[MAPbI_3]_3$	0.852	0.897	1.004	1.525	1.530	1.703	16.088
4	$[MAPbI_3]_4$	1.139	1.181	1.359	2.046	2.056	2.293	22.578
5	$[MAPbI_3]_5$	1.434	1.467	1.811	2.556	2.600	2.891	29.031
6	$[MAPbI_3]_6$	1.720	1.752	2.105	3.09	3.107	3.478	35.545
7	$[MAPbI_3]_7$	2.011	2.038	2.447	3.612	3.630	4.070	42.025
8	$[MAPbI_3]_8$	2.303	2.325	2.826	4.139	4.174	4.665	48.509
9	$[MAPbI_3]_9$	2.597	2.615	3.262	4.648	4.705	5.264	54.962
10	$[MAPbI_3]_{10}$	2.886	2.900	3.549	5.182	5.226	5.851	61.476
11	$[MAPbI_3]_{11}$	3.178	3.190	3.969	5.689	5.757	6.448	67.925
12	$[MAPbI_3]_{12}$	3.468	3.478	4.266	6.229	6.266	7.039	74.453
13	$[MAPbI_3]_{13}$	3.761	3.766	4.713	6.739	6.810	7.637	80.909
14	$[MAPbI_3]_{14}$	4.051	4.055	5.059	7.261	7.337	8.231	87.395
15	$[MAPbI_3]_{15}$	4.341	4.342	5.356	7.801	7.851	8.820	93.929

acceptor-donor (acid-base) complex system whose formation mechanism relies on the same fundamental principle of electron-give and -take policy.

The data in Table 1 show that the least of the ΔQ is to be accompanied with the $MAPbI_3$ building block in the $[MAPbI_3]_{n = 1–15}$ series. It is roughly 0.278 *e*. This value is presumably too large compared to those reported for a wide variety of conventional and unconventional hydrogen bonding interactions documented in the literature.[24] Note that there have been versatile number of intermolecular hydrogen bonding interactions appeared in recent years, [25] which play their role as intermolecular gels to hold the molecular domains together in complex configurations, assisting in the novel design of functional materials.[26] These interactions can be merged into broad types. These can be either outer (weak), or inner (strong) type. [27] According to Mulliken's connotation, [27] the formation of outer type intermolecular interactions is generally weak because the electric charge rearrangement between interacting species is very minor on complex formation and is therefore accompanied with very small amount of charge transfer (typically << 0.10 *e*) between the interacting species when they are at equilibrium; [28] the $(H_2O)_2$ dimer is an example of an outer complex wherein the intermolecular charge transfer is very marginal (ΔQ ≈ 10 *me*). [29]

Table 2: Charge transfer (ΔQ/*e*) for the $[CsPbI_3]_{n = 1–10}$ systems, obtained with M06-2X/DZP level of theory using five population schemes employed. Included is the chain length (length/Å) for all these systems.

n	Clusters	QTAIM	Becke	Mulliken	Hirshfeld	VDD	Length
1	$[CsPbI_3]_1$	0.066	0.162	0.204	0.351	0.385	3.003
2	$[CsPbI_3]_2$	0.139	0.471	0.485	0.846	0.909	9.576
3	$[CsPbI_3]_3$	0.216	0.777	0.782	1.348	1.443	16.075
4	$[CsPbI_3]_4$	0.293	1.080	1.081	1.850	1.984	22.564
5	$[CsPbI_3]_5$	0.370	1.394	1.786	2.352	2.503	29.039
6	$[CsPbI_3]_6$	0.447	1.700	1.679	2.853	3.050	35.510
7	$[CsPbI_3]_7$	0.525	2.016	1.979	3.354	3.577	41.952
8	$[CsPbI_3]_8$	0.602	2.325	2.279	3.855	4.117	48.449
9	$[CsPbI_3]_9$	0.679	2.640	2.578	4.356	4.652	54.914
10	$[CsPbI_3]_{10}$	0.757	2.954	2.877	4.856	5.191	61.374

By contrast, the (Mulliken) inner complexes are consequences of significant rearrangement of charges between the interacting partners. So, they are accompanied with large amount of charge transfers between the interacting species (typical values ΔQ >> 0.10 *e*),[28, 30-31] contributing largely to the effective stabilizations of the resulting complex configurations. Whereas the outer complexes are largely distributed in the literature, covering many areas of research in chemistry, materials and drug design, crystallography, and biology, [24, 31-32] there are only a limited number inner complexes documented in the literature.[28, 30, 33-34] The studies of Hill *et al.,* [28] Bloemink *et al.,* [30] Poleshchuk *et al.,* [33] and S. N. Eustis *et al.*[34]

are typical examples. It is recently demonstrated that induction (polarization) is the primary interaction that accounts for such large transfers of charge between the electron donor and acceptor,[28a] which can be viewed as a metric for understanding charge transfer between the interacting monomers.

6.3.2 The structure and property relationship

The most striking of the data of Table 1 is that as the number *n* in the $[MAPbI_3]_{n=1–15}$ systems increases the length of the •••Pb–I•••Pb–I••• chain increases. In line with this, the ΔQ increases additively. For instance, for the $[MAPbI_3]_2$ dimer, *r*(Pb–I•••Pb–I) ≈ 9.544 Å and ΔQ ≈ 0.560 *e*, with the latter displaying the extent of intermolecular charge transfer, which is almost twice larger than that found for the building block. For the $[MAPbI_3]_2$ trimer, *r*(•••Pb–I•••Pb–I•••) ≈16.088 Å and ΔQ ≈ 0.852 *e*, in which, the ΔQ is approximately thrice larger than that found for the $[MAPbI_3]$ block. For the largest $[MAPbI_3]_{15}$ system, the *r*(•••Pb–I•••Pb–I•••) and ΔQ are as large as ≈ 93.929 Å and 4.34 *e* respectively, indicating a substantial ΔQ.

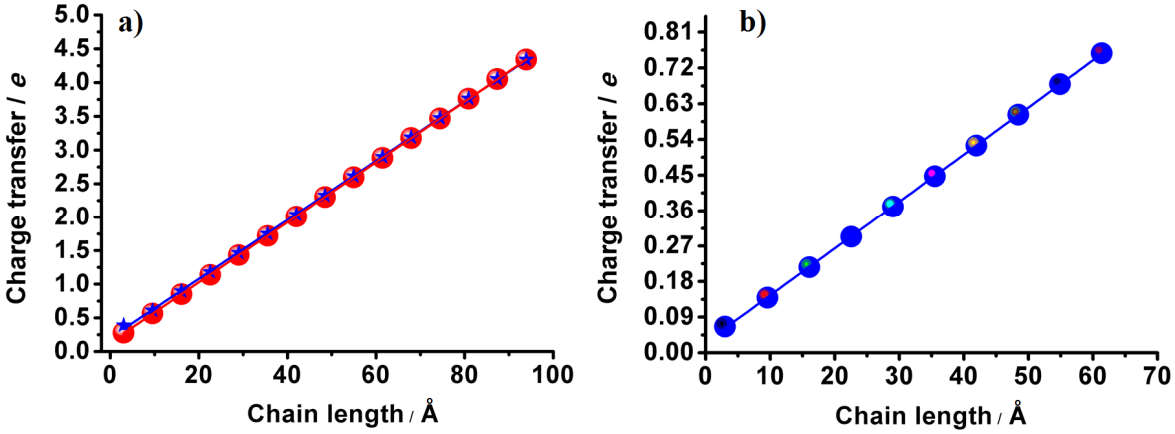

Fig. 3: a) Dependence of the QTAIM (•) and NPA (*) intermolecular charge transfers (ΔQ/*e*) on the lengths of the perovskite chains for the $[MAPbI_3]_{n = 1–15}$ series. b) Dependence of the QTAIM intermolecular charge transfers (ΔQ/*e*) on the lengths of the perovskite chains for the $[CsPbI_3]_{n = 1–10}$ cluster series. Each data set is fitted to a linear equation, with Adj. $R^2 \approx 0.99999$.

The $[CsPbI_3]$ molecular block, on the other hand, is also accompanied with some appreciable amount of intermolecular charge transfer between Cs^+ and PbI_3^-. It is taking place

in the same direction over longer distances, similarly as observed for [$MAPbI_3$], i.e., it will transfer from the negatively charged PbI_3^- to the positively charged species Cs^+. The feature in general is not very unusual for any donor-acceptor pair comprising a Lewis acid and a Lewis base. However, the extent of charge transferred between the monomers forming the [$CsPbI_3$] building block is substantially smaller than that found for the [$MAPbI_3$] building block. For instance, and with the same QTAIM level of theory, the ΔQ is calculated to be 0.066 *e* for [$CsPbI_3$], which is about 4.21 times smaller than that calculated for the [$MAPbI_3$] block. Similarly, with the increase of the cluster size *n* in $[CsPbI_3]_n$, the ΔQ is indeed increased in a manner analogous to that observed for the corresponding $[MAPbI_3]_{n = 1–15}$ clusters, but with a substantially smaller magnitude. Analysis shows that the ΔQ increases additively with the sequential increase of *n* (*n* up to 10) in $[CsPbI_3]_n$, with $0.066 < \Delta Q < 0.757$ *e*. As expected, the longest cluster $[CsPbI_3]_{10}$ is also found to be accompanied with a very large ΔQ of 0.757 *e* (see Table 2 for details about ΔQ and chain length for all the Cs-based cluster systems).

Figs. 3a and b present the desired relationship between the chain length and the QTAIM based ΔQ for the $[MAPbI_3]_{n = 1–15}$ and $[CsPbI_3]_{n = 1–10}$ series, respectively. The linear regression analysis between them for each series shows that each data set can be described by a linear function of the form $\Delta Q = a \times r + b$, where a and b are constants. The regression coefficients of these fits were such that Adj. $R^2 \approx 1$.

The same relationship can also be established when the ΔQ evaluated with the Mulliken, NPA, Hirshfeld, Becke and VDD population schemes will be individually plotted against the chain length for both the series. This is, as for example, illustrated in Fig. 4 for the $[MAPbI_3]_{n = 1–15}$ series. In particular, Fig. 4a illustrates the linear relationship between the ΔQ and the size *n* of the cluster, with the former evaluated with the various population schemes employed. Fig. 4b establishes the relationship between the charge transfers evaluated with QTAIM and those with the other five population methods. Although a linear relationship is found for each data set, the results show that the varied nature of the mathematical formulations involved for the development of each of these five population schemes do not affect the qualitative nature of the relationship established between ΔQ and *n*.

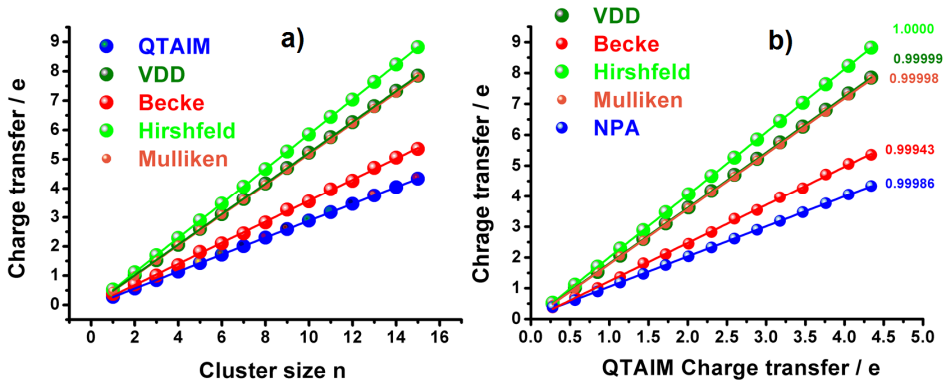

Fig. 4: a) Dependence of the extent of the intermolecular charge transfer ($\Delta Q/e$) [emanated using QTAIM, VDD, Becke, Hirshfeld, and Mulliken population analyses] on the size *n* of the $[MAPbI_3]_{n = 1–15}$ clusters. Shown in b) is the dependence of the intermolecular charge transfer evaluated with QTAIM on that calculated with the VDD, NPA Becke, Hirshfeld, and Mulliken population analyses. Each data set is fitted to a linear equation, with Adj. $R^2 \approx 1$ (exact values shown in b).

As a side note, we emphasize that the magnitudes of the ΔQ evaluated with QTAIM are substantially smaller than those evaluated with the other five population schemes $[MAPbI_3]_{n=1–15}$ series. In particular, it is found that while the ΔQ evaluated with the NPA are in excellent match with QTAIM for the clusters, and those evaluated with the Becke population method are somehow in good match with the QTAIM (~ < 1.2 times larger). On the other hand, the Hirshfeld, Mulliken and VDD have generated the ΔQ that are approximately 2.0, 1.8 and 1.8 times larger than the QTAIM estimates. A similar result is obtained for the $[CsPbI_3]_{n=1–15}$ series with the other five population schemes employed (see Table 2 for details), however the NPA analysis could not have performed with this series because of spurious basis set inconsistency problem.

6.4 Conclusion

We have identified three types of charge transfer mechanism accompanying the formation of the $[MAPbI_3]$ and $[CsPbI_3]$ building blocks in 0D, as well as the $[MAPbI_3]_{n=2–15}$ and $[CsPbI_3]_{n=2–10}$ supramolecular systems in 1D. The dominant yet direct charge transfer mechanism is found to be intermolecular, and is occurring between the interacting monomers in a direction from the negatively charged Lewis bases to the positively charged Lewis acids. That is, the ΔQ is taking place in this direction: $PbI_3^- \rightarrow CH_3NH_3^+$ for $[MAPbI_3]_{n=1–15}$, and $PbI_3^- \rightarrow Cs^+$ for $[CsPbI_3]_{n=1–10}$. The second mechanism is what we referred it to as the super-exchange charge transfer, occurring between the Pb ion core of the PbI_3^- anion and the LUMO of the $CH_3NH_3^+$ cation. The same mechanism is found to occur between the PbI_3^- anion and the Cs^+ cation for the $[CsPbI_3]$ system. Moreover, it was found that there is no direct metal–carbon bond in either of these perovskite systems, thus these should not have called as organometallic.

While the stabilities of the $[MAPbI_3]_{n=1–15}$ and $[CsPbI_3]_{n=1–10}$ cluster systems can assumedly be determined largely through the Coulomb type electrostatic component of the interactions involved, the charge transfer (polarization) component does substantially responsible for the formation of the intermolecular dative bonding interactions for which the trihalide perovskite clusters in 0 and 1D display their sole existence in the gas phase. An analogous argument may be applicable to the $MAPbI_3$ and $CsPbI_3$ systems in the solid state, as the gas phase geometries recover the skeletal 1D architectures of the low-temperature orthorhombic geometries of the corresponding systems observed in the solid state.

Because large intermolecular charge transfer between molecular domains is an unambiguous signature for the formation of formal covalent bonds, the I•••H–N intermolecular interactions in the electronic ground states of both the $[MAPbI_3]_{n=1–15}$ and $[CsPbI_3]_{n=1–10}$ systems are arguably comprising appreciable amount of covalent components.

The results presented also suggest that both the $[MAPbI_3]_{n=1–15}$ and $[CsPbI_3]_{n=1–10}$ systems and their large scale analogues can be regarded as charge transfer complexes. While the detailed nature of the charge-transfer and -separated states may provide additional theoretical insight into photophysics of these systems, an investigation of these features can be the topic of separate investigations. In any case, the study also showed that the application of a simple model of charge rearrangement can not only assist the fundamental physical understanding of the molecular perovskite systems both in 0 and 1D, but also impart the knowledge that atomic charge is indeed an elegant property of atoms in molecules

transferrable to any donor-acceptor acid-base systems for better understanding of the cluster physics involved.

6.5 References

1. R. G. Niemann, A. G. Kontos, D. Palles, E. I. Kamitsos, A. Kaltzoglou, F. Brivio, P. Falaras, P. J. Cameron, Halogen effects on ordering and bonding of $CH_3NH_3^+$ in $CH_3NH_3PbX_3$ (X = Cl, Br, I) hybrid perovskites: A vibrational spectroscopic study, *J. Phys. Chem. C* 2016, 120, 2509-2519.
2. C. C. Stoumpos, C. D. Malliakas, J. A. Peters, Z. Liu, M. Sebastian, J. Im, T. C. Chasapis, A. C. Wibowo, D. Y. Chung, A. J. Freeman, B. W. Wessels, M. G. Kanatzidis, Crystal growth of the perovskite semiconductor $CsPbBr_3$: A new material for high-energy radiation detection, *Cryst. Growth Des.* 2013, 13, 2722–2727.
3. D. J. Slotcavage, H. I. Karunadasa, M. D. McGehee, Light-induced phase segregation in halide perovskite absorbers, *ACS Energy Lett.* 2016, 1, 1199 – 1205.
4. C. Fai, J. Lau, X. Deng, Q. Ma, J. Zheng, J. S. Yun, M. A. Green, S. Huang, A. W. Y. Ho-Baillie, $CsPbIBr_2$ perovskite solar cell by spray-assisted deposition, *ACS Energy Lett.* 2016, 1, 573–577.
5. Z. Liu, J. A. Peters, C. C. Stoumpos, M. Sebastian, B. W. Wessels, J. Im, A. J. Freeman, M. G. Kanatzidis, Heavy metal ternary halides for room-temperature X-ray and gamma-ray detection, Proc. SPIE - Proc. SPIE *(The International Society for Optical Engineering)* 2013, 8852, 88520A.
6. National Renewable Energy Laboratory (NREL) Best Research-Cell Efficiency chart. http://www.nrel.gov/ncpv/images/efficiency_chart.jpg (2016).
7. T. A. Berhe, W.-N. Su, C.-H. Chen, C.-J. Pan, J.-H. Cheng, H.-M. Chen, M.-C. Tsai, L.-Y. Chen, A. Aregahegn Dubale, B.-J. Hwang, Organometal halide perovskite solar cells: degradation and stability**,** *Energy Environ. Sci.* 2016, **9**, 323-356.
8. R. E. Beal, D. J. Slotcavage, T. Leijtens, A. R. Bowring, R. A. Belisle, W. H. Nguyen, G. F. Burkhard, E. T. Hoke, M. D. McGehee, Cesium lead halide perovskites with improved stability for tandem solar cells, *J. Phys. Chem. Lett.* 2016, 7, 746−751.
9. a) K. A. Bush, *et al.*, 23.6%-efficient monolithic perovskite/silicon tandem solar cells with improved stability, *Nat. Energy* 2017, 2, 17009; b) M. H. Futscher, B. Ehrler, Efficiency limit of perovskite/Si tandem solar cells, *ACS Energy Lett.* 2016, 1, 863–868.
10. R. J. Sutton, et al., Bandgap-tunable cesium lead halide perovskites with high thermal stability for efficient solar cells, *Adv. Mat.* 2016, 6, 1502458.
11. W. J. Yin, Y. Yan, S. H. Wei, Anomalous alloy properties in mixed halide perovskites, *J. Phys. Chem. Lett.* 2014, 5, 3625−3631.
12. S. Yanagidaa, S. Yanagisawa, H. Segawa, Molecular orbital-based verification of conductivity of tetramethylammonium pentaiodide and pentaiodide-based electrolytes in dye-sensitized solar cells, *J. Electrochem. Soc.* 2015, 162, E263-E270
13. A. Varadwaj, P. R. Varadwaj, K. Yamashita, Organic-inorganic hybrid $CH_3NH_3PbI_3$ perovskite solar cell nanoclusters: Revealing ultra-strong hydrogen bonding and Mulliken inner complexes and their implication in materials design, 2017, https://arxiv.org/abs/1703.10286.
14. E. Belarbi, M. Vallés-Pelarda, B. C. Hames, R. S. Sanchez, E. M. Barea, H. Maghraoui-Meherzi, I. Mora-Seró, Transformation of PbI_2, $PbBr_2$ and $PbCl_2$ salts into $MAPbBr_3$ perovskite by halide exchange as an effective method for recombination reduction, *Phys. Chem. Chem. Phys.* 2017,19, 10913-1092.
15. A. Buin, P. Pietsch, J. Xu, O. Voznyy, A. H. Ip, R. Comin, E. H. Sargent, Materials processing routes to trap-free halide perovskites, *Nano Lett.*, 2014, *14*, 6281–6286.

16. K. G. Stamplecoskie, J. S. Manserab, P. V. Kamat, Dual nature of the excited state in organic–inorganic lead halide perovskites, *Energy Environ. Sci.* 2015, 8, 208–215.
17. J. P. Perdew, K. Burke, M. Ernzerhof, Generalized gradient approximation made simple, *Phys. Rev. Lett.* 1996, 77, 3865.
18. C. C. Stoumpos, C. D. Malliakas, M. G. Kanatzidis, Semiconducting tin and lead iodide perovskites with organic cations: Phase tansitions, high mobilities, and near-infrared photoluminescent properties, *Inorg. Chem.* 2013, 52, 9019.
19. K. L. Schuchardt, *et al.*, Basis Set Exchange: A Community Database for Computational Sciences, *J. Chem. Inf. Model.* 2007, 47, 1045-1052.
20. a) R.F.W. Bader, Atoms in Molecules: A Quantum Theory", Oxford University Press, Oxford (1990); b) R. S. Mulliken, Electronic Population Analysis on LCAO-MO Molecular Wave Functions. I, *J. Chem. Phys.*1955, 23, 1833–1840; c) F. L. Hirshfeld, Bonded-atom fragments for describing molecular charge densities, Theor. Chim. Acta 1977, 44: 129; d) C. F. Guerra, *et al.*, Voronoi deformation density (VDD) charges: Assessment of the Mulliken, Bader, Hirshfeld, Weinhold, and VDD methods for charge analysis, *J. Comput. Chem.* 2004, 25, 189–210; e) A. D. Becke, A multicenter numerical integration scheme for polyatomic molecules, *J. Chem. Phys.* 1988, *88*, 2547-2553.
21. Gaussian 09, Revision C.01, M. J. Frisch, *et al.*, Gaussian, Inc., Wallingford CT, 2016.
22. AIMAll (Version 16.10.31), Todd A. Keith, TK Gristmill Software, Overland Park KS, USA, 2016 (aim.tkgristmill.com).
23. T. Lu, F. Chen, Multiwfn: A multifunctional wavefunction analyzer, J. Comp. Chem. 2012, 33, 580-592.
24. R. Z. Khaliullin, *et al.*, Analysis of charge transfer effects in molecular complexes based on absolutely localized molecular orbitals, *J. Chem. Phys.* 2008, 128, 184112.
25. L. Meazza, Halogen-bonding-triggered supramolecular gel formation, *Nat. Chem.* 2013, 5, 42–47.
26. G. O. Lloyd, J. W. Steed, Anion-tuning of supramolecular gel properties, Nat. Chem. 2009, 1, 437 – 442.
27. a) R. S. Mulliken, J. Phys. Chem. 56, 801 (1952); b) R. S. Mulliken and W. B. Person, Molecular Complexes, Wiley-Interscience, New York 1969.
28. a) J. H. Hill, The halogen bond in thiirane···ClF: an example of a Mulliken inner complex, *Phys. Chem. Chem. Phys.* 2014,16, 19137-19140; b) R. A. Shaw, J. G. Hill, A. C. Legon, Halogen Bonding with Phosphine: Evidence for Mulliken inner complexes and the importance of relaxation energy, *J. Phys. Chem. A* 2016, 120, 8461–8468.
29. H. Elgabarty, R. Z. Khaliullin, T. D. Kühne, Covalency of hydrogen bonds in liquid water can be probed by proton nuclear magnetic resonance experiments, *Nat Commun.* 2015, 6:8318.
30. H. I. Bloemink, J. H. Holloway, A. C. Legon, Mulliken inner complexes $[(CH_3)_3 NCl]^+...F^-$ in pre-reactive mixtures of trimethylamine and chlorine monofluoride: identification and characterisation by rotational spectroscopy, *Chem. Phys. Lett.* 1996, 254, 59–68.
31. W. A. Herrebout, A. C. Legon, E. R. Waclawik, Is there significant intermolecular charge transfer in the ground state of the HCN···ICI complex? An answer from rotational spectroscopy, *Phys. Chem. Chem. Phys.* 1999, 1, 4961-4966.
32. J.B. Davey, A.C. Legon and E.R. Waclawik, Measurement of inter- and intramolecular charge transfer in the complex N_2···ICl from analysis of halogen nuclear quadrupole hyperfine structure in the rotational spectrum, *J. Mol. Struct.: THEOCHEM* 2000, 500, 403.
33. O. Kh. Poleshchuk and A. C. Legon, Density Functional Theory Studies of Bonding in Complexes H_3N···XY of Ammonia and Dihalogen Molecules: A Comparison with Experimental Results from Rotational Spectroscopy, *Z. Naturforsch.* 2002, 57 a, 537–543.

34. S. N. Eustis, D. Radisic, K. H. Bowen, R. A. Bachorz, M. Haranczyk, G. K. Schenter, M. Gutowski, Electron-driven acid-base chemistry: Proton transfer from hydrogen chloride to ammonia, *Science* 2007, 319, 936.
35. a) W.-J. Yin, J.-H. Yang, J. Kang, Y. Yan, S.-H. Wei, Halide perovskite materials for solar cells: a theoretical review, *J. Mater. Chem. A* 2015, 3, 8926; b) F. Zheng, *et al.*, Material innovation in advancing organometal halide perovskite functionality, *J. Phys. Chem. Lett.* 2015, 6, 4862−4872.
36. C. Motta, F. El-Mellouhi, S. Kais, N. Tabet, F. Alharbi, S. Sanvito, Revealing the role of organic cations in hybrid halide perovskite $CH_3NH_3PbI_3$, *Nat. Commun.* 2015, 6, 7026.
37. a) The reader may be interested to see Fig. 5.1 of the book 'Lecture Notes on Electron Correlation and Magnetism', by P. Fazekas (World Scientific, Singapore, 1999) that describes the superexchange between two cations via an intermediate anion involving transition metals. Section 2.5.1 describes Direct Exchange, while sections 2.5.2 discusses about Kinetic Exchange; Superexchange is discussed in Sec. 5.2 of Ch. 5 (Mott Insulators); b) C. Lambert, G. Nöll, J. Schelter, Surface and thin films Bridge-mediated hopping or superexchange electron-transfer processes in bis(triarylamine) systems, *Nat. Mat.* 2002, 1, 69 – 73; c) M. D. Todd, A. Nitzan, M. A. Ratner, Electron transfer via superexchange: a time-dependent approach, *J. Phys. Chem.* 1993, 97, 29–33; d) B. P. Paulson, J. R. Miller, W.-X. Gan, G. Closs, Superexchange and sequential mechanisms in charge transfer with a mediating state between the donor and acceptor, *J. Am. Chem. Soc.* 2005, 127, 4860–4868; e) K. Saito, T. Kikuchi, K. Mukaia, H. Sumia, Sequential or superexchange mechanism in bridged electron transfer distinguished by dynamics at a bridging molecule, *Phys. Chem. Chem. Phys.* 2009,11, 5290-5301.
38. a) A. C. Legon, Prereactive Complexes of Dihalogens XY with Lewis Bases B in the Gas Phase: A Systematic Case for the Halogen Analogue B•••XYof the Hydrogen Bond B•••HX, Angew. Chem. Int. Ed. 1999, 38, 2686-2714; b) W. A. Herrebout, A. C. Legon, E. R. Waclawik, Is there significant intermolecular charge transfer in the ground state of the HCN···ICI complex? An answer from rotational spectroscopy, *Phys. Chem. Chem. Phys.* 1999, 1, 4961-4966.
39. P. R. Varadwaj, Methylammonium lead trihalide perovskite solar cell semiconductors are not organometallic: A perspective, *Helvetica Chimica Acta*, 2017, DOI: 10.1002/hlca.201700090.
40. X. Xu, S. Li, H. Zhang, Y. Shen, S. M. Zakeeruddin, M. Graetzel, Y.-B. Cheng, M. Wang, A Power Pack Based on Organometallic Perovskite Solar Cell and Supercapacitor, *ACS Nano* 2015, 9, 1782–1787.
41. S. Sanvito, C. Motta, F. El-Mellouhi, Waltzing molecules for high-efficiency photovoltaics, SPIE *Newsroom* 2015, DOI: 10.1117/2.1201509.006060.
42. F. Weinhold, C. R. Landis, Natural bond orbitals and extensions of localized bonding concepts, *Chemistry Education Research and Practice* 2001, 2, 91–104.
43. A. Jain, S.P. Ong, G. Hautier, W. Chen, W.D. Richards, S. Dacek, S. Cholia, D. Gunter, D. Skinner, G. Ceder, K.A. Persson, The Materials Project: A materials genome approach to accelerating materials innovation, *APL Materials* 2013, 1, 011002.
44. G. Kieslich, A. L. Goodwin, The same and not the same: molecular perovskites and their solid-state analogues, *Mater. Horiz.* 2017, 4, 362-366.
45. K. T. Butler, K. Svane, G. Kieslich, A. K. Cheetham, A. Walsh, Microscopic origin of entropy-driven polymorphism in hybrid organic-inorganic perovskite materials, *Phys. Rev. B* 2016, 94, 180103.
46. A. L. Montero-Alejo, E. Menéndez-Proupin, D. Hidalgo-Rojas, P. Palacios, P. Wahnón, J. C. Cones, Modeling of thermal effect on the electronic properties of photovoltaic perovskite $CH_3NH_3PbI_3$: The case of tetragonal phase, *J. Phys. Chem. C* 2016, 120, 7976–7986.

Chapter 7. The Trihalide Perovskites: Low-Bandgap Materials for Photovoltaic Solar Cells

7.1 Introduction

In the area of materials science and nanotechnology, a major part of the current research focus has been centered on the invention of functional nanomaterials.[1-2] One of the main interests in these lies in the invention energy materials for applications in photovoltaic solar cells.[3-4] Lead-based and -free perovskite semiconductors are an integral part of these systems which have shown to have potential for converting sun light into electricity.[5-7] These systems have been studied intensively since scientists expect that these might prove to serve as better alternatives to silicon solar cells since these are thinner, more flexible, and easier to manufacture than silicon crystal as they requires a lot of energy in the manufacturing process.[8-10]

Manser *et al.* envisioned that this is a new chapter in the long and distinguished history of perovskites, which is being written with the breakthrough success of metal halide perovskites as solution-processed photovoltaic absorbers.[11] Green *et al.* have asserted that "photon conversion efficiency over 22% was confirmed in early 2016 for methylammonium lead trihalide perovskite ($CH_3NH_3PbI_3$, or $MAPbI_3$). However, it should not be forgotten that some of these record devices will maintain their record-breaking performance for periods that may be as short as 10 min. Good progress on the efficiency front since then has been made with both all perovskite and perovskite/silicon tandem cells, with confirmed efficiencies of 23.6% demonstrated for the latter." [12]

As already mentioned in previous Chapters, $MAPbI_3$ is the only semiconductor invented within the entire perovskite families that displays the high photovoltaic performance in the entire history of solar energy race, which is within 7 years period.[13-15] Because of its phenomenal performance, a large number of perovskite materials with a variety of B and M site cations have already been developed, where B and M are an integral part of the generic formula BMY_3.[16] In this formula, M is the metal cation and Y is generally the halogen,[16] or other cations such as $HCOO^-$.[17-19] The former arrangement of Y in BMY_3 produces usual trihalide perovskites (e.g., $CH_3NH_3PbY_3$),[16] whereas the latter arrangement produces metal-organic perovskites (e.g., $HC(NH_2)_2Pb(HCOO)_3$).[17-19] A list of perovskite systems with diverse B and M-site cations has been documented in recent studies.[20-21]

Ergen *et al.* have recently demonstrated the concept of graded bandgap perovskite solar cells. [22] These were an architecture of two perovskite layers ($CH_3NH_3SnI_3$ and $CH_3NH_3PbI_{3-x}Br_x$), incorporating GaN, monolayer hexagonal boron nitride, and graphene aerogel. Their experimental results show that these can perform well, with

steady-state conversion efficiencies averaging 18.4%, with a best of 21.7%, all without reflective coatings. Their data have yielded high fill factors of ~75% and high short-circuit current densities up to 42.1 mA cm^{-2}.

There have been significant research developments concerning the understanding of factors influencing the environmental degradation of the perovskite solar cell materials. [22] While many research articles demonstrate the material will degrade through photon dose, water, oxygen, heat and many other things,[23] it is just recently demonstrated that stable perovskite devices fabricated through a combination of 2D and 3D $(HOOC(CH_2)_4NH_3)_2PbI_4/CH_3NH_3PbI_3$ junctions may guarantee one-year device stability. [24] In this latter architecture, the 2D perovskite layer acts as a protective window against environmental ingredients, enabling the 3D perovskite to function similarly as it was without the hybrid arrangement to display its electricity generating ability. The 2D/3D architecture is an exceptional gradually-organized multi-dimensional interface that yields up to 12.9% efficiency in a carbon-based architecture, and 14.6% in standard mesoporous solar cells. Specifically, it has shown that the 10 × 10 cm^2 solar modules fabricated by a fully printable industrial-scale process deliver 11.2% efficiency stable for >10,000 h with zero loss in performances, measured under controlled standard conditions. This innovative stable and low-cost architecture is expected to enable the timely commercialization of perovskite solar cells. [24]

Despite significant synthetic developments and characterizations, [25-28] there have been many controversies in this area.[29-40] One such controversy is associated with the role of the organic cation in the design of $MAPbY_3$, where $Y = Br_{(3-x)}Cl_{x=1–3}$, $I_{(3-x)}Br_{x=1–3}$, $I_{(3-x)}Cl_{x=1–3}$. A group of scientists demonstrate it plays a major role in determining the electronic structure of the perovskite materials, [32-37] while others advocate the cation does not do anything significant.[30,40-41] Similarly, a number of research articles demonstrate that the dipolar cation has an important role to explain observed hysteresis and ferroelectric features of $MAPbI_3$,[42-43] while others demonstrate these are not ferroelectric materials.[44-45] Some authors have suggested this material is polar,[46] while others give experimental evidence demonstrating it is nonpolar,[42] and so on. In particular, Rakita *et al.* have showed that tetragonal $MAPbI_3$ is definitely ferroelectric, it is non-centrosymmetric and polar, claiming that the material's ferroelectric nature, can, but need not be important in a PV cell at room temperature. [42] This demonstration is contrast with those of Sharada *et al.*, in which, in this latter study, the authors have showed that this material is centrosymmetic and nonpolar.[46] It is thus understandable from these discussions that the research topic is immature, thereby needing significant future discussions to arrive at definitive conclusions on many aspects of these materials.

In this Chapter, I mainly focus on a five-fold objective. The first one involves the discussion of the results of the high level gas phase calculations of the $CH_3NH_3MY_3$ series, and shows how effective these can be to predict the bandgap of the corresponding

solid state systems with some accuracy. The second one involves the discussion of the predicted binding energies of the new NH_3XMY_3 (X = F, Cl, Br, I; Y = $Br_{(3-x)}Cl_{x=1-3}$, $I_{(3-x)}Br_{x=1-3}$, $I_{(3-x)}Cl_{x=1-3}$, and IBrCl; M = Pb, Sn) systems, and a comparison of them with those of the $CH_3NH_3MY_3$ systems to demonstrate the stability of these newly discovered materials. The third objective involves the discussion of the results of the bulk calculations associated with the new NH_3XMY_3 materials. The fourth objective involves the comparison of the nature of the intermolecular interactions in the low temperature phase of the NH_3IPbI_3 and $CH_3NH_3PbI_3$ systems, and presentation of our own perspective on the nature of these interactions for the orthorhombic phase, and to show which ways do these assist to explain the observed octahedral tilting in these systems. The final objective of this Chapter is to provide a demonstration concerning whether the NH_3XMY_3 systems can serve as possible new candidates for photovoltaics.

7.2 Computational details

Gaussian 09 package[47] was used for the electronic structure calculations in the gas phase, and Gaussview 05[48] was used for visualization of geometries and structural analysis.

The PBEPBE functional, together with the aug-cc-pVTZ (for $CH_3NH_3^+$, $-NH_3$, Cl, Br) and aug-cc-pVTZ-PP (for I, Sn and Pb)] basis sets, was employed for geometry optimization and normal mode vibrational frequency calculations; the basis sets were retrieved from the EMSL basis set exchange library.[49] The use of the pseudo potential basis set for the heavy atoms Pb and I is due to the fact that the Dunning's all-electron correlated aug-cc-pVTZ basis set is not available for these atoms.

The uncorrected binding energy, ΔE, for each member of the $MAPbY_3$, $MASnY_3$ and NH_3IPbY_3 series, where Y = $Br_{(3-x)}Cl_{x=1-3}$, $I_{(3-x)}Br_{x=1-3}$, $I_{(3-x)}Cl_{x=1-3}$, and IBrCl, was calculated using Eqn. 1 given below, where E is the total electronic energy of the individual species involved.

$$\Delta E\ (BMY_3) = E\ (BMY_3) - E\ (B^+) - E\ (MY_3^-) \quad \ldots\ldots\ldots\ldots\ldots\ldots\ldots\ldots\ldots\ldots\ldots\ldots\ldots\ldots\ (1)$$

The basis set superposition error (BSSE) corrected binding energy, ΔE^{corr}, for each member of the $MAPbY_3$, $MASnY_3$ and NH_3XPbY_3 series was calculated using Eqn. 2 given below. The uncorrected binding energies for all the binary perovskite cluster systems examined were basis set superposition error (BSSE) corrected using the standard counterpoise procedure of Boys and Bernardi. [50]

$$\Delta E^{corr}\ (BMY_3) = \Delta E\ (BMY_3)\ + BSSE \quad \ldots\ldots\ldots\ldots\ldots\ldots\ldots\ldots\ldots\ldots\ldots\ldots\ldots\ (2)$$

The reliability of the DFT estimates of the binding energies was examined by performing similar calculations with the Coupled Cluster calculations incorporating Single and Double excitations in conjunction with the cc-pVTZ (for $CH_3NH_3^+$, $-NH_3$, Cl, Br) and cc-pVTZ-PP (for I, Sn and Pb), as well as by performing single points at the CCSD(T) levels on the CCSD energy-minimized geometries of the binary clusters examined, where T refers the triples excitation. [47]

Periodic DFT calculations were carried out using the Vienna Ab initio Simulation Package (VASP), [51] a plane wave electronic structure code. The standard PBE functional, together with the projector augmented wave (PAW) potential method, was used for this purpose. PAW is a generalization of the pseudopotential and linear augmented-plane-wave methods, enabling density functional theory calculations to be performed with greater computational efficiency.[52]

For reasons outlined later, as well as for reasons discussed in a recent study, [53] both Γ-centered and Monkhorst-Pack type k-meshes were used in this calculations to account for the Brillouin zone integration. The size of the k-point mesh was 10 × 8 × 10 and 8 × 8 × 10 for orthorhombic and tetragonal phases, respectively. The kinetic energy cut-off was set to 520 eV. For the cubic phase, an 8 × 8 × 8 type k-point mesh was used, with same kinetic energy cut-off.

Both kcal mol^{-1} and eV are used in this Chapter throughout the discussion.

7.3 Results and discussion

7.3.1 Gas phase geometries

The ten energy-minimized geometries of the $CH_3NH_3PbY_3$ series are illustrated in

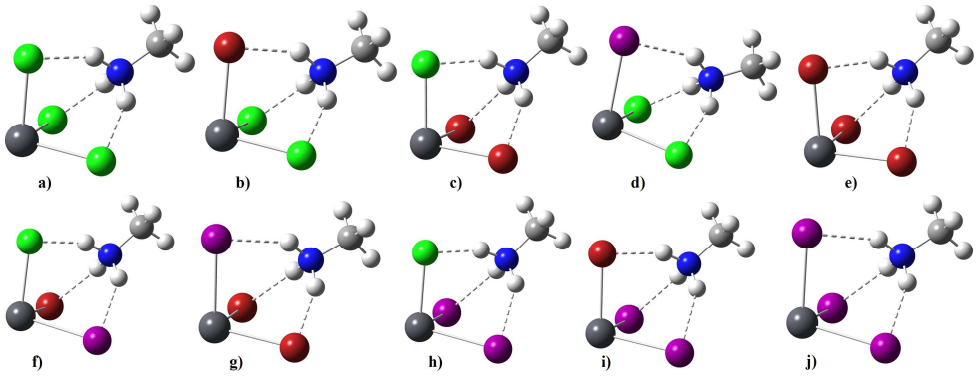

Fig. 1: Illustration of [PBEPBE/aug-cc-pVTZ(for $CH_3NH_3^+$, Cl, Br)/aug-cc-pVTZ-PP(for PbI_3^-)] energy-minimized gas-phase geometries of the ten-membered $CH_3NH_3PbY_3$ molecular building blocks, where Y = $Br_{(3-x)}Cl_{x=1-3}$, $I_{(3-x)}Br_{x=1-3}$, $I_{(3-x)}Cl_{x=1-3}$, and IBrCl. These include from top left a) $MAPbCl_3$, b) $MAPbBrCl_2$, c) $MAPbBr_2Cl$, d) $MAPbICl_2$, e) $MAPbBr_3$, f) MAPbIBrCl, g) $MAPbIBr_2$, h) $MAPbI_2Cl$, i) $MAPbI_2Br$, and j) $MAPbI_3$. Relative stabilities are given in eV. Relative stabilities can be inferred from the energy data listed in Table 1.

Fig. 1. These are all stable against their constituent monomers. The fluorine is not included into this list because perovskites with same architectures with fluorine are not yet experimentally synthesized. To our estimation, the presence of fluorine in the PbY_3^- inorganic framework in the solid state would cause complete proton transfers from the ammine group of the organic cation, causing eventual sublimation of the fluorinated species.

Similar to the geometrical configurations presented in Fig. 1, the binary complexes of the $CH_3NH_3SnY_3$ series are also found to be stable in the gas phase. In contrary, the NH_3XPbY_3 series is constructed for the first time during this thesis work, which was achieved by changing the B-site cation from $CH_3NH_3^+$ to NH_3X^+ (X = F, Cl, Br, I). These are also stable against their constituent monomers.

The CH_3NH_3X (X = Cl, Br, I) ion-pairs have been used the precursor gases for $CH_3NH_3^+$ in $CH_3NH_3PbI_3$. It may be understood that the NH_3X_2 (X = F, Cl, Br, I) molecular ion-pairs could serves as precursor gases for NH_3X^+ (X = F, Cl, Br, I) in NH_3XPbY_3. Experimental evidence of the inorganic cations such as NH_3F^+ [54-55] and NH_3Cl^+ [56] are previously documented. Fig. 2 compares the electronic structures of CH_3NH_3X with those of the NH_3X_2 systems in the gas phase.

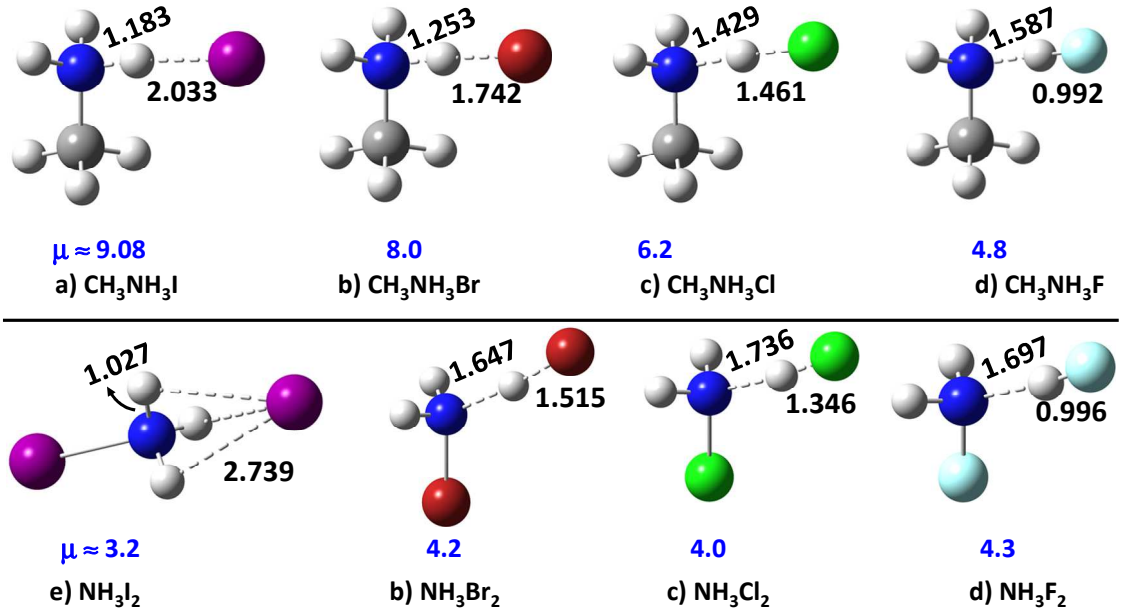

Fig. 2: Comparison of the molecular geometries of CH_3NH_3X (X = F, Cl, Br, I) (upper panel) with the corresponding ones of NH_3X_2 (X = F, Cl, Br, I) (lower panel), obtained with PBEPBE. Shown are selected N–H and X•••H distances (in Å), and electric dipole moments μ (in D). In ball-and-stick models: iodine: purple; bromine: dark-red; chlorine: green: fluorine: cyan; carbon: grey; nitrogen: blue; and hydrogen: grey-white.

7.3.2 Comparison of gas phase binding energies for the $BPbY_3$ series ($B = NH_3I^+$, $CH_3NH_3^+$)

Table 1 compares the PBEPBE level binding energies for the $CH_3NH_3PbY_3$ series with those of the $CH_3NH_3SnY_3$ and NH_3IPbY_3 series, all computed with the same level of theory. As expected, the ΔE for the complexes of the $CH_3NH_3SnY_3$ series are weaker than those of the corresponding ones for the $CH_3NH_3PbY_3$ series. Interestingly, however, the ΔE for the NH_3IPbY_3 series are found to be significantly larger than those of the former two series. That is, the intermolecular interactions in NH_3IPbY_3 are much larger than those in $CH_3NH_3SnY_3$ and NH_3IPbY_3, revealing more stability.

The ΔE, no matter whether uncorrected or BSSE corrected, for all the halide perovskites above are significantly large. These are incomparable with those proposed for the very strong (~30.0 – 40.0 kcal mol^{-1}), strong (~15 – 30 kcal mol^{-1}), moderate (~ 4–15 kcal mol^{-1}), weak (0.25 – 4.0 kcal mol^{-1}) and van der Waals (~ 0.25 kcal mol^{-1}).[57-58] One of the strongest hydrogen bonded systems containing significant amount of covalency is the F^{-}•••H–F, with its ΔE close to the covalent limit, –1.73 eV (–40.0 kcal mol^{-1}).[57-58] The above result suggests that strongly bound intermolecular interactions comprising appreciable amount of covalent components are very promising for the sophisticated design of novel functional nanomaterials for device applications. As suggested in Chapter

Table 1: Gas phase stabilities of $MAPbY_3$, $MASnY_3$ and NH_3IPbY_3 series, where Y = $Br_{(3-x)}Cl_{x=1-3}$, $I_{(3-x)}Br_{x=1-3}$, $I_{(3-x)}Cl_{x=1-3}$, and IBrCl. Calculations were carried out with [PBEPBE/aug-cc-pVTZ (for $CH_3NH_3^+$, $-NH_3$, Cl, Br)/aug-cc-pVTZ-PP (for I, Pb, SnI_3^- and PbI_3^-)].

Complexes	$MAPbY_3$		$MASnY_3$		NH_3IPbY_3	
	ΔE	ΔE^{corr}	ΔE	ΔE^{corr}	ΔE	ΔE^{corr}
$BMCl_3$	-116.54	-116.22	-113.56	-113.27	-121.29	-120.97
$BMBrCl_2$	-115.01	-114.67	-112.26	-111.95	-119.82	-119.47
$BMBr_2Cl$	-113.48	-113.11	-110.99	-110.64	-118.31	-117.97
$BMICl_3$	-113.26	-112.99	-110.62	-110.38	-118.25	-117.94
$BMBr_3$	-111.95	-111.54	-109.72	-109.35	-116.77	-116.41
BMIBrCl	-111.71	-111.41	-109.37	-109.10	-116.69	-116.41
$BMIBr_2$	-110.14	-109.81	-108.12	-107.82	-115.14	-114.85
BMI_2Cl	-109.91	-109.70	-107.80	-107.59	-115.09	-114.87
BMI_2Br	-108.31	-108.07	-106.54	-106.32	-113.51	-113.26
BMI_3	-106.46	-106.30	-104.97	-104.82	-111.78	-111.60

[a] Values in kcal mol^{-1}
[b] Eqn (1).
[c] Eqn (2).

4, the strength of the intermolecular interactions in these perovskites can be grouped into a new class, thereby we have recommended to refer them as *ultra-strong* hydrogen bonding interactions that have implication in the design of sophisticated functional nanomaterials.

The unusually large binding energies calculated for the dimers formed of ammine protons of $CH_3NH_3^+$ [or of NH_3X^+ (X = F, Cl, Br, I)] and the coordinated Y atoms of either SnY_3^-, or PbY_3^-, give further indication about substantial covalency of the intermolecular hydrogen bonding interactions in $CH_3NH_3SnY_3$, $CH_3NH_3PbY_3$ and NH_3IPbY_3. This is an observation which is against many interpretations already distributed in the entire perovskite literature that demonstrate these interactions are purely ionic. [59]

7.3.3 Relationship between binding energy and bandgap for the BMY_3 series (B = $CH_3NH_3^+$; M = Sn^{2+}, Pb^{2+})

Castelli *et al.*[60] have performed electronic structure calculations for 240 perovskites comprising the B-site cations as Cs, CH_3NH_3 and $HC(NH_2)_2$, the M-site cations as Sn and Pb divalent ions, and the Y-site anions as the halogen derivative of the same, or mixed type. The bandgaps for all the 240 perovskites were predicted to span over a region from 0.5 to 5.0 eV. As the authors noted, the trend for bandgaps for any of the ten-membered perovskite series they examined was: BMI_3 < BMI_2Br < BMI_2Cl < $BMIBr_2$ < BMIBrCl < $BMBr_3$ < $BMICl_2$ < $BMBr_2Cl$ < $BMBrCl_2$ < $BMCl_3$. This trend was independent of the nature of the B- and M-site cations in BMY_3. Not only is this, but the same authors have also found that the above trend is independent of the nature of the geometrical changes associated with the four temperature phases of the BMY_3 trihalide perovskite systems they investigated. That is, the trend was persistent for the two orthorhombic, one tetragonal, and one cubic phases for the various trihalide perovskite bulk series they examined.

The geometries of the ten-membered $CH_3NH_3PbY_3$ blocks energy-minimized in the gas phase are illustrated in Fig. 1. These are analogous with those of their corresponding bulk geometries in the pseudocubic phase, with the C–N bond in the (111) direction (cf. Fig. 6).

The uncorrected and corrected stabilization energies for these binary complexes are listed in Table 1. These suggest that the both ΔE and ΔE^{corr} are the least for the heaviest member ($CH_3NH_3SnI_3$) and the largest for the lightest member ($CH_3NH_3SnCl_3$) for the $CH_3NH_3SnY_3$ series, with ΔE^{corr} values lying between –104.82 and –113.27 kcal mol^{-1} (–4.545 and –4.912 eV, respectively). For the $CH_3NH_3PbY_3$ series, the ΔE^{corr} lie between –106.30 and –116.22 kcal mol^{-1} with the smallest and largest values of it found

for the heaviest ($CH_3NH_3PbI_3$) and lightest ($CH_3NH_3PbCl_3$) members of the series as well. Moreover, the preference of the ΔE^{corr} follows this order: BMI_3 < BMI_2Br < BMI_2Cl < $BMIBr_2$ < $BMIBrCl$ < $BMBr_3$ < $BMICl_2$ < $BMBr_2Cl$ < $BMBrCl_2$ < $BMCl_3$ for both the $CH_3NH_3SnY_3$ and $CsSnY_3$ series, a trend which is same as that found for the bandgaps for the corresponding series (*vide supra*).[60] These results demonstrate the potential importance of gas phase calculations in revealing the correct trend in the bandgap for materials of these kinds.

An approximately similar trend is also observed for ΔE of the NH_3IPbY_3 series. However, it is not perfect. The reason is obviously due to the fact that the BSSE corrected energies ΔE^{corr} for NH_3IPbBr_3 and $NH_3IPbIBrCl$ were virtually the same, and those of $NH_3IPbIBr_2$ and NH_3IPbI_2Cl were altered. This result suggests the spurious nature of the BSSE for which the expected trend between the corrected energies for the series is not reflected.

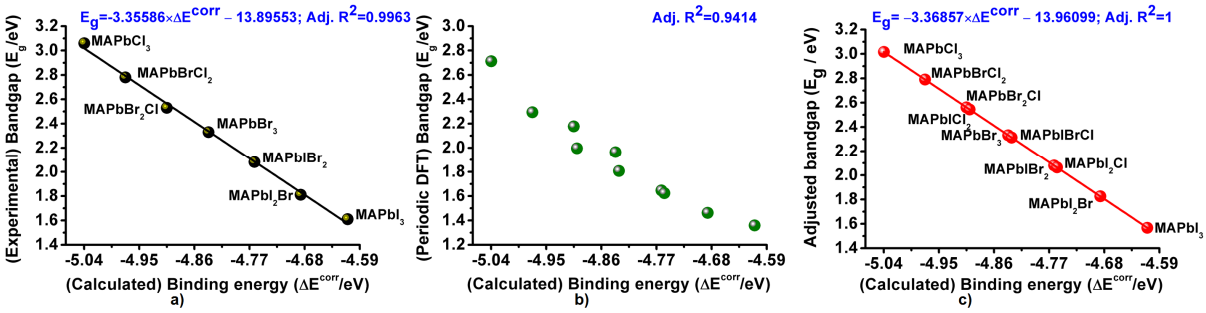

Fig. 3: Dependence a) of the experimentally reported onset of optical absorption (bandgap E_g/eV) on the basis set superposition corrected binding energy (ΔE^{corr}/eV), b) of the periodic DFT based bandgap of Castelli *et al.*[60] on the on the basis set superposition corrected binding energy (ΔE^{corr}/eV), and c) of the adjusted bandgap (eV) on the basis set superposition corrected binding energy (ΔE^{corr}/eV) for the ten-membered $CH_3NH_3PbY_3$ series, where Y = $Br_{(3-x)}Cl_{x=1–3}$, $I_{(3-x)}Br_{x=1–3}$, $I_{(3-x)}Cl_{x=1–3}$, and IBrCl. 1 eV = 23.06 kcal mol^{-1} (see Table 1 for details).

Fig. 3a) illustrates the desired dependence of the experimentally reported onset of optical absorption for the $CH_3NH_3PbY_3$ perovskite solar cells[61] on the ΔE^{corr} calculated for the corresponding building blocks. This analysis has accounted for seven data points associated with seven members of this family since the experimental E_g for the other three members of the series (out of a total of ten) are either unavailable in the literature, or the data are controversial. [62-64] For instance, the actual nature of the chlorine in $MAPbI_{3-x}Cl_x$ is controversial. The reaction mechanism leading to the formation and crystallization of pure iodide and chlorine-containing perovskite films remain unsolved. [63] The bandgap for the $CH_3NH_3PbI_2Cl$ obtained using first principles calculation was

close to 1.6 eV. This was measured to remain nearly identical to that of the tetragonal phase of the $CH_3NH_3PbI_3$ perovskite system, ~1.50 – 1.61 eV. Such a close agreement between the bandgaps of $CH_3NH_3PbI_2Cl$ and $CH_3NH_3PbI_3$ is probably due to the miscibility of Cl in the parent $CH_3NH_3PbI_3$ lattice, since a Cl content on the order of 1% was inferred by comparison of the X-ray diffraction (XRD) patterns with $CH_3NH_3PbI_3$ samples and by X-ray photoelectron spectroscopy (XPS) analysis.[24–26]Others claimed that a limited Cl content in $CH_3NH_3PbI_{3-x}Cl_x$ can be speculated on the basis of the calculated sizable destabilization energy of $CH_3NH_3PbI_2Cl$ (0.16 eV taking $CH_3NH_3PbI_3$ as a reference) because of the comparatively large difference in atomic radii between Cl and I. [64] We furthermore note that the experimentally available bandgaps for all the members of the $CH_3NH_3PbY_3$ series do not correspond to the pseudocubic phase. For example, there have been a range of values reported for the bandgap of the $CH_3NH_3PbI_3$ material that are in the 1.50 – 1.67 eV, which cover all the three phases. There is virtually a small difference in the bandgap values passing from one phase to the other phase of the system. For example, the the low-temperature orthorhombic phase has a bandgap of 1.61 eV, whereas that for the room temperature tetragonal and pseudocubic phases are ca. 1.55 and 1.67 eV, respectively, all within 0.17 eV. We have therefore used the experimentally values that are reported with a reasonable degree of chemical accuracy. Also, it should be remembered that the reported experimental bandgaps were not separately determined with respect to the rotation/orientation of the B-site cation orientation; what are reported are an average value, obtained from the photoluminesence spectra.

We have thus considered that the most stable conformation is likely to be dominant species in the solution, as well as in the solid state. We have used the ΔE^{corr} of these conformations in the fitting analysis. And, the seven members of the $CH_3NH_3PbY_3$ family used for the fitting analysis were $MAPbI_3$, $MAPbI_2Br$, $MABIBr_2$, $MAPbBr_3$, $MAPbBr_2Cl$, $MAPbBrCl_2$ and $MAPbCl_3$.

All the E_g data were fitted to a linear Eqn of the form: $E_g = a \times \Delta E^{corr} + b$, where a is the slope and b is the intercept. The linear regression analysis gave the square of the adjusted regression coefficient (Adj R^2) to be ≈ 0.9963, and the relationship that well describes the data points in the fit is represented by: $E_g = -3.35586 \times \Delta E^{corr} - 13.89553$. This relationship shows that provided ΔE^{corr} is known computationally, one can certainly predict the bandgap of the remaining members that have been experimentally missing for the $CH_3NH_3PbY_3$ series.

Fig. 3a also presents the fact that the heaviest $CH_3NH_3PbI_3$ perovskite block, which is structurally and energetically *least stable* compared to the other nine members of the $CH_3NH_3PbY_3$ family, is accompanied with the smallest energy gap between the VB maximum and the CB minimum. And, upon replacing the iodine atom by other halogen derivative in $CH_3NH_3PbI_3$ in a stepwise manner the stability of the modified perovskite block containing either purely Br-, or purely Cl-, or mixed halogen derivative,

is increasingly being more stable both geometrically and energetically. The rationalization is perhaps in agreement with the similar view provided by others for some of these systems based on experimental data.[65] For instance, the $CH_3NH_3PbI_{3-x}Br_x$ trihalide perovskite system with large amount of bromine content is more stable than that containing the iodine content. In particular, the $CH_3NH_3PbI_{3-x}Br_x$ mixed halide system with Br content < 10% gives rise to better PCE, while that with > 20% Br content provides better photostability. [65]

Fig. 3b) presents the dependence of the E_g on the ΔE^{corr} for the $CH_3NH_3PbY_3$ series. However, this time, the E_g are taken from the study of Castelli *et al.*,[60] which were evaluated with the GPAW code using periodic DFT. [66] The authors adopted several approximations to estimate the bandgaps for the studied perovskite systems. In specific, they have used the GLLB-SC potential of Gritsenko, van Leeuwen, van Lenthe, and Baerends (GLLB), [67] since the authors believe that it predicts bandgaps within 0.1 eV relative to G0W0 for this class of systems,[68] with the potential included the PBEsol correlation for solids (-SC).[69] The optical bandgap E_g was obtained in that study using the relationship given by: $E_g = E^{KS}_{gap} + \Delta_{xc} - \Delta_{soc} - \Delta_{e-h}$, where Δ_{xc} is different for each system, E^{KS}_{gap} is the Kohn-Sham bandgap, and Δ_{soc} and Δ_{e-h} are *ad hoc* corrections accounting for spin-orbit and exciton effects, respectively.

Table 2: Some selected physical properties of the $CH_3NH_3PbY_3$ series, where Y = $Br_{(3-x)}Cl_{x=1-3}$, $I_{(3-x)}Br_{x=1-3}$, $I_{(3-x)}Cl_{x=1-3}$, and IBrCl.[a]

Block	ΔE^{corr} [b]	E_g (Predicted)[c]	E_g (Castelli *et al.*)[d]	E_g (Expt.)[e]
$MAPbI_3$	-4.610	1.567	1.359	1.61
$MAPbI_2Br$	-4.686	1.825	1.462	1.81
$MAPbI_2Cl$	-4.757	2.064	1.624	--
$MAPbIBr_2$	-4.762	2.080	1.646	2.08
MAPbIBrCl	-4.831	2.313	1.807	--
$MAPbBr_3$	-4.837	2.332	1.964	2.33
$MAPbICl_2$	-4.900	2.544	1.997	--
$MAPbBr_2Cl$	-4.905	2.562	2.177	2.53
$MAPbBrCl_2$	-4.973	2.790	2.294	2.78
$MAPbCl_3$	-5.040	3.016	2.712	3.06

[a] The properties include the BSSE corrected PBEPBE binding energies (ΔE^{cor}/eV), the PBEPBE predicted bandgap (E_g(Predicted)/eV), the bandgap reported by of Castelli *et al.* (E_g(Castelli *et al.*)/eV) and the experimentally reported bandgap (E_g(Expt.)/eV).
[b] Eqn (2).
[c] This work.
[d] Ref. 60
[e] Ref. 61.

While several approximations were accounted for the accurate calculation of the bandgaps for the hybrid organic-inorganic and purely inorganic perovskite solar cells systems, [60] the dependence of the predicted bandgaps of Castelli *et al.*, [60] for the pseudocubic systems on the calculated ΔE^{corr} is found not to be excellent for the $CH_3NH_3PbY_3$ series. For the $CH_3NH_3SnY_3$ series, a similar dependency is revealed. However, for the $CsPbY_3$ and $CsPbY_3$ series, the predicted bandgap data were worse than expected since we found no such dependence between ΔE^{corr} and E_g for these two series, and is certainly a consequence of the scattering of the periodic DFT data.

Table 2 gives the detailed comparison of bandgaps obtained with different methods for the $CH_3NH_3PbY_3$ series. Table 3 presents the same for the $CH_3NH_3SnY_3$ series.

Fig. 3c) is obtained by plotting the adjusted E_g against the computed ΔE^{corr} for $CH_3NH_3PbY_3$ series. The former values were evaluated by fitting the experimental E_g and computed ΔE^{corr} data sets to a linear equation of the form: $E_g = b \times \Delta E^{corr} + c$, in which case, Adj $R^2 \approx 1$. The mathematical equation that best describes data in Fig. 3c) is represented by the relationship given by: $E_g = -3.36857 \times \Delta E^{corr} - 13.96099$.

Table 3: Some selected physical properties of the $CH_3NH_3SnY_3$ series, where Y = $Br_{(3-x)}Cl_{x=1-3}$, $I_{(3-x)}Br_{x=1-3}$, $I_{(3-x)}Cl_{x=1-3}$, and IBrCl.[a]

Block	ΔE^{corr} [b]	E_g (Predicted.)[c]	E_g (Castelli *et al.*)[d]	E_g (Expt.)[e]
$MASnI_3$	-4.545	1.295	0.438	1.30
$MASnI_2Br$	-4.610	1.564	0.555	1.56
$MASnI_2Cl$	-4.665	1.791	0.778	---
$MASnIBr_2$	-4.675	1.832	0.710	1.75
MASnIBrCl	-4.731	2.060	1.421	---
$MASnBr_3$	-4.742	2.106	1.10	2.15
$MASnICl_2$	-4.786	2.289	1.544	---
$MASnBr_2Cl$	-4.798	2.336	1.695	---
$MASnBrCl_2$	-4.855	2.570	1.914	---
$MASnCl_3$	-4.912	2.806	2.226	---

[a] The properties include the PBEPBE-based BSSE corrected binding energies (ΔE^{corr}/eV), the PBEPBE predicted bandgap (E_g(Predicted)/eV), the bandgap reported by of Castelli et al. (E_g(Castelli *et al.*)/eV) and the experimentally reported bandgap (E_g(Expt.)/eV).
[b] Eqn (2).
[c] Predicted through a linear regression analysis (see text for discussion).
[d] Ref. 60
[e] Ref. 70

7.3.4 Accuracy of DFT-PBEPBE compared to the CCSD(T) binding energies

Table 4 lists the CCSD(T) binding energies for the $CH_3NH_3PbY_3$ and $CH_3NH_3SnY_3$ series, all computed using the electronic energies of the interacting species with Gaussian 09.[47] While the PBEPBE calculated ΔE's for these dimers listed in Table 1 show that these are somehow underestimated compared to the corresponding CCSD(T) energies, the inclusion of the effect of the BSSE at the later level produces ΔE^{corr} values that are comparable with the corresponding ones evaluated with the PBEPBE. Also, it is apparent that from the data of Tables 1 and 4 that the BSSE is small with DFT compared to that of CCSD(T), and that this kind of spuriously large BSSE contribution with the same basis set with CCSD(T) is not very surprising.[71-72] Nevertheless, the general conclusion that the binding energies of the $CH_3NH_3SnY_3$, $CH_3NH_3PbY_3$ and NH_3IPbY_3 systems are unusually large cannot be changed by changing the level of theory. These results signify further that the strongly bound interaction energies can be accurately modelled with density functionals such as PBEPBE, whose energies can be comparable with the results of the very expensive CCSD(T) calculations.

Table 4: Gas phase stabilization energies of $MAPbY_3$ and $MASnY_3$ series, where Y = $Br_{(3-x)}Cl_{x=1-3}$, $I_{(3-x)}Br_{x=1-3}$, $I_{(3-x)}Cl_{x=1-3}$, and IBrCl. Calculations were carried out with [CCSD(T)/cc-pVTZ(for $CH_3NH_3^+$, Cl, Br)/cc-pVTZ-PP(for I, SnI_3^- and PbI_3^-)//CCSD/cc-pVTZ(for $CH_3NH_3^+$, Cl, Br)/cc-pVTZ-PP(for I, Pb, SnI_3^- and PbI_3^-)].[a]

Complexes	$MAPbY_3$		$MASnY_3$	
	ΔE	ΔE^{corr}	ΔE	ΔE^{corr}
$BMCl_3$	-118.65	-115.36	-114.24	-111.31
$BMBrCl_2$	-116.84	-113.43	-112.77	-109.70
$BMBr_2Cl$	-115.08	-111.54	-111.37	-108.15
$BMICl_2$	-114.8	-111.58	-110.94	-108.01
$BMBr_3$	-113.36	-109.66	-110.08	-106.70
BMIBrCl	-113.07	-109.69	-109.60	-106.51
$BMIBr_2$	-111.33	-107.78	-108.31	-105.04
BMI_2Cl	-111.02	-107.80	-107.86	-104.91
BMI_2Br	-109.27	-105.88	-106.60	-103.45
BMI_3	-107.19	-103.95	-104.92	-101.88

[a] Values in kcal mol^{-1}
[b] Eqn (1).
[c] Eqn (2).

7.3.5 PBEPBE predicted gas-phase stabilities for the complexes of the NH_3XPbY_3 series

Forty eight perovskite dimers are examined for the NH_3XPbY_3 series (X = F, Cl, Br, I), including the NH_3FPbF_3 and $NH_3FPbFCl_2$ series. Table 5 lists the DFT binding energies for these complexes, and the geometries are analogous to those reported in Fig. 1 for $CH_3NH_3PbY_3$. The data show that the NH_3XPbF_3 series is most stable, whereas the NH_3XPbI_3 series is least stable. This might not unexpected because the fluorine in PbF_3^- is strongly electronegative than the halogens in $PbCl_3^-$, $PbBr_3^-$ and PbI_3^-, which causes relatively stronger attraction to the electrophile in NH_3X^+ at the close proximity.

The strongest dimer of the NH_3XPbY_3 series of forty eight compounds is NH_3FPbF_3. The ΔE for this dimer is ca. –162.73 kcal mol^{-1}, a value which is substantially larger than the bond dissociation energies of various widely known covalent coordinate bonds. For instance, this energy is much larger than the experimentally reported bond dissociation energies of 31.1, 59.0, 71.9, 80.8 and 85.1 kcal mol^{-1} for Au–Pb, Pb–Cl, Pb–Br, Pb–Pb and Pb–F covalent coordinate bonds, respectively.

For a given Y in NH_3XPbY_3 (X = F, Cl, Br, I), the following energetic preference is revealed: NH_3FPbY_3 > NH_3ClPbY_3 > NH_3BrPbY_3 > NH_3IPbY_3. For instance, for the NH_3XPbI_3 series, the preference of the ΔE is in this order: NH_3FPbI_3 > NH_3FPbI_3 > NH_3BrPbI_3 > NH_3IPbI_3. This is again in consistent with the large electronegativity and the basicity of the fluorine compared to those of the other halogen atoms of the series, for which, the $–NH_3$ part is more electropositive in $[F–NH_3]^+$ compared to the other three, that is, $[F–NH_3]^+$ > $[Cl–NH_3]^+$ > $[Br–NH_3]^+$ > $[I–NH_3]^+$. Nevertheless, the above result suggests that the fluorine in molecular PbF_3^- is a potential hydrogen bond acceptor compared to other halogen atoms in PbY_3^-, that is, the ability of the hydrogen bond formation is in this order: F > Cl > Br > I. Interestingly, this is a trend which is opposite to the ability of the covalently bound halogen derivative in forming halogen bond (Chapters 2-3), that is, in this order: F < Cl < Br < I. The latter feature is attributed to be the polarizability of the halogen derivative that increases in the series in this order: F < Cl < Cl < Br.[73]

Note that the NH_3XPbY_3 are stable in the gas phase. This does not guarantee that all these can be stable in the solid state. This can be inferred from the recent study of Volonakis *et al.*,[74] who have recently exploited the geometries of several double perovskites Cs_2InAgX_6 ($X = Cl^-, Br^-, I^-$). The authors have considered two specific attributes for their initial screening of the geometries of these compounds. These are the so-called the phonon dispersion relations (dynamical stability) and the quaternary onvex hulls (thermodynamic stability). [75] Because the ionic radius of In^{3+} is too small (In^{3+} = 0.8 Å) relative to coordinate 6 I− anions (I^- = 2.2 Å), the authors found from their analysis that the only possible In/Ag halide double perovskites that may be amenable to synthesis are those with Cl, mixed Cl/Br, and possibly Br. This screening has guided them with the

eventual synthesis and characterization of the Cs_2InAgX_6 (X = Cl^-, Br^-) direct bandgap double perovskites in the solid state.

Table 5: Gas phase stabilization energies for the NH_3XPbY_3 series comprising forty eight members, where Y = $Br_{(3-x)}Cl_{x=1-3}$, $I_{(3-x)}Br_{x=1-3}$, $I_{(3-x)}Cl_{x=1-3}$, and IBrCl, and X = F, Cl, Br, I. Calculations were carried out with PBEPBE.[a]

Complexes	ΔE^b	$\Delta E^{cor\ c}$	Complexes	ΔE^b	$\Delta E^{cor\ c}$
NH_3FPbF_3	-162.73	-162.17	NH_3FPbBr_3	-131.77	-131.41
NH_3ClPbF_3	-154.77	-154.19	$NH_3ClPbBr_3$	-125.48	-125.09
$NH_3FBrPbF_3$	-150.31	-149.77	$NH_3BrPbBr_3$	-121.99	-121.61
NH_3IPbF_3	-143.83	-143.29	NH_3IPbBr_3	-116.77	-116.41
$NH_3FPbFCl_2$	-151.32	-150.91	$NH_3FPbIBrCl$	-131.77	-131.48
$NH_3ClPbFCl_2$	-142.56	-142.15	$NH_3ClPbIBrCl$	-125.39	-125.11
$NH_3FBrPbFCl_2$	-137.92	-137.51	$NH_3BrPbIBrCl$	-121.91	-121.62
$NH_3IPbFCl_2$	-131.30	-130.91	$NH_3IPbIBrCl$	-116.69	-116.41
NH_3FPbCl_3	-137.16	-136.82	$NH_3FPbIBr_2$	-129.85	-129.52
$NH_3ClPbCl_3$	-130.43	-130.09	$NH_3ClPbIBr_2$	-123.66	-123.33
$NH_3FBrPbCl_3$	-126.74	-126.41	$NH_3BrPbIBr_2$	-120.26	-119.95
NH_3IPbCl_3	-121.29	-120.97	$NH_3IPbIBr_2$	-115.14	-114.85
$NH_3FPbBrCl_2$	-135.43	-135.08	NH_3FPbI_2Cl	-129.81	-129.59
$NH_3ClPbBrCl_2$	-128.83	-128.47	NH_3ClPbI_2Cl	-123.60	-123.38
$NH_3BrPbBrCl_2$	-125.19	-124.83	NH_3BrPbI_2Cl	-120.20	-119.98
$NH_3IPbBrCl_2$	-119.82	-119.47	NH_3IPbI_2Cl	-115.09	-114.87
NH_3FPbBr_2Cl	-133.60	-133.28	NH_3FPbI_2Br	-127.84	-127.58
$NH_3ClPbBr_2Cl$	-127.15	-126.80	NH_3ClPbI_2Br	-121.86	-121.54
$NH_3BrPbBr_2Cl$	-123.56	123.22	NH_3BrPbI_2Br	-118.49	-118.24
NH_3IPbBr_2Cl	-118.31	-117.94	NH_3IPbI_2Br	-113.51	-113.26
$NH_3FPbICl_2$	-133.64	-133.38	NH_3FPbI_3	-125.72	-125.52
$NH_3ClPbICl_2$	-127.11	-126.82	NH_3ClPbI_3	-119.85	-119.64
$NH_3BrPbICl_2$	-123.55	-123.26	NH_3BrPbI_3	-116.67	-116.46
$NH_3IPbICl_2$	-118.25	-117.97	NH_3IPbI_3	-111.78	-111.60

[a] Values in kcal mol^{-1}
[b] Eqn (1).
[c] Eqn (2).

7.3.6 Gas phase enthalpy and free energies for $CH_3NH_3MI_3$ and NH_3IMI_3 (M = Sn, Pb)

Table 6 compares the gas phase binding energies, the BSSE corrected binding energies, the change in the enthalpy energies, the change in the free energies for $CH_3NH_3SnI_3$, $CH_3NH_3PbI_3$, NH_3ISnI_3 and NH_3IPbI_3. While these properties were evaluated with the PBEPBE/Def2-TZVVPPD the pseudo potential basis set, the BSSE with this basis set is found to be very marginal regardless of the nature of the binary geometries investigated. Moreover, the binding energies (ΔE) and the BSSE corrected binding energies (ΔE^{corr}) for the above mentioned configurations are comparable with those evaluated with the Dunning's type triple-ξ basis set (*vide supra*).

Table 6: PBEPBE/Def2-TZVVPPD comparison of the binding energies (ΔE), the BSSE corrected binding energies (ΔE^{corr}), the reaction enthalpies (ΔH) and the free energies (ΔG) between the $CH_3NH_3MI_3$ and NH_3IMI_3 (M = Sn, Pb).[a]

Property	$CH_3NH_3PbI_3$	$CH_3NH_3SnI_3$	NH_3IPbI_3	NH_3ISnI_3
ΔE[b]	-106.29	-104.83	-111.62	-110.06
ΔE^{corr} [c]	-106.18	-104.71	-111.48	-109.91
ΔH[d]	-104.23	-103.24	-109.57	-108.57
ΔG[e]	-93.13	-92.24	-98.12	-97.44

[a] Values in kcal mol^{-1} (1 eV = 23.0609 kcal mol^{-1}).
[b] Eqn (1).
[c] $\Delta H(BMI_3) = H(BPbI_3) - H(B^+) - H(MI_3^-)$
[d] $\Delta G(BMI_3) = G(BPbI_3) - G(B^+) - G(MI_3^-)$

Assuming that B^+ and MI_3^- as the two fragments of the BMI_3 (M = Sn, Pb) systems, we have calculated the reaction enthalpies (ΔH) and free energies (ΔG) at 298.15 K. As such, both ΔH and ΔG are found to be all large and negative for $CH_3NH_3SnI_3$, $CH_3NH_3PbI_3$, NH_3ISnI_3 and NH_3IPbI_3 systems, suggesting their thermodynamical stabilities.

Also, we assumed the following standard reactions for the formation of the aforementioned perovskites systems.

$$CH_3NH_3MI_3 \rightarrow MI_2 + CH_3NH_3I, \text{ where M = Sn, Pb}$$

$$NH_3IMI_3 \rightarrow MI_2 + NH_3I_2, \text{ where M = Sn, Pb}$$

Accordingly, the ΔH and ΔG for the two reactions above are evaluated using the following two relations.

$$\Delta H(CH_3NH_3MI_3) = H(CH_3NH_3MI_3) - H(MI_2) - H(CH_3NH_3I), (M = Sn, Pb)$$

$$\Delta G(CH_3NH_3MI_3) = G(NH_3IMI_3) - G(MI_2) - G(NH_3I_2), (M = Sn, Pb)$$

The calculated ΔH and ΔG for the above reactions for $CH_3NH_3PbI_3$ and NH_3IPbI_3 are presented in Table 7. Given these emerge from different reaction mechanisms, the magnitudes of these are different from those summarized in Table 6. Even so, it is apparent that the formation of the NH_3XMY_3 perovskite systems might not be unlikely in the solid state. We argue this because ΔH and ΔG for $CH_3NH_3PbI_3$ are nearly comparable in sign and magnitude with the corresponding properties estimated for NH_3IPbI_3. The results show that the latter system is somehow less stable than the former system, which is presumably the consequence of increasingly large entropic contribution, $T\Delta S$.

Table 7: PBEPBE/Def2-TZVVPPD comparison of the reaction enthalpies (ΔH) and the free energies (ΔG) between the $CH_3NH_3MI_3$ and NH_3IMI_3 (M = Pb).

Property	$CH_3NH_3PbI_3$	NH_3IPbI_3
ΔH	-34.08	-27.98
ΔG	-23.16	-15.63

[a] Values in kcal mol^{-1} (1 eV = 23.0609 kcal mol^{-1}).

Politzer *et al.*[76] have recently demonstrated that halogen bonding in the gas phase is often thermodynamically unstable, because of the loss of entropy incurred when the translational and rotational motions of the free molecules are constrained by the formation of the complex. This produces a large negative $T\Delta S$ term, which can in many instances dominate ΔH and result in positive free energy ΔG ($\Delta G = \Delta H - T\Delta S > 0$). The stronger the interaction (more negative ΔH), the more rigid is the complex and the more negative is $T\Delta S$. However $T\Delta S$ generally approaches a limiting value; for sufficiently strong interactions, therefore, ΔH dominates and $\Delta G < 0$, *i.e.* thermodynamic stability. This view is consistent with the results presented both in Table 6 and 7.

In solution and solid phases, the situation is complicated by additional factors, the overall effect of which can produce $\Delta G < 0$ even in cases that are thermodynamically unstable in the gas phase. As Politzer *et al.* stated, [76] it should be kept in mind that $\Delta G > 0$ does not totally preclude an interaction; it simply means that the equilibrium constant is less than one.

7.3.7 The Goldschmidt tolerance factor

In 1926, [77] Goldschmidt has proposed a mathematical expression equivalent to Eqn. 3 for understanding the stability and distortion of BMY_3 crystal structures.[78-79]

$$t = \frac{r_B + r_Y}{\sqrt{2}(r_M + r_Y)} \quad \text{.....(3)}$$

In this Eqn, r_B is the effective ionic radius of the B-site cation, r_M is the effective ionic radius of the M-site cation, and r_Y is the ionic effective radius of the Y-site anion. The importance of this factor is discussed elsewhere.[78-81]

For ideal $BPbX_3$ (X = Cl, Br, I) perovskites, *t* is 1, otherwise for distorted ones it varies between 0.80 and 1.11.[80] This latter range is obtainable when the effective radii for B-site cation for perovskite structures vary between 1.60 Å and 2.50 Å.[82] For instance, Park reported an effective ionic radius of 1.8 Å for the $CH_3NH_3^+$ cation, which, according to him, is thus suitable for forming perovskite structure upon its combination with lead trihalide anion. [82] It should be noted that there have been a variety of values suggested for the ionic radius of $CH_3NH_3^+$. For example, Choi *et al.,* [83] Saliba *et al.*, [84] and Amat *et al.*[85] have used a value of 2.70 Å, Kieslich *et al.,* [86] whereas Levchuk *et al.*[88] and Zhou *et al.*[88] have reported a value of 2.17 Å for the effective radius of the cation. Similarly, the effective ionic radius of $CH_3NH_3^+$ was calculated according to a rigid sphere model with free rotation of its centre of mass, and a value of 1.74 Å is reported.[89a] However, a recent study of Jishi demonstrated a value of 2.23 Å for its ionic radius,[89b] thereby demonstrating different values for the ionic radius of the cation that result from different calculation methods. These results not only enable us to question on the accuracy of the radius of the cation, but on the necessity and reliability of the requirement of the Goldschmidt tolerance factor as a metric to judge whether or not certain compounds do adopt the perovskite structure.

Note that *t* for $CH_3NH_3PbI_3$ is reported to be 0.83,[82,90] whereas that for $CsPbI_3$ is ca. 0.85.[91-92] Based on the range proposed for *t* above, these two values signify significant deviation from ideal perovskite structure. The ionic radii proposed by Shannon[93] and those revised recently have been used for the above purpose.[90]

$t < 1$ is not only a signature of an octahedral distortion, but also the lowering of crystal symmetry. Both these two geometrical features affect electronic properties of the resulting compound. For other perovskite systems, such as alkali metal halide perovskites, $0.813 < t < 1.107$,[80] and for cubic oxide perovskites, $0.89 < t < 1$. [94]

Most of the known perovskites have *t* values in the range 0.75 – 1.00. While the use of this range as a metric might be useful, it should not be regarded a *sufficient condition* to judge whether or not a given geometry can have the perovskite architecture.

This is suggestive of the study of Li *et al.*,[80] in which, it was shown that for some oxide systems with *t* within the most favorable range (0.8–0.9) no perovskite structure is stable. Also, the perovskite compounds such as $RbPbF_3$, $TlPbI_3$, $RbSnI_3$, $KFeCl_3$, and $CsBeF_3$, *etc.*, do not obey the aforementioned rule. $CH(NH_2)_2PbI_3$ ($FAPbI_3$) another example.[91]

Several other studies relevant with the tolerance factor can be found elsewhere.[65, 86,95-98]

7.3.8 The octahedral factor

In BMY_3 octahedra, the octahedral factor t_μ is defined as the ratio between ionic radii of atoms coordinated to each other. Assuming the hard sphere model and non-overlapping ions, the minimum radius for the B-site cation in six fold coordination is $0.414\,r_Y$, where r_Y is the anionic radius.

For BMY_3 systems, t_μ is defined by Eqn. 4.

$$t_\mu = \frac{r_M}{r_Y} \quad \text{..... (4)}$$

In this Eqn, r_M is the radius of the metal cation and r_Y is radius of the anion coordinated with the metal ion.

For stable $BPbY_3$ perovskites, $0.442 \leq t_\mu \leq 0.895$. This range does not account for the two abnormal systems ($TlMnI_3$ and $CsBeI_3$). If it does so, then $0.377 \leq t_\mu \leq 0.895$. Note that there are many systems exist in the literature with $0.414 \leq t_\mu \leq 0.732$, but these are non-perovskite compounds.

Since this factor does not depend on the size of the B-site cation, the same range of values can be applicable to a variety of B-site cations.

The combination of *t* with t_μ assists to build the two-dimensional structural map, which might serve as an efficient predictive tool in determining the formability of perovskite componds.[80]

Note that most of the perovskite systems exploited in this study (see discussions below) will have t_μ in the above range.

Thus, the values for *t* and t_μ are 0.822 and 0.541 for $MAPbI_3$ and 0.772 and 0.541 for $BPbI_3$.[89a, 100]

Volonakis *et al.* have obtained (t_μ, *t*) values of (0.54, 0.94), (0.50, 0.93) and (0.44, 0.91) for Cs_2InAgX_6 double perovskites, with X = Cl−, Br−, and I−, respectively. According to these authors,[74] whereas these parameters fall within the range of stability of standard halide perovskites,[80] therefore these are not very informative.

7.3.9 Bulk geometries for NH_3IPbI_3 and their comparison with those of $CH_3NH_3IPbI_3$

Several geometries of NH_3IPbI_3 were manually constructed using combined application of Gaussview 5[48] and Vesta software,[101] and their coordinates were relaxed with PBE/PAW using VASP employing periodic boundary condition.[51] Figs. 4–7 provide structural evidence about the various energy-minimized geometries of the NH_3IPbI_3 system. These four are analogous with the geometries discussed in the literature for the $CH_3NH_3PbI_3$ perovskite system, consisting the orthorhombic (*Pmna*), tetragonal (*I4/mcm*), monoclinic (*Pm*) and cubic (*Pm3m*) phases.[102-103]

The ionic radii for haloammonium ions NH_3I^+, NH_3Br^+, NH_3Cl^+ and NH_3F^+ are estimated to be roughly around 2.4, 2.2, 2.0, and 1.8 Å, respectively. These values are well within the 1.60–2.50 Å range recommended to form perovskite structures (*vide supra*).[82]

The orthorhombic geometry of the $CH_3NH_3PbI_3$ system, which belongs to the low temperature phase ($T < 165^o$), is known to be the most stable, Fig. 4 (top). This is not very surprising since the I•••H–N intermolecular hydrogen bonding interactions in this geometry between the PbI_3^- host (inorganic) and the $CH_3NH_3^+$ guest (organic) species are very strong. These are responsible for the observed tilting of the PbI_6^{4-} octahedra found for this geometry. Encouragingly, a similar result is obtained for the corresponding NH_3IPbI_3 system, with its overall geometry being stabilized by a set of I•••H–N intermolecular hydrogen bonding interactions.

Figs. 4–7 compare the calculated lattice constants for the NH_3IPbI_3 geometries with the corresponding $CH_3NH_3PbI_3$ geometries. Apparently, the lattice constants for both these systems are distinguished. As expected, the lattice constants of NH_3IPbI_3 in all the three principal directions are somehow larger compared to corresponding ones calculated for the $CH_3NH_3PbI_3$ system, which are not unexpected since the size of the B-site cation NH_3I^+ in the former system is increasingly larger than that of $CH_3NH_3^+$. To give an example, we cite that the lattice constants *a*, *b* and *c* were ca. 8.871, 13.126 and 8.636 Å, for $CH_3NH_3PbI_3$, respectively, whereas those for NH_3IPbI_3 were 9.135, 13.732 and 8.739 Å, respectively.

Another noticeable feature of the orthorhombic NH_3IPbI_3 system is that the octahedral tilting is less severe compared to that of $CH_3NH_3PbI_3$. This is evident of the Pb–I–Pb tilt angles. For instance, the Pb–I–Pb angles in the $CH_3NH_3PbI_3$ geometry are ca. 163.8 (along *b*-axis) and 150.6^o (along *a*- and *c*-axes), respectively, whereas those in NH_3IPbI_3 are 165.9^o (along *b*-axis) and 157.1^o (along *a*- and *c*-axes), respectively. Weller *et al.*[103] have demonstrated that the PbI_6^{4-} octahedra are slightly distorted in the experimental structure of orthorhombic $CH_3NH_3PbI_3$. As such, the experimentally observed values were such that Pb–I–Pb was 161.94^o (along *b*-axis) and 150.75^o (along *a*- and *c*-axes), with the average Pb–I–Pb bond angle was 154.51^o.

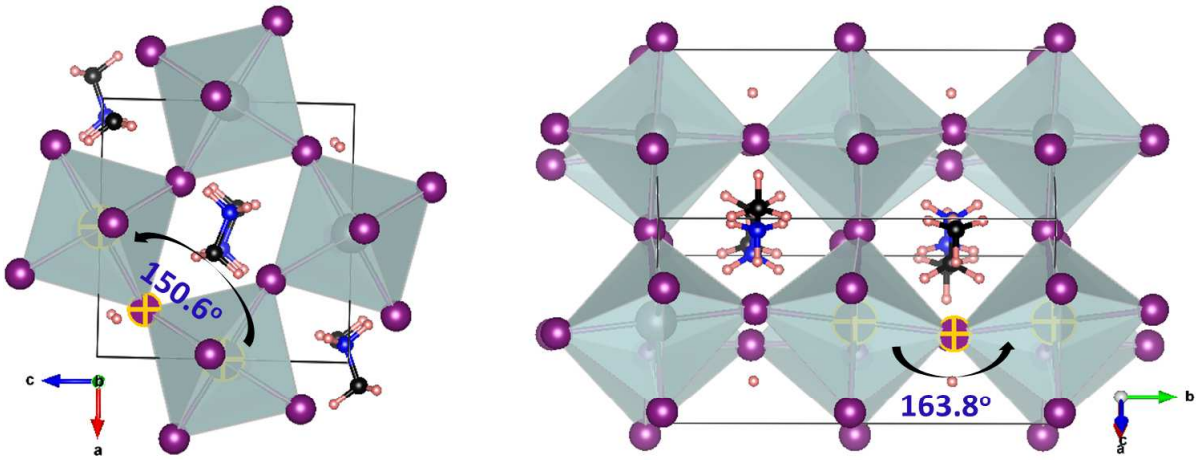

$a = 8.871$ Å; $b = 13.126$ Å; $c = 8.636$ Å;
$\alpha \approx \beta \approx \gamma \approx 90^{o}$
$CH_3NH_3PbI_3$ (orthorhombic)

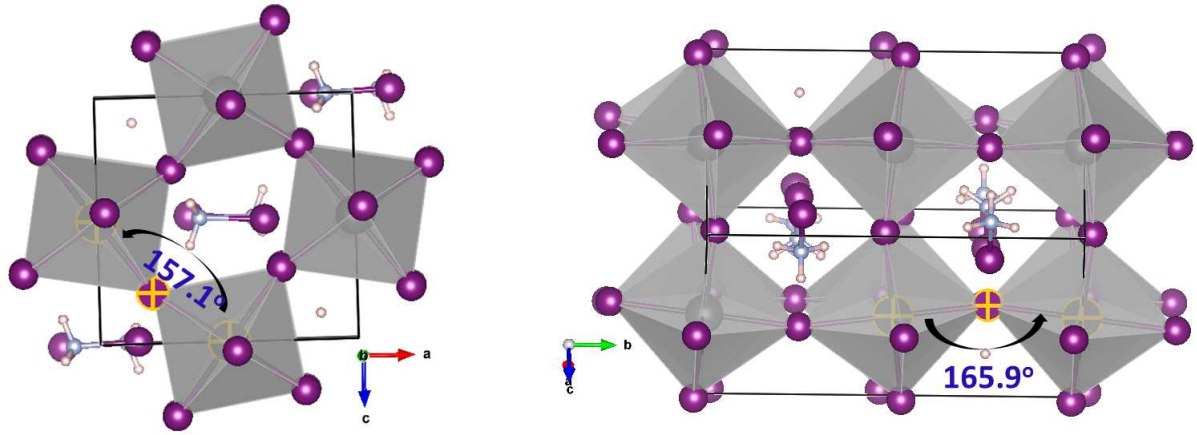

$a = 9.135$ Å; $b = 13.732$ Å; $c = 8.739$ Å;
$\alpha \approx \beta \approx \gamma \approx 90^{o}$
NH_3IPbI_3 (orthorhombic)

Fig. 4: Polyhedral views of PBE/PAW relaxed geometries of the NH_3IPbI_3 and $CH_3NH_3PbI_3$ bulks in the orthorhombic phase ($a \neq b \neq c$; $\alpha = \beta = \gamma = 90^{o}$). Optimized lattice constants are shown for each case. Also, for both cases, the Γ-centered $10 \times 8 \times 10$ k-point mesh was used.

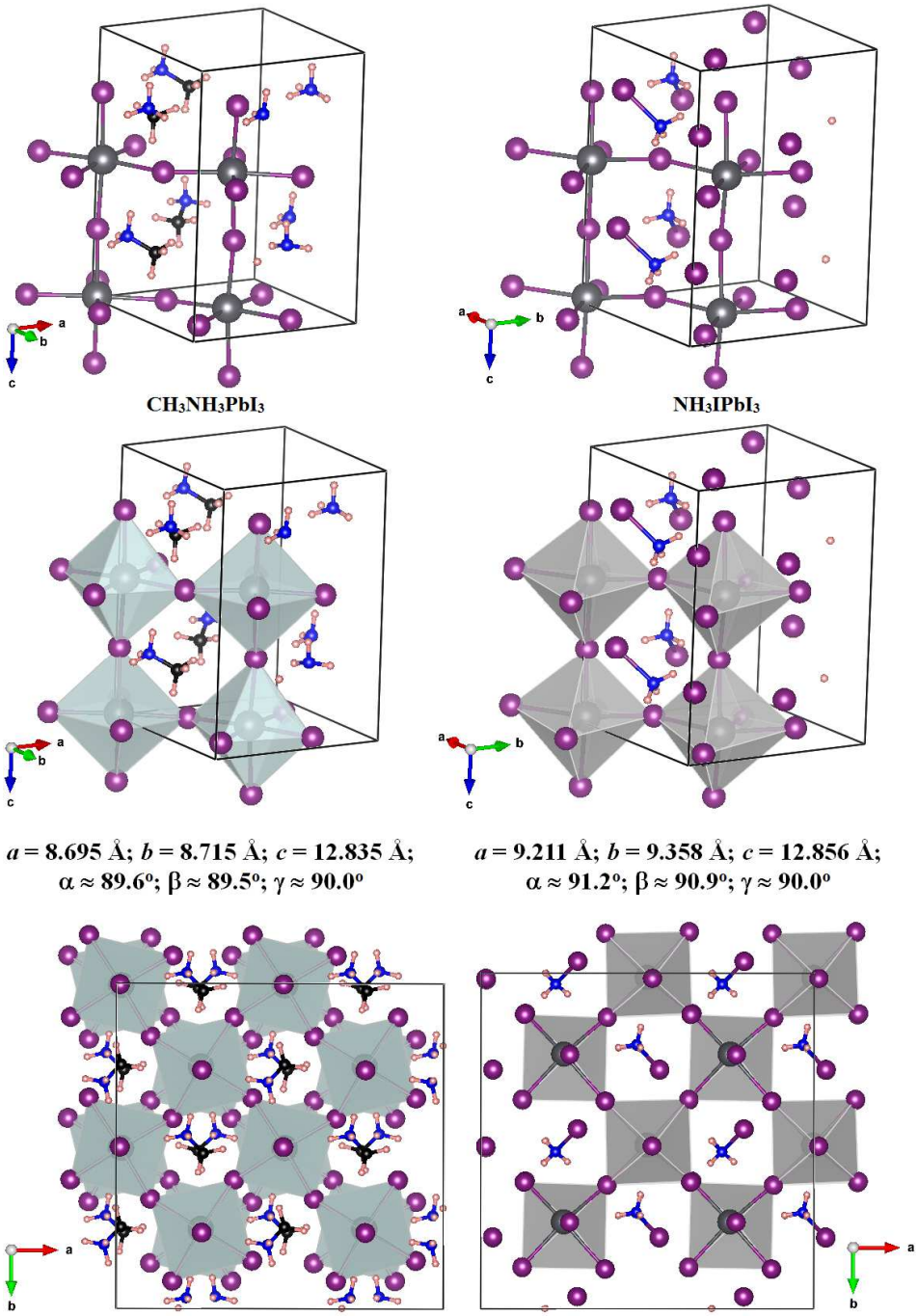

Fig. 5: Ball-and-stick (right top) and polyhedral (intermediate and bottom, right) views of PBE/PAW relaxed geometry of the NH_3IPbI_3 bulk in the tetragonal phase ($a \approx b \neq c$; $\alpha \approx \beta \approx \gamma \approx 90^o$). For comparison, the corresponding relaxed (reported) geometries are illustrated for $MAPbI_3$ (left). Optimized lattice constants are shown for the bulks for both cases. The 2× 2 × 2 supercell model geometries are illustrated for both cases for clarity (bottom).

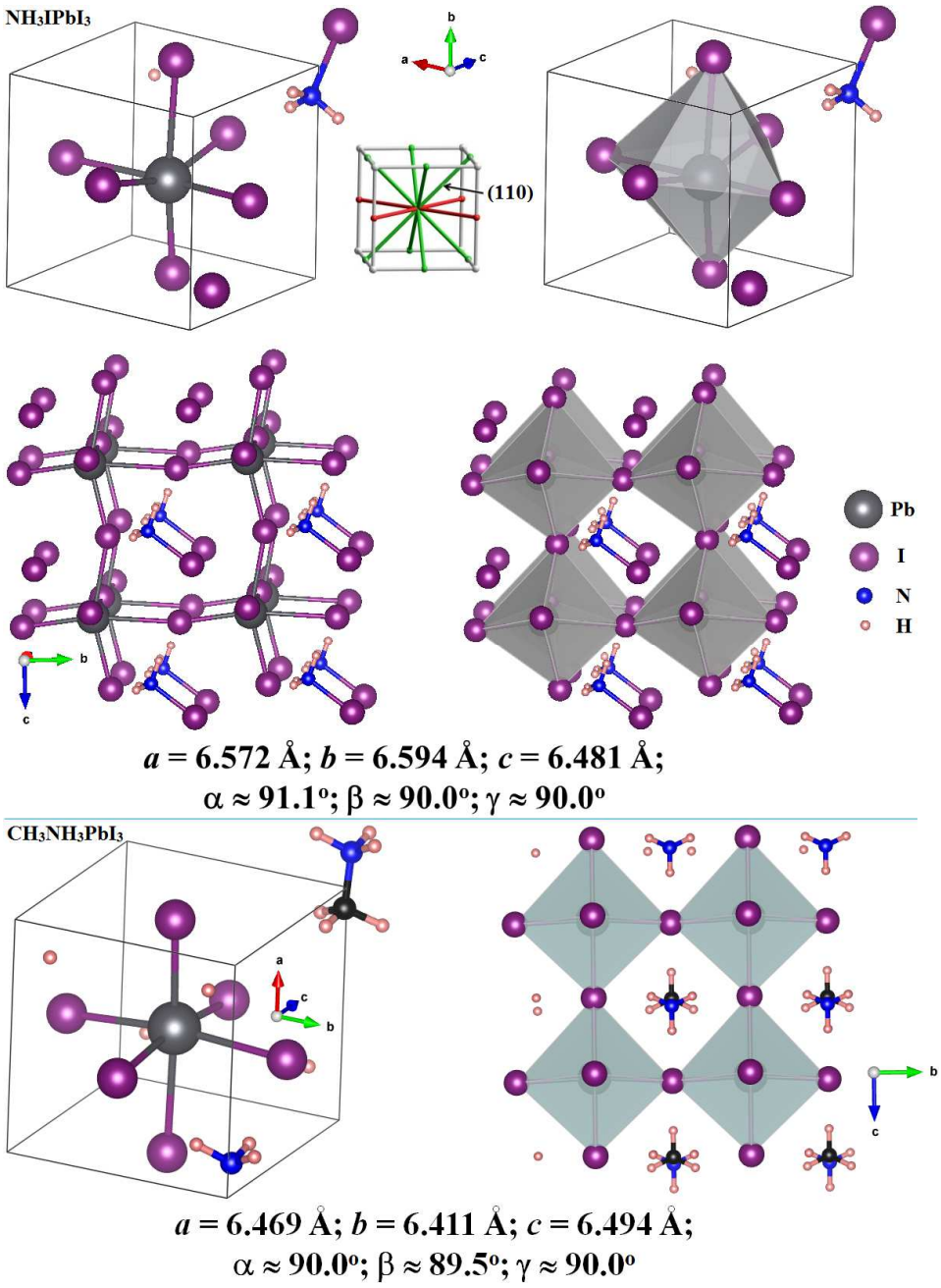

Fig. 6: Ball-and-stick and polyhedral views of PBE/PAW relaxed geometry of the NH_3IPbI_3 bulk in the monoclinic phase (top), and b) their corresponding 2×2×2 supercell geometries (intermediate). The N–I bond of the iodoammonium cation is along the (011) direction. For comparison, the monoclinic bulk and 2×2×2 supercell geometries of the $MAPbI_3$ perovskite are depicted (bottom). Optimized lattice constants are shown for both the bulk systems.

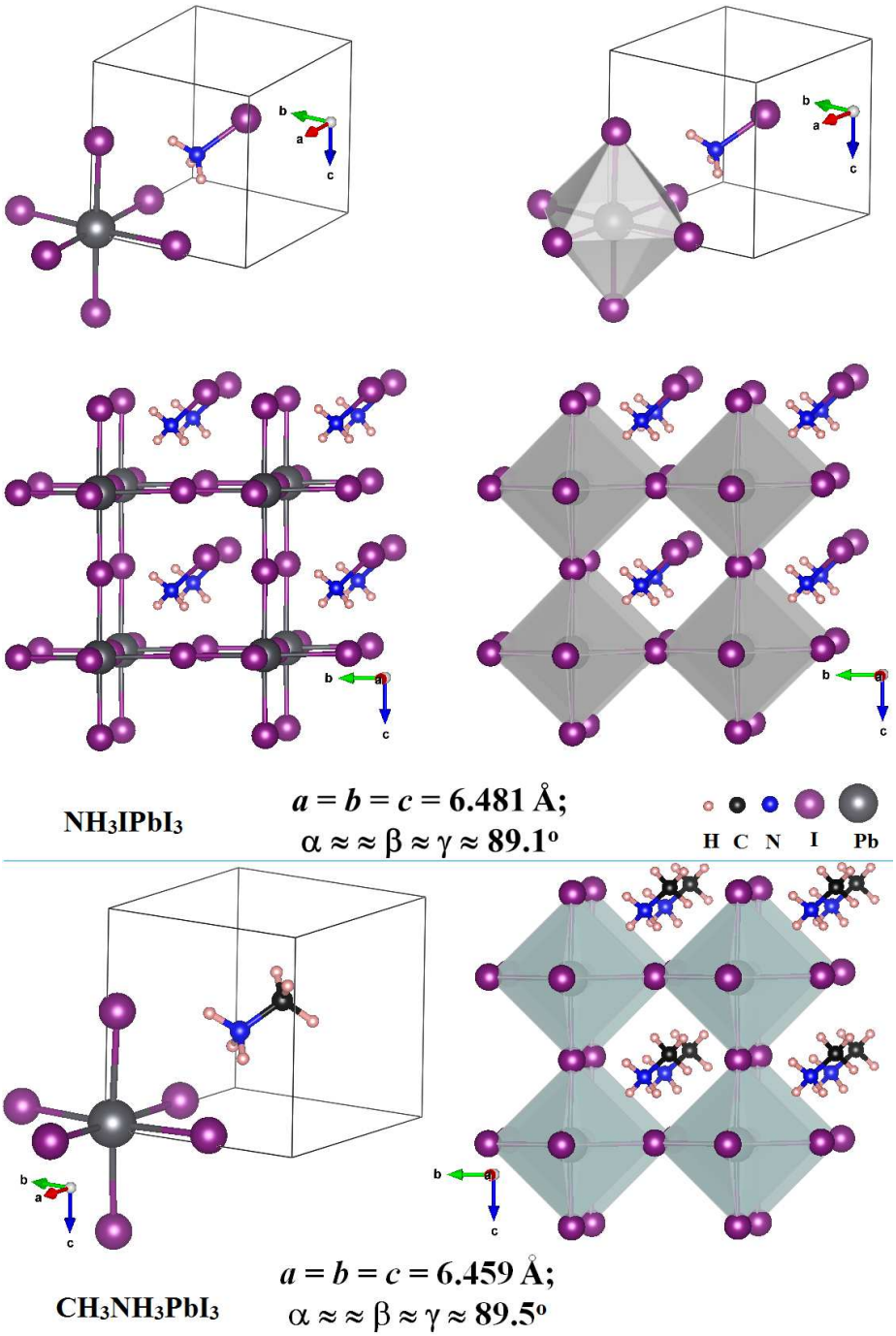

Fig. 7: Ball-and-stick and polyhedral views of PBE/PAW relaxed geometry of the NH_3IPbI_3 bulk in the cubic phase (top), and their corresponding 2×2×2 supercell geometries (intermediate). The N–I bond of the iodoammonium cation is along the (111) direction. For comparison, the related cubic and 2×2×2 supercell geometries of the $MAPbI_3$ are depicted (bottom). Optimized lattice constants are shown for the bulks for both cases.

As one passes from the orthorhombic (Fig. 4) to the tetragonal geometry (Fig. 5) to the monoclinic (Fig. 6) to the cubic geometry (Fig. 7) of the NH_3IPbI_3 system, the extent of octahedral tilting is diminished. This is a feature identical with that observed for $CH_3NH_3PbI_3$.[103] As expected, the tilting is found to be least in the monoclinic geometry, Fig. 6, and diminishingly small in the cubic geometry of NH_3IPbI_3.

Fig. 7 compares the relaxed structure of NH_3IPbI_3 with that of $CH_3NH_3PbI_3$ in the cubic phase. For both cases, the B-site cation is corner facing, with N–X (X = I, C) bond is aligned along the (111) direction. This is an orientation of the B-site cation that was experimentally observed for $CH_3NH_3PbI_3$. Since the cubic configuration of the $CH_3NH_3PbI_3$ system belongs to the high-temperature phase (327 K), [103-104] it is like that the analogous geometry of the NH_3IPbI_3 might be stable in high temperature phase as well. Note that both these geometries can be represented by the *Pm3m* space-group symmetry, which can also be described by $a^0a^0a^0$ the Glazer's notation.[105]

In contrary, the 3D structure of the tetragonal phase, which is supposedly stable at room temperature for $CH_3NH_3PbI_3$ ($165 < T < 327$ K), belongs to the *I4/mcm* space group, Fig. 5 (bottom-left). In this geometry, the PbI_6 octahedra do not show any alternative tilting along the *a*- and *b*-axes. However, there exists marginal out-of-phase tilting along the *c*-axis. In the Glazer's notation, [105] this tilting is perhaps in line with the $a^0a^0c^-$ tilt pattern.

7.3.10 Intermolecular interactions in NH_3IPbI_3: A geometry based perspective

Fig. 8 illustrates the schematic for the topology of intermolecular bonding interactions in the orthorhombic geometry of NH_3IPbI_3. It indicates that there may be four distinct contacts between the inorganic host and the iodoammonium cation. Three of these are associated with the three ammine protons that are involved in three distinct modes of intermolecular interactions with the coordinated iodides of the inorganic cage; two are equivalent and the other is long-ranged. The contact distance associated with each of the former two is ca. 2.659 Å, whereas that with the latter one is ca. 3.274 Å. These three are also indicative of hydrogen bonding, with the former two are relatively stronger than the latter one, inferred from the pronounced differences in the I•••H intermolecular bond distances.

The van der Waals radii for H and I are 1.20 and 2.04 Å, respectively.[106] The sum of these two radii is ca. 3.24 Å. Apparently, the intermolecular contact distances for the two I•••H(–N) contacts are significantly smaller than the sum of the van der Waals radii radii of I and H atoms, 3.24 Å, giving some evidence about the presence of strong hydrogen bonding interaction.[107-109] These are seemingly the main contributor responsible for the pronounced octahedral tilting observed for the orthorhombic geometry of

NH_3IPbI_3, Fig. 4. Similar rationalizations have been previously made for $CH_3NH_3PbI_3$.[110-112]

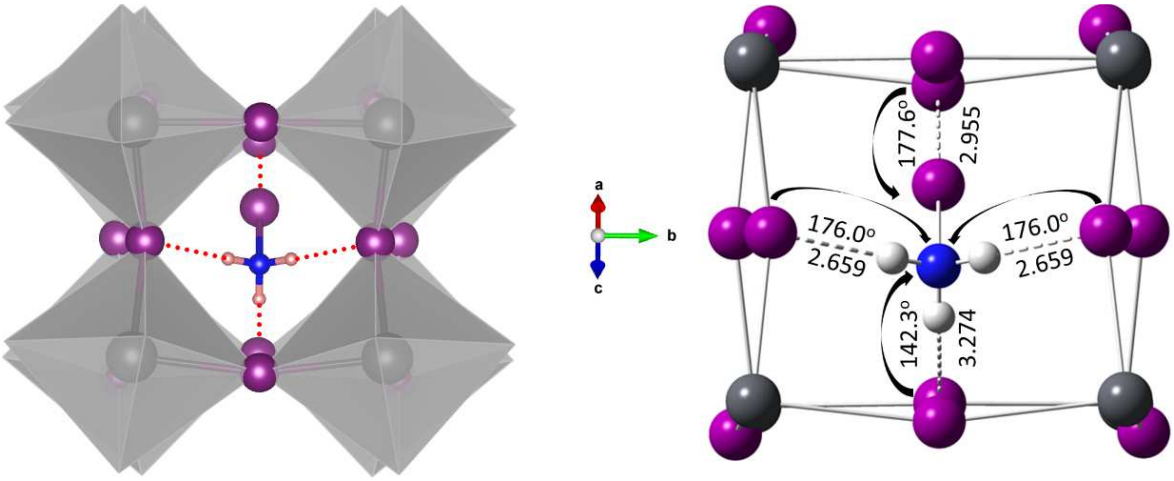

Fig. 8: Nature of intermolecular interaction topologies in the orthorhombic geometry of NH_3IPbI_3. Both polyhedral (left) and ball-and-stick (right) models are illustrated for clarity. Selected bond distances (in Å) and bond angles (°) are shown. Nitrogen: blue, Iodine: purple, Lead: grey, Hydrogen: (light-red/grey-white). The dotted lines represent intermolecular noncovalent interactions.

Noticeable in Fig. 8 is an I•••I–N intermolecular contact. The intermolecular distance for this contact is ca. 2.955 Å. Again, this is much smaller than the sum of the van der Waals radii two iodine atoms, 4.08 Å, thereby giving significant evidence about possibility of halogen bonding. Both I•••H–N hydrogen bonded and I•••I–N halogen bonded interactions in NH_3IPbI_3 are observed to be directional. This is reminiscent of the I•••H–N and I•••I–N bond angles, in which, the former and latter are close to 176.0 and 177.6°, respectively. This observation is in line with the common notion that halogen bonding is more directional than hydrogen bonding.[114]

There is another I•••H–N contact in the NH_3IPbI_3 geometry shown in Fig. 8, with r(I•••H) is ca. 3.274 Å. It is indeed weak. This is evident of the longer intermolecular bond distance, which is also longer than the van der Waals radii sum of H and I atoms, 3.240 Å. The ∠I•••H–N for this interaction is 142.3°.

The above results show that the overall structural stability of the orthorhombic phase of the NH_3IPbI_3 system is collectively arising from contributions due to hydrogen and halogen bonding interactions.

For the orthorhombic $CH_3NH_3PbI_3$ geometry, it was experimentally observed that at T ~ 100 K the centroid of the $CH_3NH_3^+$ cation lies near the center of the inorganic cage.[103] Even so, it could form reasonably strong hydrogen bonded interactions with the iodides of the inorganic core, with I•••H–N distances of 2.613 and 2.808 (×2) Å.

For the experimentally reported tetragonal geometry of $CH_3NH_3PbI_3$ (T ~ 180 K), the $[PbI_3]^-$ framework was considerably less distorted than in the orthorhombic phase, with ∠Pb–I–Pb were 157.9 and 180° (average Pb–I–Pb bond angle 165.3°). The intermolecular hydrogen bonding interactions between the $–NH_3$ group and the iodide framework of the inorganic cage were weaker, determined to be 3.18(1) and 3.15(2) Å.[103]

Fig. 9 compares the intermolecular interactions in cubic NH_3IPbI_3 with those of the corresponding $CH_3NH_3PbI_3$ system. Because of symmetry, all the three I•••H–N interactions formed between the ammonium protons of the B-site cation and the coordinated iodides of the inorganic cage in either NH_3IPbI_3, or $CH_3NH_3PbI_3$, are equivalent. For instance, r(I•••H) ≈ 2.652 Å and ∠I•••H–N ≈ 150.4° for each of three I•••H–N hydrogen bonds in NH_3IPbI_3, whereas r(I•••H) ≈ 2.680 Å and ∠I•••H–N ≈ 151.4° for each of the three I•••H–N hydrogen bonds in $CH_3NH_3PbI_3$. These results also suggest that the I•••H–N contacts in NH_3IPbI_3 are shorter than those in $CH_3NH_3PbI_3$. This result demonstrates that the intermolecular interactions are stronger in the former than in the latter geometry. Interestingly, this conclusion is in agreement with the observed difference in the gas phase binding energies calculated for these two systems, in which, the ΔE were –106.3 and –111.60 kcal mol^{-1} for the I•••H–N hydrogen bonding interactions in $CH_3NH_3PbI_3$ and NH_3IPbI_3, respectively, thereby stressing the importance of gas phase calculations to infer the chemistry of bulk materials.

Furthermore, it is found that the I•••H–C contact distances in $CH_3NH_3PbI_3$ are relatively longer. For instance, r(I•••H) ≈ 3.554 Å and ∠I•••H–C ≈ 135.6° for the I•••H–C contacts. While these are weaker, these should be not be underrepresented since these do contribute to overall structural stability of the $CH_3NH_3PbI_3$ system. An analogous interaction in NH_3IPbI_3 could be the I•••I(–N) halogen bond contact, in which, r(I•••I) ≈ 3.997 Å and ∠I•••I–N ≈ 139.4°. Even though these are weak these assist in explaining the observed octahedral tilting in the orthorhombic geometry of either NH_3IPbI_3 or $CH_3NH_3PbI_3$. Chapter 4 discusses this in more detail for the latter system.

Experimentally, it was observed for the cubic $CH_3NH_3PbI_3$ perovskite that the Pb–I–Pb angles are approximately 180° and the organic cation was orientationally disordered inside the unit cell. It could be found oriented along the three unit cell directions. For instance, it was aligned along the [111] (diagonal), the [011] (edge), and

the [100] (face) directions of the unit cell. The weak I•••H–N and I•••H–C interaction distances in cubic $CH_3NH_3PbI_3$ were reported to 3.12(2) Å and 3.52(2) Å.[103]

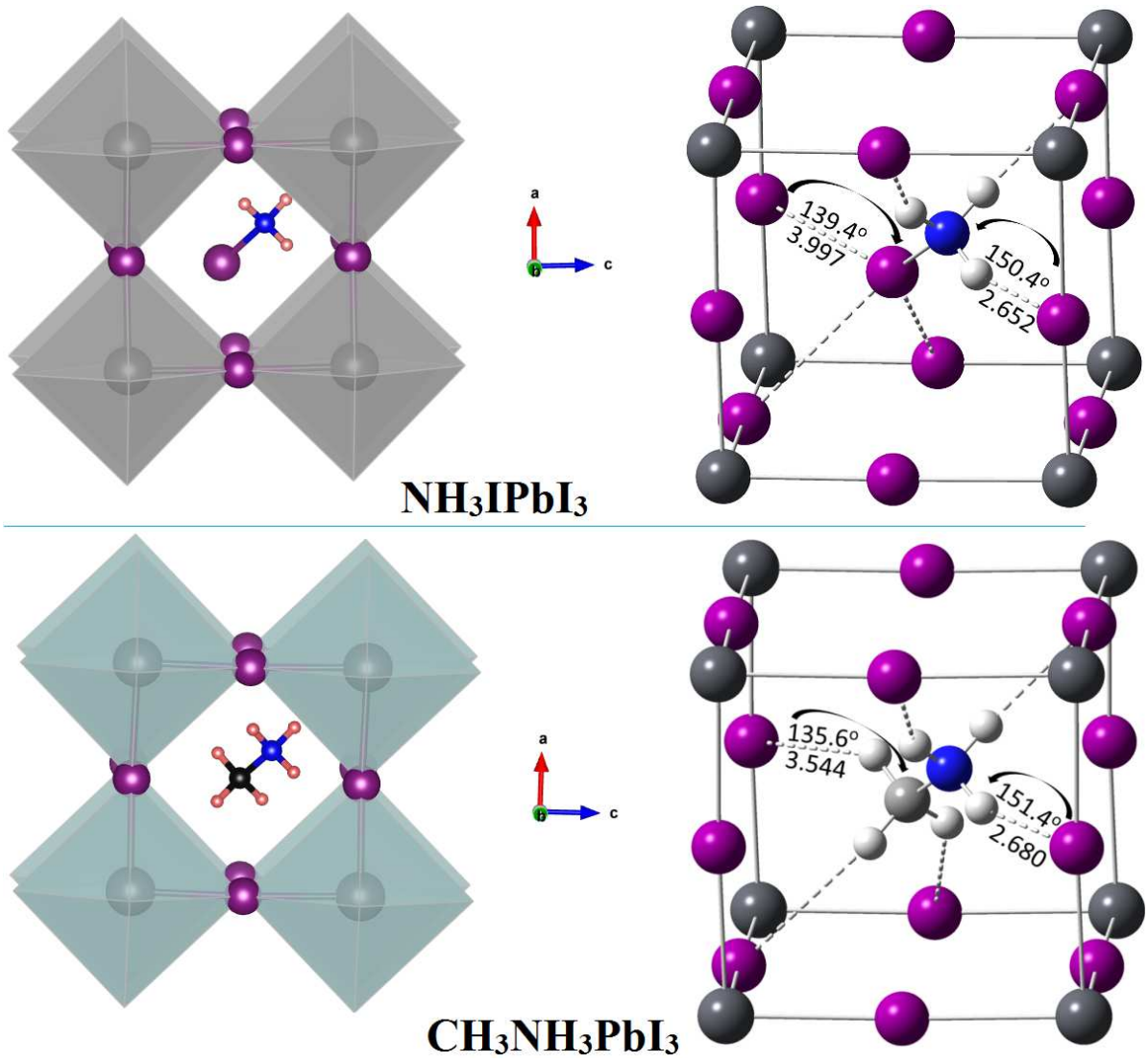

Fig. 9: Comparison of the nature of the intermolecular interaction topologies between the cubic geometries of NH_3IPbI_3 (top) and $CH_3NH_3PbI_3$ (bottom). Both polyhedral and ball-and-stick models are illustrated for clarity. Selected bond distances (in Å) and bond angles (°) are shown. The dotted lines represent intermolecular noncovalent interactions. Nitrogen: blue, Iodine: purple, Lead: grey, Hydrogen: (light-red in polyhedral model/grey-white in ball-and-stick model).

7.3.11 Intermolecular interactions in NH_3IPbI_3: A QTAIM perspective

It is not possible to discuss in detail the interaction topologies of bonding interactions for all the geometries of NH_3IPbI_3. We rather focus on the room temperature cubic geometries. Fig. 10 illustrates the molecular graphs for cubic NH_3IPbI_3 and $CH_3NH_3PbI_3$, produced employing quantum theory of atoms in molecules (QTAIM).[115-117] These involve various topologies of bonding interaction. As discussed in Chapters 2-4, these topologies can be inferred by looking at the bond critical points and bond paths that show up between nuclei of atoms that are bonded with each other.

From the molecular graph shown in Fig. 10b, it is apparent that each proton on N of $CH_3NH_3^+$ in the cubic geometry of $CH_3NH_3PbI_3$ is involved with a single I•••H intermolecular interaction. Since these three intermolecular interactions are equivalent, the charge densities at the I•••H(–N) bond critical points are also equivalent, with $\rho_b \approx$ 0.0179 a.u. In contrary, each proton on the methyl group is involved with three I•••H(–C) type interactions with the coordinated iodide atoms. Of these three, two are equivalent and the other is slightly stronger, evident of the charge density values, ρ_b: 0.0022 *vs.* 0.0032 a.u. Regardless of whether these are strong or weak, the sign of the Laplacian of the charge density at these bond critical points are all positive, signifying closed-shell electrostatic interactions. [115-117]

Similarly, the molecular graph in Fig. 10a shows that the $–NH_3$ group in NH_3I^+ is involved in three I•••H(–N) equivalent interactions in NH_3IPbI_3. The charge density at the bcps of these interactions is ca. 0.0189 a.u. This value is indeed larger than that of the corresponding interactions found for $CH_3NH_3PbI_3$, in agreement with the corresponding trend in the binding energies as noted above. In addition, the I atom in NH_3I^+ is found to be involved weakly with all the neighboring I atoms of the inorganic perovskite cage. As such, there are nine I•••I(–N) halogen bonded contacts, which are not unusual given the latter halogen atoms are polarizable and dispersive. Of these, there are six that are equivalent and are having ρ_b of 0.0023 a.u. The other three that are also equivalent with each other are relatively stronger, and having ρ_b of 0.0074 a.u.

These QTAIM results suggests that, relying solely on the intermolecular bond distances, as well as on the "less than the sum of the van der Waals radii" alone, which has been numerously practiced in the perovskite literature, can mislead to wrong conclusions. Thus care must be taken especially when the nature of the intermolecular interaction between the inorganic host and the inorganic/organic guest species are considered to be examined in perovskite systems.

In our judgement, it is always recommended to use an appropriate charge density model to account for possible interactions in systems this type, and beyond.

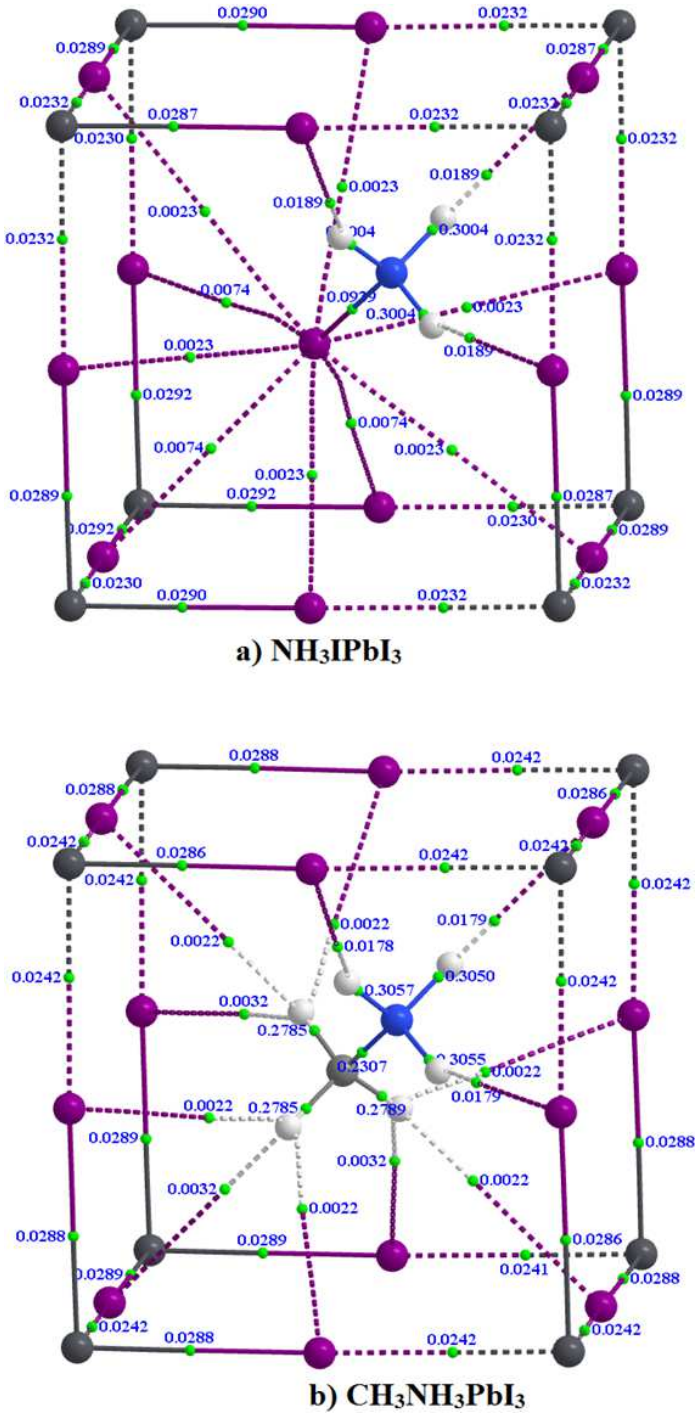

Fig. 10: QTAIM based comparison of the detailed nature of the intermolecular interaction topologies in the cubic geometries of a) NH_3IPbI_3 and b) $CH_3NH_3PbI_3$. The solid and dotted lines indicate possible intermolecular noncovalent interactions, which are actually molecular bond paths according to the definition of QTAIM.[115] The tiny green spheres between atoms (balls) represent the bond critical points. Electron charge density values (in a.u.) are shown at the (3 –1) bond critical points.

7.3.12 The bandgap and Shockley-Queisser limit

A most important property of any semiconducting material is the bandgap, symbolically represented by E_g. It is an intrinsic property of all solids, and in accord with the band theory of solid, it refers to the difference energy between the Valence Band Maximum (VBM) and Conduction Band Minimum (Scheme 1a).[118-119] There are a specific type of materials that are generally accompanied with a small non-overlapping gap between the VBM and CBM, which are neither good insulators nor conductors, these are the so-called semiconductors. [120]

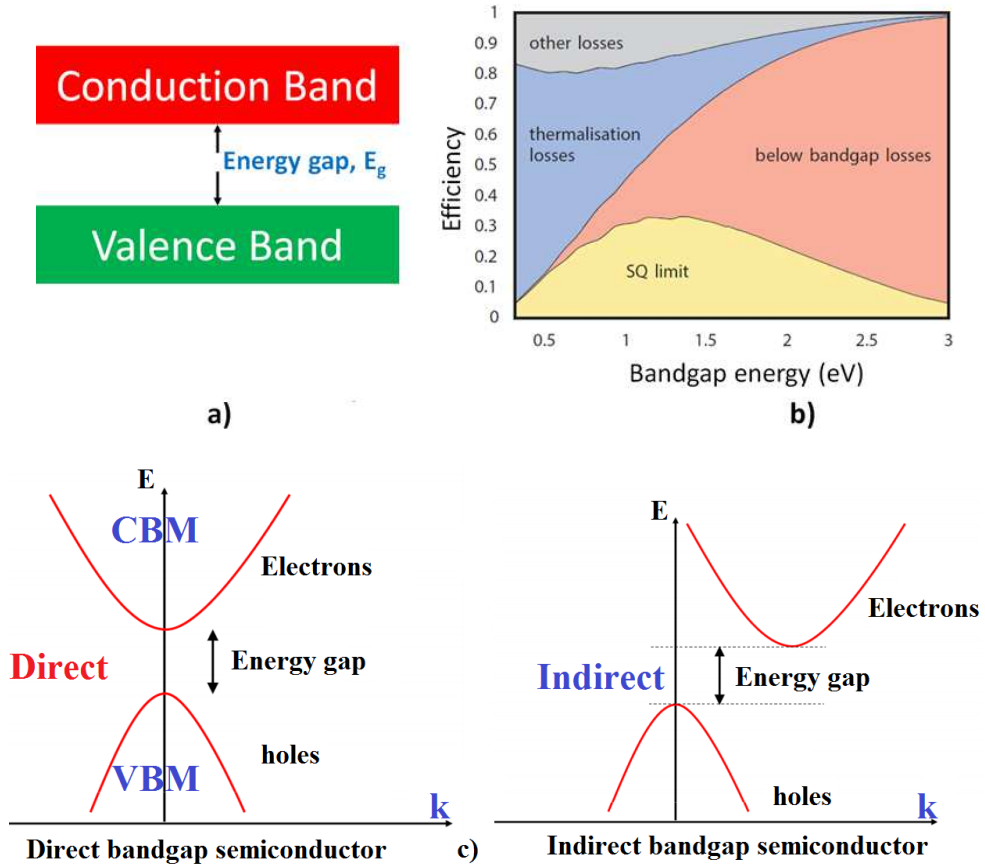

Scheme – 1: a) Definition of bandgap, E_g; b) Major losses in the Shockley-Queisser limit (AM1.5 spectrum was used as incident light for this estimation); c) Definitions of direct and indirect bandgaps, showing the valence and conduction bands appear as parabolas, with the electron energy E being a quadratic function of its momentum k (E = f(k)).

The character of bandgap for a semiconductor can either be *direct* or *indirect*. The CBM (minimal energy state in the conduction band) is characterized by a certain crystal

k-vector in the Brillouin zone. Similarly, the VBM (maximal energy state in the valence band) is characterized by a certain crystal k-vector. When these two k-vectors for both VBM and CBM are the same, the bandgap is called a "direct", Scheme 1c. When they are not the same, it is then called as "indirect". According to Wiki, [121] the band gap is called "direct" if the momentum of electrons and holes is the same in both the conduction band and the valence band; an electron can directly emit a photon. In an "indirect" gap, a photon cannot be emitted because the electron must pass through an intermediate state and transfer momentum to the crystal lattice.

Direct bandgap materials includes some III-V compounds such as InAs, GaAs, whereas indirect bandgap materials include Si and Ge, as well as compounds of the III-V elements (viz. AlSb).[120-121]

Most of materials reported till date are characterized by the bandgap. The theoretical limit for single-junction solar cells is usually referred to as the Shockley-Queisser (SQ) limit.[124] The SQ efficiency limit for the AM1.5 spectrum is about 33.7 % assuming a single p-n junction with a bandgap of 1.34 eV. This means an ideal solar cell will be able to convert 33.7% of the total sunlight (1000 W/m^2) falling on it into electricity (337 W/m^2). For AM0, the SQ limit is 30.1% at 1.26 eV. The most popular solar cell material, silicon, has a less favorable band gap of 1.1 eV, resulting in a maximum efficiency of about 32%. Modern commercial mono-crystalline solar cells produce about 24% conversion efficiency, the losses due largely to practical concerns like reflection off the front surface and light blockage from the thin wires on its surface. The major loss mechanisms that are taken into account in the Shockley-Queisser limit are illustrated in Scheme 1b. The major losses are non-absorbed photons below the bandgap and thermalised energy of photons above the bandgap. The other losses are due to the voltage loss because of thermal radiation and the fill factor being different from 100%.

7.3.13 The accuracy of the bandgap for the cubic phase of $CH_3NH_3PbI_3$: A benchmark study

Previous periodic DFT calculations have suggested that molecular rotations and orientation of the $CH_3NH_3^+$ cation can lead to a dynamic change of the band structure of $CH_3NH_3PbI_3$, responsible to explain the slow carrier recombination and the superior solar energy conversion efficiency. In specific, Motta *et al.* have performed periodic DFT calculations for the cubic phase of the $CH_3NH_3PbI_3$ system, in which case, they considered two specific orientations for the $CH_3NH_3^+$ cation.[125] Their results have showed that when the $CH_3NH_3^+$ cation orients along the [011] direction, an *indirect* band gap is present with an energy of 1.629 eV. And ordering the cation along the [111] direction has led to a *direct* gap of 1.611 eV.

Note that in these calculations the authors have accounted for the fully relativistic spin–orbit coupling interaction by VASP.[51] A projector augmented wave

pseudopotential, together with plane wave basis set energy cutoff of 520 eV, was invoked. In addition, the Brillouin zone integration was performed using 8 × 8 × 8 *k*-point mesh centered at the Γ point, and the correction to the PBE was done within the method of Tkatchenko and Scheffler (DFT-TS) to account for dispersion dominant van der Waals interactions.

As mentioned above, the nature of the calculated bandgap for the $CH_3NH_3PbI_3$ material was found to be oppositely with respect to the directional preference of the organic cation inside the inorganic perovskite cage. Because of this reason, the authors could demonstrate that *$CH_3NH_3PbI_3$ is a 'dynamical' bandgap semiconductor*, in which the exact position of the conduction band minimum depends on the particular spatial arrangement of the organic molecular ions. Moreover, it was suggested that the extended carrier lifetimes in $CH_3NH_3PbI_3$ might be a consequence of the 'dynamical' position of the conduction band minimum forming a basin around a high-symmetry point in the *k*-space. These results were demonstrated to be robust against bandgap corrections and spin–orbit interaction and deliver an absorption spectrum in good agreement with experimental data near the absorption edge.

The authors of this study have demonstrated that the computational results and the interpretations they have provided are not a *computational artifact*. [125] This is evident of their statement such as "… We have carefully verified that the indirect bandgap is not an artifact of our computation method. First, we analyzed the relaxation in a 2 × 2 × 2 (96 atoms) supercell to establish whether further low-symmetry configurations are possible …"

Considering the results of the above study into account, [125] we have conducted a benchmark study using periodic DFT to re-examine the "character" of the bandgap and the nature of the conduction band minimum for CH_3NH_3PbI. An interest towards this was to verify whether $CH_3NH_3PbI_3$ should be regarded as a 'dynamical' bandgap semiconductor as suggested in the article of the *Nat. Commun.*[125]?

Table 1 summarizes the computed bandgaps for the two orientations of the organic cation inside the perovskite cage in $CH_3NH_3PbI_3$. These were calculated using the PBE functional, together with a plane wave basis set energy cut-off of 520 eV. The Brillouin zone integration was performed using 8 × 8 × 8 *k*-point centered at and not at the Γ point (e.g., Monkhorst Pack), with the former setting is in consistent with at adopted by Motta *et al.*[125]

The above selection of the k-point grid/mesh is probably consistent with the VASP manual[126] that recommends to use even meshes (e.g. 8 × 8 × 8) for up to $n = 8$. From there on odd meshes are more efficient (e.g. 11 × 11 × 11). However, it should be kept in mind that the number of divisions is often totally unrelated to the total number of k-points and to the precision of the grid. Therefore, an 8 × 8 × 8 might be more accurate

than a 9 × 9 × 9 grid. For fcc, an 8 × 8 × 8 grid is approximately as precise as an 8 × 8 × 8 mesh. A documentation on the choice of the k-point mesh can be found elsewhere.[127]

In addition to the 8 × 8 × 8 *k*-point centered at and not at the Γ, a number of other settings for the k-point were adopted for the relaxation of the geometry of the 12 atoms unit cell of cubic $CH_3NH_3PbI_3$. These include the $n \times n \times n$ (n = 3–20) k-point meshes centered at and not at the Γ point.

From the bandgap data summarized in Table 8 and Appendix 1 for $CH_3NH_3PbI_3$, it is obvious that the "character" of the bandgap in a particular orientation of the organic cation depends on the nature of the k-point mesh, as well as that on the nature of the NELM tag, the latter sets the maximum number of electronic SC (self-consistency) steps to be performed during relaxation of the geometry. For instance, for the (011) orientation of the organic cation, the bandgap was calculated to be *indirect* for k-point meshes such as 3 × 3 × 3, 11 × 11 × 11, 13 × 13 × 13, 15 × 15 × 15, 17 × 17 × 17, or 19 × 19 × 19 when these each was centered at Γ, whereas that calculated with all the remaining k-point meshes is *direct*. Similarly, there were several such occasions, such as 3 × 3 × 3, 5 × 5 × 5, 12 × 12 × 12, 13 × 13 × 13, or $n \times n \times n$ (n = 15–20), in which cases, the bandgap was calculated to be *indirect*, and in these cases, the k-point mesh was not

Table 8: Dependence of bandgap (E_g) on the nature of k-point mesh for $CH_3NH_3PbI_3$ in the cubic phase. [a, b]

	011				111			
k-point mesh	Γ	Nature	M	Nature	Γ	Nature	M	Nature
3 × 3 × 3	3.084	Indirect	3.084	Indirect	3.268	Indirect	3.266	Indirect
4 × 4 × 4	1.788	Direct	2.542	Direct	1.646	Direct	2.755	Indirect
5 × 5 × 5	2.214	Direct	2.216	Indirect	2.404	Direct	2.404	Direct
6 × 6 × 6	1.681	Direct	2.032	Direct	1.580	Direct	2.167	Direct
7 × 7 × 7	1.920	Direct	1.920	Direct	2.017	Direct	2.017	Direct
8 × 8 × 8	1.657	Direct	1.857	Direct	1.581	Direct	1.916	Direct
9 × 9 × 9	1.811	Direct	1.810	Direct	1.844	Direct	1.844	Direct
10 × 10 × 10	1.657	Direct	1.778	Direct	1.581	Direct	1.793	Direct
11 × 11 × 11	1.755	Indirect	1.754	Direct	1.754	Direct	1.754	Direct
12 × 12 × 12	1.657	Direct	1.737	Indirect	1.581	Direct	1.724	Direct
13 × 13 × 13	1.724	Indirect	1.724	Indirect	1.701	Direct	1.701	Direct
14 × 14 × 14	1.657	Direct	1.714	Direct	1.581	Direct	1.683	Direct
15 × 15 × 15	1.706	Indirect	1.706	Indirect	1.669	Direct	1.669	Direct
16 × 16 × 16	1.657	Direct	1.700	Indirect	1.581	Direct	1.657	Direct
17 × 17 × 17	1.695	Indirect	1.722	Indirect	1.647	Direct	1.647	Direct
18 × 18 × 18	1.657	Direct	1.690	Indirect	1.581	Direct	1.639	Direct
19 × 19 × 19	1.687	Indirect	1.686	Indirect	1.632	Direct	1.632	Direct
20 × 20 × 20	1.657	Direct	1.683	Indirect	1.581	Direct	1.627	Direct

[a] Values in eV.
[a] NELM = 80.

centered at Γ (i.e., at Monkhorst M). For the remaining k-point meshes examined at M, the bandgap of the material is found to be *direct*. Apparently, these results show that changing the size of the k-point mesh drives the nature of the bandgap from *indirect* to *direct*, and *vice-versa*.

A similar character for the bandgap is notable for the (111) orientation of the organic cation in cubic $CH_3NH_3PbI_3$. Setting NELM at 20 has the bandgap is calculated to be *indirect* for k-point meshes such as 3 × 3 × 3, 4× 4 × 4, or 11 × 11 × 11, whereas at all the other 15 settings of the k-point mesh, it is found to be *direct*. When NELM was set at 80, only two k-point meshes 3 × 3 × 3 and 4× 4 × 4 were found to be *indirect* at M, and at the remaining settings of the k-point mesh, it is found to be *direct*. Evidently, the variable "character" of the bandgap (from *direct* to *indirect* and so on) with respect to the changed nature of the k-point mesh for the same orientation of the organic cation is nothing other than *a computational artifact*. This should not therefore be attributed to "dynamics" of the molecular cation since it has nothing to do with the "dynamics" of the organic cation inside the interior of inorganic cage.

Note that it is experimentally observed that the organic cation rotates and reorients inside the inorganic cage interior.[103-104] It can therefore be understandable that these motions are dynamical by nature, a consequence of thermodynamics. Conspicuously, the alignment of the organic cation along the (111) direction, or that along the (011) direction, has some effect on the magnitude of the bandgap of $CH_3NH_3PbI_3$. This is not unexpected since the organic cation perturbs the internal volume of the perovskite cage through rotation as is needed for such a motion inside it. The change in the volume is indeed a consequence of subtle electronic structure changes through strain, as well as of marginal distortions to the PbI_6^{4-} octahedra, which collectively affects the magnitude of the bandgap for the $CH_3NH_3PbI_3$ material. For instance, either with the 8 × 8 × 8 mesh or with the 20 × 20 × 20 mesh, the bandgap of the $CH_3NH_3PbI_3$ in regard to the two orientations (111) and (011) of MA is calculated to be 1.581 and 1.657 eV, respectively. These bandgap values are both *direct* at R. The small change 0f 0.076 eV between the two magnitudes of the bandgap in regard to the two orientations of the organic cation is certainly attributed to its dynamical motion, but its character would remain the same.

The above result might be in disagreement with the interpretation of Motta *et al.*[125] According to the authors, when MA is aligned along the (111) direction, the bandgap is direct and measures at 1.423 eV. The absorption profile then increases monotonically from that value, indicating the possibility of direct transitions across the band edges. In contrast, when $CH_3NH_3^+$ is placed along (011), the bandgap is indirect, and it is slightly larger than that found for the corresponding system with the alignment of MA along the (111) orientation. In particular, for the (011) orientation, a direct gap of 1.611 eV and an indirect one of 1.629 eV were found, with the shape of

the absorption spectrum was quite different from that found for system with the (111) orientation. These results are somehow in agreement with the results of Table 8.

Table 9: PBE/PAW predicted bandgaps for the NH_3XPbY_3 series comprising forty eight members, where Y = $Br_{(3-x)}Cl_{x=1–3}$, $I_{(3-x)}Br_{x=1–3}$, $I_{(3-x)}Cl_{x=1–3}$, and IBrCl, and X = F, Cl, Br, I. The pseudocubic geometries were considered with the B-site cation aligned along the (111) direction.[a,b]

BMY_3	6×6×6	Nature	8×8×8	Nature	BMY_3	6×6×6	Nature	8×8×8	Nature
NH_3FPbF_3	3.420	Indirect	3.000	Indirect	$NH_3FPbFCl_2$	3.181	Indirect	3.095	Indirect
NH_3ClPbF_3	3.068	Indirect	2.959	Indirect	$NH_3ClPbFCl_2$	2.772	Indirect	2.648	Indirect
$NH_3FBrPbF_3$	2.641	Indirect	2.550	Indirect	$NH_3BrPbFCl_2$	2.330	Indirect	2.225	Indirect
NH_3IPbF_3	2.557	Indirect	2.485	Indirect	$NH_3IPbFCl_2$	2.272	Indirect	2.198	Indirect
NH_3FPbCl_3	2.785	Direct	2.654	Direct	$NH_3FPbIBrCl$	2.298	Direct	2.121	Direct
$NH_3ClPbCl_3$	2.487	Indirect	2.392	Indirect	$NH_3ClPbIBrCl$	2.077	Indirect	1.995	Indirect
$NH_3FBrPbCl_3$	1.936	Indirect	1.847	Indirect	$NH_3BrPbIBrCl$	2.063	Indirect	1.993	Indirect
NH_3IPbCl_3	1.881	Indirect	1.811	Indirect	$NH_3IPbIBrCl$	2.271	Indirect	2.233	Indirect
$NH_3FPbBrCl_2$	2.581	Direct	2.43	Direct	$NH_3FPbIBr_2$	2.193	Direct	2.017	Direct
$NH_3ClPbBrCl_2$	2.310	Indirect	2.216	Indirect	$NH_3ClPbIBr_2$	1.753	Indirect	1.667	Indirect
$NH_3BrPbBrCl_2$	2.037	Indirect	1.955	Indirect	$NH_3BrPbIBr_2$	1.69	Indirect	1.621	Indirect
$NH_3IPbBrCl_2$	2.308	Indirect	2.243	Indirect	$NH_3IPbIBr_2$	1.978	Indirect	1.921	Indirect
NH_3FPbBr_2Cl	2.460	Direct	2.298	Direct	NH_3FPbI_2Cl	2.215	Indirect	2.024	Direct
$NH_3ClPbBr_2Cl$	2.319	Indirect	2.212	Indirect	NH_3ClPbI_2Cl	2.104	Indirect	2.001	Indirect
$NH_3BrPbBr_2Cl$	1.734	Indirect	1.623	Indirect	NH_3BrPbI_2Cl	1.518	Indirect	1.412	Indirect
NH_3IPbBr_2Cl	1.735	Indirect	1.636	Indirect	NH_3IPbI_2Cl	1.47	Indirect	1.444	Indirect
$NH_3FPbICl_2$	2.376	Direct	2.212	Direct	NH_3FPbI_2Br	2.122	Direct	1.929	Direct
$NH_3ClPbICl_2$	2.131	Indirect	2.029	Indirect	NH_3ClPbI_2Br	2.02	Indirect	1.916	Indirect
$NH_3BrPbICl_2$	1.995	Indirect	1.907	Indirect	NH_3BrPbI_2Br	1.391	Indirect	1.28	Indirect
$NH_3IPbICl_2$	2.060	Indirect	2.051	Indirect	NH_3IPbI_2Br	2.032	Indirect	1.979	Indirect
NH_3FPbBr_3	2.361	Direct	2.198	Direct	NH_3FPbI_3	2.032	Direct	1.831	Direct
$NH_3ClPbBr_3$	2.211	Indirect	2.116	Indirect	NH_3ClPbI_3	1.918	indirect	1.828	Indirect
$NH_3BrPbBr_3$	1.632	Indirect	1.536	Indirect	NH_3BrPbI_3	1.323	indirect	1.232	Indirect
NH_3IPbBr_3	1.551	Indirect	1.472	Indirect	NH_3IPbI_3	1.237	indirect	1.159	Indirect

[a] Values in eV
[a] NELM = 80

In conclusion, our current finding suggests that the character of the bandgap of $CH_3NH_3PbI_3$ is independent of the nature of the orientational and rotational degrees of freedom of the organic cation inside the cuboctahedral cage. The previously drawn conclusion that the $CH_3NH_3PbI_3$ is a dynamical semiconductor may be true since the orientation of the organic species slightly perturbs the magnitude of the bandgap, but its character will remain the same. The other conclusion that suggests “the change of the character of the bandgap of material” through rotational motion may be incorrect

since it *is simply a computational artifact*. Evidently, it seems to us that caution must be taken to select an appropriate k-point mesh for modeling of halide based perovskite systems falling into the same class of compounds, otherwise misleading conclusions can be easily derived.

7.3.14 Selection of an appropriate k-point mesh for predicting bandgaps for the NH_3XPbY_3 series

In order to select an appropriate k-point mesh to model the NH_3XPbY_3 systems with a reasonable degree of chemical accuracy, we have investigated in the last section the performance of various k-point meshes in predicting the nature of the bandgap for the $CH_3NH_3PbI_3$ system. The geometry of this system was cubic and the orientation of the organic cation was either along the (011) direction, or along the (111) direction. As demonstrated, the magnitude of the bandgap was found to be sensitive to the nature of the k-point mesh for a specific orientation of the organic cation. While the predicted nature of the bandgap was variable with respect to the nature of the k-point mesh (Table 8), it was quite clear that the very dense k-point sampling such as the $20 \times 20 \times 20$ (8000 k-points over the full Brillouin zone) may be good to get insight into the correct nature and magnitude of bandgap regardless of the nature of the orientation of the organic cation. Given the result obtained from this specific k-point mesh is comparable with those obtained with even k-point meshes such as $8 \times 8 \times 8$, $10 \times 10 \times 10$, $12 \times 12 \times 12$, or $18 \times 18 \times 18$, *etc.*, and given these calculations with larger k-point sampling are computationally expensive, we thus have opted for a smaller k-point meshes, such as $6 \times 6 \times 6$ and $8 \times 8 \times 8$, to relax the geometries of the NH_3XPbY_3 systems in pseudocubic phase. Also, we have used $10 \times 8 \times 10$ and $8 \times 8\times 10$ k-point meshes for the relaxation of the geometries of the orthorhombic and tetragonal phases of the NH_3IPbI_3 system, similarly as that described by Feng *et al.*[53] for the corresponding geometries of the $CH_3NH_3PbI_3$ system.

7.3.15 Prediction of bandgaps for the NH_3XPbY_3 series in the pseudocubic phase

Table 9 summarizes the bandgaps for forty eight NH_3XPbY_3 systems examined for the pseudocubic geometries, with the haloammonium cation aligned along the (111) direction. Except for NH_3FPbY_3, the bandgaps for the remaining systems are found to be *indirect*, with the E_g values for all systems ranging between 1.237 and 3.420 eV (for NH_3IPbI_3 and NH_3FPbF_3, respectively). For NH_3FPbY_3, the bandgap was *direct*.

For the NH_3XPbY_3 series with a given Y, the bandgap decreases increasing the size of the halogen X in NH_3X^+ from F through Cl to Br to I. For instance, the bandgaps are 1.831, 1.828, 1.232 and 1.159 eV for NH_3FPbI_3, NH_3ClPbI_3, NH_3BrPbI_3 and NH_3IPbI_3, respectively. This trend in the bandgap in this specific series is consistent with

that found for the gas phase binding energies of the corresponding systems (Table 5). That is, this result shows that strongly bound systems are accompanied with larger bandgaps.

Moreover, by keeping nature of the X site species fixed and by varying the nature of the Y-site halogen content, the bandgap of the resulting material can be tuned in a wide range from 1.831 to 3.420 eV. These results suggest that the bandgaps of the NH_3XPbY_3 materials can be changeable in dual manner by changing the nature of the halogen content both in the X- and Y-sites, enhancing the flexibility of the tunability of bandgap compared to $CH_3NH_3^+$.

While performing the bandgap analysis of the NH_3XPbI_3 systems (X = F, Cl, Br, I), we had choose rather a high-dense k-point mesh, $12 \times 12 \times 12$. In the analysis, we have found no change in the character of the bandgap with this setting for NH_3IPbI_3, NH_3BrPbI_3 and NH_3FPbI_3 when the results were compared to those found with the $8 \times 8 \times 8$ k-point mesh. However, for the NH_3ClPbI_3 system, the character of the bandgap could switch from *direct* to *indirect* when the k-point even grid was not centered at Γ-point, Table 10. We have therefore performed another benchmark study for this system, as well as for the other three systems of this specific four-membered series. The results for the latter three systems are summarized in Tables 11–13.

Table 10: Dependence of bandgap on the nature of k-point mesh for pseudocubic NH_3ClPbI_3.[a]

	(011) direction				(111) direction			
k-point	Γ	Nature	Monkhorst	Nature	Γ	Nature	Monkhorst	Nature
$6 \times 6 \times 6$	1.340	Indirect	1.314	Indirect	1.603	Direct	1.918	Indirect
$7 \times 7 \times 7$	1.340	Indirect	1.340	Indirect	1.881	Indirect	1.879	Indirect
$8 \times 8 \times 8$	1.288	Indirect	1.316	Indirect	1.603	Direct	1.834	Indirect
$9 \times 9 \times 9$	1.320	Indirect	---	---	1.783	Indirect	1.780	Indirect
$10 \times 10 \times 10$	1.274	Indirect	1.302	Indirect	1.603	Direct	1.752	Indirect
$11 \times 11 \times 11$	1.311	Indirect	1.311	Indirect	1.732	Direct	1.727	Direct
$12 \times 12 \times 12$	1.278	Indirect	1.296	Indirect	1.603	Direct	1.704	Direct
$13 \times 13 \times 13$	1.294	Indirect	1.294	Indirect	1.691	Direct	1.686	Direct
$14 \times 14 \times 14$	1.278	Indirect	1.283	Direct	1.603	Direct	1.672	Direct
$15 \times 15 \times 15$	1.285	Indirect	1.285	Direct	1.666	Direct	1.661	Direct
$16 \times 16 \times 16$	1.278	Indirect	1.280	Direct	1.603	Direct	1.652	Direct
$17 \times 17 \times 17$	1.278	Indirect	1.285	Direct	1.650	Direct	1.645	Direct
$18 \times 18 \times 18$	1.278	Indirect	1.280	Direct	1.603	Direct	1.639	Direct
$19 \times 19 \times 19$	1.281	Indirect	1.281	Direct	1.639	Direct	1.634	Direct
$20 \times 20 \times 20$	1.274	Indirect	1.277	Direct	1.603	Direct	1.630	Direct

[a] Values in eV.

Table 11: Dependence of bandgap (E_g) on the nature of k-point mesh for cubic NH_3FPbI_3.[a]

	(011) direction				(111) direction			
k-point	Γ	Nature	Monkhorst	Nature	Γ	Nature	Monkhorst	Nature
$6\times6\times6$	1.617	Direct	2.032	Direct	1.617	Direct	2.032	Direct
$7\times7\times7$	1.910	Direct	1.910	Direct	1.910	Direct	1.910	Direct
$8\times8\times8$	1.618	Direct	1.831	Direct	1.618	Direct	1.831	Direct
$9\times9\times9$	1.777	Direct	1.777	Direct	1.777	Direct	1.777	Direct
$10\times10\times10$	1.618	Direct	1.740	Direct	1.618	Direct	1.740	Direct
$11\times11\times11$	1.618	Direct	1.713	Direct	1.713	Direct	1.713	Direct
$12\times12\times12$	1.618	Direct	1.694	Direct	1.618	Direct	1.694	Direct
$13\times13\times13$	1.679	Direct	1.679	Direct	1.679	Direct	1.679	Direct
$14\times14\times14$	1.618	Direct	1.668	Direct	1.618	Direct	1.668	Direct
$15\times15\times15$	1.659	Direct	1.659	Direct	1.659	Direct	1.659	Direct
$16\times16\times16$	1.618	Direct	1.652	Direct	1.618	Direct	1.652	Direct
$17\times17\times17$	1.647	Direct	1.647	Direct	1.647	Direct	1.647	Direct
$18\times18\times18$	1.618	Direct	1.642	Direct	1.618	Direct	1.642	Direct
$19\times19\times19$	1.639	Direct	1.639	Direct	1.639	Direct	1.639	Direct
$20\times20\times20$	1.614	Direct	1.636	Direct	1.614	Indirect	1.636	Direct

[a] Values in eV.

Table 12: Dependence of bandgap (E_g) on the nature of k-point mesh for cubic NH_3BrPbI_3.[a]

	(011) direction				(111) direction			
k-point	Γ	Nature	Monkhorst	Nature	Γ	Nature	Monkhorst	Nature
$6\times6\times6$	1.063	Indirect	1.322	Indirect	1.003	Indirect	1.236	Indirect
$7\times7\times7$	1.283	Indirect	1.283	Indirect	1.208	Indirect	1.208	Indirect
$8\times8\times8$	1.003	Indirect	1.232	Indirect	0.919	Indirect	1.163	Indirect
$9\times9\times9$	1.168	Indirect	1.168	Indirect	1.089	Indirect	1.089	Indirect
$10\times10\times10$	1.024	Indirect	1.133	Indirect	0.950	Indirect	1.050	Indirect
$11\times11\times11$	1.128	Indirect	1.128	Indirect	1.049	Indirect	1.049	Indirect
$12\times12\times12$	1.002	Indirect	1.110	Indirect	0.919	Indirect	1.033	Indirect
$13\times13\times13$	1.084	Indirect	1.084	Indirect	1.003	Indirect	1.003	Indirect
$14\times14\times14$	1.013	Indirect	1.072	Indirect	0.934	Indirect	0.989	Indirect
$15\times15\times15$	1.071	Indirect	1.071	Indirect	0.992	Indirect	0.992	Indirect
$16\times16\times16$	1.002	Indirect	1.063	Indirect	0.919	Indirect	0.984	Indirect
$17\times17\times17$	1.050	Indirect	1.050	Indirect	0.968	Indirect	0.968	Indirect
$18\times18\times18$	1.008	Indirect	1.045	Indirect	0.927	Indirect	0.962	Indirect
$19\times19\times19$	1.046	Indirect	1.046	Indirect	0.965	Indirect	0.965	Indirect
$20\times20\times20$	1.002	Indirect	1.041	Indirect	0.919	Indirect	0.961	Indirect

[a] Values in eV.

Table 13: Dependence of bandgap (E_g) on the nature of k-point mesh for cubic NH_3IPbI_3.[a]

	(011) direction				(111) direction			
k-point	Γ	Nature	Monkhorst	Nature	Γ	Nature	Monkhorst	Nature
$6 \times 6 \times 6$	1.003	Indirect	1.236	Indirect	1.063	Indirect	1.322	Indirect
$7 \times 7 \times 7$	1.208	Indirect	1.208	Indirect	1.283	Indirect	1.283	Indirect
$8 \times 8 \times 8$	0.919	Indirect	1.163	Indirect	1.003	Indirect	1.232	Indirect
$9 \times 9 \times 9$	1.089	Indirect	1.089	Indirect	1.168	Indirect	1.168	Indirect
$10 \times 10 \times 10$	0.950	Indirect	1.050	Indirect	1.024	Indirect	1.133	Indirect
$11 \times 11 \times 11$	1.049	Indirect	1.049	Indirect	1.128	Indirect	1.128	Indirect
$12 \times 12 \times 12$	0.919	Indirect	1.033	Indirect	1.002	Indirect	1.110	Indirect
$13 \times 13 \times 13$	1.003	Indirect	1.003	Indirect	1.084	Indirect	1.084	Indirect
$14 \times 14 \times 14$	0.934	Indirect	0.989	Indirect	1.013	Indirect	1.072	Indirect
$15 \times 15 \times 15$	0.992	Indirect	0.992	Indirect	1.071	Indirect	1.071	Indirect
$16 \times 16 \times 16$	0.919	Indirect	0.984	Indirect	1.002	Indirect	1.063	Indirect
$17 \times 17 \times 17$	0.968	Indirect	0.968	Indirect	1.050	Indirect	1.050	Indirect
$18 \times 18 \times 18$	0.927	Indirect	0.962	Indirect	1.008	Indirect	1.045	Indirect
$19 \times 19 \times 19$	0.965	Indirect	0.965	Indirect	1.046	Indirect	1.046	Indirect
$20 \times 20 \times 20$	0.919	Indirect	0.961	Indirect	1.002	Indirect	1.133	Indirect

[a] Values in eV.

As can be seen from Table 10, and for the (111) orientation of the B-site cation in NH_3ClPbI_3, and except for $7 \times 7 \times 7$ and $9 \times 9 \times 9$ k-point grids centered at Γ-point, the nature of the bandgap is calculated to be *direct*. For the $7 \times 7 \times 7$ and $9 \times 9 \times 9$ k-point meshes, the bandgap is found to be *indirect*. The nature of the bandgap is found to remain the same when the $n \times n \times n$ (n = 6–10) k-point meshes were not centered at Γ-point. However, an enhancement of the size of the $n \times n \times n$ k-point sampling (n = 13–20) with "Γ" replaced by "Monkhorst" in the KPOINT file has turned the bandgap of the system to be *direct*. A similar attribute is also noticeable for the bandgap data obtained for this system with the B-site cation along the (011) direction. However, in this case, all types of k-point grids centered at Γ-point have resulted the *character* of the bandgap to be *indirect*, and when "Γ" replaced by "Monkhorst", the bandgap could become *indirect* for $n \times n \times n$ k-point sampling (n = 6–10), and *direct* for the remaining dense meshes, revealing a computational artifact.

An analogous result was found for the NH_3FPbI_3 system. In this case, all types of k-point meshes tested could reflect the *character* of the bandgap to be *direct*. However, yet surprisingly, the dense k-point grid, $20 \times 20 \times 20$, centered at Γ-point has resulted in an *indirect* bandgap for the bulk material, demonstrating a computational artifact.

These results further suggest that one should be very careful and should perform a benchmark study in order to provide any definitive conclusion on the *character* of bandgap for any new material. It would always be advantageous if experimental

photoluminesence optical spectra for such new materials are at hand for comparison, which might greatly assist to validate the reliability of the theoretical method as well.

By contrast, and for NH_3IPbI_3 and NH_3BrPbI_3, there were no variation in the *character* of the bandgap regardless of the nature of the k-point grids, as well as the nature of the "Γ" or "Monkhorst". In both cases, an indirect bandgap is found for both the orientations of the B-side cation (cf. Tables 12 and 13).

Thus considering the persistently repeating results obtained from the high k-point grids centered at Γ, it can be concluded that the bandgap for the pseudocubic NH_3FPbI_3 is *direct* regardless of the orientation of the B-site cation. For the pseudocubic NH_3ClPbI_3, it is both *direct* and *indirect*, thereby dynamic. For the NH_3XPbI_3 (X = I, Br) systems, it is *indirect* with respect to the orientation of the B-site cation. The *direct* nature of the bandgap suggests possibility of radiative recombination, where an electron in the conduction band can annihilate with a hole in the valence band to release (emission) an excess energy as a photon. This is, however, not possible when bandgap of the material is *indirect*, such as that found for most of the other pseudocubic geometries of NH_3XPbY_3, as in this case the photons cannot carry crystal momentum, in which case, the law of conservation of crystal momentum might not be fulfilled. In this latter case, the involvement of the phonon makes this process much less likely to occur in a given span of time, which is why radiative recombination is far *slower* in indirect band gap materials than *direct* band gap ones. This is why light-emitting and laser diodes are almost always made of direct band gap materials, and not indirect band gap ones (like silicon). [128]

7.3.16 Prediction of bandgaps for the NH_3XPbI_3 series in the orthorhombic phase.

Figs. 11-12 illustrates the four relaxed geometries for the NH_3XPbI_3 series (X = F, Cl, Br, I), obtained with PBE/PAW in conjunction with the 10 × 8 × 10 k-point mesh centered at Γ. The lattice constants for each of these systems is consistent with what might be expected for an orthorhombic phase, that is, $a \neq b \neq c$, and $\alpha = \beta = \gamma = 90^o$. For instance, for NH_3ClPbI_3, a = 8.916 Å, b = 13.235 Å, c = 8.720 Å, and $\alpha = \beta = \gamma = 90.0^o$. For all cases, $a \approx c < b$, which is indicative of the *Pnma* space group.

Table 14: Predicted PBE/PAW bandgap (E_g) for the orthorhombic phase of the NH_3XPbI_3 (X = F, Cl, Br, I) systems.[a]

System	Bandgap (non-SOC)	Nature	Bandgap (SOC)	Nature	Difference[b]
NH_3FPbI_3	1.929	Direct	1.048	Direct	0.881
NH_3ClPbI_3	1.621	Direct	0.891	Direct	0.730
NH_3BrPbI_3	1.446	Direct	0.768	Direct	0.687
NH_3IPbI_3	1.364	Direct	0.673	Direct	0.691

[a] Values in eV

[b] Difference of bandgap between SOC and non-SOC

The bandgap, without incorporating the effect of SOC, is found to be the largest for NH_3FPbI_3 and the least for NH_3IPbI_3, Table 14. This ordering is same as that found for the corresponding systems in the pseudocubic phase (Table 9). In all cases, the *character* of the bandgap is to found be *direct*.

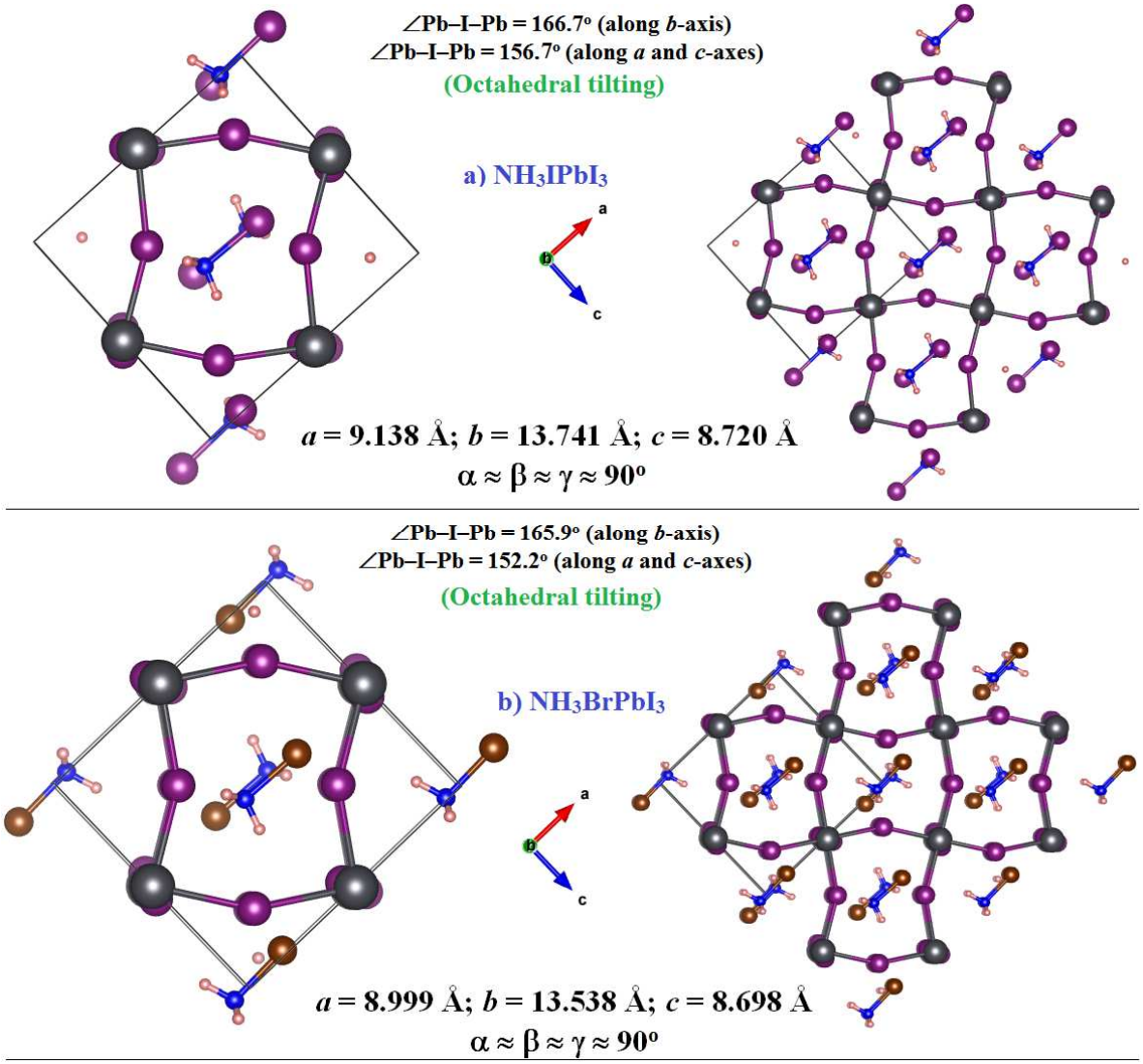

Fig. 11: Ball-and-stick models for the NH_3XPbI_3 (X = I, Br) series in the orthorhombic phase. Selected titling bond angles and lattice constants are shown for comparison. Nitrogen: blue, Iodine: purple, Bromine: dark-red, Lead: grey, Hydrogen: light-red.

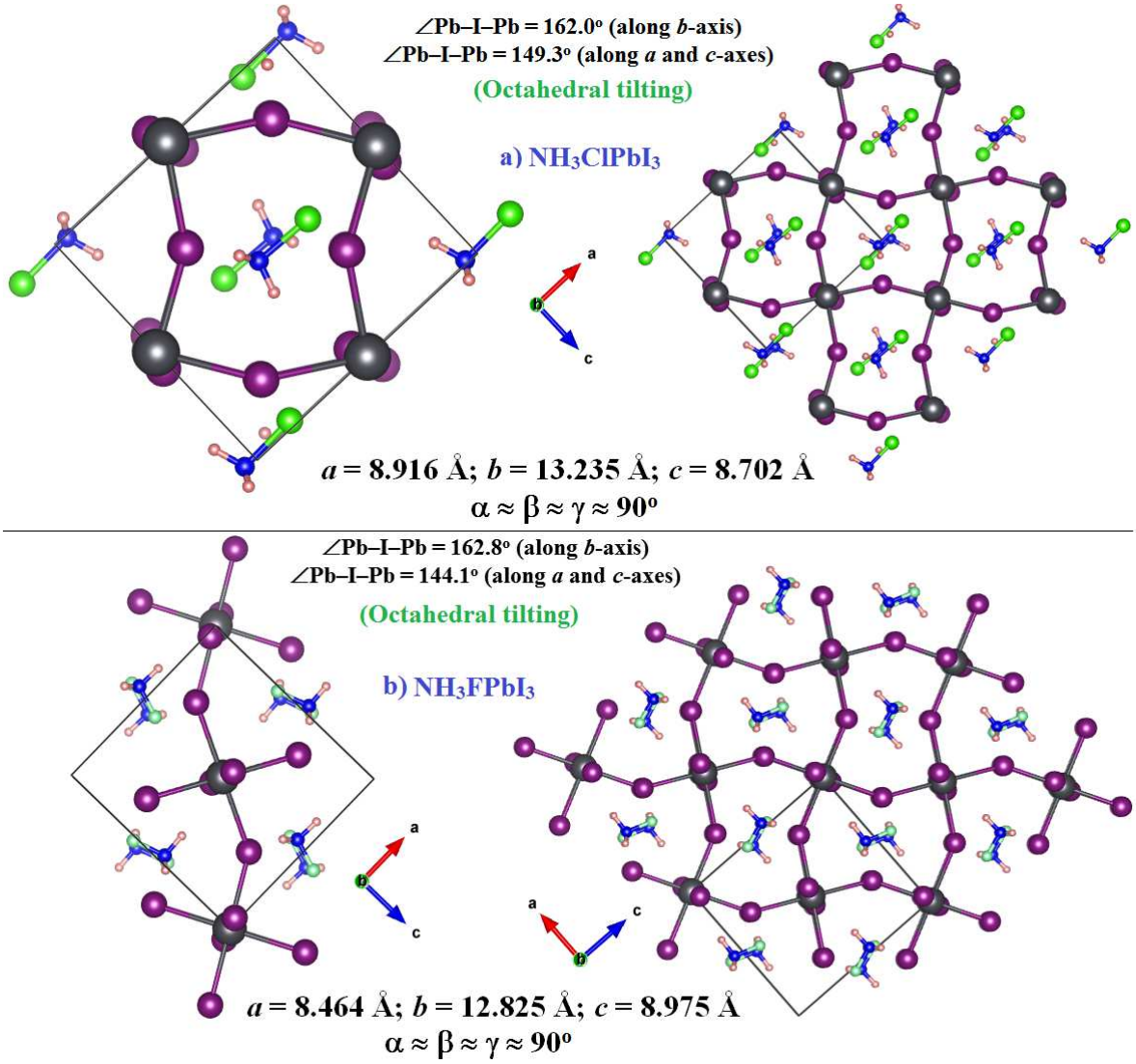

Fig. 12: Ball-and-stick models for the NH_3XPbI_3 (X = Cl, F) series in the orthorhombic phase. Selected titling bond angles and lattice constants are shown for comparison. Nitrogen: blue, Iodine: purple, Chlorine: green, Fluorine: deep-cyan, Lead: grey, Hydrogen: light-red.

7.3.17 Structural stabilities and lattice constants for the NH_3XPbY_3 series (X = Y = F, Cl, Br, I) in the orthorhombic phase

Fig. 13 compares the energy-minimized geometries and the lattice constants for the NH_3XPbY_3 (X = Y = F, Cl, Br, I) series. These each is orthorhombic, with *Pnma* space group. In all cases, the tilting of the PbY_6^{4-} octahedra is prominent, but the extent of this is the largest for the NH_3FPbY_3 system. This is minimally associated with the Pb–Y–Pb angle along the *b*-axis, and maximally along the *a*- and *c*-axes, similarly as found for the $CH_3NH_3PbI_3$ system (*vide supra*). In average, the extent of tilting is found to be in this order: $NH_3IPbY_3 < NH_3BrPbY_3 < NH_3ClPbY_3 < NH_3FPbY_3$. Interestingly, however, this preference of octahedral titling is found not to be along with the common belief that perovskites with highest tilting octahedra will be good for the generation of low bandgap materials, Table 15.[110-112] We have found that the bandgap for this series increases as the extent of octahedral tilting increases.

Table 15: PBE/PAW predicted bandgaps (E_g) for the orthorhombic phase of the NH_3XPbY_3 (X = Y = F, Cl, Br, I) systems.[a]

System	Bandgap (non-SOC)	Nature	Bandgap (SOC)	Nature	Difference [b]
NH_3FPbF_3	3.238	Direct	3.092	Direct	0.146
$NH_3ClPbCl_3$	1.913	Indirect	1.514	Direct	0.399
$NH_3BrPbBr_3$	1.508	Indirect	0.918	Direct	0.590
NH_3IPbI_3	1.364	Direct	0.673	Direct	0.691

[a] Values in eV

[b] Difference of bandgap between SOC and non-SOC

7.3.18 Geometrical strabilities and bandgaps of the NH_3XSnI_3 series (X = F, Cl, Br, I)

Figs. 14–17 illustrates the relaxed geometries of the tin analogues, the NH_3XSnI_3 series (X = F, Cl, Br, and I). These are all stable in the orthorhombic phase. The tilting of the SnI_6^{4-} octahedra is found to be less pronounced compared to that found for the corresponding NH_3XPbI_3 analogues discussed in the previous sections. For instance, the ∠Sn–Cl–Sn is close to 164.3° (along *b*-axis) and 151.9° (along *b*- and *c*-axes) for NH_3ClSnI_3 (Fig. 16), whereas the ∠Pb–Cl–Pb is close to 162.0° (along *b*-axis) and 149.3° (along *b*- and *c*-axes) (Fig. 12a). Similarly, the ∠Sn–I–Sn is close to 168.0° (along *b*-axis) and 160.8° (along *b*- and *c*-axes) for NH_3ISnI_3 (Fig. 14), whereas the ∠Pb–I–Pb is close to 166.7° (along *b*-axis) and 156.7° (along *b*- and *c*-axes) (Fig. 11a). The only discrepancy is noted for the NH_3BrSnI_3 geometry, in which, the tilting is pronounced in all the three directions. For instance, the ∠Sn–I–Sn are close to 149.7° (along *a*-axis), 161.8° (along *b*-axis) and 155.9° (along *c*-axis), Fig. 15.

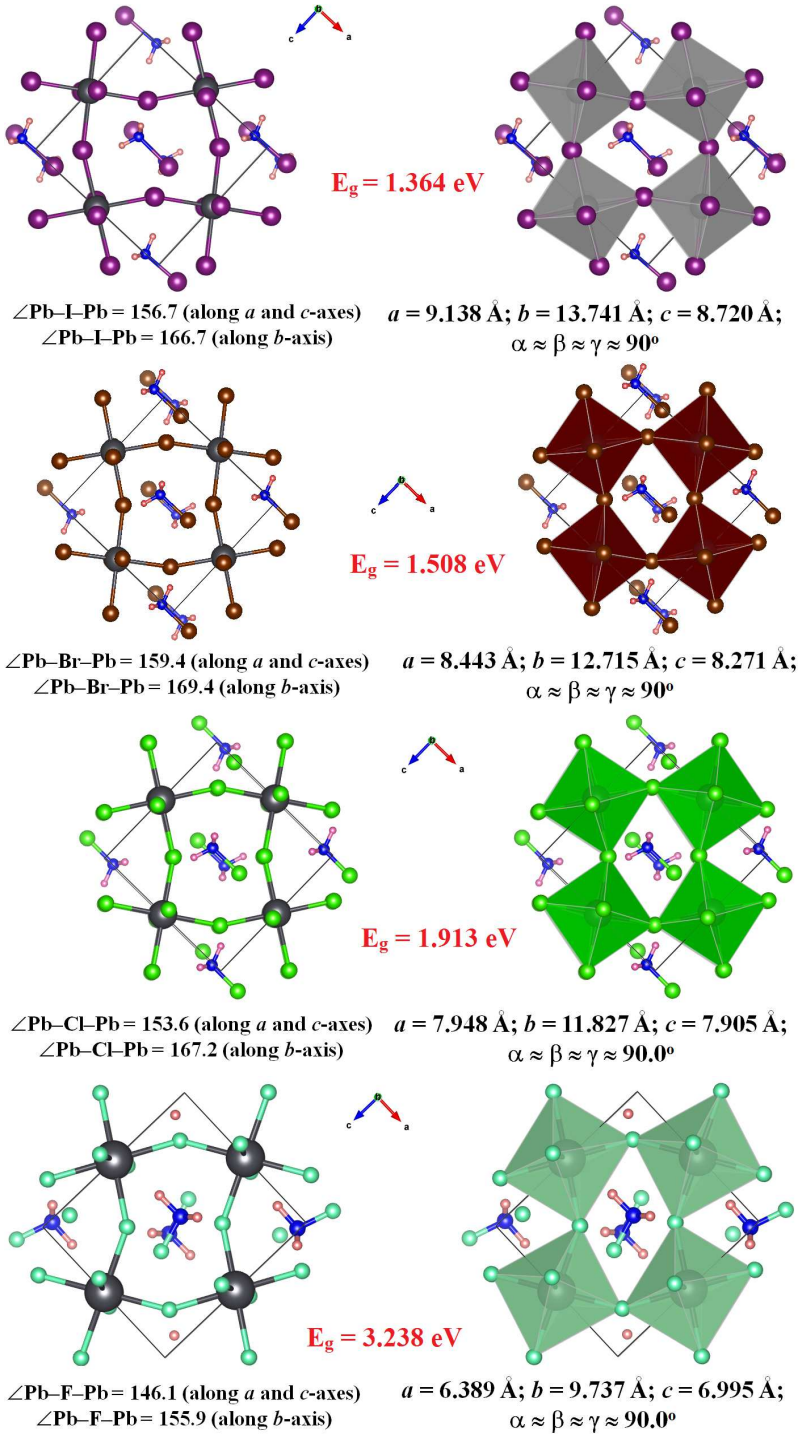

Fig. 13: Comparison of the relaxed geometries and lattice constants for the NH_3XPbY_3 (X = Y = F, Cl, Br, I) series. Both ball-and-stick and polyhedral models are illustrated for clarity. Selected titling bond angles, and bandgaps (no-SOC) are listed. Nitrogen: blue, Iodine: purple, Bromine: dark-red, Chlorine: green, Fluorine: deep-cyan, Lead: grey, Hydrogen: light-red.

While other two phases (tetragonal and pseudocubic) of the tin based NH_3XSnI_3 systems are yet to be exploited, we confirm that the pseudocubic geometries for the aforementioned series is also stable. Fig. 18 clarifies it in more detail, and without any specific bias the k-point mesh used for geometry relaxation and bandgap calculation was 12 × 12 × 12. Apparently, all these are stable theoretically, and are low bandgap materials, either *direct* or *indirect*, determined by the nature of the B, M and Y site ions in BMY_3.

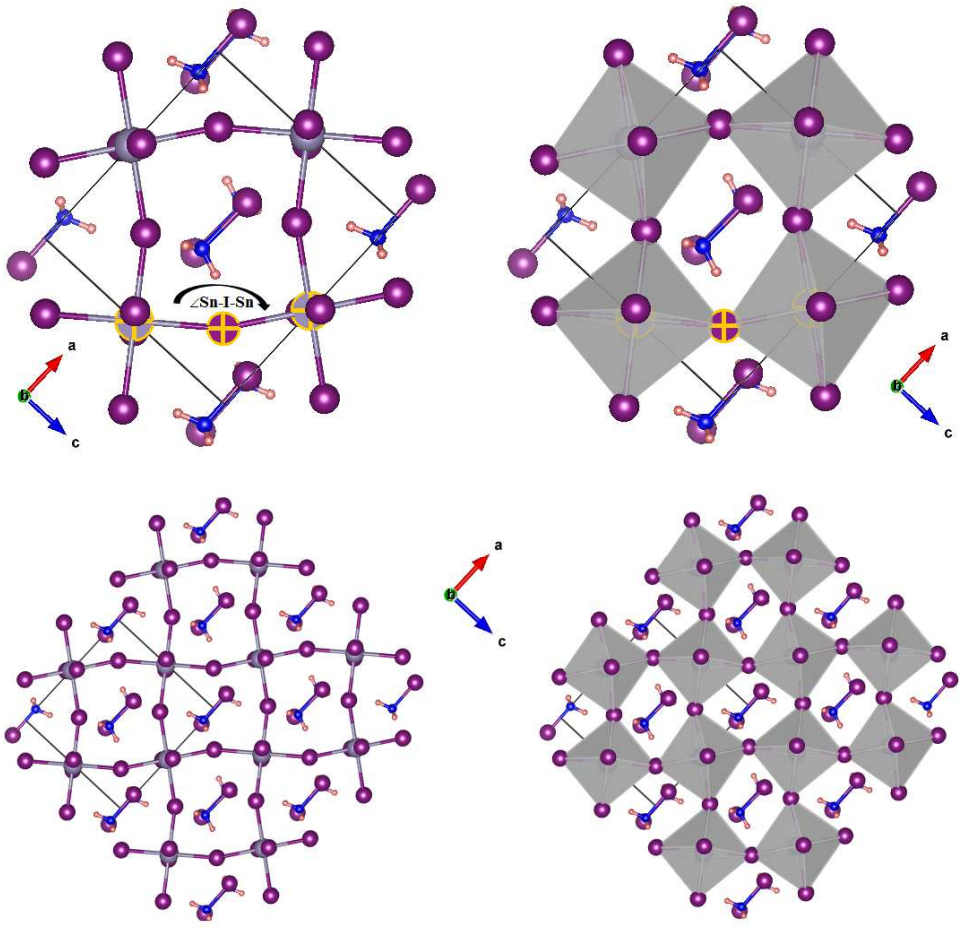

Fig. 14: Various views for the relaxed geometry of the NH_3ISnI_3 bulk, and its 2×2×2 supercell geometries in the orthorhombic phase. The nature of the tilting angles associated with the SnI_6^{4-} octahedra and the lattice constants are listed at the bottom.

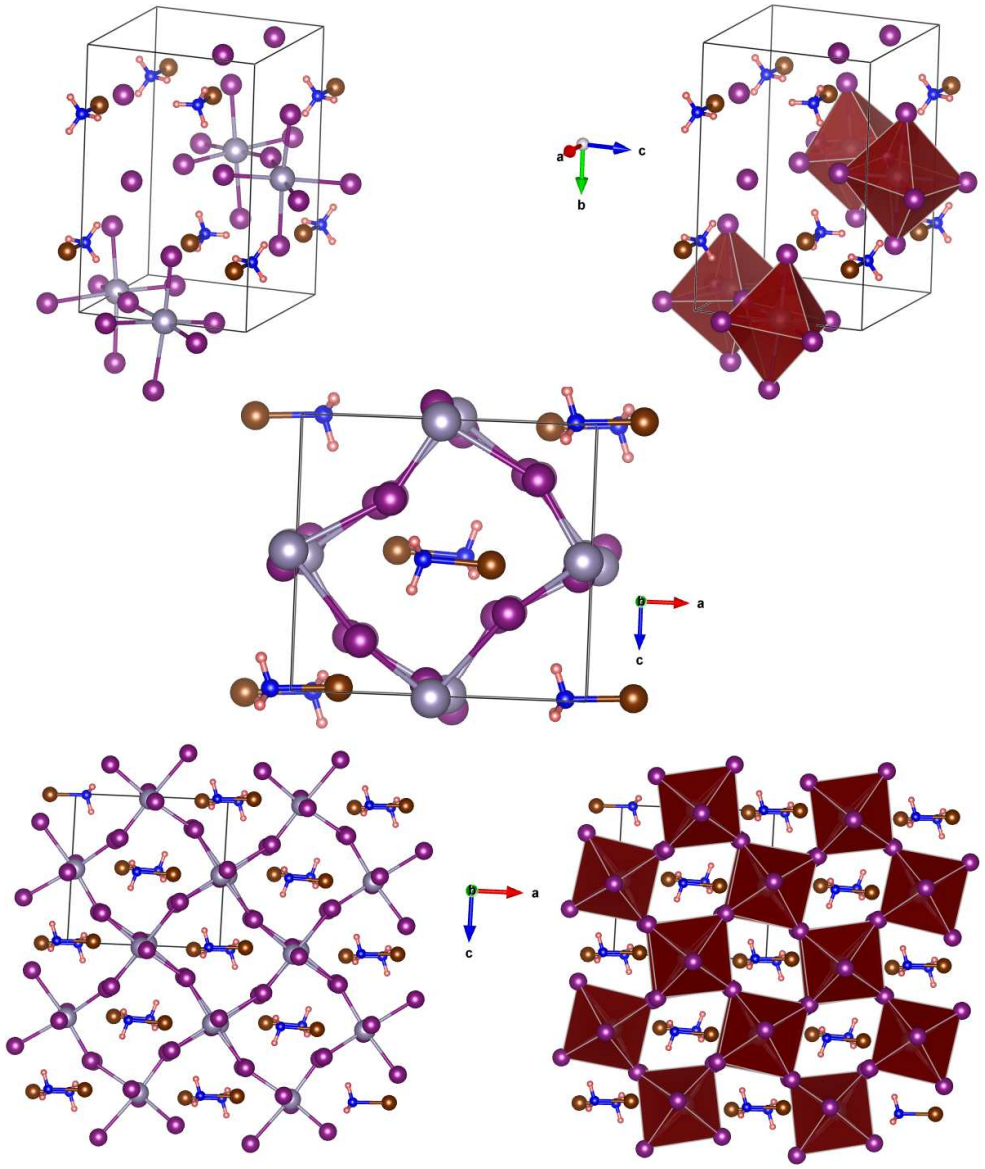

Fig. 15: Various views for the relaxed geometry of the NH_3BrSnI_3 bulk, and its 2×2×2 supercell geometries in the orthorhombic phase. The nature of the tilting angles associated with the SnI_6^{4-} octahedra and the lattice constants are listed at the bottom.

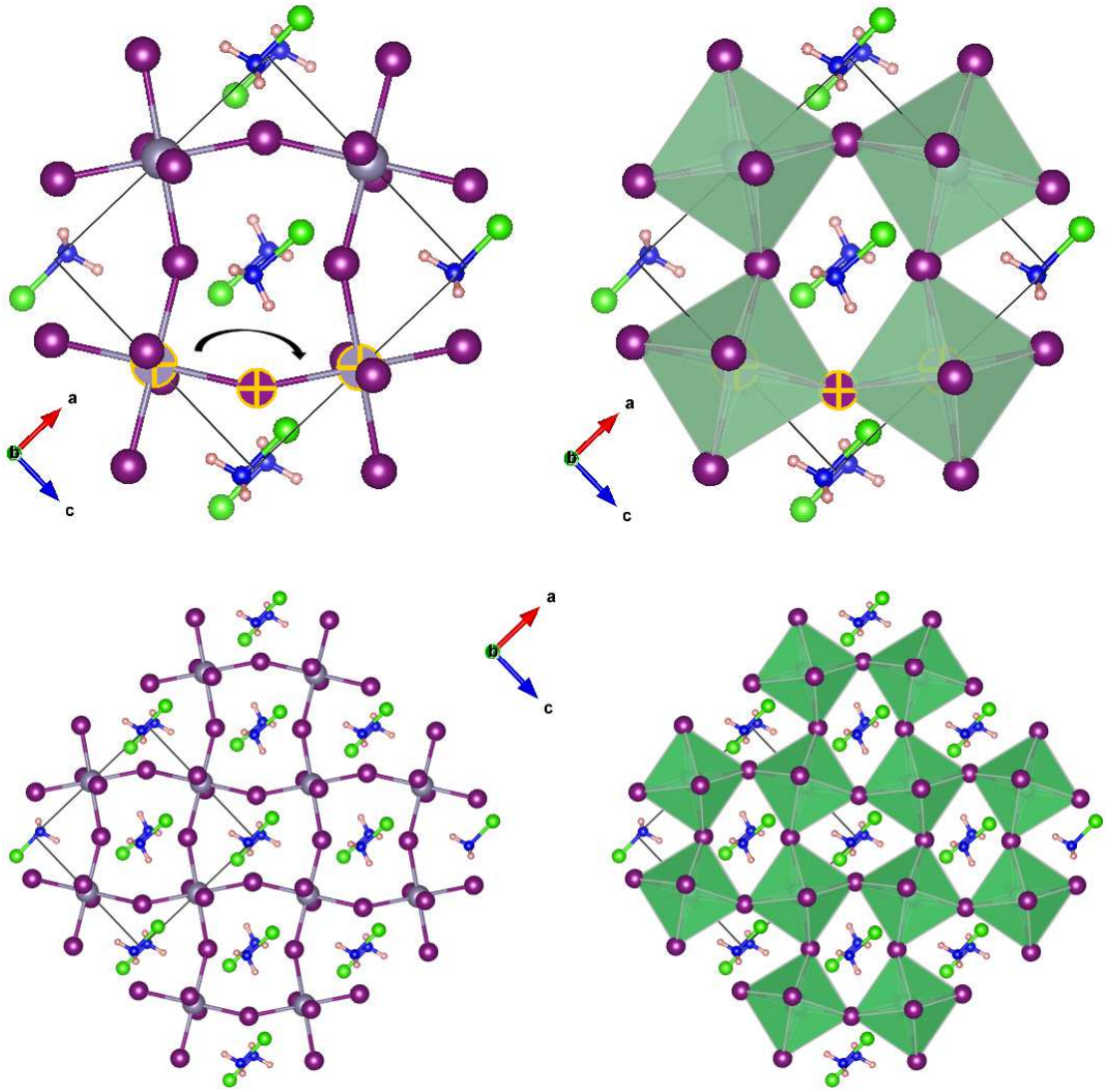

Octahedral Tilting

∠Sn–Cl–Sn = 151.9° (along *a* and *c*-axes)
∠Sn–Cl–Sn = 164.3° (along *b*-axis)

Lattice Constants

$a = 8.786$ Å; $b = 13.054$ Å; $c = 8.618$ Å;
$\alpha \approx \beta \approx \gamma \approx 90.0°$

Fig. 16: Various views for the relaxed geometry of the NH_3ClSnI_3 bulk, and its 2×2×2 supercell geometries in the orthorhombic phase. The nature of the tilting angles associated with the SnI_6^{4-} octahedra and the lattice constants are listed at the bottom.

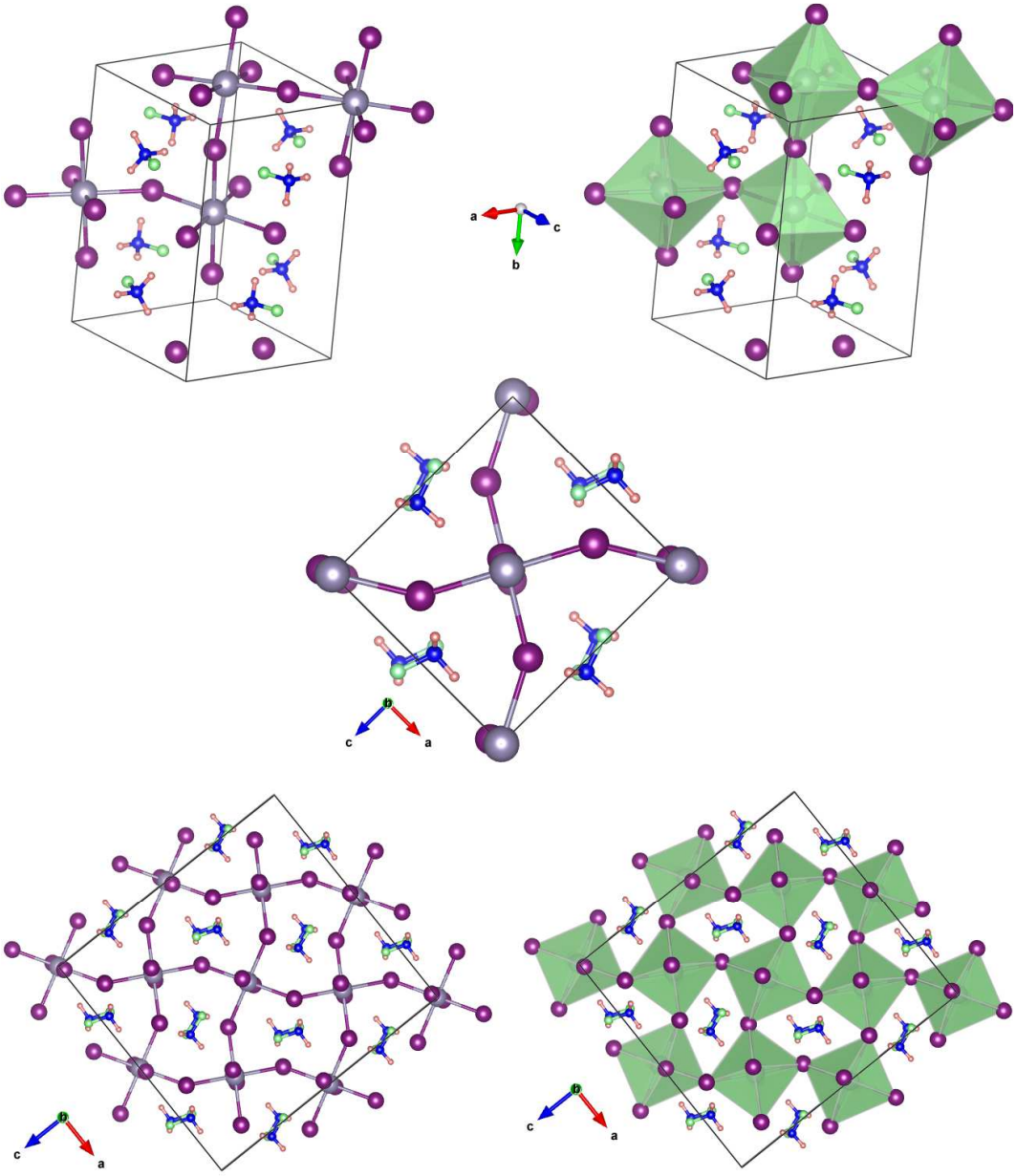

Fig. 17: Various views for the relaxed geometry of the NH_3FSnI_3 bulk, and its 2×2×2 supercell geometries in the orthorhombic phase. The nature of the tilting angles associated with the SnI_6^{4-} octahedra and the lattice constants are listed at the bottom.

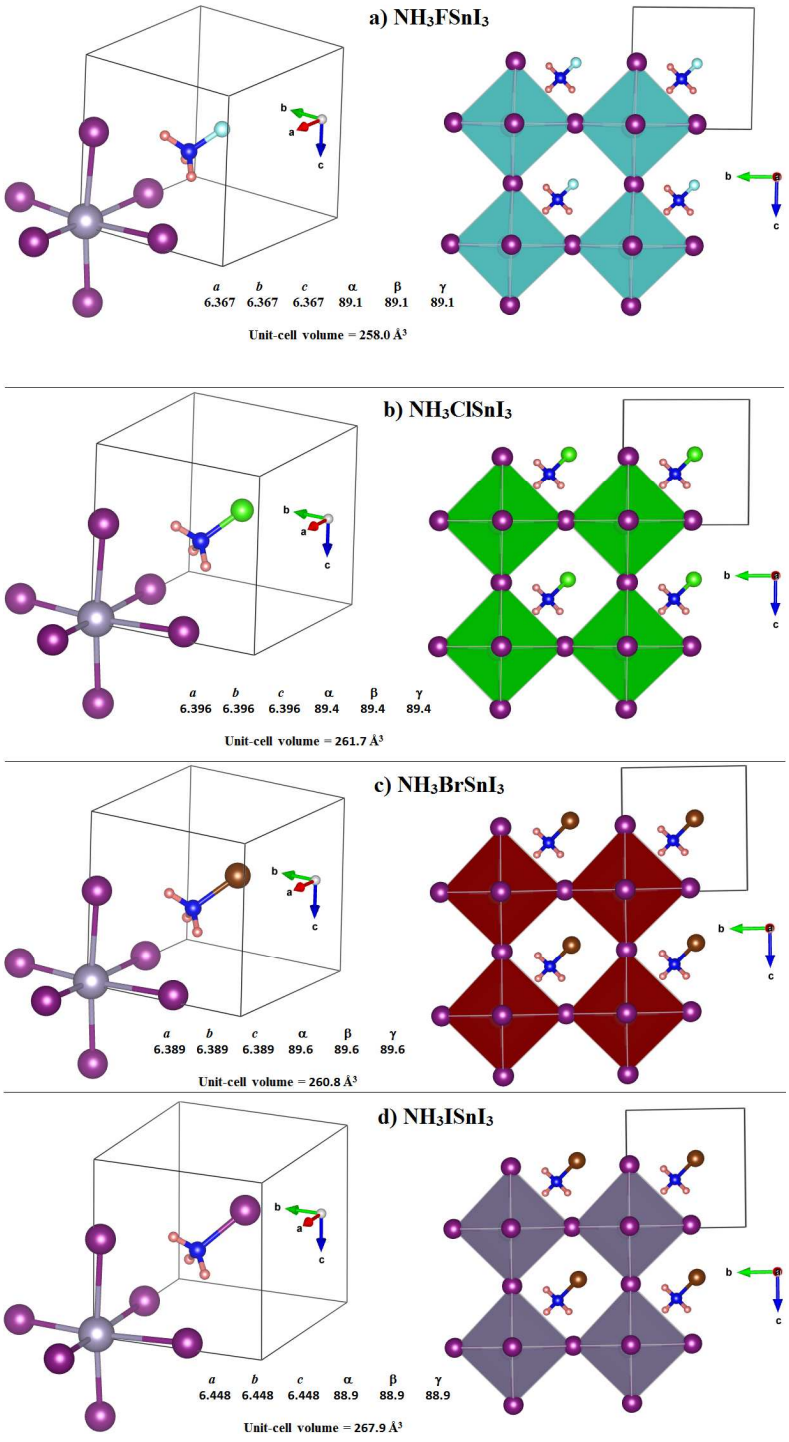

Fig. 18: The relaxed geometries of the NH_3XSnI_3 (X = F, Cl, Br, I) bulks in the cubic phase, with the B-site cation along the (111) orientation. The 2×2×2 supercell geometries are shown for clarity. The lattice constants are listed for comparion.

Table 16: PBE/PAW predicted bandgaps (E_g) for the orthorhombic phase of the NH_3XSnI_3 (X = F, Cl, Br, I) series.[a]

System	Bandgap (non-SOC)	Nature	Bandgap (SOC)	Nature	Difference
NH_3FSnI_3	0.917	Direct	0.667	Direct	0.250
NH_3ClSnI_3	0.660	Direct	0.486	Direct	0.174
NH_3BrSnI_3	1.186	Indirect	1.092	Indirect	0.094
NH_3ISnI_3	0.525	Direct	0.348	Direct	0.177

[a] Values in eV

Table 17: Predicted PBE/PAW bandgap (E_g) for the pseudocubic phase of the NH_3XSnI_3 (X = F, Cl, Br, I) series.[a,b]

System	Bandgap (non-SOC)	Nature	Bandgap (SOC)	Nature	Difference [c]
NH_3FSnI_3	0.652	Direct	0.419	Direct	0.235
NH_3ClSnI_3	0.662	Direct	0.434	Direct	0.228
NH_3BrSnI_3	0.203	Indirect	0.022	Indirect	0.181
NH_3ISnI_3	0.207	Indirect	0.182	Indirect	0.025

[a] Values in eV

[b] Γ-centered $12 \times 12 \times 12$ k-point mesh was used both for structure relaxation and bandgap calculation.

[c] Difference of bandgap between SOC and non-SOC

7.3.19 Relativistic effects: Spin-orbit coupling

Christensen and Seraphin published their seminal paper on relativistic effects in the band structure of gold several decades ago, [129] although the significance of spin-orbit effects was recognized in 1965 by Anderson *et al.*[130] and Loucks[131] during their exploration of properties in solid lead. Since then many of the solid state calculations incorporate scalar relativistic effects to evaluate solid state band structure properties of compounds containing heavy elements. These effects are responsible for the valence s contraction (direct relativistic effect) and the expansion of the d and f shells (indirect relativistic effect) through the increased nuclear screening by the direct relativistic effects.[132-133] For heavy elements spin-orbit coupling (SOC) effects need to be considered since these increase roughly with Z^2, where Z is the nuclear charge.[134] However, from a most recent study of Volonakis *et al.*,[74] it seems that the spin-orbit

effects are unimportant for first and second row transition elements, as well as for third and fourth row main group elements. For instance, these authors have showed that spin−orbit effects to be unimportant for In/Ag double perovskites, [74] even though it is not so in $MAPbI_3$. [135]

A relativistically corrected Hamiltonian $\hat{H}$ is generally takes the following form:

$$\hat{H} = \hat{H}_0 + \hat{H}_{SO} \quad \text{..... (5)}$$

In Eqn (5), the first term $\hat{H}_0[\hat{H}_0 = \frac{\hat{P}^2}{2m_e} + V(r)]$ on the RHS is the usual zeroth order nonrelativistic Hamiltonian of Kohn−Sham noninteracting system and the second term is the relativistic effect or spin orbital coupling (SOC), which is usually treated as a perturbation term in DFT calculations. The Eqn for $\hat{H}_{SO}$ is given by:

$$H_{SO} = \frac{\hbar}{4m_0^2c^2}\vec{\sigma}.[\vec{p}\times\vec{\nabla}V(r)] \quad \text{..... (6)}$$

In this Eqn, $\hbar$ is the Plank's constant, m_0 is the mass of free electron, c is the speed of light, σ is the Pauli spin operator, p is the momentum operator, and $\nabla V(r)$ is the gradient of the scalar Coulomb potential between a valence electron and nucleus. Since *V(r)* varies quickly near the nucleus of an atom, its gradient would change rapidly with *r* as well. It is thus expected that the core region of an atom plays the significant role in SOC correction, which would be prominent for heavy atoms such as lead.

In solids, electrons experience electric fields from atoms in the lattice. There are two origins for local fields in a crystal. The first one deals with bulk inversion asymmetry (BIA), which can be explained by the Dresselhaus spin-orbit interaction, and the second one deals with structural inversion asymmetry (SIA), which can be explained by the Rashba spin-orbit interaction. [136] The Rashba-Dresselhaus effect is a consequence of SOC when combined with a local electric field, leading to the k-dependent splitting of the dispersion curves (energy bands) in the k-space. The underlying details of these features have been discussed in recent studies.[136-137]

While the relativistic effect is not an integral part of the local density approximation (LDA) or generalized gradient approximation (GGA) based density functionals, it is quite apparent that such functionals provide a reasonable estimate for the bandgaps for materials of different varieties, [118-119] including those involve heavy metals. [74, 137] The PBE functional employed in this study is one among many of them that has been vastly used for estimating the electronic structure and properties of semiconductor materials.[138-140] It has readily been understood that PBE underestimates the bandgaps of $CH_3NH_3PbX_3$ (X = Cl, Br, I) compounds. [137,140] Inclusion of SOC has a negative effect on

the bandgaps, causing a further decrease of its magnitude. [53, 135, 137,140] Even so, there have been many recent studies, which have accounted for such routine calculations at the PBE level to show that SOC has some pronounced effect on the bandgap. [53,137,140] By contrast, the many-body perturbation GW method (single particle Green's function G and the screened Coulomb interaction W) significantly overestimates the band gaps of the any system.[141] Inclusion of the SOC correction to GW results in the bandgaps that are in good agreement with experimental values.[142] In this sense, it has been believed that the GW + SOC is relatively more accurate than PBE + SOC for the electronic band dispersions. Also, the HSE06 functional predicts band gaps that can be comparable with experimental ones, [143] and the HSE06 + SOC approach slightly underestimates the bandgaps. [53] Use of this functional for modeling is as expensive as that of GW + SOC.

It is also not new to scientists that for $CH_3NH_3PbI_3$ the conduction band comprises mainly the Pb 6p character, whereas the valence band comprises I 5p + Pb 6s. For the $CH_3NH_3PbBr_3$ perovskite the conduction band comprises mainly the Pb 6p-like states, whereas the valence band comprises Br 4p + Pb 6s. Similarly, for $CH_3NH_3PbCl_3$, the conduction band comprises mainly the Pb 6p character, whereas the valence band comprises Cl 3p + Pb 6s. These built the band structure, as well as the density of states (DOS) spectra.

Fig. 19 illustrates the band structure of the $CH_3NH_3PbI_3$ system, with the organic cation aligned along the (111) and (011) directions. In realistic situation, the four high symmetry k-points are those of the cubic structure with Pm3m space group, which are Γ, R, M and X. While the static picture of the $CH_3NH_3PbX_3$ systems formally has *P*1 symmetry, we have exploited the band structure of the $CH_3NH_3PbI_3$ around the four high symmetry k-points. As expected, a direct bandgap is predicted at a high symmetry k-point, the so-called R point. This result is in decent agreement with those of Liu *et al.*, [140] in which, the bandgap reported by these authors for the $CH_3NH_3PbI_3$ bulk with PBE was 1.58 eV without SOC, which is close to our corresponding value of 1.581 eV.

According to Whalley et al., [137] SOC is not expected to have a large impact on the structural properties of the Pb-based compounds as the (empty) conduction band is mainly affected. By the Hellmann-Feyman theorem, the force on atoms depends only on the electron density, which is provided by the occupied orbitals. It is already known from earlier studies that the first-order effect of SOC is the downshift of the bandgap of the material, which can be as large as 1 eV.[144] This is not unexpected since the three 6p degenerate orbitals ($6p_x$, $6p_y$ and $6p_z$) of the Pb^{2+} ion are split, causing apart in energy. For $CH_3NH_3PbI_3$, the effect of SOC on the bandgap is as large as 1.0 and 1.114 eV for $CH_3NH_3PbI_3$ for the (011) and (111) orientations, respectively. Liu *et al.* have reported a difference value of 1.13 eV between SOC and non-SOC bandgaps for $CH_3NH_3PbI_3$. [144] Nevertheless, for both orientations of the organic cation, Rashba-Dresselhaus splitting of

the conduction band minimum is evident in the SOC incorporated band structures, Fig. 19.

Table 18: PBE/PAW predicted bandgap (E_g) for the pseudocubic phase of the $CH_3NH_3PbI_3$ systems.[a,b]

	(011) orientation				(111) orientation			
	Bandgap (non-SOC)	Nature	Bandgap (SOC)	Nature	Bandgap (non-SOC)	Nature	Bandgap (SOC)	Nature
$8\times8\times8$	1.657	Direct	0.657	Direct	1.581	Direct	0.467	Direct
$9\times9\times9$	1.811	Direct	0.817	Direct	1.844	Direct	0.869	Direct
$10\times10\times10$	1.657	Direct	0.657	Direct	1.581	Direct	0.468	Direct
$11\times11\times11$	1.755	Indirect	0.731	Indirect	1.754	Direct	0.752	Direct
$12\times12\times12$	1.657	Direct	0.657	Direct	1.581	Direct	0.468	Direct
$13\times13\times13$	1.724	Indirect	0.683	Direct	1.701	Direct	0.672	Direct
$14\times14\times14$	1.657	Direct	0.657	Direct	1.581	Direct	0.468	Direct
$15\times15\times15$	1.706	Indirect	0.656	Direct	1.669	Direct	0.618	Direct

[a] Values in eV

[b] Liu *et al*. have reported without and with SOC incorportated bandgaps of 1.58 and 0.45 eV for $CH_3NH_3PbI_3$.[140]

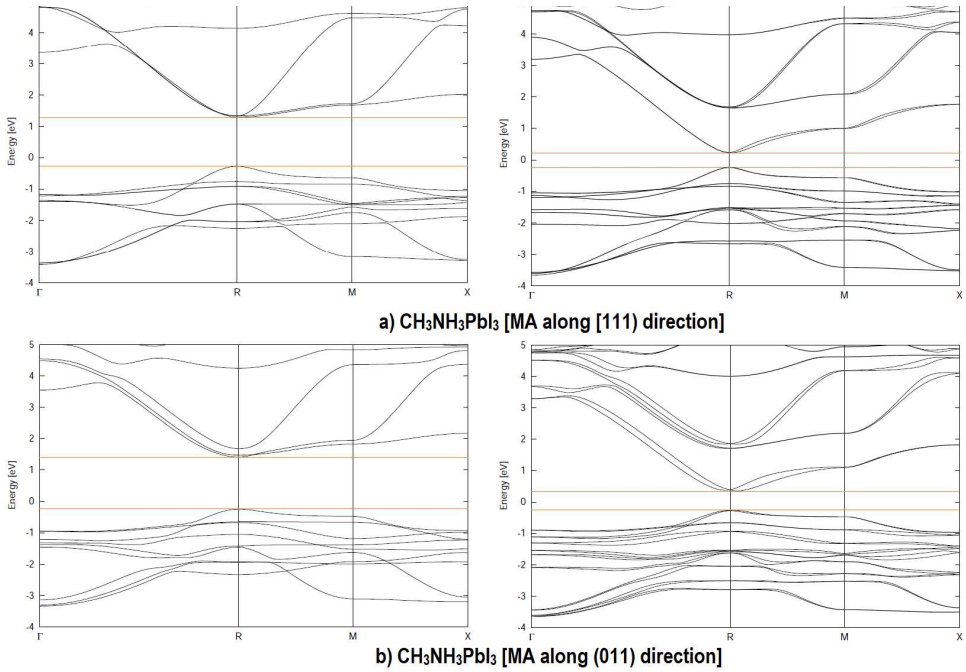

Fig. 19: Comparison of with and without SOC incorporated band structures for the $CH_3NH_3PbI_3$ in the pseudocubic phase, with the B-site cation aligned along the (111) and (011) directions. Rashba-Dresselhaus splitting of the conduction band minimum is evident in the SOC incorporated band structures. The labeling of the special k-points points are those of the cubic perovskite structure with $Pm\bar{3}m$ space group, retrieved from bilbao crystallographic server.[149] The $8\times8\times8$ k-point mesh centered at Γ was used both for geometry relaxation and band structre calculations.

Tables 14 and 15 summarize the bandgaps for orthorhombic NH_3XPbY_3 (X = F, Cl, Br, I) and NH_3XPbY_3 (X = Y = F, Cl, Br, I) without and with SOC. As expected, we did indeed see a significant downshift of the bandgap after incorporating SOC, which could be as large as 1 eV. For NH_3FPbF_3, however, we could see an abnormal behavior. In fact, while this system contains the heavy atom Pb, it does not show any such pronounced downshift of the bandgap. For instance, the bandgap for the system without SOC is ca. 3.238 eV, whereas that with SOC is 3.092 eV (Table 15), showing a marginal effect of SOC on the bandgap when the X- and Y-site ions are both fluorine. Nevertheless, upon passing the NH_3XPbY_3 (X = Y = F, Cl, Br, I) series from F through Cl to Br to I, the trend in the reduction of the bandgap is as follows: F < Cl < Br < I (Table 15).

Table 19: PBE/PAW predicted bandgap (E_g) for the pseudocubic phase of the NH_3XPbI_3 systems.[a]

System	Bandgap (non-SOC)	Nature	Bandgap (SOC)	Nature	Bandgap (non-SOC)	Nature	Bandgap (SOC)	Nature
	(111) orientation				(011) orientation			
NH_3FPbI_3	1.618	Direct	0.612	Direct	1.785	Direct	0.755	Indirect
NH_3ClPbI_3	1.598	Direct	0.556	Direct	1.278	Indirect	0.641	Direct
NH_3BrPbI_3	1.002	Indirect	0.493	Direct	1.410	Indirect	0.739	Indirect
NH_3IPbI_3	0.919	Indirect	0.505	Direct	1.604	Indirect	1.038	Indirect

[a] Values in eV

[a] Γ centered $8 \times 8 \times 8$ and $12 \times 12 \times 12$ k-point meshes were used for geometry relaxation and band structure calculations, respectively. SOC single points were carried out with Γ centered $12 \times 12 \times 12$ k-point mesh.

A similar result is also obtained for the pseudocubic geometries of the NH_3XPbY_3 (X = Y = F, Cl, Br, I) compounds. As can be see from Table 19, the reduction of the bandgap is as large as 1.006, 1.042, 0.509, and 0.414 eV for NH_3FPbI_3, NH_3ClPbI_3, NH_3BrPbI_3 and NH_3IPbI_3, respectively, when the orientation of the B-site cation is along (111). However, when the orientation of the cation is constrained along the (011) direction, the reduction of the bandgaps became 1.030, 0.637, 0.671 and 0.566 eV for the corresponding geometries, respectively. These results unequivocally demonstrate that the influence of SOC on bandgap is not systematic, meaning that it is not found to be the largest for the heaviest member and the smallest for the lightest member of the series. For instance, while the NH_3IPbI_3 system is found to be the heaviest member of the series comprising heavy elements such as I and Pb, yet the effect of SOC is found to be the least of 0.414 and 0.566 eV for the (111) and (011) orientations of the B-site cation in $BPbI_3$. It is also notable from the data of Table 19 that for both the orientations of the B-site cation, the magnitude of the reduction of the bandgap due to SOC is the largest when the B-site cation is NH_3F^+, and the least when it is NH_3I^+. These results further suggest that SOC

corrected bandgaps do controlled not only by the orientation of the B-site ion inside the perovskite cage, but also by the size of the halogen in NH_3X^+. The same order of preference in the decrease of the bandgap due to SOC is notable from data presented in Table 14 for the orthorhombic geometry of the NH_3XPbY_3 (X = Y = F, Cl, Br, I) systems.

From Tables 16 and 17, it is notable that the pronounced reduction of bandgap due to SOC is not observed for the NH_3XSnY_3 compounds both in the orthorhombic and cubic phases. The magnitude of the reduction in the bandgap is as large as 0.25 eV, which is associated with the lightest member (NH_3FSnI_3) of the series, but not with the heaviest one (NH_3ISnI_3).

Another striking feature of Table 19 is that for the (111) orientation of the B-site cation the bandgaps for NH_3XPbI_3 (X = F, Cl) were found as direct, whereas those for the NH_3FPbI_3 (X = Br, I) systems were indirect. Incorporating SOC, the bandgaps for the latter two systems were found to be direct. For the (011) orientation, on the other hand, the bandgap for NH_3FPbI_3 was calculated to be direct, whereas those for the remaining NH_3XPbI_3 (X = Cl, Br, I) systems were found to be indirect. Inclusion of SOC has turn the character of the bandgap from direct to indirect for NH_3FPbI_3, and indirect to direct for NH_3ClPbI_3, while those for the remaining two compounds, NH_3XPbI_3 (X = Br, I), remain the same with and without SOC. An identical result is obtained for the NH_3BrSnI_3 system in which the SOC has driven the bandgap of this material from indirect to direct. In general, without SOC, a doubly spin-degenerate band with a single maximum is expected, both for VBM and CBM. Including the effects of SOC and inversion-symmetry breaking, these each splits up into two spin-split bands shifted with respect to each other in k-space by k_0. This is the so-called Rashba splitting, and the strength of SOC is quantified by the Rashba parameter α,[148] where $\alpha = 2E_0/k_0$ (E_0 is the minimum depth at the central high symmetry point in k-space). The transitions from indirect to direct and *vice-versa* noted as above could be the many body effect of the SOC as a consequence of Rashba splitting of the conduction band in the k-space since the splitting of the VBM is very marginal and can be neglected since the effect is somehow indistinguishable, see Figs. 19 (for $CH_3NH_3PbI_3$) and Figs. 23-24 (for NH_3XPbI_3 (X = F, Cl, Br, I)).

Discussions analogous to the above have also been reported elsewhere. For instance, Azarhoosh *et al.*[145] and Wang *et al.*[145] have recently showed theoretically that Rashba splitting of the conduction band is also evident of $MAPbI_3$, leading to a slightly indirect transition 50 to 75 meV below the direct bandgap. This has been attributed to the strong effect of SOC in the MAPI crystal, and since the spin-splitting scales approximately with Z^2, the valence band is less affected than the conduction band.[145] On the other hand, the experimental results of Ke *et al.* have showed that the existence of the transition of direct to indirect band gap in $CH_3NH_3PbI_3$ film is induced by changing organic content CH_3NH_3I precursor molecule.[147]

7.3.20 Comparison of band structures for the NH_3XPbI_3 (X = F, Cl, Br, I) series in the orthorhombic phase

Detailed electronic band structures of the NH_3XPbY_3 series in the orthorhombic phase are illustrated in Figs. 20 and 21 for (X = F, Cl) and (X = Br, I), respectively. For all cases, and without SOC, the bandgap is found to be direct at Γ-point. While using the term direct, one might refer to a vertical forward transition following the Franck–Condon principle ($\Delta k = 0$). A transition in the backward direction is equally allowed, leading generally to a fast radiative recombination (–hν) of photogenerated electrons (e^-) and holes (h^+) belonging to the CB and VB, respectively.

With SOC, and for all the four systems above, the magnitude of the bandgap has decreased to some extent. Even so, the character of the bandgap remains the same, meaning it is direct at the high-symmetry Γ-point. This result may indicate that these systems are ideal for applications in thin film photovoltaics.

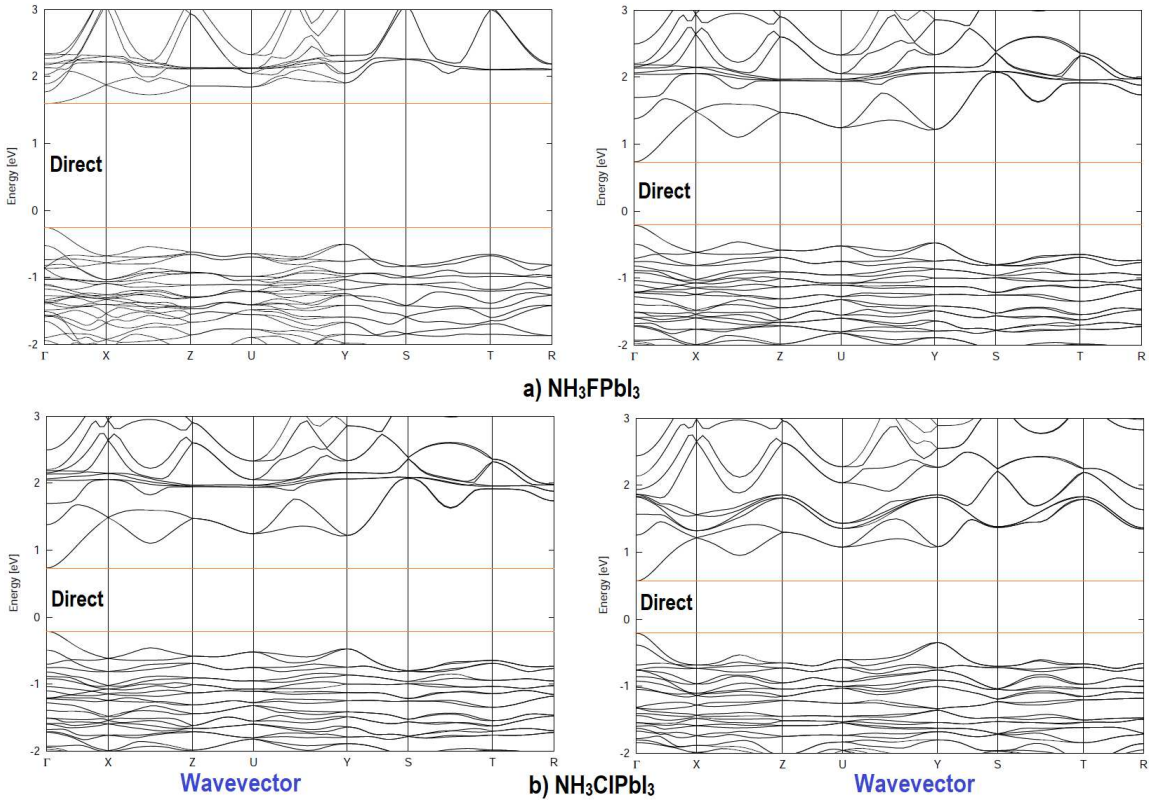

Fig. 20: Comparison of with and without SOC incorporated electronic band structures for the NH_3XPbI_3 (X = F, Cl) series in the orthorhombic phase. The labeling of the special points are those of the orthorhombic perovskite structure with *Pnma* space group, retrieved from bilbao crystallographic server.[149]

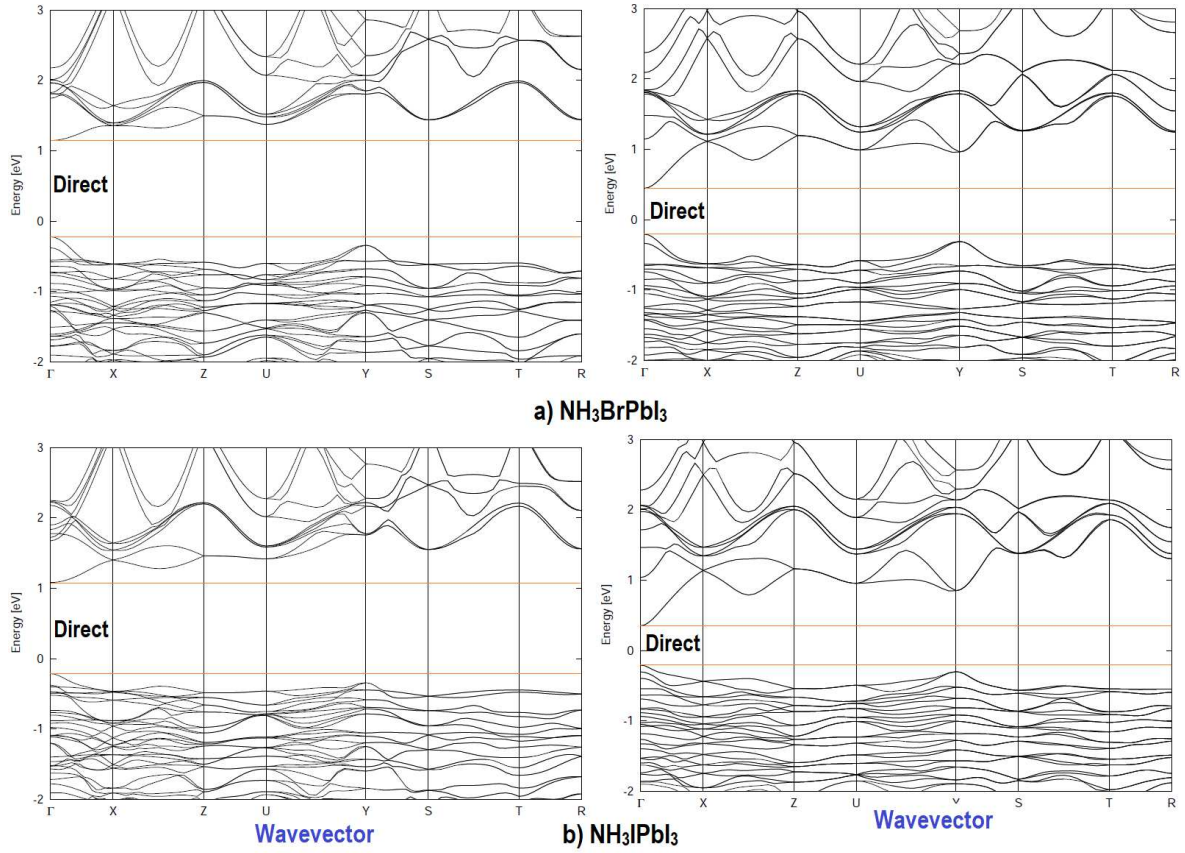

Fig. 21: Comparison of with and without SOC incorporated band structures for the NH_3XPbI_3 (X = Br, I) series in the orthorhombic phase. The labeling of the special points are those of the orthorhombic perovskite structure with *Pnma* space group, retrieved from bilbao crystallographic server.[149]

As already mentioned above, the bandgaps for $NH_3ClPbCl_3$ and $NH_3BrPbBr_3$ are calculated to be indirect. This is evident of Fig. 22, in which, the VBM is located at the hight symmetry Γ point and the CBM at the nearby high symmetry k-point called the X-point. However, incorporating SOC, both the orthorhombic geometries of NH_3XPbY_3 (X = Y = Cl, Br) have band extrema at the Γ point, revealing a transition of the character of the bandgap from indirect to direct.

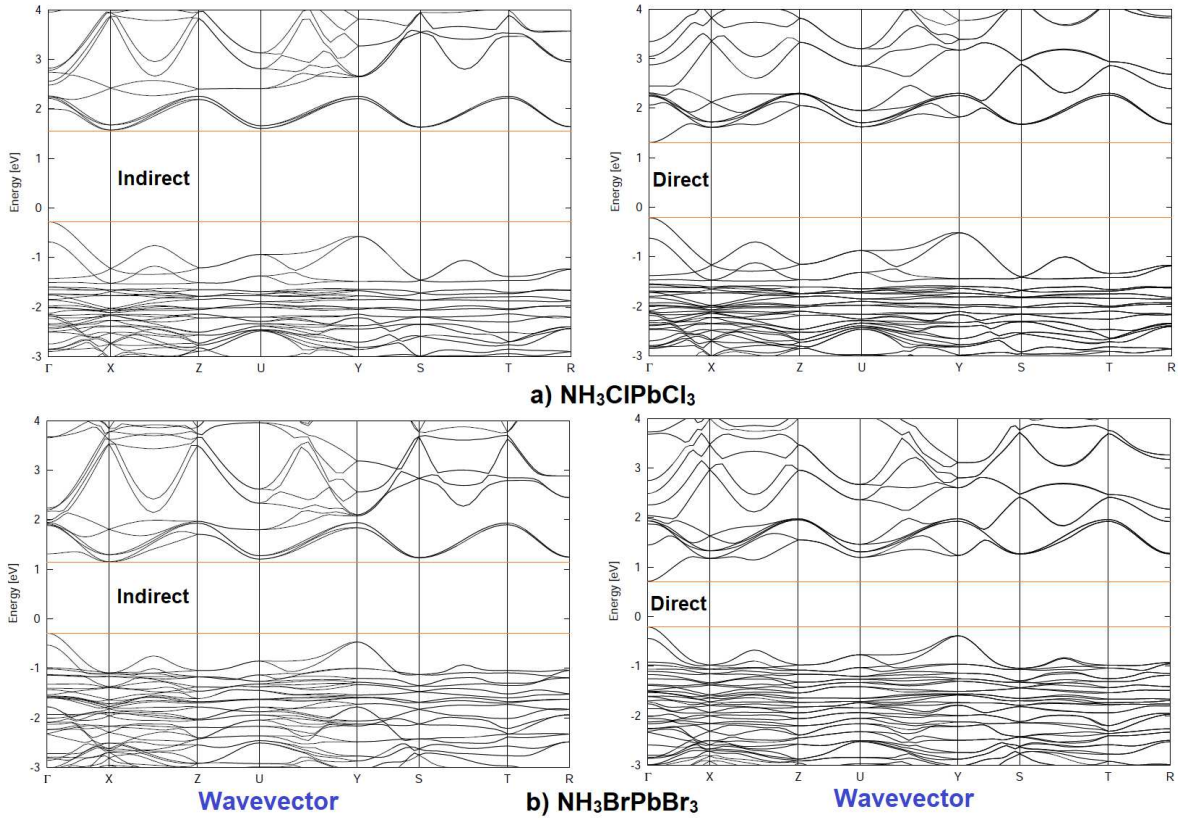

Fig. 22: Comparison of with and without SOC incorporated PBE band structures for the NH_3XPbY_3 (X = Y = Cl, Br) series in the orthorhombic phase. The labeling of the special points are those of the orthorhombic perovskite structure with *Pnma* space group, retrieved from bilbao crystallographic server.[149]

7.3.21 Comparison of electronic band structures for the NH_3XPbI_3 (X = F, Cl, Br, I) series in the pseudocubic phase

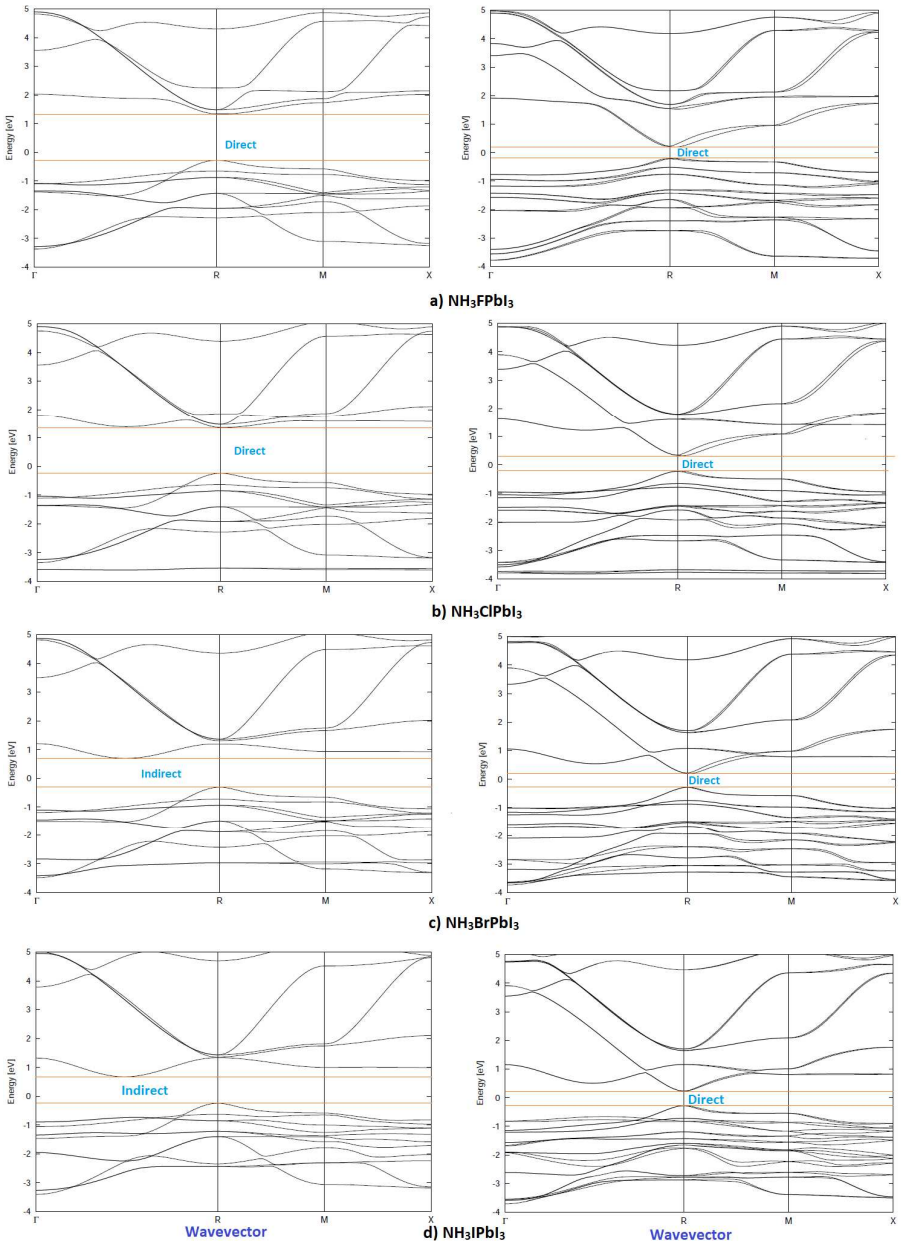

Fig. 23: Comparison of with and without SOC incorporated band structures for the NH_3XPbI_3 (X = F, Cl, Br, I) series in the pseudocubic phase, with the B-site cation aligned along the (111) direction. Rashba-Dresselhaus splitting of the conduction band minimum is evident in the SOC incorporated band structures. The labeling of the special points are those of the cubic perovskite structure with $Pm\bar{3}m$ space group, retrieved from bilbao crystallographic server.[149]

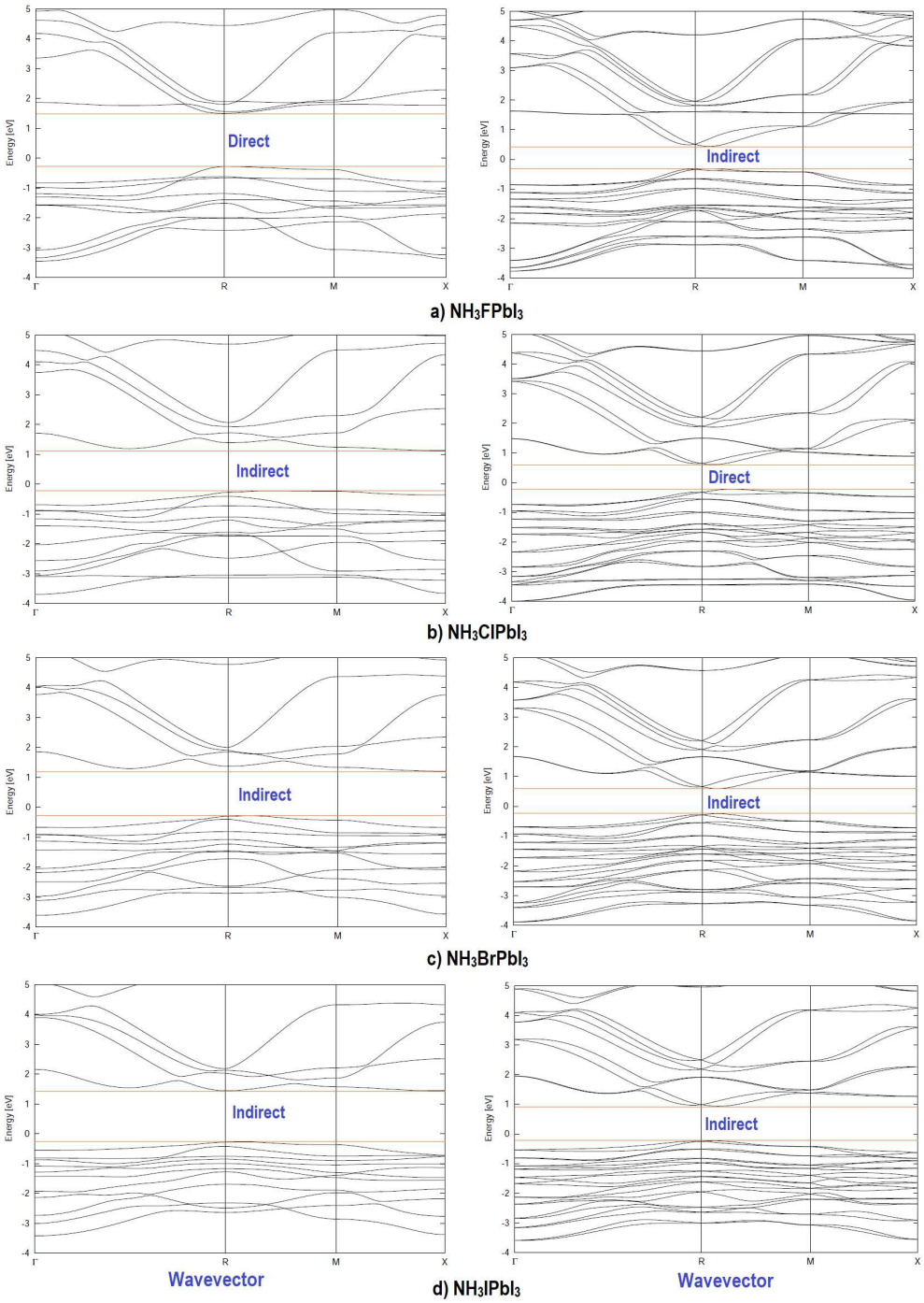

Fig. 24: Comparison of with and without SOC incorporated band structures for the NH_3XPbI_3 (X = F, Cl, Br, I) series in the pseudocubic phase, with the B-site cation aligned along the (011) direction. Rashba-Dresselhaus splitting of the conduction band minimum is evident in the SOC incorporated band structures. The labeling of the special points are those of the cubic perovskite structure with $Pm\bar{3}m$ space group, retrieved from bilbao crystallographic server.[149]

Figs. 23 and 24 presented the detailed electronic band structures of the NH_3XPbI_3 (X = F, Cl, Br, I) series in the pseudocubic phase, with the B-site cation aligned along the (111) and (011) directions, respectively. For each case, either the VBM or the CBM is degenerate and there is no splitting observed for either of these bands at the band extrema. This is not the case for these bands after including the effects of the SOC. As such, there is clearly a doublet splitting noticeable for each system regardless of the orientation of the B-site cation in $BPbY_3$, enabling bandgap transitions from indirect to direct and vice-versa. In particular, it is found that the bandgaps for NH_3BrPbI_3 and NH_3IPbI_3 are indirect for the (111) orientation of the B-site cation. We call it indirect because the transition involved is non-vertical by nature. In this case, the photoexcitation of VB electrons is only possible through the involvement of lattice phonons, whose energy and momentum are either borrowed from or released to the solid.[150]

With SOC, the bandgap transition for these latter systems became direct. Similarly, for the (011) orientation of the B-site cation, the direct bandgap transits to

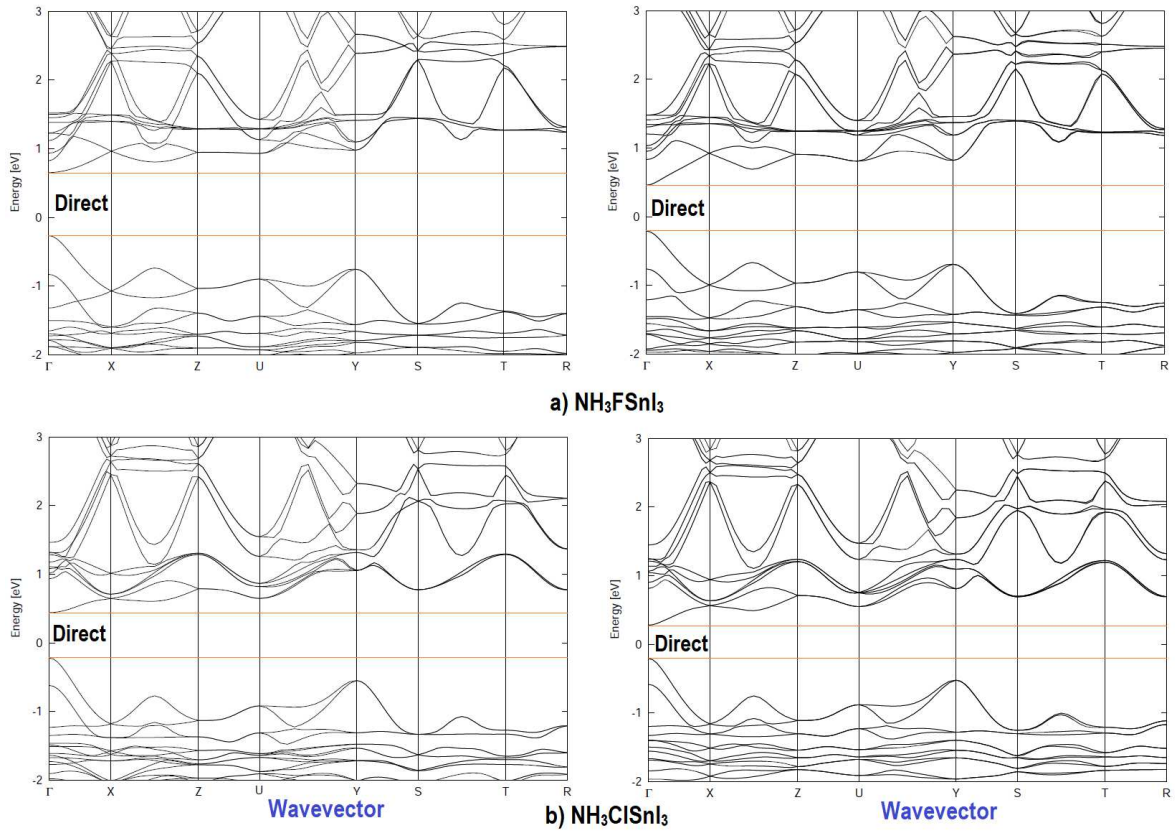

Fig. 25: Comparison of with and without SOC incorporated band structures for NH_3XSnI_3 (X = F, Cl) series in the orthorhombic phase. The labeling of the special points are those of the orthorhombic perovskite structure with *Pnma* space group, retrieved from bilbao crystallographic server.[149]

indirect for NH_3FPbI_3, and that of NH_3ClPbI_3 transits from indirect to direct. For the remaining systems, no such transitions were notable of Fig. 23 and 24, even though all these systems display the importance of SOC and emergence of band splitting. Another observation is that the Rashba splitting is more prominent when the B-site cation is aligned along the (011) direction compared to that aligned along the (111) direction.

The direct to indirect transition of the bandgap has been experimentally inferred for $CH_3NH_3PbI_3$, [9] as well as for the $CH_3NH_3PbBr_3$[146] system in the pseudocubic phase. It was shown that increasing pressure leads to a decrease in Rashba splitting, driving the character of the band structure from indirect to direct.

Fig. 25 and 26 presents the detailed electronic band structures of the NH_3XSnI_3 (X = F, Cl, Br, I) series in the orthorhombic phase. Except for NH_3BrSnI_3, the bandgaps for all the other three geometries containing F, Cl and I NH_3X^+ are found to be direct at Γ. For the NH_3BrSnI_3 system, the bandgap is found to be indirect. The VBM centers at Γ, whereas the CBM centers at the nearby high symmetry k-point called X-point.

Fig. 27 presents the the detailed electronic band structures of the NH_3XSnI_3 (X =

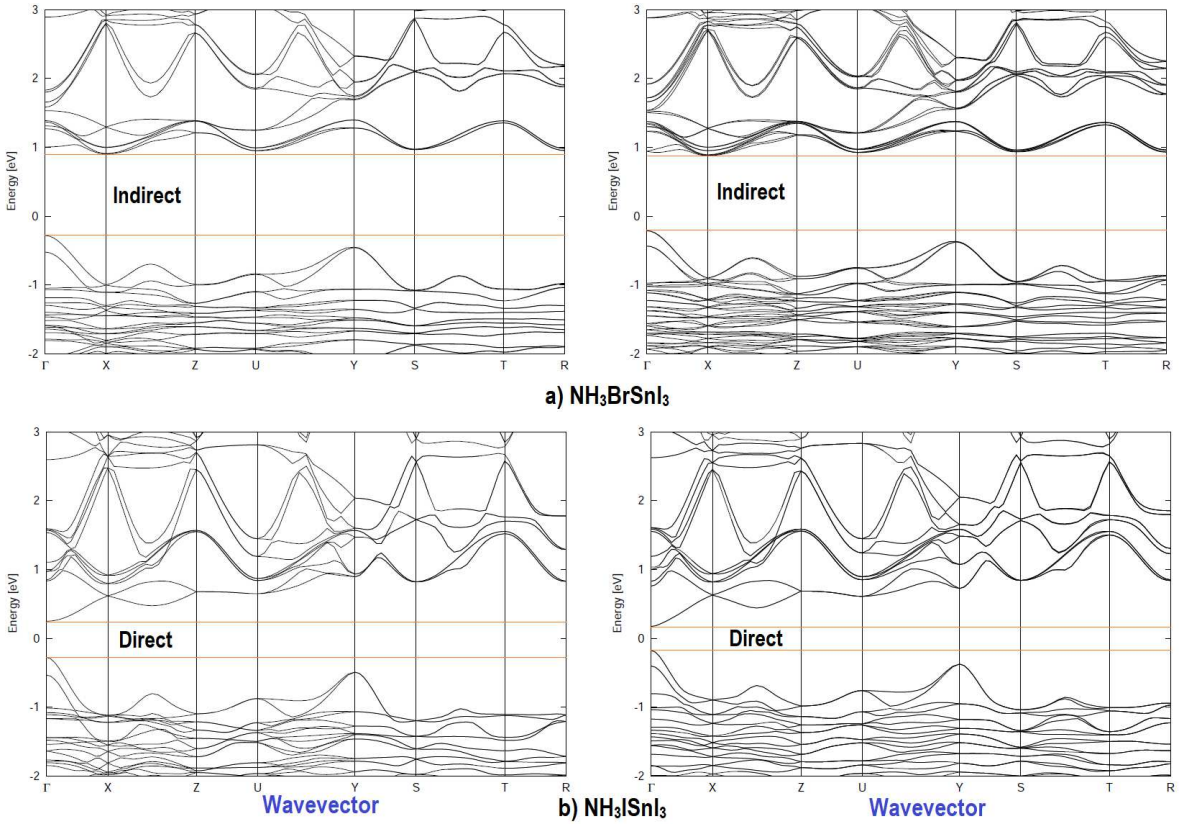

Fig. 26: Comparison of with and without SOC incorporated PBE band structures for NH_3XSnI_3 (X = Br, I) series in the orthorhombic phase. The labeling of the special points are those of the orthorhombic perovskite structure with *Pnma* space group, retrieved from bilbao crystallographic server.[149]

F, Cl) series in the pseudocubic phase; Fig. 18 illustrates their geometries. The bandgaps for these materials are calculated to be very small, values lying between 0.65 and 0.66 eV. These two are direct bandgap materials, showing their importance for application in photovoltaics. The attribute is similar to those found for the NH_3XPbI_3 (X = F, Cl) systems. In all these cases, the Rashba splitting of the CBM is sharply evident, but is very marginal. Its importance might be neglected since it does not cause any such major role to drive the transition from direct or indirect, and so on.

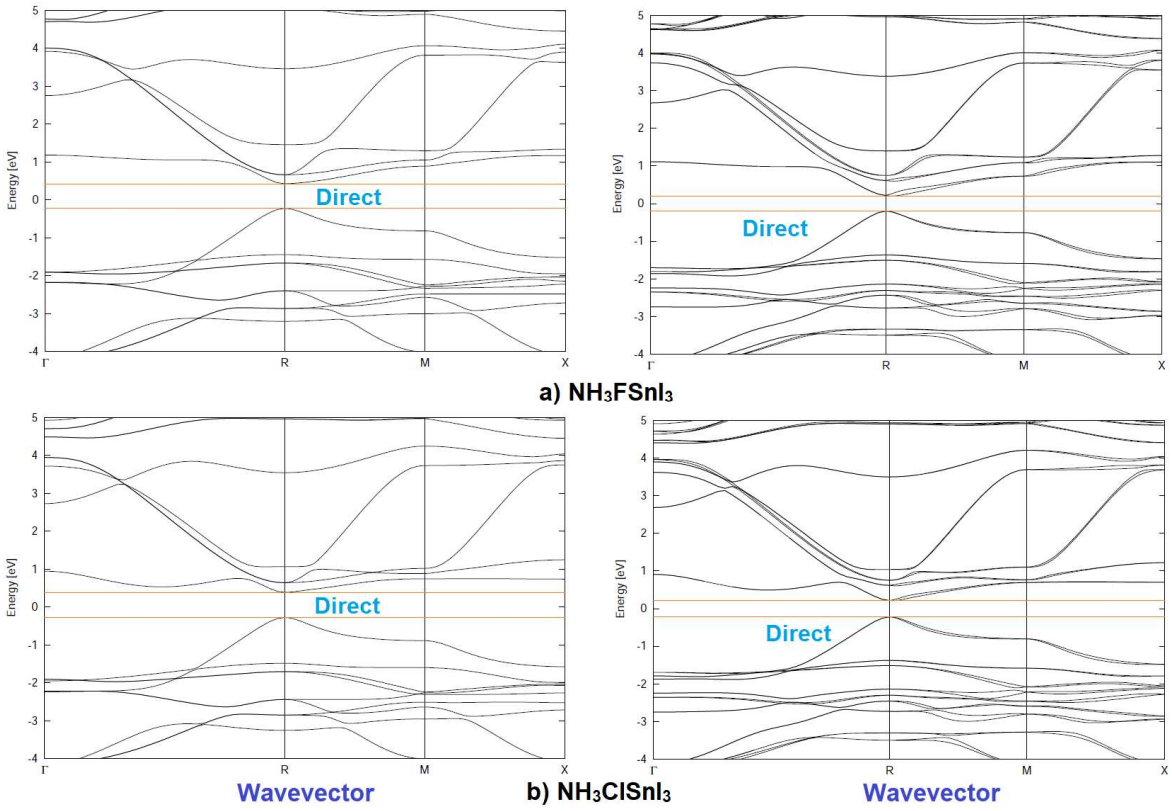

Fig. 27: Comparison of with and without SOC incorporated PBE band structures for NH_3XSnI_3 (X = F, Cl) series in the pseudocubic phase, with the B-site cation aligned along the (111) direction. Rashba-Dresselhaus splitting of the conduction band minimum is evident in the SOC incorporated band structures. The labeling of the special points are those of the cubic perovskite structure with $Pm\bar{3}m$ space group, retrieved from bilbao crystallographic server.[149]

Fig. 28 presents the PBE electronic band structures of the NH_3XSnI_3 (X = I, Br) series in the pseudocubic phase; Fig. 18 illustrates their geometries. The bandgaps for these materials are also calculated to be very small, values varying between 0.207 and 0.203 eV. These two are indirect bandgap materials, which can be comparable with similar materials already established in the literature. For instance, Si is an indirect material,[151-152] in which, the VBM and CBM energies occur at different values of the crystal momentum ($\Delta k \neq 0$), but is one of the important photovoltaic materials. However, as Volonakis *et al.*[74] have recently been asserted that Cs_2BiAgX_6 (X = Cl, Br) have synthesized and found to exhibit band gaps in the visible range. However, the band gaps of these compounds are indirect, which is not ideal for applications in thin film photovoltaics. Nevertheless, for NH_3XSnI_3 (X = I, Br), the Rashba splitting of the CBM is sharply evident, but is very marginal. Thus its importance might be neglected since it does not seem causing any such major role to drive the transition from direct or indirect, and so on.

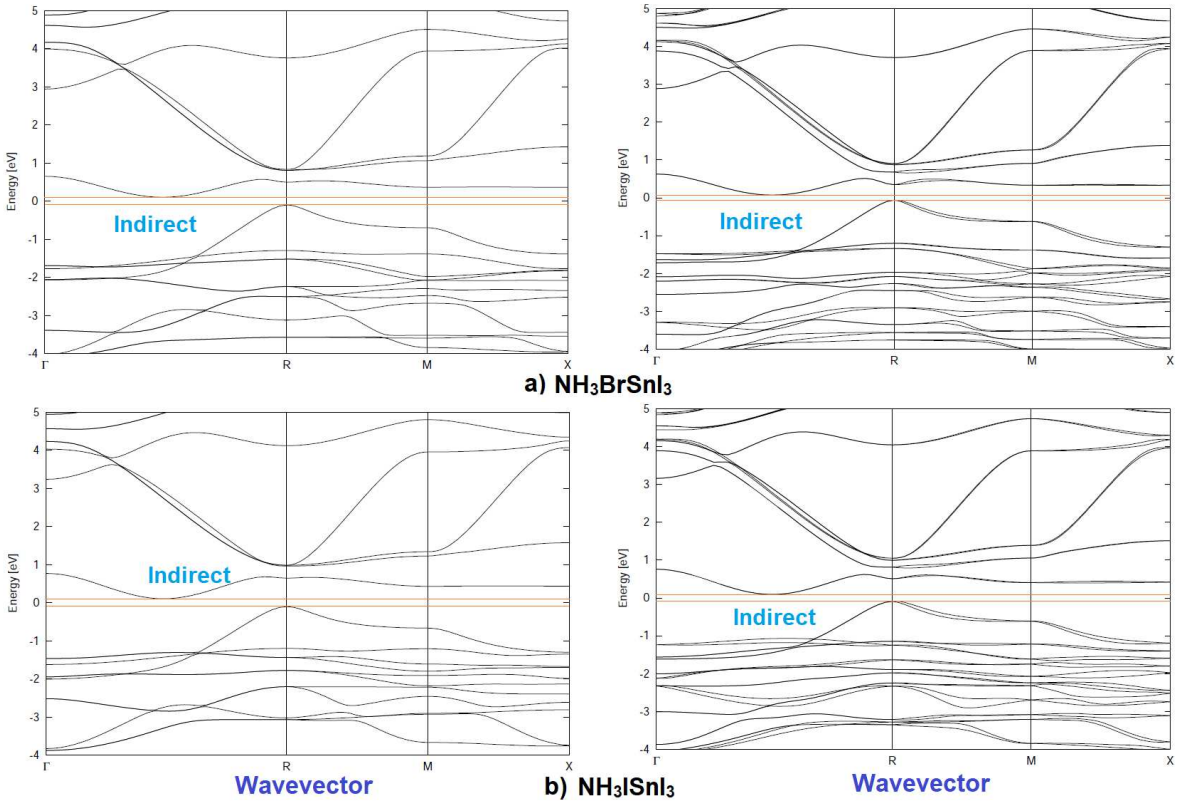

Fig. 28: Comparison of with and without SOC incorporated PBE band structures for NH_3XSnI_3 (X = Br, I) series in the cubic phase, with the B-site cation aligned along the (111) direction. Rashba-Dresselhaus splitting of the conduction band minimum is evident in the SOC incorporated band structures. The labeling of the special points are those of the cubic perovskite structure with $Pm\bar{3}m$ space group, retrieved from bilbao crystallographic server.[149]

7.3.22 DOS spectra for $CH_3NH_3PbI_3$

As already indicated above, the valence band maximum for $CH_3NH_3PbI_3$ is built through the combination of I 5p and Pb 6s orbitals. The conduction band minimum is shown to be composed of Pb 6p orbital character. This is evident of Fig. 30.

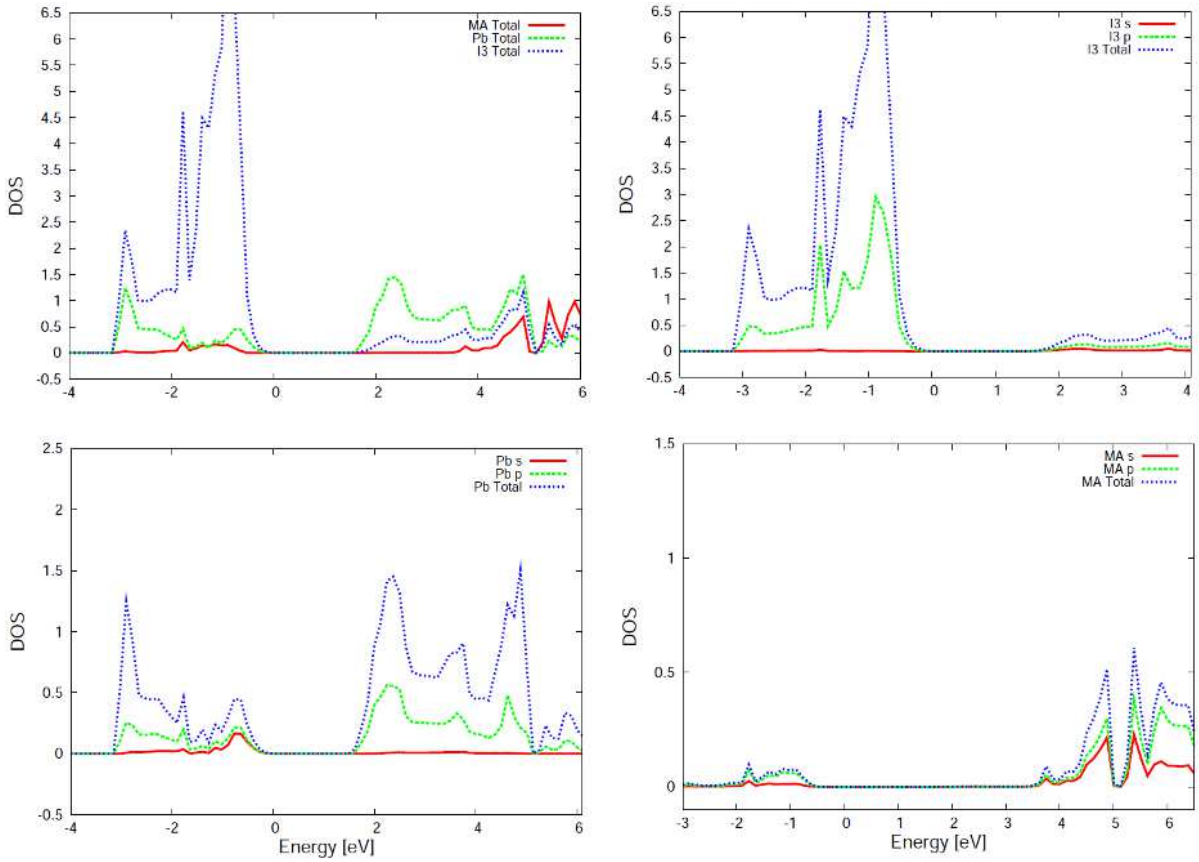

Fig. 30: DOS spectra for $CH_3NH_3PbI_3$

7.3.23 DOS spectra for NH_3XPbI_3 (X = F, Cl, Br, I) series

From Figs. 31, it is apparent that the nature of the DOS spectra is substantially different from that found for $CH_3NH_3PbI_3$. In this case, it seems to us that the valence band for NH_3IPbI_3 is built through the combination of I 5p (I of both PbI_3^- and NH_3I^+) and Pb 6s orbital characters. In contrary, the conduction band is composed of Pb 6p (anti-bonding) orbital character.

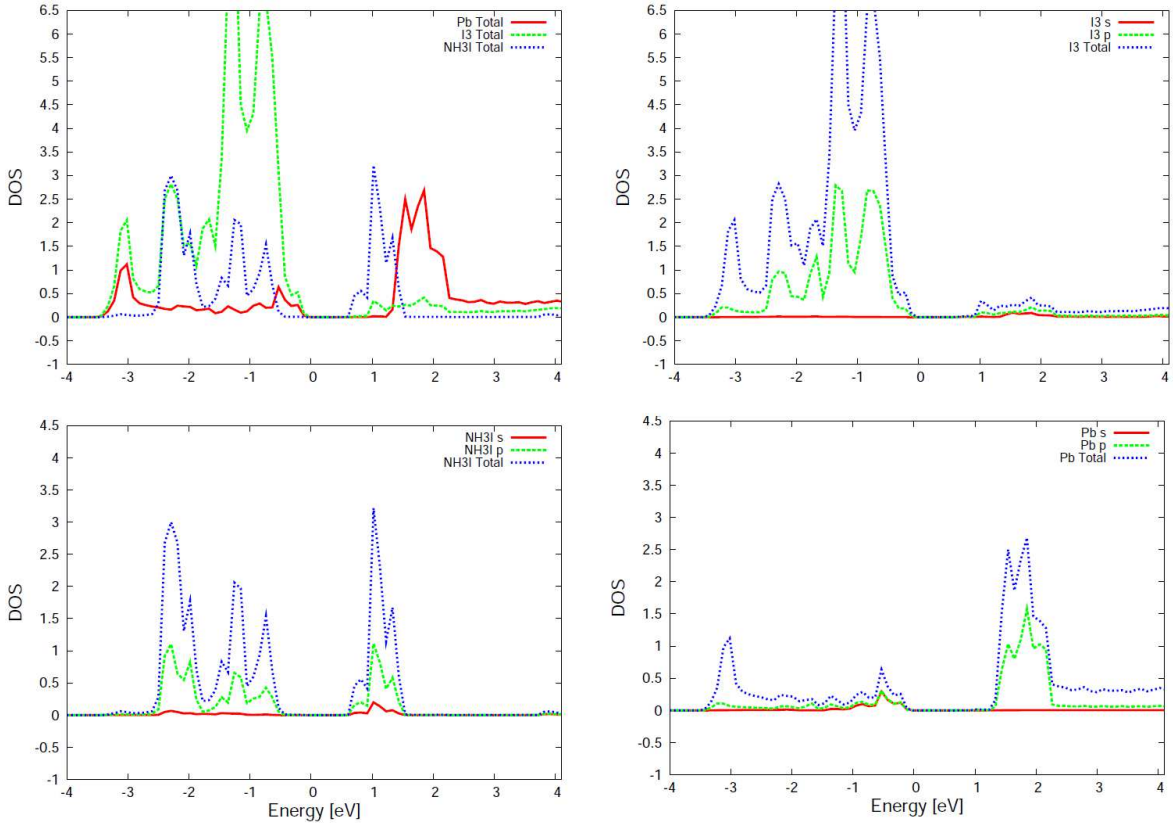

Fig. 31: DOS spectra for NH_3IPbI_3

A similar profile is evident of the DOS spectra for NH_3BrPbI_3 (Fig. 32) and NH_3ClPbI_3 (Fig. 33). However, the DOS for NH_3FPbI_3 (Fig. 34) is comparable with that of $CH_3NH_3PbI_3$. These results show that the presence of heavier halogen atoms in the B-site cations can contribute to some extent compared to those does not contain the halogen atoms. This is obviously due to their dispersive nature.

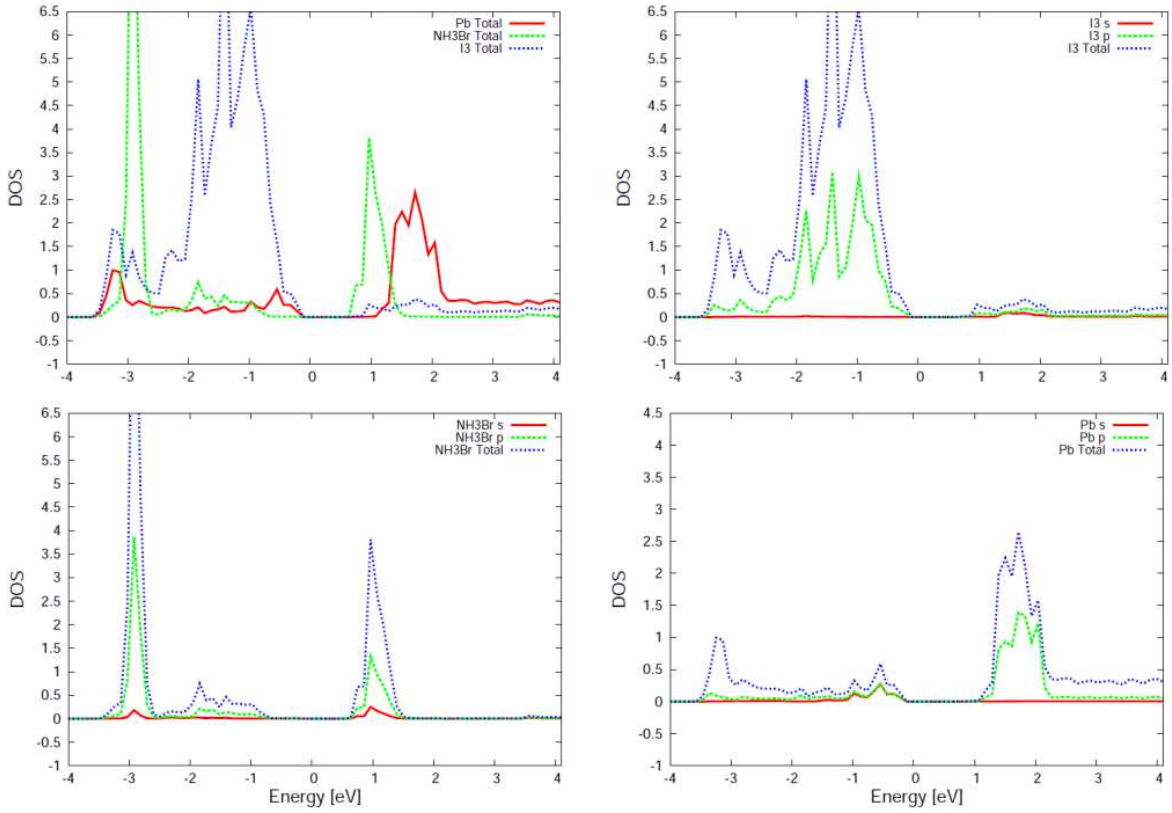

Fig. 32: DOS spectra for NH_3BrPbI_3

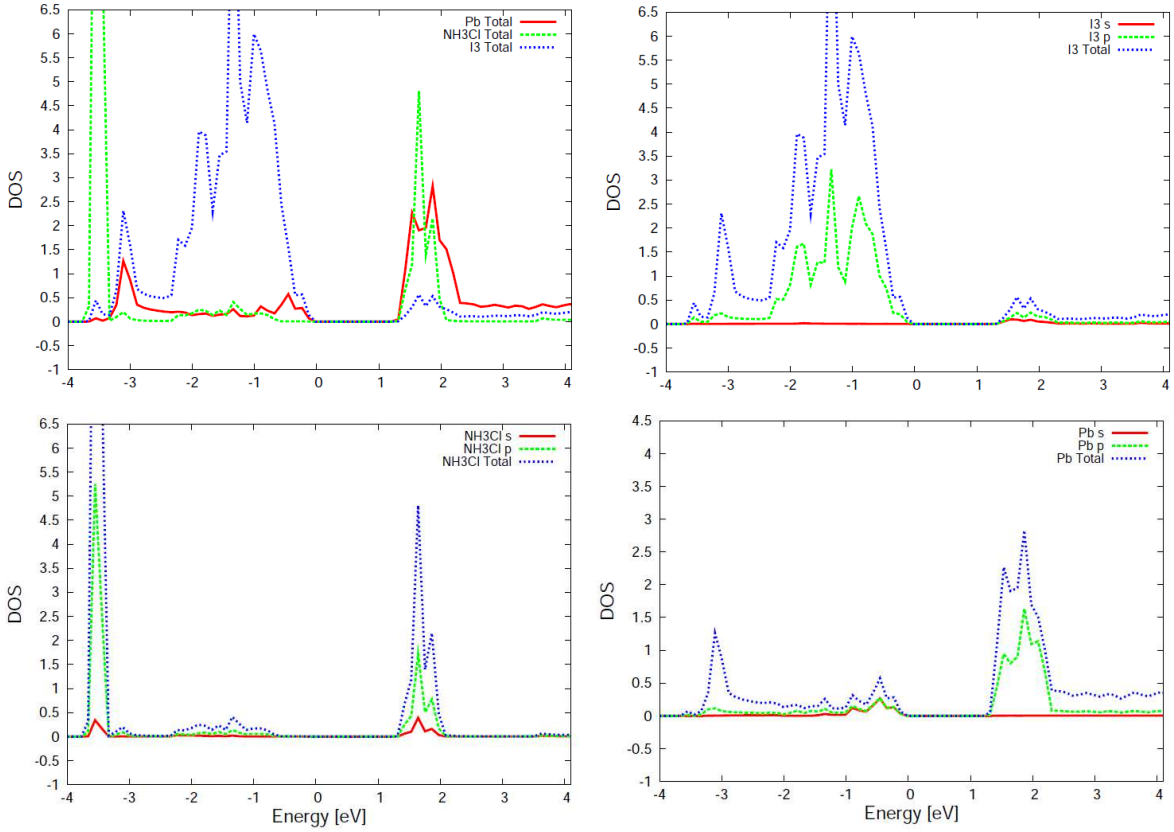

Fig. 33: DOS spectra for NH_3ClPbI_3

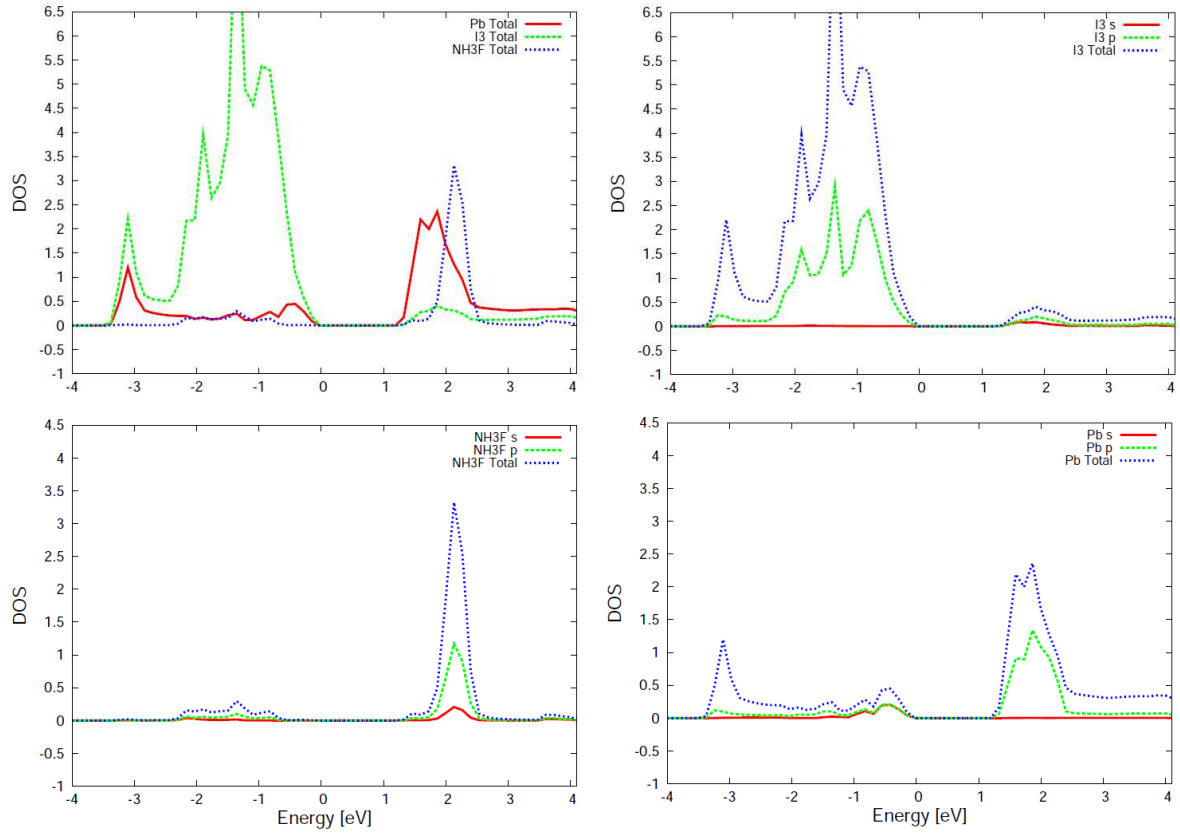

Fig. 34: DOS spectra for NH_3FPbI_3

7.3.24 Effective masses for charge carriers (electrons and holes)

For any semiconductor crystal to conduct reasonable amount of electric current, it must be able generate substantial amount of mobile charge carriers. That is, it should be able to generate electrons in the CB and holes in the VB. And that there would be no net current flow out of or into the crystal without an external field.

At an applied external electric field accompanied by an external potential difference, these carriers would move. This would be resulting in net current flow. However, it should be kept in mind that the flow would be slow if the mass of these carriers would be very high.

In general, the energy of a free particle (electron) can be described by the following Eqn., since its potential energy $V(r) = 0$.

$$E = \frac{P^2}{2m} \quad \text{……..……(5)}$$

Since the particle has dual character, and in case of solid, it should be written as

$$E = \hbar k \quad \text{……..……(5)}$$

Equating these two equations and taking it's the second derivative, we lead to Eqn (6).

$$\frac{1}{m} = \frac{1}{\hbar^2}\frac{\partial^2 E}{\partial k^2} \quad \text{……..(6)}$$

Thus, for an electron and for a hole, Eqn. 6 can be written as

$$\frac{1}{m_e^*} = \frac{1}{\hbar^2}\frac{\partial^2 E}{\partial k^2} \quad \text{……...(7)}$$

$$\frac{1}{m_h^*} = \frac{1}{\hbar^2}\frac{\partial^2 E}{\partial k^2} \quad \text{……...……(8)}$$

Within the domain of the parabolic approximation described by Eqns 7 and 8, we have estimated the effective mass of the hole associated with the valence band maximum, m_h^*. In the same, we have also estimated the effective mass of the electron associated with the conduction band, m_e^*.

The anisotropic effects of the dispersion in the first Brillouin zone have also considered, and the average values computed at high symmetry k-points along the band edges were estimated using Eqn. 9, and the results are presented in Table 20.

As expected, the effective masses of both the charge carriers are found to be small, which are comparable with those already reported for $MAPbI_3$. Incorporating SOC, these were further reduced to some little extent, as expected. For instance, Georgi *et al.* have reported the SOC incorporated effective masses of photogenerated electrons and holes for $MAPbI_3$ to be $m_e^* = 0.23m_0$ and $m_h^* = 0.29m_0$, respectively. [153]

Table 20: Mean hole and electron effective masses for NH_3XPbI_3 (X = F, Cl, Br, I), all computed with PBE/PAW level of theory without and with SOC. [a,b]

System	Property	Cubic	Cubic	Ortho	Ortho
		non-SOC	SOC	non-SOC	SOC
NH_3FPbI_3	$\frac{m^*_h}{m_0}$	0.25	0.18	0.37	0.33
	$\frac{m^*_e}{m_0}$	0.43	0.13	0.32	0.24
NH_3ClPbI_3	$\frac{m^*_h}{m_0}$	0.23	0.17	0.32	0.28
	$\frac{m^*_e}{m_0}$	0.38	0.12	0.35	0.22
NH_3BrPbI_3	$\frac{m^*_h}{m_0}$	0.21	0.16	0.32	0.28
	$\frac{m^*_e}{m_0}$	0.39	0.12	0.36	0.21
NH_3IPbI_3	$\frac{m^*_h}{m_0}$	0.21	0.18	0.42	0.37
	$\frac{m^*_e}{m_0}$	0.46	0.13	0.37	0.19

[a] The NH_3I^+ cation is aligned along the (111) direction in the cubic phase.
[b] SOC: inclusion of the effects of spin-orbit coupling.
[c] m_0 is the effective mass of the free electron.

7.4 Conclusions

This chapter has introduced the underlying physical chemistry and chemical physics of perovskite solar cell materials. In particular, it has delineated the gas phase binding chemistry of various BMY_3 perovskite compounds. It has uncovered the fact that there is a chemistry between gas phase and the solid state for these materials, which has revealed as the relationship between binding energy and bandgap. It was shown that accurate bandgaps can be predictable with the knowledge of gas phase binding energies.

Considering gas phase binding energy and structural and conformational stabilities as guiding tools, a series of new compounds, NH_3XMY_3 (M = Pb, Sn), has been predicted. These are shown as stable in the bulk phase. These are found to have bandgaps that are comparable with those of the $CH_3NH_3MY_3$ analogues, where M = Pb and Sn.

I have demonstrated using benchmark calculations with PBE and various k-point meshes that caution must be taken into account when interpreting the nature of the bandgap of any perovskite material predicted by the VASP software. The character of the bandgap calculated with some k-point meshes centered at and not at Γ can be different for any given compound, which can mislead to arrive at various wrong conclusions. It is always recommended to perform a benchmark calculation to test the reliability of the results obtained with a given k-point mesh.

There have been too many views persisting in the literature on the exact nature of the conduction and valence band extrema in halide perovskites, and the topic is under debate. It has been often demonstrated that the organic cation has no contribution to the either of these bands, but there are only a few studies that report the cation indeed contributes to these bands below 0.5 eV. However, changing the B-site cation MA by the NH_3X^+ cations, it is found that the contribution of the haloammonium cation to both VB and CB might not be very small.

Moreover, the estimation of effective masses of charge carriers, and the exploration of the natures of the electronic band structures, and DOS spectra have showed that the NH_3XMI_3 (X = F, Cl, Br, I) compounds can be competitive with the $CH_3NH_3MY_3$ systems. It is found that NH_3XMI_3 perovskites are direct bandgap materials in the low temperature orthorhombic phase. In the room temperature cubic phase, several of them are found to be direct and dynamical, thereby perhaps good for application in photovoltaics. This is a result which is somehow comparable with those have been demonstrated for the $CH_3NH_3PbI_3$ light harvester and related other perovskite solar cell semiconductors.

7.5 References

1. F. K. Kessler, et al., Functional carbon nitride materials — design strategies for electrochemical devices, Nature Reviews Materials, 2017, 17030, DOI: 10.1038/natrevmats.2017.30.
2. H. F. Liang, H. N. Alshareef, A Plasma-Assisted Route for the Rapid Preparation of Transition-Metal Phosphides for Energy Conversion and Storage, Small Methods 2017, 1, 1700111
3. Y. Yin, D. Talapin, The chemistry of functional nanomaterials, Chem. Soc. Rev., 2013, 42, 2484-2487.
4. D. Forgács , *et al.*, Efficient Monolithic Perovskite/Perovskite Tandem Solar Cells, Adv. Energy Mat. 2017, 7, 10.1002/aenm.201602121.
5. J. Zhao, *et al.*, Is Cu a stable electrode material in hybrid perovskite solar cells for a 30-year lifetime? Energy Environ. Sci., 2016,9, 3650-3656.
6. X. Qiu, *et al.*, From unstable CsSnI3 to air-stable Cs_2SnI_6: A lead-free perovskite solar cell light absorber with bandgap of 1.48 eV and high absorption coefficient, Solar Energy Materials and Solar Cells, 2017, 159, 227-234.
7. D. Wang, Stability of perovskite solar cells, Solar Energy Materials and Solar Cells 2016, 147, 255-275.
8. A. T. Barrows, *et al.*, Monitoring the Formation of a $CH_3NH_3PbI_{3-x}Cl_x$ Perovskite during Thermal Annealing Using X-Ray Scattering, Adv. Funct. Mat., 2016, DOI: 10.1002/adfm.201601309.
9. E. M. Hutter, *et al.*, Direct–indirect character of the bandgap in methylammonium lead iodide perovskite, Nature Materials 2017, 16,115–120.
10. M. Jacoby, The future of low-cost solar cells Perovskite and other emerging photovoltaic technologies grab headlines. But will they ever come to market? c&en 2016, 94, 30.
11. J. S. Manser, Intriguing Optoelectronic Properties of Metal Halide Perovskites, Chem. Rev. 2016, 116, 12956–13008.
12. M. A. Green, A. Ho-Baillie, Perovskite Solar Cells: The Birth of a New Era in Photovoltaics Chem. Rev., 2016, 116, 12956–13008.
13. K. Kojima, Y. Teshima, Y. Shirai, T. Miyasaka, Organometal halide perovskites as visible-light sensitizers for photovoltaic cells, *J. Am. Chem. Soc.* 2009, 131, 6050-6051.
14. M. M. Lee, J. Teuscher, T. Miyasaka, T. N. Murakami, H. J. Snaith, Efficient hybrid solar cells based on meso-superstructured organometal halide perovskites, *Science* 2012, 338, 643–647.
15. S. Luo, W. A. Daoud, Crystal Structure Formation of $CH_3NH_3PbI_{3-x}Cl_x$ Perovskite, Materials 2016, 9, 123.
16. Under the spotlight: The organic–inorganic hybrid halide perovskite for optoelectronic applications, nanotoday 10, 2015, 355.
17. W. Li, A. Thirumurugan, P. T. Barton, Z. Lin, S. Henke, H. H.-M. Yeung, M. T. Wharmby, E. G. Bithell, C. J. Howard, A. K. Cheetham, Mechanical tunability via hydrogen bonding in metal–organic frameworks with the perovskite architecture, *J. Am. Chem. Soc.* 2014, 136, 7801–7804.
18. M. Mączka, A. Ciupa, A. Gągor, A. Sieradzki, A. Pikul, B. Macalik, M. Drozd, Perovskite metal formate framework of $[NH_2\text{-}CH(+)\text{-}NH_2]Mn(HCOO)_3$]: phase transition, magnetic, dielectric, and phonon properties, *Inorg Chem.* 2014, 53, 5260-8.
19. a) R. E. Marsh, On the structure of $Zn(C_4H_8N_2O_6)$, *Acta Crystallogr. C* 1986, 42, 1327−1328; (b) A. Rossin, M. R. Chierotti, G. Gi□mb□sti□ni, R. Gobetto, M. Peruzzini,

Amine-templated polymeric Mg formates: crystalline scaffolds exhibiting extensive hydrogen bonding, *CrystEngComm* 2012, 14, 4454−4460.
20. M. Becker, *et al.*, Formation of hybrid ABX_3 perovskite compounds for solar cell application: first-principles calculations of effective ionic radii and determination of tolerance factors, Dalton Trans. 2017, 46, 3500.
21. F. Zheng, *et al.*, Material Innovation in Advancing Organometal Halide Perovskite Functionality, J. Phys. Chem. Lett. 2015, 6, 4862–4872.
22. O. Ergen, *et al.*, Graded bandgap perovskite solar cells, Nature Materials 2017, 16, 522–525.
23. T. A. Berhe, *et al.*, Organometal halide perovskite solar cells: degradation and stability, Energy Environ. Sci. 2016, 9, 323-356.
24. G. Grancini, *et al.*, One-Year stable perovskite solar cells by 2D/3D interface engineering, Nature Communications 2017, 8, 15684.
25. Zhijun Ning, *et al.*, Quantum-dot-in-perovskite solids, Nature 2015, 523, 324-328.
26. N. J. Jeon *et al.*, Compositional engineering of perovskite materials for high-performance solar cells, Nature 2015, 517, 476-480.
27. M. I. Saidaminov, *et al.*, High-quality bulk hybrid perovskite single crystals within minutes by inverse temperature crystallization, Nat. Commun. 2015, 6, 7586.
28. W. Zhang, *et al.*, Ultrasmooth organic–inorganic perovskite thin-film formation and crystallization for efficient planar heterojunction solar cells, Nat. Commun. 2015, 6, 6142.
29. I. Borriello, G. Cantele, D. Ninno, Ab initio investigation of hybrid organic-inorganic perovskites based on tin halides, *Phys. Rev. B*, 2008, 77, 235214.
30. L. D. Whalley, J. M. Frost, Y.-K. Jung, A. Walsh, Perspective: Theory and simulation of hybrid halide perovskites, *J. Chem. Phys*. 2017 146, 220901.
31. F. Brivio, A. B. Walker, A. Walsh, Structural and electronic properties of hybrid perovskites for high-efficiency thin-film photovoltaics from first-principles, *APL Mater*. 2013, 1, 042111.
32. Y. Wang, N. Song, L. Feng, X. Deng, Effects of Organic Cation Additives on the Fast Growth of Perovskite Thin Films for Efficient Planar Heterojunction Solar Cells, *ACS Appl. Mater. Interfaces* 2016, 8, 24703–24711.
33. M. Salado, L. Calio, R. Berger, S. Kazim, S. Ahmad, Influence of the mixed organic cation ratio in lead iodide based perovskite on the performance of solar cells, *Phys Chem Chem Phys*. 2016 18, 27148-27157.
34. E. Mosconi, A. Amat, Md. K. Nazeeruddin, M. Grätzel, F. De Angelis, First-Principles Modeling of Mixed Halide Organometal Perovskites for Photovoltaic Applications, *J. Phys. Chem. C*, 2013, 117, 13902–13913.
35. E. Mosconi, C. Quarti, T. Ivanovska, G. Ruani, F. De Angelis, Structural and electronic properties of organo-halide lead perovskites: a combined IR-spectroscopy and ab initio molecular dynamics investigation, *Phys. Chem. Chem. Phys.*, 2014,16, 16137-16144.
36. A. M. A. Leguy, *et al.*, The dynamics of methylammonium ions in hybrid organic–inorganic perovskite solar cells, *Nat.Commun.* 2015, 6, 7124, doi:10.1038/ncomms8124.
37. J. Berry, *et al.*, Hybrid Organic–Inorganic Perovskites (HOIPs): Opportunities and Challenges, *Adv. Mater*. 2015, 27, 5102–5112.
38. G. R. Berdiyorov, F. El-Mellouhi, M. E. Madjet, F. H. Alharbi, S. N. Rashkeev, Electronic transport in organometallic perovskite $CH_3NH_3PbI_3$: The role of organic cation orientations, *Appl. Phys. Lett.* 2016, 108, 053901.
39. T. Chen, B. J. Foley, C. Park, C. M. Brown, L. W. Harriger, J. Lee, J. Ruff, M. Yoon, J. J. Choi, S.-H. Lee, Entropy-driven structural transition and kinetic trapping in

formamidinium lead iodide perovskite, *Sci. Adv.*, 2016, 2, e1601650 DOI: 10.1126/sciadv.1601650.
40. S. Sanvito, C. Motta, F. El-Mellouhi, Waltzing molecules for high-efficiency photovoltaics, *SPIE Newsroom*, 2015, DOI: 10.1117/2.1201509.006060.
41. C. Motta, F. El-Mellouhi, S. Kais, N. Tabet, F. Alharbi, S. Sanvito, Revealing the role of organic cations in hybrid halide perovskite $CH_3NH_3PbI_3$, *Nat. Commun.* 2015, 6, 7026.
42. Y. Rakita, *et al.*, Tetragonal $CH_3NH_3PbI_3$ is ferroelectric, PNAS 2017, 114, E5504-E5512.
43. E. Strelcov, *et al.*, $CH_3NH_3PbI_3$ perovskites: Ferroelasticity revealed, Sci. Adv. 2017, 3, e1602165DOI: 10.1126/sciadv.1602165
44. M. U. Rothmann, *et al.*, Direct observation of intrinsic twin domains intetragonal $CH_3NH_3PbI_3$, Nat. Commun. 2017, 8, 14547, DOI: 10.1038/ncomms14547
45. Z. Fan, *et al.*, Ferroelectricity of $CH_3NH_3PbI_3$ perovskite, J. Phys. Chem. Lett. 2015, 6, 1155–1161.
46. G. Sharada, *et al.*, Is $CH_3NH_3PbI_3$ Polar? J. Phys. Chem. Lett. 2016, 7, 2412–2419.
47. Gaussian 09, Revision C.01, M. J. Frisch, G. W. Trucks, H. B. Schlegel, G. E. Scuseria, M. A. Robb, J. R. Cheeseman, G. Scalmani, V. Barone, B. Mennucci, G. A. Petersson, H. Nakatsuji, M. Caricato, X. Li, H. P. Hratchian, A. F. Izmaylov, J. Bloino, G. Zheng, J. L. Sonnenberg, M. Hada, M. Ehara, K. Toyota, R. Fukuda, J. Hasegawa, M. Ishida, T. Nakajima, Y. Honda, O. Kitao, H. Nakai, T. Vreven, J. A. Montgomery, Jr., J. E. Peralta, F. Ogliaro, M. Bearpark, J. J. Heyd, E. Brothers, K. N. Kudin, V. N. Staroverov, R. Kobayashi, J. Normand, K. Raghavachari, A. Rendell, J. C. Burant, S. S. Iyengar, J. Tomasi, M. Cossi, N. Rega, J. M. Millam, M. Klene, J. E. Knox, J. B. Cross, V. Bakken, C. Adamo, J. Jaramillo, R. Gomperts, R. E. Stratmann, O. Yazyev, A. J. Austin, R. Cammi, C. Pomelli, J. W. Ochterski, R. L. Martin, K. Morokuma, V. G. Zakrzewski, G. A. Voth, P. Salvador, J. J. Dannenberg, S. Dapprich, A. D. Daniels, Ö. Farkas, J. B. Foresman, J. V. Ortiz, J. Cioslowski, and D. J. Fox, Gaussian, Inc., Wallingford CT, 2009.
48. GaussView, Version 5, Roy Dennington, Todd A. Keith, and John M. Millam, Semichem Inc., Shawnee Mission, KS, 2009.
49. EMSL basis set library. This is available via: https://bse.pnl.gov/bse/portal (last retrieved July 24, 2017).
50. S. F. Boys and F. Bernardi, The calculation of small molecular interactions by the differences of separate total energies, Mol. Phys. 2017, 19, 553.
51. a) G. Kresse, J. Hafner, Ab initio molecular dynamics for liquid metals, *Phys. Rev. B* 1993, 47, 558; b) G. Kresse, J. Hafner, Ab initio molecular-dynamics simulation of the liquid-metal-amorphous-semiconductor transition in germanium, *Phys. Rev. B* 1994, 49, 14251; c) G. Kresse, J. Furthmüller, Efficiency of ab-initio total energy calculations for metals and semiconductors using a plane-wave basis set, *Comput. Mat. Sci.* 1996, 6, 15; d) G. Kresse, J. Furthmüller, Efficient iterative schemes for ab initio total-energy calculations using a plane-wave basis set, *Phys. Rev. B* 1996, 54:11169; e) P. E. Blöchl, O. Jepsen, O. K. Andersen, Improved tetrahedron method for Brillouin-zone integrations, *Phys. Rev. B* 1994, 49, 16223–16233.
52. a) P.E. Blöchl, Projector augmented-wave method, Phys. Rev. B 1994, 50, 17953; b) G. Kresse, and J. Joubert, From ultrasoft pseudopotentials to the projector augmented wave method, Phys. Rev. B 1999, 59, 1758.
53. J. Feng, B. Xiao, Crystal Structures, Optical Properties, and Effective Mass Tensors of $CH_3NH_3PbX_3$ (X = I and Br) Phases Predicted from HSE06, J. Phys. Chem. Lett. 2014, 5, 1278–1282.

54. V. Grakauskas, A. H. Remanick, K. Baum, The synthesis of fluorammonium salts, J. Am. Chem. Soc. 1968, 90, 3839–3841.
55. V.Grakauskas, Fluorammonium trifluoromethanesulfonate, J. Inorg. Nucl. Chem.1973, 35, 3034.
56. S. Schneider, R. Haiges, T. Schroer, J. Boatz, K. O. Christe, The $[NH3Cl]^+$ ion, Angew. Chem. Int. Ed. 2004, 43, 5213 –5217.
57. H. Szatyłowicz, Structural aspects of the intermolecularhydrogen bond strength: H-bondedcomplexes of aniline, phenol andpyridine derivatives, *J. Phys. Org. Chem.*2008, 21 897–914.
58. G. R. Desiraju, Hydrogen Bridges in Crystal Engineering: Interactions without Borders, *Acc. Chem. Res*. 2002, 35, 565–573.
59. a) H. Fang, P. Jena, Molecular origin of properties of organic–inorganic hybrid perovskites: The big picture from small clusters, *J. Phys. Chem. Lett.* 2016, 7, 1596–1603; b) Q. Yao, H. Fang, K. Deng, E. Kan, P. Jena, Superhalogens as building blocks of two-dimensional organic–inorganic hybrid perovskites for optoelectronics applications, *Nanoscale* 2016, 8, 17836-17842; c) H. Fang, P. Jena, Super-ion inspired colorful hybrid perovskite solar cells, *J. Mater. Chem. A* 2016, 4, 4728.
60. a) I. E. Castelli, J. M. García-Lastra, K. S. Thygesen, K. W. Jacobsen, Bandgap calculations and trends of organometal halide perovskites, *APL Materials* 2014, 2, 081514 (References therein); b) Computational Materials Repository, Organometal Halide Perovskites, https://cmr.fysik.dtu.dk/organometal/organometal.html#organometal (last retrieved July 24, 2017).
61. R. G. Niemann, *et al.*, Halogen effects on ordering and bonding of $CH_3NH_3^+$ in $CH_3NH_3PbX_3$ (X = Cl, Br, I) hybrid perovskites:a vibrational spectroscopic study, *J. Phys. Chem. C* 2016, 120, 2509-2519.
62. K. Galkowski, *et al.*, Determination of the exciton binding energy and effective masses for the methylammonium and formamidinium lead tri-halide perovskite family, Energy Environ. Sci., 2016,9, 962-970.
63. G. Pellegrino, *et al.*, Texture of $MAPbI_3$ Layers Assisted by Chloride on Flat TiO2 Substrates, J. Phys. Chem. C, 2015, 119, 19808–19816.
64. W.-L. Yan, G.-H. Lu, F. Liu, Effect of Chlorine Substitution on Lattice Distortion and Ferroelectricity of $CH_3NH_3PbI_3$, J. Phys. Chem. C 2016, 120, 17972−17977.
65. M. A. Green, A. Ho-Baillie, H. J. Snaith, The emergence of perovskite solar cells, *Nat. Photon. 2014* 8, 506–514.
66. a) J. J. Mortensen, L. B. Hansen, and K. W. Jacobsen, *Phys. Rev. B* 2005, 71, 035109; b) J. Enkovaara, C. Rostgaard, J. J. Mortensen, J. Chen, M. Dulak, L. Ferrighi, J. Gavnholt, C. Glinsvad, V. Haikola, H. A. Hansen *et al., J. Phys. Condens. Matter* 2010, 22, 253202.
67. O. Gritsenko, R. van Leeuwen, E. van Lenthe, and E. J. Baerends, *Phys. Rev. A* 1995, 51, 1944.
68. R. Dalven, Empirical relation between energy gap and lattice constant in cubic semiconductors, *Phys. Rev. B* 1973, 8, 6033.
69. I. E. Castelli, T. Olsen, S. Datta, D. D. Landis, S. Dahl, K. S. Thygesen, and K. W. Jacobsen, *Energy Environ. Sci.* 2012, 5, 5814.
70. F. Hao, C. C. Stoumpos, D. H. Cao, R. P. H. Chang, M. G. Kanatzidis, Lead-free solid-state organic–inorganic halideperovskite solar cells, Nat. Photon. 2014, 8, 489.
71. S. Scheiner, Geometries and energies, Ch 2, in: Hydrogen Bonding: A Theoretical Perspective, Oxford University Press, Inc., 1997.

72. C. D. Sherrill, Counterpoise Correction and Basis Set Superposition Error, 2010; this is available via: http://vergil.chemistry.gatech.edu/notes/cp.pdf (last retrieved July 24, 2017).
73. G. Cavallo, P. Metrangolo, R. Milani, T. Pilati, A. Priimagi, G. Resnati, G. Terraneo, The halogen bond, *Chem. Rev.* 2016, 116, 2478–2601.
74. G. Volonakis, *et al.*, $Cs_2InAgCl_6$: A New Lead-Free Halide Double Perovskite with Direct Band Gap, J. Phys. Chem. Lett. 2017, 8, 772−778.
75. G. Hautier, Accuracy of Density Functional Theory in Predicting Formation Energies of Ternary Oxides from Binary Oxides and its Implication on Phase Stability. Phys. Rev. B: Condens. Matter Mater. Phys. 2012, 85, 155208.
76. P. Politzer, J. S. Murray, Enthalpy and entropy factors in gas phase halogen bonding: compensation and competition, CrystEngComm 2013, 15, 3145-3150.
77. V. M. Goldschmidt, Die Gesetze der Krystallochemie, Die Naturwissenschaften, 1926, 21, 477–485, doi:10.1007/bf01507527.
78. X. Liu, *et al.*, Tolerance factor and the stability discussion of ABO_3-type ilmenite, Journal of Materials Science: Materials in Electronics, 2008, 20, 323–327.
79. M. Becker, T. Klüner, M. Wark, Formation of hybrid ABX_3 perovskite compounds for solar cell application: first-principles calculations of effective ionic radii and determination of tolerance factors, Dalton Trans. 2017, 46, 3500–3509.
80. C. Li, X. Lu, W. Ding, L. Feng, Y. Gao, Z. Guo, Formability of ABX_3 (X = F, Cl, Br, I) halide perovskites, Acta Cryst. 2008 B64, 702–707.
81. M. Rini, *et al.*, Control of the electronic phase of a manganite by mode-selective vibrational excitation, Nature 2007, 449, 72-74.
82. N.-G., Park, Perovskite solar cells: an emerging photovoltaic technology, materialstoday 2015, 18, 65-72.
83. H. Choi, J. Jeong, H. B. Kim, S. Kim, B. Walker, G. H. Kim and J. Y. Kim, *Nano Energy*, 2014, **7**, 80–85.
84. M. Saliba, *et al.*, Cesium-containing triple cation perovskite solar cells: improved stability, reproducibility and high efficiency, Energy Environ. Sci. 2016, 9, 1989-1997.
85. A. Amat, *et al.*, Cation-Induced Band-Gap Tuning in Organohalide Perovskites: Interplay of Spin−Orbit Coupling and Octahedra Tilting, Nano Lett. 2014, 14, 3608−3616.
86. G. Kieslich, S. Sun, A. Cheetham, An extended tolerance factor approach for organic-inorganic perovskites, Chem. Sci. 2015, 6, 3430–3433.
87. I. Levchuk, *et al.*, Brightly Luminescent and Color-Tunable Formamidinium Lead Halide Perovskite $FAPbX_3$ (X = Cl, Br, I) Colloidal Nanocrystals, Nano Lett., 2017, 17, 2765–2770.
88. Y. Zhou, *et al.*, Exceptional Morphology-Preserving Evolution of Formamidinium Lead Triiodide Perovskite Thin Films via Organic-Cation Displacement, J. Am. Chem. Soc. 2016, 138 5535–5538.
89. a) J. Navas, A. Sanchez-Coronilla, J. J. Gallardo et al., "Revealing the role of Pb2+ in the stability of organic-inorganic hybrid perovskite CH3NH3Pb1 − xCdxI3: an experimental and theoretical study, Phys. Chem. Chem. Phys. 2015, 17, 23886–23896, 2015; b) R. A. Jishi, Modified Becke-Johnson exchange potential: improved modeling of lead halides for solar cell applications, AIMS Materials Science, 2016, 149-159. doi: 10.3934/matersci.2016.1.149.
90. W. Travis, *et al.*, On the application of the tolerance factor to inorganic and hybrid halide perovskites: a revised system, Chem. Sci., 2016, 7, 4548

91. Z. Li, M. Yang, J.-S. Park, S.-H. Wei, J. J. Berry, K. Zhu, Stabilizing Perovskite Structures by Tuning Tolerance Factor: Formation of Formamidinium and Cesium Lead Iodide Solid-State Alloys, Chem. Mater. 2016, 28, 284–292.
92. C. H. Hendon, R. X. Yang, L. A. Burton, A. Walsh, Assessment of polyanion (BF_4^- and PF_6^-) substitutions in hybrid halide perovskites J. Mater. Chem. A, 2015, 3, 9067.
93. R. D. Shannon, Revised Effective Ionic Radii and Systematic Studies of Interatomic Distances in Halides and Chalcogenides, Acta Cryst. 1976, A32 751-767. The data contained in the database is available at: http://abulafia.mt.ic.ac.uk/shannon/ (last retrieved July 25, 2017)
94. M. Johnsson, P. Lemmens, Handbook of Magnetism and Advanced Magnetic Materials, John Wiley & Sons, Ltd., 2007.
95. A. Kumar, A.S. Verma, S.R. Bhardwaj, Prediction of Formability in Perovskite-Type Oxides, The Open Applied Physics Journal, 2008, 1, 11-19.
96. J. A. Brehm, J. W. Bennett, M. R. Schoenberg, I. Grinberg, A. M. Rappe, The structural diversity of ABS_3 compounds with d0 electronic configuration for the B-cation, J. Chem. Phys. 2014, 140, 224703. Modified Goldschmidt tolerance factor calculator for ABX3 compounds is available at: https://jaramillo.mit.edu/modified-goldschmidt-tolerance-factor-calculator-abx3-compounds (last retrieved July 25, 2017).
97. S. G. Kang, First-principles examination of low tolerance factor perovskites, 2017, 10.1002/qua.25420
98. T. Sato, S. Takagi, S. Deledda, B. C. Hauback, S. Orimo, Extending the applicability of the Goldschmidt tolerance factor to arbitrary ionic compounds Sci. Rep. 2016, 6, 23592.
99. G. S. Rohere, Structure and Bonding in Crystalline Materials, New York, Cambridge University Press, 2001.
100. Hybrid Perovskite, CH3NH3PbI3, for Solar Applications: An Experimental and Theoretical Analysis of Substitution in A and B Sites Antonio Sánchez-Coronilla, Journal of Nanomaterials Volume 2017, 2017, https://doi.org/10.1155/2017/9768918
101. K. Momma and F. Izumi, "VESTA 3 for three-dimensional visualization of crystal, volumetric and morphology data," J. Appl. Crystallogr. 2011, 44, 1272-1276.
102. A. Jain, S.P. Ong, G. Hautier, W. Chen, W.D. Richards, S. Dacek, S. Cholia, D. Gunter, D. Skinner, G. Ceder, K.A. Persson, The Materials Project: A materials genome approach to accelerating materials innovation APL Materials, 2013, 1, 011002.
103. M. T. Weller, O. J. Weber, P. F. Henry, A. M. Di Pumpo, T. C. Hansen, Complete structure and cation orientation in the perovskite photovoltaic methylammonium lead iodide between 100 and 352 K *Chem. Commun.* 2015, 51, 4180.
104. C. C. Stoumpos, C. D. Malliakas, M.i G. Kanatzidis, Semiconducting tin and lead iodide perovskites with organic cations: Phase transitions, high mobilities, and near-infrared photoluminescent properties, *Inorg. Chem.* 2013, 52, 9019–9038.
105. A. M. Glazer, The classification of tilted octahedra in perovskites, *Acta Cryst*. 1972, B28, 3384-3392.
106. S. Alvarez, A cartography of the van der Waals territories, *Dalton Trans.* 2013, 42, 8617-8636.
107. E. Arunan, *et al.*, Definition of the hydrogen bond (IUPAC Recommendations 2011), *Pure Appl. Chem*. 2011, 83, 1637–1641.
108. E. Arunan, Definitions of a hydrogen bond. This is available via: http://ipc.iisc.ernet.in/~arunan/iupac/iupac/Definition_of_HydrogenBond.pdf (last retrieved on June 19, 2017); References therein.
109. Varadwaj

110. J.-H. Lee, N. C. Bristowe, P. D. Bristowe, A. K. Cheetham, Role of hydrogenbonding and its interplay with octahedral tilting in $CH_3NH_3PbI_3$, *Chem. Commun.* 2015, 51, 6434.
111. J. -H. Lee, N. C. Bristowe, J. H. Lee, S. -H. Lee, P. D. Bristowe, A. K. Cheetham, H. M. Jang, Resolving the physical origin of octahedral tilting in halide perovskites, *Chem. Mater.* 2016, 28, 4259–4266.
112. J.H. Lee, J.-H. Lee, E.-H. Kong, H. M. Jang, The nature of hydrogen bonding interaction in the prototypic hybrid halide perovskite, tetragonal $CH_3NH_3PbI_3$, *Sci. Rep.* 2016, 6, 21687, doi:10.1038/srep21687.
113. G. R. Desiraju, *et al.*, Definition of the halogen bond (IUPAC Recommendations 2013), *Pure Appl. Chem.* 2013, 85, 1711-1713.
114. A. Priimagi, *et al.*, The Halogen Bond in the Design of Functional Supramolecular Materials: Recent Advances, Acc. Chem. Res. 2013, 46, 2686–2695.
115. R. F. W. Bader, Atoms in Molecules A Quantum Theory, Oxford University Press, Oxford, 1990.
116. R. F. W. Bader, T. T. Nguyen-Dang, and Y. Tal, A topological theory of molecular structure, *Rep. Prog. Phys.* 1981, 44, 893 948.
117. R. F. W. Bader, Atoms in Molecules, http://www.wiley.com/legacy/wileychi/ecc/samples/sample02.pdf. (last retrieved July 26, 2017).
118. J. M. Crowley, *et al.*, Resolution of the Band Gap Prediction Problem for Materials Design, J. Phys. Chem. Lett. 2016, 7, 1198–1203.
119. Y. Zhao, D. G. Truhlar, Calculation of semiconductor band gaps with the M06-L density functional Yan Zhao and J. Chem. Phys. 130, 074103, 2009.
120. R. Geiger, T. Zabel, H. Sigg, Group iv direct band gap photonics: methods, challenges, and opportunities, Front. Mater. 2015, https://doi.org/10.3389/fmats.2015.00052 (last retrieved July 26, 2017).
121. A document on "Direct and indirect band gaps From Wikipedia, the free encyclopedia" can be available at: https://en.wikipedia.org/wiki/Direct_and_indirect_band_gaps (last retrieved July 26, 2017).
122. A. Belghachi, Theoretical Calculation of the Efficiency Limit for Solar Cells, http://dx.doi.org/10.5772/58914.
123. Losses and Efficiency Limits, https://ocw.tudelft.nl/wp-content/uploads/solar_energy_section_10_1_10_2.pdf (last retrieved July 26, 2017).
124. W. Shockley, H. J. Queisser, Detailed Balance Limit of Efficiency of p-n Junction Solar Cells, Journal of Applied Physics, 1961, 32, 510-519; doi:10.1063/1.1736034.
125. C. Motta, F. El-Mellouhi, S. Kais, N. Tabet, F. Alharbi, S. Sanvito, Revealing the role of organic cations in hybrid halide perovskite $CH_3NH_3PbI_3$, *Nat. Commun.* 2015, 6, 7026, doi:10.1038/ncomms8026.
126. A document on "Number of k-points, and method for smearing". This is available at: https://cms.mpi.univie.ac.at/vasp/vasp/Number_k_points_method_smearing.html (last retrieved July 26, 2017).
127. A document on "Choice of the k-point mesh". This is available at: https://th.fhi-berlin.mpg.de/th/fhi98md/doc/main/node15.html (last retrieved July 26, 2017).
128. V. Kocevski, O. Eriksson, J. Rusz, Transition between direct and indirect band gap in silicon nanocrystals, Phys. Rev. 2013, B87, 245401.

129. N. Egede Christensen, B. O. Seraphin, Relativistic Band Calculation and the Optical Properties of Gold Phys. Rev. 1971, B4, 3321.
130. J. R. Anderson, A. V. Gold Fermi Surface, Pseudopotential Coefficients, and Spin-Orbit Coupling in Lead, Phys. Rev. 1965, 139, A1459
131. T. L. Loucks, Relativistic Electronic Structure in Crystals. I. Theory, Phys. Rev. 1965, 139, A1333
132. Pyykko, Relativistic effects in structural chemistry, Chem. Rev. 1988, 88, 563.
133. N. E. Christensen, S. Satpathy, and Z. Pawlowska, Bonding and ionicity in semiconductors, Phys. Rev. B 1987, 36, 1032.
134. A. Hermann, J. Furthmüller, H. W. Gäggeler, P. Schwerdtfeger, Spin-orbit effects in structural and electronic properties for the solid state of the group-14 elements from carbon to superheavy element, Phys. Rev. 2010, 82, 155116.
135. J. Even, L. Pedesseau, J.-M. Jancu, C. Katan, Importance of Spin-Orbit Coupling in Hybrid Organic/Inorganic Perovskites for Photovoltaic Applications. J. Phys. Chem. Lett. 2013, 4, 2999.
136. A. Manchon, H. C. Koo, J. Nitta, S. M. Frolov, R. A. Duine, New perspectives for Rashba spin–orbit coupling, Nature Materials 2015, 14, 871–882.
137. L. D. Whalley, J. M. Frost, Y.-K. Jung, A. Walsh, Perspective: Theory and simulation of hybrid halide perovskites J. Chem. Phys. 2017, 146, 220901.
138. B. Schatschneider, S. Monaco, A. Tkatchenko, J.-J. Liang, Understanding the Structure and Electronic Properties of Molecular Crystals Under Pressure: Application of Dispersion Corrected DFT to Oligoacenes, J. Phys. Chem. A, 2013, 117, 8323–8331.
139. L. Schimka, J. Harl, G. Kresse, Improved hybrid functional for solids: The HSEsol functional, J. Chem. Phys. 2011, 134, 024116.
140. S. Liu, F. Zheng, N. Z. Koocher, H. Takenaka, F. Wang, A. M. Rappe, Ferroelectric Domain Wall Induced Band Gap Reduction and Charge Separation in Organometal Halide Perovskites, J. Phys. Chem. Lett. 2015, 6, 693−699.
141. S. Botti, M. A. L. Marques, Strong Renormalization of the Electronic Band Gap due to Lattice Polarization in the G W Formalism, Phys. Rev. Lett. 2013, 110, 226404.
142. P. Umari, E. Mosconi, F. De Angelis, Relativistic GW calculations on $CH_3NH_3PbI_3$ and $CH_3NH_3SnI_3$ Perovskites for Solar Cell Applications, Sci. Rep. 2014, 4, 4467.
143. V. Krukau, O. A. Vydrov, A. F. Izmaylov, G. E. Scuseria, Influence of the exchange screening parameter on the performance of screened hybrid functionals, J. Chem. Phys. 2006, 125, 224106.
144. F. Brivio, K. T. Butler, A. Walsh, M. van Schilfgaarde, Atomistic origins of high-performance in hybrid halide perovskite solar cells, Nano Lett. 2014, 14, 2584-90.
145. P. Azarhoosh, S. McKechnie, J. M. Frost, A. Walsh, M. van Schilfgaarde, Research Update: Relativistic origin of slow electron-hole recombination in hybrid halide perovskite solar cells, APL Materials 2016, 4, 091501.
146. T. Wang, B. Daiber, J. M. Frost, S A. Mann, E. C. Garnett, A. Walsh, B. Ehrler, Indirect to direct bandgap transition in methylammonium lead halide perovskite, Energy Environ. Sci., 2017, 10, 509.
147. X. Ke, J. Yan, A. Zhang, B. Zhang, Y. Chen, Optical band gap transition from direct to indirect induced by organic content of $CH_3NH_3PbI_3$ perovskite films, Appl. Phys. Lett. 2015, 107, 091904.
148. D. Niesner, M. Wilhelm, I. Levchuk, A. Osvet, S. Shrestha, M. Batentschuk, C. Brabec, T. Fauster, Giant Rashba Splitting in $CH_3NH_3PbBr_3$ Organic-Inorganic Perovskite, Phys. Rev Lett. 2016, 117, 126401.

149. The k-vector types and Brillouin zones of the space groups of crystals can be obtained from the bilbao crystallographic server. This is available at: http://www.cryst.ehu.es/ (last retrieved July 28, 2017).
150. J.-E. Moser, Slow recombination unveiled, Nat. Mat. 2017, 16, 4-5.
151. Goetzberger, Adolf et.al. *Crystalline Silicon Solar Cells*. Chichester: John Wiley & Sons Ltd., 1998.
152. Green, Martin A. *Solar Cells: Operating Principles, Technology, and System Applications*. Englewood Cliffs: Prentice-Hall, Inc., 1982.
153. G. Giorgi, *et al.*, Small Photocarrier Effective Masses Featuring Ambipolar Transport in Methylammonium Lead Iodide Perovskite: A Density Functional Analysis J. Phys. Chem. Lett., 2013, 4, 4213–4216.

Chapter 8. General Conclusion

This thesis has summarized the outcome of two main aspects of the chemistry of noncovalent interactions. The first one involved the fundamental understanding of these interactions through first-principles calculations, and the outcome is that a new classification scheme has emerged and proposed. The second one involved the utilization of these understandings to develop a set of new materials suitable for application in photovoltaics. That is, I have employed the underlying the fundamental chemistry of noncovalent bonding interactions to develop engineered materials that might be suitable for photovoltaic solar cell technology.

Chapters 2-3 of the thesis have dealt with the exploration of the fundamental chemistry of the reactivity of covalently bonded halogens in neutral molecules, especially involving the fluorine. It is showed that the negative fluorine in the perfluorobenzene molecule has adequate potential to attract the negative sites in another same/different molecule, a finding which is at odd to the common belief that similarly charged species do always repel each other. While this interaction is weakly compared to any standard π•••π stacking and π•••σ interactions ubiquitous between aromatic compounds when both are in proximity, this cannot be overlooked since this kind of unusual attraction between the fluorine atoms can lead to the formation of complex geometries that might have implication in materials design. Similar interactions have already demonstrated experimentally recently, and have been distributed in many geometries in the solid state, which are yet to be fully exploited. Some of our studies have already inspired other researchers to conduct similar researches to understand the reactivity of fluorine in molecules.

Chapters 4-6 have introduced the fundamental gas phase chemistry of the bonding features of one of the largely studied perovskite systems, the so-called methylammonium lead triiodide perovskite. The gas phase results discussed have not only resembled the chemistry of molecular conformations identified in the solid state, but also showed that this system can be regarded as a Mulliken Inner Complex in its block form. Based on the magnitude of stabilization energies and the nature of the intermolecular geometries, a modified classification scheme is introduced in this thesis in the area of noncovalent interactions. In particular, possibility of another class of strongly bound intermolecular interactions is proposed, which was an aid to the four common types of intermolecular interactions already established in the literature. This study has recommended to refer this class of interactions to as *ultra-strong* type. Such a classification scheme was possible based on the exploration of various characteristic properties of the $MAPbI_3$ system and its other halogenated derivatives falling into the same class of compounds. The proposed classification is expected to assist researchers for their identification of similar

intermolecular interactions in molecular complex systems of diverse type. The various characteristic features discussed in this thesis for iodide perovskite blocks might be used as guiding tools for the futuristic design of functional materials for photovoltaics and other optoelectronic applications.

Several established concepts of the area of noncovalent interactions have introduced in the area of halide based perovskites to enhance the understanding of their fundamental chemistry. In particular, I have showed that the ground state charge transfer between the interacting partner species in halide perovskites should not just be realized as just intermolecular in the ground electronic state. The complete charge transfer process has shown to follow a three-step mechanism. The first step has involved the formation of the lead triiodide anion species within the domain of the monomer. The second step has involved the formal intermolecular charge transfer between the HOMO and LUMO orbitals, a standard type of charge transfer which is commonly invoked to understand the formation of any kind of intermolecular complex. The third step has involved a super-exchange intermolecular charge transfer feature, occurring between the coordinated Pb ion and the LUMO of the organic cation in $MAPbI_3$. It is a kind of an intermolecular charge transfer, which is rare in hydrogen bonded complex systems. Similar charge transfer mechanisms have found to operate between the interacting monomers to form the $CsPbI_3$ system in 0D and its 1D derivatives in their respective ground electronic states. These results have enabled us to demonstrate that this kind of three-step charge transfer phenomena is ubiquitous in halide based perovskite systems, and that it should not overlooked.

The thesis has also introduced the concept of cooperativity in the area of halide perovskites, a phenomenon which is not only useful for the understanding of intermolecular interactions in many body systems, but also powerful for materials design. To this end, it was showed that the emergence of the supramolecular analogues of $CH_3NH_3PbI_3$, or $CsPbI_3$, from the building blocks is a consequence of additive cooperativity, which is synergestic. This result should be interesting to experimentalists who have been involved in the experimental vapor phase deposition to synthesize high quality $CH_3NH_3PbI_3$, or something similar.

There have been a long standing discussion in the literature debating that “octahedral tilting” is a solid state effect. It is this important metric which is responsible to explain the observed low bandgap for many Sn and Pb based perovskites. In specific, it has often demonstrated that larger the tilting of the PbI_6 octahedra in $CH_3NH_3PbI_3$ larger would be the bandgap. However, in this thesis, it is showed that octahedral tilting is not just a solid state effect. It can be pronounced in the gas phase, wherein no external agencies are allowed to act on the skeletons of the perovskite building blocks. The specific result shows that gas phase calculations can be used as a guiding tool for

modeling any new perovskite systems, and to my estimation, such calculations can be very useful if these are proformed before the bulk phase calculations.

Understanding chemical interactions between molecular fragments, such as those presented in Chapters 2–7, have greatly assisted us to theoretically develop some new perovskite materials. In particular, the results of our gas phase calculations presented in Chapters 4–5 and 7 have enabled us the understanding of the general nature of the local structures and energetic stabilities of pure and mixed halide perovskite compounds in the cubic phase (containing 12 atoms in the unit cell, as in $MAPbI_3$). The binding energies were calculated to be so high, which are actually several times larger than the covalent limit (–40 kcal mol^{-1}). This specific feature served as a guiding tool for the eventual discovery of a set of new perovskite materials, involving the NH_3XPbY_3 series, where X = F, Cl, Br and I. These, within the dimeric model approximation, have stabilization energies that are larger than those of the corresponding systems of the $CH_3NH_3PbY_3$ and $CH_3NH_3SnY_3$ series, thereby can be typified as *ultra-strong* type. The corresponding bulk calculations have enabled us to characterize these as either direct, or indirect bandgap materials, or even a combination of both characters. The bandgaps for many of them were so low that these might serve as better, or even comparable, functional materials relative to the widely and vastly studied halide perovskite semiconductors such as $CH_3NH_3PbY_3$ and $CH_3NH_3SnY_3$. Since these latter systems are expected to have tremendous future in the development of photovoltaic solar cells for future energy from sun light, it is thus expected that the materials developed and proposed in this study might serve as another set of possible candidates competitive with $CH_3NH_3PbY_3$. Although most of these newly discovered systems are not yet thoroughly exploited theoretically, or experimentally, it is expected that several theoretical and experimental attempts will prove whether or not the newly proposed hypoethetical materials can be practically adaptive for significant future research.

It is evident from Chapter 7 that many of the NH_3XPbY_3 systems are needed to be exploited both theoretically and experimentally since these systems have been least exploited. Many faicinating optoelectronic properties are yet to be modelled for these sysrems, which would include estimation of dielectric constants, optical spectra, point defects, ferroelectric behaviour, and exciton binding energy, among others.